Jordan Journal of Mechanical and Industrial Engineering (JJMIE)

JJMIE is a high-quality scientific journal devoted to fields of Mechanical and Industrial Engineering. It is published by Hashemite University in cooperation with the Jordanian Scientific Research and Innovation Support Fund, Ministry of Higher Education and Scientific Research.

EDITORIAL BOARD

Editor-in-Chief

Prof. Ali M. Jawarneh

Assistant Editors

Dr. Ahmad AlMigdady
Dr. Mohannad Jreissat

Editorial Board

Prof. Tariq A. ALAzab
Al Balqa Applied University

Prof. Adnan A. Bashir
The Hashemite University

Prof. Ibrahim Abu-Alshaikh
Jordan University

Prof. Mohammed Ali Almomani
Jordan University of Science and Technology

Prof. Nabil Beithou
Tafila technical University

Prof. Hitham M. Tlilan
The Hashemite University

THE INTERNATIONAL ADVISORY BOARD

Khaled Abou-El-Hossein
Nelson Mandela University, South Africa

Hosni Abu-Mulaweh
Purdue University, USA

Habil. Salman Ajib
Hochschule Ostwestfalen-Lippe, Germany

Abdelsalam Al-Sarkhi
King Fahd University, Saudi Arabia

Mohammad Khasawneh
Binghamton University, U.S.A

Afzal Khan
University of Engineering and Technology, Pakistan

Mohd Sapuan Salit
University Putra, Malaysia

Shyh-Chour Huang
National Kaohsiung University of Science and Technology, Taiwan

Suhil Kiwan
Jordan University of Science and Technology, Jordan

Amer Ababneh
Hashemite University, Jordan

Naseem Sawaqed
Mutah University, Jordan

Rebhi Damseh
Al-Balqa Applied University, Jordan

Safwan Al-Qawabah
Al-Zaytoonah University, Jordan

Mohammed Al-Nawafleh
Al-Hussein Bin Talal University, Jordan

Hubert Roth
Siegen University, German

Eiyad Abu-Nada
Khalifa University, UAE

Petr A. Nikrityuk
University of Alberta, CANADA

Editorial Board Support Team

Language Editor

Dr. Baker M. Bani-khair

Publishing Layout

Eng. Ali Abu Salimeh

SUBMISSION ADDRESS

Prof. Ali M. Jawarneh, Editor-in-Chief
Jordan Journal of Mechanical & Industrial Engineering,
Hashemite University,
PO Box 330127, Zarqa, 13133 , Jordan
E-mail: jjmie@hu.edu.jo

Hashemite Kingdom of Jordan

Hashemite University

Jordan Journal of Mechanical and Industrial Engineering

JJMIE

An International Peer-Reviewed Scientific Journal

Financed by Scientific Research Support Fund

Volume 16 Number 4, September 2022

http://jjmie.hu.edu.jo/

ISSN 1995-6665

Jordan Journal of Mechanical and Industrial Engineering (JJMIE)

JJMIE is a high-quality scientific journal devoted to fields of Mechanical and Industrial Engineering. It is published by Hashemite University in cooperation with the Jordanian Scientific Research and Innovation Support Fund, Ministry of Higher Education and Scientific Research.

Introduction: The Editorial Board is very committed to build the Journal as one of the leading international journals in mechanical and industrial engineering sciences in the next few years. With the support of the Ministry of Higher Education and Scientific Research and Jordanian Universities, it is expected that a heavy resource to be channeled into the Journal to establish its international reputation. The Journal's reputation will be enhanced from arrangements with several organizers of international conferences in publishing selected best papers of the conference proceedings.

Aims and Scope: *Jordan Journal of Mechanical and Industrial Engineering* (JJMIE) is a refereed international journal to be of interest and use to all those concerned with research in various fields of, or closely related to, mechanical and industrial engineering disciplines. *Jordan Journal of Mechanical and Industrial Engineering* aims to provide a highly readable and valuable addition to the literature which will serve as an indispensable reference tool for years to come. The coverage of the journal includes all new theoretical and experimental findings in the fields of mechanical and industrial engineering or any closely related fields (Materials, Manufacturing, Management, Design, Thermal, Fluid, Energy, Control, Mechatronics, and Biomedical). The journal also encourages the submission of critical review articles covering advances in recent research of such fields as well as technical notes.

Guide for Authors

Manuscript Submission:
High-quality submissions to this new journal are welcome now and manuscripts may be either submitted online or email.

Online: For online and email submission upload one copy of the full paper including graphics and all figures at the online, submission site, accessed via http://jjmie.hu.edu.jo. The manuscript must be written in MS Word Format. All correspondence including notification of the Editor's decision and requests for revision, takes place by e-mail and via the Author's homepage, removing the need for a hard-copy paper trail

Submission address and contact :
Prof. Ali M. Jawarneh
Editor-in-Chief
Jordan Journal of Mechanical & Industrial Engineering, Hashemite University
PO Box 330127, Zarqa, 13115, Jordan
E-mail: jjmie@hu.edu.jo

Types of contributions*:* Original research papers and Technical reports

Corresponding author: Clearly indicate who is responsible for correspondence at all stages of refereeing and publication, including post-publication. Ensure that telephone and fax numbers (with country and area code) are provided in addition to the e-mail address and the complete postal address. Full postal addresses must be given for all co-authors.

Original material: Submission of an article implies that the work described has not been published previously (except in the form of itstan abstract or as part of a published lecture or academic thesis), that it is not under consideration for publication elsewhere, tha publication is approved by all authors and that, if accepted, it will not be published elsewhere in the same form, in English or in any other language, without the written consent of the Publisher. Authors found to be deliberately contravening the submission guidelines on originality and exclusivity shall not be considered for future publication in this journal.

Withdrawing: If the author chooses to withdraw his article after it has been assessed, he shall reimburse JJMIE with the cost of reviewing the paper.

Manuscript Preparation:

General: Editors reserve the right to adjust style to certain standards of uniformity. Original manuscripts are discarded after .publication unless the Publisher is asked to return original material after use. Please use MS Word for the text of your manuscript

Structure: Follow this order when typing manuscripts: Title, Authors, Authors title, Affiliations, Abstract, Keywords, Introduction, Main text, Conclusions, Acknowledgements, Appendix, References, Figure Captions, Figures and then Tables. Please supply figures imported into the text AND also separately as original graphics files. Collate acknowledgements in a separate section at the end of the article and do not include them on the title page, as a footnote to the title or otherwise.

Text Layout: Use 1.5 line spacing and wide (3 cm) margins. Ensure that each new paragraph is clearly indicated. Present tables and figure legends on separate pages at the end of the manuscript. If possible, consult a recent issue of the journal to become familiar with layout and conventions. All footnotes (except for table and corresponding author footnotes) should be identified with superscript Arabic numbers. To conserve space, authors are requested to mark the less important parts of the paper (such as records of experimental results) for printing in smaller type. For long papers (more than 4000 words) sections which could be deleted without destroying either the sense or the continuity of the paper should be indicated as a guide for the editor. Nomenclature should conform to that most frequently used in the scientific field concerned. Number all pages consecutively; use 12 or 10 pt font size and standard fonts.

Corresponding author: Clearly indicate who is responsible for correspondence at all stages of refereeing and publication, including post-publication. The corresponding author should be identified with an asterisk and footnote. Ensure that telephone and fax numbers (with country and area code) are provided in addition to the e-mail address and the complete postal address. Full postal addresses must be given for all co-authors. Please consult a recent journal paper for style if possible.

Abstract: A self-contained abstract outlining in a single paragraph the aims, scope and conclusions of the paper must be supplied.

Keywords: Immediately after the abstract, provide a maximum of six keywords (avoid, for example, 'and', 'of'). Be sparing with abbreviations: only abbreviations firmly established in the field may be eligible.

Symbols: All Greek letters and unusual symbols should be identified by name in the margin, the first time they are used.

Units: Follow internationally accepted rules and conventions: use the international system of units (SI). If other quantities are mentioned, give their equivalent quantities in SI

Maths: Number consecutively any equations that have to be displayed separately from the text (if referred to explicitly in the text).

References: All publications cited in the text should be presented in a list of references following the text of the manuscript.

Text: Indicate references by number(s) in square brackets in line with the text. The actual authors can be referred to, but the reference number(s) must always be given.

List: Number the references (numbers in square brackets) in the list in the order in which they appear in the text.

Examples:

Reference to a journal publication:

[1] M.S. Mohsen, B.A. Akash, "Evaluation of domestic solar water heating system in Jordan using analytic hierarchy process". Energy Conversion & Management, Vol. 38 (1997) No. 9, 1815-1822.

Reference to a book:

[2] Strunk Jr W, White EB. The elements of style. 3rd ed. New York: Macmillan; 1979.

Reference to a conference proceeding:

[3] B. Akash, S. Odeh, S. Nijmeh, "Modeling of solar-assisted double-tube evaporator heat pump system under local climate conditions". 5th Jordanian International Mechanical Engineering Conference, Amman, Jordan, 2004.

Reference to a chapter in an edited book:

[4] Mettam GR, Adams LB. How to prepare an electronic version of your article. In: Jones BS, Smith RZ, editors. Introduction to the electronic age, New York: E-Publishing Inc; 1999, p. 281-304

Free Online Color : If, together with your accepted article, you submit usable color and black/white figures then the journal will ensure that these figures will appear in color on the journal website electronic version.

Tables: Tables should be numbered consecutively and given suitable captions and each table should begin on a new page. No vertical rules should be used. Tables should not unnecessarily duplicate results presented elsewhere in the manuscript (for example, in graphs). Footnotes to tables should be typed below the table and should be referred to by superscript lowercase letters.

Notification: Authors will be notified of the acceptance of their paper by the editor. The Publisher will also send a notification of receipt of the paper in production.

Copyright: All authors must sign the Transfer of Copyright agreement before the article can be published. This transfer agreement enables Jordan Journal of Mechanical and Industrial Engineering to protect the copyrighted material for the authors, but does not relinquish the authors' proprietary rights. The copyright transfer covers the exclusive rights to reproduce and distribute the article, including reprints, photographic reproductions, microfilm or any other reproductions of similar nature and translations.

Proof Reading: One set of page proofs in MS Word format will be sent by e-mail to the corresponding author, to be checked for typesetting/editing. The corrections should be returned within 48 hours. No changes in, or additions to, the accepted (and subsequently edited) manuscript will be allowed at this stage. Proofreading is solely the author's responsibility. Any queries should be answered in full. Please correct factual errors only, or errors introduced by typesetting. Please note that once your paper has been proofed we publish the identical paper online as in print.

JJMIE

Volume 16, Number 4, September. 2022
ISSN 1995-6665

Jordan Journal of Mechanical and Industrial Engineering

JJMIE

Volume 16, Number 4, September. 2022
ISSN 1995-6665

Jordan Journal of Mechanical and Industrial Engineering

JJMIE

Volume 16, Number 4, September. 2022
ISSN 1995-6665
Pages 459 – 469

Jordan Journal of Mechanical and Industrial Engineering

Wear Performance of Asbestos-Free Brake Pad Materials

B. D. Bachchhav[*], K. N. Hendre

Department of Mechanical Engineering, All India Shri Shivaji Memorial Society's College of Engineering, Pune, Maharashtra- 411 001, India.

Received 6 Feb 2022 *Accepted 9 Jun 2022*

Abstract

Brake lining performance is influenced by configuration of friction material, functional speeds, load, and temperature. Asbestos friction materials are injurious to human health and, therefore, replacement is needed, hence an alternate material with desired tribo-mechanical properties is to be investigated. In this paper, the wear characterestics of two asbestos-free friction materials sliding against grey cast iron disc were investigated. A metallic based (*viz:*AF-22) and fine brass based (*viz:*CL-3003) were prepared by compression moulding process that required pin samples. Wear experiments were performed using a Pin-on-disc tribo-tester. The wear rates were compared under various temperature, sliding speed, and pressure conditions using Taguchi's L_9 orthogonal array. The wear rate of AF-22 was observed between 2.01 to 2.17 mm^3/N.m., and for CL-3003 (1.49 to 1.66 mm^3/N.m). Ranking of the parameters based on the experimental findings and the S/N ratio analysis was done. Temperature is the most influencing parameter, i.e. 82.96% for AF-22 and 87.95% for CL-3003 material. The EDS technique was used to understand material composition. At various magnifications, SEM images of brake pad materials were investigated. Further investigation under in-situ condition is recommended for these materials.

Keywords: Asbestos-free, Wear, Brake Materials, Taguchi Method, Pin-on-Disc, SEM, EDS.

1. Introduction

The brake system must be highly reliable as it safeguards the human life. In modern vehicles, disc brakes are mostly preferred over drum brakes due to its high heat disspation rate and light weight. Brake pads, located in brake calipers facing each other, exert pressure on the disc to stop the wheel by friction, which in turn generates heat at the interface. Friction materials are found to wear linearly at lower disc temperature, however at high temperature and pressure wear tend to be exponential thus reduces useful life of brake pads. Appropriate selection of friction materials for brake pads largely affects performance of a system. The brake padmaterials are among the most multifaceted composite materials due to variety of base materials, i.e., metals, ceramic and polymers. Mettalic based or non-asbestos organic (NAO) materials are most preferred for commercial brake pads. In recent times, many researchers had investigated non-asbestos based organic (NAO) materials as a replacement to the traditional brake pad materials having superiortribo-characterestics, such as being lighter in weight and having improved durability. Most commonly used brake pad materials and thier tribological impact when used with interface disc on the entire braking system were reviewd. The right composition of binders, additives, fillers, and abrasives ensure minimum stopping distance and wear that helps in reducing frictional noise against a metallic disc [1].

The diversity in chemical and physical properties makes it more complex to find the right composition and mixing. Asbestos-based friction compounds have been used so far due to their tribo-mechanical performance, however, they are now banned due to the health risks they impose. Research is being done to formulate envoirnment friendly brake pad materials that are as good as asbestos having similarly good mechanical, thermal, frictional and anti-wear qualities. Developments of agro-waste-based palm kernel fibers [2], periwinkle shell [3-4], maize husks agreo-waste [5-6] brake materials is being done. Wear behaviour of fiber reinforced phenolic composites under different conditions of applied loads and speeds were evaluated and showed improved wear resistance as compared to asbestos [7].

Performance of asbestos and non-asbestos organic materials used in commercial brake pads and their comparision based on crtitical properties need to be evaluated. In particular, the properties required to friction materials which are resistant to wear, thermal fatigue, shear and compression during braking, low sensitivity to environmental conditions, such as water, oil and corrosive salts, thermal stability and oxidation, and a stable friction coefficient under different conditions and time. Binders, reinforcements, friction modifiers, and fillers are commonly used in friction materials; nevertheless, their composition changes with applications, technical advancements, and potential environmental impact. Till now, manufacturers' experience has probably played a larger role than any other attributes in the development of

---

[*] Corresponding author e-mail: bdbachchhav@aissmscoe.com.

friction materials. The Analytic Hierarchy Process (AHP) was used to assess critical attributes for a variety of brake pad materials, the important parameters for braking application was ranked [8]. The analysis, on the other hand, was mostly based on qualitative features.

Friction and wear characteristics of asbestos-free rubber resin bonded metallic brake Pad materials sliding against EN 31 disc were evaluated using Pin-on-disc apparatus and found that temperature is the most dominating parameter in increasing friction and wear [9-10]. A conductive rock-fibers/metallic fibres and thermo-graphite were tried as an alternative to Cu additives and found improvement in their properties other than physical and mechanical properties [11-12]. A role of Cu powder and its amount in a friction material were evaluated. It was found that 10 wt. % of Cu is the optimum amount for better tribological, thermo-physical and mechanical behavoiur of friction materials [13]. Palm slag along with phenolic and metallic binders have shown their potential to use as filler material in brake pad composites [14]. Use of natural fibres, such as coconut fibres reinforced with aluminium showed better physico-mechanical performance at 5-10 % of coconut fibre [15]. An effect of contact area on worn mass were experimented using Taguchi method and validated by finite element simulation [16].

In friction linings, wear occurs principally by adhesion, abrasion, tribo-chemical reactions and ablation. The brake drum or disc, as well as the friction material, wear at a high rate during the early burnishing or wearing of the brakes[17-19].

By the time the primary braking drum or disc asperities have been rounded, the wear rates of the brake linings have stabilized. Brake torque, sliding speed, temperature effects, and brake usage frequency are the influencing parameters on wear [20]. Formation of tribo-chemical film on the counrface disc surface, the analysis of friction bands and wear particals, and an effect of temperature variation through SEM analysis were done to investigate wear mechanism [21-22]. Formation of third body film acts as a wear resistant substance during sliding wear tests. Use of solid lubricant powder, such as graphite, molendinumdisulphide and other iron oxides controls the friction at lower level [23]. Investigations on tribo-performance of brake pad materials were evaluated using pin-on-disc tribometer[23-24], reciprocating sliding test set-up[13, 16-18, 25], brake dynamometers disc brake test etc [26-27] .

In recent past, researchers tried to understand wear meachanism in braking system. Gawande et al., compared and investigated tribological behavior of non-asbestos with asbestos brake pad material using dry abrasion test under different loading conditions. It is observed that contact pressure and the covered distance have significant impact on weight loss, and also vary linearly, however, an effect of interface temperature was not under consideration for this study [28].

Till now, there are hardly any research studies that discuss the effect of interface temperature on wear behavior of friction material. An objective of this paper is to study wear performance of metallic based (AF-22) and fine brass based (CL-3003) friction materials under changing working conditions of temperature, sliding velocity, pressure and sliding distance. Friction materials were developed by compression moulding process and prepared to a sample suitable for pin-on-disc apparatus. Furthermore, Scanning electron microscopy (SEM), energy dispersive X-ray microanalysis (EDX) were used to understand wear mechanism in detail. Thermal stability was analysed by Thermogravimetric analysis (TGA). Through extensive quantitative analysis utilising the Taguchi technique, this research presents preliminary examinations of wear performance of brake pad materials as a suitable alternative to asbestos friction material.

2. Materials and Methods

2.1. Materials

Two asbestos-free metallic based friction materials were manufactured from CO-EFF friction bands, Pune, India, viz: AF-22 and CL-3003. Proper mixing fibers, resins, fillers and additives were carried out in a sigma mixer. A preform was prepared in 50 tonne capacity hydraulic press. Heat and pressure was applied during compaction and then curing was done at 150ºC. After curing, the composites were ejected from the mould cavity. The test samples were cut from the pad segment and after turning and grinding operations brought into required pin size. The grey cast iron disc was used throughout the experimentations. Disc and bottom surface of pin was ground and polished so as to reproduce interface conditions as precise as possible. A metallic filler-based rubber resin bonded (AF-22) and a fine brass-based organic and inorganic reinforcing fibres with specific synthetic rubber modified resins (CL-3003) and their physicsl properties are mentioned in Table 1.

Table 1. Physical properties **of** brake pad Materials

Materials	Density (g/cm^3)	Compressive Strength (N/mm^2)	Transverse Bending Strength (N/mm^2)
AF-22	2.12	165	78
CL-3003	1.90	190	85

2.2. EDS analysis of Friction Materials

Energy dispersive spectroscopy (EDS) analysis of brake friction materials were carried out. Table 2 shows the main compounds and wt % contribution of commertial NOA (Non-asbestos) brake pad materials.

Table 2. Main compounds and their % contribution, in the brake pad materil

Compounds	AF-22 [wt. %]	CL-3003 [wt. %]
C	31.70	37.77
O	27.72	32.19
Si	12.74	12.67
Ba	7.57	0.00
Sb	6.79	4.16
Ca	6.68	2.92
Mo	3.59	5.00
Al	2.09	3.51
Mg	1.11	1.46
Na	0.00	0.31

The EDS spectra and elemental content of AF-22 material are shown in figure 1. Ingredients include C, Si, Ba, Sb, Ca, Mo, and Al among others. Due to higher concentration of rubber resin, C (Carbon) and Si (Silicon) provides higher strength. It also includes elemental properties of Ba (Barium), Sb (Antimony), Ca (Calcium) and Mo (Molybdenum).

Figure 2 displays the CL-3003 material's EDS spectrum and elemental makeup. It lists elements, such as C, Si, Mo, Sb, Al, Ca, Mg, and so on. Table 2 shows the EDS elemental composition for CL-3003. From Energy Dispersive Spectroscopy plots it can be revealed that, as the additive concentration increases C (Carbon) and Si (Silicon) wt % content increases due to the high cross linkage of organic (hydrocarbon chain of rubber) fiber material. Elemental raw Si and its intermetallic compounds are semiconductors and used as alloy integrals to provide more resistance to the aluminum, magnesium and other metals. Metallurgic silicon with 98-99 % purity with Mo (Molybdenum) enhances harden-ability, toughness of steel and improves strength.

2.3. Thermogravimetric analysis

Thermal stability of both samples were investigated using a thermogravimetric analyzer. Figure 3 shows a thermo-gravimetric examination of the AF-22 material in an oxygen-rich environment. By subjecting each raw material to an identical TGA run and computing the onset temperature of the corresponding change in mass, the thermal stability of the raw materials in the formulation was conformed. Figure 3 demonstrates that the rubber crumb particles exhibited the lowest thermal stability, with a mass loss beginning of 200 °C and a 100 % mass loss by 580 °C.

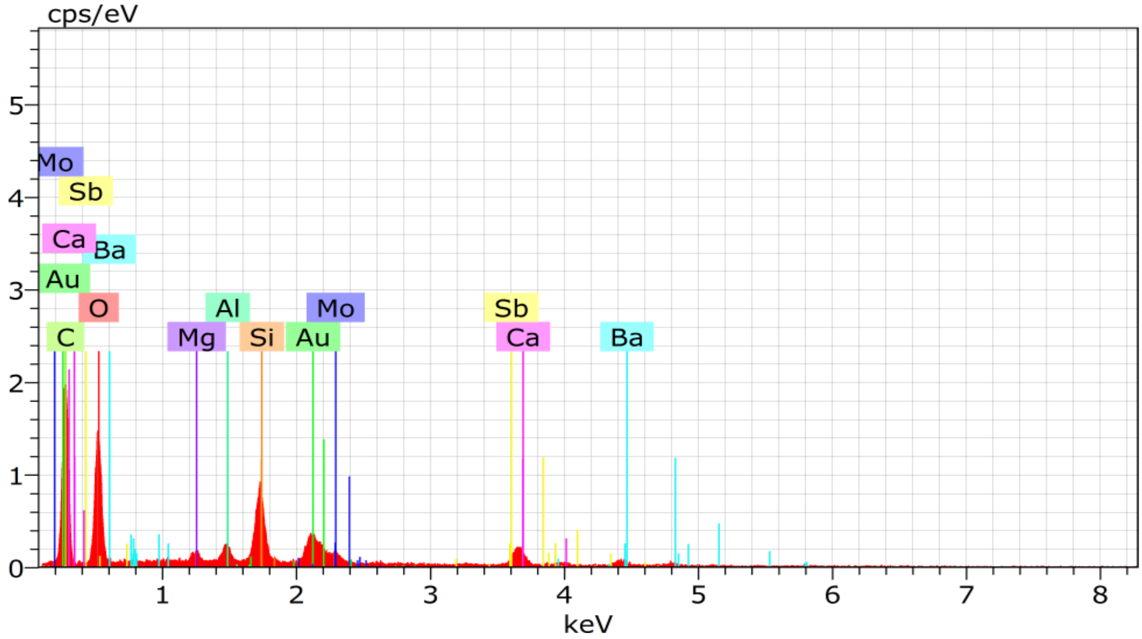

Figure 1. EDS spectrum for AF-22 brake pad material sample as detected

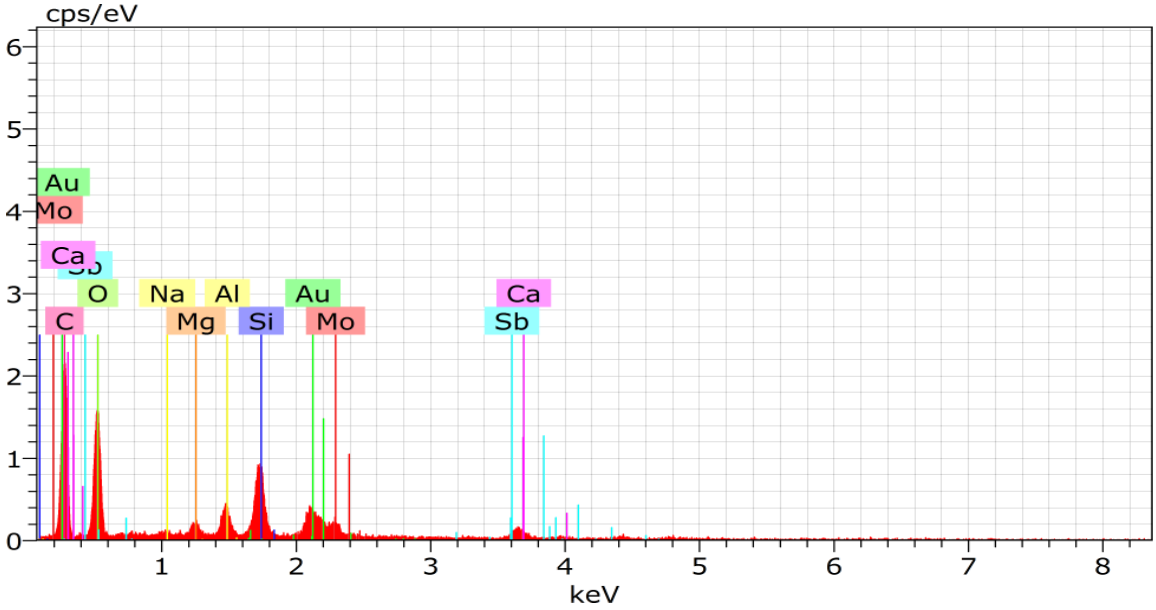

Figure 2. EDS spectrum for CL-3003 brake pad material sample as detected

The direction of mass shift is indicated by the positive and negative notation. The raw materials thermal stability differed greatly in terms of onset temperature, percentage mass change, and rate of mass change. A slow and continuous thermal degradation precedes the primary thermal event, accounting for a 1.55 percent mass loss before 200 °C onset temperature of. Once the major thermal degradation event has passed, the oxidation of metallic compounds within the formulation, such as iron, steel, and antimony, obatined a mass gain between 600 °C and 800 °C.

Figure 4 shows a typical result for a thermo-gravimetric examination of the CL-3003 friction material in an oxygen-rich environment. Brass oxide has a low beginning of mass loss of 285.1 °C for a refractory oxide, but only 1.8 percent of its mass is lost during this early degradation step, as illustrated in figure no. 6. Antimony tri-sulphide had a mixed mass change, with the initial mass loss occurring at 200 °C and the secondary mass gain occurring at 600 °C due to the metal's oxidation.

After a well-defined starting temperature, both ferrous-based iron and steel materials gained mass as a function of temperature. With no start temperature and a total mass loss of 38.4 percent at 600 °C, the minerals perlite and vermiculite had the best thermal stability. The thermal stability of fibrous materials, particularly aramid and natural fibres as illustrated in figure 6, is of particular relevance in this study.

Thermal stability of AF-22 and CL3003 was compared by TGA in order to correlate with hot performance of brake linings. CL-3003 material found shows better thermal stability and less susceptible to thermal fade.

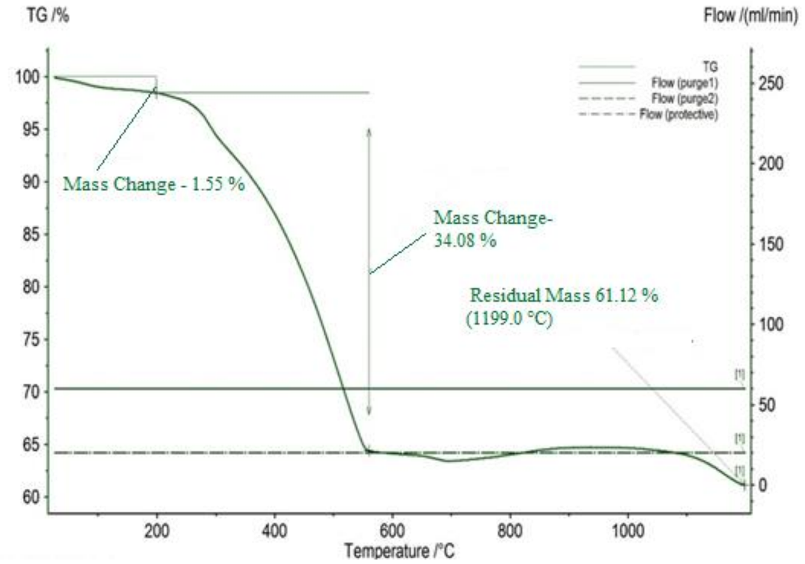

Figure 3. AF-22 brake material thermal analysis

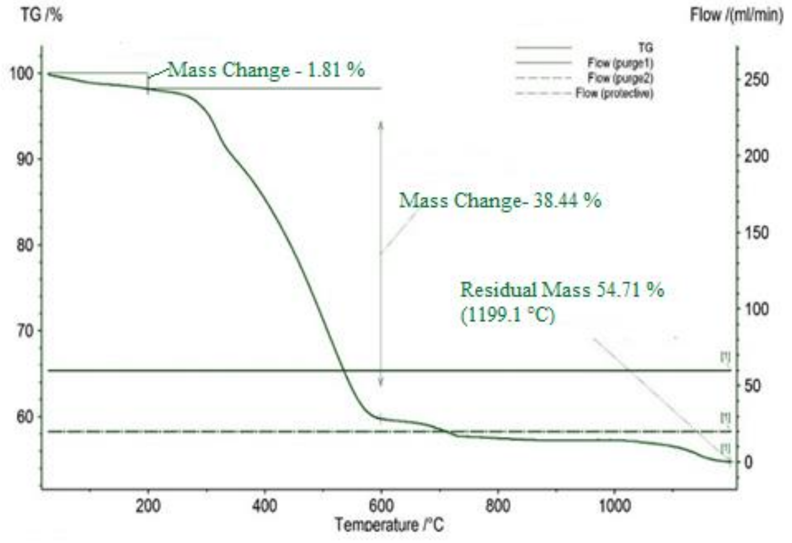

Figure 4. CL-3003 brake material thermal analysis

3. Experimentation

3.1. Sample Preperation:

The pin of 8 mm in diameter was ground and flattened on the bottom surface to ensure full surface contact. The bottom surface of pin is polished with ceramic paper to ensure uniform initial suface roughness through the samples. The combined surface integrity of pin and disc surface is ensured not more than 1.6 µm for all experiments. Roughness of the specimen as well as counterface disc was measured before the test by a Taylor Hobson surface roughness tester, using a cut-off value of 0.8 mm. A Grey Cast Iron (GCI) disc hardened to 60 HRC, of 165 mm in diameter and 10 mm thick, rotates through a powered spindle.

DUCOM (TR-20LE) "Pin-on-disc" test-rig (Figure 5) was used to perform experiments. Experiments were performed using ASTM G99 standard at room temperature under dry conditions. For the experimental study, parameters that correlate to actual braking operations, such as disc sliding speed, brake pad holding pressure, and so on, were deemed to be within their realistic range. In order to achieve sliding velocity between 2.10 to 6.30 m/s, track radius is adjusted between 25 to 75 mm and disk is rotated with a speed range between 200 to 2000 rpm. An interface temperature was varied as 50^0C, 100^0C, and 150^0C. The data acquisition system measures amount of linear wear using WINDUCOM 2010 software which then conveted into wear rate (mm^3/N.m).

3.2. Plan of Experiments

Experimental design based on Taguchi's orthogonal arrays was used in this work. Considering time and economy. Tagichi's orthogonal arrays are preferred over traditional factorial design of experiments. Furthermore, Tagichi's orthogonal array (OA) give more consistency and reproducibility of results.

During experimentation, many external factors which are not designed into standard set of experiments are influencing output response. An effect of these external factors on out-put response is termed as "noise". The signal to noise ratio (S/N ratio) measures sensitivity of the ourput response to the non-controllable factors i.e. noise. S/N ratio is expressed in terms of mean square deviation (MSD). In braking operations, the wear rate is desired to be lower, therefore a lower S/N ratio is considered, since smaller is better is considered as an objective function. MSD and SN ratios can be calculated using equation (1) and (2), for smaller is better [29].

$$MSD = (W_1^2 + W_2^2 + W_3^2 + \text{-----} W_n^2)/Y \quad (1)$$

Where MSD = mean square deviationfrom the true value of the output characteristics.

$$S/N = -10_{\log}(MSD) \quad (2)$$

Where Y is the number of observations and *W* is the wear rate that has been measured.

The L_9 (3^4) array was chosen with two repetations for the experimentation. The column was allocated the factors. The experiment plan consisted of 9 tests (array rows), with the first column representing Temperature (T), the second column representing Sliding Velocity (V), the third column representing Pressure (P), the fourth column representing Sliding Distance (D).

The wear rate (W_R), the reaction of unit load and sliding distance was investigated in terms of specific wear ratein (mm^3/Nm). Specific wear rate is found to be more accurate method to specify wear as compared to weight loss or linear wear method. To enable for study of the variance of the results and S/N ratios, the tests were duplicated twice, yielding a total of 18 observations each for AF-22 and CL3003 material. The weight difference approach was used to determine wear. The parameters and their levels are listed in table 3.

Table 3. Factors and their levels

	Levels			Units
Factors	1	2	3	
Temperature (T)	50	100	150	^{0}C
Sliding Velocity (V)	2.10	4.20	6.30	m/s
Pressure (P)	1	2	3	N/mm^2
Sliding Distance (D)	4000	8000	12000	m

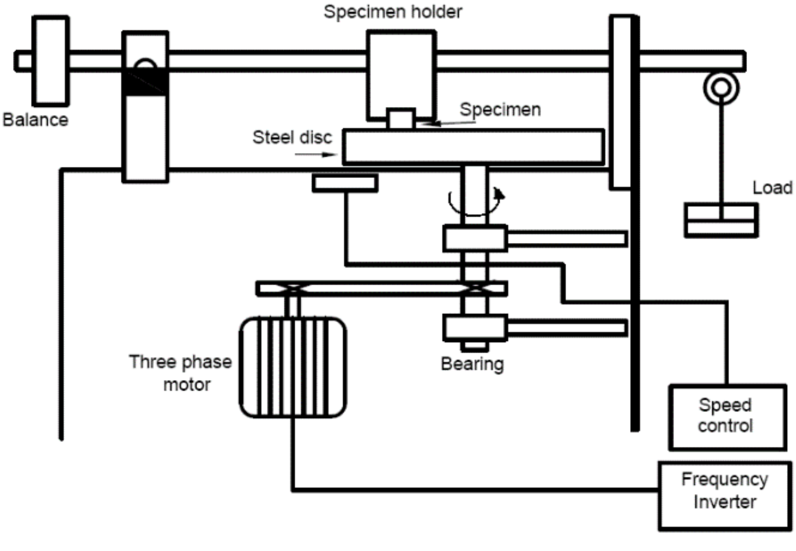

Figure 5. Pin-on-disc set-up

4. Results and Discussion

4.1. Wear Characterestics of AF-22 Material

Linear wear in µm was converted into volumetric loss of material and specific wear rate is calculated in $mm^3/N.m$.Table 4 illustrates the experimental findings for the AF-22 brake material in terms of wear rate.The spread around a target value is expressed by the signal-to-noise ratio (S/N). The smaller the spread, the higher the S/N ratio.

The parameters for wear were ranked using MINITAB18, Taguchi Design Software, as shown in response table 5.

The main effect for the S/N ratios for wear rate is plotted as shown in Fig. 6. SN ratio plot is exactly reverse to that of mean value plot. Hence, wear rate will be highest at 150^0C temperature, 6.3 m/s sliding velocity, 3 MPa pressure and 1.2 km of sliding distance.

Using MINITAB software analysis of variance was calculated as shown in Table 6. Percentage contribution of influencing factors were estimated using the pure sum of squares method.Temperature is most influencing parameter (82.96%) followed by pressure (6.80%), sliding velocity (5.77%), and sliding distance (4.48 %) that are statistically significant to control wear. Tempurature along with pressure cause loosening of matrix material and formulation of granulated wear particles under friction. These granuals further act as a third body particals and lead to more wear of pad material. The binders and fillers plays an important role in controlling wear. Gawande et al., observed linear relationship between wear rate, load and sliding distance; however the effect of temperature was not considered in their study [28]. Using MINITAB software yielded a mathematical equation for specific wear rate (equation 3).

Specific Wear Rate =

$$1.9239 + 0.00106\,T + 0.0071\,V + 0.0167P + 0.000003D \qquad (3)$$

Table 5. Response table for S/N ratios

Level	Temperature (T)	Sliding Velocity (V)	Pressure (P)	Sliding Distance (D)
1	-6.241	-6.473	-6.447	-6.460
2	-6.656	-6.504	-6.545	-6.545
3	-6.682	-6.601	-6.587	-6.574
Delta	0.442	0.127	0.141	0.114
Rank	1	3	2	4

Table 6. Analysis of variance for wear rate (AF-22)

Source	DF	Seq SS	Adj MS	Contribution (%)
(T)	2	0.02142	0.01071	82.96%
(V)	2	0.00148	0.00074	5.77%
(P)	2	0.00175	0.00087	6.80%
(D)	2	0.00115	0.00057	4.48%
Error	0	0.00000	0.00000	0.0000
Total	8	0.02582		100.00%

Table 4. Experimental results for AF-22 brake materials

Run	Levels				Specific Wear Rate x 10^{-5} $mm^3/N.m$		Specific Wear Rate x 10^{-5} $mm^3/N.m$	S/N Ratio
	T	V	P	D	WR_1	WR_2		
1	50	2.10	1	4000	2.01	2.00	2.005	-6.042
2	50	4.20	2	8000	2.05	2.06	2.055	-6.256
3	50	6.30	3	12000	2.10	2.09	2.095	-6.423
4	100	2.10	2	12000	2.16	2.15	2.155	-6.668
5	100	4.20	3	4000	2.15	2.14	2.145	-6.628
6	100	6.30	1	8000	2.15	2.16	2.155	-6.668
7	150	2.10	3	8000	2.17	2.16	2.165	-6.709
8	150	4.20	1	12000	2.15	2.14	2.145	-6.628
9	150	6.30	2	4000	2.16	2.17	2.165	-6.709

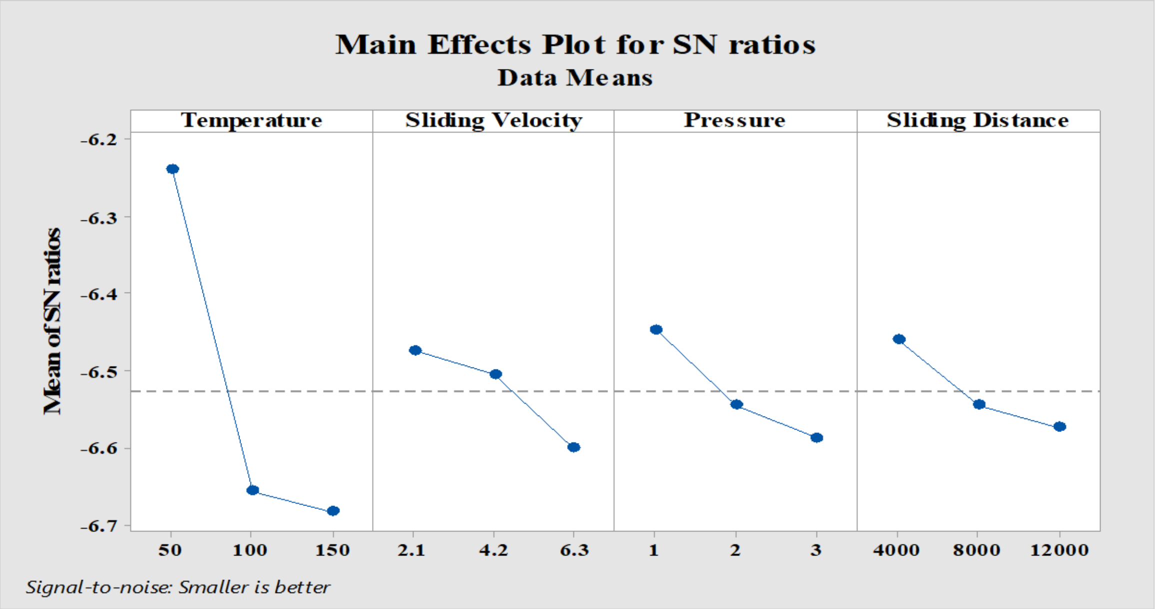

Figure 6. Main effect plot for SN ratios for AF-22 Material

4.2. Wear Characterestics of CL-3003 Material

Table 7 shows the experimental results for CL-3003 friction material.

Fig. 7 shows the main effects plot for the S/N ratios for wear for various parameters such as temperature, sliding velocity, pressure, and sliding distance.

The parameters for wear were ranked using MINITAB, Taguchi Design Software, as shown in response table 8.

The scatter around a target value is expressed by the signal-to-noise ratio (S/N). S/N ratios for wear rate, parameter ranking, and ANOVA are calculated using MINITAB, Taguchi design software. Percentage contribution of influencing factors estimated using the pure sum of squares method.

Table 7. Experimental results for CL-3003 brake materials

Run	Levels				Specific Wear Rate x 10^{-5} (mm^3/N.m)		Mean Specific Wear Rate x 10^{-5} (mm^3/N.m)	S/N Ratio
	T	V	P	D	WR_1	WR_2		
1	50	2.10	1	4000	1.50	1.49	1.495	-3.492
2	50	4.20	2	8000	1.54	1.55	1.545	-3.778
3	50	6.30	3	12000	1.57	1.56	1.565	-3.890
4	100	2.10	2	12000	1.63	1.62	1.625	-4.217
5	100	4.20	3	4000	1.62	1.61	1.615	-4.163
6	100	6.30	1	8000	1.64	1.65	1.645	-4.323
7	150	2.10	3	8000	1.65	1.66	1.655	-4.376
8	150	4.20	1	12000	1.66	1.65	1.655	-4.376
9	150	6.30	2	4000	1.65	1.64	1.645	-4.323

Table 8. Response table for S/N ratios

Level	Temperature (T)	Sliding Velocity (V)	Pressure (P)	Sliding Distance (D)
1	-3.721	-4.029	-4.064	-3.993
2	-4.235	-4.106	-4.106	-4.159
3	-4.358	-4.179	-4.143	-4.161
Delta	0.638	0.150	0.079	0.168
Rank	1	3	4	2

Table 9. Analysis of variance for wear rate (CL-3003)

Source	DF	Seq SS	Adj MS	Con (%)
(T)	2	0.02286	0.01143	87.95%
(V)	2	0.00106	0.00053	4.10%
(P)	2	0.00026	0.00013	1.03%
(D)	2	0.00180	0.00090	6.92%
Error	0	0.00000	0.0000	0.0000
Total	8	0.02582		100.00%

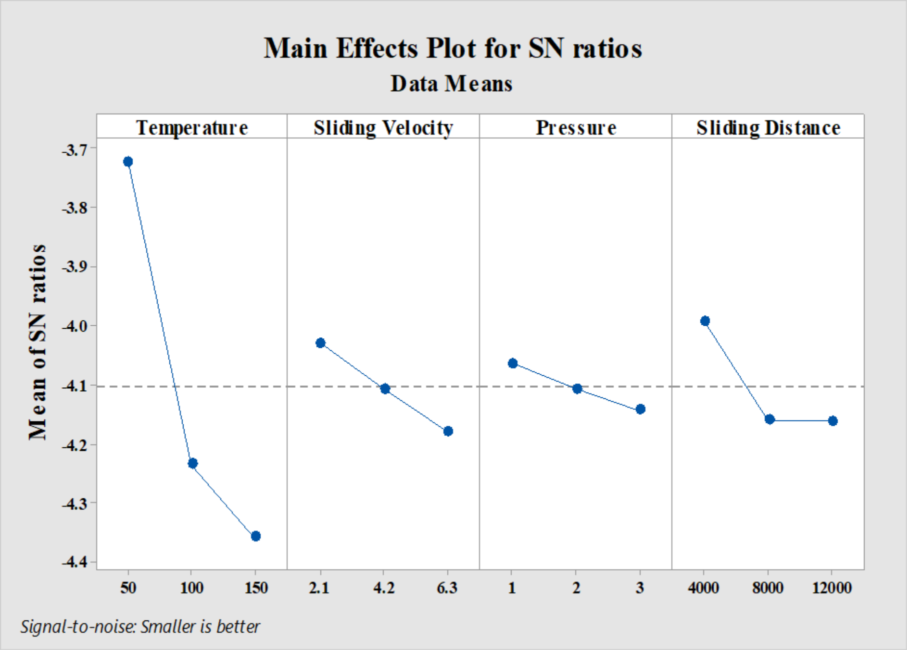

Figure7. Main effect plot for S/N ratioCL-3003 Material

Table 9 shows the results of the ANOVA for wear. Temperature (87.95%) is the highest influencing parameter followed by sliding distance (6.92%), sliding velocity (4.10%) and pressure (1.03%) on wear. Similar effect of parameters are observed on wear characterestics of other non-asbestos materials [9, 24, 28].

Mathematical equation for specific wear rate (Equation 4) obtained is as follows:

Specific Wear Rate= 1.4183 +0.001167T + 0.00635V + 0.0067P+0.000004D(4)

It is observed that the specific wear rate of AF-22 material is around 24 % more than that of CL-3003 material. For both the materials Tempurature is most predominent parameter which affects on wear, however it is more in case of CL 3003. Pressure is least contributing parameter for CL3003, however, it is second largest contributing parameter for AF-22. This may be due to more weight (%) of Mo in CL3003. Similar results for load and sliding distance were obtained by Gawande et al., (2020) for CL 3003 material; however they have not considered interface temperature.

4.3. Wear Mechanism

The base matrix SEM image before test shows chunk, segments and block images of AF-22 compound in figure 8a at 10000 x magnifications. C and Si weight percent are higher due to the presence of rubber resin, as carbon gives hydrocarbon close fit bonding for higher strength. AF-22 also comprises elemental properties of Ba (Barium), Sb (Antimony), Ca (Calcium), and Mo (Molybdenum).

The segmental sections of CL-3003 were measured by SEM, as illustrated in figures 8b. Because of the high cross linking of organic (hydrocarbon chain of rubber) fibred material, it can be concluded from EDS plots that, as concentration increases, content of C and Si weight percent increases. Elemental raw Si and its intermetallic compounds are semiconductors that are used as alloy integrals to give aluminum, magnesium, and other metals better resistivity. Metallurgic silicon with a purity of 98-99 percent and Mo (Molybdenum) improves steel hardenability, toughness, and strength.

After the test, in AF-22 material a brittle and chipped surface shows a typical abrasive wear and tribochemical reactions which is a function of phony surface layer (Fig. 9a). The resultant discontinuity will increase residual stresses leading to develop brittle cracks.

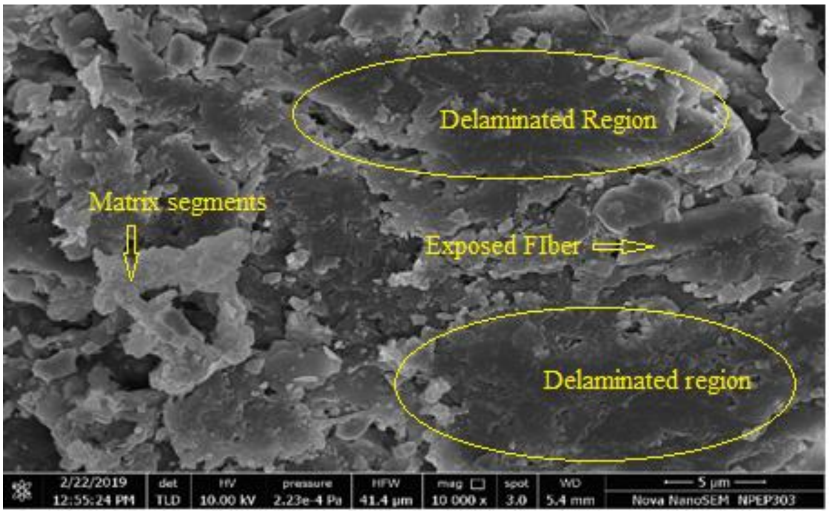

Figure 8. a) AF-22 brake material sample SEM image at 10,000 x magnification

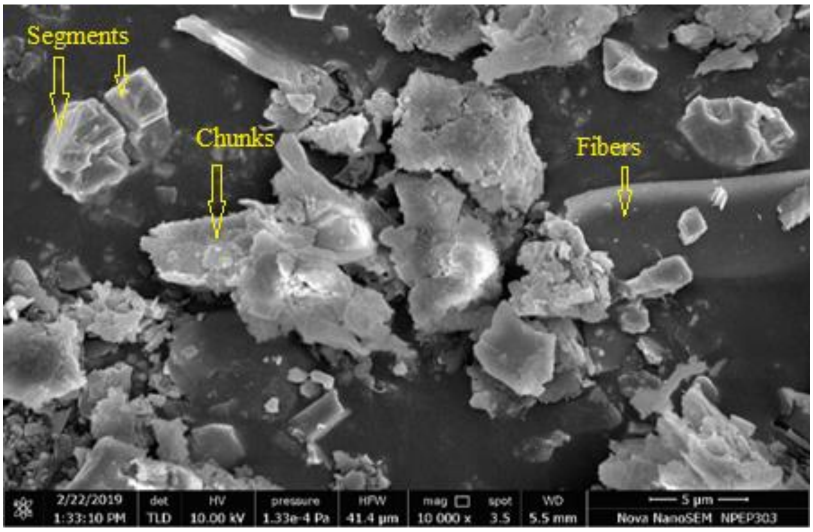

Figure 8. b) CL-3003 brake pad material sample SEM image at 10,000 x magnification

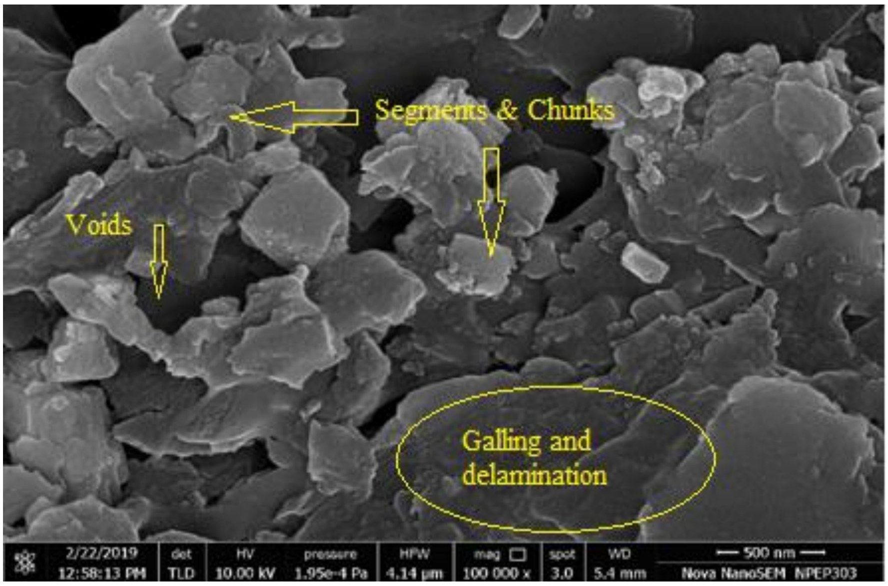

Figure 9. a) AF-22 brake material sample SEM image at 1,00,000 x magnification

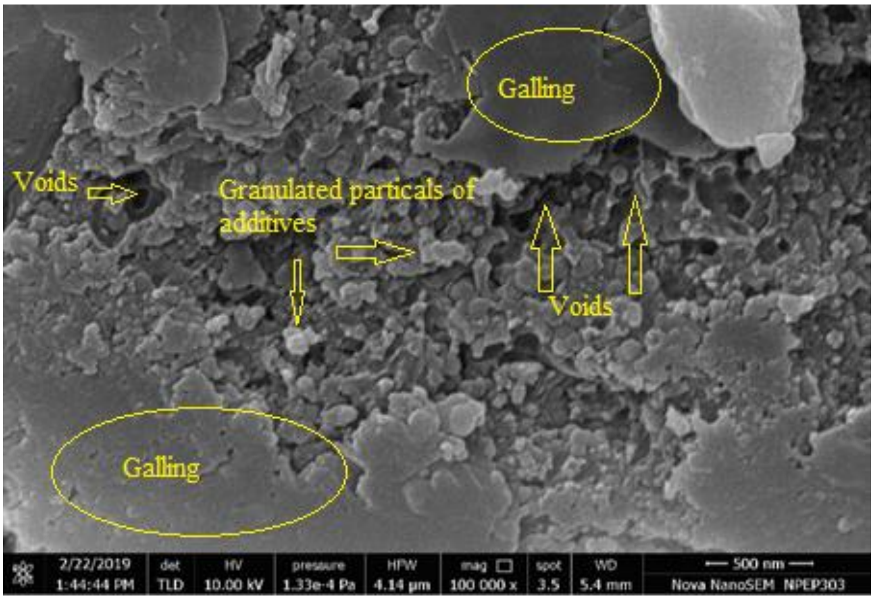

Figure 9. b) CL-3003 brake pad material sample SEM image at 1,00,000 x magnification

At high temperature, softening of matrix phase resulted in ploughing of metallic fibres in CL-3003 material. Frictional heating and pressure tends to melt metallic additives which leads to loose binders and granulated particals causing more wear. Dettachement of these particles will cause three body abrasive wear. This suggests reason for increasing wear with temperature. Interface temperature strongly controls the properties of ingredients of friction material. The mechanical integrity of the compacted wear debris becomes weaker due to increase in temperature and thermal degradation occurs. This is also depends on initial micro-aspirity on pin as well as on disc surface. Whitening of the grain boundry region observed due to stress whitening of matrix material.

In this study, the researcher has compared tribological behavior of two non-asbestos materials viz: AF-22 and CL-3003, and it is observed that CL-3003 material shows less wear rate than AF-22, hence is a better substitute material. Wear rate of friction materials at temperature below 150^0 C is linear; however due to thermanl degradation at high temperate it may be exponential. Wear performance is also affected by composition especially binder materials alongwith temperature, pressure and speed [9,24,28]. Similarly , wear volume is directly proportional to applied load, speed, sliding time and speed in Fibre Reinforced Al And Al-Alloy Metal Matrix Composites also [30-31].

Wear rate of metallic filler-based rubber resin bonded (AF-22) is more than organic and inorganic reinforcing fibres with specific synthetic rubber modified resins based (CL-3003) material. Metling of metal additives and formation of hot spots due to frictional heating is the main cause of increase in wera rate of AF-22. Hence, resin and fillers and their proportion is most important while formulating novel brake pad materials.

Few principal process parameters were taken into consideration for this study, however; for more understanding of wear mechanism due to frictional heating a systematic study under '*in-situ*' condition is suggested.

5. Conclusion

Wear performance of two asbestos- free brake pad materials sliding against a grey cast iron disc were evaluated and compared. The wear performance of compression moulded brake pad materials has been effectively analysed using Taguchi's analysis approach. The wear rate of AF-22 was observed between 2.01 to 2.17 mm^3/N.m., which is higher than CL-3003 (1.49 to 1.66 mm^3/N.m).Ranking of the parameters have been done and it was observed that temperature is most influeincing parameter for both the materials. Linear relationship was observed between specific wear rate and tempurature, pressure, sliding velocity and sliding distance for both materials.When compared to the AF-22 friction material, CL-3003 has a higher heat conductivity. Adhessive deformation of metallic additives in AF-22 contribute considerably in loss of friction due to excessive temperature causing 'fade'.The thermal degradation of the ingredients controls the wear mechanism. Based on Scanning electron microscopy images, thermal degradation causes exponential rise in wear rate. This will lead to engineers that wear rate can be minimised by controlling interface temperature between brake pads and disc either externally and (or) by adding solid lubricants in existing materials. In terms of material, CL-3003 friction material outperforms AF-22. To anticipate the commercial usage of brake pad materials, detailed investigations involving more combinations can be carried out to generate databank for futuristic material.

Acknowledgment

The authors gratefully welcome The Institution of Engineers (India) for financial support for conducting research and development on this topic.

References

[1] Borawski, A. "Conventional and unconventional materials used in the production of brake pads – review". Science and Engineering of Composite Materials, Vol. 27, No. 1,2020, pp. 374-396.

[2] Ikpambese, K. K., Gundu D. T. and Tuleun L. T. "Evaluation of palm kernel fibers (PKFs) for production of asbestos-free automotive brake pads". Journal of King Saud University–Engineering Sciences,Vol. 28, 2016, pp, 10–118.

[3] Aku, S. Y., Yawas D. S., Madakson P. B. and Amaren S. G. "Characterization of periwinkle shell as asbestos-free brake pad materials", The Pacific Journal of Science and Technology,Vol. 13, No. 2, 2012, pp. 57-63.

[4] Yawas, D. S., Aku, S. Y. and Amaren, S. G. "Morphology and properties of periwinkle shell asbestos-free brake pad". Journal of King Saud University, Engineering Sciences, Vol. 28, 2016, pp. 103-109.

[5] Olabisi, A. I., Ademoh, N. A. and Boye, T. E. "Development of asbestos-free automotive brake pad using ternary agro-waste fillers". Journal of Multidisciplinary Engineering Science and Technology, Vol. 3, No. 7, 2016, pp. 5307-5327.

[6] Ademoh, N. A. andOlabisi, A. I. "Development and evaluation of maize husks asbestos-free based brake pad". Industrial Engineering Letters,Vol. 5, No. 2, 2015, pp. 67-80.

[7] Ilanko, A., K. and Vijayaraghavan, S. "Wear behavior of asbestos-free eco-friendly composites for automobile brake materials". Friction, Vol. 4, No. 2, 2016, pp. 144-152.

[8] Hendre, K. N. and Bachchhav, B. D. "Critical Property Assessment of Novel Brake Pad Materials by AHP". Journal of Manufacturing Engineering, Vol. 13, No. 3, 2018, pp. 148-151.

[9] Hendre, K. N. and Bachchhav, B. D. "Friction and Wear Characteristics of Rubber Resin-Bonded Metallic Brake Pad Materials". International Journal of Engineering and Advanced Technology, Vol. 8, No. 6, 2019a, pp. 1312-1316.

[10] Hendre, K. N. and Bachchhav, B. D. "Frictional Characteristics of Brake Pad Materials Alternate to Asbestos". International Journal of Engineering and Advanced Technology, Vol. 9, No. 2, 2019b, pp. 694-698.

[11] Aranganathan, N. andJayashreeBijwe, "Development of copper-free eco-friendly brake-friction material using novel ingredients", Wear, Vol. 352–353,2016, pp. 79-91.

[12] Leonardi, M., Menapace, C., Matejka, V., Gialanella, S. and Straffelini, G. "Pin-on-disc investigation on copper-free friction materials dry sliding against cast iron" Tribology International, Vol. 119, 2018, pp. 73-81.

[13] Kumar, M. and Bijwe J. "Non-asbestos organic (NAO) friction composites: role of copper; its shape and amount". Wear, Vol. 270, 2011, pp. 269–280.

[14] Ruzaidi C. M., Kamarudin H., Shamsul J. B., Mustafa Al Bakri A. M. and Liyana J. "Mechanical properties and morphology of palm slag, calcium carbonate and dolomite filler in brake pad composites". Applied Mechanics and Materials,Vol. 313(314), 2013, pp. 174-178.

[15] Maleque M. A., Atiqah A., Talib R. J. and Zahurin H. "New natural fibre reinforced aluminium composite for automotive brake pad". International Journal of Mechanical and Materials Engineering, Vol. 7, No. 2, 2012, pp. 166-170.

[16] Hatam, A. and Khalkhali, A., "Simulation and sensitivity analysis of wear on the automotive brake pad". Simulation Modelling Practice and Theory, Vol. 84, 2018, pp. 106-123.

[17] Verma, P., Menapace, L., Bonfanti, A., Ciudin, R., Gialanella, S. and Straffelini, G "Braking pad-disk system: wear mechanisms and formation of wear fragments". Wear, Vol. 322(323), 2015, pp. 251-258.

[18] Gui, L., Wang, X., Fan, Z. and Zhang, F. "A simulation method of thermo-mechanical and tribological coupled analysis in dry sliding system". Tribology International, Vol. 103, 2016, pp. 121-131.

[19] Jose, C., Chanchi, G., Gregory, A. M., James, G. C., Geoffrey, W. R., George and C. C. "Hysteretic behaviour of asymmetrical friction connections using brake pads of D3923".. Structures, Vol. 16, 2018, pp.164-175.

[20] Khairnar, H. P., Phalle V. M. and Mantha S. S. "Estimation of automotive brake drum shoe interface friction coefficient under varying conditions of longitudinal forces using Simulink".Friction, Vol. 3, No. 3, 2015, pp. 214-227.

[21] Surya Rajan B., Sai Balaji M. A. and Velmurugan C. "Correlation of field and experimental test data of wear in heavy commercial vehicle brake liners".Friction,Vol. 5, No. 1, 2017, pp. 56-65.

[22] Wang W. J., Wang F., Gu K. K., Ding H. H., Wang H. Y., Guo J., Liu Q. Y. and Zhu M. H. "Investigation on braking tribological properties of metro brake shoe materials". Wear, , Vol. 330(331), 2015, pp. 498-506.

[23] W. Österle, C. Deutsch, T. Gradt, G. Orts-Gil, T. Schneider and A.I.Dmitriev."Tribological screening tests for the selection of raw materials for automotive brake pad formulations". Tribology International, Vol. 73, 2014, pp. 148-155

[24] Hendre, K. N. and Bachchhav, B. D. "Tribological behavior of non-asbestos brake pad material", Materials Today: Proceedings, Vol. 38, 2021, pp. 2549-2554.

[25] Lee, S., and Jang Ho. “Effect of plateau distribution on friction instability of brake friction materials”. Wear, Vol. 400, No. 401, 2018, pp. 1-9.

[26] Rongping, Y., Peter, F., and Yafei Lu “Performance and evaluation of eco-friendly brake friction materials”. Tribology International, Vol. 43, Issue 11, 2010,pp. 2010-2019.

[27] Polajnar, M., Kalin, M., Thorbjornsson, I., Thorgrimsson, J. T., Valle, N. and Botor-Probierz, A. “Friction and wear performance of functionally graded ductile iron for brake pads”. Wear, Vol.382, 2017, pp. 85-94.

[28] Gawande, S.H., Raibhole, V.N. and Banait, A.S. “Study on Tribological Investigations of Alternative Automotive Brake Pad Materials”. J Bio TriboCorros, Vol. 6, No.93, 2020, pp. 1-10.

[29] Roy Ranjit K. ‘Design of Experiments Using the Taguchi Approach’, Van Nostrand, New York, 1996.

[30] Ramadan J. Mustafa. “Abrasive Wear of Continuous Fibre Reinforced Al And Al-Alloy Metal Matrix Composites”. Jordan Journal of Mechanical and Industrial Engineering, Vol. 4, No. 2, 2010, pp. 246-255.

[31] Dixit, G., Khan, M., M. “Sliding Wear Response of an Aluminium Metal Matrix Composite: Effect of Solid Lubricant Particle Size”.Jordan Journal of Mechanical and Industrial Engineering, Vol. 8, No. 6, 2014, pp. 351-358.

JJMIE

Volume 16, Number 4, September. 2022
ISSN 1995-6665
Pages 471 – 483

Jordan Journal of Mechanical and Industrial Engineering

An Accuracy and Efficiency Study on the Use of Symmetrical Numerical Models of Electronic Packages under Various Loading Conditions

Mohammad A. Gharaibeh*

Department of Mechanical Engineering, Faculty of Engineering, The Hashemite University - Zarqa, 13133, Jordan

Received 4 Jul 2021 *Accepted 13 Jun 2022*

Abstract

This paper investigates the accuracy, validity, and the efficiency of the use of symmetry-based finite element models in simulating the mechanical behavior of board-level electronic assemblies under various loading conditions. In this investigation, ANSYS software was adopted to build the quarter-symmetry of the full geometric models, and to conduct the analysis. Various analysis types, including static, modal, harmonic, transient and spectrum analysis were considered. The results of the symmetric model were extensively compared to those of the full model in each analysis type. Based on this comprehensive comparison, it is recommended to use the symmetrical numerical models in static, transient and spectrum analysis types. However, the use of such models is not generally encouraged in eigenvalue problems like modal analysis. For harmonic analysis, a cautious use of the symmetry models, combined with full solution methods, is encouraged. Additionally, a data on the computational cost, such as solution time and memory usage, of the use of symmetric models was reported. Finally, the computational efficiency results showed high preference in using quarter symmetry models over full models..

Keywords: Finite Element Modeling, Symmetric models, electronic packages, computational efficiency.

1. Introduction

Board-level electronic packages analysis is of great interest over the world [1, 2]. In real-life, electronic products are subjected to various static as well as dynamic loading conditions [3]. Over the years, finite element method (FEM) has been proven to be effective in the analysis and characterization of board-level electronic assemblies [4, 5]. One major hand-waving concern in building accurate and efficient finite element analysis (FEA) models of electronic systems is the computational cost and solution time due to the wide range complexity of the electronic structure [6]. To overcome this issue, researchers have constantly adopted, wherever possible, the use of symmetrical FEA models. For example, Pitarresi et al. [7] considered half-symmetry FE models in the analysis of board-level electronic packages under drop impact. Luan et al. [8] used quarter-symmetry models in the investigations of thin-profile fine-pitch ball grid array (TFBGA) and quad flat no-lead (QFN) packages in impact loadings as well. Many other researchers have adopted symmetrical computational models of board-level electronic vehicles in drop and shock loading condition [9-14]. For static bending, Zhang et al. [15] considered quarter symmetry in the analysis of pad cratering failures of plastic ball grid array (PBGA) systems. Baber and Guven [16] applied half-symmetry, quarter-symmetry and one-eighth-symmetry FE models in their reliability and fatigue life assessment of electronics under static bending and thermal cycling tests. Farley et al. [17] employed half-symmetry simulations in the investigations of the fatigue characteristics of copper traces in packages subjected to cyclic bending. In addition to drop and bending tests, symmetrical models have been widely used in the analysis of board-level electronic packages under thermal cycling [18-21], harmonic and random vibrations [22-26] and combined temperature-vibration loading conditions [27, 28].

Although the symmetry FE models have been widely considered, other researchers analyzed full models. The definition of full models mean that no symmetry was incorporated, and the full geometry of electronic board was modeled and hence analyzed. Xia et al. [29-31], Tang et al. [32], Gharaibeh [33-36] and Gharaibeh et al. [37-41] have used such full models in the fatigue life and reliability evaluations of board-level electronic assemblies under harmonic as well as random vibration excitations. Full models were also adopted in the study for electronics under drop/impact [42, 43], static bending [44] and combined loading conditions [44-49].

In addition to the assessment of the failure of electronic packages, full finite element models were applied the studies that obtain the in-plane material properties (modulus of elasticity, shear modulus and Poisson’s ratio) of printed circuit boards (PCB) using finite element model

---

* Corresponding author e-mail: mohammada_fa@hu.edu.jo.

updating techniques [50-52]. Such studies include the execution of modal analysis to obtain the natural frequencies and mode shapes of the electronic structures. The use of full and symmetrical models is continuously seen in other engineering applications [53-58].

As it is seen from the previous literature survey, both symmetry-based and full computational models were used in various kinds of analysis. However, there is a lack of understanding about when and how to use full or symmetry models to achieve computationally effective models, in terms of computer memory usage and solution time, without affecting accuracy. For this reason, the aim of the current paper is to provide extensive finite element study on the accuracy and efficiency of the use of both full and symmetrical models of board-level electronic packages under various conditions including static, modal, harmonic, transient and spectrum analysis-type problems.

We start by introducing the details of the test vehicle considered in this study followed by the finite element modeling details and a brief introduction on all the analysis types tested throughout the analysis. The comparison results between full and symmetry-based models are presented subsequently. Finally, this paper summarized the findings and provided recommendations on the use of full and/or symmetry models in the suitable analysis type and loading condition.

2. Description of the Problem

As mentioned earlier, this work aims to test the accuracy, validity and efficiency of the use of symmetrical finite element models of board-level electronic packages subjected to various loading conditions. Consequently, the loading conditions considered in this paper include, static loading, impact loading, random as well as harmonic vibration loadings and natural frequency and mode shape analysis. In summary, static, dynamic and eigenvalue problems were considered.

The board-level configuration evaluated in this work appears in Figure 1. This configuration is assembled from a squared printed circuit board (PCB) with $76 \times 76\ mm^2$ in-plane dimensions and a $1\ mm$ thickness, an Amkor CABGA 256 Integrated Circuit (IC) component of 16 × 16 full area array SAC305 solder interconnects. This highly symmetric squared configuration was purposefully chosen to create a quarter-symmetric and full finite element models, as will be described in the following section.

3. Finite Element Modeling

In this paper, ANSYS commercial software Release 19.0, installed on a personal computer (PC) with an Intel ® Core ™ i7-4790 central processing unit (CPU) at 3.60 GHz processer and 8 Gigabytes of RAM, was adopted to create the FE models and to execute all the analysis types considered in the present work.

In the analysis, two types of FE models were investigated: Full model and Quarter-Symmetry (QS) model. In the full model, shown in Figure 2(a), the previously described test sample was modeled with full geometric properties. In contradiction, the QS model only one quarter was modeled, Figure 2(b), per the geometric symmetry of the tested configuration. In both full and QS models, only linear elastic material properties were used for all parts of the electronic assembly. The purpose of selecting elastic material behavior is directed towards the validity and efficiency of the use of symmetric computational models in various types of analysis as it does not provide or report any reliability or fatigue data. Material Properties used in the present study are listed in Table 1.

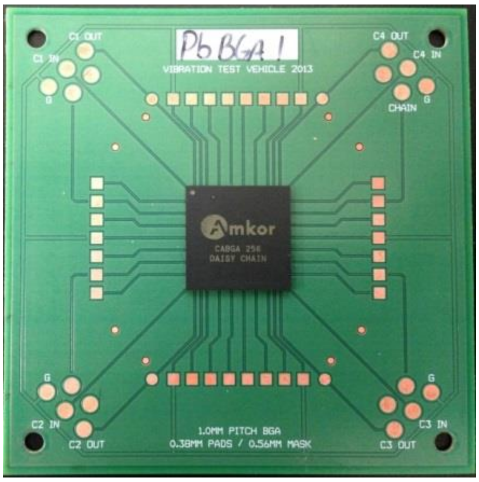

Figure 1. Test Board Details.

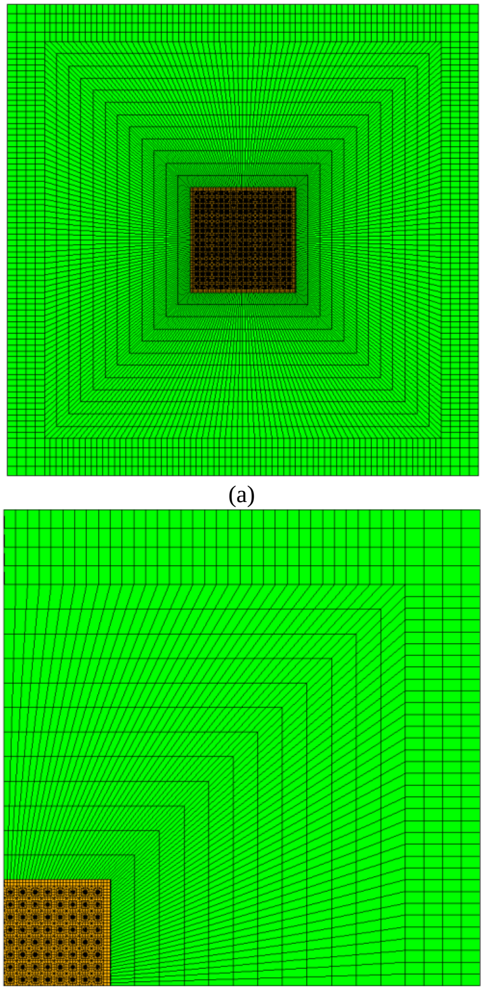

(a)

(b)

Figure 2. Finite element models (a) full model (b) quarter symmetry model.

Table 1. Linear elastic material properties used in the FE model.

Material Parameter	PCB	Component	Solder joints SAC305	Copper pads
Young's Modulus (GPa)	32.0	27.0	43.0	120.0
Poisson's ratio	0.24	0.25	0.36	0.30
Density (kg/m^3)	3000	1100	7400	8800

For mesh properties, SOLID 185 ANSYS element with full integration properties was used in both full and QS models. Additionally, care was taken to generate the same mesh characteristics, i.e., element size and distribution, and to eliminate the effect of mesh discrepancies in QS and full model and in each model as well. In the full model, 178,880 elements and 220,294 nodes were generated while the symmetric model contained 44,270 elements and 55,330 nodes.

For the boundary conditions, the full model was constrained in all directions at each corner of the PCB. The QS model was restrained at the top-right corner of the PCB in all directions and the symmetry boundary conditions were applied on the planes of symmetry.

The analysis types simulated in the current investigation included static, modal, harmonic, transient and spectrum analysis. For analysis robustness, ANSYS Sparse Solver was adopted to solve for the full and symmetry models in all analysis types considered.

In static analysis, a self-weight of $1g$ was applied, where g is the acceleration of gravity and $g = 9.81\, m/s^2$. Although it is straightforward and well-known that in static problems both QS and full models are expected to produce the same results, it was reported here for completeness.

In modal analysis, the first ten natural frequencies and mode shapes of the symmetry-based and the full model were calculated. Mathematically, modal analysis is an eigenvalue value problem in which the natural frequencies are the eigenvalues, and the mode shapes are the eigenvectors. Although, it does not provide any strain or stress data, but it provides important dynamic characteristics of the tested structure and it is widely used in the process of evaluating the in-plane material properties of the PCBs and other electronic structure.

Harmonic analysis was also incorporated in the present study to ensure the validity of the use of the symmetric FEA models in dynamic problems with steady-state response. In ANSYS, two harmonic analysis methods are available: Full method and Mode superposition method [57]. The full method is the most straightforward solution method for conducting a harmonic analysis as it uses the full system matrices without matrix reduction to compute the harmonic response, i.e., displacements, in a single pass. However, it is computationally expensive. The second method, the mode superposition (MSUP) method, is faster and less computationally intensive as it sums the factored eigenvectors (mode shapes) of a previously conducted modal analysis to compute the harmonic response. However, to calculate stresses and strains of the analyzed structure, it requires a second solution step; the expansion pass step, The MSUP method accuracy, which highly depends on the number of the mode shapes incorporated in the solution, the higher the better.

In the present work, harmonic analysis was adopted to simulate the base excitation vibration problem of the test piece. A base input acceleration of $1g$ was applied on the fixed locations, i.e., PCB 4 corners in the full models and the top-right corner in the QS model. The damping ratio used in this analysis is 0.5%, as extracted from a previous study of the author [33]. For completeness, both solution methods, full and MSUP, were simulated. In MSUP, two cases were tested. The first case (MSUP 05), only five model shapes were incorporated in the simulation and the second case (MSUP 15), fifteen modes were included in the solution.

Another important analysis type tested in this investigation is transient analysis. This type of analysis is commonly used to solve for dynamic problems with transient response. As in harmonic analysis, two solution methods are available in conducting a transient analysis in ANSYS: full and mode superposition (MSUP) method [57]. The properties, advantages, and disadvantages of each solution method here are the same of those discussed in harmonic analysis. In electronic packages research, transient analysis is widely used for simulating drop tests. In the present study, the shock profile of JEDEC B-condition [58] with a standard half-sine wave base acceleration of $1500g$ input level and pulse duration of $0.5\, msec$ was considered. The load application procedure and damping ratio use in transient analysis are similar to those of the previously discussed harmonic analysis. Additionally, full and mode superposition with MSUP 05 and MSUP 15 methods were studied in this type of analysis.

The last analysis type performed in this study is spectrum analysis. ANSYS spectrum analysis is commonly used to simulate base excitation random vibrations problems. In ANSYS, random vibration problem with spectrum analysis is also called power spectral density (PSD) analysis [53]. Mathematically, PSD is a statistical measure that is defined as the root-mean-square (RMS) value of a given random variable. In random vibration simulations, it is always assumed that the dynamic input loading has a zero mean, and it follows the properties of Gaussian or normal distributions. During the solution process of a PSD analysis, it requires a combination of the mode shapes, which are to be obtained from modal analysis. More mode combinations lead to more accurate results, similar to MSUP method in harmonic and transient analyses. In the present work, a base acceleration with a PSD input level of $1\, g^2/Hz$ with a damping ratio of 0.5% was applied at the fixed locations, as previously presented in harmonic and transient analysis. In the mode combination step, two cases were simulated MSUP 05 and MSUP 15 to combine five and fifteen mode shapes during the analysis, respectively.

4. Results and Discussions

4.1. Static Analysis

As mentioned earlier, it is straightforward and well-known that the results of the static solution in full and symmetric models are expected to be in exact match.

However, this paper comes to document all of that along with other analysis types for completeness. The results of static analysis are depicted in Figure 3 and Figue 4. Figure 3 presents a contour plot for the out-of-plane displacements from both QS and full models and Figue 4 shows the von Mises stress of the solder joints area array. Apparently, displacement and stress results from both model types are the same as expected, which further validates the efficiency and accuracy of the use symmetry-based numerical models in such kind of problems.

4.2. Modal Analysis

Modal analysis results, i.e., natural frequencies and mode shapes, from both model configurations are included in Table 1 and Table 2. From Table 1, it is clearly observed that natural frequencies in the full and QS models, i.e., eigenvalues, do not match, except for the first mode. Same observations can be noted in Table 3. It can be explained that not all mode shapes are symmetric and that most of the eigenvectors are antisymmetric (axisymmetric). By taking a deeper look into the results, it could be seen that the natural frequencies and operating deflection shapes of the fourth and sixth modes of the full model are matching the second and third modes of the symmetry-based model, respectively. This is because that these two specific modes are symmetric. While all other shown mode shapes are antisymmetric, they differ in the QS model and the full model.

Here, it can be concluded that the symmetry-based computational models cannot be used in the analysis of eigenvalue problems like modal analysis as well as buckling analysis.

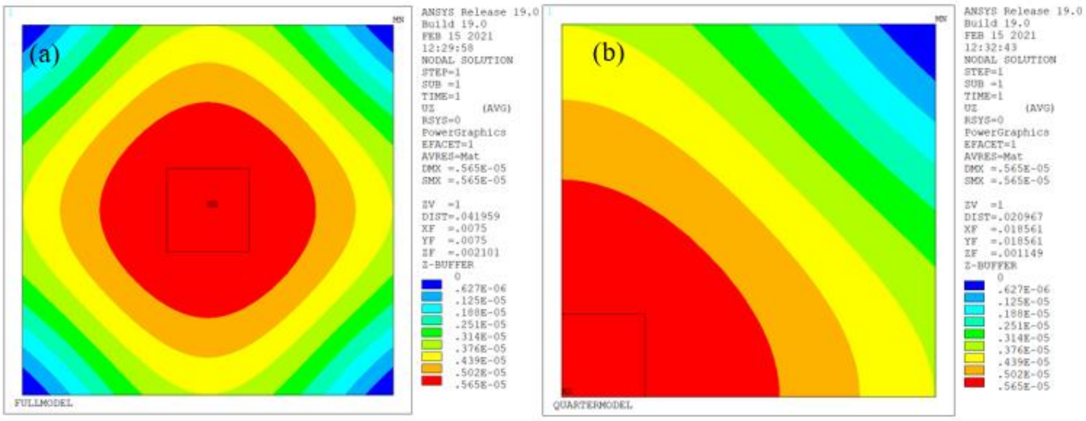

Figure 3. Contour plots for the out-of-plane deflections using (a) full and (b) QS models.

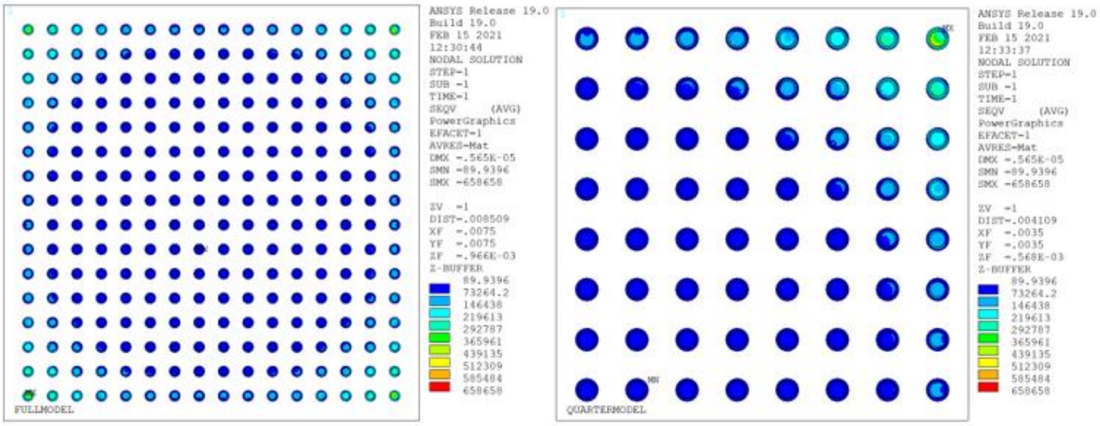

(a) (b)

Figure 4. Contour plots for the solder area array von Mises stresses using (a) full and (b) QS models.

Table 2. Natural frequency comparison between full and QS models.

Mode #	Full model natural frequency [Hz]	QS model natural frequency [Hz]
1	235.85	235.85
2	502.97	712.98
3	502.97	1283.5
4	712.98	2622.0
5	1213.7	3509.1
6	1283.5	4035.7
7	1497.0	4623.9
8	1497.0	6479.3
9	2056.1	7883.8
10	2221.6	8374.2

4.3. Harmonic Analysis

As stated previously, harmonic analysis was performed to simulate the base excitation with harmonic input problem on both QS and full model systems. Three cases, including full, MSUP 05 and MSUP 15, were considered. Figure 5shows the out-of-plane displacements at the board center frequency functions for all simulated cases in frequency range from 1 Hz to 15 KHz. As shown in Figure 5(a), the board transverse deflections from both QS and full models, using full solution methods, are exactly the same and right on top of each other. This concludes that the use of symmetry based FEA models is totally valid and accurate. For Figure 5(b) and Figure 5(c), the PCB deflections are not the same from the full and the QS model. Specifically, for MSUP 05 solution method (Figure 5(b)). For MSUP 15 (Figure 5(c)), the board deflections are in better match with the full solution methods as more mode shape, i.e., eigenvectors, were invoked in the solution. As a result, while using symmetric models in harmonic analysis with mode superposition, care must be taken, and sufficient number of mode shapes has to be included in the solution. For safe use of symmetry-based models in harmonic analysis, the use of the full solution method is highly encouraged for best accuracy. For a closer look, Figure 6shows the board deformations for all solution methods as extracted from full and QS models, respectively. For Figure 6(a), it is obviously seen that the data of MSUP 15 matches the results of the full solution method while MSUP 05 misses the resonant peaks for excitation frequencies exceeding 3 KHz. This is due to the fact that MSUP 15 uses 15 modes in the solution while MSUP 05 uses only 5 modes. Such findings lead to the statement that even when using full numerical models, careful selection of the number of modes to be incorporating the mode superposition method is strictly essential. If this is not easily obtained, the use of full solution method is strongly recommended. Figure 6(b) depicts the deflections all solution methods as extracted from the symmetry based FEA model. This shows that the use of full solution method, even in symmetric models, provides accurate and valid results compared to full models. However, the use of MSUP methods is not encouraged as important details will be missed which leads to erroneous results.

In summary, the use of symmetry-based models in harmonic analysis is valid and efficient only if full solution method is performed. Otherwise, erroneous and maybe disastrous results might be achieved. Additionally, if mode superposition solution methods were used, in both full and symmetric models, the inclusion of sufficient number of mode shapes is required.

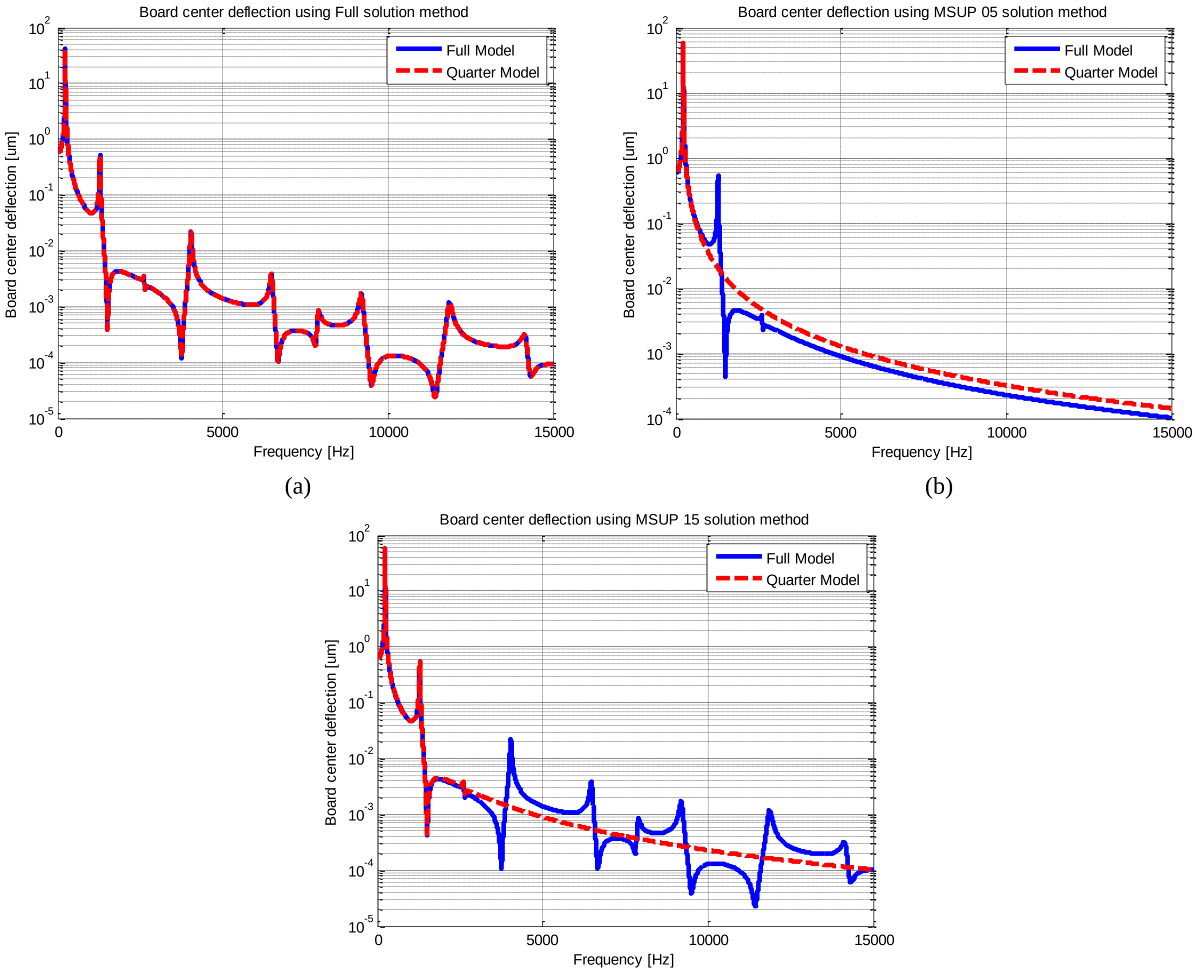

(a) (b)

(c)

Figure 5. Board deflection frequency response from both full and QS models using (a) full (b) MSUP 05 and (c) MSUP 15 methods.

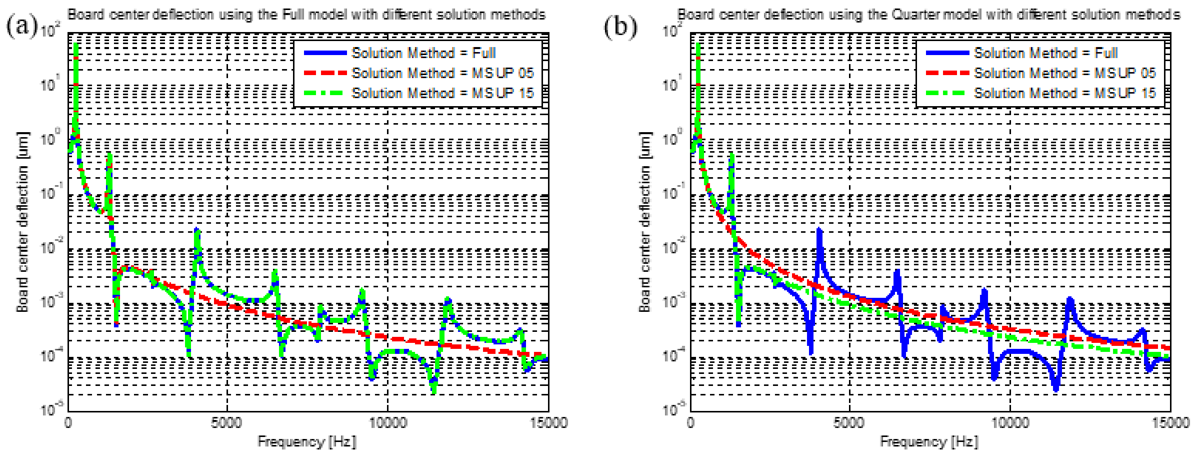

Figure 6. Board deflections frequency response using different solution methods in (a) full and (b) QS model.

4.4. Transient Analysis

The purpose of performing transient analysis in this study is to ensure the validity of using symmetric modes of board-level electronic packages under drop/impact loading. Figure 7 shows the results of the comparison of board transverse deflection time response from both full and QS models using all solution techniques, full, MSUP 05 and MSUP 15. Such findings proves that the results of the symmetry based numerical model perfectly matches those of the full model, for all solution techniques. However, as shown in Figure 8which compares all three solution methods as performed in QS and full models, the use of mode superposition may not yield to the same results of the full solution method, especially after the time exceeds 0.01 seconds. As a result, the use of full solution method is highly favorable for best solution accuracy. Additionally, the adoption of the symmetry based FEA models is also valid and proven to be accurate especially if combined with full solution method.

4.5. Spectrum Analysis

In this paper, the spectrum analysis, or PSD analysis, was used to simulate the random vibration problem of electronic packages at the board-level. As mentioned earlier, the PSD analysis requires the combination of mode shapes which are extracted from modal analysis. Hence, two combinations were investigated in this work: MSUP 05 and MSUP 15 in which 5 and 15 modes were invoked in the solution, respectively. Figure 9 and Figure 10 show the three-sigma (3σ) von Mises stress in the solder area array in both FEA models using MSUP 05 and MSUP 15 solution methods, respectively. The (3σ) von Mises stress means that the probability that solder stresses will exceed this (3σ) stress value is less than 0.3% of the time [39]. This (3σ) von Mises stress value is a commonly used criterion in the fatigue life estimation of electronic assemblies under random vibration [1-2, 29-31, 39]. Back to the stress results, it is shown that the solder stress distributions from the symmetry-based mode and the full model, in MSUP 05 and MSUP 15, and both models proves that the maximum solder stress occurs in the outermost interconnect. Additionally, both full and QS models and solution methods result in the same stress values. For example, the maximum solder stress is 13.7 MPa in all models and solution techniques.

The discussions above prove that the symmetric FEA models are efficient, valid, and safe to use in any of the tested solution methods during the simulation of a spectrum analysis.

4.6. Computational Efficiency

This work introduces a comparison between the symmetry-based and full numerical models in terms of solution time and random-access memory (RAM) usage of the computer machine used throughout the analysis. **Table 4** lists all the solution time and the total RAM usage for all analysis types performed in this study. In general, and as expected, the QS model requires less time and memory than the full model. For example, in static analysis, the QS-to-full-model ratio ($QS/Full$) for solution time is 7.54% and for memory usage is 38.92% which shows great computational advantage of the symmetric model over the full model without losing solution accuracy. Thus, the consideration of symmetry-based numerical models in static analysis type problems is highly encouraged. A similar statement can be made in the use of transient and spectrum analysis types. However, for modal and harmonic analysis, the use of full models is strongly recommended as the solution accuracy is given the priority over the computational costs.

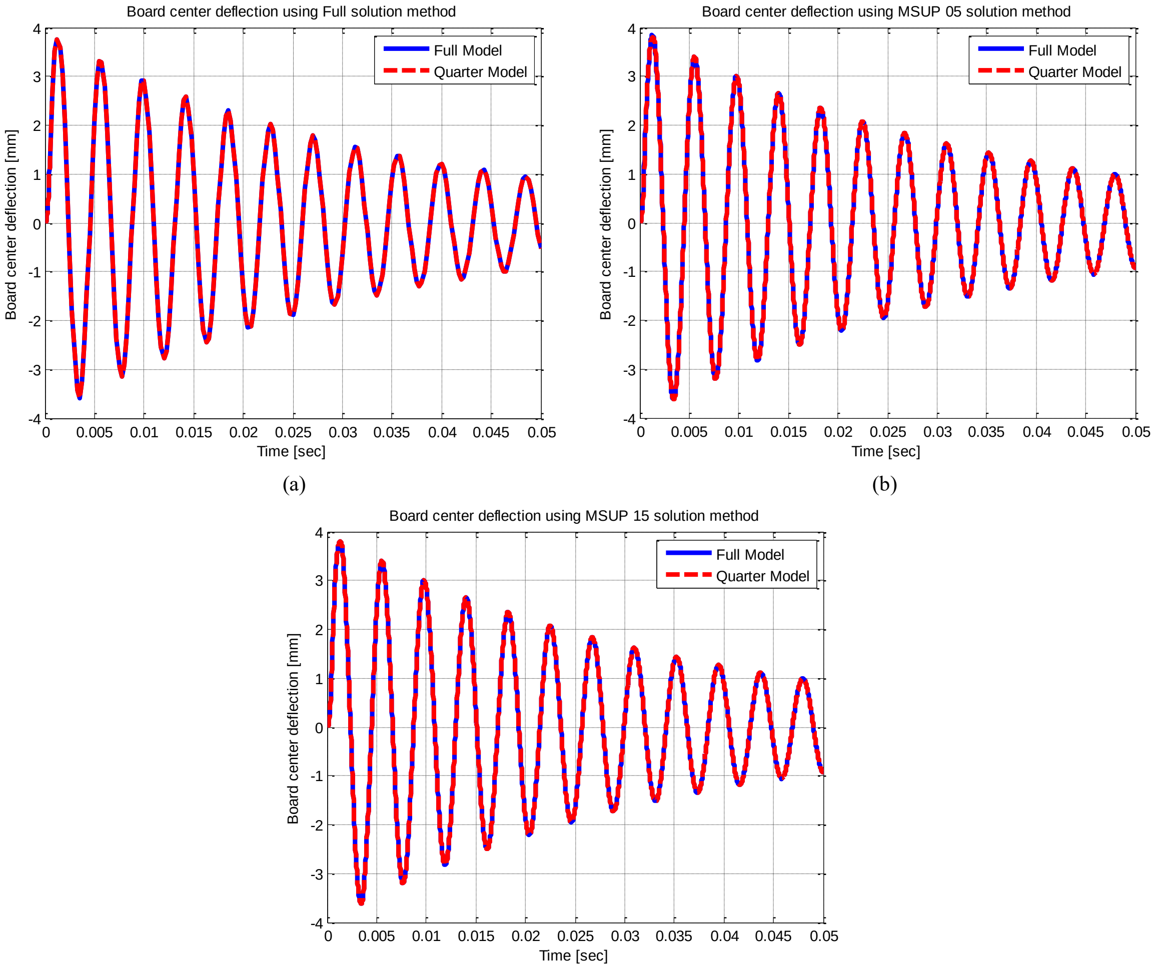

(a)

(b)

(c)

Figure 7. Board deflection time response from both full and QS models using (a) full (b) MSUP 05 and (c) MSUP 15 methods.

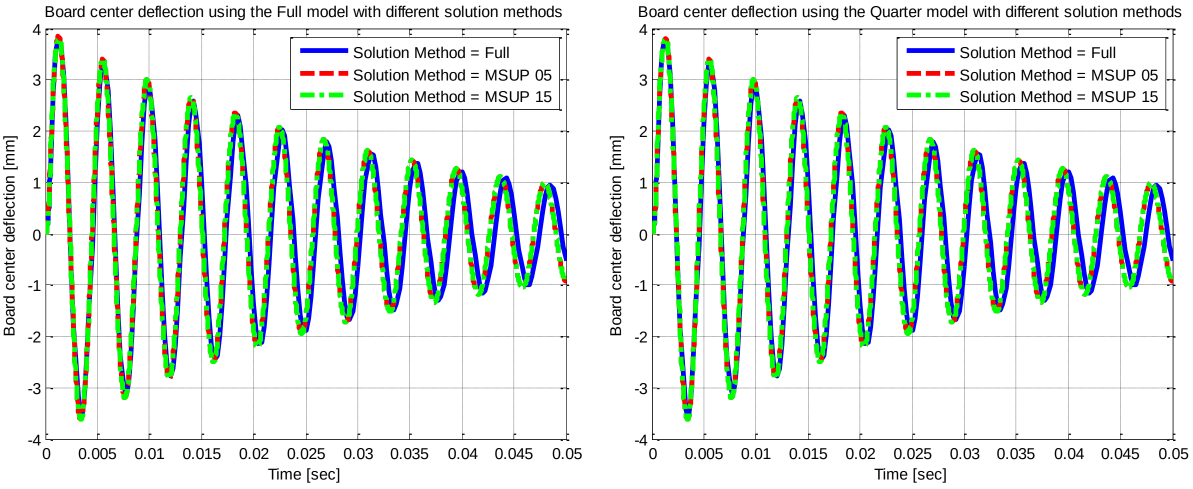

(a)

(b)

Figure 8. Board deflections time response using different solution methods in (a) full and (b) QS model.

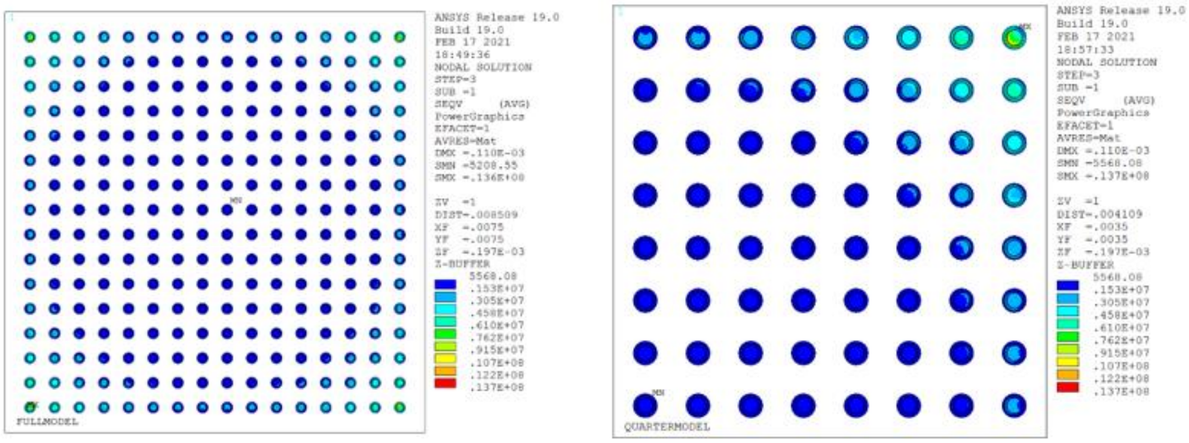

(a) (b)

Figure 9. Three-sigma solder area array von Mises stresses using MSUP 05 in (a) full, and (b) QS models.

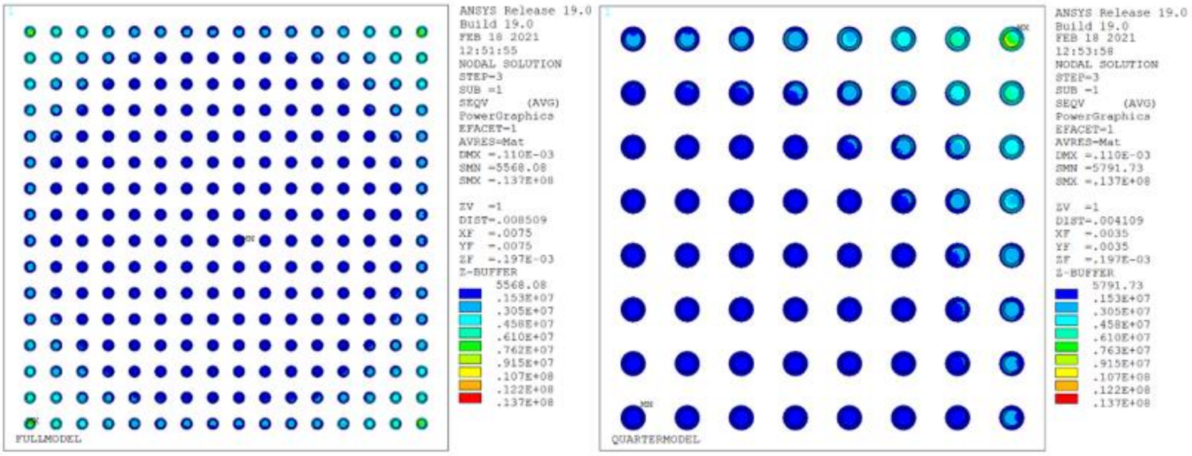

(a) (b)

Figure 10. Three-sigma solder area array von Mises stresses using MSUP 15 in (a) full, and (b) QS models.

Table 3. Mode shape comparison between full and QS models.

Mode #	Full Model Mode Shape	QS Model Mode Shape
1	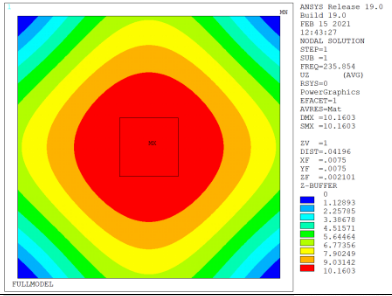	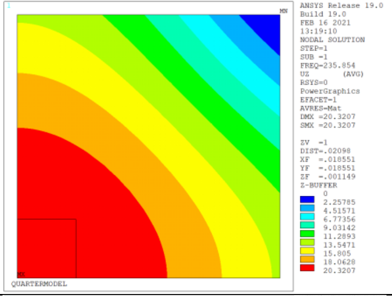
2	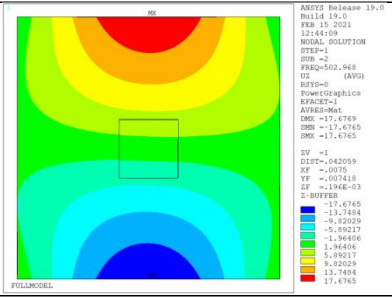	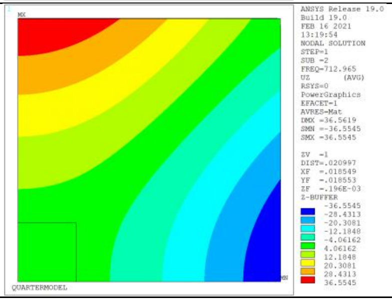

<table>
<tr>
<td>3</td>
<td></td>
<td>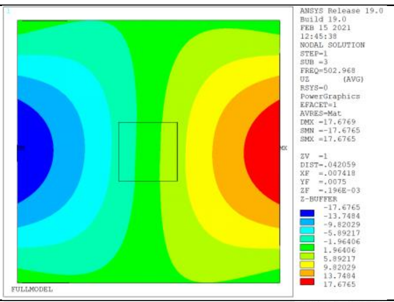
ANSYS Release 19.0
Build 19.0
FEB 15 2021
12:45:38
NODAL SOLUTION
STEP=1
SUB =3
FREQ=502.968
UZ (AVG)
RSYS=0
PowerGraphics
EFACET=1
AVRES=Mat
DMX =17.6769
SMN =-17.6765
SMX =17.6765
ZV =1
DIST=.042059
XF =.007418
YF =.0075
ZF =.196E-03
Z-BUFFER
-17.6765
-13.7484
-9.82029
-5.89217
-1.96406
1.96406
5.89217
9.82029
13.7484
17.6765
MN
MX
FULLMODEL</td>
<td>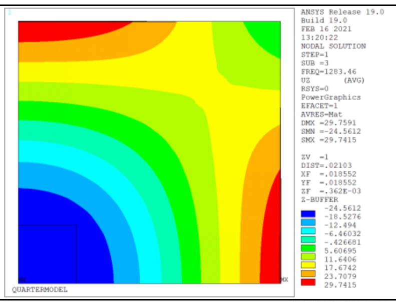
ANSYS Release 19.0
Build 19.0
FEB 16 2021
13:20:22
NODAL SOLUTION
STEP=1
SUB =3
FREQ=1283.46
UZ (AVG)
RSYS=0
PowerGraphics
EFACET=1
AVRES=Mat
DMX =29.7591
SMN =-24.5612
SMX =29.7415
ZV =1
DIST=.02103
XF =.018552
YF =.018552
ZF =.362E-03
Z-BUFFER
-24.5612
-18.5276
-12.494
-6.46032
-.426681
5.60695
11.6406
17.6742
23.7079
29.7415
MX
QUARTERMODEL</td>
</tr>
<tr>
<td>4</td>
<td></td>
<td>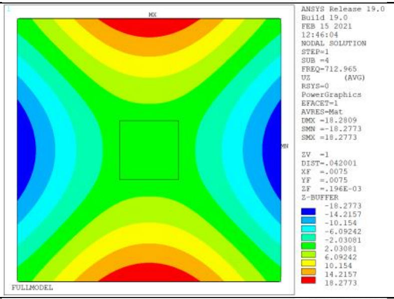
ANSYS Release 19.0
Build 19.0
FEB 15 2021
12:46:04
NODAL SOLUTION
STEP=1
SUB =4
FREQ=712.965
UZ (AVG)
RSYS=0
PowerGraphics
EFACET=1
AVRES=Mat
DMX =18.2809
SMN =-18.2773
SMX =18.2773
ZV =1
DIST=.042001
XF =.0075
YF =.0075
ZF =.196E-03
Z-BUFFER
-18.2773
-14.2157
-10.154
-6.09242
-2.03081
2.03081
6.09242
10.154
14.2157
18.2773
MX
MN
FULLMODEL</td>
<td>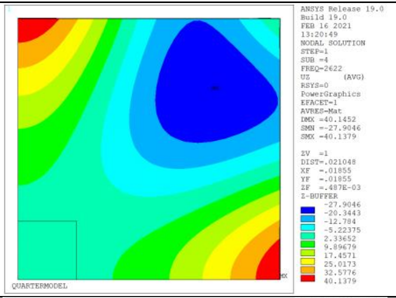
ANSYS Release 19.0
Build 19.0
FEB 16 2021
13:20:49
NODAL SOLUTION
STEP=1
SUB =4
FREQ=2622
UZ (AVG)
RSYS=0
PowerGraphics
EFACET=1
AVRES=Mat
DMX =40.1452
SMN =-27.9046
SMX =40.1379
ZV =1
DIST=.021048
XF =.01855
YF =.01855
ZF =.487E-03
Z-BUFFER
-27.9046
-20.3443
-12.784
-5.22375
2.33652
9.89679
17.4571
25.0173
32.5776
40.1379
MN
MX
QUARTERMODEL</td>
</tr>
<tr>
<td>5</td>
<td></td>
<td>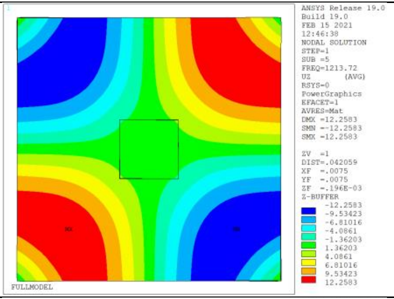
ANSYS Release 19.0
Build 19.0
FEB 15 2021
12:46:38
NODAL SOLUTION
STEP=1
SUB =5
FREQ=1213.72
UZ (AVG)
RSYS=0
PowerGraphics
EFACET=1
AVRES=Mat
DMX =12.2583
SMN =-12.2583
SMX =12.2583
ZV =1
DIST=.042059
XF =.0075
YF =.0075
ZF =.196E-03
Z-BUFFER
-12.2583
-9.53423
-6.81016
-4.0861
-1.36203
1.36203
4.0861
6.81016
9.53423
12.2583
MX
MN
FULLMODEL</td>
<td>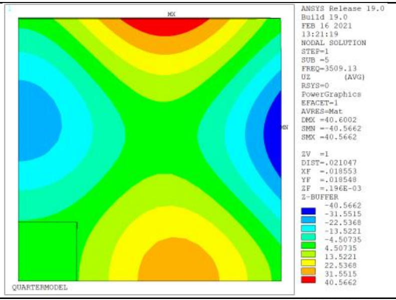
ANSYS Release 19.0
Build 19.0
FEB 16 2021
13:21:19
NODAL SOLUTION
STEP=1
SUB =5
FREQ=3509.13
UZ (AVG)
RSYS=0
PowerGraphics
EFACET=1
AVRES=Mat
DMX =40.6002
SMN =-40.5662
SMX =40.5662
ZV =1
DIST=.021047
XF =.018553
YF =.018548
ZF =.196E-03
Z-BUFFER
-40.5662
-31.5515
-22.5368
-13.5221
-4.50735
4.50735
13.5221
22.5368
31.5515
40.5662
MX
MN
QUARTERMODEL</td>
</tr>
<tr>
<td>6</td>
<td></td>
<td>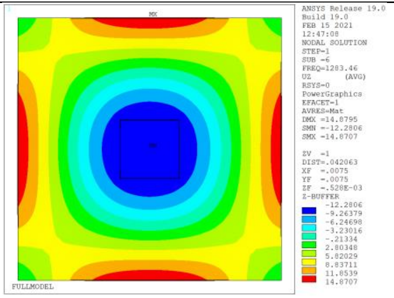
ANSYS Release 19.0
Build 19.0
FEB 15 2021
12:47:08
NODAL SOLUTION
STEP=1
SUB =6
FREQ=1283.46
UZ (AVG)
RSYS=0
PowerGraphics
EFACET=1
AVRES=Mat
DMX =14.8795
SMN =-12.2806
SMX =14.8707
ZV =1
DIST=.042063
XF =.0075
YF =.0075
ZF =.520E-03
Z-BUFFER
-12.2806
-9.26379
-6.24698
-3.23016
-.21334
2.80348
5.82029
8.83711
11.8539
14.8707
MX
MN
FULLMODEL</td>
<td>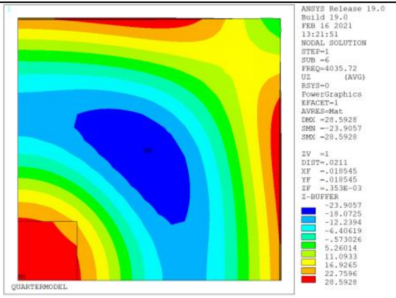
ANSYS Release 19.0
Build 19.0
FEB 16 2021
13:21:51
NODAL SOLUTION
STEP=1
SUB =6
FREQ=4035.72
UZ (AVG)
RSYS=0
PowerGraphics
EFACET=1
AVRES=Mat
DMX =28.5928
SMN =-23.9057
SMX =28.5928
ZV =1
DIST=.0211
XF =.018545
YF =.018545
ZF =.353E-03
Z-BUFFER
-23.9057
-18.0725
-12.2394
-6.40619
-.573026
5.26014
11.0933
16.9265
22.7596
28.5928
MN
QUARTERMODEL</td>
</tr>
<tr>
<td>7</td>
<td></td>
<td>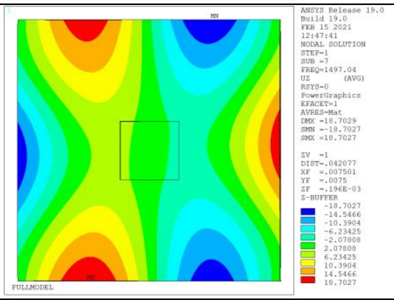
ANSYS Release 19.0
Build 19.0
FEB 15 2021
12:47:41
NODAL SOLUTION
STEP=1
SUB =7
FREQ=1497.04
UZ (AVG)
RSYS=0
PowerGraphics
EFACET=1
AVRES=Mat
DMX =18.7029
SMN =-18.7027
SMX =18.7027
ZV =1
DIST=.042077
XF =.007501
YF =.0075
ZF =.196E-03
Z-BUFFER
-18.7027
-14.5466
-10.3904
-6.23425
-2.07808
2.07808
6.23425
10.3904
14.5466
18.7027
MN
MX
FULLMODEL</td>
<td>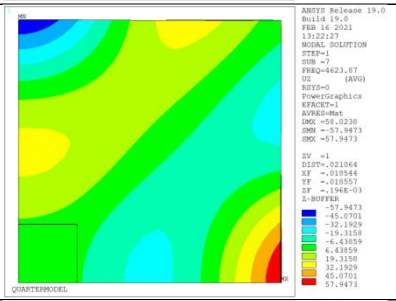
ANSYS Release 19.0
Build 19.0
FEB 16 2021
13:22:27
NODAL SOLUTION
STEP=1
SUB =7
FREQ=4623.87
UZ (AVG)
RSYS=0
PowerGraphics
EFACET=1
AVRES=Mat
DMX =58.0238
SMN =-57.9473
SMX =57.9473
ZV =1
DIST=.021064
XF =.018544
YF =.018557
ZF =.196E-03
Z-BUFFER
-57.9473
-45.0701
-32.1929
-19.3158
-6.43859
6.43859
19.3158
32.1929
45.0701
57.9473
MN
MX
QUARTERMODEL</td>
</tr>
<tr>
<td>8</td>
<td></td>
<td>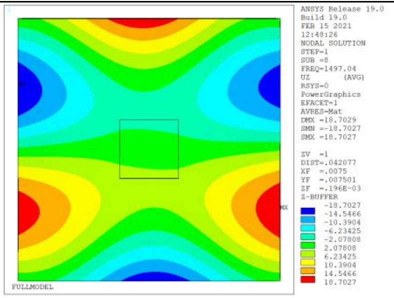
ANSYS Release 19.0
Build 19.0
FEB 15 2021
12:48:26
NODAL SOLUTION
STEP=1
SUB =8
FREQ=1497.04
UZ (AVG)
RSYS=0
PowerGraphics
EFACET=1
AVRES=Mat
DMX =18.7029
SMN =-18.7027
SMX =18.7027
ZV =1
DIST=.042077
XF =.0075
YF =.007501
ZF =.196E-03
Z-BUFFER
-18.7027
-14.5466
-10.3904
-6.23425
-2.07808
2.07808
6.23425
10.3904
14.5466
18.7027
MN
MX
FULLMODEL</td>
<td>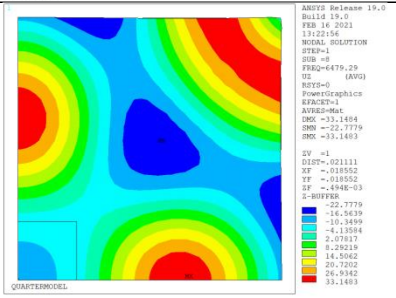
ANSYS Release 19.0
Build 19.0
FEB 16 2021
13:22:56
NODAL SOLUTION
STEP=1
SUB =8
FREQ=6479.29
UZ (AVG)
RSYS=0
PowerGraphics
EFACET=1
AVRES=Mat
DMX =33.1484
SMN =-22.7779
SMX =33.1483
ZV =1
DIST=.021111
XF =.018552
YF =.018552
ZF =.494E-03
Z-BUFFER
-22.7779
-16.5639
-10.3499
-4.13584
2.07817
8.29219
14.5062
20.7202
26.9342
33.1483
MN
MX
QUARTERMODEL</td>
</tr>
</table>

<table>
<tr>
<td>9</td>
<td>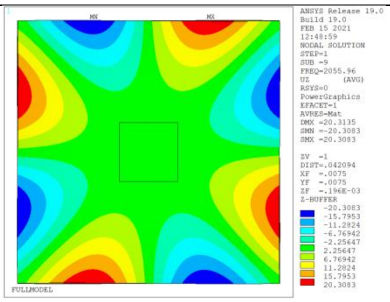
</td>
<td>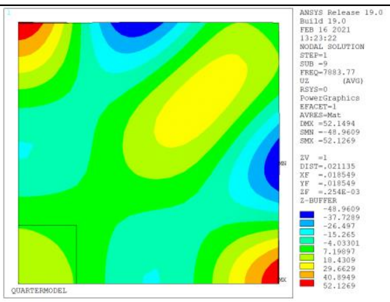
</td>
</tr>
<tr>
<td>10</td>
<td>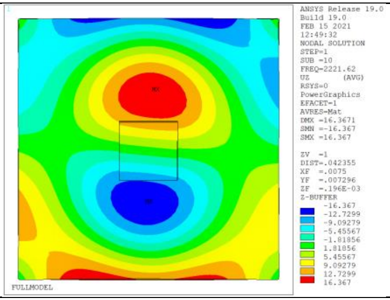
</td>
<td>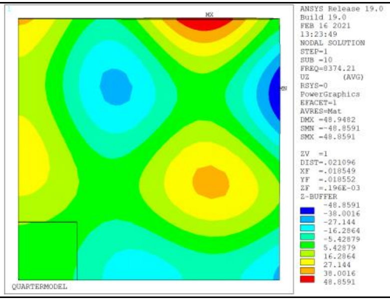
</td>
</tr>
</table>

Table 4. Computational efficiency data.

<table>
<tr><td colspan="10">STATIC ANALYSIS</td></tr>
<tr><td>Model type</td><td colspan="3">Full Model</td><td colspan="3">QS Model</td><td colspan="3">$\frac{QS}{Full} \times 100\%$</td></tr>
<tr><td>Memory usage (MB)</td><td colspan="3">2549.0</td><td colspan="3">992.0</td><td colspan="3">38.92%</td></tr>
<tr><td>Solution time (sec)</td><td colspan="3">140.6</td><td colspan="3">10.60</td><td colspan="3">7.54%</td></tr>
<tr><td colspan="10">MODAL ANALYSIS</td></tr>
<tr><td>Model Type</td><td colspan="3">Full Model</td><td colspan="3">QS Model</td><td colspan="3">$\frac{QS}{Full} \times 100\%$</td></tr>
<tr><td>Memory usage (MB)</td><td colspan="3">2157</td><td colspan="3">1082</td><td colspan="3">50.16%</td></tr>
<tr><td>Solution time (sec)</td><td colspan="3">106.1</td><td colspan="3">29.9</td><td colspan="3">28.18%</td></tr>
<tr><td colspan="10">HARMONIC ANALYSIS</td></tr>
<tr><td>Model Type</td><td colspan="3">Full Model</td><td colspan="3">QS Model</td><td colspan="3">$\frac{QS}{Full} \times 100\%$</td></tr>
<tr><td>Solution Method</td><td>Full</td><td>MSUP 05</td><td>MSUP 15</td><td>Full</td><td>MSUP 05</td><td>MSUP 15</td><td>Full</td><td>MSUP 05</td><td>MSUP 15</td></tr>
<tr><td>Memory usage (MB)</td><td>2929.0</td><td>4590.0</td><td>4759.0</td><td>2283.0</td><td>1764.0</td><td>1756.0</td><td>77.94%</td><td>38.43%</td><td>38.43%</td></tr>
<tr><td>Solution time (sec)</td><td>395878.6</td><td>73.8</td><td>180.3</td><td>14803.0</td><td>10.5</td><td>43.2</td><td>3.74%</td><td>14.22%</td><td>23.96%</td></tr>
<tr><td colspan="10">TRANSIENT ANALYSIS</td></tr>
<tr><td>Model Type</td><td colspan="3">Full Model</td><td colspan="3">QS Model</td><td colspan="3">$\frac{QS}{Full} \times 100\%$</td></tr>
<tr><td>Solution Method</td><td>Full</td><td>MSUP 05</td><td>MSUP 15</td><td>Full</td><td>MSUP 05</td><td>MSUP 15</td><td>Full</td><td>MSUP 05</td><td>MSUP 15</td></tr>
<tr><td>Memory usage (MB)</td><td>4885.0</td><td>4590.0</td><td>4759.0</td><td>1500.0</td><td>1764.0</td><td>1756.0</td><td>30.71%</td><td>38.43%</td><td>38.43%</td></tr>
<tr><td>Solution time (sec)</td><td>3298.6</td><td>69.9</td><td>102.6</td><td>730.9</td><td>13.9</td><td>71.3</td><td>22.16%</td><td>19.89%</td><td>69.49%</td></tr>
<tr><td colspan="10">SPECTRUM ANALYSIS</td></tr>
<tr><td>Model Type</td><td colspan="3">Full Model</td><td colspan="3">QS Model</td><td colspan="3">$\frac{QS}{Full} \times 100\%$</td></tr>
<tr><td>Solution Method</td><td colspan="2">MSUP 05</td><td>MSUP 15</td><td colspan="2">MSUP 05</td><td>MSUP 15</td><td colspan="2">MSUP 05</td><td>MSUP 15</td></tr>
<tr><td>Solution time (sec)</td><td colspan="2">4158.0</td><td>4158.0</td><td colspan="2">1911.0</td><td>1903.0</td><td colspan="2">45.96%</td><td>45.77%</td></tr>
<tr><td>Solution time (sec)</td><td colspan="2">100.6</td><td>253.9</td><td colspan="2">28.0</td><td>53.2</td><td colspan="2">27.83%</td><td>20.95%</td></tr>
</table>

5. Conclusions

This work introduced an accuracy and efficiency study on the use of symmetry-based finite element models of board-level electronic packages subjected to various types of loadings. ANSYS commercial software was adopted in the quarter symmetry model and the full models to perform all the analysis types. Both model types were executed in various problem types including static, modal, harmonic, transient and spectrum analysis. Additionally, solutions methods, as full and mode superposition methods, were considered. Furthermore, this paper reported some data on the computational efficiency metrics including solution time and total memory usage of all model and analysis types conducted. As a result of this study, we recommend the use of symmetric numerical models in static, transient and spectrum analysis types. However, the use of such models is not recommended in eigenvalue problems like modal analysis. For harmonic analysis, a cautious use of the symmetry models, combined with full solution methods, is encouraged. Finally, the computational efficiency results showed high preference in using quarter symmetry models over full models.

References

[1] Gharaibeh, M. A., & Makhlouf, A. S. H. (2020). Failures of electronic devices: solder joints failure modes, causes and detection methods. In *Handbook of Materials Failure Analysis* (pp. 3-17). Butterworth-Heinemann.

[2] Gharaibeh, M. A. (2020). Analytical solutions for electronic assemblies subjected to shock and vibration loadings. In *Handbook of Materials Failure Analysis* (pp. 179-203). Butterworth-Heinemann.

[3] Gharaibeh, M. A. (2015). *Finite element modeling, characterization and design of electronic packages under vibration*. PhD Dissertation, State University of New York At Binghamton, Binghamton, NY, USA.

[4] Gharaibeh, M., Su, Q., Pitarresi, J., & Anselm, M. (2013). Modeling and characterization for vibration. *Universal Instruments Advanced Research in Electronic Assemblies Consortium, Conklin, NY*, 12-13.

[5] Gharaibeh, M., Pitarresi, J., & Anselm, M. (2013). Strain correlation: Finite element modeling and experimental data. *Universal Instruments Advanced Research in Electronic Assemblies Consortium, Conklin, NY*, 12-13.

[6] Pitarresi, J. M., & Akanda, A. (1993). Random vibration response of a surface mount lead/solder joint. (pp. 207-217), *Advances in electronic packaging*, *4*(1).

[7] Pitarresi, J., Roggeman, B., Chaparala, S., & Geng, P. (2004, June). Mechanical shock testing and modeling of PC motherboards. In *2004 Proceedings. 54th Electronic Components and Technology Conference (IEEE Cat. No. 04CH37546)* (Vol. 1, pp. 1047-1054). IEEE.

[8] Luan, J. E., Tee, T. Y., Goh, K. Y., Ng, H. S., Baraton, X., Bronner, R., & Kujala, A. (2005, April). Drop impact life prediction model for lead-free BGA packages and modules. In *EuroSimE 2005. Proceedings of the 6th International Conference on Thermal, Mechanial and Multi-Physics Simulation and Experiments in Micro-Electronics and Micro-Systems, 2005.* (pp. 559-565). IEEE.

[9] Tee, T. Y., Ng, H. S., Lim, C. T., Pek, E., & Zhong, Z. (2004). Impact life prediction modeling of TFBGA packages under board level drop test. *Microelectronics Reliability*, *44*(7), 1131-1142.

[10] Lall, P., Shantaram, S., Angral, A., & Kulkarni, M. (2009, May). Explicit submodeling and digital image correlation based life-prediction of leadfree electronics under shock-impact. In *2009 59th Electronic Components and Technology Conference* (pp. 542-555). IEEE.

[11] Dhiman, H. S., Fan, X., & Zhou, T. (2009, May). JEDEC board drop test simulation for wafer level packages (WLPs). In *2009 59th Electronic Components and Technology Conference* (pp. 556-564). IEEE.

[12] Wu, M. L., & Lan, J. S. (2018). Reliability and failure analysis of SAC 105 and SAC 1205N lead-free solder alloys during drop test events. *Microelectronics Reliability*, *80*, 213-222.

[13] Wu, M. L., & Lan, J. S. (2018). Prediction of Fatigue Resistance in Lead-Free Ni-Doped SAC 1205 Solder Alloys Using a Rate-Dependent Material Model and Subjected to Drop Tests. *IEEE Transactions on Components, Packaging and Manufacturing Technology*, *8*(10), 1777-1787.

[14] Che, F., Luan, J. E., Goh, K. Y., & Baraton, X. (2009, December). Drop impact life model development for FBGA assembly with lead-free solder joint. In *2009 11th Electronics Packaging Technology Conference* (pp. 656-662). IEEE.

[15] Zhang, Q., Lo, J. C., & Lee, S. R. (2017, May). Pad Cratering Based Failure Criterion for the Life Prediction of Board Level Cyclic Bending Test. In *2017 IEEE 67th Electronic Components and Technology Conference (ECTC)* (pp. 448-455). IEEE.

[16] Baber, F., & Guven, I. (2016, May). Solder Joint Fatigue Life Prediction of Electronic Packages Using Combined FEA and Peridynamics. In *2016 IEEE 66th Electronic Components and Technology Conference (ECTC)* (pp. 225-231). IEEE.

[17] Farley, D., Zhou, Y., Dasgupta, A., & DeVries, J. W. C. (2012). An adaptive Cu trace fatigue model based on average cross-section strain. *Microelectronics Reliability*, *52*(11), 2763-2772.

[18] Motalab, M., Mustafa, M., Suhling, J. C., Zhang, J., Evans, J., Bozack, M. J., & Lall, P. (2013, May). Correlation of reliability models including aging effects with thermal cycling reliability data. In *2013 IEEE 63rd Electronic Components and Technology Conference* (pp. 986-1004). IEEE.

[19] Chaparala, S. C., Roggeman, B. D., Pitarresi, J. M., Sammakia, B. G., Jackson, J., Griffin, G., & McHugh, T. (2005). Effect of geometry and temperature cycle on the reliability of WLCSP solder joints. *IEEE transactions on components and packaging technologies*, *28*(3), 441-448.

[20] Johnson, Z. (1999, June). Implementation of and extensions to Darveaux's approach to finite-element simulation of BGA solder joint reliability. In *1999 Proceedings. 49th Electronic Components and Technology Conference (Cat. No. 99CH36299)* (pp. 1190-1195). IEEE.

[21] Wu, K. C., Lee, C. H., & Chiang, K. N. (2016, May). Characterization of thermal cycling ramp rate and dwell time effects on AF (Acceleration Factor) Estimation. In *2016 IEEE 66th Electronic Components and Technology Conference (ECTC)* (pp. 251-256). IEEE.

[22] Wong, T. E., Reed, B. A., Cohen, H. M., & Chu, D. W. (1999, June). Development of BGA solder joint vibration fatigue life prediction model. In *1999 Proceedings. 49th Electronic Components and Technology Conference (Cat. No. 99CH36299)* (pp. 149-154). IEEE.

[23] Fan, X., Pei, M., & Bhatti, P. K. (2006, May). Effect of finite element modeling techniques on solder joint fatigue life prediction of flip-chip BGA packages. In *56th Electronic Components and Technology Conference 2006* (pp. 9-pp). IEEE.

[24] Yeh, C. L., Lai, Y. S., & Wang, C. C. (2006, October). Finite element analysis procedure for board-level swept sine

vibration tests. In *2006 International Microsystems, Package, Assembly Conference Taiwan* (pp. 1-4). IEEE.

[25] Zhou, Y., Al-Bassyiouni, M., & Dasgupta, A. (2009). Vibration durability assessment of Sn3. 0Ag0. 5Cu and Sn37Pb solders under harmonic excitation. *Journal of Electronic Packaging*, *131*(1).

[26] Perkins, A., & Sitaraman, S. K. (2004, June). Vibration-induced solder joint failure of a ceramic column grid array (CCGA) package. In *2004 Proceedings. 54th Electronic Components and Technology Conference (IEEE Cat. No. 04CH37546)* (Vol. 2, pp. 1271-1278). IEEE.

[27] Eckert, T., Krüger, M., Müller, W. H., Nissen, N. F., & Reichl, H. (2010, June). Investigation of the solder joint fatigue life in combined vibration and thermal cycling tests. In *2010 Proceedings 60th Electronic Components and Technology Conference (ECTC)* (pp. 1209-1216). IEEE.

[28] Eckert, T., Muller, W. H., Nissen, N. F., & Reichl, H. (2009, May). A solder joint fatigue life model for combined vibration and temperature environments. In *2009 59th Electronic Components and Technology Conference* (pp. 522-528). IEEE.

[29] Xia, J., Li, G., Li, B., & Cheng, L. (2016). Optimal design for vibration reliability of package-on-package assembly using FEA and taguchi method. *IEEE Transactions on Components, Packaging and Manufacturing Technology*, *6*(10), 1482-1487.

[30] Xia, J., Li, G., Li, B., Cheng, L., & Zhou, B. (2017). Fatigue life prediction of package-on-package stacking assembly under random vibration loading. *Microelectronics Reliability*, *71*, 111-118.

[31] Xia, J., Cheng, L., Li, G., & Li, B. (2017). Reliability study of package-on-package stacking assembly under vibration loading. *Microelectronics Reliability*, *78*, 285-293.

[32] Tang, H., Wu, Z., & Lui, Z. (2012, August). Random vibration simulation and analysis of PoP solder joints with different structure parameters. In *2012 13th International Conference on Electronic Packaging Technology & High Density Packaging* (pp. 1168-1171). IEEE.

[33] Gharaibeh, M. A., Su, Q. T., & Pitarresi, J. M. (2016). Analytical solution for electronic assemblies under vibration. *Journal of Electronic Packaging*, *138*(1).

[34] Su, Q., Pitarresi, J., Gharaibeh, M., Stewart, A., Joshi, G., & Anselm, M. (2014, May). Accelerated vibration reliability testing of electronic assemblies using sine dwell with resonance tracking. In *2014 IEEE 64th Electronic Components and Technology Conference (ECTC)* (pp. 119-125). IEEE.

[35] Su, Q. T., Gharaibeh, M. A., Stewart, A. J., Pitarresi, J. M., & Anselm, M. K. (2018). Accelerated vibration reliability testing of electronic assemblies using sine dwell with resonance tracking. *Journal of Electronic Packaging*, *140*(4).

[36] Gharaibeh, M. A. (2018). Reliability analysis of vibrating electronic assemblies using analytical solutions and response surface methodology. *Microelectronics Reliability*, *84*, 238-247.

[37] Gharaibeh, M. (2018). Reliability assessment of electronic assemblies under vibration by statistical factorial analysis approach. *Soldering & Surface Mount Technology*.

[38] Gharaibeh, M., Stewart, A. J., Su, Q. T., & Pitarresi, J. M. (2019). Experimental and numerical investigations of the vibration reliability of BGA and LGA solder configurations and SAC105 and 63Sn37Pb solder alloys. *Soldering & Surface Mount Technology*.

[39] Gharaibeh, M. A. (2020). A numerical study on the effect of the fixation methods on the vibration fatigue of electronic packages. *Microelectronics Reliability*, *115*, 113967.

[40] Gharaibeh, M. A., & Pitarresi, J. M. (2019). Random vibration fatigue life analysis of electronic packages by analytical solutions and Taguchi method. *Microelectronics Reliability*, *102*, 113475.

[41] Gharaibeh, M. A., Su, Q. T., & Pitarresi, J. M. (2018). Analytical model for the transient analysis of electronic assemblies subjected to impact loading. *Microelectronics Reliability*, *91*, 112-119.

[42] Wang, W., Robbins, D., & Glancey, C. (2016, May). Simulation Model to Predict Failure Cycles in Board Level Drop Test. In *2016 IEEE 66th Electronic Components and Technology Conference (ECTC)* (pp. 1886-1891). IEEE.

[43] Park, S., Shah, C., Kwak, J., Jang, C., Pitarresi, J., Park, T., & Jang, S. (2007, May). Transient dynamic simulation and full-field test validation for a slim-PCB of mobile phone under drop/impact. In *2007 Proceedings 57th Electronic Components and Technology Conference* (pp. 914-923). IEEE.

[44] Farley, D., Zhou, Y., Askari, F., Al-Bassyiouni, M., Dasgupta, A., Caers, J. F. J., & DeVries, J. W. C. (2009, April). Copper trace fatigue models for mechanical cycling, vibration and shock/drop of high-density PWAs. In *EuroSimE 2009-10th International Conference on Thermal, Mechanical and Multi-Physics Simulation and Experiments in Microelectronics and Microsystems* (pp. 1-9). IEEE.

[45] Lin, E., Jiang, Q., & Dasgupta, A. (2016, May). Effect of isothermal aging on harmonic vibration durability of SAC305 interconnects. In *2016 15th IEEE Intersociety Conference on Thermal and Thermomechanical Phenomena in Electronic Systems (ITherm)* (pp. 761-765). IEEE.

[46] Pang, J. H. L., Wong, F. L., Heng, K. T., Chua, Y. S., & Long, C. E. (2013, May). Combined vibration and thermal cycling fatigue analysis for SAC305 lead free solder assemblies. In *2013 IEEE 63rd Electronic Components and Technology Conference* (pp. 1300-1307). IEEE.

[47] Gharaibeh, M. (2020). Experimental and numerical fatigue life assessment of SAC305 solders subjected to combined temperature and harmonic vibration loadings. *Soldering & Surface Mount Technology*.

[48] Wang, M., & Wells, B. (2016, May). Substrate trace modeling for package warpage simulation. In *2016 IEEE 66th Electronic Components and Technology Conference (ECTC)* (pp. 516-523). IEEE.

[49] Lall, P., Yadav, V., Zhang, D., & Suhling, J. (2018, May). Reliability of SAC Leadfree Solders in Automotive Underhood Temperature-Vibration. In *2018 17th IEEE Intersociety Conference on Thermal and Thermomechanical Phenomena in Electronic Systems (ITherm)* (pp. 1255-1269). IEEE.

[50] Xu, F., Li, C. R., Jiang, T. M., & Zhang, D. P. (2016). Fatigue life prediction for PBGA under random vibration using updated finite element models. *Experimental Techniques*, *40*(5), 1421-1435.

[51] Zhang, B., Liu, P. K., Ding, H., & Cao, W. (2010). Modeling of board-level package by Finite Element Analysis and laser interferometer measurements. *Microelectronics Reliability*, *50*(7), 1021-1027.

[52] Gharaibeh, M. (2018). Finite element model updating of board-level electronic packages by factorial analysis and modal measurements. *Microelectronics International*.

[53] Gharaibeh, M. A., Ismail, A. A., Al-Shammary, A. F., & Ali, O. A. (2019). Three-Material Beam: Experimental Setup and Theoretical Calculations. Jordan Journal of Mechanical and Industrial Engineering, 13(4).

[54] Obaidat, M. H., Al Meanazel, O. T., Gharaibeh, M. A., & Almomani, H. A. (2016). Pad Cratering: Reliability of Assembly Level and Joint Level. Jordan Journal of Mechanical and Industrial Engineering, 10(4).

[55] Cao, Z., Liang, N., Zeng, S., & Gang, X. (2022). Dynamic Response Analysis of the Impact Force of Steel Wheel on the

Elastic Half-Space. Jordan Journal of Mechanical and Industrial Engineering, 16(1).

[56] Bolar, G. (2022). 3D Finite Element Method Simulations on the Influence of Tool Helix Angle in Thin-Wall Milling Process. Jordan Journal of Mechanical and Industrial Engineering, 16(2).

[57] Hadoush, A. (2020). Finite Element Formulation of Internally Balanced Blatz–Ko Material Model. Jordan Journal of Mechanical and Industrial Engineering, 14(2).

[58] Arumugam, A., & Pramanik, A. (2020). Review of Experimental and Finite Element Analyses of Spot Weld Failures in Automotive Metal Joints. Jordan Journal of Mechanical and Industrial Engineering, 14(3).

[59] ANSYS, Inc. (January 2018). ANSYS Mechanical APDL Structural Analysis Guide, Release 19.0.

[60] JEDEC Solid State Technology Association. (2003). Board level drop test method of components for handheld electronic products. *JEDEC Standard JESD22-B111*.

JJMIE

Volume 16, Number 4, September. 2022
ISSN 1995-6665
Pages 485 – 492

Jordan Journal of Mechanical and Industrial Engineering

Axial Flux BLDC Motor Liquid Cooling System: Modelling and Experimental Analysis

Tarsisius Kristyadi*, Marsono, Sahril Sayuti

Mechanical Engineering, InstitutTeknologi Nasional Bandung Indonesia

Received 30 Aug 2021 *Accepted 15 Jun 2022*

Abstract

The paper describes the effect of cooling media and temperature on 20 KW axial flux BLDC motor performance using numerical and experimental analysis. The motor is applied in electric car with initially as natural air cooling, and it is modified as liquid cooling. Numerical and experimental analysis shows that cooling temperature has significant effect on power and efficiency of motor. Lower cooling temperatures produce higher motor power and efficiency. Based on experimental investigation, maximum power of water cooled BLDC motor can generate power of 25 kW and 81.0 % efficiency, while air cooled motor produces lower power and efficiency of 19.1 kW and 65.0 % respectively. Comparative analysis of motor performance based on model and experiment were presented as well. Maximum motor power calculated by model is slightly higher than that measured by experiment. It can be explained that in modeling, the friction losses on the bearings are neglected, while in the experiment, the friction loss remains a variable that affects the motor power output.

Keywords: BLDC, axial flux, cooling, liquid, power.

1. Introduction

The development of electric vehicles encourages researchers to make these vehicles more efficient. Some of the studies aimed to improve the transmission system [1] and the electric motor performance. Air cooled axial flux BLDC motor used to drive electric cars loses power after several minute running due to motor overheat. Overheat on the electric motor leads to harmful effects, such as degradation of the insulation coil, demagnetization, increase of heat loss, decrease in the efficiency of the motor and reduction of the life time of the electric motor[2]. The heat generated due to the current through the windings causes an increase of temperature in various parts of the electric machine [3]. The increase in temperature reduces the insulation resistance of the windings, generates thermal stress, and reduces efficiency [4], and further causes machine failure [5].

Figure 1 shows motor performance which is affected by temperature variations. To generate torque at which is 1.65 Nm, motor at temperature 125°C requires a larger electric current compared to the motor at temperature 25ºC. Peak power motor temperature of 125°C has 1.65 Nm torque while peak power motor temperature of 25°C was at torque 2.88 Nm [6].

It is indicated that the increase in temperature of the motor can affect performance of the electric motors [7]. Overheat on the motor can be avoided by using liquid cooling instead of air cooling. Several methods to increase the cooling rate can be carried out such as the addition of fins on the heat transfer surface [8] and particle modification [9]. While the discussion of the flow characteristics numerically has also been discussed by several researchers [10]. Several studies on cooling material and cooling methods in electric motors have also been discussed in some literature [11,12,13,14].Combination of nano fluid as cooling media and spiral cooling channels were applied as motor cooling system can increase the heat transfer capability of the cooling system and to reduce operating temperature of the electric motor[11,13]. Another investigation to prevent temperature rise in electric motor was used in metal-based phase change materials [14]. To increase heat transfer in phase change material heat sink, insertion of metal foam was aplied [15].

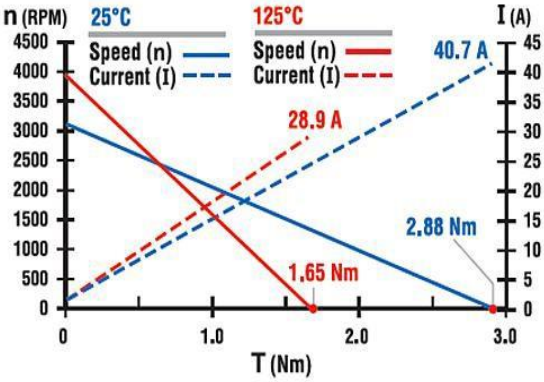

Figure 1. Comparison of BLDC motor performance with temperature variation [6]

---

* Corresponding author e-mail: kristyadi@itenas.ac.id.

For Cooling of existing motor installed on vehicle, simplified cooling modification is required. In this investigation, simplified flat waterjacket is aplied in anaxial flux BLDC motor. The goal of investigation is to determine the effectiveness of water cooling on axial flux BLDC motor numerically and experimentally.

2. Motor Description

The axial flux BLDC motor analyzed consists of the main components of the rotor, stator, bearings and casing. The motor stator consists of 2 stators where each stator consists of 12 identical cores. Armature core is made from pure iron powder with 99% Fe content mixed with carbon fiber resin as the bounding. This mixture of iron powder and resin consists of resin at 14% of the total weight of the mixture of iron powder and epoxy to form a carbon composite[16]. The stator winding (armature) uses copper wire coated with an insulator with a total diameter of 0.8 mm. The rotor on the BLDC motor consists of 8 pairs of permanent magnets. The magnets used in axial flux Brushless DC motors are neodymium types. Neodymium magnets (**NdFeB**, **NIB** or **Neo** magnet) are strong magnets that have a very wide range of applications [17,18,19,20]. This magnet is very popular for the use of electric machines based on permanent magnets. This magnetic strength can reach 440 kJ / m3, so it is suitable for use in BLDC motors [20].

Figure 2. Stator consists of core and armature

Figure 2. Shows the stator consisting of a core and copper windings forming a core and armature unit. There are 2 identical stators to form the BLDC that is analyzed. Figure 3 shows rotor piece which consists of 8 pairs of neodymium magnet. This rotor consists of 2 faces where each face is filled with 5 mm thick of magnets.

Figure 3. Magnetic rotor

General arrangement of the BLDC motor to be analyzed is described at Figure 4.

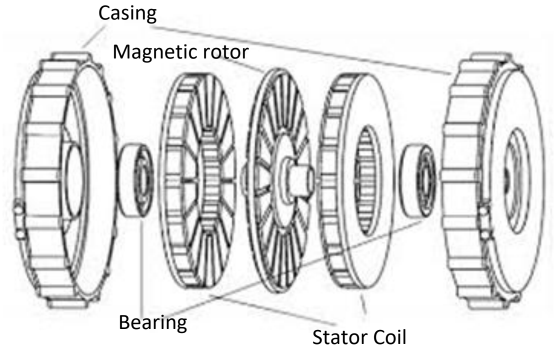

Figure 4. General arrangement of BLDC motor to be analyzed.

This motor has a nominal power of 20 kW and can produce a maximum power up to 30 kW.

Comparison between inner diameter of rotor and stator and the outer diameter is 0.58[19]. The motor has a maximum speed of 6000 rpm, powered by dc voltage of 72 v. For this analysis, the motor is initially air cooled and then liquid cooled.

3. Numerical Analysis

This paper discusses the modeling of 20 kW BLDC motor cooling process. The motor has rate power of 20 kW at voltage 72 V with 90% rate efficiency. The operation speed of the motor is about 2000-6000 rpm.Motor casing made by alluminum with dimension of 270 mm diameter and 306 mm height. In this simulation,electromagnetic losses such as corelosses and copper losses are obtained by Maxwell equation, while losses due to bearing friction are neglected[16].

3.1. ModelDescription

Heat generation on BLDC Motor losses that occur in electric motors can be classified as follows:

3.1.1. Resistive Losses

Resistive losses are generally the main component of power losses in BLDC motors and are calculated as[22]:

$$P_r = mI_{ph}^2 R_{ph} \tag{1}$$

where I_{ph}^2 is the current phase, m is the number of phases and $R_{ph}$is the resistance which varies depend on temperature[22].

3.1.2. Loss per Unit Mass due to Hysteresis (Ph)

The core stator is made of insulated silicon steel lamination. Therefore, variations in magnetic flux due to magnetic rotation produce Eddy current losses and hysteresis losses in the laminate. This loss is estimated individually for the yoke tooth stator as different variations in the inside field. Loss of mass per unit due to hysteresis, Eddy current in yoke stator and Eddy current in tooth stator is calculated as [22,23]:

$$P_h = K_h f^{\alpha} B_m^{\beta} \tag{2}$$

Where Bm is the peak density of the flux ,*f* is the frequency of the flux variation, Kh, α, β is the fitcurve calculated from the data of the loss of the laminate.

3.1.3. Eddy Current Losses on Stator Yoke (Pey)

To calculate Eddy current losses in the stator yoke, the following equation can be used [22,24]:

$$P_{ey} = K_e \frac{8}{\pi} \frac{f^2 B_m^2}{\beta_m} \tag{3}$$

Where Bm is the peak flux density,*f* is the frequency of the flux variation, βm is the arc of the tooth and width of the mast respectively in the electric radians, Ke is the curve of the fit constant calculated from the data of the loss of the laminate.

3.1.4. Eddy Current Losses on Stator Tooth (Pet)

To calculate eddy current losses in a tooth stator, the following equation can be used [24,25]:

$$P_{et} = K_e \frac{4}{\pi} \frac{f^3 B_m^2}{\alpha_{tt}} \left[2 - \frac{\pi - \beta_m}{\alpha_{tt}}\right] \tag{4}$$

where Bm is the peak flux density ,*f* is the frequency of the flux variation, α_{tt} and βm is the arc of the tooth and the pile width respectively in the electric radians, Kh, Ke, α, β are the fit curve curves calculated from the data on the loss of the laminate [25].

3.1.5. Heat Transfer Model

The heat transfer modelling is ilustraded in following figure.

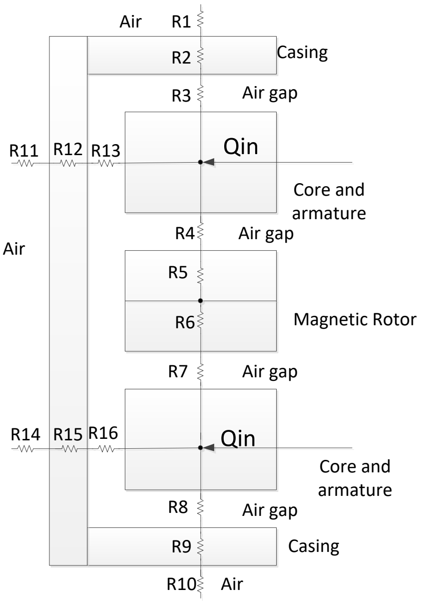

Figure 5. Thermal circuit model of air cooled motor

Figure 5 shows the thermal circuit of air cooled motor, where heat generated from core and armature is transferred to atmospheric air. Thermal circuit model of liquid cooled motor is shown in Figure 6. In this figure, heat transfer from core and armature is transferred to atmospheric air axially and also transferred to liquid cooler radially.

In this analysis, the heat transfer model is divided into 2 cases, namely the air cooled motor and the liquid cooled motor. In the first case, where the motor using air-cooling, axial heat transfer occurs from the core and armature to the outside air through the air gap by convection, to the casing by conduction, then by convection and radiation from the casing surface to the air. Whereas heat transfer in the radial direction occurs from the core and armature through the air gap by convection, through casing by conduction and continues from the surface of the casing to the outside air by radiation.

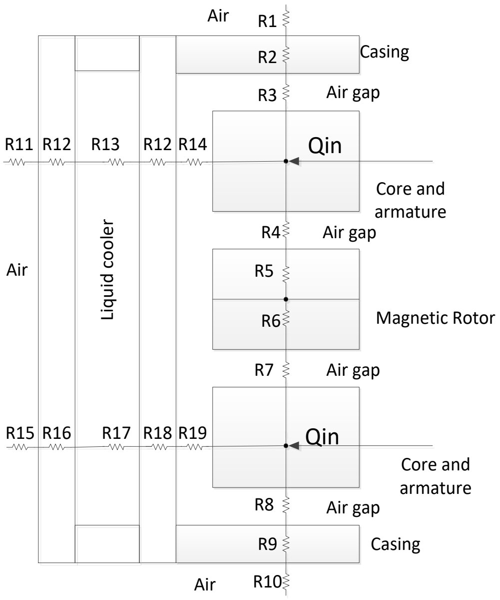

Figure 6. Thermal circuit model of liquid cooled motor

Model illustration of the first case is shown in Figure 5. In the second case as shown at Figure 6, the motor is cooled using liquid (water), the cooling process in the axial direction is the same as in the first case, while the cooling in the radial, there is an additional heat transfer mode. The additional mode occurs from inner surface of the casing to the outside air through convection in water and conduction from the inner surface to the outer surface of the casing.

Core and armature winding are heat sources on this motor that can be simplified as heat flux. In this model, air gap between the armature/core and casing, and air gap between core/armature and magnetic rotor use silicone thermal grease with a thermal conductivity of 6.2 W / mK as thick as 0.5 mm [26,27,28].

The magnitude of heat transfer$Q$ from the core and winding armature to the atmospheric air depends on the convection coefficient and therefore,its estimation becomes the routine of thermalanalysis.The heat transfer by convection is described by below equation[29]:

$$\mathrm{Q = hA(Ts - Ta)} \tag{5}$$

Where A is surface area, Ta and Tsare atmospheric and surface temperature respectively and h is convection coefficient that described as [29]:

$$h = \frac{k}{D}(0.11)[0.5Re^2 + G_r P_r]^{0.35} \tag{6}$$

where :

D is diameter

k is thermal conductivity

Re is Reynolds number

Gr is Grasoft number

Pr is Prantl number

$T_s$is Temperature of surface (casing and core)

T_a is air or liquid temperature

3.1.6. Model of Mechanical Power of Rotor

Rotorrotation is governed by the mechanical equation below[30]:

$$\boldsymbol{J_m \frac{d\omega}{dt} = T_e - T_L + D_\omega} \tag{7}$$

where$J_m$is the total momento finertia$\omega$is the rotors peed;T_e is the electromagnetic torque,$D$is the damping coefficient and T_L is the torque required to drive the load.

Rotorinertia is based on the assumption that all parts of the rotorrotate around the center of the shaft [30]:

$$\boldsymbol{J_{shaft} = 2\pi\rho L_{shaft}\left(\frac{D_{shaft}}{2}\right)^4} \tag{8}$$

3.1.7. Electrical-Mechanical Relation Model

Relation between electrical power and mechanical power is described using following equation [30,31]:

$$P_{elect} = P_{mech\,shaft} + P_r + P_h + P_{ey} + P_{et} + P_{thermal\,loss} + P_f \tag{9}$$

where $P_{mechshaft}$ is mechanical power by motor shaft, Pf is bearing friction losses which is neglected. From above equation, for numerical (modelling) analysis mechanical power generated by motor shaft is described as[30,32]:

$$P_{mech\,shaft} = P_{elect} - P_r - P_h - P_{ey} - P_{et} - P_{thermal\,loss} \tag{10}$$

In this case[31]:

$$P_{elect} = V.I \tag{11}$$

Where I is electrical current and V is voltage.

3.2. Calculation Procedure

The purpose of the simulation is to calculate the power and efficiency of the motor. Electrical energy is supplied to the motor with voltage and current parameters of 72 V and 400 A respectively. The input energy is transferred to mechanical energy (Pmech) and loses, which consists of resistive losses (Pr), hysteresis (Ph), Eddy current on stator yoke (Pey), Eddy current on stator tooth (Pet) and heat transfer loss.The boundary condition can be described as follows[34,35]:

Table 1. Boundary condition of motor model

Specify Boundary Name	Type	Specify Continuum Name	Type
Inlet	Velocity Inlet	External_Fluid	Fluid
Outlet	Pressure Out	Internal_Fluid	Fluid
Wall_Surrounding	Wall	Heatsink	Solid
Wall_Heatsink	Wall	Rotor	Solid
Wall_Rotor	Wall	Winding	Solid
Wall_Winding	Wall	Core	Solid
Wall_Core	Wall		

Actual heat transfer will occur in 3D in all directions following the temperature differences that occur. The heat source on the axial flux BLDC motor is on the winding and core where heatflux (Qin at upper stator and Qin at lower stator) are transferred axially and radially. At upper side, heat flux transmitted in axial direction will be through convection with thermal resistance of R3, conduction on casing with thermal resistance of R2 followed by radiation from casing surface to atmospheric air. In the other hand, the heat flux is transfer axially to rotor magnet by convection and conduction with thermal resistance R 4 and R5respectively. Radial heat transfer occur when heat generated by stator is transferred to surrounding air by convection (R13), then conduction (R12) and followed by radiation with thermal resistance R11. Likewise at lower side, heat flux is transferred in axial direction by convection with thermal resistance R8, conduction on casing with thermal resistance R9 followed by radiation from casing surface to atmospheric air with thermal resistance R11. The heat flux is also transferred axially to rotor magnet by convection with thermal resistance of R7 and conduction with thermal resistance R6. Similar to upper side, radial heat transfer at lower side occurs when heat generated by stator is transferred to surrounding air by convection (R16), then conduction (R15) and followed by radiation with thermal resistance R14.

Above description is the modeling of heat transfer in an air-cooled motor. While the calculation of heat transfer radially in a liquid-cooled motor, there is an additional mode, namely convection in the radial direction from the casing to the liquid cooler. Referring to the figure, convection occurs from the surface of the casing to the coolant which is symbolized by R13 on the upper side and R17 on the lower side. R12 and R16 show the conduction heat transfer resistance in the casing while R11 and R15 are radiation thermal resistance from the casing surface to atmospheric air.

3.3. Calculation Result

The first modeling is a 20 KW BLDC motor given an electrical energy and cooling by atmospheric air with temperature of 27 ^{o}C. Motor rotation at maximum speed at 6000 rpm. The analysis is focused on the thermal conditions between the stator core and the rotor, which became a heat source and requires cooling. While other losses are considered constant depending on the properties of the magnetic material, of core and coil. Figure 7 describes the temperature distribution between the stator armature, casing and magnetic rotor on the upper side of the motor axially. It is assumed that the motor is upper and lower symmetric, hence the characteristic of lower side is similar with the upper side.

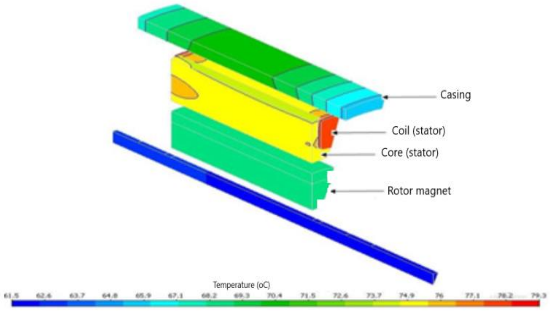

Figure 7. Temperature distribution of inner motor based on air cooled

It can be seen that maximum temperature occurs at armature especially at coil. Temperature difference between maximum and lowest temperature is about 13^{o}C. And temperature difference between casing surface at axial position is about 42°C.At radial heat transfer condition, temperature distribution of the BLDC motor can be seen at the following figure. In Figure 8 below, it can be seen that core and armature temperature are relatively uniform.

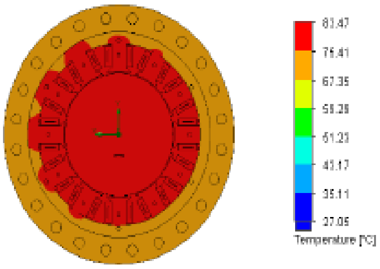

Figure 8. Motor temperature distribution at radial direction with air cooled

The casing temperature in the radial direction is also relatively hot, and the difference between the casing temperature and the air temperature is also relatively the same, which is around 42 °C.Figure 9 shows the temperature distribution in the radial direction (seen in cross section). Prediction of temperature distribution along motor casing contain fin is similar with other calculation [36].

The second modeling is a water cooled 20 kW BLDC. In this case, the motor is modified by providing a water jacket and wrapped with a second casing for the cooler. Temperature of water as liquid cooler is set as 20°C. In this condition, thermal conductivity of water is 12 W/mK [29].

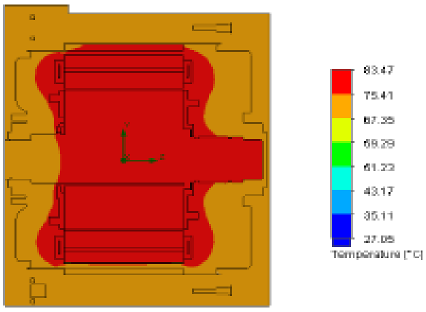

Figure 9. Cross section temperature distribution on air cooled BLDC motor

Similar with first model, temperature distribution of stator, rotor magnet and casing axially is analyzed. Figure 10 show the temperature distribution of above referred. The maximum temperature is lower than air cooling motor. Temperature difference between casing surface at axial position is about 28°C.

Temperature distribution analysis at radial direction is shown at the Figure 11. It can be seen that maximum motor temperature is relatively lower than air cooled motor. More clearly, the temperature difference between the casing surface and the water cooler is shown in the Figure 12. From the figure, the difference between the casing and the coolant reaches 47°C.

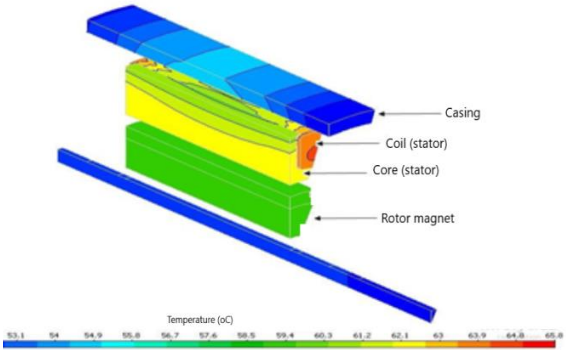

Figure 10. Temperature distribution of inner motor based on water cooled

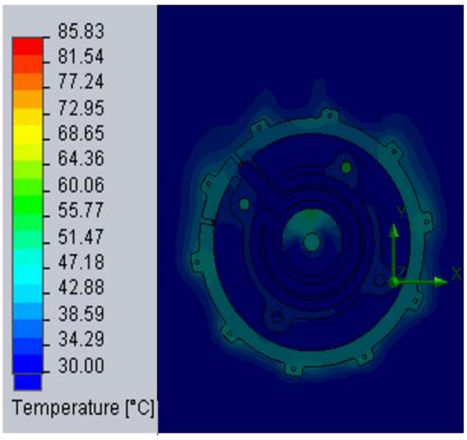

Figure 11. Water cooled Motor temperature distribution at radial direction

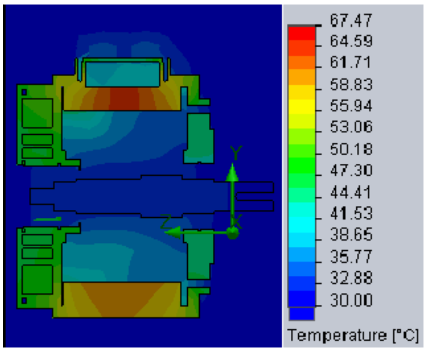

Figure 12. Cross section temperature distribution on water cooled BLDC motor

Similar calculation using various water temperature, air temperature and motor speed. Water temperature is set as 20°C, 22°C, 24°C, 50°C, 60 °C and 70°C. Ambient air temperature is varied from 27°C to 50°C. And motor speed is varied form 1500 rpm to 6000 rpm

3.3.1. Motor Power and efficiency Calculation

By using numerical analysis, based on previous calculation procedure, motor power and efficiency can be defined and summarized in the following table:

Table 2. Motor power and efficiency calculation result based on air cooled motor modelling

Air temperature $(^{oC})$	Motor speed (rpm)	Motor power (kW)	Motor efficiency
27	6000	22500	0.781
27	3000	21900	0.760
30	6000	21800	0.757
30	3000	21250	0.738
40	6000	19100	0.663
40	3000	18650	0.648
50	6000	16780	0.583
50	3000	15800	0.549

Table 3. Motor power and efficiency calculation result based on water cooled motor modelling

Water temperature (oC)	Motor speed (rpm)	Motor power (kW)	Motor efficiency
20	6000	25400	0.882
20	3000	25150	0.873
22	6000	24700	0.858
22	3000	24300	0.844
24	6000	23600	0.819
24	3000	23050	0.800
50	6000	17020	0.591
50	3000	16550	0.575
60	6000	14250	0.495
60	3000	13800	0.479
70	6000	13100	0.455
70	3000	12060	0.419

From above table, it can be seen that cooler temperature have significant effect for maximum motor power and efficiency, while motor speed give small effect.

4. Experimental Analysis

The air cooling and liquid cooling BLDC motor was tested using dynamometer test bed. The dynamometer is equipped with electronic speed sensor, power sensor, temperature sensor based on Arduino. The test bed is illustrated at Figure 13.

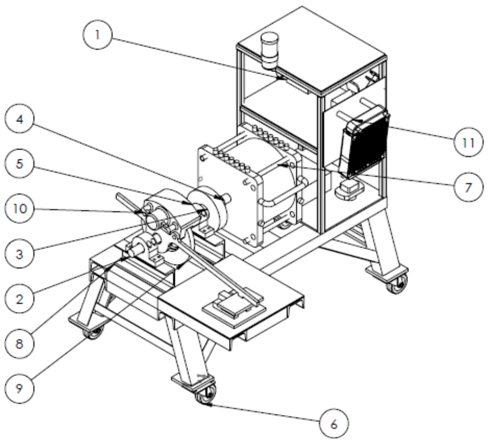

Figure 13. Motor test bed

Where:

1. Load controller
2. Speed sensor
3. 1st Coupling
4. 2nd coupling
5. Pillow block
6. Caster wheel
7. Motor
8. Bearing support
9. Temperature sensor
10. Power meter
11. Panel for instrument

The experimental analysis investigates the effect of air cooling and liquid cooling temperature on BLDC motor power. Motor speed was variated by load variation by dynamometer control. Voltage and current were set of 72 V and 400 A respectively. In first experiment, the BLDC motor was cooled by 25°C atmospheric air. The cooling temperature was set as fix. In liquid cooling case, motor was cooled by water with various temperature from 20°C to 70°C. Electrical power input was similar with air cooled case. The result of experiment is described in the following figure. In Figure 14, effect of cooling temperature on motor power is described. This figure shows that higher cooler temperature cause lower power. This is in line with the theory described in the introduction, that the higher the temperature is, the lower the magnetic strength gets, causing the motor power to decrease as well. Cooling media also has effect on motor power. Liquid cooler has higher heat transfer rate than air cooler. Higher thermal conductivity of water provides a greater cooling rate so that the stator and rotor temperatures are relatively low, resulting in higher motor power. This is shown in Figure 15. As power increases, the water cooled motor efficiency is also higher than air-cooled motors. This can be seen in the Figure 16. From Figure 15 and Figure 16, it can be seen that liquid cooling motor can produce maximum power of 25 kW and 81.0 % of efficiency, while air cooling motor can produce maximum power of 19.1 kW and 65.0% efficiency

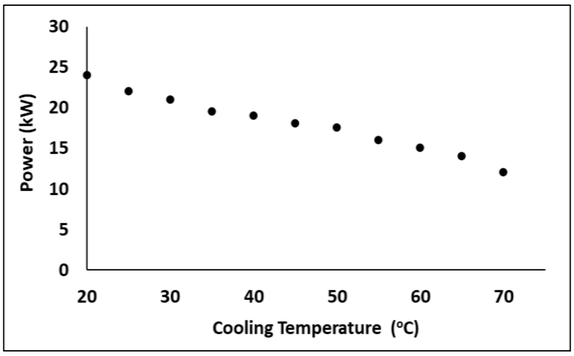

Figure 14. Effect of cooling temperature to motor power.

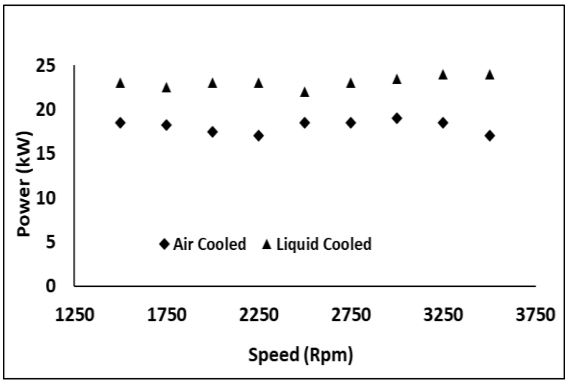

Figure 15. Motor power based on cooler type at various speed.

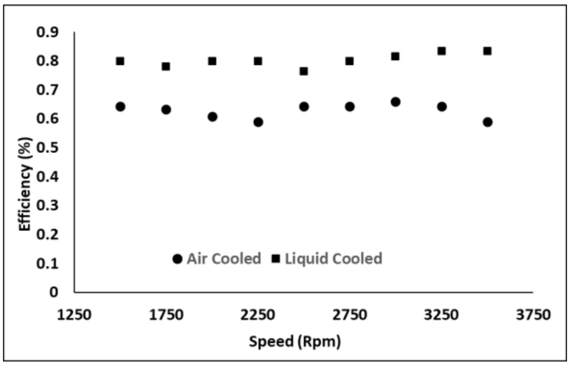

Figure 16. Motor power based on cooler type at various speed.

The final investigation is a comparative analysis of motor performance based on model and experiment. From Figure 17, it can be seen than maximum motor power calculated by model is slightly higher than that measured by experiment. It can be explained that in modeling, the friction losses on the bearings are neglected, while in the experiment, the friction loss remains a variable that affects the motor power output.

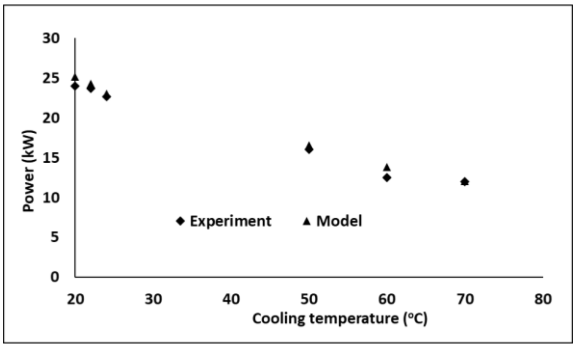

Figure 17. Comparative of motor power based on model and experiment.

5. Conclusion

Effect of cooling temperature and cooling media on axial flux BLDC motor power and efficiency were presented. 20 kW of BLDC motor performance with air cooling and water cooling was investigated numerically and experimentally. From numerical analysis, the motor power was calculated based on input power minus losses power and efficiency was calculated based power input and power output. The calculated power was compared with measured power that was conducted on motor test bed. The Numerical and experimental method shows that cooling temperature has significant effect on power and efficiency of motor. Lower of cooling temperature produces higher motor power and efficiency. Based on experimental investigation, at normal condition, maximum power of water cooled BLDC motor can generate power of 25 kW and 81.0 %efficiency, while air cooled motor produces lower power and efficiency of 19.1 kW and 65.0 % respectively. Comparative analysis of motor performance based on model and experiment was presented as well. Maximum motor power calculated by model is slightly higher than that measured by experiment. It can be explained that in modeling, the friction losses on the bearings are neglected, while in the experiment, the friction loss remains a variable that affects the motor power output

Acknowledgment

This research paper is funded from Indonesia Government in *"Penelitian Terapan Unggulan Perguruan Tinggi"* scheme year 2019.

References

[1] Qingyong Z., Wanga Y., Lina W., Luoa Y., Wua X., "Contact mechanics analysis and optimization of shape modification of electric vehicle gearbox". Jordan Journal of Mechanical and Industrial Engineering, Volume 14,Number 1, March. 2020 . P 15 – 24.

[2] Vu, Duc Thuan, "New cooling system design of bldc motor for electric vehicle using computation fluid dynamics modeling".Journal of the KSTLE Vol. 29, No. 5, October 2013, pp. 318~323.

[3] Fasil, Muhammed, "Numerical and experimental investigation of heat flow in permanent magnet brushless dc hub motor".SAE International J. Alt. Power./ Volume 4, Issue 1 (May2015).

[4] Cezario, Cassiano A., "Transient thermal analysis of an induction electric motor".18th International Congress of Mechanical Engineering November 6-11, 2005, Ouro Preto,MG

[5] Kuria, James dan Hwang, Pyung.Optimizing heat sink geometry for electric vehicle bldc motor using CFD. Kenyatta University of Agriculture andTechnology, Kenya, 2017

[6] Chandrakant, Shinde S., "Numerical and experimental analysis of heat transfer through various types of fin profiles by forced convection".International Journal of Engineering Research & Technology (IJERT) ISSN: 2278-0181 Vol. 2 Issue 7, July –2013

[7] Faiz, J., Ganji, B., Carstensen, C.E.,"Temperature rise analysis ofswitched reluctance motors due to electromagnetic losses".IEEE Trans. Magn., 2009, **45**, (7), pp. 2927–2934

[8] Samadifar M and Toghraie D., "Numerical simulation of heat transfer enhancement in a plate-fin heat exchanger using a new type of vortex generators". Aplied Thermal Engineering vol.133, March 2018, pp.671-681.

[9] Toghraie D., Afrand M.,Zadeh A.R., Akbari H.A., "Numerical investigation on the flow and heat transfer of a multi-lobe particle and equivalent spherical particles in a packed bed with considering the wall effect". International Journal of Mechanical Sciences, Vol 138-139 April 2018 pp.350-367.

[10] Toghraie D.,Moraveji A., "Computational fluid dynamics simulation of heat transfer and fluid flow characteristics in a vortex tube by considering the various parameters".International Journal of Heat and Mass TransferVol. 113, Oct. 2017, pp. 432-443

[11] Deriszadeh A, de Monte F. "On Heat Transfer Performance of Cooling Systems Using Nanofluid for Electric Motor Applications". *Entropy.* 2020; 22(1):99. https://doi.org/10.3390/e22010099

[12] Deriszadeh, F. de Monte, M. Villani and L. Di Leonardo, "Hydrothermal performance of ethylene glycol and water mixture in a spiral channel for electric motor cooling," *21st European Conference on Power Electronics and Applications (EPE '19 ECCE Europe),* 2019, pp. 1-10, doi: 10.23919/EPE.2019.8914967.

[13] Deriszadeh A, de Monte F.,"Performance evaluation of the electric machine cooling system employing nanofluid as an

advanced coolant". *ChemEngineering.* 2021;5(3):53. https://doi.org/10.3390/chemengineering5030053

[14] Deriszadeh, A, de Monte, F, & Villani, M., "Numerical thermal performance investigation of an electric motor passive cooling system employing phase change materials". *Proceedings of the ASME 2021 Heat Transfer Summer Conference collocated with the ASME 2021 15th International Conference on Energy Sustainability. ASME 2021 Heat Transfer Summer Conference.* Virtual, Online. June 16–18, 2021. V001T08A006. ASME. https://doi.org/10.1115/HT2021-63506

[15] Ahmad K. A.M, Jawarneh A.M, Ababneh A.K., Dalgamoni H.N., "Numerical investigation of the cooling performance of pcm-based heat sinks integrated with metal foam insertion". Jordan Journal of Mechanical and Industrial Engineering, Volume 15,Number 2, June. 2021. P 191 – 197.

[16] Fu, L. M., Lin, C., Chang, C. L., Chang, J., & Tsai, C. H.,"Numerical investigation into thermal behavior of brushless permanent magnet motors". Advanced Materials Research, 199–200, 1518–1522.

[17] Han, S., Jahns, T.M., Zhu, Z.Q.,"Analysis of rotor core eddy-current losses ininterior permanent magnet synchronous machines". Industry ApplicationsSociety Annual Meeting, Edmonton, Alta, October 2008

[18] NEOREC series neodymium iron boron magnet datasheet'. TDKCorporation, May 2011. Available at: http://tdk.co.jp/

[19] Constantinides, S., The demand for rare earth materials in permanentmagnets. Arnold Magnetic Technologies. Available at: http://arnoldmagnetics.com/, [Accessed 18 July 2019]

[20] Trout, S.R.,"Material selection of permanent magnets, considering thethermal properties correctly". Proc. The electric manufacturing and coilwinding conf., Cincinnati, OH, October 2001.

[21] **Gieras**, Jacek F., **Wang**, Rong-Jie, **Kamper**, Maarten J. Axial flux permanent magnet brushless machinesbook.Springer; 2008.

[22] Zhang, Y., Cheng, M.C., Pillay, P.,"Magnetic characteristics and excess eddycurrent losses". Industry Applications Society Annual Meeting, Houston, TX,2009

[23] Nalakath, S., Preindl, M., Yang, Y., "Modeling and analysis of corelosses of an IPM magnet machine for online estimation purposes". AnnualConf. of IEEE Industrial Electronics Society, Yokohama, Japan, 2015

[24] Mthombeni, T.L., Pillay, P., "Physical basis for the variation of laminationcore loss coefficients as a function of frequency and flux density". AnnualConf. on IEEE Industrial Electronics, Paris, November 2006

[25] Takahashi, N., Morishita, M., Miyagi, D., "Examination of magneticproperties of magnetic materials at high temperature using a ring specimen". IEEE Trans. Magn., 2010, **46**, (2), pp. 548–551

[26] Selection of electrical steels for magnetic cores. AK Steel. Available at:http://aksteel.com/, [Accessed 16 July 2019]

[27] Standard classification of insulating coatings for electrical steels by composition, relative ansulatingability and application. American Societyof Testing and Materials, ASTM A 976-13, 2015

[28] DuPONT NOMEX Paper Type 410.DuPONT. Available at: http://www.dupont.com, [Accessed April 2020]

[29] Chang, C.C., Cheng, C.H., Ke, M.T., "Experimental and numericalinvestigations of air cooling for a large-scale motor".Int. J. Rotating Mach, 2009, pp. 1–7

[30] Yang, Y., Arshad-Ali, K., Roeleveld, J., "State-of-the-art electrifiedpowertrains: hybrid, plug-in hybrid, and electric vehicles".Int. J. Powertrains,2016, **5**, (1), pp. 1–28

[31] Yang, Y., Schofield, N., Emadi, A.,"Integratedelectro-mechanical doublerotorcompound hybrid transmissions for hybrid electric vehicles".IEEETrans. Veh. Techno., 2016, **65**, (6), pp. 4687–4699

[32] Bilgin, B., Magne, P., Malysz, P., "Making the case for electrifiedtransportation". IEEE Trans. Transp. Electrification, 2015, **1**, (1), pp. 4–17

[33] Gerada, D., Mebarki, A., Brown, N.L., "High-speed electricalmachines: technologies, trends, and developments".IEEE Trans. Ind.Electron., 2014, **61**, (6), pp. 2946–2959

[34] Zhang, Y., Ruan, J., Huang, T., "Calculation of temperature rise in aircooledinduction motors through 3-D coupled electromagnetic fluiddynamicand thermal finite-element analysis".IEEE Trans. Magn., 2012, **48**,(2), pp. 1047–1050

[35] Yoheswaran, B., Pullen, K.R.,"Flow and convective heat transfer in disk-typeelectric machines with coolant flow". Int. Conf. on Electrical Machines(ICEM), 2014

[36] Mohammad S., "Computational fluid dynamics simulation of plate fin and circular pin fin heat sinks". Jordan Journal of Mechanical and Industrial Engineering, Volume 10,Number 2, June. 2016. P 99 – 104.

JJMIE

Volume 16, Number 4, September. 2022
ISSN 1995-6665
Pages 493 – 502

Jordan Journal of Mechanical and Industrial Engineering

Combination of Single Channel Blind Source Separation Method and Normal Distribution for Diagnosis of Bearing Faults

Mohamed Lotfi Cherrad[1,*], Hocine Bendjama[2], Tarek Fortaki[3]

[1]*Dept of Electronic Engineering, Faculty of Technology, University of Batna 2, Batna, Algeria and Searcher ., Research Center in Industrial Technologies CRTI, P.O.Box 64 Cheraga, Algiers, Algeria.*
[2] *Research Center in Industrial Technologies CRTI, P.O.Box 64 Cheraga, Algiers, Algeria.*
[3] *Dept of Electronic Engineering, Faculty of Technology, University of Batna 2, Batna, Algeria*

Received 25 Oct 2021 *Accepted 13 Jun 2022*

Abstract

In most industrial environments, vibration analysis is widely used for fault diagnosis of rolling bearings. The vibration signal measured from a bearing represents a mixture of motor vibration, rolling vibration, noise, and other sources. Due to the high cost of devices and limited space, only one sensor can be installed to measure this signal. In this paper, a feature extraction method based on Single Channel Blind Source Separation (SCBSS) and Normal Distribution (ND) is proposed for vibration monitoring of rolling element bearings. To decompose the bearing signal, SCBSS is applied for separating the different sources. Because ND is sensitive to the type of fault, it is used as criterion to find an output that contains the maximum information about the fault by removing the other sources. In fact, the obtained signal contains other vibrations which affect the correct source of fault. A second SCBSS filter is, therefore, proposed to decompose the selected source and thus improves the performance of fault diagnosis. The application of the proposed method is carried out on a deep groove ball bearing with outer race fault, ball fault, and inner race fault in order to better validate the diagnosis results.

Keywords: Vibration analysis, Fault diagnosis, Single Channel Blind Separation Source, Normal Distribution, Rolling bearing.

1. Introduction

The vibration monitoring and fault diagnosis of rotating machines is the most important strategy to guaranty the operating conditions of such equipment [1-2-3]. The main objective is to monitor and know the state of the machines at all times in order to detect a failure early [4-5].

The rolling element bearing is the most important components of rotating machines and their load capacity and reliability are subject to high demands. The malfunction of rolling bearings may cause abnormal vibration and undesirable noise [6]. Their monitoring is therefore a serious subject for researchers to improve the bearing performance.

In the industrial field, the measured vibration signal of rolling bearings is a mixture of vibration from motor, rolling element, other sources and the noise [7]. The Blind Source Separation (BSS) method, called also ICA algorithm (Independent Component Analysis), is one of the most effective methods for solving the multi-component or multi-source signal problems [8], and it is used to separate or recover unknown source signals through the signals observed in cases where the source signals cannot be acquired precisely [9].

In many cases, only one sensor can be installed for monitoring mechanical equipment due to the high cost of devices and limited space. Therefore, research on adequate single-channel separation methods to separate the sources from each other using only one sensor, is of great interest [10]. Among them we find the Single Channel Blind Source Separation method (SCBSS) [11]. SCBSS is a special case of BSS, which must satisfy the condition that the number of sensor signals is less than the number of source signals [12]. Especially, it requires only a single sensor to separate multiple source signals [13]. A large number of SCBSS applications has been studied and documented, e.g. Sun et al [14] Used an adaptive multiscale generalized morphology filter (AMGMF) combined with adaptive fast ensemble empirical mode decomposition (AFEEMD) for diagnosis of the composite failure of the rotor system. Xu et al [15] combined EEMD, PCA and Robust ICA for diagnosing of bearing faults. Xiong et al [16] proposed an algorithm based on SCBSS, Complementary EEMD and PCA for motion artifact reduction in ambulatory ECG signals. He et al [17] presented a new SCBSS based on the multi-channel mapping and Independent Component Analysis (ICA) to separate the mixed signal. In the same context, the SCBSS method is widely used in industry, especially for combined fault problems [15-17]. It effectively isolates the mechanical fault for each part individually [18]. Compared to EEMD. Although EEMD algorithm can effectively reduce the mode mixing problem, there are still problems such as empirical selection of parameters and time consuming [19]. In addition, rotating mechanical sampling signals often contain

---

[*] Corresponding author e-mail: cherradlotfi@gmail.com.

strong background noise, in which the impact signal is the main cause of EEMD aliasing. Therefore, it is necessary to filter the signal in order to reduce noise interference before EEMD decomposition

In fact, the vibration signal of rolling bearings, even without noise, is a signal with several sources or components [7]. For this purpose, there should be close attention paid to the decomposition and analysis of multi-components signals. There are several methods of decomposition exist such as: Empirical Mode decomposition [20], Wavelet Decomposition [1-21] and BSS. In the present work, the SCBSS method is applied for separating or decomposing the multi-components bearing signal into different sources in order to extract the source with useful information by eliminating the unwanted signals and interferences.

In this paper, we propose to use a combination between SCBSS and ND as a selection criterion. First, a SCBSS filter is used to decompose the measured vibration signal into a series of sources, and then the ND and its mean are employed to select the source component that contains the most characteristic fault information. The envelope spectrum is applied to explore the fault information upon the appearance of the fault characteristic frequencies.

Knowing that the signal of a bearing has several components, so there is an unclear extraction of the fault characteristics in the frequency spectrum, which affects the performance of the bearing fault diagnosis. To overcome this difficulty, the resulting signal from the SCBSS filter is again injected into the same filter. Finally, to assess the quality of recovered signal; the kurtosis, Signal-to-Noise Ratio (SNR) and Mean Square Error (MSE) are calculated for each SCBSS output.

The remaining sections are organized as follows. Section 2 presents the proposed method and the mathematical formulations of SCBSS and ND. Section 3 describes the bearing test rig and the bearing characteristic frequencies. Section 4 discusses the obtained diagnosis results and evaluates the proposed method by calculating the kurtosis, the SNR and the MSE. Finally, Section 5 presents our concluding remarks.

2. Theoretical Descriptions:

2.1. Blind Source Separation (BSS):

BSS is a signal processing technique, addressed specially for recovering multiple independent sources from their mixtures. It is closely related to Independent Component Analysis (ICA) [11]. When monitoring and fault diagnosis of mechanical equipment, the M observations, which represent the outputs of the M sensors, are the linear combinations of the N sources. In this way, the output observation of the ith sensors is defined as:

$$X_i = \sum_{j=1}^{N} a_{ij} s_j + n_i, i = 1,2,...M \qquad (1)$$

Where $X_{1,..M}$ denote the observations, $s_{1,...N}$ denote the sources, a_{ij} is the linear combination coefficient and n_i denotes the environment noise received by the ith sensor.

The noise may be considered as a source signal, in this way, the mathematical model of BSS could be shown as: ith sensor.

The linear BSS can be expressed as follows:

$$X(t) = AS(t) \qquad (2)$$

Where $X \in R^{M+1}$ is the observation vector, $A \in R^{M*N}$ the unknown mixing matrix, $S \in R^{N+1}$ the unknown source vector.

Here, assuming the mixing matrix A is invertible and the sources are statistically independent. The hypothesis of independence between the sources is physically possible because their origins are different.

The BSS is based on the estimation of the separation matrix B to calculate Y, which can be expressed as follows:

$$Y(t) = BX(t) = BAS(t) \qquad (3)$$

Where Y (t) is an estimate vector of the source signal S (t) and B is the separating matrix. The basic principle of the BSS method is illustrated in Figure (1).

2.2. Normal Distribution (ND):

ND is a super Gaussian shape [22]. It is applied, in the present work, as a selection criterion to find the source that has more information about the defect of the rolling element bearing. The ND function is given as [23]:

$$h = f\left(\frac{s}{\mu,\sigma}\right) = \frac{1}{\sigma\sqrt{2\pi}} e^{-\frac{(S-\mu)^2}{2\sigma^2}} \qquad (4)$$

Where S [$s_1, s_2 \ldots, s_N$] is a vector, μ the mean of vector S and σ its standard deviation. They are defined as follows:

$$\mu = \frac{1}{N}\sum_{i=1}^{N} S_i \qquad (5)$$

$$\sigma = \sqrt{\frac{1}{N}\sum_{i=1}^{N}(S_i - \mu)^2} \qquad (6)$$

2.3. Proposed Method:

The Figure (2) illustrates the steps of the proposed algorithm. Its principle is described as follows: first, we insert a segment of the input signal into the SCBSS filter in order to reduce the calculation time; this segment must contain the same characteristics of the original signal. After applying SCBSS filter, two outputs are resulted. In order to extract the source that contains most of the fault information and removes the unwanted signal, the ND and its mean is applied to each output. The selected signal is again injected into the SCBSS filter to obtain a clear source with useful information.

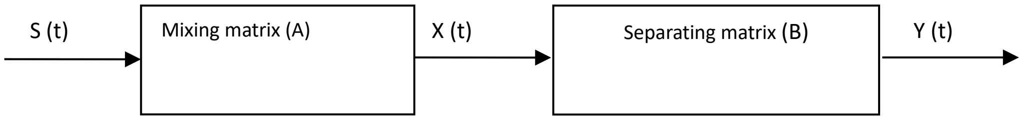

Figure 1. Principle of BSS method.

3. Experimental setup

In this study, we used the vibration data obtained from the Case Western Reserve University Bearing Data Center [24]. As illustrated in Figure (3), vibration data was collected using accelerometers, which are attached to the housing with magnetic bases. The unit of measurement is mm/s^2 (Gravity) and the duration of each vibration signal was 10 seconds. The vibration data were collected at 12000 samples per second, for four different bearing conditions: (1) Bearing without fault i.e. Normal state (N); (2) Bearing with Outer Race Fault (ORF); (3) Bearing with Ball Fault (BF) and (4) Bearing with Inner Race Fault (IRF). For ball and inner race cases, the sizes of the different faults are: 0.1778, 0.3556, and 0.5334 mm. For outer race case, the sizes of the faults are either 0.1778 or 0.5334 mm. The vibration data was recorded with four rotation speeds; 1797, 1772, 1750 and 1730 rpm corresponding respectively to 30, 29.5, 29.1 and 28.8 Hz.

The characteristic frequencies of defective bearing with ORF, BF and IRF computed at rotation frequency of 30 Hz, are respectively 107.8 Hz, 139 Hz and 161.8 Hz. The Figure (4) shows the segments of their time measurements.

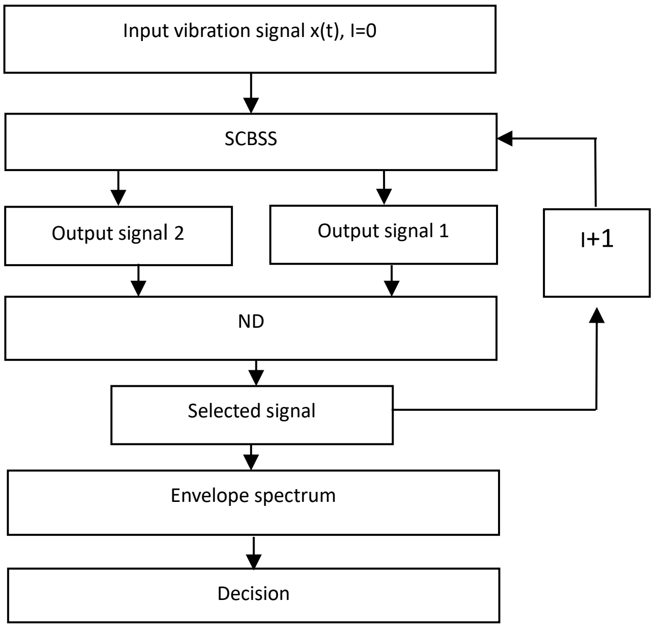

Figure 2. SCBSS-ND algorithm

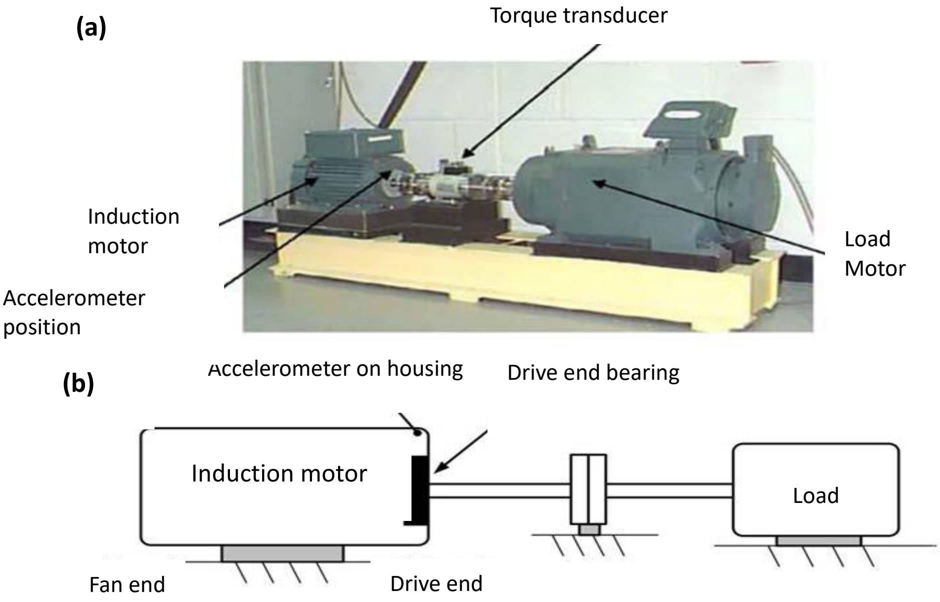

Figure 3. (a) Bearing test rig and (b) its schematic description.

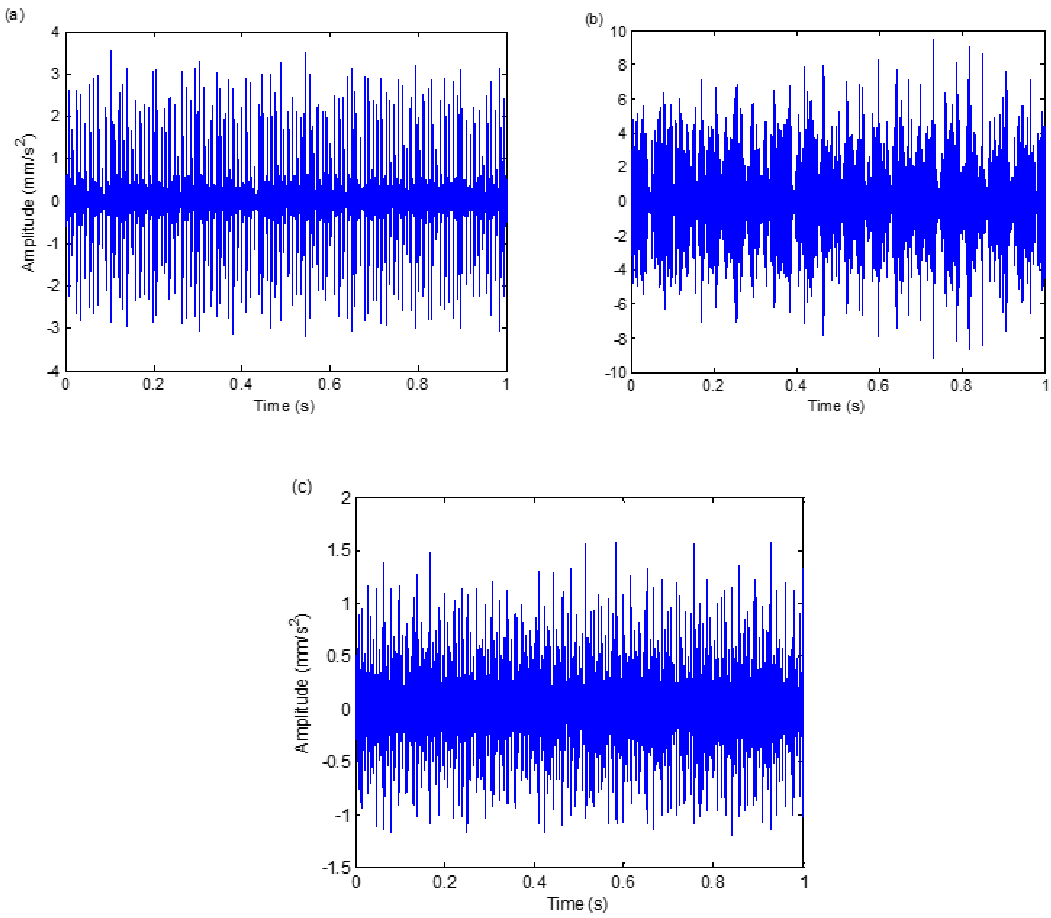

Figure 4. Measured vibration signals: (a) ORF, (b) BF and (c) IRF

4. Results and Discussion

In this section, we validate the effectiveness of the proposed method by using the SCBSS-ND algorithm and the bearing experimental signals mentioned previously. In fact, to separate the different sources by inserting the complete raw vibration signal into the SCBSS filter takes a lot of computing time. For this purpose, we truncate the original signal into segments of length, at least, 6 complete rotations as long as the motor speed is ranging from 1730 to 1797 rpm, in order to have the same characteristics of the full signal. Here the segment of length 8192 point is selected and a Blackman window to adjust this truncation is applied.

The selected signal is injected into the SCBSS filter with good control over its properties, in which the window length of this filter is 1024 and the format of the extracted sources is the same as the truncation window (Blackman window). In this section, the proposed algorithm is applied to analyze the vibration signals acquired from the rolling element bearing with the three considered conditions; ORF, BF and IRF. The shaft rotation speed is 1797 rpm (30 Hz) and the characteristic frequencies of defective bearing are 107.8 Hz for ORF, 139 Hz for BF and 161.8 Hz for IRF. The measured vibration signals are plotted in the experimental part (section 3, Figure (4) (a, b and c)).

First, the SCBSS method is used to decompose the raw fault signals acquired from a single sensor, into temporal sources in order to select, among them, the most informative. For the considered cases of rolling bearing, two outputs are resulted; source1 and source2, which are illustrated in Figure (5). This indicates physical that the measured vibration signal of rolling bearings is a multi-component signal which includes many sources and noise. The noise component is an independent source in relation to other vibration signals. Although, the vibration measured from the rolling bearing, even without noise, is a signal with several sources or components.

The ND and its mean are used to analyze the fault information of each source; they are presented in Figure (6) (a, b and c) and listed in Table (1). Based on the largest normal distribution mean values which are 1.8651, 1.0917 and 2.0682 for ORF, BF and IRF respectively, the first source, which contains the most characteristic information about the fault, is selected for all considered cases, as shown in the Table (1), the normal distributions of the source1 remain constant in all cases, and it is also symmetrical around μ on x axis, where the shape of the distribution curve is Gaussian (see, Figure (6) (left) (a, b and c)), while the normal distribution curves of the source 2 are not constant in all cases. Besides being heterogeneous and irregular, they do not have the same beginning and the same end, and they are also not symmetrical around μ on x axis (Figure (6) (right) (a, b and c)), which justify our choice of the source1, the measured vibration signal is periodic shocks contaminated by noise. For this reason, the ND of source1 is regular, while the noise distribution is random and irregular.

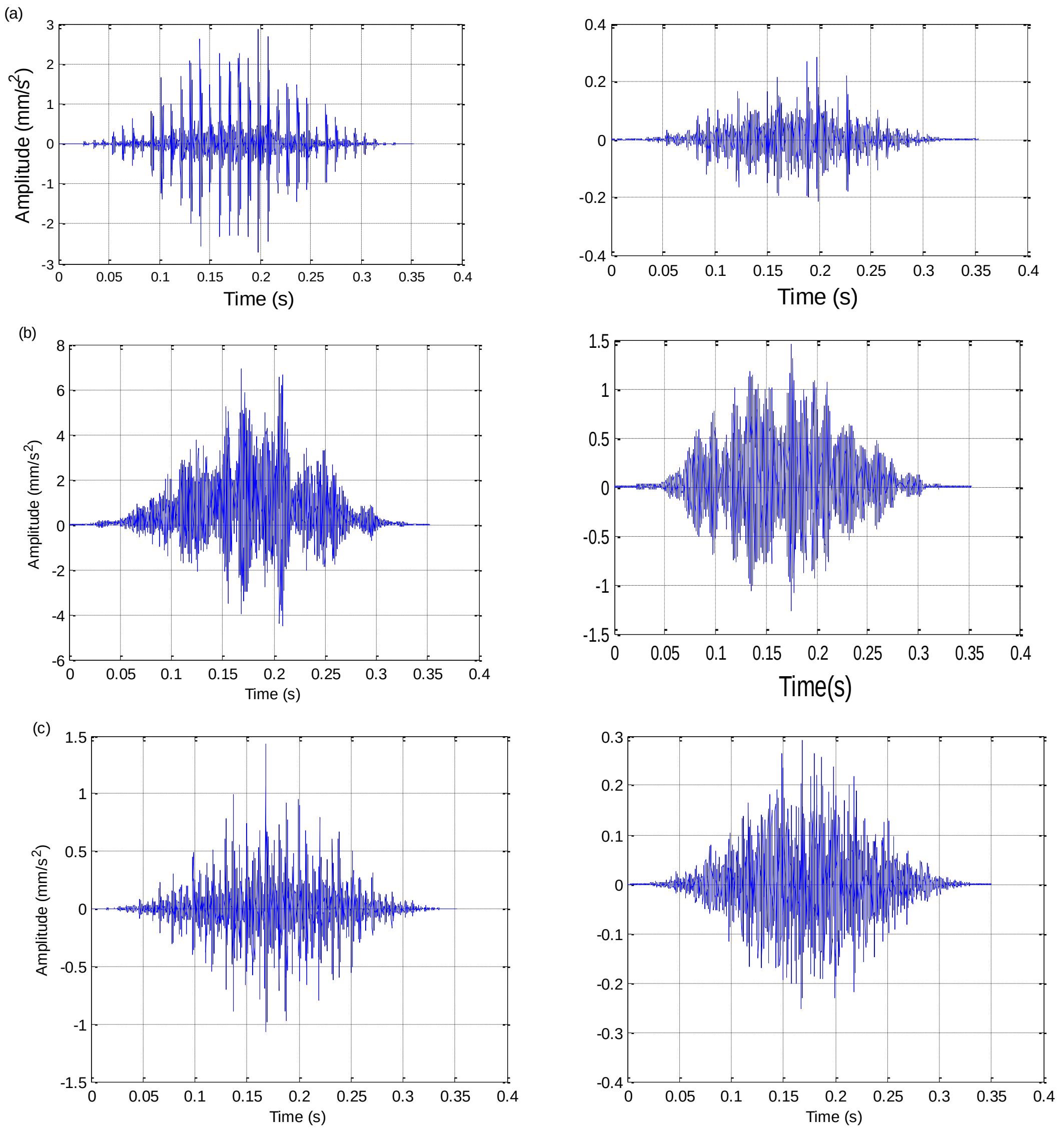

Figure 5. Temporal representation of source1 (left) and source2 (right) for the bearing with: (a) ORF, (b) BF and (c) IRF.

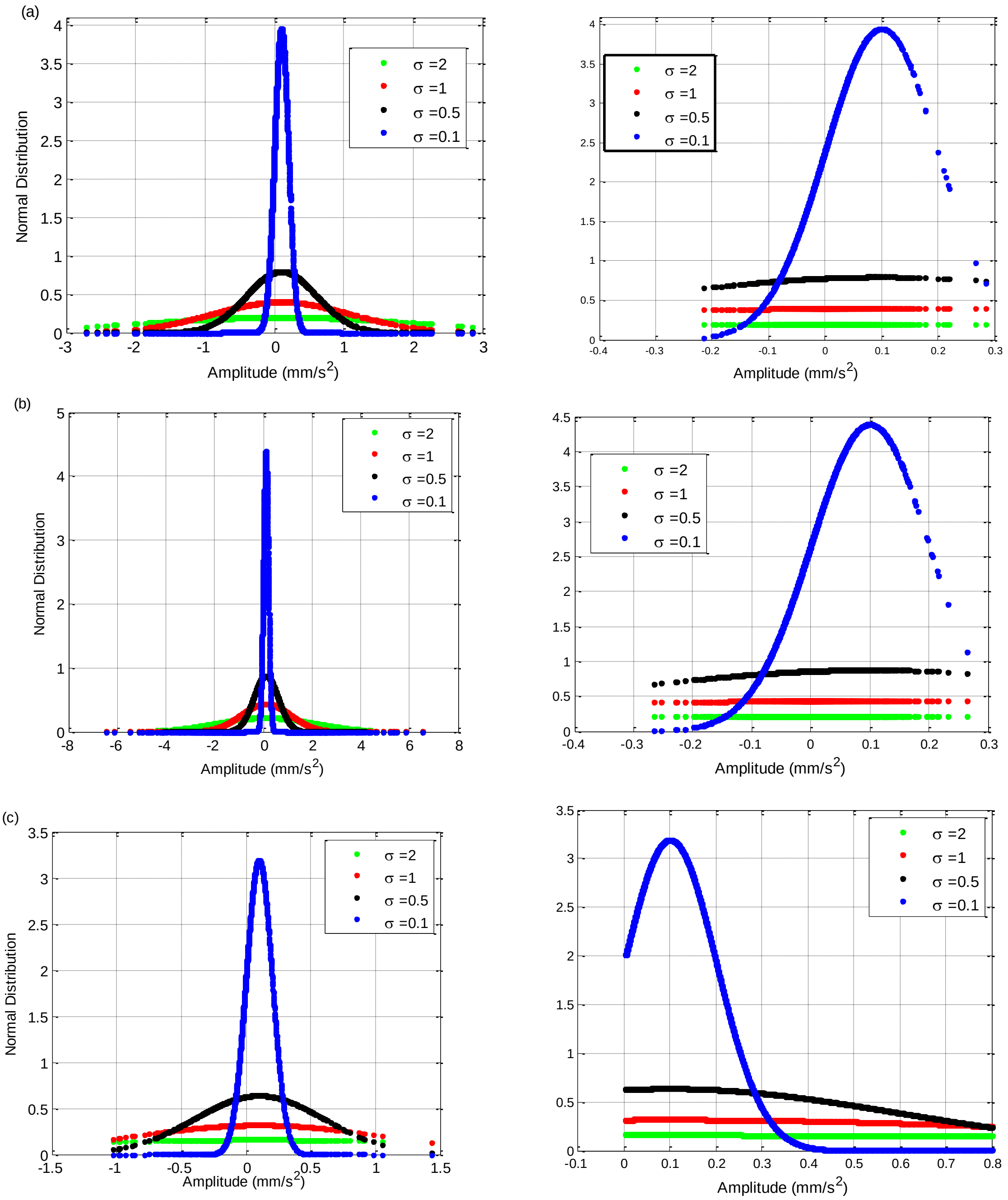

Figure 6. Normal distributions, with µ=0.1, of source1 (left) and source2 (right) for the bearing with: (a) ORF, (b) BF and (c) IRF.

Table 1. Mean of ND of the two sources (µ=0.1).

	ORF		BF		IRF	
	Source1	Source2	Source1	Source2	Source1	Source2
σ=2	0.1963	0.1992	0.1987	0.1933	0.1986	0.1533
σ=1	0.3797	0.3966	0.3464	0.3517	0.3925	0.2762
σ=0.5	0.7798	0.7071	0.5637	0.4839	0.7529	0.4113
σ=0.1	1.8651	0.6429	1.0917	0.2279	2.0682	0.5775

Figure (7) represents the envelope spectra of source1 of the rolling bearing with ORF, BF and IRF. The characteristic frequency of ORF (fORF) and its seven successive harmonics are clearly noted (see, Figure (7) (a)). These frequency components are not well detected in their exact positions as shown in Table (2). In this table, the calculated delta represents the difference between the theoretical frequency and the detected frequency of the bearing fault. On the envelope spectra of the selected source of BF and IRF cases of Figure (7) (b) and (c) respectively, the characteristic frequencies of BF and IRF are clearly detected and their first harmonics can barely be recognized with the presence of some spectral interference lines. The computed values of delta index, listed in Table (2), show that the principal harmonics are not detected in their exact positions. The presence of shocks in the signal clearly indicates the presence of the defect. They are represented on the spectrum by synchronous peaks.

The selected source, even without noise, is a multi-components signal which is again injected into the SCBSS filter to eliminate the unwanted signals in order to further improve the obtained results, are often produced by interference of vibration from motor, rolling element and other sources. The Figure (8) (a, b and c) represents respectively the time domain of source1 of the defective bearing with ORF, BF and IRF. From this figure, there is a significant decrease in parasites and the emergence of pulses appears clear and harmonious, especially in Figure (8) (a) and Figure (8) (c), as well as the noise is almost entirely eliminated, which will be more apparent on the spectrum.

The envelope spectrum of the resulting signal is illustrated in Figure (9). From Figure (9) (a), it is clear that the ORF frequency (fORF) and its two harmonics (2□fORF and 3□fORF) are exactly identified. In Figure (9) (b), the peak frequencies of BF are clearly detected, in which the first and second harmonic frequencies are also precisely identified. Finally, the characteristic frequency of IRF (fIRF) and its two successive harmonics (2□fIRF, 3□fIRF) are correctly identified (see, Figure (9) (c)). In addition, we also note from the Table (3) that the calculated values of the delta decrease for each harmonic frequency.

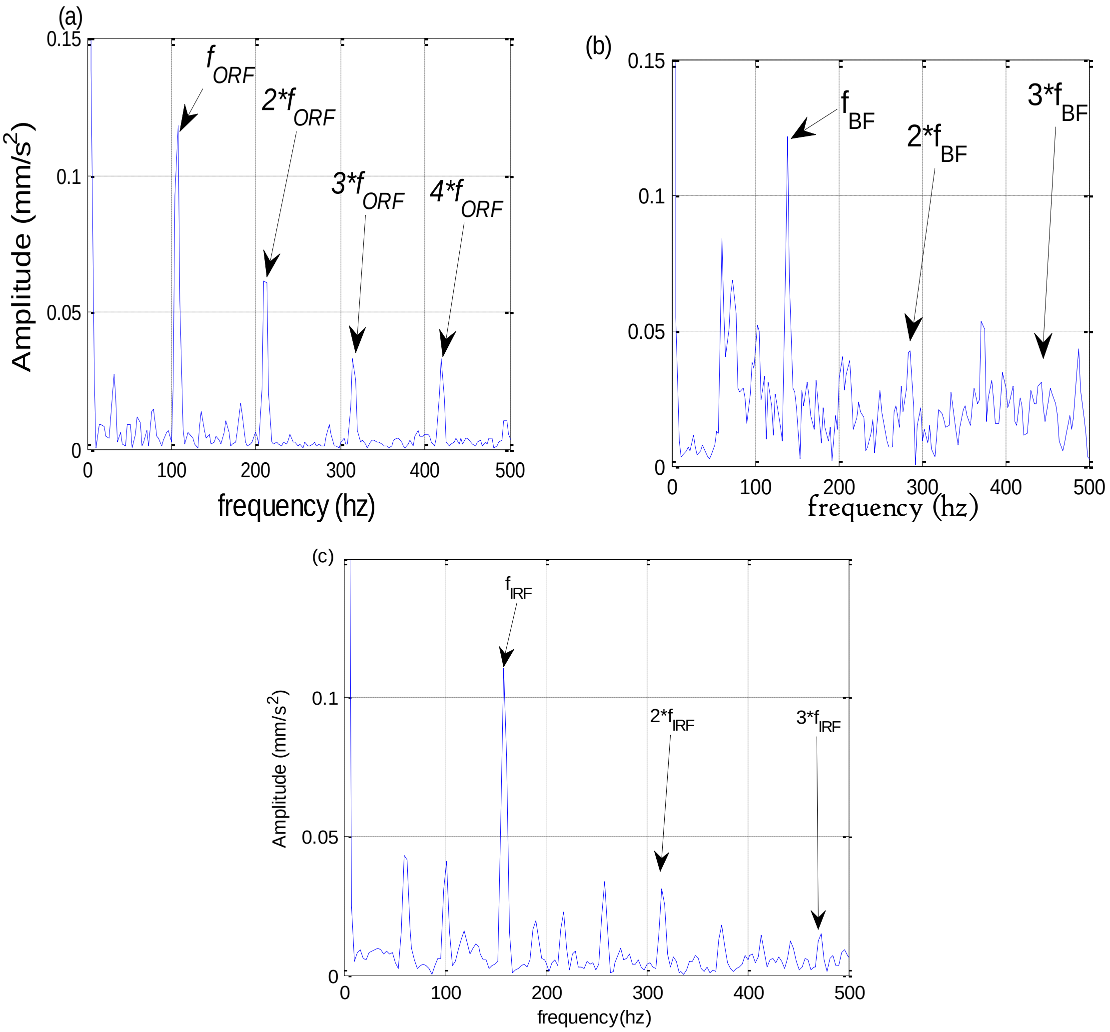

Figure 7. Frequency spectrum of source1 resulting from the first SCBSS filter: (a) ORF, (b) BF and (c) IRF.

Table 2. ORF, BF and IRF frequencies detected from the first SCBSS filter.

ORF		BF		IRF	
f_{ORF} and harmonics (Hz)	Delta (Hz)	f_{BF} and harmonics (Hz)	Delta (Hz)	f_{IRF} and harmonics (Hz)	Delta (Hz)
107.8	0	139	0	161.8	0
209.9	5.7	286.5	8.5	323.6	0
314.9	8.5	420.6	3.6	486.79	1.39
419.9	11.3	544.7	11.3	658.4	11.2

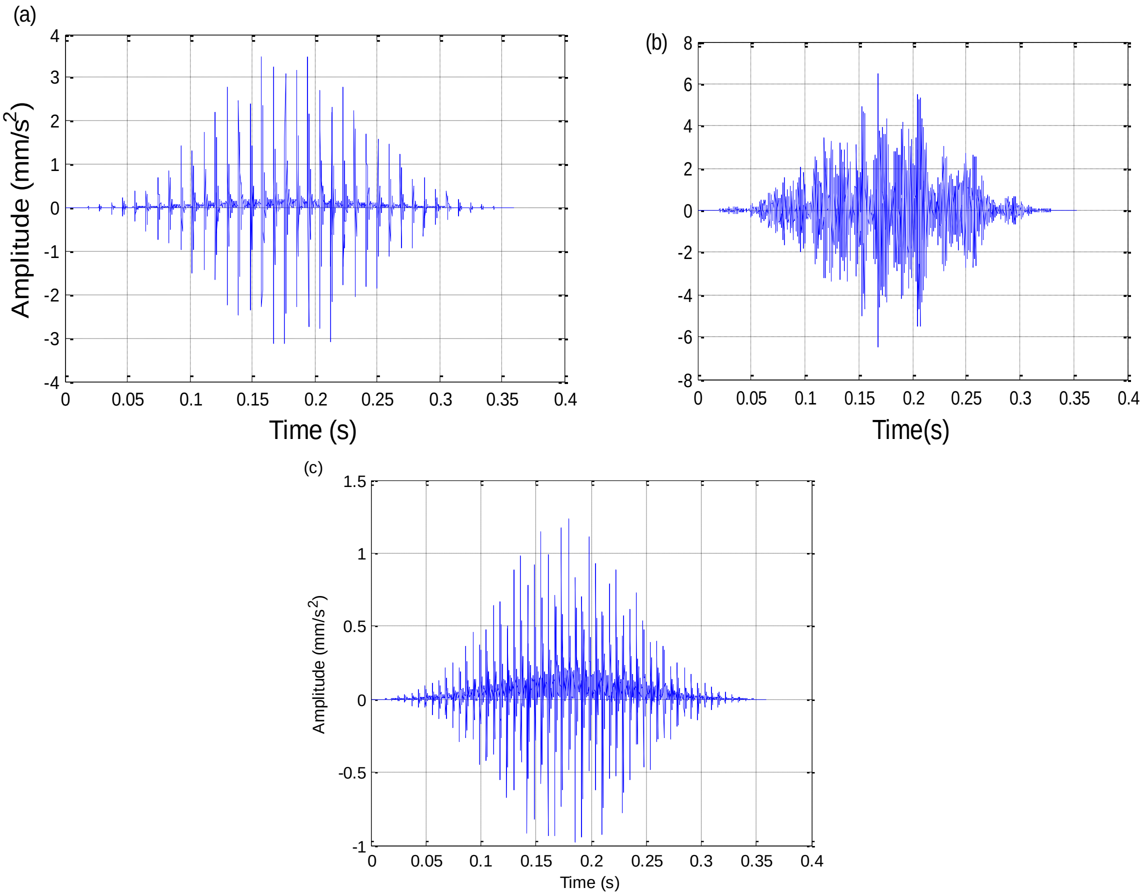

Figure 8. Temporal representation of source1 obtained from the second SCBSS filter: (a) ORF, (b) BF and (c) IRF.

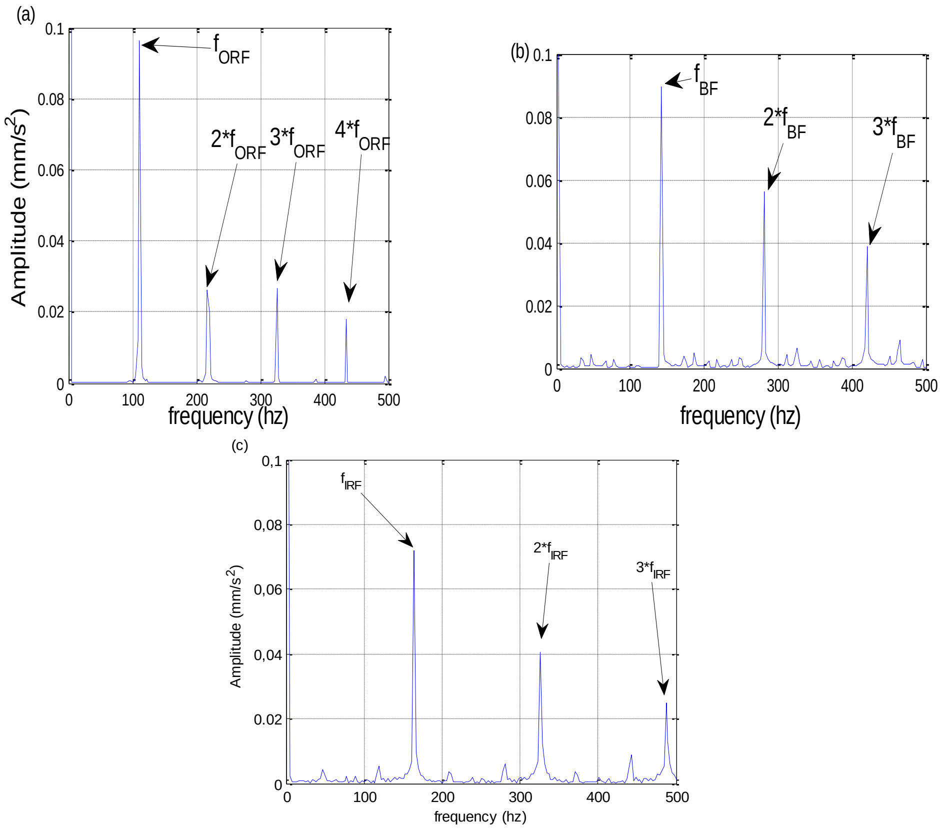

Figure 9. Frequency spectrum of source1 resulting from the second SCBSS filter :(a) ORF, (b) BF and (c) IRF.

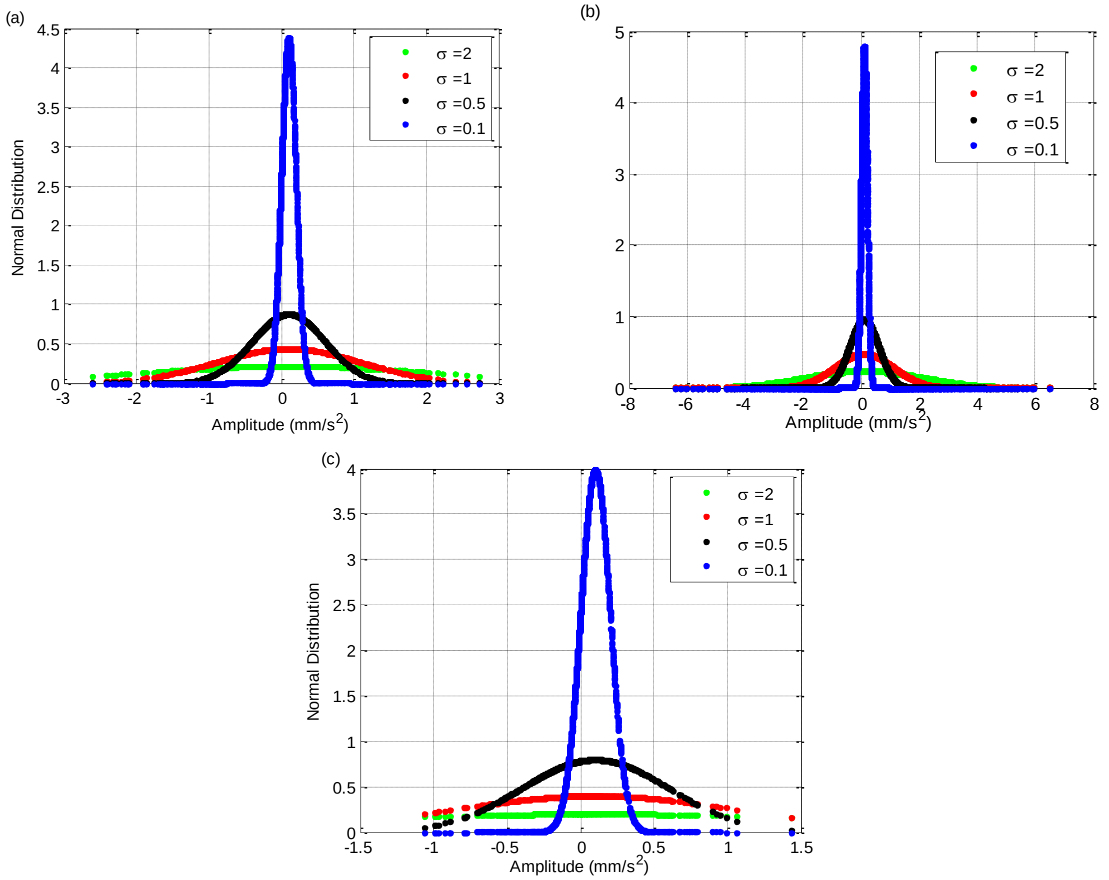

Figure 10. Normal distributions of the signal resulting from the second SCBSS filter, with μ=0, of: (a) ORF, (b) BF and (c) IRF.

Table 3. ORF, BF and IRF frequencies obtained from the second SCBSS filter.

ORF		BF		IRF	
f_{ORF} and harmonics (Hz)	Delta (Hz)	f_{BF} and harmonics (Hz)	Delta (Hz)	f_{IRF} and harmonics (Hz)	Delta (Hz)
107.8	0	139	0	161.8	0
215.6	0	278	0	323.6	0
323.4	0	420.3	3.3	485.49	0
425.5	5.7	559.4	3.4	648.4	1.2

Table 4. Mean of ND of the signal obtained from the second SCBSS filter (μ=0.1).

	ORF	BF	IRF
σ=2	0.2186	0.2191	0.1992
σ=1	0.4326	0.4361	0.3966
σ=0.5	0.8354	0.8564	0.7793
σ=0.1	2.4313	2.3767	2.3856

By comparing normal distributions and their means of vibration signals resulting from first and second SCBSS filters, the Figure (10) (a, b and c) shows that the distribution of the second signal increases over the y axis, also it is more accurate and symmetrical around μ on the x axis. Table (4) summarizes the calculated values of the means of the distributions; it shows that the obtained values from the second SCBSS filter are larger than those calculated from the first filter (see Table (1)).

In order to verify the quality of the resulting signal from SCBSS filters, Table (5) shows respectively the computed values of kurtosis, SNR and MSE. From all obtained results, the signal containing only information about rolling bearing fault is correctly recovered.

Table 5. Kurtosis, SNR and MSE values for each SCBSS.

	Kurtosis	SNR	MSE
Before applying BSS	7.706	-	-
First SCBSS	17.07	11db	8.38 *10-6
Second SCBSS	20.34	23db	2.56*10-11

5. Conclusion

This paper presents a combined method based on Single Channel Blind Source Separation (SCBSS) and Normal Distribution (ND) to analyze and detect bearing degradation. SCBSS filters are used to decompose the vibration signals measured from defective bearings with outer race fault, ball fault and inner race fault, into a series of sources. To select the source that contains the significant information about the fault, the ND and its mean are used as principal criterion.

The validation of the obtained results by the calculation of kurtosis, SNR and MSE parameters showed a precise detection of the characteristic frequencies of the bearing faults and their harmonics, by eliminating the various interferences. By comparing with BSS alone and EMD, the method proposed, in this paper, leads to the best separation performances for most types of mixture with an extraction precision of the characteristic frequencies of the bearing faults and their harmonics in the shortest possible time.

Acknowledgments

The authors would like to thank Prof. K.A. Loparo of Case Western Reserve University for providing bearing vibration data sets .This paper is also supported by Department of Electronic Engineering of University of Batna 2 and Research Center in Industrial Technologies CRTI.

References

[1] H. Bendjama, M.S. Boucherit, “Wavelets and Principal Component Analysis Method for Vibration Monitoring of Rotating Machinery’’. Journal of Theoretical and Applied Mechanics, Vol. 54, No. 2, 2016, 659-670.

[2] M. Nicodim, H. Gheorghiu, “Identification of faults rolling bearings through vibration and shock impulses analysis”. U.P.B. Sci. Bull., Series D, Vol. 73, No. 1, 2011, 63-70.

[3] S. K. Sar , R. Kumar , “Hasty Fault Diagnosis of a Rotating Machinery Hinge on Stalwart Trippy Classifier with Robust Harmonized Swan Machine” .Jordan Journal of Mechanical and Industrial Engineering Vol. 14, No.2 ,2020, 223 – 236.

[4] R. Bouhali, K. Tadjine, H. Bendjama, M. N. Saadi, “Fault diagnosis of bladed disc using wavelet transform and ensemble empirical mode decomposition”. Australian Journal of Mechanical Engineering, Vol. 18, No. sup1, 2020, S165-S175.

[5] V. V. Rao, C. Ratnam, “Estimation of Defect Severity in Rolling Element Bearings using Vibration Signals with Artificial Neural Network”. Jordan Journal of Mechanical and Industrial Engineering, Vol. 9, No. 2,2015.

[6] A. Bouzaouit, E. Hadjadj Aouel, O. Bennis, “Stochastic modeling for the follow-up the bearing degradation”. U.P.B. Sci. Bull., Series D, Vol. 79, No. 1, 2017, 209-218.

[7] M .Zhao, J. Lin, X. Xu, X. Li, “Multi-Fault Detection of Rolling Element Bearings under Harsh Working Condition Using IMF-Based Adaptive Envelope Order Analysis”, Sensors, Vol. 4, No. 11, 2014, 20320-20346.

[8] S. Delvecchio, J. Antoni, “Extraction of angle deterministic signals in the presence of stationary speed fluctuations with cyclostationary blind source separation”. Mechanical Systems and Signal Processing, Vol. 27, 2012, 350-361.

[9] A. Kouadri, K. Baiche, M. Zelmat, “Blind source separation filters-based-fault detection and isolation in a three tank system”. Journal of Applied Statistics, Vol. 41, No. 8, 2014, 1799–1813.

[10] L. Sun, K. Xie, T. Gu, J .Chen, Z. Yang, “Joint dictionary learning using a new optimization method for single-channel blind source separation”. Speech Communication, Vol. 106, 2019, 85-94.

[11] H. Wang, L. Li, X. Gong, W. Du, “Blind source separation of rolling element bearing single channel compound fault based on Shift Invariant Sparse Coding’’. Journal of Vibroengineering, Vol. 19, No. 3, 2017, 1809-1822.

[12] X. Cai, X. Wang, Z. Huang, F. Wang, “Single-Channel Blind Source Separation of Communication Signals Using Pseudo-MIMO Observations”. IEEE Communications Letters, Vol. 22, No. 8, 2018, 1616-1619.

[13] X. Li, P. Fu, “Application of Single-channel Blind Source Separation Based on EEMD in Bearing Fault Diagnosis”. China Mechanical Engineering, Vol. 25, No. 7, 2014, 924-930.

[14] H. Sun, H. Wang, J. Guo, “A single-channel blind source separation technique based on AMGMF and AFEEMD for the rotor system’’. IEEE Access, Vol. 6, 2018, 50882-50890.

[15] W. Xu, X. Yan, “Application of single channel blind separation algorithm based on EEMD-PCA-robust ICA in bearing fault diagnosis’’. International Journal of Communications, Network and System Sciences, Vol. 10, No. 8, 2017, 138-147.

[16] F. Xiong, D. Chen, “CEEMDAN- IMFx-PCA-CICA: an improved single-channel blind source separation in multimedia environment for motion artifact reduction in ambulatory ECG’’. Complex & Intelligent Systems, 2020, 1-15.

[17] P. He, T .She, W. Li, W. Yuan, “Single channel blind source separation on the instantaneous mixed signal of multiple dynamic sources ’’. Mechanical systems and signal processing, Vol. 113, 2018, 22-35.

[18] D. Yang, C. Yi, Z. Xu , Y. Zhang, M. Ge, C. Liu, “Improved tensor-based singular spectrum analysis based on single channel blind source separation algorithm and its application to fault diagnosis’’. Applied Sciences, Vol. 7, No. 7, 2017, 418.

[19] X. M. Xue, J. Z. Zhou, Y. H. Xu, W. L. Zhu ,C.S. Li, “An adaptively fast ensemble empirical mode decomposition method and its applications to rolling element bearing fault diagnosis’’, Mech. Syst. Signal Process, Vol. 62, No. 2015,2015,444-459.

[20] B. Chen, P. Yin, Y. Gao, F. Peng, “Use of the correlated EEMD and time-spectral kurtosis for bearing defect detection under large speed variation”. Mechanism and Machine Theory, Vol. 129, 2018, 162-174.

[21] J. Chebil, G. Noel, M. Mesbah, M. Deriche, “Wavelet decomposition for the detection and diagnosis of faults in rolling element bearings’’. Jordan Journal of Mechanical and Industrial Engineering, Vol. 3, No. 4, 2009, 260-267.

[22] G. Wang, R. Xue, J. Zhao, “Switching criterion for sub-and super-Gaussian additive noise in adaptive filtering”, in Signal Processing, Vol. 150, No. 5, 2018, 166-170.

[23] C. Forbes, M. Evans, N. Hastings, B. Peacock. Statistical Distributions, Hoboken, NJ, USA: Wiley, Nov. 2010.

[24] K.A. Loparo. Bearing vibration dataset, Case Western Reserve University. Available at: www.eecs. case.edu/laboratory/bearing , 2016.

JJMIE

Volume 16, Number 4, September. 2022
ISSN 1995-6665
Pages 503 – 513

Jordan Journal of Mechanical and Industrial Engineering

Enhancement of Maintenance Efficiency for Liquefied Natural Gas Plant: Operation Factors, Workforce and Productivity Control

Firas Basim Ismail[1*], Ammar Al-Bazi[2], Rami Hikmat Al-Hadeethi[3],
Mohammed Najah Mahdi[4], Abdulaziz Gaber Al-khulaqi[1]

[1]*Power Generation Unit, Institute of Power Engineering (IPE), Universiti Tenaga Nasional (UNITEN), 43000 Kajang, Selangor, Malaysia.*
[2]*School of Mechanical, Aerospace and Automotive Engineering, Coventry University, Coventry, CV1 5FB, UK*
[3]*University of Victoria, London, UK*
[4]*ADAPT Centre, School of Computing, Dublin City University, Dublin 9, Ireland*

Received 10 Dec 2021 *Accepted 20 Jun 2022*

Abstract

Nowadays, to survive in the highly competitive industries, organizations require adapting to the rapid changes in the industrial environment to deliver the products or services with high quality in accordance with the consumer's expectation. In order to achieve maximum efficiency, organizations endeavour to enhance their asset integrity, reliability, availability, productivity, maintenance practice, and concentration on safety and product quality. It is also vital to ensure the highest maintenance efficiency practice in organizations to achieve the best efficiency practice.

Therefore, this paper aims to identify the most influential factors that impact workforce productivity's Wrench Time (WT). Understanding the impacts of these factors on the WT and identifying their causes will provide a clear vision of how the management can allocate the necessary resources to eliminate these impacts.

As a methodology, random sampling is used to determine the sample of observations from a given population. This sample is then used in the pilot test that is conducted to test the reliability of the data collection method. The Day In Life Of (DILO) approach is used to collect data as an observation method that involves the supervisor's participation with the technicians throughout the whole working day. A case study based on one of the largest LNG plants in the Middle East is conducted to verify the achieved maintenance efficiency.

As a result, workforce productivity has increased to 38.1% by changing the monthly workforce plan, leading to a future roadmap to enhance maintenance efficiency by considering more related factors.

Keywords: Maintenance Efficiency, Workforce Plan and Productivity, Wrench Time, DILO.

1. Introduction

Organizations endeavour to enhance their assets' integrity, reliability, availability, and productivity and become more conscious of the product's safety and quality. This improvement leads organizations to achieve maximum performance efficiency and efficient maintenance practice. A market competition force stimulates the organization to close to decide the competitive advantages in every process [1,2].

Generally, maintenance goals in the manufacturing process contribute in several areas [3]. These goals include the plant life's accomplishment, the plant functionality, the environment and safety, the cost-effectiveness of the conservation works, and the efficiency of utilizing the resources.

In most organizations, insufficient capabilities in managing the maintenance will directly affect the company's activities by decreasing productivity, creating overstock inventory which result in inefficient performance [4,5], and [6]. Therefore, improving maintenance efficiency is vital and required by organizations to achieve the best practice of their productivity and performance with less afforded maintenance costs. As one of the maintenance measurement criteria, Wrench Time (WT) is a maintenance criterion used to measure how much time maintenance technicians spend doing actual work assignments [5]. The maintenance cost is also an important criterion [6], and it must be prioritised and minimised [7].

Improving maintenance efficiency in the power industry has been investigated in some recent literature including, but not limited to [8] who developed an improved mathematical model that evaluates the economic efficiencies of the integrated energy system, considering new constraints for maintenance including electric generation, transmission subsystems and the ability to produce and transport a variety of primary energy sources. The Analysis Of Variance (ANOVA) technique was used to analyse the effect of climate conditions on different gas or electricity transmission regions. Authors in [9] used a

---

* Corresponding author e-mail: Firas@uniten.edu.my.

quantitative approach followed by analysing secondary data of all the plant failures and stoppages during plant operation to improve maintenance strategies by examining the efficiency of the thermal power plant. [10] presented an empirically grounded research agenda for smart maintenance that reflects the heterogeneity in industrial adoption and performance of Smart Maintenance to achieve novel perspectives from strategy, organization, economics and sociology. [11] presented the power plant maintenance scheduling and particle swarm optimization (PSO) technique to ensure economical and reliable operation of the power system. Power plant maintenance scheduling of a power system based on minimization of the objective function has been proposed considering a power system's economical and reliable operation while satisfying the crew/workforce and the load demand. [12] Investigating maintenance's role in energy-saving and available maintenance approaches for energy consumption reduction. Various literature and publications on the research areas were reviewed and summarized to show the importance of maintenance and approaches commonly used for energy efficiency. [13] applied the lean maintenance techniques based on a previously developed multicriteria decision-making process that uses why Fuzzy is not part of the acronym? example: FAHP methodology to carry out diagnosis and prescription tasks. That methodology allowed the prescription of the appropriate learning techniques to resolve the primary deficiencies in maintenance efficiency.

Authors in [14] developed a predictive maintenance planning model using intelligent methods involving five main phases: data cleaning, data normalization, optimal feature selection, prediction network decision-making, and prediction. Authors in [15] presented the concept of Predictive Maintenance 4.0, the building blocks of predictive system architecture, its applications in the electrical sector and its benefits as an innovative technology. [16] proposed a new structure for the Lean Maintenance (LM) process based on a systematic literature review of a significant number of related articles that were published on LM. The process structure is designed based on the five lean principles to guide and support organizations in pursuing maintenance excellence. Authors in [17] conducted a literature review and updated survey on maintenance management of photovoltaic plants, a novel analysis of the current state and a discussion of the future trends and challenges, considering the main faults and degradation mechanisms, including the causes, effects, and the main techniques to detect, prevent and mitigate them. [18] reviewed previous practice of maintenance schedules in the electricity industry to study regulated and deregulated power systems and explore some critical features such as network considerations, fuel management, and data uncertainty.

Although the previous works considered in their maintenance focus on several factors, including energy efficiency, generation, transmission, excellence, strategy, organization, economics and sociology, none-of them investigated other more factors such as operational factors which affect the productive workforce, and this has a direct impact on the maintenance efficiency. Hence, this work aimed to investigate operational factors' impact on the maintenance efficiency rather than focusing on the data collection approach, Day In Life Of (DILO), which was previously used to improve productivity. Other practices of maintenance efficiency improvement are conducted in different industries, including but not limited to Automotive Maintenance Spare Parts [19], reliability-centred maintenance [20], integrated reliability, availability, and maintainability [21].

However, this work aims to understand the factors that impact the WT of the workforce productivity, which directly affects maintenance efficiency. The contributions of this paper are summarized as follows:

- To better understand the WT percentile of the workforce productivity, the maximum WT should be achieved and considered as an indicator used in the industry to illustrate the productivity of the maintenance activities. Measuring the WT is necessary for an organization to define targets and keep track of progress to reduce their value-adding (VA) and non-value-adding (NVA) times.
- To identify different operation factors that impact the WT and reduce the causes to enhance the WT and the maintenance efficiency. Studying the adding and non-value adding factors and developing short- and long-term plans to minimize the non-value adding time.
- To set a roadmap for the maintenance management to utilize their resources to reduce the waste and develop a long-term plan for the maximum performance of WT. Sustaining continuous improvement; developing collaboration among management and workforce, and shortening the distance and behavioural change that can lead to increase of the work productivity.

2. Research Methodology

An operational observation method is used to observe the activities and the time taken by the maintenance workforce during the working day. The continuous observation regarding what the workforce team performed during the day or more, as illustrated in the 1980s by Frederic W. Taylor, pioneered the work sampling practice [22]. Observation practice methods are widely used in research because it provides a vision that might not be accomplished with different methodologies. Many managers and researchers considered observation practice an excellent approach to data gathering compared with other processes like interviews and questionnaires [23]. As shown in Figure 1, the theoretical framework process consists of three main steps. Data input is mainly associated with operational factors that are impacting workforce productivity. Data processing begins by providing a training program to all respondents that cover the process of observation, time recording, and data collection. Data preparation is followed in three steps: identification, training, and data collection.

Furthermore, data analysis and interpretation are conducted to determine the project objectives. A pilot test was conducted with a small group of the targeted respondents to test the reliability of the observation method. The test was performed by collecting five observations per the line management decision to measure the reliability of the observation method with data collocation. The line management accepted and approved the result of the pilot test.

Data output results can be seen as determining the position of the workforce productivity according to the best practices in the industries. It can also provide the management insight to prepare for any necessary resources to enhance or improve the current position by developing an enhancement program, as shown in Figure 1.

Therefore, the research plan execution sequence is created based on the theoretical framework shown in Figure 1 and is categorized into four stages, as shown in Figure 2.

Stage 1 Research Strategy: The research strategy demonstrates the main points of the research process and the direction to achieve the objectives, which consists of nine steps.

Stage 2 Aim and Boundaries: This research aims to enhance maintenance efficiency by increasing the percentage value of the workforce productivity (Wrench Time). The maintenance department of Company A is divided into many sections and sub-section. The targeted population for this project is only the maintenance workforce for assets 1, 2, and 3 under the sub-section of Mechanical, Electrical, Instrumentation, and Control System.

Stage 3 Data Preparation: Data preparation is separated into three steps: data identification, training, and data collection. Data preparation started with identifying the different operation factors that impact workforce productivity. These factors are developed through the involvement of the maintenance senior staff, including the final approval of the line management.

Stage 4 Data Analysis: The collected quantitative data are analyzed using MS Excel. The collected data is analyzed to determine the percentage of the workforce productivity (WT), the activities executed and have a value-added or non-value-added to the productivity.

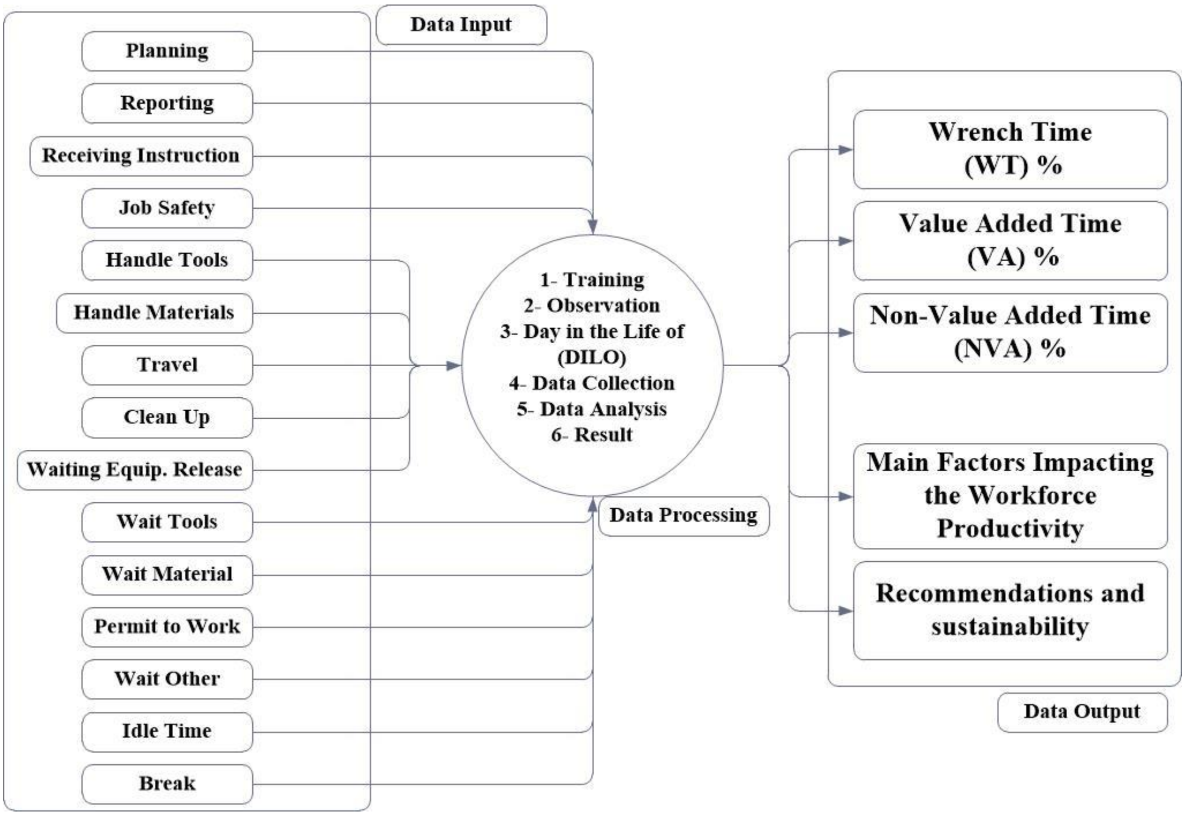

Figure 1. Proposed Research Theoretical Framework Process.

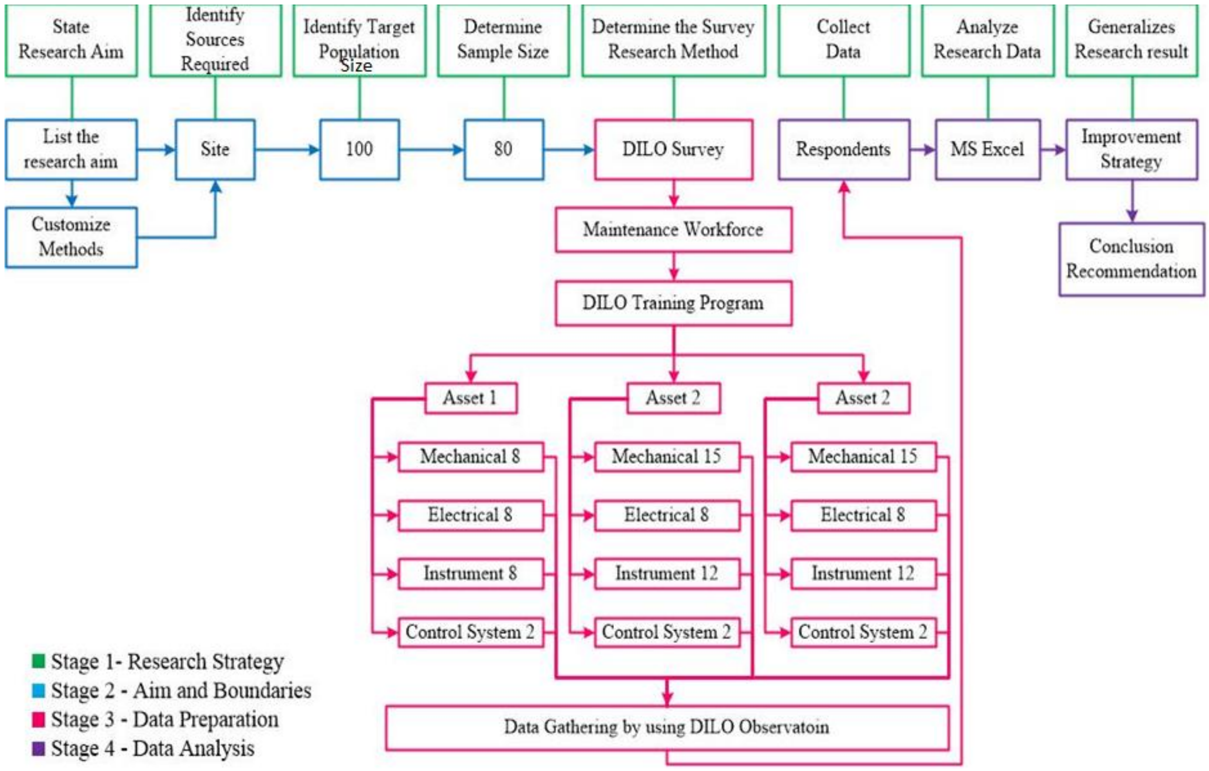

Figure 2. Research Plan Execution Sequence [24]

The operation factors that agreed to measure by observation activity using the DILO observation methods are shown in Table 1.

In order to have reliable, accurate, and trusted data, we decided that the mechanical supervisors would have to observe the instrumentation and control system teams, and the control system supervisors would observe the mechanical teams. Table 2 shows the values of each element of the OCE according to the MEI [25].

Nowadays, many companies started to measure the craft utilization time (WT) to monitor the workforce productivity, efficiency of the planning and scheduling, and other resources. Eliminating waste will enhance the workforce productivity and increase the WT, whereas the typical WT is 40%, and the best is 70%. The element values in Table 2 for craft utilization were adopted as a reference for analysing workforce productivity (WT).

Table1. Operation Factors List

Productivity	**Operation Factors**	
	Value Added (VA)	Non-Value Added (NVA)
Wrench Time	Planning	Waiting Equip. Release
	Reporting	Wait for Tools
	Receiving Instruction	Wait for Material
	Permit to work	Wait for Other
	Job Safety	Idle Time
	Handle Tools	Break
	Handle Materials.	
	Travel	
	Clean Up.	

Table 2. Range of OCE Element Values and OCE(Percentage)

	Range of OCE Element Values		
OCE Elements	Low	Medium	High
Craft Utilization (WT)	**30%**	**50%**	**70%**
Craft Performance	>80%	90%	95%
Craft Service Level	>90%	95%	98%
OCE Factor	22 %	43%	65%

3. Case study

In order to verify the achieved workforce productivity and the operation factors percentage, a case study was used in one of the liquefied natural gas plants based in the Middle East. Mode details about the company will be provided in the following section.

3.1. Company Brief

Company A is an LNG producer in the Middle East that exports the LNG to its client based on a long-term contract. The liquefaction of LNG passes through several processes, such as acid removal, dehydration, mercury removal, pre-cooling, fractionation, liquefaction, and storage. The liquefied natural gas is extracted upstream and then transported to the liquefaction facilities downstream, consisting of the process trains. The LNG is liquefied at -161^{o}C degrees, then exported to the international markets using a fleet of LNG carriers. The LNG business observed a strong development during the previous eras, which caused an increase in the LNG demand worldwide. Therefore, the LNG demand increased from 1990 to 2011 by 190 million tons. This incredible development was mainly due to the world's big traditional gas well [26]. To ensure a continuous operation and production of LNG, it is required to enhance the maintenance process efficiency of the facilities.

Understanding the current maintenance process leads to identifying the process's shortcomings, and accurately interpreting the data collected and creating an accurate analysis. Observation comprises time recording of the conservation works activities executed by the maintenance technician from 7:00 am to 4:00 pm using a Day in the Life of (DILO) method. The process sequences during the working day consist of the following steps:

- The meeting started in the early morning,7:00 am, in the workshop yard. The supervisors and their team received instructions with a quick brief from the foreman regarding maintenance tasks.
- Collect the necessary documents and drawings and reserve the spare parts if required from the warehouse.
- The supervisors gathered the team with contractors and collected the required standard tools. Occasionally, they collected a special tool from the tool container if required.
- Arrange services/support requirements from electrical, instrumentation, control system, mechanical, and logistics disciplines.
- Transportation from the maintenance building to the control room uses a pick-up car (contractors use a personal tricycle or bicycle).
- Toolbox talk (TBT) meetings are led by the supervisor, explaining the safety precautions that should be considered during the job execution.
- The supervisor picks up the permit to work (PTW) document from a control room in the morning, which has a pick-up time, as all employees are in the PTW room to get the permit to work documents.
- The night shift production supervisor approves PTW documents being ready for the next day. The day production supervisor will check for safety and hazardous requirements, including the supplementary documents. Sometimes, the production day supervisor will discuss the safety and hazard issues with the maintenance team before signing the PTW when clarification is needed.
- Once the day shift production supervisor approves the PTW, the maintenance team will move with the field operator to perform a final check and hand over the machine to maintenance.
- Upon completion of the maintenance jobs, the maintenance supervisor has to sign the PTW with the field operator prior submitted to the production supervisor. If the job is not completed, the maintenance supervisor must report that the work status will be completed by the next day.
- If a job is not completed before lunchtime (12:00 pm - 1:00 pm), the maintenance team must stop and resume it after lunch.
- Before 3:00 pm, the maintenance supervisor has to go back to the office to write the daily report, complete the work order with technical findings, and write in SAP.

3.2. Data Collection

Data Collection was conducted in Company Ain assets 1, 2, and 3 as described in the research boundaries. The collection started from 7:00 am to 4:00 pm using the day in the life of (DILO) method. The data collection was divided into three stages: part of the data was collected in July, the second in August, and the third in September 2014. The data is divided into three stages to examine the operation factors that impact workforce productivity. Four observers (Supervisors) collected data from different disciplines (Mechanical. Electrical, Instrumentation, and Control systems) each month by supervising and monitoring the technicians throughout the whole working day, including monitoring and recording the tasks carried out and the time taken to complete them.

In order to have reliable, accurate and trusted data, the instrument and control system teams and supervisors will observe the mechanical teams. The observers collected the total number of observations was 80 during the three months based on the population and sampling size rules. The data collection was done based on the developed plan for each discipline every day. See Table 3 for the workforce plan and 3-5 for the monthly observation plan.

Table 3. Workforce Plan for Observation(Values)

Discipline	Population	Sample Size	July	August	September
Mechanical	38	31	31	31	31
Instruments	32	26	26	26	26
Electrical	24	20	20	20	20
Control System	6	3	3	3	3
Total DILO	100	80	80	80	80

Table 4 shows the number of conducted observations by each discipline for the three months of July, August and September, and the final participant result was 100% achievement.

Table 4. Monthly DILO Plan (Values and Percentages)

Crew	July	August	September	Percentage
Mechanical	10	10	10	100%
Instruments	9	9	9	100%
Electrical	6	6	6	100%
Control System	2	1	2	100%
Total DILO	27	26	27	100%

The observation plan table shows how many observations were planned for everyday to be collected by the observers. See Figure 3 for the observation plans for September.

3.3. Data Analysis

Data analysis will concentrate on the workforce productivity (WT) and determine percentages of the activities that are executed but do not have an added value to the productivity, and this can be transferred to either value-added or non-value-added time. The collected quantitative data are analysed by using the statistical methods analysis software. An MS Excel software is used to analyse the collected data using the DILO observation method. Figure 4 shows the productivity and non-Productivity tasks.

The analysis focuses on the WT, value-added time (VA), and non-value added time (NVA). Data analysis is divided into three parts; part one will analyse the collected data using MS Excel to identify the major percentile of operation factors related to each month (July, August, and September) and then interpret the variation between each one. This will provide insight and recommendations for question two. Along with this analysis, determine the percentile of WT, value-added time and non-value added time. This leads to accomplishing question number one. The last part of this study concentrates on the program development to monitor the improvement of the workforce productivity by establishing a roadmap plan for observation methods to be applied at different intervals to appraise the result deviations.

The data collected through the observation by the observers were 80 DILO for each month, based on the population and sample size as described in Table 5.

4. Result

Data analysis of the maintenance process observation of the workforce team activities is conducted in July, August, and September, as presented in Table 6 and Figure 5.

Table 5. Workforce Plan for Observation (Values)

Discipline	Population	Sample Size	July	August	September
Mechanical	38	31	31	31	31
Instruments	32	26	26	26	26
Electrical	24	20	20	20	20
Control System	6	3	3	3	3
Total DILO	100	80	80	80	80

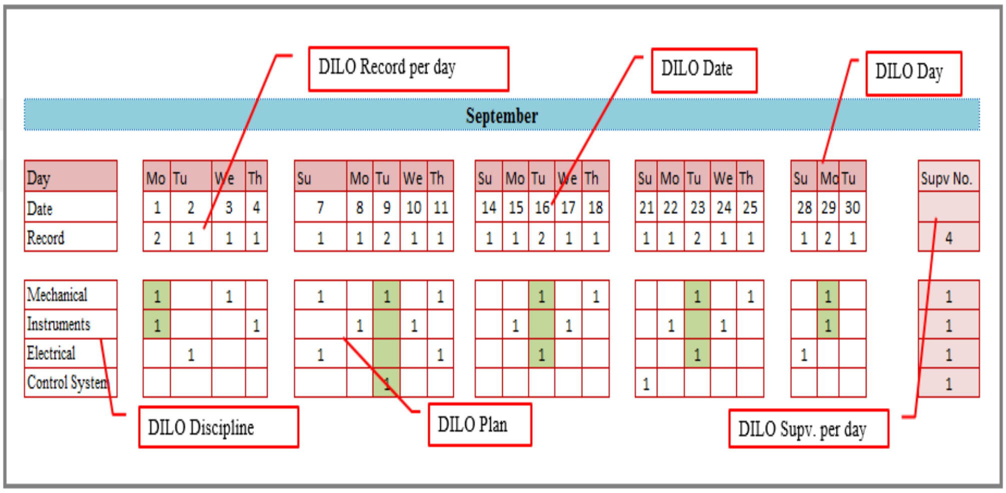

Figure 3. Observation Plan (Values)

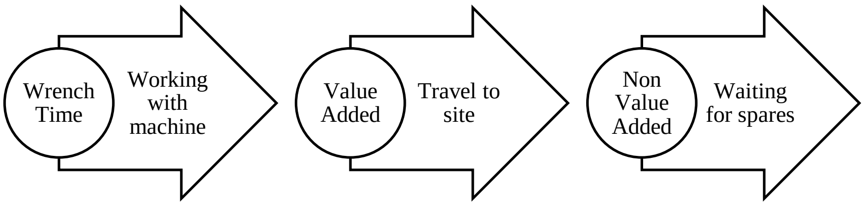

Figure 4. Productivity and Non-Productivity Tasks

Table 6. Accumulative Observation Result (Percentage)

Accumulative Observation					
Operation Factors	% Jul	% Aug	% Sep	% Avg.	Productivity
Wrench Time	37.0%	38.0%	39.2%	38.1%	38.1%
Planning	7.7%	7.4%	7.3%	7.4%	
Reporting	4.6%	4.6%	4.7%	4.6%	
Receiving Instruction	2.4%	2.6%	2.4%	2.5%	
Job Safety	2.6%	2.8%	2.7%	2.7%	
Handle Tools	2.3%	2.8%	2.5%	2.5%	
Handle Materials.	2.8%	2.3%	3.2%	2.8%	
Travel	13.1%	12.7%	12.2%	12.7%	
Permit to Work	5.4%	5.6%	5.9%	5.7%	
Clean Up.	2.1%	2.3%	2.4%	2.3%	43.1%
Waiting Equip. Release	2.3%	2.5%	2.0%	2.3%	
Wait Tools	1.3%	1.2%	0.6%	1.0%	
Wait Material	1.7%	2.3%	2.2%	2.1%	
Wait Other	1.7%	0.9%	1.0%	1.2%	
Idle Time	1.9%	1.1%	1.2%	1.4%	
Break	11.1%	10.9%	10.6%	10.9%	18.9%

Operation factors (added value and non-added value) were the significant causes of the underutilization of the workforce productivity caused by more time consumed in travel, breaks, planning, and permits to work and report. The wrench time of the workforce productivity is 38.1%, below the medium range score of 50% according to the Maintenance Excellence Institute standard. According to the finding, a proposed roadmap was developed to diminish the losses in the maintenance business process and then to enhance the maintenance efficiency by improving the wrench time of the workforce productivity.

The observation results demonstrated the key factors that affected the workforce productivity (WT), and to decrease the waste generated through; travel, breaks, planning, permits to work, and reporting, management needs to assign the necessary resources. The percentage value of each operation factor is presented in Table 8.

In Table 8, travel, break, planning, permit to work, and reporting are the major factors that impact the workforce productivity determined by the three-month observation and the percentile distribution of the workforce productivity (WT), value-adding, non-value adding time and major factors.

According to the key operation factor values demonstrated in the percentage trends in Figure 7, there were a few positive developments in Travel, Break, and Planning throughout the research. The changes were heading in a negative direction for factor permit to work. On the other hand, the change in Permit to work is negative. This change is due to the change in workforce behavior during short-term periods of being monitored, and usually they soon return to their previous practices.

Table 8. Major Factor of VA and NVA(Percentage)

Item	July	August	September	Mean %
Travel	13.1%	12.7%	12.2%	12.7%
Break	11.1%	10.9%	10.6%	10.9%
Planning	7.7%	7.4%	7.3%	7.4%
Permit to work	5.4%	5.6%	5.9%	5.7%
Reporting	4.6%	4.6%	4.7%	4.6%
Total	41.90%	41.20%	40.70%	41.30%

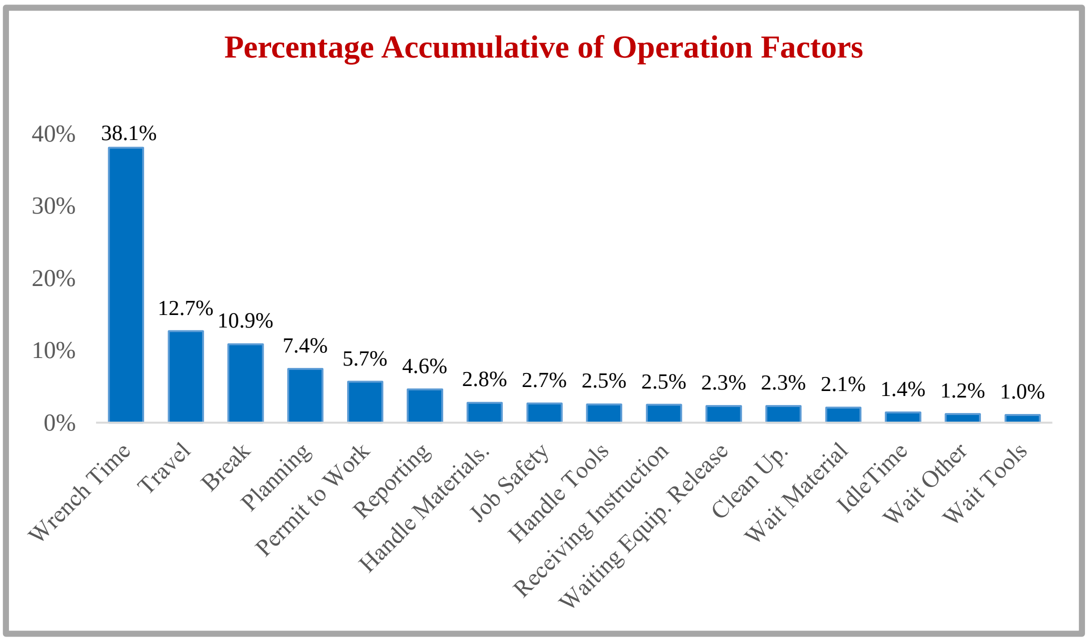

Figure 5. Percentage Accumulative of Operation Factors(Percentage)

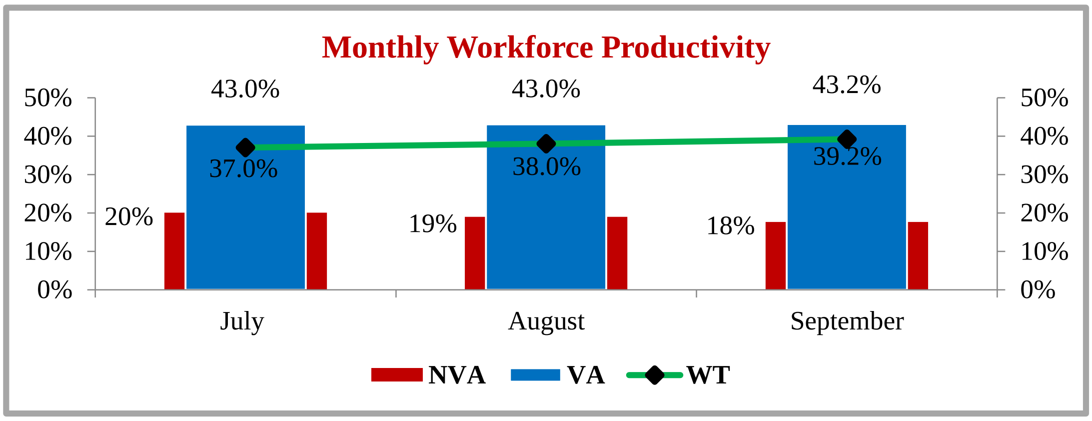

Figure 6. Monthly Percentile Distribution of WT, VA, and NVA(Percentage)

Reporting factor has approximately changed by 0.10% during the three-month observation. These changes are out of control since the observation was focused only on the maintenance workforce team, and the Permit to Work (PTW) team is from another department. Table 9 shows the main reasons behind the excessive time-consuming operation factor.

These require close follow-up by the management with the help of the monitoring tools to manage and sustain the Workforce Productivity (WT), as demonstrated in Figure 8.

The dashboard, presented in Figure 10, consists of an accumulative observation table, operation factors monthly trends, percentage accumulative of operations factors, VA and NVA, monthly workforce productivity, and overall workforce productivity.

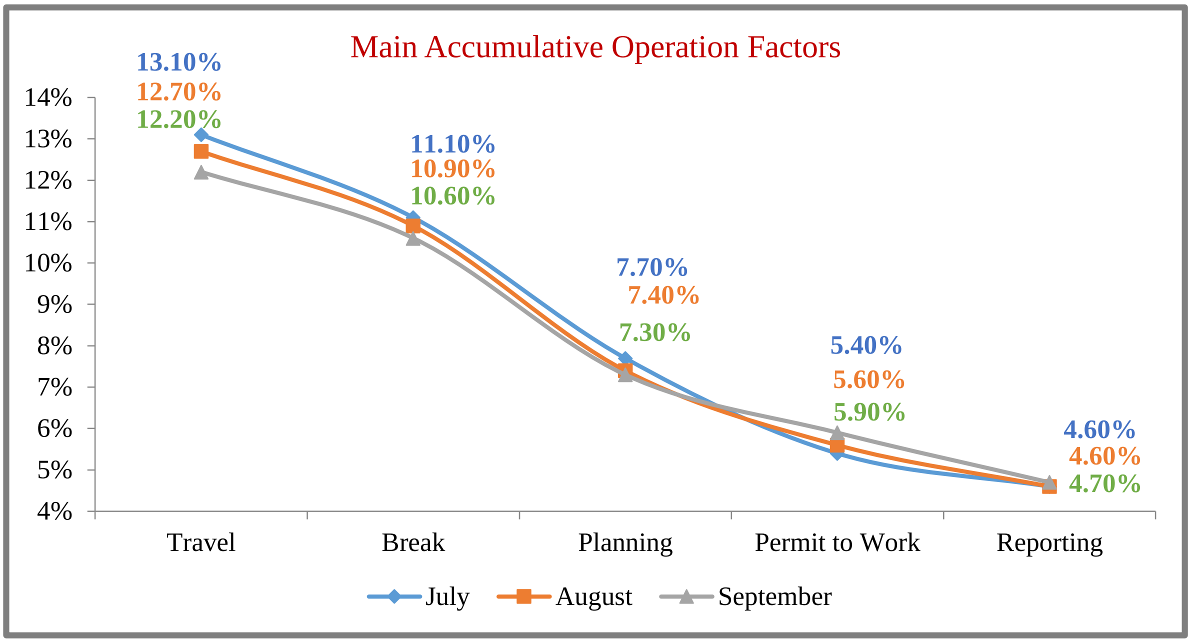

Figure 7. The trend of Main Accumulative Operation Factors (Percentage)

Table 9. Reasons for Excessive Time

Travel	Break	Planning	Permit to Work	Reporting
Wide area facilities and shortage of transportation **Long trips from workshop to control room to field and back to the workshop** **Minimum two trips per day in the same observation took three to four trips per day.** **Using bicycle or tricycle for commuting from workshop to field and vice versa**	The workforce team does not follow the company rule by spending more than one hour during the lunch break. The unofficial teatime break between 9:00am to 10:30 am consumed by the workforce team is unconventional.	Involved in tasks contrary to the job description. Scheduling role was assigned to the senior technicians. Unavailability of the scheduler team within the planning section. Unavailability of the integrated planning of maintenance activities. A shortcoming in communication between different departments. Planning consumes time for data collection and interpretation.	PTW issuance takes more time due to the unavailability of the day supervisor, field operator, and unready machines for intervention or crowded with the maintenance team during the peak time of the PTW issuance process. PTW team is from the production department and was not considered in this study. The same shortcoming in the PTW process occurred every day	An updated work order in SAP with a complete technical finding. Inter the time writing (working hour) related to each workforce member and technically complete the work order. Update the contractor register with the total number of contractors involved in the daily activities

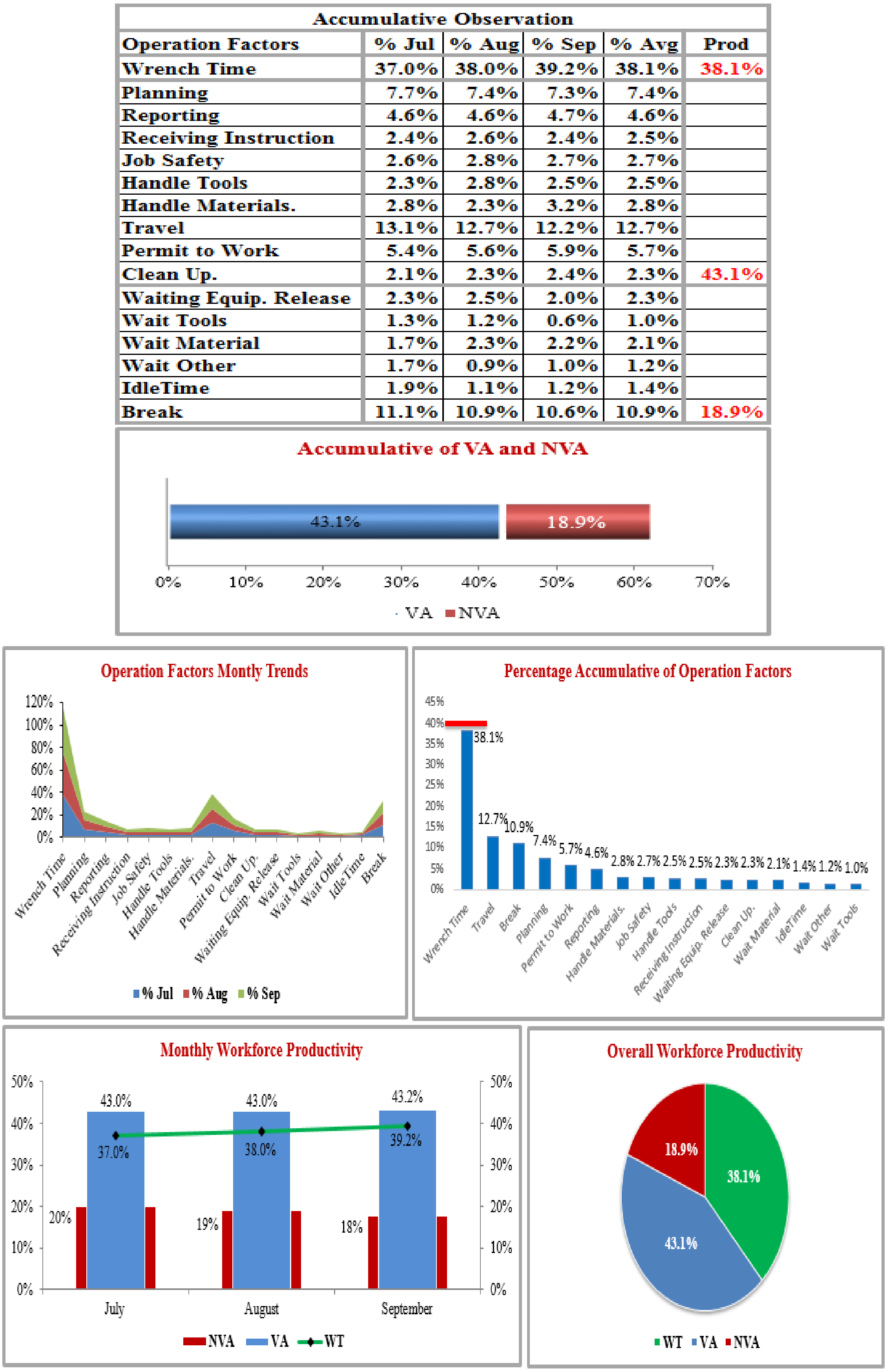

Accumulative Observation

Operation Factors	% Jul	% Aug	% Sep	% Avg	Prod
Wrench Time	37.0%	38.0%	39.2%	38.1%	38.1%
Planning	7.7%	7.4%	7.3%	7.4%	
Reporting	4.6%	4.6%	4.7%	4.6%	
Receiving Instruction	2.4%	2.6%	2.4%	2.5%	
Job Safety	2.6%	2.8%	2.7%	2.7%	
Handle Tools	2.3%	2.8%	2.5%	2.5%	
Handle Materials.	2.8%	2.3%	3.2%	2.8%	
Travel	13.1%	12.7%	12.2%	12.7%	
Permit to Work	5.4%	5.6%	5.9%	5.7%	
Clean Up.	2.1%	2.3%	2.4%	2.3%	43.1%
Waiting Equip. Release	2.3%	2.5%	2.0%	2.3%	
Wait Tools	1.3%	1.2%	0.6%	1.0%	
Wait Material	1.7%	2.3%	2.2%	2.1%	
Wait Other	1.7%	0.9%	1.0%	1.2%	
IdleTime	1.9%	1.1%	1.2%	1.4%	
Break	11.1%	10.9%	10.6%	10.9%	18.9%

Figure 8. Workforce Productivity (WT) Monitoring Dashboard(Percentage)

5. Comparison study

The following chart describes the changes and effects of the workforce productivity and utilization and how they influence the maintenance performance and KPI. Maintenance KPI has many measuring indicators that measure the maintenance department's performance, and budget is one of these indicators. Operating the maintenance department within the approved planned budget means that the department utilizes the available resources without developing any losses in the maintenance process activities. Figure 9 presents a comparison conducted for Workforce Productivity Utilization.

6. Conclusion and Future Work

In this study, the factors that directly impact maintenance efficiency were identified. The percentile of the WT, VA, NVA, and the main operation factors that impact workforce productivity were investigated as it relates to the improvement program to sustain and enhance the current maintenance efficiency situation. The productivity losses were minimised to increase maintenance efficiency and workforce utilization.

The Day In the Life Of (DILO) approach was used to determine the factors' percentages. This was achieved through observation of the complete maintenance activities process from start to finishing of the working day. The random Sampling technique and Pilot Test were also used in this study to acquire a proper sample size and to test the reliability of the data collection method, respectively.

Based on the final result from 38.1% to 64.9% of the observation survey, it has been concluded that maintenance efficiency depends on workforce productivity; improved productivity was interconnected with cost-effectiveness, leading to improved maintenance performance.

In future work, developing standard operation factors for different industries is required since the industrial environment varies from one industry to another. It is also recommended that standardizing the operation factors would create standard percentile ranges of the productivity that can be used as a reference to measure the workforce productivity of any organization.

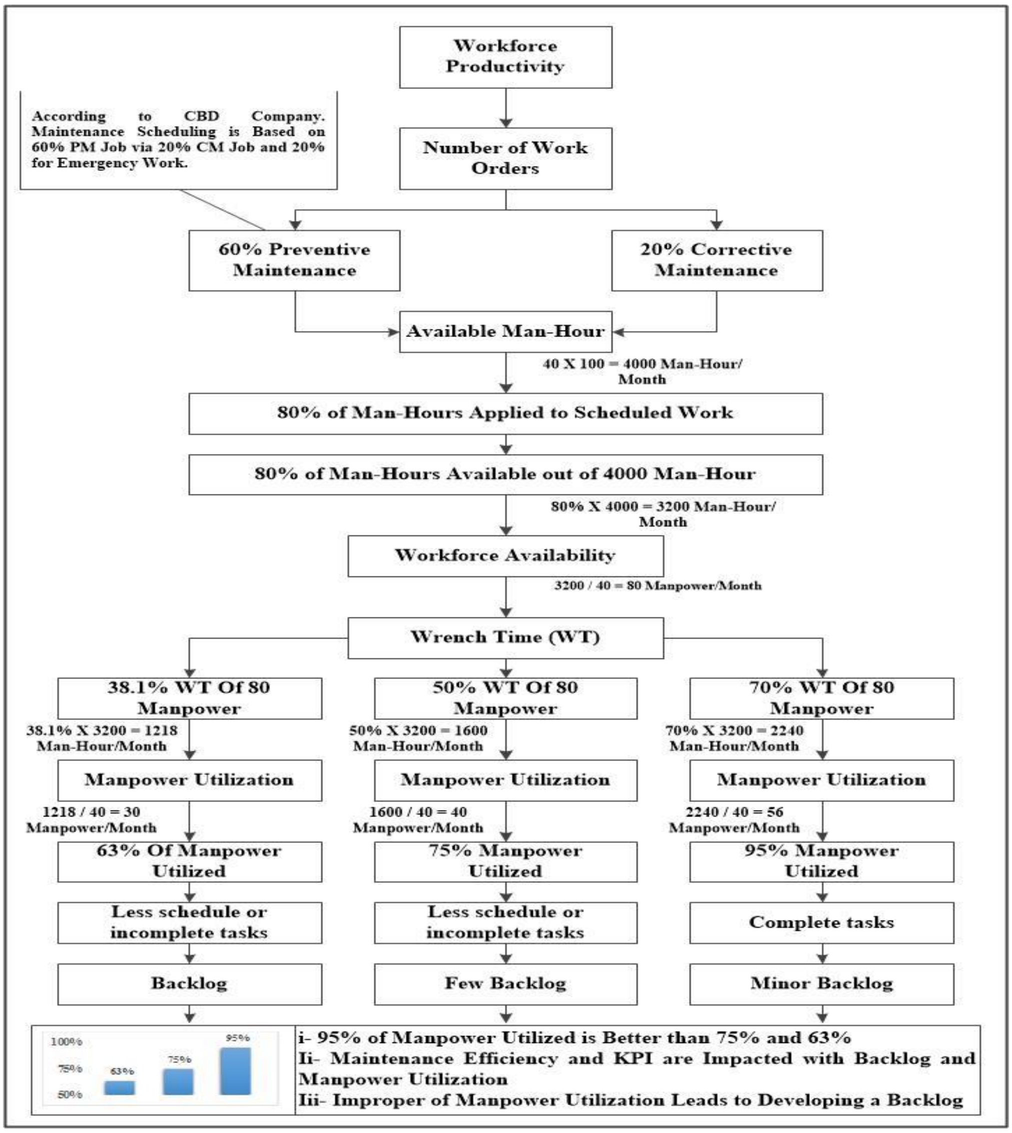

Figure 9. Workforce Productivity Utilization Comparison(Percentage)

References

[1] Tortorella G.L., Fogliatto F.S., Cauchick-Miguel P.A., Kurnia S., and Jurburg D., "Integration of Industry 4.0 technologies into Total Productive Maintenance practices," International Journal of Production Economics, Vol. 240, pp. 108-224, 2021.

[2] Pintelon, L., Pinjala, S.K. and Vereecke, A. (2006), "Evaluating the effectiveness of maintenance strategies", Journal of Quality in Maintenance Engineering, Vol. 12 No. 1, pp. 7-20. https://doi.org/10.1108/13552510610654501

[3] Rivera Rubio E.M., "Sistema de gestión del mantenimiento industrial". 2011.

[4] Patterson J.W., Fredendall L. D., Kennedy W. J., and A. McGee, "Adapting total productive maintenance to Asten, Inc," Production and Inventory Management Journal, Vol. 37, pp. 32, 1996.

[5] Sari E., Ma'aram A., Shaharoun A.M., Chofreh A.G., Goni F.A., Klemeš J.J. "Measuring sustainable cleaner maintenance hierarchical contributions of the car manufacturing industry". Journal of Cleaner Production, Vol. 312, pp. 127717, 2021. https://doi.org/10.1016/j.jclepro.2021.127717.

[6] Dias J., Nunes E., and Sousa S. "Productivity Improvement of Transmission Electron Microscopes-A Case Study," Procedia Manufacturing, Vol. 51, pp. 1559-1566, 2020.

[7] Chin H.H., Varbanov P.S., Klemeš J.J., Benjamin M.F.D., and Tan R.R. "Asset maintenance optimisation approaches in the chemical and process industries-A review" Chemical Engineering Research and Design. Vol. 164, pp. 162-194, 2020.

[8] Azadeh A, Fekri M, Asadzadeh S, Barazandeh B, Barrios B. A unique mathematical model for maintenance strategies to improve energy flows of the electrical power sector. Energy Exploration & Exploitation. Vol. 34(1), pp 19-41. 2016. doi:10.1177/0144598715623665

[9] Modiba T., Telukdarie A. "Maintenance Strategy Optimization of a Thermal Power Plant ". IEEE International Conference on Industrial Engineering and Engineering Management, 2021.

[10] Bokrantz J., Skoogh A., Berlin C., Wuest T., Stahre J."Smart Maintenance: a research agenda for industrial maintenance management". International Journal of Production Economics, Vol. 224, June 2020, pp 107547

[11] Velayutham P., Ismail F.B. "Review on Power Plant Maintenance and Operational Performance", MATEC Web of Conferences 225, 05003 (2018) https://doi.org/10.1051/matecconf/201822505003 UTP-UMP-VIT SES 2018

[12] Firdaus N., Samat H.A., Mohamad N. "Maintenance for Energy efficiency: A Review", IOP Conference Series Materials Science and Engineering 530(1):012047, 2019. DOI: 10.1088/1757-899X/530/1/012047

[13] Duran O., Capaldo A., Acevedo P.A.D. "Lean Maintenance Applied to Improve Maintenance Efficiency in Thermoelectric Power Plants", Energies. Vol. 10(10), pp 1653,2017 DOI: 10.3390/en10101653

[14] Abidi M.H., Mohammed M.K., Alkhalefah H. "Predictive Maintenance Planning for Industry 4.0 Using Machine Learning for Sustainable Manufacturing", Sustainability 2022.

[15]Righetto S.B., Izumida M.A. Martins, Carvalho E.G., Hattori L.T. and De Francisci S. "Predictive Maintenance 4.0 Applied in Electrical Power Systems". IEEE Power & Energy Society Innovative Smart Grid Technologies Conference (ISGT), 2021, pp. 1-5, doi: 10.1109/ISGT49243.2021.9372230.

[16] Mostafa S., Lee S.-H., Dumrak J., Chileshe N., Soltan H. "Lean thinking for a maintenance process", Production & Manufacturing Research, Vol. 3(1), pp 236-272, 2015.

[17] Gonzalo P., Marugán A.P., Márquez A.G., Pedro F. "Survey of maintenance management for photovoltaic power systems", Renewable and Sustainable Energy Reviews, Vol. 134, pp 110347, 2020.

[18] Froger A., Gendreau M., Mendoza J.E., Pinson E., Rousseau L.-M. "Maintenance scheduling in the electricity industry: a literature review", European Journal of Operational Research. Vol 251 (3), pp.695-706, 2016.

[19] Li J. "Distributed Multi-level Inventory Algorithms for Automotive Maintenance Spare Parts Based on Centralized Control Model". Jordan Journal of Mechanical and Industrial Engineering (JJMIE), Vol. 14 (1), 2020

[20] Afefy I.H., Mohib A., El-kamash A.M. , Mahmoud M.A. "A New Framework of Reliability Centered Maintenance". Jordan Journal of Mechanical and Industrial Engineering (JJMIE), Vol. 13 (3), 2019.

[21] Aly M.F., Afefya I.H., Abdel-Magied R.K., Abd Elhalim E.K. "A Comprehensive Model of Reliability, Availability, and Maintainability (RAM) for Industrial Systems Evaluations", Jordan Journal of Mechanical and Industrial Engineering (JJMIE), Vol. 12 (1), 2018.

[22] Al-Najjar B. and Alsyouf I. "Selecting the most efficient maintenance approach using fuzzy multiple criteria decision making". International journal of production economics.Vol. 84, pp. 85-100, 2003.

[23] Mobley R.K. "An introduction to predictive maintenance", Elsevier, 2002

[24] Wireman T. "How to calculate return on investment for maintenance improvement projects". In ASME Citrus Engineering Symposium, 1997, pp. 27-43.

[25] Ralph W. "Measuring Overall Craft Effectiveness (OCE)", 2001.

[26] KFraser. "Facilities management: the strategic selection of a maintenance system," Journal of Facilities Management, 2014.

JJMIE

Volume 16, Number 4, September. 2022
ISSN 1995-6665
Pages 515 – 528

Jordan Journal of Mechanical and Industrial Engineering

The Time Dependent Poisson's Ratio of Nonlinear Thermoviscoelastic Behavior of Glass/Polyester Composite

Raed Naeem Hwayyin[*], Azhar Sabah Ameed

University of Technology/ Electromechanical Department, Baghdad-Iraq

Received 20 Mar 2022 *Accepted 11 Jun 2022*

Abstract

The study predicted an equation describing the time-dependent Poisson's ratio by describing the nonlinear thermoviscoelastic behavior of the composite material depending on experimental results. The composite creep specimens are prepared from polyester resin reinforced with mat chopped. The experimental creep tests contribute to characterizing the behavior of nonlinear thermoviscoelastic material by determining relaxation stress as a function of time, strain, and, temperature. The Poisson's ratio was determined by taking into account the effect of temperature and time at different stresses. The creep tests were performed at various temperatures of 30, 40, 50, and, 60 C^o and at different stresses which described the thermoviscoelastic behavior of the composite material. The study was concluded with a mathematical model to describe the Poison's ratio function, taking into consideration its effect on the thermoviscoelastic behavior of the composite material. The maximum effect of time on the Poisson's ratio was decreasing by an average ratio of 9.87% at a temperature of 60 C^o and stress of 12.3MPa while the maximum effect of the temperature on Poisson's ratio was at an average ratio of 17.59% at a stress 12.3 MPa. In addition, the equation of Poisson's ratio $\nu(t, T)$ was found for the thermoviscoelastic behavior of the composite material. Finally, the mathematical model describes the failure behavior of the composite material used in the manufacture of tanks, boat hulls, and structures.

Keywords: Poisson's ratio, nonlinear, thermoviscoelastic.

Nomenclature

$\varepsilon(t,T)$	Strain as function of time and temperature	mm
T	Temperature	C^o
$\varepsilon(\sigma)$	Time independent strain (function of applied stress).	
t	Time	min
A(t)	Cross section area as function of time	mm^2
F	Force	N
$\varepsilon_T(t,T)$	Lateral strain as function of time and temperature	mm
b(t)	Lateral dimension as function of time	mm
b_o	Initial lateral dimension	mm
L(t)	Longitudinal dimension as function of time	mm
L_o	the gauge length of the specimen in millimeters.	
$\varepsilon_L(t,T)$	Longitudinal strain as function of time and temperature	mm
$\nu(t,T)$	Poisson's ratio as function of time and temperature	-----
$\sigma(t,T)$	Stress relaxation as function of time and temperature	MPa
$ns(\sigma,T)$	Slope of creep stress as function of stress and temperature	----
$n(\sigma,T)$	Slope of creep strain as function of stress and temperature	----
$\nu(t, T)$	the Poisson's ratio as a function of time and temperature	
t	Time	min
t_k	Thickness	mm

1. Introduction

The mechanical behavior of polymeric materials is characterized by describing their time-dependent properties in shear or simple tension (creep). Global interest and growing demand for sustainable energy development lead to the preservation of future generations by preserving the environment and natural resources. Conservation of natural resources through improved mechanical properties and applications of multi-system components, such as composites and structural elements. Entire structures require further optimization of materials and a deeper understanding of the influence of temperature and pressure on time dependence [1]. The primary importance of the Poisson ratio lies in determining the mechanical properties of any material which can be found through experimental tests to measure the mechanical properties. Characteristics dependent on the Poisson ratio include plane fatigue, fracture stiffness, indentation resistance, acoustic wave propagation, thermal shock

---

[*] Corresponding author e-mail: 10596@uotechnology.edu.iq.

resistance, and critical torsion. In general, the Poisson ratio is treated as a parameter that varies from one polymer to another [2]. The study tested Poisson's ratio in three ranges of less than 0.2. Properties materials where the conventional elasticity is between (-1, 0.5). The study predicts the roots of the relationships of quadratic functions divided into three ranges ($-1< \nu \leq 0$), ($0\leq \nu \leq 0.2$), and ($0.2 \leq \nu <0.5$).The researchers investigated the three main issues in dealing with the calculation of the Poisson's ratio of polymers: anisotropy, strain dependence, and strain rate. They depend on mechanical properties, where they adopted an isotropic according to classical elasticity theory [3]. The study investigated materials, such as concrete and polymers under uniaxial load that exhibit creep under continuous axial load resulting in axial and transverse strain. They discussed the expected evolution concerning the time (increasing, decreasing, non-monotonic) of Poisson's viscous ratio[4]. The study determined the Poisson's ratio and Young modulus of red beans at different moisture levels and for a different loading rate, the study concluded that the Young modulus decreased with increasing the humidity percentage to predict the deformation behavior of red beans[5]. The study investigated the phenomenological relationships between Poisson's ratio of behavior and response materials under specific loading conditions. They analyzed different loading conditions on specimens and their effect on material properties. It included an inclusive study of the phenomenological relationships of the Poisson's ratio and the response, where the results confirmed that the Poisson's ratio adopts experimental results. They obtained two-dimensional (2D) strains under the influence of the process of creep or relaxation[6]. The researchers investigated the resistance of materials to deformation under mechanical loads rather than a change in volume as Poisson's ratio provides a measure of the performance of any material during strained elasticity. The study set numerical limits between (0.5 to -1) that are suitable for all isotropic materials. Through new experiments and methods leading to material synthesis, the Poisson ratio means an understanding of the mechanical properties of modern materials [7]. The researcher presented the definition of Poisson's ratio as an elastic constant representing the ratio of lateral contraction to elongation in the infinitesimal uniaxial extension of a homogeneous isotropic body. In viscoelastic materials, the Poisson ratio is a function of time that depends on the time system chosen to measure it[8]. The study presented that the Poisson ratio, in general, is a function that depends on time or a complex dynamic frequency that depends on its magnitude (in the frequency domain). The study presents that viscoelastic Poisson's ratio has a different time dependence based on the test method used. The relationship between Poisson's ratio in creep and relaxation can be developed. The viscoelastic Poisson's ratio does not need to be continuously increased over time and it does not have to be monotonic over time[9]. The study adopted the micro/Nanoindentation tester (NANOVEA) to find the modulus of elasticity, stiffness, and accumulation. Low carbon steel AISI1018, alloy steel AISI 4340, and, aluminum alloy 6061 were used as a case study. The study conducted a specific element analysis using a three-dimensional symmetric model to find a relationship between Poisson's ratio and material stress. The Poisson ratio was modeled from 0 to 0.48 to determine the effect of Poisson's ratio on the properties of the elastic-plastic where the properties were verified through the laboratory results. The study investigated that the Poisson's ratio is not considered to be physically stable in viscoelastic materials, but rather is a function that depends on time for polymeric. [10].The researchers developed a new 3D model of the thermoplastic viscoelastic behavior of unidirectional reinforced composite materials by applying Maxwell's model[11].The study investigated the determination of the viscoelastic behavior at different stress levels and the determination of the stress relaxation at different temperatures, Fancey's latch model [12]. Concerning long-term tests, two widely accepted test methods are stress relaxation and creep [13–17].Changes in the mechanical properties of composite materials are related to changes in viscoelastic behavior [18-20] being mainly dependent on stress (creep) and strain (stress relaxation) levels and temperature. Differently from vegetable fiber-reinforced composites [18, 21], structural composites have microstructural changes related to the resin as a reflection of stress/strain variation. If the imposed stress/strain exceeds the maximum resistance of the composite, matrix/fiber de-bonding fiber breakage and destruction of matrix interlayers between fibers can occur.The study built a mathematical model to describe the problem of soft shells for the manufacture of composite materials for thin layers and to determine the deformation and residual stress [22]. They investigated the effect of Poisson's ratio and geometry on the stress concentration factor through triaxial stress on circular and square columns that have a U-notch. They described the elastic stress concentration as a function of Poisson's ratio.[23].The study examined polymers reinforced with short fibers at different periodic and constant loads and showed a decrease in the life of the polymer depending on the loading time and the amount of loading. The study concluded that it is possible to extend the life of failure with the development of rigidity of the compound by examining the damage path that can be used in predicting failure in reality [24]. The study examined four models of multi-layer of beams under constant stress to describe the viscoelastic behavior to limit the effect of the delamination fracture behavior [25].The study suggested a model based on Maxwell's model to show the effect of interior design factors on the viscoelastic-elastic relaxation coefficient E (t)[26]. The study investigated the physical aging of the viscoelastic behavior of epoxy material experimentally at different temperatures and times. The study showed that the aging shift factor is more affected by time than by temperature[27].The importance of the current study in describing the new mathematical model of the thermal viscoelastic behavior of composite materials used in tanks, boat hulls, and structures under constant stress over time and studying the effects of this behavior on the Poisson's ratio $\nu(t, T)$. In addition, the study determines the relaxation stress by taking into account temperature, stress, and strain. The aim of the present study is to describe the Poisson's ratio as a function $\nu(t, T)$ of the nonlinear thermoviscoelastic behavior of the composite material at different stresses according to ASTM creep specimens standard.

2. Theoretical Analysis

Mathematical models and in particular the energy function of time behavior describe the creeping behavior of viscoelastic materials with good accuracy and over a wide time range. The following mathematical model gives a good description of the creep of viscoelastic materials under constant stress[24]:

$$\varepsilon(t) = \varepsilon(\sigma).t^n \tag{1}$$

The time-dependent strain function ε(t) can be determined by defining the variables involved in it by taking the logarithm of both sides of the equation, which results in a line graph having a slope representing the magnitude of the time-dependent strain equation constant. The viscoelastic behavior affected by temperature and the viscoelastic material properties, such as creep compliance, stress relaxation function, and the modulus of elasticity (E), is a function of time, strain, and temperature E(t, ε, T)[25]. As the applied load is constant during the creep process, the cross-section area of the specimens can be determined by [26]:

$$A(t) = \frac{F}{\sigma(t)} \tag{2}$$

in the creep test, the very small variation in thickness of specimens (t_k) is neglected, where the lateral strain b(t) represented a lateral strain of specimen cross-section ε_T(t). The variation in the thickness of specimen (t_k) is neglected then the variation of the cross-section with time is attributed to variation in lateral dimension b(t) the equation (2) can now be written as; The lateral strain can be calculated as[27];

$$\varepsilon_T = \frac{b_2(t)-b_1(t)}{b_o} \tag{3}$$

The longitudinal strain can be calculated as follows;

$$\varepsilon_T = \frac{L(t_2)-L(t_1)}{L_o} \tag{4}$$

The transverse strain ε_T in terms of Poisson's ratio is written as[28]:

$$\varepsilon_T = -\nu.\varepsilon_L = \frac{-\nu.\sigma_L}{E(t,\varepsilon,T)} \tag{5}$$

The time depending on Poisson's ratio is determined by[28]:

$$\nu(t) = -\frac{\varepsilon_T(t)}{\varepsilon_L(t)} \tag{6}$$

3. Material And Methods

3.1. Material

The study conducted experimental creep tests for a composite material consisting of polyester (matrix) that has properties shown in Table 1 and supported by random fiberglass (mat chopped) with specifications shown in Table 2 [29], with a volumetric fraction of 0.26 by determining the weight of the materials that consist of the composite material with additive hardener 0.01%, where the polyester was cast at room temperature. The creep specimens were cut using a CNC machine according to their standard dimensions. The research adopted creep specimens according to the standard creep test specimen (Standard Creep Test ASTM-D2990)[30] as shown inFigures1-a and b.

Table 1. Mechanical Properties of Polyester resin [29]

Properties	Value
Specific Density (at 20 C°)	1.22
Tensile Stress at Break	65 N/mm^2
Elongation at break (50mm gauge length)	3.0 %
Modulus of Elasticity	3600 N/mm^2
Density (ρ)	1268 kg/m^3
Rockwell Hardness	M70

Table 2. Mechanical Properties of E-glass Fibers [29]

Glass type	Specific gravity	σ_{ult} (MPa)	Modulus Of Elasticity (GPa)	Liquids temperature C°
E-glass	2.58	3450	72.5	1065

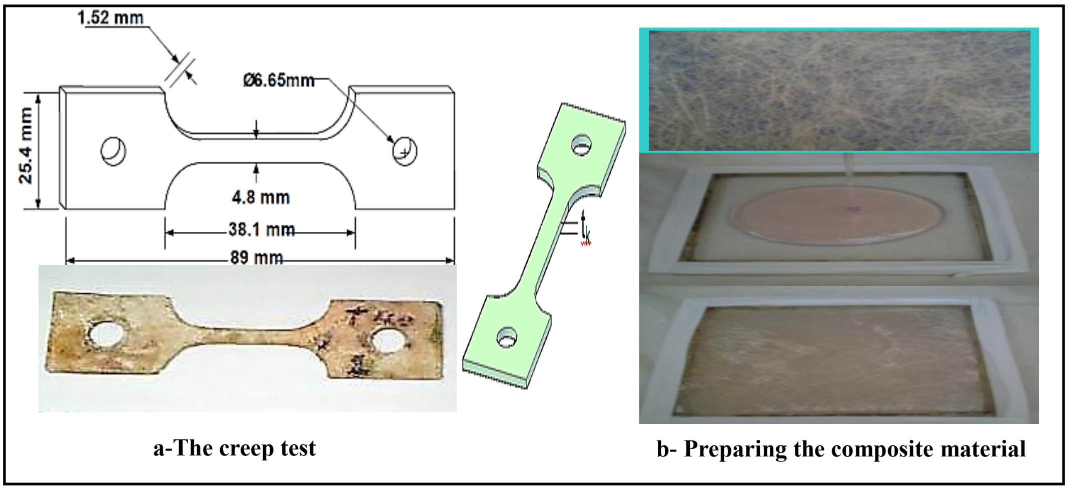

a-The creep test

b- Preparing the composite material

Figure 1. **a**-The Standard creep test specimen ASTM-D2990 [30]
b- Preparing the composite creep specimens

3.2. Methods

3.2.1. Nonlinear Behavior Of Composite Material

The study determined the range of non-linear behavior of the material by two creep tests required at a high-stress level, where the two creep tests do not satisfy the linear behavior of strain and stress conditions of the composite material as shown in equation (7) and (8), where the behavior of composite material will be considered nonlinear [31]:

$$\frac{\varepsilon_1(t_1)}{\sigma_1} = \frac{\varepsilon_2(t_1)}{\sigma_2} \tag{7}$$

$$\frac{\varepsilon_1(t_2)}{\sigma_1} = \frac{\varepsilon_2(t_2)}{\sigma_2} \tag{8}$$

The nonlinear thermoviscoelastic constitutive equation was derived using the concept of the linear principle, but it is extended to the nonlinear behavior range. Thermoviscoelastic has considered the response of viscoelastic material as very sensitive to the temperature variation uncounted in many engineering applications. The difficulty is mainly due to the nonlinear relationship between stress, strain, and, temperature. A method of direct experimental determines the kernel functions of the constitutive equation under variable loading, strain, and, temperature.

3.2.2. The Stress Relaxation

The relation between creep compliance and the stress relaxation function in viscoelastic behavior can be described by plotting the experimental data. Plotting the stress with time at different strains according to the log-log scale to find the slope of different strains n(ε). The stress relaxation can be expressed in the following equation [32]:

$$\sigma(t) = \sigma(\varepsilon).\, t^{n(\varepsilon)} \tag{9}$$

Stress relaxation is defined as a gradual decrease in stress with time under a constant strain. This behavior of composite is studied by applying a constant strain to the specimen and measuring the stress required to maintain that strain as a function of time [32] where relaxation stress was determined through the experimental results according to them the following equation at different strains and temperatures shown in (AppendixA):

$$\sigma(t,\varepsilon,T) = \sigma(\varepsilon,T).\, t^{ns(\varepsilon,T)} \tag{10}$$

Where,

$$\sigma(\varepsilon,T) = f_B(T).\, \varepsilon + f_A(T) \tag{11}$$

And ns(ε,T) as shown in (Appendix B)

$$ns(\varepsilon,T) = f_{ANS}(\varepsilon) + f_{BNS}(\varepsilon).\, T + f_{CNS}(\varepsilon).\, T^2 + f_{DNS}(\varepsilon).\, T^3 + f_{EDS}(\varepsilon).\, T^4 \tag{12}$$

The specimens have the rectangular cross-sectional area dependent on time and temperature during the creep test as the following:

$$A(t) = b(t,T).\, t_k \tag{13}$$

4. Results and Discussion

The complexity in describing the nonlinear thermoviscoelastic behavior of a composite material theoretically makes experimental results an appropriate way to predict this behavior in a mathematical model according to the specific conditions in which experimental tests were conducted, such as time, strain, and temperature. A new relation for Poisson's ratio as a function of time and stress is developed from the above-mentioned analysis. This relation of the thermo-time dependent Poisson's ratio can be written as the following [29]:

$$\nu(t,T) = -\frac{\varepsilon_T(t,T)}{\varepsilon_L(t,T)} \tag{14}$$

The variation in lateral dimension b(t). Equation (2) can now be written as [31];

$$b(t,T) = \frac{F}{t_k\,.\,\sigma(t,\varepsilon,T)} \tag{15}$$

The lateral strain can be calculated as [31];

$$\varepsilon_T(t,T) = \frac{b(t_2,T) - b(t_1,T)}{b_o} \tag{16}$$

Or, the transverse strain εT in terms of Poisson's ratio is written as [32]:

$$\varepsilon_T = -\nu\,\varepsilon_L = \frac{-\nu\,\sigma_L}{E} \tag{17}$$

Where, The longitudinal strain predicate by experimental results (Appendix C):

$$\varepsilon_L(t,\sigma,T) = \varepsilon(\sigma,T).\, t^{n(\sigma,T)} \tag{18}$$

Where,

$$n(\sigma,T) = f_{NA}(T) + f_{NB}(T).\, \sigma + f_{NC}(T).\, \sigma^2 \tag{19}$$

The results in Figure 2 show the effect of increasing the temperature on the Poisson's ratio, where it was found that Poisson's ratio increased by 16.15% when the temperature was raised from 30 C° to 60C°, so it was found that the maximum effect of increasing the time leads to a decrease of the Poisson's ratio by 8.15%at temperature 50 C° and stress 6.9 MPa. The Poisson's ratio decreases with time caused by a decrease in the transverse strain rate relative to the longitudinal strain in creep specimens due to the resistance of the composite material specimens with the time which agrees with the behavior of the Poisson's ratio in the study [31].

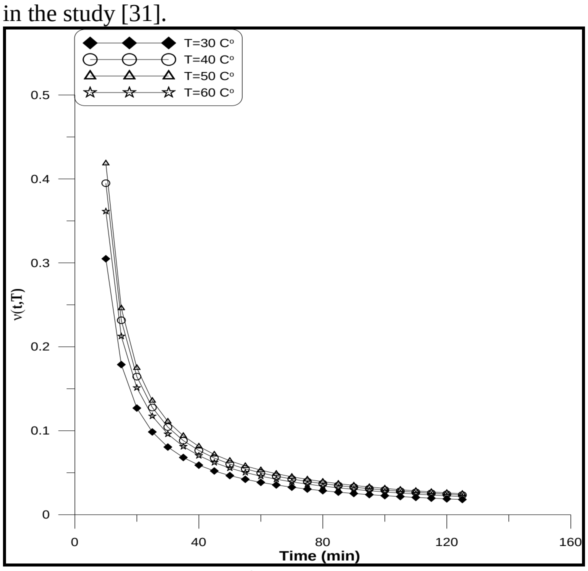

Figure 2. The relationship of the Poisson's ratio with time at stress 6.9 MPa and ε(T) is equal to 0.07 at different temperatures.

The results in Figure 3 showed an increase in the Poisson's ratio by an average ratio of 9.82% as a result of increasing the temperature from 30 C° to 60 C°at stress 8.24MPawhile increasing time leads to a maximum decrease in Poisson's ratio by 8.84% at temperature 40 C° and stress 8.24MPa.The Poisson's ratio increased with an average ratio of 9.82% as a result of increasing the temperature from 30C° to 60 C° and the maximum decrease in Poisson's ratio by 9.65% is due to increasing the time of applying the constant stress on the creep specimens at a temperature of 40 C° and stress of 9.6 MPa as shown in Figure 4.

The results in Figure 5 show the effect of increasing the temperature on the Poisson's ratio, where it was found that there was an increase of the Poisson ratio by an average ratio of 7.55% when the temperature was raised from 30 C^{o} to 60C^{o}at stress11 MPa, while Figure 6 presents the increase of Poisson's ratio by an average ratio of 10.26% as a result of increasing the temperature from 30 C^{o} to 60 C^{o} while maximum increasing of the time of applied stress leads to a decrease in Poisson's ratio by 25.9% at temperature 60 C^{o} and stress 11 MPa, so it increases by 10.6% at temperature 50 C^{o} and stress 12.3 MPa due to a decrease in the change ratio in the cross-section area of creep specimens.

The decrease in the change rate of Poisson's ratio is due to the decrease in the effect of raising the temperature with increasing the effect of the stress compared to the time effect on the specimens, which became the most effective factor in the events of longitudinal strain relative to the transverse. Comparing the experimental results of Figures 2, 3, 4, 5, and 6 show increasing the stress from (6.9 to 12.3) MPa to an increase in the Poisson's ratio with ratios (15.5%, 9.41%, 6.71%, 7.26%, and, 10.4%) at different temperature with fixing ε(T)at 0.12.Because the increase in stress causes an increase in the transverse strain of creep specimens relative to the longitudinal strain due to increasing the Poisson's ratio, which refers to the start of occurrence in the failure. In a specific period of time before failure, an increase in the transverse strain occurs more than in the longitudinal strain which is a symmetry to the necking phenomenon behavior in ductile materials, thus it can be considered as an indicator of starting failure occurrence of the composite material having the same composition. The change in the longitudinal and transverse strain depends on the movement of dislocations in the internal structure of the composite material specimens with the duration of the stress applied to it in addition to the temperature factor.

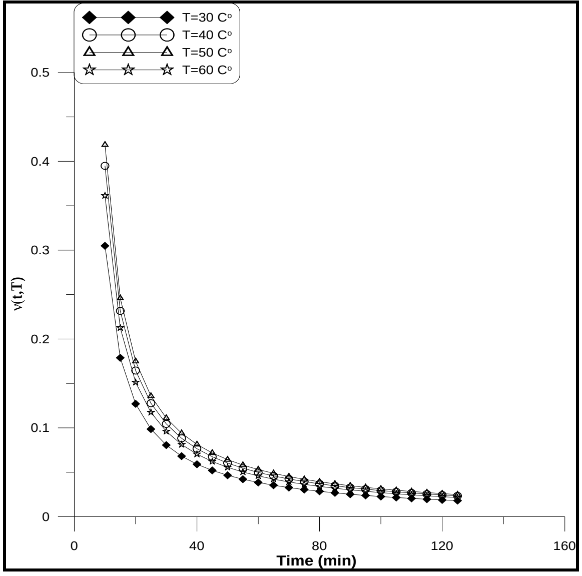

Figure 3. The relationship of the Poisson's ratio with time at stress 8.24 MPa and ε(T) is equal to 0.07 at different temperatures

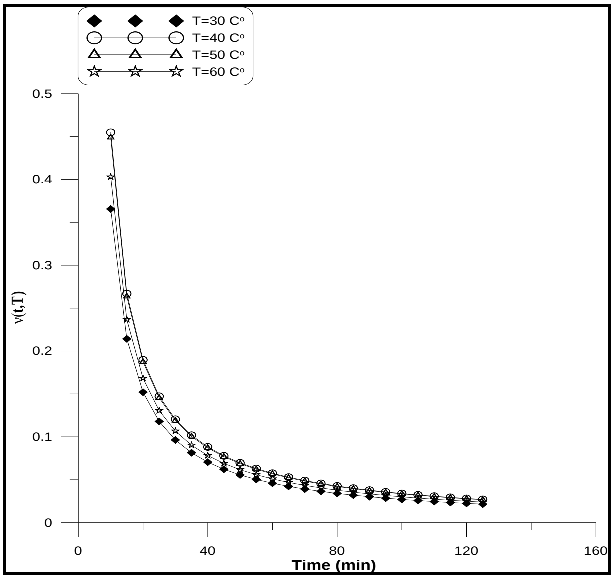

Figure 4. The relationship of the Poisson's ratio with time at stress 9.6 MPa and ε(T) is equal to 0.07 at different temperatures

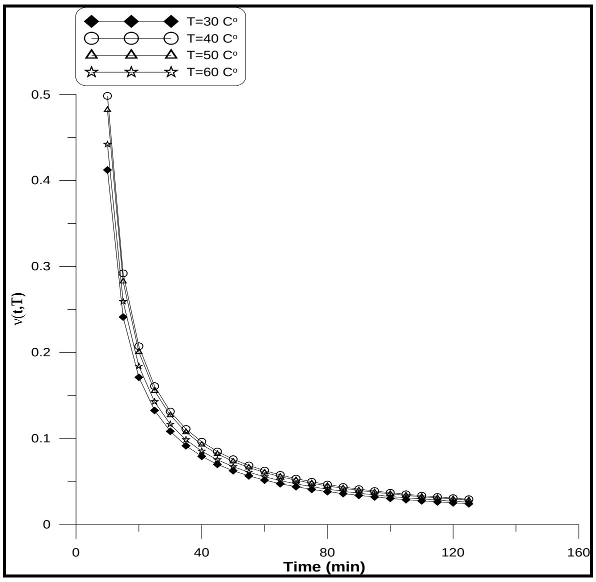

Figure 5. The relationship of the Poisson's ratio with time at stress 11 MPa and ε(T) is equal to 0.07 at different temperatures

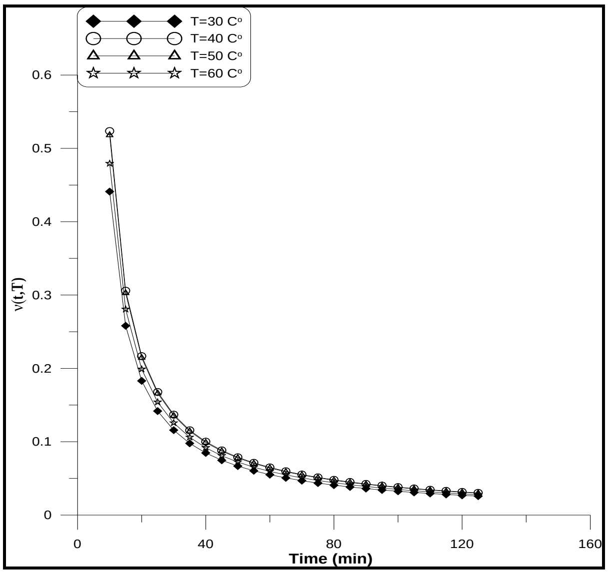

Figure 6. The relationship of the Poisson's ratio with time at stress 12.3 MP andε(T) is equal to 0.07 at different temperatures

Comparing the results in the Figures 7, 8, 9,10, and 11 it appears that the increase in the Poisson's ratio by 15.2%, 9.31%, 6.42%, 7.96%, and 10.1% when increasing the stresses from 6.9 to 12.3MPaof different temperature at fixing ε(T)at 0.12.The behavior of the material in changing the Poisson ratio, which depends on the instantaneous rate of change in the cross-section area of the specimens, which increases at first of loading and then decreases due to the movement of dislocations in the microstructure in the composite material and the redistribution of stress concentration in it, followed by limited increase before the final failure occurs.

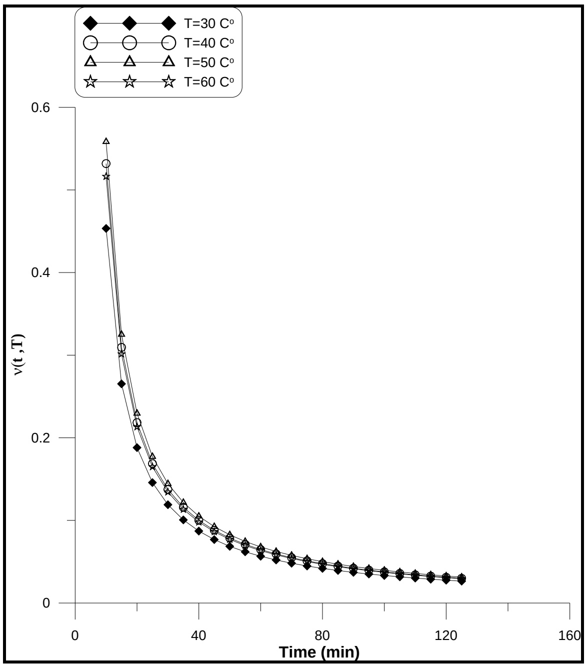

Figure7. The relationship of the Poisson's ratio with time at stress 6.9 MPa and ε(T) is equal to 0.12 at different temperatures

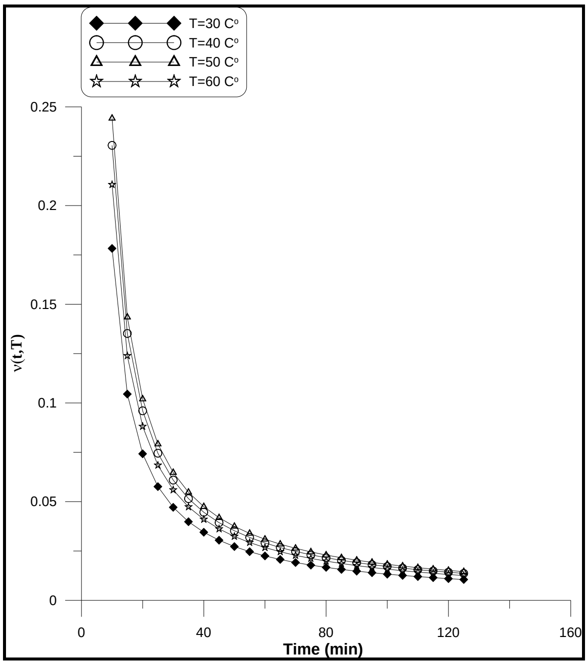

Figure 8 . The relationship of the Poisson's ratio with time at stress 8.24 MPa and ε(T) is equal to 0.12 at different temperatures

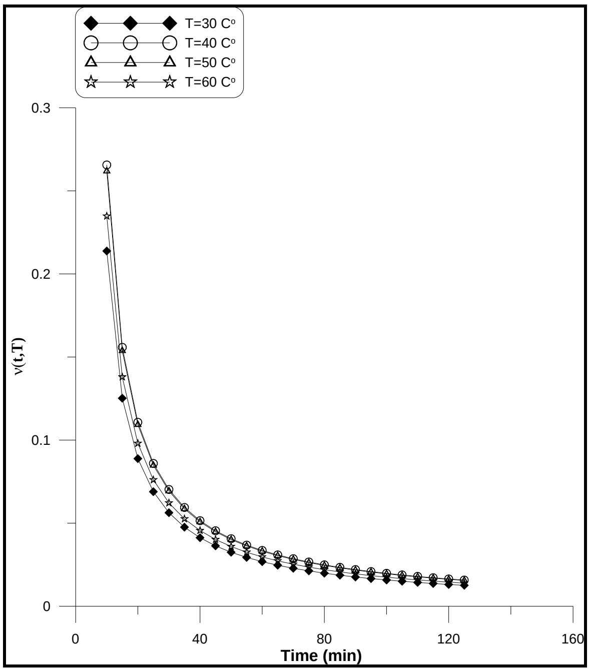

Figure 9. The relationship of the Poisson's ratio with time at stress 9.6 MPa and ε(T) is equal to 0.12 at different temperatures

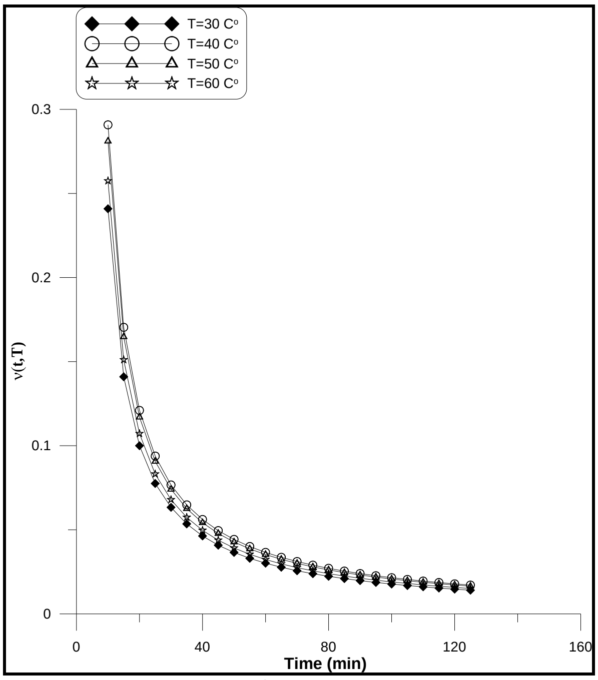

Figure10. The relationship of the Poisson's ratio with time at stress 11 MPa and ε(T) is equal to 0.12 at different temperatures

The experimental results in Figures 12, 13, 14, 15, and 16 describe the vary the increasing ratio of Poisson ratio which starts increasing then decreasing followed by limited increasing refer to the failure start occur in creep specimens.The Poisson ratio of different temperatures increased with ratios of 15.5%, 9.44%, 6.74%, 7.28%, and 10.4% as a result of increasing the stress from 6.9 to 12.3MPa at fixing ε(T)at 0.17.

The results in Figure17 display The effect of stress on Poisson's ratio at a temperature of 30 C°. It was found that the Poisson's ratioincreases by 15.5 %while increasing with a ratioof 9.47 % as shown in Figure 18 at a temperature of40C° when stress increases from 6.9 MPa to 12.3 MPa.

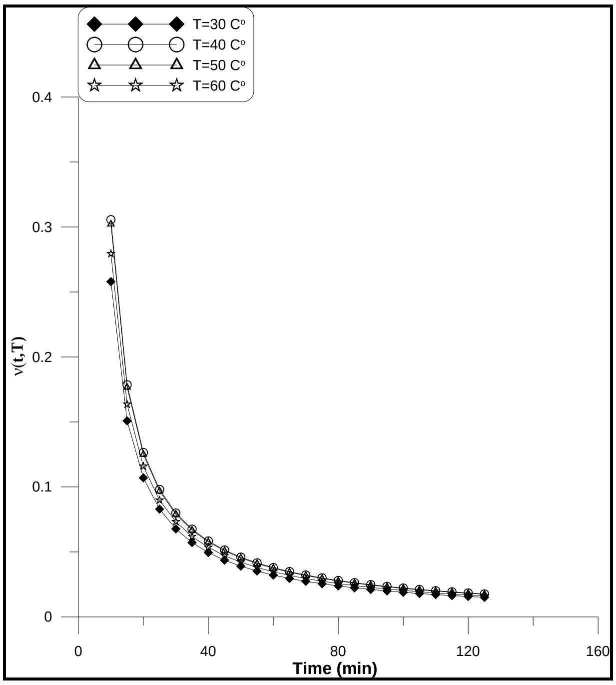

Figure 11. The relationship of the Poisson's ratio with time at stress 12.3 MPa and ε(T) is equal to 0.12 at different temperatures

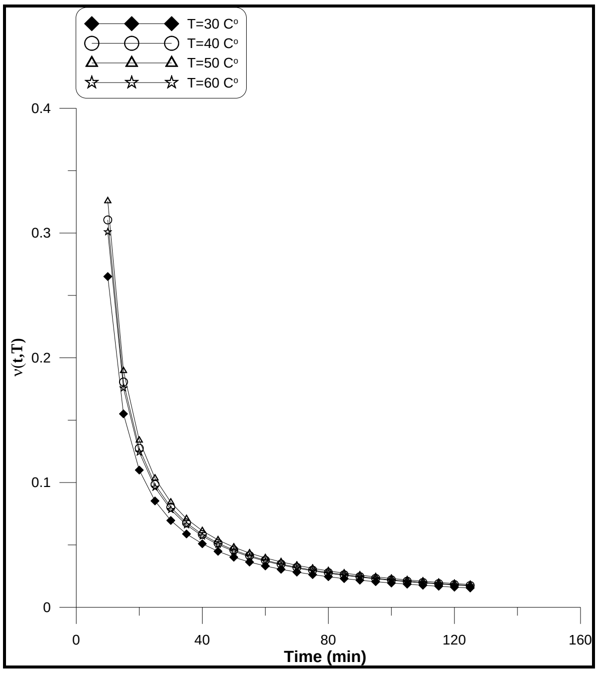

Figure 12 . The relationship of the Poisson's ratiowith time at stress 6.9 MPa and ε(T) is equal to 0.17 at different temperatures

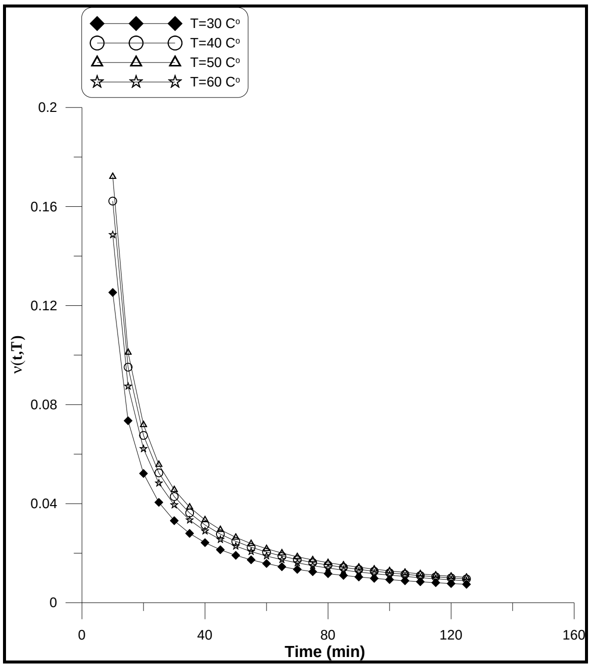

Figure 13 . The relationship of the Poisson's ratiowith time at stress 8.24 MPa and ε(T) is equal to 0.17 at different temperatures

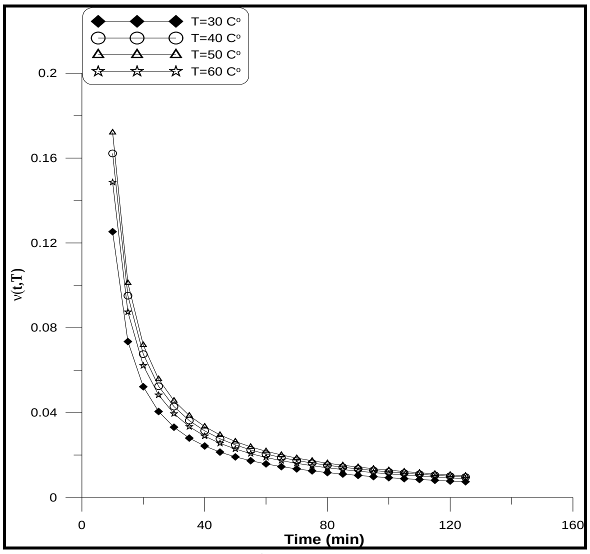

Figure 14. The relationship of the Poisson's ratiowith time at stress 9.6 MPa and ε(T) is equal to 0.17 at different temperatures

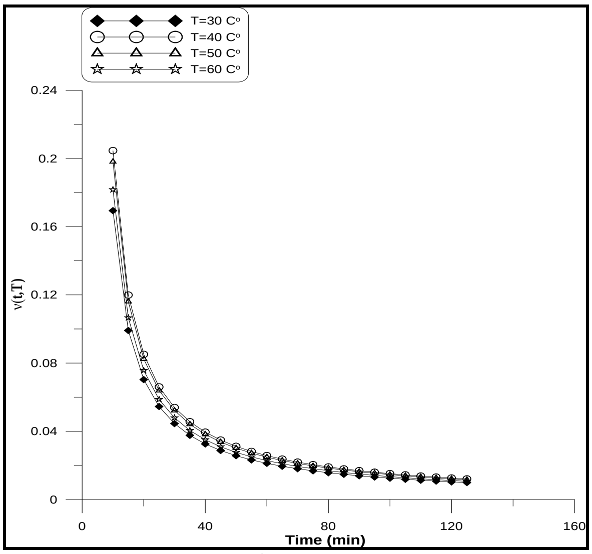

Figure 15. The relationship of the Poisson's ratio with time at stress 11 MPa and ε(T) is equal to 0.17 at different temperatures

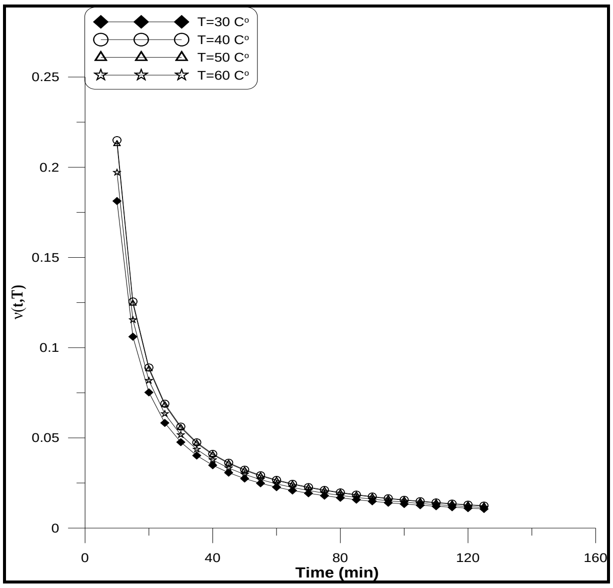

Figure 16. The relationship of the Poisson's ratio with time at stress 12.3 MPa and ε(T) is equal to 0.17 at different temperatures

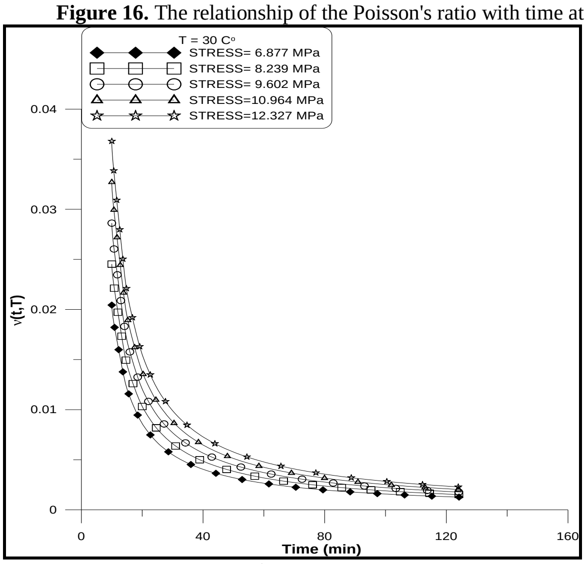

Figure 17. The relationship of the Poisson's ratio with time at temperature 30 and ε(T) is equal to 0.07 at different stresses

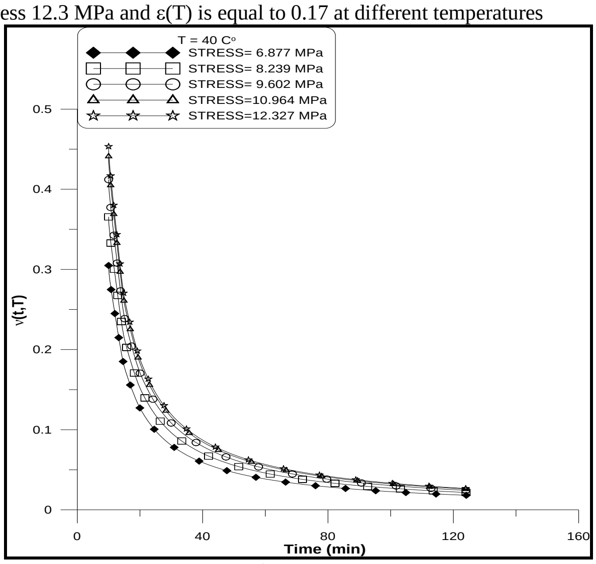

Figure 18. The relationship of the Poisson's ratio with time at temperature 40 C° and ε(T) is equal to 0.07 at different stresses

Figure19 displays The effect of stress on Poisson's ratio at a temperature of 50 C^o. It was found that the Poisson's ratio increases by 7.2 % while increasing with a ratio of 10.2 % as shown in Figure 10at temperature 60 C^o when stress increases from 6.9 MPa to 12.3 MPa when fixing ε(T)at 0.07.

The three-dimensional Figure21 showed the effect of temperature on the Poisson's ratio as a function of time ν(t, T) at stress 6.9 MPa. The decrease in the change of the Poisson's ratio over time is due to the material's resistance to elongation as a result of the rearrangement of dislocations movement in the microstructure of the composite material specimens, while the effect of increasing the temperature from 30 C^o to 50 C^o leads to increase the Poisson's ratio by 27.5%and followed by decreasing with ratio 15.6 % in the interval between 50 C^o to 60 C^{o}with fixing ε(T)at 0.07.

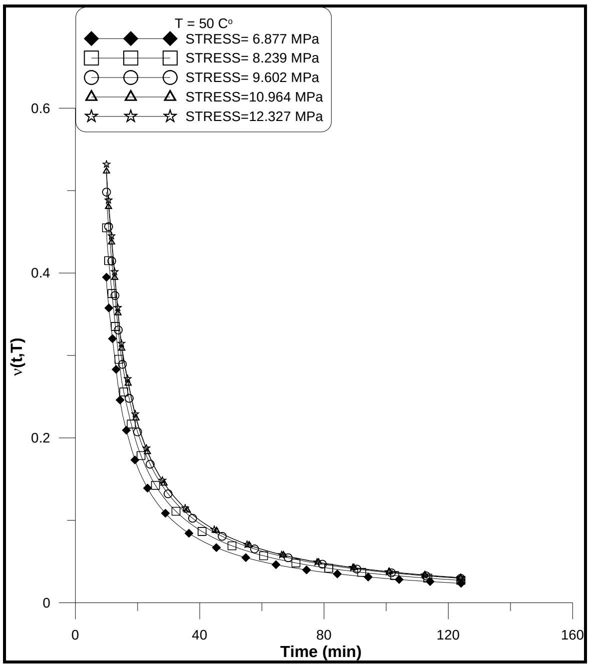

Figure 19. The relationship of the Poisson's ratio with time at temperature 50 C^{o}and ε(T) is equal to 0.07 at different stresses

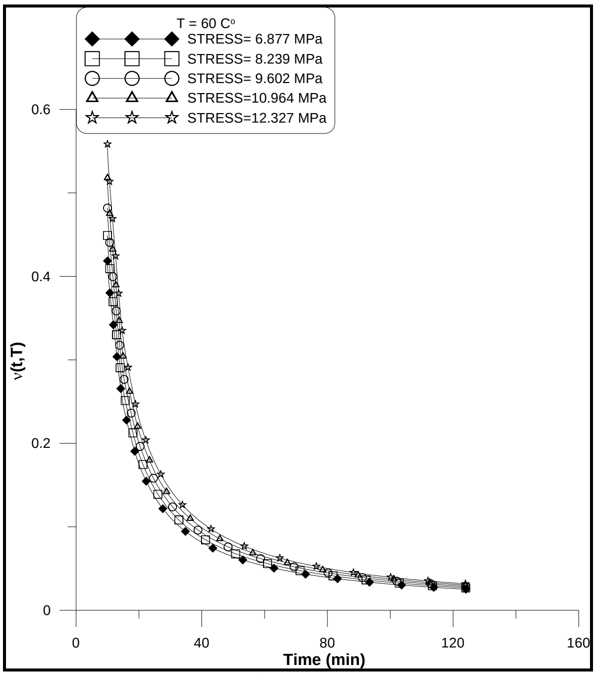

Figure 20. The relationship of the Poisson's ratio with time at temperature 60 C^{o}and ε(T) is equal to 0.07 at different stresses

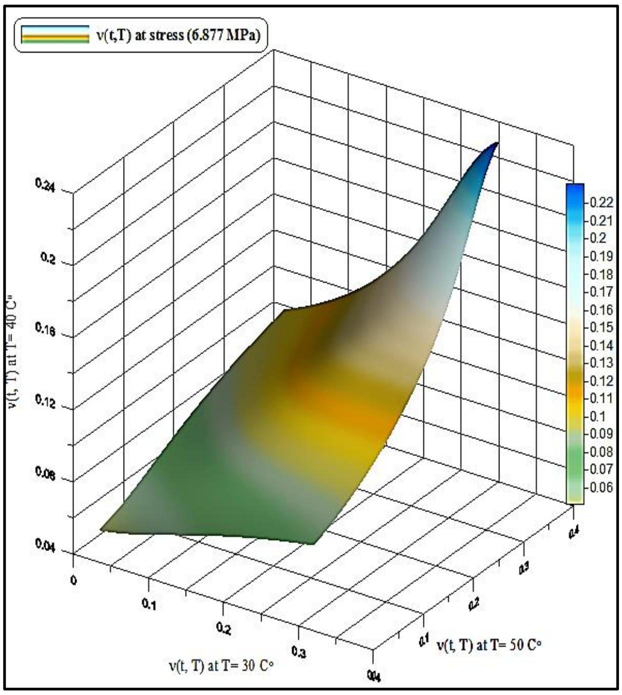

Figure 21. The relationship of the Poisson's ratioν(t,T) with time and Temperatureat stress 6.9 MPa

The three-dimensional figure shows the effect of both time and temperature between 30 to 50 C^{o} at a stress of 8.24MPa which increases in Poisson's ratio by 19% followed by decreases in a ratio of 10.25% in the range of temperature between 50 Co to 60 C^{o}. The occurrence of a decrease in the Poisson ratio indicates a decrease in the transverse strain compared to the longitudinal strain, which is an indicator of the start of failure. The value of the Poisson's ratio ν (t, T) is between (0.06) and its highest value (0.21). The figure shows the overlapping effect of increasing the temperature and time, which leads to an increase in the value of the Poisson's ratio that occurs due to the increase in the transverse strain in the test samples before the fracture occurs, as shown in Figure 22. Meanwhile, the effect of increasing temperature from 30 to 50 C^{o}leads to an increase in the Poisson's ratio by 14.7% at stress 9.6 MPa as shown in Figure 23.

The 3-Dimensional Figure24 showed the effect of increasing the temperature from 30 C^{o} to 50 C^{o} leads to an increase in the Poisson's ratio by an average ratio of 7.88% at stress 11 MPa,while the Poisson's ratio increased by an average ratio of 17.59% at stress 12.3 MPa as shown in Figure 25.

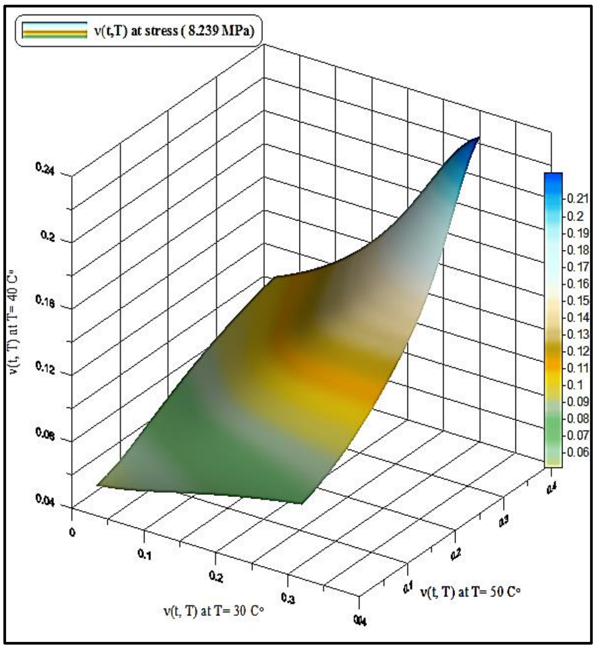

Figure 22. The relationship of the Poisson's ratio ν(t, T) with time and Temperature at stress 8.24 MPa

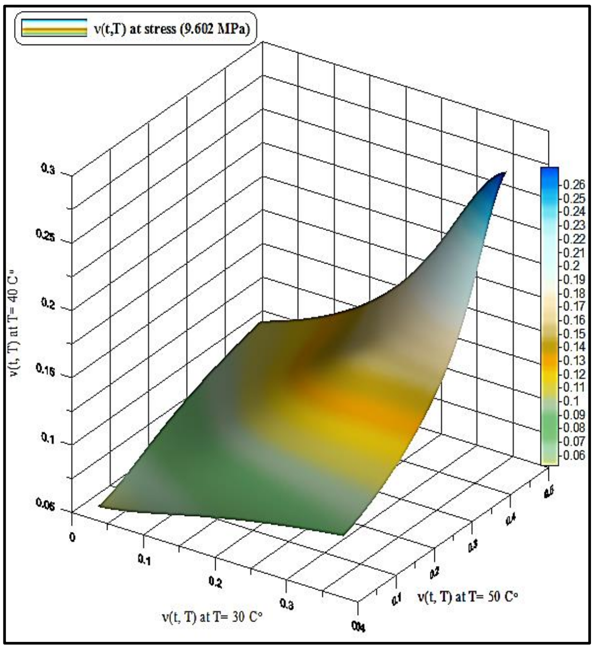

Figure 23. The relationship of the Poisson's ratio ν(t, T) with time and Temperature at stress 9.6 MPa

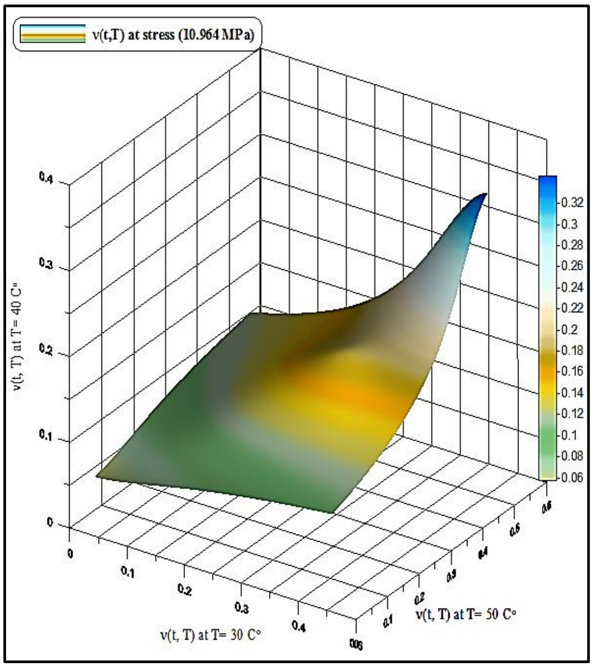

Figure 24. The relationship of the Poisson's ratio ν(t, T) with time and Temperature at stress 11 MPa

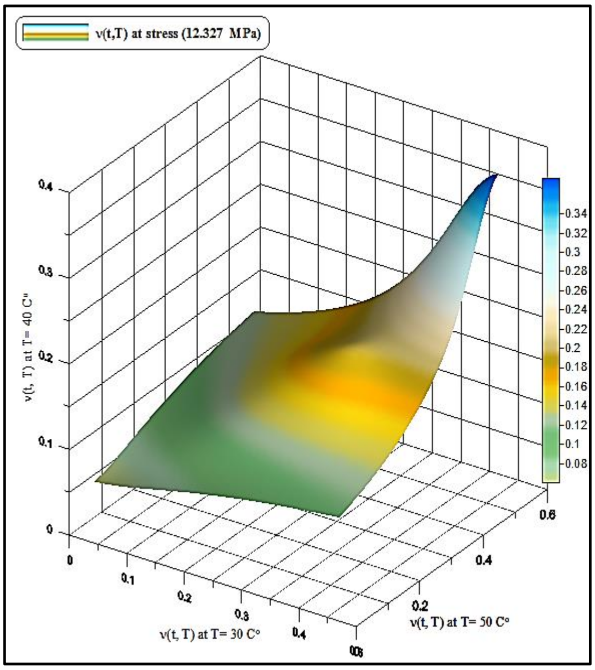

Figure 25. The relationship of the Poisson's ratio ν(t, T) with time and Temperature at stress 12.3 MPa

In the above three-dimensional figures, it is observed that there was an increase in the Poisson's ratio at temperature40 C^{o} compared to the smooth rise in it at other temperatures, as there was an increase in the Poisson's ratio with applying the stress giving the composite specimens the suitable time to gain maximum elongation strain through a creep test. Figure 26 shows the decrease in the percentage change occurring in the Poisson's ratio, which is a function of time and temperature with an increase in stress since the decrease in stress gave the specimen the necessary time for longitudinal elongation before the failure occurred. The lowest change occurred in the Poisson's ratio at stress 11 MPa, where the specimen reached its maximum resistance to prevent the occurrence of failure, followed by a slight increase in the change at stress 12.3 MPa which is considered the stress that will lead to failure and the increase resulting from the internal redistribution of stresses in the specimen due to a higher dislocation movement in the creep test of the composite specimens and then failure occurs.

The study found that the maximum effect of time on the Poisson's ratio $\nu(t, T)$ was at the time in the range of 10-60 minutes and led to a decrease in the Poisson's ratio by a ratio of 9.87% due to an increase the amount of instantaneous change in cross-section area of creep specimens at temperature 60 C^{o} and stress12.3MPa. The maximum effect of the temperature on Poisson's ratio was at an average ratio of 17.59%at stress 12.3MPa.The highest effect of stress on Poisson's ratio was an increase of 33.44% as a result of increasing stress in intervals between 11MPa to 12.3MPa when temperature 30 C^{o} and strain 0.12.It was observed that the decrease in the effect of increasing the temperature and stress on Poisson's ratio is an indication of the beginning of failure in the composite specimens during the creep test, especially at intervals between 50 to 60 C^{o}.

Conclusions

The conclusion of the research is to build a mathematical model describing the Poisson's ratio $\nu(t, T)$ as a function of the time and temperature of composite materials. The study found the maximum effect of the temperature on Poisson's ratio was at 17.59% at stress 12.3MPa at a time of 30 minutes so that, the Poisson's ratio increased by a maximum ratio of 2.77% when the stress increased by 16.53% which mean that the temperature's effect 6.3 times of the stress's effect at this condition. The experimental results refer to the maximum increase ratio that occurred in the Poisson's ratio by an increase of 33.44% as a result of increasing stress in the interval between 11 MPa to 12.3MPa when temperature 30 C^{o} and strain 0.12. Finally, the mathematical model covers a wide range of cases to describe the behavior of the composite material at constant loads with time to predict the time of failure in it from the change that occurs in Poisson's ratio $\nu(t, T)$ that are used in the manufacture of tanks and structures.

Acknowledgements

We would like to thank the University of Technology-Iraq, especially the Electromechanical Engineering Department.

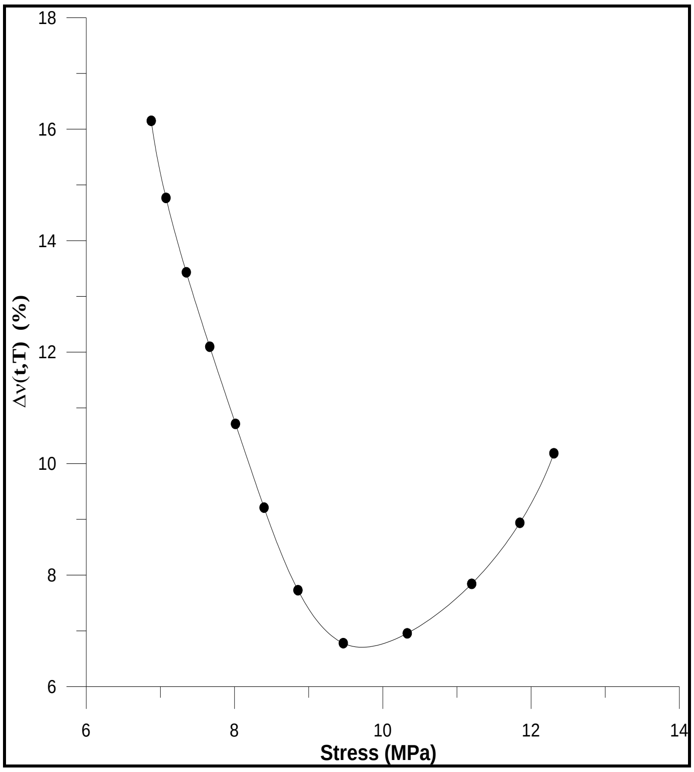

Figure 26. The relationship of average change of Poisson's ratio $\Delta\nu(t, T)$ at different stresses

References

[1] Emri and M. Gergesova, "Time-Dependent Behavior Of Solid Polymers", EOLSS Publishers/ UNESCO, United Kingdom, 2010.

[2] K. E. EVANS, "Mechanical Properties and Testing of Polymers", Springer Science Business Media Dordrecht, 1999.

[3] P.H. Mott and C.M. Roland, "Limits ToPoisson’s Ratio In Isotropic Materials, Chemistry Division",Code 6120, Naval Research Laboratory, Washington DC 20375-5342, 2009,1-12.

[4] J. Sanahuja and L. Charpin, "Concrete Basic Creep And Poisson’s Ratios: Back To Basics Of Viscoelasticity And Applications", 23ème CongrèsFrançais de Mécanique, Lille, 28 au 1er, 2017, 1-15.

[5] Mostafa KianiDehKiani, Hossein Maghsoudi and Said Minaei, "Determination Of Poisson’s Ratio And Young's Modulus Of Red Bean Grains", Journal of Food Process Engineering, 2009,1-10.

[6] Harry H. Hilton, "Elastic AndViscoelastic Poisson’s Ratios: The Theoretical Mechanics Perspective", Materials Sciences and Applications, Vol.8, 2017, 291-332.

[7] G. N. Greaves, A. L. Greer, R. S. Lakesand T. Rouxel, "Poisson’s Ratio And Modern Materials", NATURE MATERIALS, Vol. 10, 2011, 823-837.

[8] N.W. Tschoelgl, Poisson’s Ratio in Linear Viscoelasticity – A Critical Review, Mechanics of Time-Dependent Materials ,Vol.6, 2002, 3–51.

[9] R. S. Lakes · A. Wineman, On Poisson’s Ratio in Linearly Viscoelastic Solids, J Elasticity, DOI 10.1007/s10659-006-9070-4, Vol. 85, 2006, 45–63.

[10] MD Mehadi Hassan, Effect of Poisson’s Ratio on Material Properties Characterization by Nanoindentation with a Cylindrical Flat Tip Indenter, South Dakota State University, Theses and Dissertations, 2016, 1-60.

[11] Jun-Jun Zhai, Xiang-Xia Kong, and Lu-Chen Wang," Thermo-Viscoelastic Response Of 3D Braided Composites Based On A Novel FsmsfeMethod", Materials, ,https://doi.org/10.3390/ma14020271, Vol. 14,No. 271, 2021.,2-18.

[12] Heitor L. Ornaghi Jr., JoséHumberto S. Almeida Jr., Francisco M. Monticeli and, Roberta M. Neves," Stress Relaxation, Creep, And Recovery Of Carbon Fiber Non-Crimp Fabric Composites",Composites Part C: Open Access, Vol.3, 2020.

[13] N Obaid, MT Kortschot, M Sain, "Modeling And Predicting The Stress Relaxation Of Composites With Short And Randomly Oriented Fibers", Materials (Basel) 10, doi: 10.3390/ma10101207., 2017, 1–11.

[14] N Obaid, MT Kortschot, M Sain, "Predicting The Stress Relaxation Behavior Of Glass- Fiber Reinforced Polypropylene Composites", Compos. Sci. Technol. 161, doi: 10.1016/j. ,2018, 85–91.

[15] AA Gusev, LS. Kern, "Frequency Domain Finite Element Estimates OfViscoelas- Tic Stiffness Of Unidirectional Composites", Compos. Struct. 194, doi: 10.1016/j., 2018, 445–453.

[16] Y Xie, Y Xiao, J Lv, Z Zhang, Y Zhou, Y Xue, "Influence of creep on preload relaxation of bolted composite joints: Modeling and numerical simulation", Compos. Struct. 245, doi: 10.1016/j,2020.

[17] HL Ornaghi Jr, RM Neves, FM Monticeli, JHS Almeida Jr, Viscoelastic characteristics of carbon fiber-reinforced epoxy filament wound laminates, Compos. Commun. 21 ,doi: 10.1016/j.coco.2020.100418 ,2020.

[18] MS Sreekala, MG Kumaran, R Joseph, S Thomas, Stress-relaxation behaviour in com- posites based on short oil-palm fibres and phenol formaldehyde resin, Compos. Sci. Technol. 61 ,doi: 10.1016/S0266-3538(00)00214-1, 2001, 1175–1188,

[19] Ornaghi Jr HL, Almeida Jr JHS, Monticeli FM, Neves RM, CioffiMO,"Time- temperature behavior of carbon /epoxy laminates under creep loading", Mech. Time- Depend. Mater.,10.1007/s11043-020-09463-z, 2020,1–14.

[20] JHS Almeida Jr, HL Ornaghi Jr, N Lorandi, PB Bernardo, SC Amico, Creep and inter- facial behavior of carbon fiber reinforced epoxy filament wound laminates, Polym. Compos. 39 2199–2206, doi: 10.1002/pc, 2017.

[21] HSP Silva, HL Ornaghi Jr, JHS Almeida Jr, AJ Zattera, SC Amico, "Mechanical Behav- IorAnd Correlation Between Dynamic Fragility And Dynamic Mechanical Properties Of Curaua Fiber Composites", Polym. Compos, doi: 10.1002/pc, 2014.

[22] N.Al-Klouba, M. A. Nawafleh, M. Tarawnehc and, F. Al-Ghathiana, "A Mathematical Study for Investigation the Problems of Soft Shells Materials", Jordan Journal of Mechanical and Industrial Engineering, Vol.4, No.3, 2010, 418 – 423.

[23] H. M. Tlilan, " Effect of Poisson’s Ratio on the Elastic Strain Concentration Factor of Notched Bars under Static Tension and under Pure Bending", Jordan Journal of Mechanical and Industrial Engineering, Vol.4, No.6, 2010, 757 – 778.

[24] Gabriel Stadler , Andreas Primetzhofer , Michael Jerabek , Gerald Pinter, and Florian Grün, " Investigation Of The Influence Of Viscoelastic BehaviourOn The Lifetime Of Short Fibre Reinforced Polymers", Polymers ,doi:10.3390/polym12122874, Vol.12, Issue 12, , 2874, 2020, 1-13.

[25] Victor Rizov, "Influence Of The Viscoelastic Material Behaviour On The Delamination In Multilayered Beam", Procedia Structural Integrity, Published by Elsevier B.V, Vol. 25, 2020, 88–100.

[26] FernándezPelayo, David Blanco , Pedro Fernández , Javier González and Natalia Beltrán, " Viscoelastic BehaviourOf Flexible Thermoplastic Polyurethane Additively Manufactured Parts: Influence Of Inner-Structure Design Factors", Polymers, Vol. 13, Issue 14, 2021, 1-15.

[27] S.G. Nunesa,d,e, R. Joffe, N. Emami, P. Fernberg, S. Saseendran, A. Esposito, S. C. Amico, J. Varna ,"Physical Aging Effect On Viscoelastic Behavior Of Polymers", Composites Part C: Open Access, Vol.7, 2022, 1-5.

[28] R. S. Lakes, "The Time-Dependent Poisson's Ratio Of Viscoelastic Materials Can Increase Or Decrease", Cellular Polymers, Vol.11, 1992,466-469.

[29] William N. Findley ,JamesSlai and KasifOnaran.“ Creep and Relaxation of Nonlinear Viscoelastic Material”, North-Holland Publishing,1976.

[30] Muhsin J. Jweeg, Adnan M. Al-SultanyandRaedNaeemHwyyin, "Nonlinear Analysis of Thermoviscoelasticity of Laminated Composites", Eng. & Tech. Journal, Vol. 28, No.14, 2010, 1-19.

[31] Azhar Sabah Ameed, "Poisson's Ratio as a Function of Time in Composite Material of Viscoelastic Behavior by Depending on Creep Test", Eng. & Tech. Journal, Vol.29, No.3, 2011, 488-498.

[32] Amelie Renault, Luc Jaouen,Franck Sgard and NoureddineA., "Direct QuasistaticMeasurement of AcousticalPorous Material Poisson Ratio",University Sherbrook ,Canada,2010.

[33] Reihart T.J.&others, Engineered Materials Handbook Volume-1Composites, ASM. International, 1987.

[34] Standard Creep Test ASTM-D2990.

[35]William N. Findley, James S. Lai, Kasif Onaran, "Creep And Relaxation Of Nonlinear Viscoelastic Materials", North-Holland Publishing Company, Volume 18, Pages 1-372 , 1976.

[36] Sabah Khammass, Samira K. Rad and Muhsin J.Jweeg, "Linear and Nonlinear Behavior of Viscoelastic Thin Plates Subjected to Uniform Distributed Loading", phd. Thesis, Al-Mustansiriyah University -College of engineering, Pages1 – 178, 2006.

Appendices

Appendix–A. The experimental function of stress as a function of strain and temperature

$$f_B(T) = -4041.75 + 484.083.T - 18.3113\,.T^2 + 0.28793\,.T^3 - 0.00161287.T^4 \tag{A.1}$$

$$f_A(T) = 496.922 - 52.069.T + 1.87278\,.T^2 - 0.0284644\,.T^3 + 0.000155193.T^4 \tag{A.2}$$

$$\sigma(\varepsilon,T) = f_B(T).\,\varepsilon + f_A(T) \tag{A.3}$$

Appendix–B. The experimental fitting of (ns) which is the slope of logarithm of stress as a function of strain and temperature

$$f_{ANS}(\varepsilon) = 2.89798 - 64.9958\,.\varepsilon + 252.399.\,\varepsilon^2 \tag{B.1}$$

$$f_{BNS}(\varepsilon) = -0.252621 + 5.59588\,.\varepsilon - 21.305.\,\varepsilon^2 \tag{B.2}$$

$$f_{CNS}(\varepsilon) = 0.008076 - 0.176779.\,\varepsilon + 0.658348\,.\varepsilon^2 \tag{B.3}$$

$$f_{DNS}(\varepsilon) = -0.000113913 + 0.00245404\,.\varepsilon - 0.00896002.\,\varepsilon^2 \tag{B.4}$$

$$f_{ENS}(\varepsilon) = 5.98297\mathrm{E} - 007 - 1.26821\mathrm{E} - 005.\,\varepsilon + 4.55375\mathrm{E} - 005.\,\varepsilon^2 \tag{B.5}$$

$$ns(\varepsilon,T) = f_{ANS}(\varepsilon) + f_{BNS}(\varepsilon).T + f_{CNS}(\varepsilon).T^2 + f_{DNS}(\varepsilon).T^3 + f_{ENS}(\varepsilon).T^4 \tag{B.6}$$

Appendix–C. The experimental fitting of the strain as a function of strain, stress, and, temperature

$$f_{NA}(T) = -7.36306 + 0.63538.T - 0.0201105.T^2 + 0.000280252.T^3 - 1.45469\mathrm{E} - 006.T^4 \tag{C.1}$$

$$f_{NB}(T) = 1.71764 - 0.146934.T + 0.00460911.T^2 - 6.35792\mathrm{E} - 005.T^3 + 3.2681\mathrm{E} - 007.T^4 \tag{C.2}$$

$$f_{NB}(T) = -0.0852624 + 0.00719369.T - 0.000222179.T^2 + 3.02208\mathrm{E} - 06.T^3 - 1.535\mathrm{E} - 008.T^4 \tag{C.3}$$

$$n(\sigma,T) = f_{NA}(T) + f_{NB}(T).\,\sigma + f_{NC}(T).\,\sigma^2$$

$$\varepsilon(t,\sigma,T) = \varepsilon(\sigma,T).\,t^{n(\sigma,T)}$$

JJMIE

Volume 16, Number 4, September. 2022
ISSN 1995-6665
Pages 529 – 542

Jordan Journal of Mechanical and Industrial Engineering

A Comprehensive Review on 3D Printing Technology: Current Applications and Challenges

Archisman Dasgupta*, Prasenjit Dutta

Department of Production Engineering, National Institute of Technology, Agartala, Tripura west, 799046, India

Received 20 Mar 2022 *Accepted 11 Jun 2022*

Abstract

The key advantages of 3D printing technology include design freedom, customization, pollution prevention, the capacity to construct advanced systems, and rapid prototyping. In this paper, a concise overview of the fundamental 3D printing techniques, materials, and their advancement in emerging fields is presented. Besides, the significant potential of additive manufacturing in medical, aeronautical, architecture, and defensive structures are discussed in detail. The latest developments in materials, comprising alloys, polymer composites, ceramics, and concrete are also discussed. Finally, the key processing issues and computer design limitations of 3D printing technology is described. In short, this study presents a survey of the advantages and disadvantages of 3D printing as a baseline for possible future research work.

Keywords: Additive manufacturing; 3D printing applications; Materials; Key challenges.

Nomenclature

3DP	3D printing
AM	Additive manufacturing
CAD	Computer-aided design
SLA	Stereolithography
FDM	Fused deposition modeling
PBF	Powder bed fusion
SLS	Selective laser sintering
SLM	Selective laser melting
IJP	Inkjet printing
LOM	Laminated object manufacturing
DED	Direct energy deposition
CC	Contour crafting
QD	Quantum Dot

1. Introduction

3D printing (3DP) is a technology for creating a variety of shapes and intricate patterns using three-dimensional data modelling [1], [2].The process entails printing several layers of material on top of one another. Charles Hull invented this technique in 1986 through a procedure called stereolithography followed by further advancements, for instance, fused deposition modelling, powder bed fusion, contour crafting, and inkjet printing, etc.[3].Over the decades, 3DP has progressed, using diverse procedures, equipment and materials and can handle production and logistical activities. Additive manufacturing (AM)is extensively being used nowadays in various areas, especially construction, prototype manufacturing, and biomechanics. The implementation of 3DP in architectural projects is restricted, despite the benefits of decreased waste, increased design freedom, and mechanization. [4], [5].

As AM technology advances, its application in a variety of fields expands as well. One of the primary reasons for this technology's increased accessibility is the expiration of existing inventions that enabled engineers to create modern 3D printing machines. Latest advancements have lowered the expense of 3D printers, enabling them to be used in more areas including institutions, residences, hospitals, and laboratories. Previously, design engineers utilized 3DP widely to create decorative and practical models because of its quick and cost-effective prototyping capabilities. Thus, the usage of 3DP has resulted in a significant reduction in the expenses associated with product development[6].

However, in recent times 3DP has been widely implemented in a variety of companies, from prototype to finished items. Owing to the increased expenses associated with developing a specially designed product for individual customers, manufacturers have struggled with product customization. Conversely, AM enables low-cost 3D printing of limited numbers of customized products. It is particularly advantageous in the medical sector, where customized items for each individual are frequently required[7]. Wohlers Associates predicted that by 2020, around 50% of the commercial product will be manufactured by 3DP[1]. However, to further enhance the

---

* Corresponding author e-mail: archismandg@gmail.com.

benefits of 3DP for the public, much research is needed on this technology[5].

The emerging agreement in favour of implementing 3DP is that it will improve system efficiencies, design flexibility, and customization. Metals, polymers, ceramics, and concrete are some of the materials that are commonly utilized in 3DP.Usually, modern 3DP metals and alloys are used in the aircraft industry since conventional procedures are extremely time-consuming, complicated, and expensive. Ceramics are mostly utilized in the additive manufacture of scaffolds, while concrete is the primary material applied in the additive manufacturing of structures. Nevertheless, the poor mechanical characteristics and anisotropic behaviour of 3D printed objects continue to constrain the possibility of mass printing. As a result, an optimized 3D printing design is vital in protecting defect susceptibility and anisotropic performance. Additionally, variations in the printed conditions affect the final product's appearance[8].AM is proficient in creating components in a wide range of dimensions, from microscopic to massive. Yet, the quality of printed items is reliant on the technique's precision and the scale of the print. For example, micro-scale additive manufacturing has difficulties with resolutions, surface integrity, and multilayer adhesion, necessitating the use of comment procedures like sintering. Besides, the scarcity of materials accessible for 3DP creates barriers to the widespread use of this technology in a variety of sectors. As a result, there is a necessity for the development of appropriate material for 3DP.Moreover, additional study is required to improve the mechanical characteristics of 3D printed components[9].

The benefits of the 3DP technique will continue to manifest as a result of ongoing scientific research which should be carried out to comprehend and eradicate the limits that prevent this technology from being used. AM-oriented Computer-aided design (CAD) systems are only a few of the critical characteristics that must be implemented[10].A distinct feature of 3DP is its capacity for mass customization, which means manufacturing a number of individualized products in a way that every item is unique. 3DP eliminates the additional cost associated with mold creation and tooling for a customized component. Consequently, bulk fabrication of a large number of similar components can be as economically efficient as producing a similar number of unique individualized products. The transition between alternative designs is simple, incurring minimal additional costs and requiring no particular planning. Additionally, AM offers the possibility of mass-producing complicated shapes including lattice structures, where the implementation of conventional manufacturing technologies like casting is complicated and requires additional time for processing[11]. However, advances in production rate and cost savings must be accomplished using machine design advancements. Furthermore, the high price and lengthy processing time associated with the AM method continue to be significant impediments to large-scale production[12]. This article will offer an in-depth examination of 3DP techniques, including the major processes used, the materials utilized, their present predicament, and applicability in a variety of sectors. Additionally, this report also presents knowledge gaps and problems in deploying this technology.

2. Different basic methods of 3DP

To fulfill the need for printing complicated objects at high resolutions, AM methods have been created. Fused deposition modeling is still the most popular technique of 3DP that primarily utilizes polymer filaments. Also, AM of powders in 3DP via selective laser sintering, selective laser melting, or liquid binding, as well as inkjet printing, contour crafting, stereolithography, direct energy deposition, and laminated object manufacturing, are the primary methods of AM[13], [14].These procedures are concisely described in the subsequent sub-sections, along with respective benefits and the materials needed for each approach. **Figure 1** depicts a schematic diagram of the primary techniques of AM.

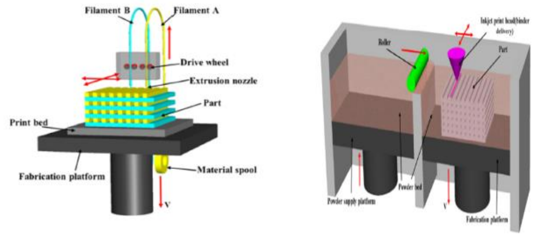

(a) Fused deposition modelling (b) Inkjet printing

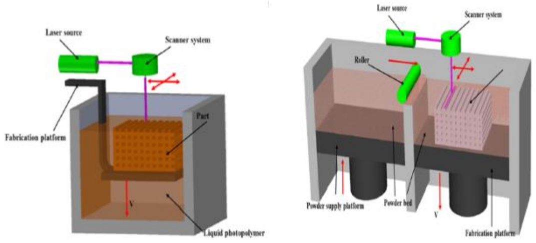

(c) Stereolithography (d) Powder bed fusion

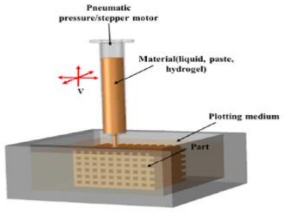

(e) 3D Plotting

Figure 1. Schematic diagram of the various 3DP methods[15]

2.1. *Stereolithography (SLA)*

SLA is one of the oldest techniques used in AM. It initiates a chain reaction on a film of resin by ultraviolet light or an electron beam. Once activated, the monomers immediately change to polymer chains. Following polymerization, a design is established within the resin layer to serve as a support for the subsequent layers. After the printing is completed, the unreacted resin is retrieved. Several printed parts may require a post-processing intervention, like heating or photocuring, to produce the necessary mechanical characteristics. Ceramic-polymer composites (silicon oxycarbide) can be printed using the diffusion of ceramic particles in monomers.SLA produces high-quality components at a resolution of as little as 10 µm. Moreover, it is a somewhat slower and costly technique, with a fairly restricted selection of printing materials[16].

2.2. Fused deposition modeling (FDM)

A filament of a thermoplastic is utilized in the FDM technique to print3D layers of different materials. The filament is warmed up to a quasi-condition at the nozzle before being dispensed onto the base or over formerly produced layers. The thermoplasticity of the filament is critical for this process because it enables the filament to merge together throughout the printing and then harden at ambient conditions. The layer's depth, the filament's breadth, and alignment, and the air gaps are the primary operating factors that influence the structural qualities of printed components. The primary source of structural fragility is observed to be inter-layer misalignment. However, the primary advantages of FDM are cost-effectiveness, high efficiency, and flexibility. whereas, the primary disadvantages of this process are poor mechanical qualities, layer-by-layer appearances, poor surface integrity, and a restrictive choice of thermoplastics[17].

2.3. Powder bed fusion (PBF)

PBF methods involve the application of fine layers of ultrafine particles that are distributed and packed firmly together on a platform. Particles of layers are fused collectively using a laser beam or a binder. Successive layers of particles are started rolling over the preceding layers and cemented permanently till the finished three-dimensional item is constructed. The excessive powder is subsequently vacuumed away and, when required, additional treatment including coating, sintering, or infiltration is accomplished. The dispersion of powder type and packaging, which define the densities of the printed item, is the primary critical aspects affecting the technique's performance.The laser must be utilized with particles that have a minimal melting temperature, while liquid binders must be employed in all other cases. Selective laser sintering (SLS) is being utilized to process a wide range of polymers, metals, and alloy powders. However, selective laser melting (SLM) can be employed on a limited number of metals, including steel and aluminium[18].

2.4. Inkjet printing (IJP)

IJP is a widely used technique for the AM of ceramics. It is utilized to print sophisticated and expensive ceramic objects for purposes like tissue engineering. The injecting nozzle is used to infuse and inject a persistent ceramic solution, such as zirconium oxide powder, into the substrate in the form of bubbles, where it solidifies into a pattern strong enough to support future layers of printed materials. This process is quick and reliable, which gives designers and printers greater choice when developing and printing complicated shapes. Ceramic inks are classified into two categories: wax-based inks and liquid suspensions. To settle wax-based inks, they are melted and applied onto a cold substrate. By contrast, liquid suspensions are stabilized through the process of liquid evaporation[19].

2.5. Laminated object manufacturing (LOM)

LOM is among the earliest industrially accessible AM processes, which is based upon layer-by-layer cutting.Using a mechanized cutter or a laser, consecutive layers are accurately sliced and then fused firmly, or vice versa. This procedure is especially advantageous for the thermal joining of ceramic or metallic materials because it simplifies the design of internal features by eliminating excess material prior to bonding. After cutting, the extra materials can be retrieved and reused.LOM is compatible with a wide range of materials, including polymer composites, ceramics, paper, and metal-filled tapes[20].

2.6. Direct energy deposition (DED)

DED has been employed in the production of super alloys with exceptional performance. This technique is also referred to as laser engineered net shaping, laser solid forming, directed light fabrication, direct metal deposition, electron-beam AM, and wire-arc AM.DED utilizes an electron beam that is targeted specifically on the little part of the substrate while concurrently melting a feedstock material. After the electron beam has moved, the molten material is placed and bonded to the melted substrates and hardened. This technology is frequently utilized in aeronautical applications utilizing titanium, Inconel, stainless steel, and aluminum, and related alloys[21].

2.7. 3D Plotting

3D plotting is a technique that involves extruding a viscous liquid from a pressurized injector (syringe) in order to construct three-dimensional shapes of materials. The syringe head may revolve in three dimensions whereas the substrate remains stable. This allows for the layer-by-layer assembly of discharged materials. Curing processes can be triggered mainly by UV light or by distributing two reactive chemicals utilizing a blending nozzle. Materials can be transported to a plotting surface to complete the curing reaction in some instances. The fluidity of the material and the rates of deposition are related to the accuracy of the ultimate printed items. The primary benefit of this approach is that it allows for materials flexibility.3D plotting printers allow solutions, pastes, and hydrogels. A short-term, fatal material may be required to maintain the printed component, as raw viscous materials have poor rigidity, which can cause complicated structures to crash[22].**Table 1** presents a comparative analysis of various 3DP technologies.

2.8. Direct write technique

Direct Writing (DW), sometimes called Robo-casting, is a layer-by-layer production technology focused on extrusion and is appropriate for complicated structures. Composites, ceramics, biomaterials, and shape memory alloys are among the materials that can be utilized for DW. DW is useful for a variety of applications, from biological to optics, because of its simplicity and cost-effectiveness.

Recent DW research has revealed a trend toward developing novel materials. This method is divided into three main categories: (a) extrusion-based DW, (b) continuous droplet-based DW, and (c) energy-assisted DW, which allow for the production of functional and industrial parts complex shapes, and scales [21].

Table 1: A summary of the primary 3DP methods[10], [15], [23]

Method	Materials	Applications
SLA	Resin and its monomers	Prototyping, and biomedical
FDM	Thermoplastic and fibre-reinforced polymers	toys, advanced composite parts and rapid prototyping,
PBF	Powders of metals, alloys, and polymers	Electronics, biomedical, lightweight structures, aerospace and heat exchangers
IJP	Dispersed particles in a liquid Ceramic	Large structures, buildings, and biomedical
LOM	Ceramics, paper, polymer composites, and metal rolls	Electronics, and foundry industries
DED	Powders of metals and alloys	Retrofitting, aerospace, repair, biomedical, and cladding
DW	Composites, ceramics, biomaterials, and shape memory alloys	Industrial complex parts

3. Applications of 3DP in various fields

3.1. Biomaterials and bio-fabrications

Today, the medical sector accounts for 11% of the entire AM industry and is expected to be a major driver of AM innovation and expansion[24].Bio-fabrication is the process of fabricating tissues and organs via bio-printing, bio-assembly, and maturation. The primary distinction amongst bio fabrication and traditional AM is the incorporation of cells into the created biomaterials to make bio-inks. The integration of bio-ink printing with laser-induced forward transfer, inkjet printing, and robotic dispensing enables the production of bio-inks[25].The biomaterials are developed into the appropriate pattern and tissues using bimolecular and cells. Biomaterials serve as scaffolds and physiological clues for the formation of the tissue matrix, whereas biomolecules direct the tissue rejuvenation processes[26].Numerous bio-inks and cells will be merged with increasingly sophisticated organs and tissues. Also, improved imaging will enable the accurate determination of the size, shape, and structure of faulty components. Additionally, by utilizing homologous cells from the client, the chance of refusal of the created implant is decreased. In vitro fabrication of cartilage, bone, aortic valves, branched vascular trees, and microbial tracheal splints are already accomplished[3].In situ tissues creation, to heal tissues and organs immediately inside the body is yet another critical objective of biofabrication, that has also been accomplished to a certain degree with skin, bone, and cartilage[27].

Likewise, bio-fabricated components will be employed as prototypes for toxicity studies, and cancer simulations[28].Commercially accessible materials for 3DP of biomedical applications are illustrated in **Table 2**.

Table 2: Commercially accessible materials for 3DP of biomedical applications[29]–[33]

Material	Uses	Chemical structure
Polyethylene oxide	Tablets	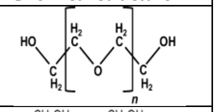
Cellulose polymer	Oral dosage in the form of tablets	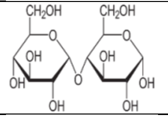
Polyglycolic acid	Custom implants for antibiotic delivery	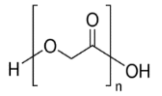
Acrylonitrile butadiene styrene	Osteoid medical cast	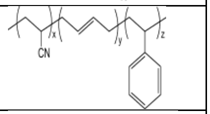
Ethylene-vinyl acetate	Intrauterine and subcutaneous devices	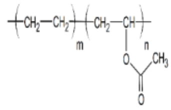
Polycaprolactone	Scaffolding for bone tissue engineering, tablets loaded with nano-capsules, and vaginal rings,	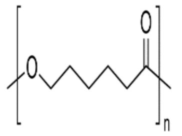
Polylactic acid	Vaginal rings, implants, microneedles, multi-compartment capsular device, beads, catheters, and discs	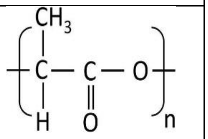
Polyvinyl alcohol	Tablets, orodispersable films, and multi-compartment capsular device	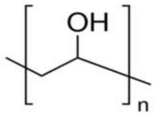

The production of vascularized organs is a significant problem in biofabrication. Due to the fact that huge organs require blood arteries to function metabolically, technologies for creating complicated vascular systems and neuropathy needs to be developed[23].Zhang et al. discussed current advancements in three-dimensional bioprinting of blood veins and functionally vascularized tissues. Due to the existing limitations of printing at high resolutions on a microscopic level, and also due to the absence of mechanical qualities for vasculature cells, additional investigation, and improvement in this field is necessary to manufacture 3DP tissues[34]. Nevertheless, recent advancements in adaptable bio-ink demonstrate AM's promise for tissue creation of sensitive human body organs. Bioreactors have been investigated in conjunction with elements that stimulate angiogenesis and neuropathy in order to develop bioprinted components with the required qualities. The combination of various bioinks and AM processes demonstrates optimistic possibilities in the fabrication of human cell structures[35].Moreover, in situ printing technology for tissue rejuvenation is a cutting-edge concept that will revolutionize the medical business.

The pharmaceutical companies will also gain significant benefits from AM.As a result, drug production and delivery methods will undergo dramatic changes. In 2015, the Food and Drug Administration(FDA)certified the first AM medication[26].There are several novel AM drug delivery technologies being investigated, including oral, prosthetic, and topical drug delivery methods.AM may be used to manipulate the release profile of pharmaceuticals by altering the three-dimensional shape, morphology, and location of the active participants in drug delivery methods.AM is used to develop novel pharmaceutical products, including hydrogels, antimicrobial micropatterns, artificial extrinsic scaffolds, micropores bioactive glass structures, nanocapsules, and multi-layered pharmaceuticals[36].AM is also transforming the implantation market, as it enables the development of patient-specific prosthetics[37].

For instance, **Figure 2** illustrates a custom-made Jig used to enhance cryoablation needle positioning. Currently, the production of pipelines incorporates image analysis of the person's body, its refinement, implant designing, and production, all of which are accomplished through the use of CAD programs[3].A dependable and premium AM technology can rapidly build biologically complicated shapes. Although patient-specific AM prosthetics are now accessible, the majority of those have been utilized solely in clinical studies with the client's explicit consent[38].Reliability of procedures and components will also be valuable in the long run for permanent legislative certification. Implants can also incorporate intricate geometrical characteristics. For instance, low-stiffness, high-strength lattice architectures have been investigated in order to reduce stress shields among the implants and the bones[39]. Biomimetics can be used to influence certain lattice patterns. AM's free-form capabilities enable the combination of this physical function with many other aspects like tissue implantation, restoration, nutrition, wastes, and antimicrobial delivery, biodegradability, and bio-resorbability. Additionally, lattices with graded architectures may alter the local characteristics, optimizing the implant's behavior. For instance, the lattice may be stiffer on the inside to withstand greater weights and porous on the outside to aid in bones in growth[40], [41].

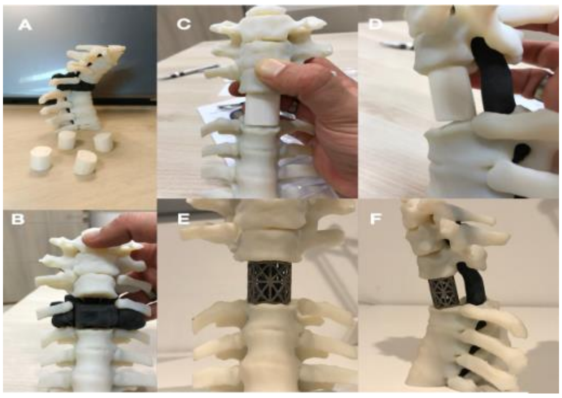

Figure 2. Jig optimized for cryoablation needle positioning using 3DP[42]

3.2. *Aviation and aerospace*

Aeronautical equipment including aircraft components, gas turbines, and heat exchangers could be made or replaced via AM[43].Non-metal AM techniques like SLA, multijet modelling, and FDM are used to rapidly prototype components and fabricate fittings as well as interior design comprised of plastic, ceramic, and composites[44].DED methodology is utilized to fabricate big structural elements because it is less precise but faster than PBF technology. Because of the accuracy of PBF technologies, system development and integration with various functions can be optimized. This approach is mostly utilized for smaller; more complicated components.GE Aviation is utilizing PBF machines to make its latest series of jet engine parts that have complicated designs for improved cooling channels and supports. The life span has been increased fivefold. The needed number of items was decreased from 18 to 1, and the overall weight was decreased by 25%[45].Non-metallic components also play a significant role in the aircraft sector.SLA, MJP, and FDM methods can be used to make plastics, ceramics, and composites. Stratasysbegan using FDM in conjunction with numerous aviation industries, including Piper Aircraft, Bell Helicopter, and NASA, for rapid prototyping, tooling, and part production[46].For example, **Figure 3** depicts a 3DP multi-stable architectural structure and a protecting structure for Mars artifacts.AM of high-temperature ceramics is a promising topic of research at the moment. Modern and sophisticated production methods are used to create high-performance aircraft parts. These components are exposed to corrosion, impact stress, and repetitive temperature cycles, all of which can result in flaws or fractures.Due to the high cost of these components, replacement is preferable over maintenance[47].

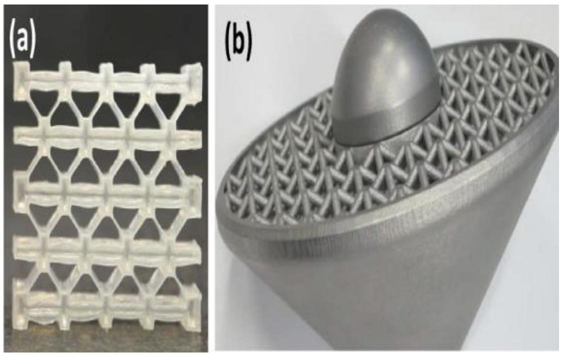

Figure 3. (a) Multi-stable crafted object created by 3DP (b) Protecting structure for Mars created 3DP[48]

In comparison to traditional welding procedures, AM technology can fix metal parts with exceptional accuracy and minimum energy consumption. A laser beam forms metallurgical connections among the component and the repairing metal that is added. This technology produces little deformation and is suitable for complicated and thin-walled aircraft structures[47].Additionally, AM can be used to replace materials that are not weldable or parts that are prone to deformation.DED machines disseminate and melt metal powder over the wounded region, whereas computer numerical control(CNC)machinery enhances the repairing quality. This approach enables better construction capacity, improved precision, and superior surface quality[49].The additional material exhibits superior fatigue qualities to the existing wrought material while keeping dimensional tolerances. Further, this technology minimizes the decaying of mechanical characteristics induced by thermal loads and can easily heal damages of any substances. Maintenance costs have been estimated at 50% of the cost of remanufacturing the component[50].Automated solutions are now being designed to identify damages, match the initial computer-aided design(CAD) model with the actual equipment, and replace defective parts using AM and CNC machinery.AM also can impact the supply networks for spares. Dispersed manufacturing of spares will minimize operational costs and delays, while also reducing the burden on supply chain management and logistical informatics. Simultaneously, AM will enhance consumer satisfaction, adaptability, efficiency, and resilience against supply chain interruptions. Such improvements, although, would occur if the pricing of AM machines and materials decreases[51].Further, AM can make antique components without relying on outdated equipment, molds, and die.For instance, maintaining and modernizing F-15 aircraft utilizing AM has resulted in significant cost reductions.3DP technologies have already exhibited impressive capabilities, ranging from quick prototyping to finished part manufacture and semi-automatic maintenance[23].

3.3. Buildings and structures

About 3% of the whole AM business is devoted to architectural projects[52].Nevertheless, this domain is still in its adolescence, having been employed in household structures for the first time in 2014 and demonstrating tremendous promise ever since. Recent years have seen an increase in interest in mechanized building construction using 3DP technologies. It can transform the building sector and enable astronauts to erect structures on the moon more easily[53].It enables substantial time and resources savings during construction. Casting, molding, and extrusion are all conventional procedures utilized in the construction process.3DP can be used where there will be limitations, such as geometric complexity in the construction sector. As a result, its effectiveness is based on its capacity to construct precisely, which opens up several design options. Khoshnevis invented the contour crafting (CC) technique for mechanized design and constructions, as well as for aerospace uses. Owing to its capability to utilize in-situ resources, it is well suited for low-income accommodation and the fabrication of lunar shelters[54].In 2014, the first 3DP residential construction was created in Amsterdam using the FDM process. Dus Architects carried the proposal forward to display the printer's mobility while minimizing material waste and logistic expenses, thus clearing the way for its adoption in the construction sector. Also in 2014WinSun, a Chinese architecture business, bulk printed apartment dwellings in less than 24 hours in Shanghai. However, WinSun experienced a number of hurdles over the project's length, including issues related to fragility, architecture service compatibility, and indirect printing[55].

Companies which utilise 3D printing technology in the fabrication of automobile structures gain significant market competitive advantages over their contenders. Furthermore, using 3DP, vehicle manufacturing companies can adapt to complex geometry and accomplish distinct customising capability when creating unique vehicle parts for the world market. Moreover, the prolonged utilisation of 3D printing technologies has allowed automobile producers to create prototypes and one-of-a-kind concept cars that also perform an important role in characterising the prospect of vehicles technologies. As a result, comprehensive investigation is required to determine the effect of this technology in revolutionising the world - wide car production industry[56].

Few years ago, Lim et al. suggested three large-scale 3DP procedures suited for the construction sector, each with its own set of advantages and disadvantages depending on the materials used and the applying processes. D-shape and concrete printing both are frame-mounted and gantry-mounted processes that are normally completed off-site. Besides, the CC process can be employed for on-site operations when installed on a robot and crane[57].Additionally, Nadal described the approaches for scaling up ordinary desktop 3DP.Nevertheless, other issues arise, like material waste and inaccuracy, which are typically more labour-intensive[58].

Hager et al. developed a potential process comparable to CC that utilizes cementations materials, thermoplastics, and ceramic products and has the potential to revolutionize the architectural sector in the long run. The initial onsite contour crafts structure was constructed using a sand-cement mixture.CC method is frequently referred to as the first practical AM technology for structure construction. By contrast, the D-shape approach employs the powder deposition procedure, which involves the employment of a chemical substance, including a chlorine-based liquid, to fuse the powder. The technique yields structural components with excellent mechanical qualities. Nonetheless, the regulatory directions and increased service requirements continue to be the primary drawbacks of this strategy[59].Cesaretti et al. also explored the feasibility of employing the D-shape printing process in hostile spatial situations and utilizing the available materials[60].**Figure 4** illustrates a construction utilizing 3DP technology.

Figure 4. Construction using 3DP technology[61]

4. Materials used for 3D printing

4.1. Polymers and composites

Polymers are the foremost used materials in the 3DP industries because of their versatility and flexibility of incorporation into various 3DP processes[62]. Thermoset filaments, reactive monomers, resins, and powders are all examples of polymers used in AM. Wohlers Associates' yearly business analysis indicates that photopolymer-generated prototypes accounted for over 50% of the 3DP market in industrial sectors. Yet, photopolymers' thermo - mechanical characteristics should be enhanced further[63].For example, depending on the difference in Ultraviolet radiation and intensities, the microstructure and alignments of 3DP polymers are dependent upon layer thickness. Conversely, it's also believed that plastics for SLS are the second most essential type of 3DP[63].Polystyrene, polyamides, and thermoplastic elastomers are all examples of SLS polymers. Photopolymer-based technologies provide consistency, thin layers, and high accuracy. Additional advancements utilizing novel resins have resulted in increased rigidity and thermal tolerance. Numerous 3DP techniques can be used to treat thermoplastic polymers. While sustaining an optimal resin viscosity at low temperatures is a significant hurdle to overcome when utilizing polylactic acid[64].At the moment, polylactic acid-based composites are being utilized to fabricate 3DP tissue engineering scaffolds.FDM is frequently utilized to fabricate low-melting-point thermoplastics and polymer composites. However, environmentally acceptable polymeric materials with good physical qualities are critical for FDM since commonly used commercialized polymers for 3DP, such as acrylonitrile-butadiene-styrene copolymers and polylactic acid, do not fulfil the necessary requirements[65].According to Song et al., polylactic acid produced by 3DP exhibits excellent mechanical qualities when compared to injection-moldedpolylactic acid. Additionally, post-tensioning organic fiber reinforcement inserted in the polylactic acid matrix enhanced mechanical characteristics, which is a promising advancement in 3DP[66], [67]. The polymer composite parts produced by 3DP technology are shown in **Figure 5.**

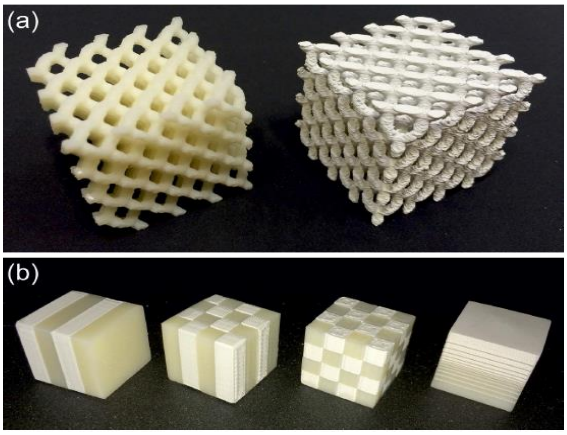

Figure 5. Polymer composite parts produced by 3DP technology (a) rod connected diamond photonic crystals, (b) 1D, 2D, and 3D periodic structure[68]

Nanoparticles can be incorporated into a 3DP item individually, mechanically, with occasional stoppages, or by mixing them in the matrix material[69], [70].While the use of nanoparticles and AM has various benefits, one of the most important advantages is that the products' uniformity can be enhanced. Nanocomposites have gained interest from a variety of organizations owing to their desirable qualities, which include high thermal conductivity, enhanced fire resistance, superior strength, and low weight. When nanoparticles are incorporated and mixed into parent materials via 3DP, significant potential for nanocomposite synthesis occurs. Thus, improving the durability of nanocomposites, as well as their pricing and thermal instability, may provide benefits and potential prospects[71], [72].Elliott et al. explored the influence of adding Quantum Dot (QD) nanoparticles onto a photopolymer resin using the polyjet 3DP method.QD is a form of nanoparticles with a dimension of 2–20 nm and the ability to absorb UV rays. It was discovered that introducing nanoparticles alters the rheology of the substance. By combining this material with 3DP technology, a final object with distinctive optical qualities is developed[73].3DP of polymeric materials has evolved over the decades, allowing for the investigation and exploration of unique materials. The combination of 3DP and a polymer matrix composite enables commercial manufacturing with superior features and physical characteristics. Even so, the lack of printed materials that enable the process of 3DP to be used to a wider range of commercial uses for high-performance composites is still a significant barrier[74].The inclusion of fibre reinforcement could perhaps improve the physical qualities of polymeric materials, which is an enticing breakthrough in 3D printing. Recent times, researchers noted that continuous fibre reinforcement for enhancing the physical characteristics of 3D-printed polymeric materials has proven difficult [106], [107]. Tekinalp et al. investigated the difficulties attributed to 3D printing fiber - reinforced polymer composites and assessed the load bearing capacity of carbon fibre composite parts. The specimens made with FDM had a substantial increment in strength and stiffness[75], [108].

4.2. Metals and alloys

Metal AM has tremendous growth potential. This technique has been primarily employed in the aviation sector for testing, development, and smart functions. Additionally, it is employed in the biomedical, defense, and automobile sectors[24]. In comparison to traditional fabrication techniques, metal AM enables the creation of complicated shapes with unique interfaces. Titanium and its alloys, steel alloys, a few aluminium alloys, nickel alloys, and a few cobalt and magnesium-based metals are all optimized for AM applications. Particularly, titanium and its alloys are high-performance materials that are widely utilized in a variety of sectors. They are characterized by significant machining expenses and a long lead time when manufactured using traditional techniques. Thus, AM can provide major financial gains by allowing for the production of extremely complicated structures at a reduced cost and with fewer wastages[76].Ti-6Al-4V has undergone extensive research and is now being utilized commercially in the aeronautical and healthcare areas.AM frequently employs steels including austenitic stainless steels, maraging steels, precipitation hardenable stainless steels, and tool steels. These alloys are suitable for common purpose usage as well as those requiring great hardness and strength, including tools or molding[77].Austenitic steels and precipitation-hardenable stainless steels are especially susceptible to the effects of AM parameters. Currently, only a few aluminium alloys are employed in AM for a variety of purposes[78]. In comparison to titanium alloys, they are easier to machine and less expensive. As a result, commercial demand for titanium alloys for AM has been diminished. Additionally, some high-performance aluminium alloys are difficult to weld and have a high reflectivity for the laser wavelengths usually employed in AM[79].Furthermore, the low viscosity of molten aluminium precludes the formation of a wide melting pool. Superior thermal conductivity of aluminium minimizes inner thermal stresses and enables rapid AM procedures[80].With reference to the metallurgy of SLM Al-Si alloys, a typical microstructure with overlapped melt pools is illustrated in **Figure 6.**

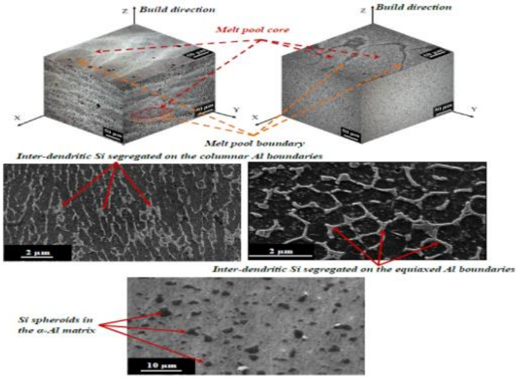

Figure 6. A typical microstructure of SLM Al-Si alloys[81]

For high-temperature usage, nickel-based superalloys like Inconel 625 and Inconel 718 have been produced, whereas, CoCr alloys are being investigated for medicinal and dermatological applications. Additional materials, including magnesium, and copper alloys, are being studied for medical purposes[82].In general, densely packed components generated via AM are of equivalent, if not superior quality to traditionally manufactured components. To achieve such results, it is vital to control porosity and morphology. The primary imperfection that results in fracture propagation is porosity that may be regulated by adjusting the imparted volume energy as well as the feedstock quality[83].Low levels of imposed energy cause the material to produce abnormally shaped cavities. However, an abundance of energy results in the formation of circular pores. The feedstock's performance can be enhanced by employing denser powder beds and smaller particles to enhance flowability and uniformity[84]. Also, the existence of impurities and the alloy's purity should be maintained.AM metal parts have fine microstructures than conventionally made metallic parts, resulting in greater yield and final strengths. Conversely, their microstructure is anisotropic and is assessed by the direction of construction.As a result, anisotropy of material characteristics is quite prevalent, with greater strength and strain in the directions of printing. Additionally, surface roughness and material imperfections influence the fractured behaviour and fatigue strength of AM parts. Higher surface roughness leads to enhanced stress concentration and a more rapid failure rate when subjected to fatigue loading. Furthermore, intrinsic material flaws and poor layer binding reduce the fatigue resistance of AM components. Post-manufacturing operations minimize residue porosity, alter the morphology, and minimize surface imperfections[85].

4.3. Concrete

The architectural industry has benefited from the expansion of AM technology. A comparable technique to IJP, termed CC, has been invented as the primary technique for the AM of structural components. To extrude the concrete mixture, this technology employs bigger nozzles and higher pressures[86].To provide a flawless finishing rather than a layer-by-layer impression, trowel-like equipment is coupled to the printer. At the moment, 3DP technology for construction is in adolescence. As a result, the technology's life-cycle efficiency has not been confirmed[86].Contemporary scientific work on 3DP concrete structures has resulted in the development of novel technologies and materials that are briefly reviewed below. The foremost critical feature of effective CC is the concrete's fresh attributes. Extrusion of complicated structures demands a high level of workability.Gosselin et al. invented a printing technique that separates the accelerator and the premixed mortar and then blends them at the printhead prior to extrusion. The properties of the premixed mortar can be managed for a prolonged duration of time using this technology without compromising the initial strength of the printed layers necessary for successful layer construction.By employing a six-axis robotic system and managing the behaviour of materials before and after the extrusion process, this technology might be capable of fabricating complicated units and without the use of transitory support[87].Paul et al. studied various concrete combinations and discovered that tribological features of the mixture, particularly its thixotropic behaviour, affect the printing and pumping of these mixtures[88].Perrot et al. proposed a mathematical model focused on the rheological behaviour of cement mixtures to optimize the construction rate while avoiding fracture and deformation of the bottom layers[89]. Zhong et al. examined a 3DP nanocomposite geopolymer, for example, a non-portland cement concrete treated with alkali.To achieve a higher resolution, a mixture of quick-setting cement and polyvinyl alcohol composite has been used. However, layer deformation and the creation of voids in between layers were detected and are found to be less apparent when the specimens are post-cured in water[90].Xia and Sanjayan examined the 3DP powder-based structure in a geopolymer matrix. The powder bed is composed of powdered blast furnace slag, sand, and anhydrous sodium silicate, which acts as an alkali activator. The fluid-binder is composed of water and a trace of 2-Pyrrolidone.With geometrical inflation; the 3DP blocks have a low tensile strength of 0.9 MPa. The specimens were post-treated in alkaline solutions at 60°C to improve their strength to 16.5 MPa. Nevertheless, treatments with an alkaline and subjected to elevated temperatures are thought unlikely in full-scale 3DP objects. It is also necessary to evaluate the endurance of 3DP constructions[91].For instance, when compared to traditional concrete, a 3DP construction may experience increased water evaporation due to the absence of formwork to guard from air exposure. As a result, contraction and the danger of fracturing can be increased. Thus, powder-bed AM requires more development in order to produce high-strength constructions[23].

4.4. Ceramic

AM has established itself as a critical technology for manufacturing sophisticated ceramics for biomedical and bioengineering applications. Regardless of the printing precision, the layer-by-layer structure and constrained material availability are the primary hurdles for 3DP of ceramics. Post-processing sintered ceramic components to achieve the required structure is a lengthy and expensive operation[19].As a result, 3DP of complex shapes accompanied by sintering has grown in popularity (**Figure 7**).

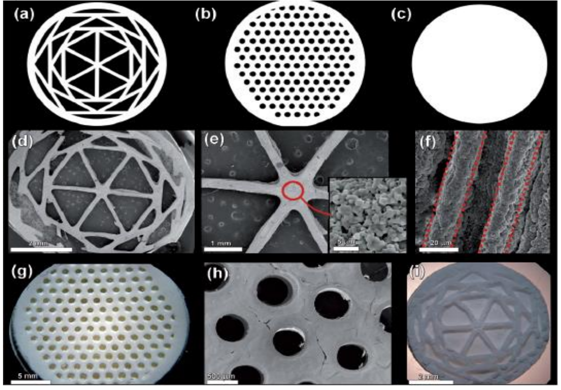

Figure 7. 3D printed ceramic structures[92]

3DP of porous ceramics or lattices resulted in several benefits through the development of new lighter materials customized for specific purposes. Ceramic scaffolds for biomedical applications have improved in terms of convenience and speed when compared to conventional casting and sintering procedures. Moreover, 3DP technology enables precise control over the porosity of lattices[93].

Numerous techniques and materials have been researched in order to improve the physical characteristics of 3DP ceramic lattices as compared to ancient techniques.IJP, PBF, and SLA are the primary technologies for 3DP of ceramics.IJP is considered to be the primary approach for producing thick ceramic specimens which do not require post-treatment.For IJP, a consistent solution with controllable rheology which flows readily, may not choke at the nozzle, and has an efficient drying procedure is necessary[94].Cracking and flattening of the printed filament is also considered to be a critical feature of IJP, with the viscoelastic behaviour of the inks playing an important role[95].SLS is another popular technique for 3DP of ceramic powders. Nevertheless, the thermal shock caused by fusion heating and cooling to room temperature might result in the production of cracks in ceramic components[96]. For ceramic-matrix composites, a technology called selective laser gelation has been developed that integrates SLS with sol-gel technology. For ceramic powders which do not readily fuse or melt at the lowered laser heating temperature, binders with lower melting temperatures are utilized. This process is referred to as indirect SLS and is most frequently employed to create ceramic-polymer and ceramic-glass composites[97].

Ceramics' particle size distribution also has an impact on their flowability, density, and shrinkage during printing. It is demonstrated that increasing the proportion of smaller particles lowered the flowability of a glass-ceramic combination, resulting in a reduced printing resolution and increased shrinkage. Furthermore, because the glass-ceramic powder has a reduced bulk density, it shrinks more during sintering[98]. **Table 3** summarizes the primary applications, advantages, and disadvantages of the 3DP materials.

Table 3: A summary of the primary uses, advantages, and disadvantages of the primary 3DP materials[23]

Materials	Uses	advantages	disadvantages
Polymers and composites	Medical, sports, architecture, biomedical aerospace, and automotive	Cost-effective, fast prototyping, mass customization, and complex structures	A limited selection of polymers and weak mechanical properties
Metals and alloys	Military, automotive, aerospace, and biomedical	Mass customization, multifunctional optimization, fewer assembly components, and reduced material waste	Dimensional inaccuracy, a limited selection of alloys, and poor surface finish
Concrete	Construction, and infrastructure	Less labor required and no need for formwork	Anisotropic mechanical properties, layer-by-layer appearance, and poor inter-layer adhesion
Ceramics	Aerospace, biomedical, chemical industries, and automotive	Reduced fabrication time, controlling porosity of lattices, and microstructure	A limited selection of printable ceramics

5. Key challenges of 3DP technology

Despite the advantages of 3DP, which include creative freedom, personalization, and the capability to build complicated shapes, there are significant limitations that would require additional research and innovation. Among these disadvantages are excessive costs, restricted uses in massive constructions, poorer and anisotropic mechanical qualities, etc. Irrespective of the time and cost of 3DP, that should be determined for each usage, four major issues inherent in AM are described[23], [99].**Figure 8** illustrates a few microstructural defects in 3DP polymer samples.

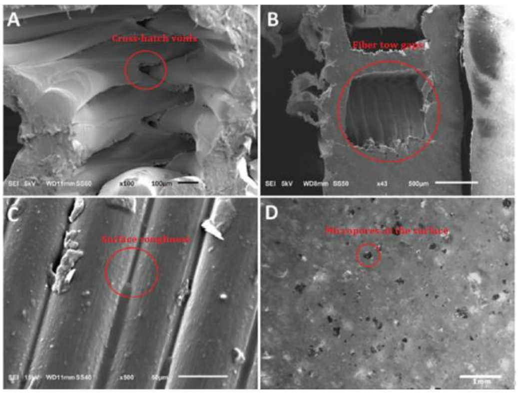

Figure 8: Microstructural defects in 3D-printed, unreinforced polymer specimens[100]

5.1. Void formation

The creation of voids between successive layers of materials is among the primary disadvantages of 3DP technology. The increased porosity caused by AM can be rather large, reducing mechanical performances owing to decreased interfacial adhesion between printed layers. The extent to which voids emerge is significantly dependent on the 3DP method and material used. The development of voids is much more prevalent in processes that utilize filament of materials, like FDM or CC, and is believed to be amongst the primary faults that lead to poorer and anisotropic mechanical characteristics. Additionally, this void creation can cause subsequent layer deformation. Increased filament thickness lowers porosity and cohesiveness in a 3DP composite utilizing the FDM process. It leadsto an enhancement in water intake and a decrease in tensile strength[101].

5.2. Microstructure and mechanical properties

One of the primary difficulties in AM technology is anisotropic behaviour. Due to the complexity of layer-by-layer printing; the structure of the material within every layer is distinct from the microstructure at the layer borders. Owing to the anisotropic nature of the material, the mechanical properties of the 3DP part are varied in the vertical plane than in the horizontal plane[102].Whenever metals and alloys are printed using SLS or SLM, succeeding layers reheat the borders of the preceding layer, resulting in a distinct grain structure and anisotropic behaviour. The laser beams heat penetration into the individual layer is critical for not only managing the sintering operation but also for reducing anisotropic characteristics. The alterations in morphological and textural behaviour in the transverse direction lead to increased strength and ductility in 3DP titanium alloy using the SLM process as contrasted to the longitudinal direction[103].

5.3. Divergent from design to execution

The primary tool for designing 3D printable parts is CAD software. Due to the constraints of AM, the printed part may contain a few faults that were not expected in the manufactured component. The CAD system utilizes both solid geometry and boundaries.It often approximates the model using tessellation principles. Transferring CAD data into a 3DP item, frequently leads to flaws and faults, especially on curvatures. While a super fine tessellation may partially fix this issue, however, the calculated processing and printing will be time-consuming and difficult. As a result, post-processing by heating to correct these flaws is often contemplated. To minimize the difference between design and execution, it would be required to prepare and determine the part's optimal alignment, split the portion into adequate layers, and produce supportive elements[104].

5.4. Layer-by-layer appearance

Due to the nature of AM technology, layer-by-layer aesthetics is another issue. Whenever the 3DP part is disguised in the final design, the aesthetic may be irrelevant– for example in bioengineered scaffolds. In some purposes, including architecture, toys, and aircraft, a uniform surface is favored over the layer-by-layer appearance. Physical or chemical post-processing techniques, including sintering, can eliminate that fault but raise production time and expense[105 - 108].

6. Summary/Conclusion

The greatest advantages of 3DP technology include design freedom, mass customization, and the capacity to build complicated shapes with minimum wastage. A detailed assessment of 3DP methods, materials, and the state of the art in popular applications across multiple industries was conducted. Additionally, the primary issues associated with the nature of 3DP were explored. FDM is among the most widely used 3DP technologies due to its cheap cost, accessibility, and fast processing speed. It was initially developed for 3DP of polymer filaments but has now been repurposed to print a variety of other materials. FDM is primarily employed for rapid prototyping, but the mechanical characteristics and precision of the printed items are lower than those produced by powder-bed technologies. Furthermore, SLA is a pioneering technology of 3DP that is mostly utilized with photopolymers to create highly precise items. Nevertheless, it is a time-consuming and intricate process that is constrained for selective materials.

Polymers are the most often used materials for rapid prototyping. By reinforcing polymers with fibers and nanomaterials, the mechanical characteristics of the 3DP composite were improved.The three primary methods of 3DP used for metals and alloys are SLS, SLM, and DED.Due to a restricted number of metals and alloys suitable for 3DP technology, modern techniques must be adapted to a greater range.Ceramics have permitted the development of sophisticated ceramic lattices for a variety of purposes, including ceramic scaffolds used for tissue engineering.Recent improvements have focused on developing a concrete mixture with superior flowability, processability, mechanical strength, and aesthetics.AM has made a significant contribution to contemporary biomaterial research and innovation for prototyping complicated and customized structures with patient-specific requirements. Yet, it faces obstacles such as resource scarcity and regulatory concerns. While the continuous scientific investigation of materials and processes has aided in overcoming a few of these obstacles, there is still scope for improvements. Considering its radical potential for developing innovative products, 3DP technology requires additional research to compete with existing technologies in the mass manufacturing of everyday goods due to its higher cost and production time. However, AM has advanced tremendously during the last few years. Increased investment, research, and advancement will result in a rapid transition from conventional production to 3DP technology.

References

[1] N. Hossain, M. A. Chowdhury, M. B. A. Shuvho, M. A. Kashem, and M. Kchaou, “3D-Printed Objects for Multipurpose Applications,” *Journal of Materials Engineering and Performance 2021 30:7*, vol. 30, no. 7, pp. 4756–4767, Mar. 2021, doi: 10.1007/S11665-021-05664-W.

[2] H. Alzyod and P. Ficzere, “The Influence of the Layer Orientation on Ultimate Tensile Strength of 3D Printed Poly-lactic Acid,” *Jordan Journal of Mechanical and Industrial Engineering*, vol. 16, no. 3, 2022.

[3] A. A. Zadpoor and J. Malda, “Additive Manufacturing of Biomaterials, Tissues, and Organs,” *Annals of Biomedical Engineering 2016 45:1*, vol. 45, no. 1, pp. 1–11, Sep. 2016, doi: 10.1007/S10439-016-1719-Y.

[4] P. Kumar, D. K. Rajak, M. Abubakar, S. G. M. Ali, and M. Hussain, “3D Printing Technology for Biomedical Practice: A Review,” *Journal of Materials Engineering and Performance 2021 30:7*, vol. 30, no. 7, pp. 5342–5355, Apr. 2021, doi: 10.1007/S11665-021-05792-3.

[5] R. A. García-León, J. A. Gómez-Camperos, and H. Y. Jaramillo, “Scientometric Review of Trends on the Mechanical Properties of Additive Manufacturing and 3D Printing,” *Journal of Materials Engineering and Performance 2021 30:7*, vol. 30, no. 7, pp. 4724–4734, Feb. 2021, doi: 10.1007/S11665-021-05524-7.

[6] B. Berman, “3-D printing: The new industrial revolution,” *Business Horizons*, vol. 55, no. 2, pp. 155–162, Mar. 2012, doi: 10.1016/J.BUSHOR.2011.11.003.

[7] J. W. Stansbury and M. J. Idacavage, “3D printing with polymers: Challenges among expanding options and opportunities,” *Dental Materials*, vol. 32, no. 1, pp. 54–64, Jan. 2016, doi: 10.1016/J.DENTAL.2015.09.018.

[8] O. Ivanova, C. Williams, and T. Campbell, “Additive manufacturing (AM) and nanotechnology: promises and challenges,” *Rapid Prototyping Journal*, vol. 19, no. 5, pp. 353–364, 2013, doi: 10.1108/RPJ-12-2011-0127.

[9] M. Vaezi, H. Seitz, and S. Yang, “A review on 3D micro-additive manufacturing technologies,” *The International Journal of Advanced Manufacturing Technology 2012 67:5*, vol. 67, no. 5, pp. 1721–1754, Nov. 2012, doi: 10.1007/S00170-012-4605-2.

[10] W. Xu *et al.*, “3D printing for polymer/particle-based processing: A review,” *Composites Part B: Engineering*, vol. 223, p. 109102, Oct. 2021, doi: 10.1016/J.COMPOSITESB.2021.109102.

[11] T. Sivarupan *et al.*, “A review on the progress and challenges of binder jet 3D printing of sand moulds for advanced casting,” *Additive Manufacturing*, vol. 40, p. 101889, Apr. 2021, doi: 10.1016/J.ADDMA.2021.101889.

[12] Z. Chen *et al.*, “3D printing of ceramics: A review,” *Journal of the European Ceramic Society*, vol. 39, no. 4, pp. 661–687, Apr. 2019, doi: 10.1016/J.JEURCERAMSOC.2018.11.013.

[13] BhushanBharat and CaspersMatt, “An overview of additive manufacturing (3D printing) for microfabrication,” *Microsystem Technologies*, vol. 23, no. 4, pp. 1117–1124, Apr. 2017, doi: 10.1007/S00542-017-3342-8.

[14] M. Mao *et al.*, “The Emerging Frontiers and Applications of High-Resolution 3D Printing,” *Micromachines 2017, Vol. 8, Page 113*, vol. 8, no. 4, p. 113, Apr. 2017, doi: 10.3390/MI8040113.

[15] X. Wang, M. Jiang, Z. Zhou, J. Gou, and D. Hui, “3D printing of polymer matrix composites: A review and prospective,” *Composites Part B: Engineering*, vol. 110, pp. 442–458, Feb. 2017, doi: 10.1016/J.COMPOSITESB.2016.11.034.

[16] M. FP, F. J, and G. DW, “A review on stereolithography and its applications in biomedical engineering,” *Biomaterials*, vol. 31, no. 24, pp. 6121–6130, Aug. 2010, doi: 10.1016/J.BIOMATERIALS.2010.04.050.

[17] O. A. Mohamed, S. H. Masood, and J. L. Bhowmik, “Optimization of fused deposition modeling process parameters: a review of current research and future prospects,” *Advances in Manufacturing 2015 3:1*, vol. 3, no. 1, pp. 42–53, Feb. 2015, doi: 10.1007/S40436-014-0097-7.

[18] C. Y. Yap *et al.*, “Review of selective laser melting: Materials and applications,” *Applied Physics Reviews*, vol. 2, no. 4, p. 041101, Dec. 2015, doi: 10.1063/1.4935926.

[19] N. Travitzky *et al.*, “Additive Manufacturing of Ceramic-Based Materials,” *Advanced Engineering Materials*, vol. 16, no. 6, pp. 729–754, Jun. 2014, doi: 10.1002/ADEM.201400097.

[20] J. Li, T. Monaghan, T. T. Nguyen, R. W. Kay, R. J. Friel, and R. A. Harris, “Multifunctional metal matrix composites with embedded printed electrical materials fabricated by ultrasonic additive manufacturing,” *Composites Part B: Engineering*, vol. 113, pp. 342–354, Mar. 2017, doi: 10.1016/J.COMPOSITESB.2017.01.013.

[21] I. Gibson, D. Rosen, and B. Stucker, “Introduction and Basic Principles,” *Additive Manufacturing Technologies*, pp. 1–18, 2015, doi: 10.1007/978-1-4939-2113-3_1.

[22] A. Gannarapu and B. A. Gozen, “Freeze-Printing of Liquid Metal Alloys for Manufacturing of 3D, Conductive, and Flexible Networks,” *Advanced Materials Technologies*, vol. 1, no. 4, Jul. 2016, doi: 10.1002/ADMT.201600047/FULL.

[23] T. D. Ngo, A. Kashani, G. Imbalzano, K. T. Q. Nguyen, and D. Hui, “Additive manufacturing (3D printing): A review of materials, methods, applications and challenges,” *Composites Part B: Engineering*, vol. 143, pp. 172–196, Jun. 2018, doi: 10.1016/J.COMPOSITESB.2018.02.012.

[24] Wohlers Associates, “Wohlers Annual Report: Additive Manufacturing and 3D Printing State of the Industry,” 2021.

[25] C. L. Ventola, “Medical Applications for 3D Printing: Current and Projected Uses,” *Pharmacy and Therapeutics*, vol. 39, no. 10, p. 704, Oct. 2014, Accessed: Aug. 07, 2021. [Online]. Available: /pmc/articles/PMC4189697/.

[26] N. J, M. RD, M. CM, K. MA, and K. A, “A new chapter in pharmaceutical manufacturing: 3D-printed drug products,” *Advanced drug delivery reviews*, vol. 108, pp. 39–50, Jan. 2017, doi: 10.1016/J.ADDR.2016.03.001.

[27] V. Keriquel *et al.*, “In situ printing of mesenchymal stromal cells, by laser-assisted bioprinting, for in vivo bone regeneration applications,” *Scientific Reports 2017 7:1*, vol. 7, no. 1, pp. 1–10, May 2017, doi: 10.1038/s41598-017-01914-x.

[28] W. C, T. Z, Z. Y, Y. R, L. L, and S. W, “Three-dimensional in vitro cancer models: a short review,” *Biofabrication*, vol. 6, no. 2, 2014, doi: 10.1088/1758-5082/6/2/022001.

[29] G. A, B. AB, H. GB, G. S, and B. AW, “3D printing of modified-release aminosalicylate (4-ASA and 5-ASA) tablets,” *European journal of pharmaceutics and biopharmaceutics : official journal of Arbeitsgemeinschaft*

fur Pharmazeutische Verfahrenstechnik e.V, vol. 89, pp. 157–162, 2015, doi: 10.1016/J.EJPB.2014.12.003.

[30] F. J, Y. X, and J. Y, "3D printing of vaginal rings with personalized shapes for controlled release of progesterone," *International journal of pharmaceutics*, vol. 539, no. 1–2, pp. 75–82, Mar. 2018, doi: 10.1016/J.IJPHARM.2018.01.036.

[31] C. H *et al.*, "A comparative analysis of scaffold material modifications for load-bearing applications in bone tissue engineering," *International journal of oral and maxillofacial surgery*, vol. 35, no. 10, pp. 928–934, Oct. 2006, doi: 10.1016/J.IJOM.2006.03.024.

[32] S. G, M. W, B. AB, T. KM, and G. S, "In vitro characterisation of terbutaline sulphate particles prepared by thermal ink-jet spray freeze drying," *International journal of pharmaceutics*, vol. 447, no. 1–2, pp. 165–170, Apr. 2013, doi: 10.1016/J.IJPHARM.2013.02.045.

[33] M. A, M. A, P. F, F. A, Z. L, and G. A, "3D printed multi-compartment capsular devices for two-pulse oral drug delivery," *Journal of controlled release : official journal of the Controlled Release Society*, vol. 268, pp. 10–18, Dec. 2017, doi: 10.1016/J.JCONREL.2017.10.008.

[34] Z. Zhang, B. Wang, D. Hui, J. Qiu, and S. Wang, "3D bioprinting of soft materials-based regenerative vascular structures and tissues," *Composites Part B: Engineering*, vol. 123, pp. 279–291, Aug. 2017, doi: 10.1016/J.COMPOSITESB.2017.05.011.

[35] J. W *et al.*, "Direct 3D bioprinting of perfusable vascular constructs using a blend bioink," *Biomaterials*, vol. 106, pp. 58–68, Nov. 2016, doi: 10.1016/J.BIOMATERIALS.2016.07.038.

[36] U. ID, C. L, and P. A, "Three-dimensional drug printing: a structured review," *Journal of the American Pharmacists Association : JAPhA*, vol. 53, no. 2, pp. 136–144, 2013, doi: 10.1331/JAPHA.2013.12217.

[37] W. X *et al.*, "Topological design and additive manufacturing of porous metals for bone scaffolds and orthopaedic implants: A review," *Biomaterials*, vol. 83, pp. 127–141, Mar. 2016, doi: 10.1016/J.BIOMATERIALS.2016.01.012.

[38] I. Campbell, D. Bourell, and I. Gibson, "Additive manufacturing: rapid prototyping comes of age," *Rapid Prototyping Journal*, vol. 18, no. 4, pp. 255–258, Jun. 2012, doi: 10.1108/13552541211231563.

[39] H. P, M. L, K. C, S. RF, and M. FA, "Cellular Ti-6Al-4V structures with interconnected macro porosity for bone implants fabricated by selective electron beam melting," *Acta biomaterialia*, vol. 4, no. 5, pp. 1536–1544, Sep. 2008, doi: 10.1016/J.ACTBIO.2008.03.013.

[40] R. Sharma, R. Singh, R. Penna, and F. Fraternali, "Investigations for mechanical properties of Hap, PVC and PP based 3D porous structures obtained through biocompatible FDM filaments," 2018, doi: 10.1016/j.compositesb.2017.08.021.

[41] Z. Hu *et al.*, "Design of ultra-lightweight and high-strength cellular structural composites inspired by biomimetics," *Composites Part B: Engineering*, vol. 121, pp. 108–121, Jul. 2017, doi: 10.1016/J.COMPOSITESB.2017.03.033.

[42] L. R, R. G, S. K, K. M, and L. Z, "Use of 3-Dimensional Printing Technology in Complex Spine Surgeries," *World neurosurgery*, vol. 133, pp. e327–e341, Jan. 2020, doi: 10.1016/J.WNEU.2019.09.002.

[43] C. K. Chua, K. F. Leong, and C. S. Lim, "Rapid prototyping: Principles and applications, third edition," *Rapid Prototyping: Principles and Applications, Third Edition*, pp. 1–512, Jan. 2010, doi: 10.1142/6665.

[44] L. Yin, J. Doyhamboure-Fouquet, X. Tian, and D. Li, "Design and characterization of radar absorbing structure based on gradient-refractive-index metamaterials," *Composites Part B: Engineering*, vol. 132, pp. 178–187, Jan. 2018, doi: 10.1016/J.COMPOSITESB.2017.09.003.

[45] "Layer by Layer | MIT Technology Review." https://www.technologyreview.com/2011/12/19/20869/layer-by-layer/ (accessed Aug. 07, 2021).

[46] "Additive Manufacturing for Innovative Design and Production | MIT xPRO." https://learn-xpro.mit.edu/additive-manufacturing?utm_medium=ppc&utm_source=google&utm_campaign=amx&utm_term=industrial 3d printing&utm_content=aw-c&utm_term=industrial 3d printing&utm_campaign=Lifetime+Campaign+-+Additive+Manufacturing+-+C+(Run+11)&utm_source=adwords&utm_medium=ppc&hsa_acc=5861714288&hsa_cam=8553314852&hsa_grp=90248772881&hsa_ad=448051485815&hsa_src=g&hsa_tgt=kwd-43641086169&hsa_kw=industrial 3d printing&hsa_mt=b&hsa_net=adwords&hsa_ver=3&gclid=CjwKCAjw3riIBhAwEiwAzD3TiU46-oEYiMRAVrS4rS45k684Bq0obuqb9qR26sg3Rw1uVtJ_NYkqfxoC9acQAvD_BwE (accessed Aug. 07, 2021).

[47] B. Graf, A. Gumenyuk, and M. Rethmeier, "Laser Metal Deposition as Repair Technology for Stainless Steel and Titanium Alloys," *PhPro*, vol. 39, pp. 376–381, 2012, doi: 10.1016/J.PHPRO.2012.10.051.

[48] S. S *et al.*, "Multistable Architected Materials for Trapping Elastic Strain Energy," *Advanced materials (Deerfield Beach, Fla.)*, vol. 27, no. 29, pp. 4296–4301, Aug. 2015, doi: 10.1002/ADMA.201501708.

[49] J. Ruan, K. Eiamsa-Ard, J. Zhang, and F. W. Liou, "AUTOMATIC PROCESS PLANNING OF A MULTI-AXIS HYBRID MANUFACTURING SYSTEM," 2002, Accessed: Aug. 07, 2021. [Online]. Available: https://proceedings.asmedigitalcollection.asme.org.

[50] I. L. de Camargo, J. F. P. Lovo, R. Erbereli, R. T. Coelho, I. B. da Silva, and C. A. Fortulan, "An Overview of Laser Engineered Net Shaping of Ceramics," *Matéria (Rio de Janeiro)*, vol. 25, no. 1, Apr. 2020, doi: 10.1590/S1517-707620200001.0916.

[51] L. Chen, Y. He, Y. Yang, S. Niu, and H. Ren, "The research status and development trend of additive manufacturing technology," *The International Journal of Advanced Manufacturing Technology 2016 89:9*, vol. 89, no. 9, pp. 3651–3660, Aug. 2016, doi: 10.1007/S00170-016-9335-4.

[52] B. Kianian, "3D Printing and Additive Manufacturing State of the Industry, Annual Worldwide Progress Report: Chapters titles: The Middle East, and other countries," *Wohlers Report - 3D Printing and Additive Manufacturing State of the Industry*, vol. 22, p. 344, 2017, Accessed: Aug. 08, 2021. [Online]. Available: https://researchspace.auckland.ac.nz/handle/2292/46626.

[53] N. Labeaga-Martínez, M. Sanjurjo-Rivo, J. Díaz-Álvarez, and J. Martínez-Frías, "Additive manufacturing for a Moon village," *Procedia Manufacturing*, vol. 13, pp. 794–801, 2017, doi: 10.1016/J.PROMFG.2017.09.186.

[54] B. Khoshnevis, "AUTOMATED CONSTRUCTION BY CONTOUR CRAFTING-RELATED ROBOTICS AND INFORMATION TECHNOLOGIES," vol. 13, no. 1, pp. 5–19, 2004, Accessed: Aug. 08, 2021. [Online]. Available: www.calearth.org.

[55] P. Wu, J. Wang, and X. Wang, "A critical review of the use of 3-D printing in the construction industry," *Automation in Construction*, vol. 68, pp. 21–31, May 2016, doi: 10.1016/J.AUTCON.2016.04.005.

[56] A. S. Elakkad, "3D Technology in the Automotive Industry," *International Journal of Engineering Research and*, vol. V8, no. 11, Nov. 2019, doi: 10.17577/IJERTV8IS110122.

[57] S. Lim, R. A. Buswell, T. T. Le, S. A. Austin, A. G. F. Gibb, and T. Thorpe, "Developments in construction-scale additive manufacturing processes," *Automation in Construction*, vol. 21, no. 1, pp. 262–268, Jan. 2012, doi: 10.1016/J.AUTCON.2011.06.010.

[58] A. Nadal, J. Pavón, and O. Liébana, "3D printing for construction: A procedural and material-based approach," *Informes de la Construccion*, vol. 69, no. 546, 2017, doi: 10.3989/IC.16.066.

[59] I. Hager, A. Golonka, and R. Putanowicz, "3D Printing of Buildings and Building Components as the Future of Sustainable Construction?," *Procedia Engineering*, vol. 151, pp. 292–299, Jan. 2016, doi: 10.1016/J.PROENG.2016.07.357.

[60] G. Cesaretti, E. Dini, X. De Kestelier, V. Colla, and L. Pambaguian, "Building components for an outpost on the Lunar soil by means of a novel 3D printing technology," *Acta Astronautica*, vol. 93, pp. 430–450, 2013, doi: 10.1016/j.actaastro.2013.07.034.

[61] "3D Printing: The Future of Construction - 3Dnatives." https://www.3dnatives.com/en/3d-printing-construction-310120184/ (accessed Aug. 08, 2021).

[62] A. M. Al-Huneidei and I. S. Jalham, "Studying the Properties of Polymer blends Sheets for Decorative Purposes," *Jordan Journal of Mechanical and Industrial Engineering*, vol. 7, no. 1, 2013.

[63] L. SC, L. R, S. J, G. M, and M. R, "Polymers for 3D Printing and Customized Additive Manufacturing," *Chemical reviews*, vol. 117, no. 15, pp. 10212–10290, Aug. 2017, doi: 10.1021/ACS.CHEMREV.7B00074.

[64] Y. Zhuang *et al.*, "3D–printing of materials with anisotropic heat distribution using conductive polylactic acid composites," *Materials & Design*, vol. C, no. 126, pp. 135–140, Jul. 2017, doi: 10.1016/J.MATDES.2017.04.047.

[65] S. FS, N. KV, Z. MY, M. AV, K. SD, and E. YZ, "Mechanical properties and shape memory effect of 3D-printed PLA-based porous scaffolds," *Journal of the mechanical behavior of biomedical materials*, vol. 57, pp. 139–148, Apr. 2016, doi: 10.1016/J.JMBBM.2015.11.036.

[66] Y. Song, Y. Li, W. Song, K. Yee, K.-Y. Lee, and V. L. Tagarielli, "Measurements of the mechanical response of unidirectional 3D-printed PLA."

[67] Albarnawi, Alkhair. The effects of content and surface modification of filler on the mechanical properties of selective laser sintered polyamide12 composites. *Jordan Journal of Mechanical and Industrial Engineering*. 8. 265-274, 2014.

[68] F. Castles *et al.*, "Microwave dielectric characterisation of 3D-printed BaTiO3/ABS polymer composites," *Scientific Reports 2016 6:1*, vol. 6, no. 1, pp. 1–8, Mar. 2016, doi: 10.1038/srep22714.

[69] A. Chiappone *et al.*, "Study of graphene oxide-based 3D printable composites: Effect of the in situ reduction," *Composites Part B: Engineering*, vol. 124, pp. 9–15, Sep. 2017, doi: 10.1016/J.COMPOSITESB.2017.05.049.

[70] S. Dul, L. Fambri, and A. Pegoretti, "Fused deposition modelling with ABS–graphene nanocomposites," *Composites Part A: Applied Science and Manufacturing*, vol. C, no. 85, pp. 181–191, Jun. 2016, doi: 10.1016/J.COMPOSITESA.2016.03.013.

[71] Q. T. Nguyen, T. Ngo, P. Tran, P. Mendis, M. Zobec, and L. Aye, "Fire performance of prefabricated modular units using organoclay/glass fibre reinforced polymer composite," *Construction and Building Materials*, vol. 129, pp. 204–215, Dec. 2016, doi: 10.1016/J.CONBUILDMAT.2016.10.100.

[72] J. Song, C. Chen, and Y. Zhang, "High thermal conductivity and stretchability of layer-by-layer assembled silicone rubber/graphene nanosheets multilayered films," *Composites Part A: Applied Science and Manufacturing*, vol. 105, pp. 1–8, Feb. 2018, doi: 10.1016/J.COMPOSITESA.2017.11.001.

[73] A. M. Elliott, O. S. Ivanova, C. B. Williams, and T. A. Campbell, "AN INVESTIGATION OF THE EFFECTS OF QUANTUM DOT NANOPARTICLES ON PHOTOPOLYMER RESIN FOR USE IN POLYJET DIRECT 3D PRINTING."

[74] G. Alaimo, S. Marconi, L. Costato, and F. Auricchio, "Influence of meso-structure and chemical composition on FDM 3D-printed parts," *Composites Part B: Engineering*, vol. C, no. 113, pp. 371–380, Mar. 2017, doi: 10.1016/J.COMPOSITESB.2017.01.019.

[75] H. L. Tekinalp *et al.*, "Highly oriented carbon fiber–polymer composites via additive manufacturing," *Composites Science and Technology*, vol. 105, pp. 144–150, Dec. 2014, doi: 10.1016/J.COMPSCITECH.2014.10.009.

[76] S. Gorsse, C. Hutchinson, M. Gouné, and R. Banerjee, "Additive manufacturing of metals: a brief review of the characteristic microstructures and properties of steels, Ti-6Al-4V and high-entropy alloys," *http://www.tandfonline.com/action/journalInformation?show=aimsScope&journalCode=tsta20#.VmBmuzZFCUk*, vol. 18, no. 1, pp. 584–610, Dec. 2017, doi: 10.1080/14686996.2017.1361305.

[77] H. Attar, M. Calin, L. Zhang, S. Scudino, and J. Eckert, "Manufacture by selective laser melting and mechanical behavior of commercially pure titanium," *ECU Publications Post 2013*, vol. 593, pp. 170–177, Jan. 2014, doi: 10.1016/j.msea.2013.11.038.

[78] L. E. Murr *et al.*, "Microstructures and Properties of 17-4 PH Stainless Steel Fabricated by Selective Laser Melting," *Journal of Materials Research and Technology*, vol. 1, no. 3, pp. 167–177, Oct. 2012, doi: 10.1016/S2238-7854(12)70029-7.

[79] C. Brice, R. Shenoy, M. Kral, and K. Buchannan, "Precipitation behavior of aluminum alloy 2139 fabricated using additive manufacturing," *Materials Science and Engineering A*, vol. 648, pp. 9–14, Nov. 2015, doi: 10.1016/J.MSEA.2015.08.088.

[80] K. Bartkowiak, S. Ullrich, T. Frick, and M. Schmidt, "New Developments of Laser Processing Aluminium Alloys via Additive Manufacturing Technique," *Physics Procedia*, vol. 12, no. PART 1, pp. 393–401, Jan. 2011, doi: 10.1016/J.PHPRO.2011.03.050.

[81] N. T. Aboulkhair, M. Simonelli, L. Parry, I. Ashcroft, C. Tuck, and R. Hague, "3D printing of Aluminium alloys: Additive Manufacturing of Aluminium alloys using selective laser melting," *Progress in Materials Science*, vol. 106, p. 100578, Dec. 2019, doi: 10.1016/J.PMATSCI.2019.100578.

[82] A. G. Demir and B. Previtali, "Additive manufacturing of cardiovascular CoCr stents by selective laser melting," *Materials & Design*, vol. 119, pp. 338–350, Apr. 2017, doi: 10.1016/J.MATDES.2017.01.091.

[83] A. T. Sutton, C. S. Kriewall, M. C. Leu, and J. W. Newkirk, "Powder characterisation techniques and effects of powder characteristics on part properties in powder-bed fusion processes," *http://dx.doi.org/10.1080/17452759.2016.1250605*, vol. 12, no. 1, pp. 3–29, Jan. 2016, doi: 10.1080/17452759.2016.1250605.

[84] T. Vilaro, C. Colin, and J. D. Bartout, "As-Fabricated and Heat-Treated Microstructures of the Ti-6Al-4V Alloy Processed by Selective Laser Melting," *Metallurgical and Materials Transactions A 2011 42:10*, vol. 42, no. 10, pp. 3190–3199, May 2011, doi: 10.1007/S11661-011-0731-Y.

[85] "Additively Manufactured Inconel 718: Microstructures and Mechanical Properties - Dunyong Deng - Google Books."

[86] M. R. Khorramshahi and A. Mokhtari, "Automatic Construction by Contour Crafting Technology," *Emerging Science Journal*, vol. 1, no. 1, pp. 28–33, Jul. 2017, doi: 10.28991/ESJ-2017-01113.

[87] C. Gosselin, R. Duballet, P. Roux, N. Gaudillière, J. Dirrenberger, and P. Morel, "Large-scale 3D printing of ultra-high performance concrete – a new processing route for

architects and builders,” *Materials & Design*, vol. 100, pp. 102–109, Jun. 2016, doi: 10.1016/J.MATDES.2016.03.097.

[88] B. Panda, N. A. N. Mohamed, S. C. Paul, G. B. Singh, M. J. Tan, and B. Šavija, “The Effect of Material Fresh Properties and Process Parameters on Buildability and Interlayer Adhesion of 3D Printed Concrete,” *Materials*, vol. 12, no. 13, Jul. 2019, doi: 10.3390/MA12132149.

[89] A. Perrot, D. Rangeard, and A. Pierre, “Structural built-up of cement-based materials used for 3D-printing extrusion techniques,” *Materials and Structures 2015 49:4*, vol. 49, no. 4, pp. 1213–1220, Feb. 2015, doi: 10.1617/S11527-015-0571-0.

[90] J. Zhong, G. X. Zhou, P. G. He, Z. H. Yang, and D. C. Jia, “3D printing strong and conductive geo-polymer nanocomposite structures modified by graphene oxide,” *Carbon*, vol. 117, pp. 421–426, Jun. 2017, doi: 10.1016/J.CARBON.2017.02.102.

[91] M. Xia and J. Sanjayan, “Method of formulating geopolymer for 3D printing for construction applications,” *Materials & Design*, vol. C, no. 110, pp. 382–390, Nov. 2016, doi: 10.1016/J.MATDES.2016.07.136.

[92] E. M. Hernández-Rodríguez *et al.*, “Prospective use of the 3D printing technology for the microstructural engineering of Solid Oxide Fuel Cell components,” *Boletin de la Sociedad Espanola de Ceramica y Vidrio*, vol. 53, no. 5, pp. 213–216, Sep. 2014, doi: 10.3989/CYV.252014.

[93] Y. Wen *et al.*, “3D printed porous ceramic scaffolds for bone tissue engineering: a review,” *Biomaterials Science*, vol. 5, no. 9, pp. 1690–1698, Aug. 2017, doi: 10.1039/C7BM00315C.

[94] B. Derby, “Additive Manufacture of Ceramics Components by Inkjet Printing,” *Engineering*, vol. 1, no. 1, pp. 113–123, Mar. 2015, doi: 10.15302/J-ENG-2015014.

[95] M. Rosa *et al.*, “Zirconia nano-colloids transfer from continuous hydrothermal synthesis to inkjet printing,” *Journal of the European Ceramic Society*, vol. 39, no. 1, pp. 2–8, Jan. 2019, doi: 10.1016/J.JEURCERAMSOC.2017.11.035.

[96] F. H. Liu, Y. K. Shen, and Y. S. Liao, “Selective laser gelation of ceramic-matrix composites,” *Composites Part B: Engineering*, vol. 42, no. 1, pp. 57–61, Jan. 2011, doi: 10.1016/J.COMPOSITESB.2010.09.011.

[97] E. Vorndran *et al.*, “3D Powder Printing of β-Tricalcium Phosphate Ceramics Using Different Strategies,” *Advanced Engineering Materials*, vol. 10, no. 12, pp. B67–B71, Dec. 2008, doi: 10.1002/ADEM.200800179.

[98] C. Sun *et al.*, “Effect of particle size gradation on the performance of glass-ceramic 3D printing process,” *Ceramics International*, vol. 1(PA), no. 43, pp. 578–584, Jan. 2017, doi: 10.1016/J.CERAMINT.2016.09.197.

[99] H. SJ, “Porous scaffold design for tissue engineering,” *Nature materials*, vol. 4, no. 7, pp. 518–524, 2005, doi: 10.1038/NMAT1421.

[100] C. Oztan *et al.*, “Microstructure and mechanical properties of three dimensional-printed continuous fiber composites:,” *https://doi.org/10.1177/0021998318781938*, vol. 53, no. 2, pp. 271–280, Jul. 2018, doi: 10.1177/0021998318781938.

[101] W. Zhang, R. Melcher, N. Travitzky, R. K. Bordia, and P. Greil, “Three-Dimensional Printing of Complex-Shaped Alumina/Glass Composites,” *Advanced Engineering Materials*, vol. 11, no. 12, pp. 1039–1043, Dec. 2009, doi: 10.1002/ADEM.200900213.

[102] T. Mühler, C. M. Gomes, J. Heinrich, and J. Günster, “Slurry-Based Additive Manufacturing of Ceramics,” *International Journal of Applied Ceramic Technology*, vol. 12, no. 1, pp. 18–25, Jan. 2015, doi: 10.1111/IJAC.12113.

[103] T. Niendorf, S. Leuders, A. Riemer, H. A. Richard, T. Tröster, and D. Schwarze, “Highly Anisotropic Steel Processed by Selective Laser Melting,” *Metallurgical and Materials Transactions B 2013 44:4*, vol. 44, no. 4, pp. 794–796, May 2013, doi: 10.1007/S11663-013-9875-Z.

[104] W. Oropallo and L. A. Piegl, “Ten challenges in 3D printing,” *Engineering with Computers 2015 32:1*, vol. 32, no. 1, pp. 135–148, Jun. 2015, doi: 10.1007/S00366-015-0407-0.

[105] N. Coniglio, T. Sivarupan, and M. El Mansori, “Investigation of process parameter effect on anisotropic properties of 3D printed sand molds,” doi: 10.1007/s00170-017-0861-5.

[106] Hwayyin, R. N., Hammood, A. S., & Ameed, A. S. The Effect of Acrylic Reinforcement with Different Types of Composite Material on the Impact Energy. *Jordan Journal of Mechanical and Industrial Engineering*, *16*(3), 2022.

[107] Ghalme, S. G. Improving Mechanical Properties of Rice Husk and Straw Fiber Reinforced Polymer Composite through Reinforcement Optimization. *Jordan Journal of Mechanical and Industrial Engineering*, 15(5), 2021.

[108] Kazem, B., & Khawwaf, J. Estimation Bending Deflection in an Ionic Polymer Metal Composite (IPMC) Material using an Artificial Neural Network Model. *Jordan Journal of Mechanical and Industrial Engineering*, *10*(2), 2016.

JJMIE

Volume 16, Number 4, September. 2022
ISSN 1995-6665
Pages 543 – 556

Jordan Journal of Mechanical and Industrial Engineering

Impact of Discrete Multi-arc Rib Roughness on the Effective Efficiency of a Solar Air Heater

Arwa M. Kadhim, Mena S. Mohammed, Ammar A. Farhan*

Department of Energy Engineering, University of Baghdad, 10071, Baghdad, Iraq

Received 29 Mar 2022 *Accepted 14 Jun 2022*

Abstract

Artificial roughness on the absorber plate of a Solar Air Heater (SAH) is a popular technique for increasing its effective efficiency. The study investigated the effect of geometrical parameters of discrete multi-arc ribs (DMAR) installed below the SAH absorber plate on the effective efficiency. The effects of major roughness factors, such as number of gaps (N_g = 1-4), rib pitch (p/e = 4-16), rib height (e/D = 0.018-0.045), gab width (w_g/e = 0.5-2), angle of attack (α = 30°-75°), and Reynolds number (Re= 2000-20000) on the performance of a SAH are studied. The performance of the SAH is evaluated using a top-down iterative technique. The results show that as Re rises, SAH-effective DMAR's efficiency first ascends to a specified value of Re to attain the maximum values then falls. The useful energy gained via SAH-DMAR is higher by an average of 12% when compared to smooth SAH. According to the findings, the effective efficiency of SAH-DMAR is 9.4% higher than that of smooth SAH. The maximum thermal efficiency of SAH-DMAR and smooth SAH is 81.1 % and 74.7 %, respectively.

Keywords: SAH, effective efficiency, DMAR, rib roughness.

Nomenclature

A_p	aperture area of the SAH (m^2)
b	half-height of the v-channel (m)
cp_a	specific heat of the air (J/kg K)
D	hydraulic diameter
e/D	rib height
f	friction factor
h_1	coefficient of convective heat transfer between the absorber plate and air (W/m^2 K)
h_2	coefficient of convective heat transfer between the bottom plate and air (W/m^2 K)
h_r	coefficient of radiative heat transfer between absorbing and bottom plates (W/m^2 K)
h_w	coefficient heat transfer of wind (W/m^2K)
I	insolation (W/m^2)
k_a	thermal conductivity of air (W/m K)
k_i	thermal conductivity of the glass wool (W/m K)
L_c	Length of SAH (m)
$\dot{m}_a$	air mass flow rate (kg/s)
N_g	gap numbers
Nu	Nusselt number
p/e	rib pitch
P_m	mechanical power consumed by the fan (W)
Q_u	useful energy (W)
Re	Reynolds number
T_a	air temperature (K)
T_{ai}	inlet air temperature (K)
T_{am}	ambient temperature (K)
T_{ao}	outlet air temperature (K)
T_{mb}	bottom plate temperature (K)
T_{mp}	absorber plate temperature (K)
t_i	bottom insulation thickness (m)
U_b	coefficient of bottom heat loss (W/m^2 K)
U_t	coefficient of top heat loss (W/m^2 K)
V_{in}	inlet air velocity (m/s)
V_w	wind speed (m/s)
W_c	Width of SAH (m)

Greek letters

α_p	absorber plate absorptance
β	collector inclined angle (°)
σ	Stefan–Boltzmann constant (W/m^2 K^4)
ρ_a	air density (kg/m^3)
μ_a	air viscosity (Pa s)
η_t	Thermal efficiency (%)
ε_p	absorber plate emittance
ε_b	back plate emittance
τ_c	cover transmittance
ε_c	cover emittance
η_{eff}	effective efficiency (%)
ΔP	pressure drop (Pa)

1. Introduction

Significant energy demand due to population increase has resulted in an unsustainable reliance on rapidly depleting fossil fuel reserves. Because of increased consumption, prices are expected to soar, maybe above inflation. Additionally, because of the environmental threat posed by this, the world society has been driven to adopt renewable energy as a means of attaining sustainable growth[1,2]. Solar energy is a sustainable source of energy that produces no pollution. It is employed in a wide variety of residential and industrial applications[3–5].

Solar air heaters (SAHs) are a type of heat exchanger that captures solar energy and transmit it to the air moving through them[6]. SAH is simple to produce and affordable

---

* Corresponding author e-mail: ammarali@uobaghdad.edu.iq.

to manufacture. It has a few drawbacks; one of which is that the poor coefficient of heat transfer between the heated absorber plate and the working fluid (air) results in higher heat loss and decreased efficiency. This is because the laminar sub-layer imposes a high thermal resistance on the heat transfer process [7,8]. Researchers have used both passive and active heat transfer augmentation approaches to break through this sub-layer, with passive heat transfer enhancement techniques being the most commonly investigated [9,10]. In this scenario, ribs were utilized to restrict the flow, which resulted in the separation and subsequent reattachment of the boundary layer, leading to higher turbulence.

Numerous rib configurations have been investigated numerically and experimentally to increase the rate of convective heat transfer. Initially, continuous ribs perpendicular to the main flow stream were utilized to boost the convective heat transfer rate of the turbulent flow duct [11–13]. However, any significant improvement in overall performance was offset by the larger pressure drop associated with the addition of ribs. Later, discrete ribs were used to reduce the higher pressure drop caused by the blocking effect of the ribs [10,14,15]. Saini and Saini [16] experimentally discovered that arc-shaped ribs in rectangular ducts increased the Nusselt number (Nu) by an order of 3.6 and the friction factor by 1.75 times when compared to a smooth channel. Ghritlahre et al.[17] implemented an experimental investigation on apex up and apex down ribs which give enhancement in heat transfer as compared to smooth duct SAH. Multiple arc-shaped ribs were employed by Singh et al. [18] on a heated plate with a rectangular channel. In comparison to a smooth surface, the greatest increase in Nu and friction factor was found to be 5.07 and 3.71 times.

Experiments were conducted by Pandey and Bajpai [19] to examine the thermal performance of a SAH with multi-arc-shaped ribs with gap roughness on the absorber plate. The result shows that, as the Reynolds number (Re) increases from 2100 to 21000, the thermal performance of the roughened collector is found to increase from 0.37 to 0.83, compared to 0.21 to 0.55 for the smooth SAH. Kumar et al. [12] investigated heat transfer and friction in the flow of air via rectangular ducts with S-shaped ribs on the absorber plate. The result indicates that the Nu and friction factors rise by a maximum of 4.64 and 2.71 times, respectively. Additionally, correlations for the Nu and friction factor were developed. Agrawal et al. [20] conducted experiments to determine the impact of geometrical parameters on the heat transfer coefficient and thermal efficiency of artificial roughness with a discrete double arc reverse shape. It was reported that the largest improvements in heat transfer coefficient and thermal efficiency over a smooth duct are 2.88 and 1.29, respectively. Multiple-arcrib roughness patterns with gap-shaped roughness were studied experimentally by Kumar et al. [21]. The proposed roughed solar air heater has a Nu and friction factor that are 5.76 and 6.05 times higher than the smooth SAH.

A comprehensive study of the literature carried out by Nidhul et al. [3] reveals that the arc-shaped rib pattern is superior to other rib patterns, such as a wedge, transverse, and rib-groove combination roughness. Azad et al. [22] conducted an experimental investigation on a solar air heater with a new discrete symmetrical arc rib design. The Nu and friction factor were found to be 2.26 and 3.87 times greater than those of a smooth duct, respectively. Bhuvad et al. [14] investigated the thermal-hydraulic performance of a solar air heater equipped with a new apex-up discrete arc rib roughness on the backside of the absorbing plate. At a 30° angle of attack, the maximum enhancement in thermal-hydraulic performance is 2.01. V-groove absorbing plate have also been employed to increase the surface area available for heat transfer in several studies. As a result of the increased surface area, the rate of heat transfer becomes more efficient. A V-groove absorbing plate is more efficient in absorbing heat. As the absorption rate increases, the heat transfer area of the corrugated surfaces practically doubles, increasing the temperature of the absorber plate [23].

According to the literature, artificial ribs on the absorbing surface are an effective method to enhance SAH heat efficiency. As a result, pressure drop throughout the system has increased significantly, resulting in higher power usage. In the present work, the effects of discrete multi-arc rib roughness on SAH are studied for a variety of Re values ranging from 2000 to 20000. The effect of geometrical parameters of the DMAR like N_g, p/e, w_g/e, e/D, and α on the thermal performance of the V-groove SAH is numerically investigated and validated in actual weather conditions. In addition, the effective efficiency of the SAH roughened by DMAR is estimated using a top-down iterative technique. To the best of the author's knowledge, no research study has documented the use of discrete multi-arc rib roughnesswith V-groove SAH.Thereby, the work's originality is evident in its contribution to this field of study.

2. Analytical methodology

2.1. Mathematical model

It is expected that SAH with artificial roughness will perform better than smooth surface SAH. Because of turbulence in the viscouslayer, heat transport is significantly improved. Additionally, a SAH with a triangle duct provides superior thermal performance than a SAH with a rectangular duct [13]. Fig. 1 shows a V-groove SAH having discrete multi-arc rib roughness on the absorbing plate. A 60-degree corrugation angle V-groove SAH has a 4 mm glass cover, a 1 mm absorber and backplates, and a 50 mm backside insulation. The absorber and bottom plates combine to produce a triangle-shaped duct that allows air to move through the SAH. Two identical V-groove SAHs are compared: one with discrete multi-arc rib roughness and the other without. Following are the assumptions that were made to derive the energy balance equation for each element of the V-groove SAH without altering the fundamental physical situation [24].

1. The steady-state assumption is used in the modeling of the V-groove SAH.
2. In a CV-groove SAH, one-dimensional heat transfer takes place between the various components of the system.
3. The side heat losses of the V-groove SAH are neglected, and there is no air leakage from the SAH.

The thermal behavior of the SAH with a roughened heated surface is the same as that of the smooth SAH. When insolation strikes the absorber plate, it is absorbed and then transferred to the working fluid. As a result, the same approach that is used to calculate temperatures and heat losses for smooth SAH may also be applied to roughened SAH. Fig. 2 depicts an energy flow between SAH components. Following the energy flow schematic, the energy equations for the absorbing plate, air, and bottom plate per unit area are expressed as follows:

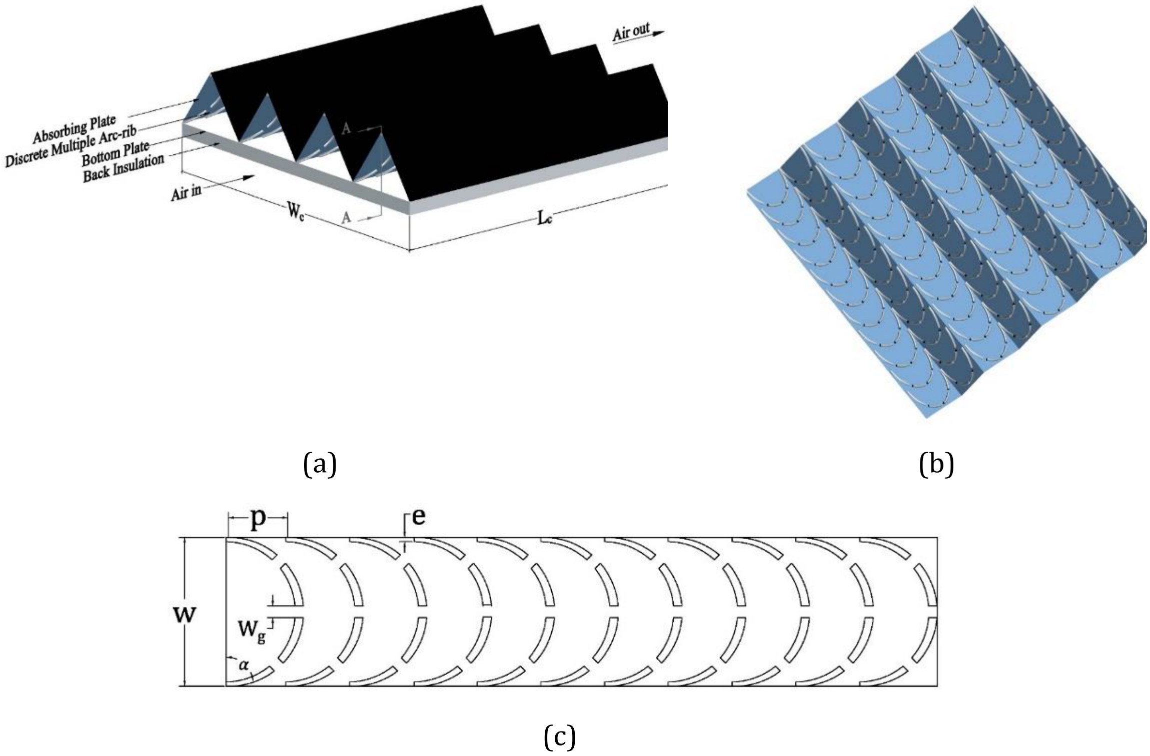

(a) (b) (c)

Figure 1. Schematic diagram of (a) SAH elements, (b) discrete multi-arc ribs on the backside of the absorbing plate, and (c) cross-sectional view of A-A

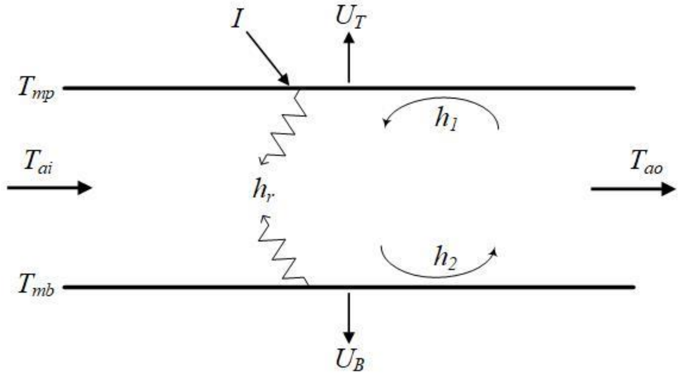

Figure 2. Schematic representation of the flow of energy between SAH components.

$$\tau_c\,\alpha_p I - U_T\left(T_{mp}-T_{am}\right) - h_r\left(T_{mp}-T_{mb}\right) - h_1\left(T_{mp}-T_a\right) = 0 \tag{1}$$

$$\frac{2\dot{m}_a c p_a}{A_p}\left(T_a - T_{ai}\right) - h_1\left(T_{mp}-T_a\right) - h_2\left(T_{mb}-T_a\right) = 0 \tag{2}$$

$$h_r\left(T_{mp}-T_{mb}\right) - h_2\left(T_{mb}-T_a\right) - U_B\left(T_{mb}-T_{am}\right) = 0 \tag{3}$$

2.2. Performance parameters of a SAH

The simplest approach to comparing the performance of a SAH is to examine its thermal efficiency. However, a SAH duct with artificial roughness led to better heat transfer, which also led to a boost in pumping power. Effective performance is based on how much energy is gained by air and how much more power is needed to pump air. Both the thermal and effective performance of the SAH should be considered when trying to find the best roughness parameters.

SAH thermal efficiency is the ratio of useful thermal energy gained by the air to the rate of solar energy that hits the heater's aperture, and is given as:

$$\eta_t = \frac{Q_u}{IA_p} = \frac{\dot{m}_a cp_a (T_{ao} - T_{ai})}{IA_p} \tag{4}$$

According to Cortes and Piacentini[25] hypothesis, SAH's net usable gain should be defined in terms of both thermal gain and the blower power consumption. As a result of the increased convective heat transfer coefficient, artificial roughness on the absorber plate improves thermal efficiency. However, this leads to a rise in pressure drop, which means that more mechanical power is needed to move air through the collector's duct. Typically, mechanical power (P_m) is provided by a blower powered by an electrical motor. It is, therefore, impossible to establish how much useful energy is gained by subtracting the motor's electrical energy consumption from the collector's thermal energy gain. The collector's energy losses must be considered when calculating the collector's net heat gain. The equivalent thermal energy (*ETE*) necessary to overcome friction is denoted by the following formula:

$$ETE = \frac{P_m}{\eta_{net}} \tag{5}$$

Where η_{net} is the net efficiency of converting thermal energy to mechanical energy conversion and is calculated as follows:

$$\eta_{net} = \eta_b \eta_m \eta_{tr} \eta_{thp} \tag{6}$$

Cortes and Piacentini[25] stated that the normal value of η_{net}, based on the common efficiency of several processes, such as blower efficiencyη_b = 0.65, electric motor efficiencyη_m = 0.88,the efficiency of electrical transmission from the power plantη_{tr} = 0.925, andthe thermal conversion efficiency of the power plantη_{thp} = 0.344, is 0.18.

The effective efficiency (η_{eff}) is defined as the ratio of net useful thermal energy gained by the air to the rate of insolation on the aperture of the collector, and is expressed as:

$$\eta_{eff} = \frac{Q_u - ETE}{IA_p} \tag{7}$$

2.3. Procedure for prediction of performance

Different system and operating parameters were used to determine the thermal and effective efficiencies of a SAH. Performance evaluation of a SAH is quantitatively carried out by a top-down iterative technique using MATLAB. The following process details the steps involved in calculating thermal and effective efficiency for a given set of roughness and operational parameter values:

Step 1. Selected values of roughness and operating parameters have been chosen such as p/e, Ng, e/D, α, w_g/e, Re, and *I*, as shown in Table 1.

Table 1. Design parameter data for the prediction model.

Parameter	Value
Length of SAH (L_c)	1 m
Width of SAH(W_c)	0.4 m
Rib pitch (p/e)	4-16
Rib height (e/D)	0.018-0.045
Rib width (W_p/w)	8
Gap numbers (N_g)	1-4
Gap width (w_g/e)	0.5-2
Angle of attack (α)	30°-75°
Bottom insulation thickness (t_i)	0.05 m
Thermal conductivity of glass wool (k_i)	0.034 W/m.°C
Absorbing plate emittance (ε_p)	0.95
Back plate emittance (ε_b)	0.95
Absorber plate absorptance (α_p)	0.96
Cover emittance (ε_c)	0.9
Cover transmittance (τ_c)	0.88
Reynolds number (*Re*)	2000 – 20,000
Insolation (*I*)	1000 W
Ambient temperature (T_{am})	25°C
Inlet air temperature (T_{ai})	25°C
Wind velocity (V_w)	2.5 m/s

Step 2. To begin the calculation, arbitrary values of T_{pm} (mean absorber plate temperature),T_{ao} (outlet air temperature), and T_{mb} (mean bottom plate temperature) are used as follows[26]:

$$T_{mp} = T_{am} + 20 \tag{8a}$$

$$T_{ao} = T_{am} + 10 \tag{8b}$$

$$T_{mb} = T_{am} + 10 \tag{8c}$$

Inlet air temperature is equal to ambient temperature, and mean air temperature (T_m) is used to evaluate the thermo-physical properties of air [27].

$$\rho_a = 1.1774 - 0.000066(T - 27) \tag{9a}$$

$$k_a = 0.02624 + 0.0000758(T - 27) \tag{9b}$$

$$\mu_a = [1.983 + 0.00184(T - 27)]10^{-5} \tag{9c}$$

$$cp_a = 1.0057 + 0.000066(T - 27) \tag{9d}$$

Step 3. Heat transfer coefficientsare calculated as follows:

The top heat loss coefficient (U_T) is obtained by combining $T_{mp}$and $T_{am}$with the correlation reported by Duffie et al. [26]

$$U_T = \left[\frac{M}{\left(\frac{C}{T_{mp}}\right)\left(\frac{T_{mp}-T_{am}}{M+f_m}\right)^{0.33}} + \frac{1}{h_w}\right]^{-1} + \left[\frac{\sigma\left(T_{mp}^2+T_{am}^2\right)\left(T_{mp}+T_{am}\right)}{\frac{1}{\epsilon_p+0.05M(1-\epsilon_p)}+\frac{2M+f_m-1}{\epsilon_c}-M}\right] \tag{10a}$$

where,*M* is the number of glass covers.

$$C = 204.429\,(\cos\beta)^{0.252} L^{-0.24} \tag{10b}$$

$$f_m = \left(\frac{9}{h_w} - \frac{30}{h_w^2}\right)\left(\frac{T_{am}}{316.9}\right)(1 + 0.091M) \tag{10c}$$

$$h_w = 5.3 + 3.7\,V_w \tag{10d}$$

The bottom heat loss coefficient (U_B) is calculated by combining the thermal conductivity (k_i) and the thickness (t_i) of the insulation[26].

$$U_B = \frac{k_i}{t_i} \tag{11}$$

The overall heat loss coefficient (U_L) is estimated as:

$$U_L = U_T + U_B \tag{12}$$

The thermal radiation coefficient (h_r) between the absorber and backplates can be estimated as:

$$h_r = \frac{\sigma\left(T_{mp}^2 + T_{mb}^2\right)\left(T_{mp} + T_{mb}\right)}{\frac{1}{\epsilon_p} + \frac{1}{\epsilon_b} - 1} \tag{13}$$

Re for equilateral triangular duct is computed as

$$\mathrm{Re} = \frac{4\,\rho_a V_{in} b}{3\,\mu_a} \tag{14}$$

where b is the half-height of the triangular duct.

For Nusselt number (Nu) inside the triangle conduit of the smooth SAH, Hollands and Shewen [28] proposed the following relationship to compute the convective heat transfer coefficient (h_1) between absorbing plate and air.

$$\mathrm{Nu}_1 = \mathrm{Nu}_o + \gamma_o \frac{b}{L_c} n, \tag{15}$$

where n is the number of collectors connected in series, and Nu_o and γ_o are functions of Re. Hollands and Shewen [28] recommended the following relations for Nu_o and γ_o:

$$\mathrm{Nu}_o = 2.821 \text{ and} \gamma_o = 0.126\mathrm{Re} \text{ for} \mathrm{Re} < 2800, \tag{16a}$$

$$\mathrm{Nu}_o = 1.9 \times 10^{-6}\mathrm{Re} \text{ and} \gamma_o = 225 \quad \text{for} \quad 2800 \le \mathrm{Re} \le 10^4, \tag{16b}$$

$$\mathrm{Nu}_o = 0.0302\mathrm{Re}^{0.74} \text{and} \gamma_o = 0.242\mathrm{Re}^{0.74} \quad \text{for } 10^4 < \mathrm{Re} < 10^5. \tag{16c}$$

An empirical equation, which was correlated by Kumar et al. [21], is used to determine the Nu_r for a SAH roughened by discrete multi-arc ribs on the absorbing plate as formula 17:

The Dittus-Boelter equation for Nu_2 is used to calculate the convective heat transfer coefficient (h_2) between the bottom plate and air [26].

$$Nu_2 = 0.023\, Re^{0.8}\ Pr^{0.4} \tag{18}$$

According to Hedayatizadeh [29], the coefficient of convective heat transfer is computed as follows:

$$h = \frac{3\, Nu\, k_a}{4\, b} \tag{19}$$

Step 4. The energy balance Eqs. (1-3) are solved by a top-down iterative program to yield new values for T_{mp}, T_{ao}, and T_{mb}. Compare these numeric values to the old ones. The comparison is based on the error value, which is the difference between the previous and current values. The procedure is repeated until all SAH temperature values are equal to or less than 0.00001.

Step 5. The value of friction factor (f_r), for the selected set of roughness parameters, is determined by the correlation developed by Kumar[21]. Whilst, f_s for smooth plate is determined using Hedayatizadeh et al. [29]relations.

$$f_s = f_o + \phi \frac{b}{L_c} n \tag{21}$$

f_o and $\phi$are functions of the Re number, determined as:

$$f_o = 13.33\mathrm{Re}^{-1} \text{and } \phi = 0.65 \qquad \text{for} \mathrm{Re} < 2800 \tag{22a}$$

$$f_o = 3.2 \times 10^{-4}\mathrm{Re}^{0.34} \text{and } \phi = 2.94\mathrm{Re}^{-0.19} \text{for } 2800 \le \mathrm{Re} \le 10^4 \tag{22b}$$

$$f_o = 0.0733\mathrm{Re}^{-0.25} \text{and } \phi = 0.51 \text{ for} 10^4 \le \mathrm{Re} \le 10^5 \tag{22c}$$

The pressure drop across the duct (ΔP) can be calculated as follows [10]:

$$\Delta P = \frac{3\rho_a L_c V_{in}^2 f}{2b} \tag{23}$$

The amount of P_m required by the blower to force air throughout the SAH can be expressed as [30]:

$$P_m = \frac{\dot{m}_a\, \Delta P}{\rho_a} \tag{24}$$

Finally, useful energy gain, thermal, and effective efficiencies are calculated by Eqs. 4 and 7, respectively.The flowchart of the top-down iterative program is shown in Fig. 3.

$$\mathrm{Nu_r} = 7 \times 10^{-5} \left(\begin{array}{c} \mathrm{Re}^{1.557} \left(\frac{\mathrm{w_g}}{\mathrm{e}}\right)^{0.028} \mathrm{N_g^{0.153}} \left(\frac{\mathrm{W_p}}{\mathrm{w}}\right)^{0.075} \left(\frac{\alpha}{60}\right)^{0.153} \left(\frac{\mathrm{p}}{\mathrm{e}}\right)^{0.385} \left(\frac{\mathrm{e}}{\mathrm{D}}\right)^{0.231} \\ \times \exp(-0.22 \ln \left(\frac{\mathrm{w_g}}{\mathrm{e}}\right)^2) \exp(-0.75 \ln\left(\mathrm{N_g}\right)^2) \exp(0.274 \left(\ln\left(\frac{\alpha}{60}\right)\right)^2) \\ \times \exp\left(-0.0001 \left(ln\left(\frac{\mathrm{W_p}}{\mathrm{w}}\right)\right)^2\right) \exp(-0.075 \left(\ln\left(\frac{\mathrm{p}}{\mathrm{e}}\right)\right)^2) \end{array} \right) \tag{17}$$

$$f_r = 0.335 \left(\begin{array}{c} \mathrm{Re}^{-0.25} \left(\frac{\mathrm{w_g}}{\mathrm{e}}\right)^{0.029} \mathrm{N_g^{0.069}} \left(\frac{\mathrm{W_p}}{\mathrm{w}}\right)^{0.079} \left(\frac{\alpha}{60}\right)^{0.132} \left(\frac{\mathrm{p}}{\mathrm{e}}\right)^{0.331} \left(\frac{\mathrm{e}}{\mathrm{D}}\right)^{0.156} \\ \times \exp(-0.152 \ln \left(\frac{\mathrm{w_g}}{\mathrm{e}}\right)^2) \exp(-0.02 \ln\left(\mathrm{N_g}\right)^2) \exp(0.148 \left(\ln\left(\frac{\alpha}{60}\right)\right)^2) \\ \times \exp\left(-0.004 \left(ln\left(\frac{\mathrm{W_p}}{\mathrm{w}}\right)\right)^2\right) \exp(-0.068 \left(\ln\left(\frac{\mathrm{p}}{\mathrm{e}}\right)\right)^2) \end{array} \right) \tag{20}$$

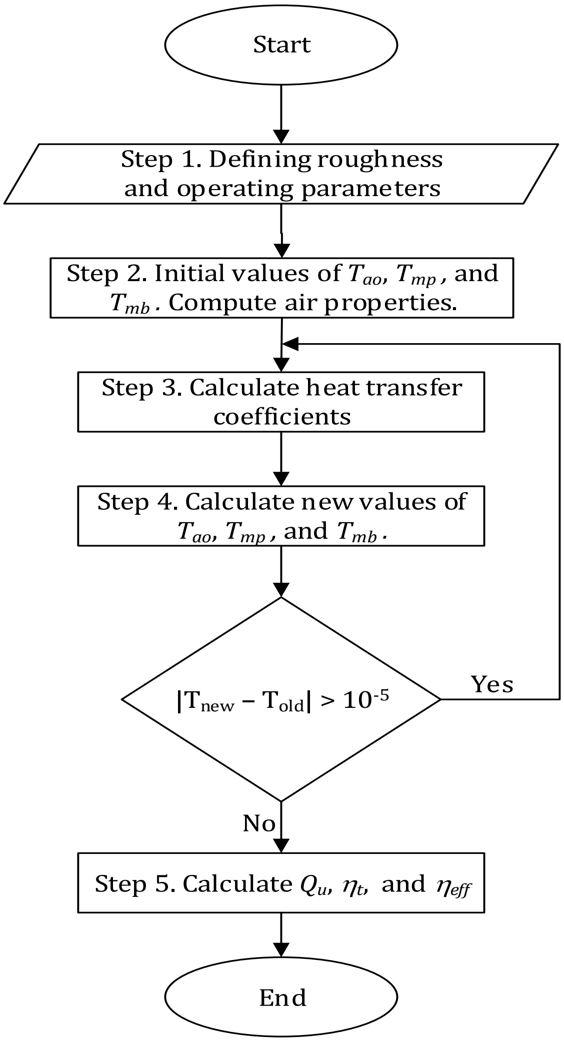

Figure 3. Flowchart for the computer program.

3. Results and discussion

The numerical solutions for different Re and roughness characteristics, such as rib height (e/D), number of gaps (N_g), gap width (w_g/e), ribpitch (p/e), and arc-angle (α) were used to calculate the T_p, Q_u,η_t, and η_{eff} of SAH roughened by DMAR, which were described further below. The results were compared to those obtained in the case of smooth ducts operating under the same conditions to investigate the improvement in T_{mp}, Q_u, η_t, and η_{eff} due to artificial roughness parameters.

Fig.4a depicts the impacts of the rib height(e/D) on the absorber plate temperature (T_p) vs the Re for the smooth SAH and SAH-DMAR at constant value of $N_g = 2$, $w_g/e = 1.25$, $p/e = 10$, and $\alpha = 45°$. When the Re is increased, the absorber plate temperature declines dramatically at first, and then very minimally at high values of Re. The absorber plate temperature of the SAH-DMAR is lower than that of the smooth collector for a given Re. The temperature of the absorber plate drops when the diameter of the roughness element, which is represented by the dimensionless term e/D, is increased. For e/D = 0.045, the lowest absorber plate temperatures are 32.01 °C, compared to 42.77 °C for smooth SAH. This reduction in the temperature of the absorber plate is caused by the breakdown of a viscous sub-layer, which prevents heat transfer from the absorbing plate to the working fluid. As a result of the roughened absorbing plate, there has been an increment in the amount of useful energy (Q_u) gained by the air as shown in Fig. 4b. It can be seen that the enhancement in thermal energy gained by air is greatest at low Re and gradually diminishes until it becomes unchangeable at Re greater than 13000. When the diameter of the roughness element is increased, the thermal energy gain increases proportionally. The reason for this is that the low e/D is immersed in the viscous sublayer. In the case of e/D = 0.045, the highest thermal energy output value is obtained at 324.16 W, which is about 8.5% greater than the value obtained with smooth SAH.

For a wide variety of e/D, the influence on thermal efficiency (η_t) is shown in Fig. 5a. The thermal performance of roughened collector is higher than that of a smooth collector, as seen in the figure. This is owing to the fact that the heightening of DMAR helps in breaking down thermal resistance at the heating surface which promotes more heat transfer from the absorbing plate to the air. As a result, thermal efficiency is improved. When Re is raised from 2000 to 20000, the maximum thermal efficiency of a roughened collector increases from 49% to 81%, corresponding to an e/D value of 0.045. Thermal efficiency increases from 47.9% to 74.7% with Re for a smooth collector. SAH thermal performance is improved due to the DMAR arrangement over the absorber plate, which allows for recurrent breakage of viscous sub-layers. In contrast, the alteration in viscous sub-layers also encourages the production of small eddies near the roughness elements, which resulted in a greater pressure drop in the SAH. Thus, to select the best value of e/D, effective efficiency (η_{eff}) is plotted against Re as shown in Fig. 5b. Better effective efficiency is associated with increased e/D and/or a higher Re. As Re approaches 13000, efficiency begins to decline for all e/D levels. Further increases in Re (above 13000) may lead to extra frictional losses that are greater than the gain in heat transfer; consequently, a decrease in effective efficiency is observed. Effective efficiency for SAH-DMAR at e/D = 0.045 is 76.6 %, while the smooth SAH has an efficiency of 70.4%. These findings showed that the optimal effective efficiency is achieved at e/D = 0.045.

Fig. 6a depicts the effect of changing gap numbers (N_g) on absorbing plate temperature. Other roughness parameters are kept constant i.e.,e/D = 0.045, w_g/e = 1.25, p/e = 10, and α = 45°throughout the investigation. As N_g increases from 1 to 3, the temperature of the absorbing plate falls, until it reaches its minimum value of 31.9 °C at N = 3. However, as the value of N_g rises over 3, the temperature of the absorbing plate rises. This can occur as a result of the roughness-elements changing discharge points. The N_g serves as discharge points, allowing the secondary flow to depart through the DMAR. The number of discharge points in the DMAR grows as the value of N_g grows. However, the absorbing plate temperature only decreased up to N_g = 3 as can be shown. This could be owing to increased local turbulence strength caused by secondary flow discharged through gaps downstream of the DMAR. Also, it could be attributed to the transverse plane's highly intense swirl flow. When N_g> 3, the secondary flow may not be strong enough to cause additional turbulence at the rib downstream, resulting in higher absorbing plate temperatures. For varying values of Ng, Fig. 6b demonstrates the fluctuation of Q_u with Re while keeping the rest roughness parameters constant. It is clear that Q_u grows for a given number of gaps until it reaches 3, after which it decreases. It can be observed that the increase in thermal energy absorbed by air is largest at Re < 10000, as opposed to Re > 10000. The gaps break down the secondary flow along the ribs, allowing the secondary flow fluid to mix with the main flow. Consequently, Q_u is increased. The maximum value of Q_u is 324.2 W is obtained at Re = 20000 and N_g = 3.

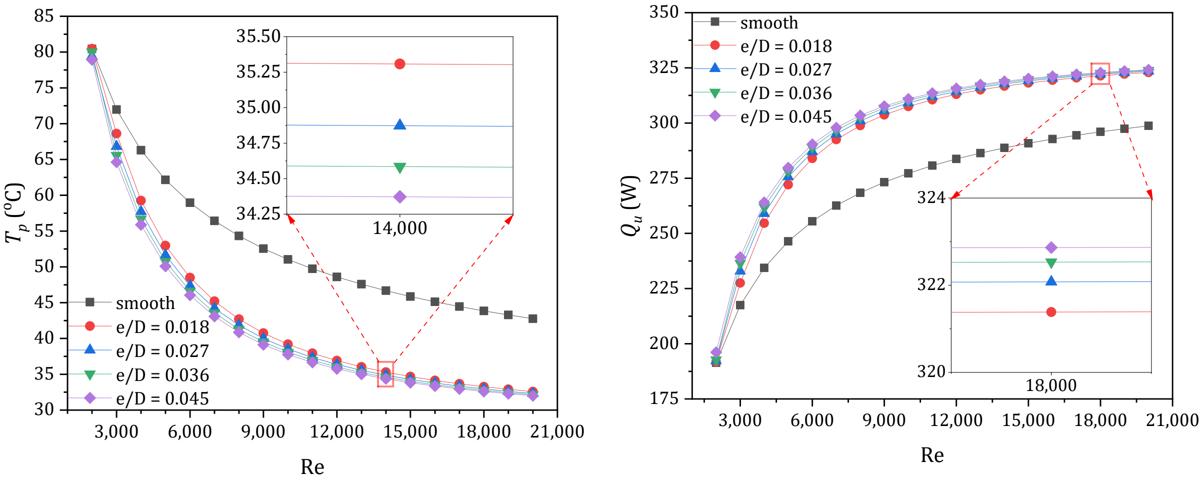

(a) (b)

Figure 4. The effect of the e/D on (a) absorber plate temperature, and (b) useful energy gain.

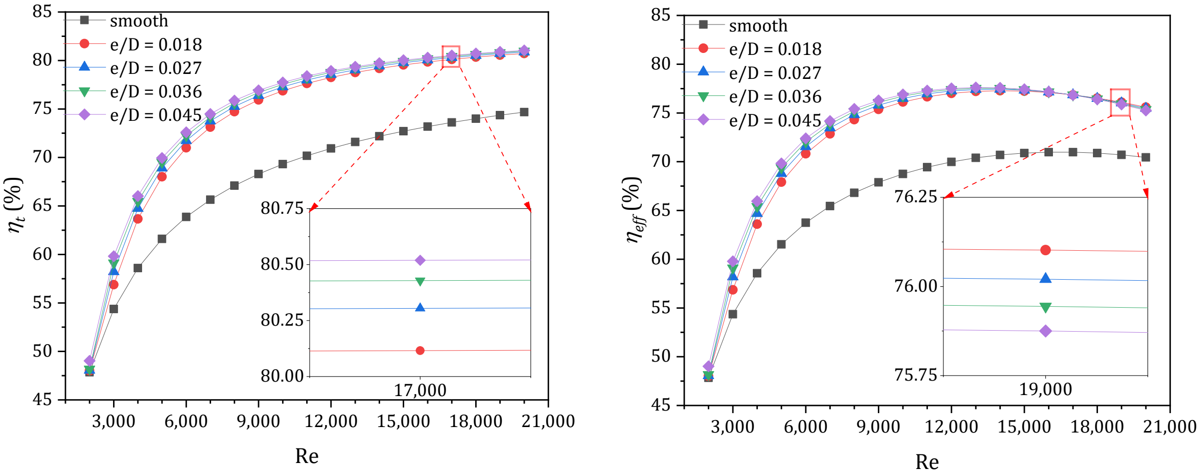

(a) (b)

Figure 5. The influence of *e/D* on (a)thermal efficiency, and (b)effective efficiency.

The influence of N_g on thermal efficiency is demonstrated in Fig. 7a. As shown in the figure, the thermal performance of a roughened collector is better than that of a smooth collector. This is because N_g assists in mixing secondary flow along the ribs with the main flow through the duct, allowing for more heat transfer from the absorber plate to the air. Therefore, thermal efficiency enhances. Furthermore, with all Re studied, thermal efficiency improves as N_g increases until $N_g = 3$, and the opposite trend is observed at higher N_g values. At Re = 20000 and N_g =3, it can be seen that the thermal efficiency of SAH-DMAR is 7.9% higher than that of smooth SAH. Fig. 7b shows the difference in effective efficiency between a SAH with and without DMAR throughout a range of Re. Effective efficiency is significantly increased for all N_g values when compared to smooth SAH until Re = 13000 when it begins to decline because of the larger pressure drop when compared to lower thermal enhancement. The best effective efficiency for SAH-DMAR is 77.6%, compared to 70.4 % for a smooth SAH at Re of 13000. Maximum effective efficiency is found at Ng of 3 based on the above findings.

Fig. 8a depicts the effect of gap width (w_g/e) on T_p for constant values of e/D, N_g, p/e, and α, i.e., 0.045, 3, 10, and 45°. It can be noted that the T_p is lowest when w_g/e = 1, and largest when w_g/e = 0.5. The amount of flow rate that occurs at the rib downstream changes dramatically when the width of the given gaps in the DMAR is changed. It is necessary for the flow leaving via the gaps to have a higher velocity at the rib downstream for better heat augmentation. Because the gap width (w_g) for $w_g/e< 1$ is relatively small, the secondary flow flowing along the rib-element is unable to find a smooth path through it, resulting in a large T_p. When $w_g/e > 1$, the w_g becomes large enough to allow a smooth secondary flow outflow from the gap, but the flow is delayed, and the T_p rises. Because the absorber plate temperature is lower, more heat gain is absorbed by the air as shown in Fig. 8b. The smooth SAH pattern has the lowest heat gain when compared to the roughened SAH pattern, which increases as Re rises, especially at low flow rates. The maximal heat gain for a SAH-DMAR is 324.2 W, compared to 298.7 W for a smooth duct, as shown in Fig. 8b.

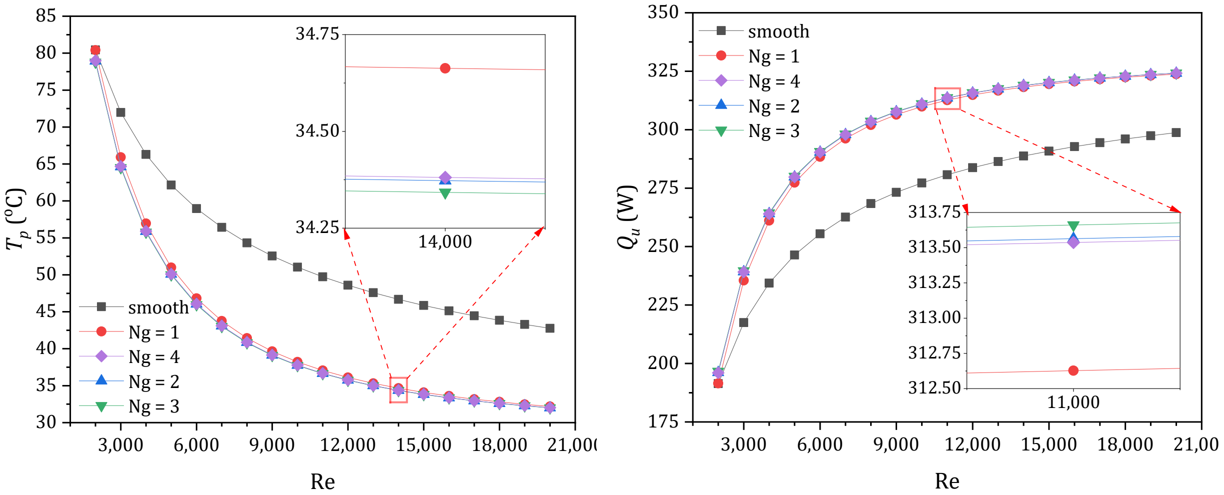

(a) (b)

Figure 6. The effect of the N_g on (a) absorber plate temperature, and (b) useful energy gain.

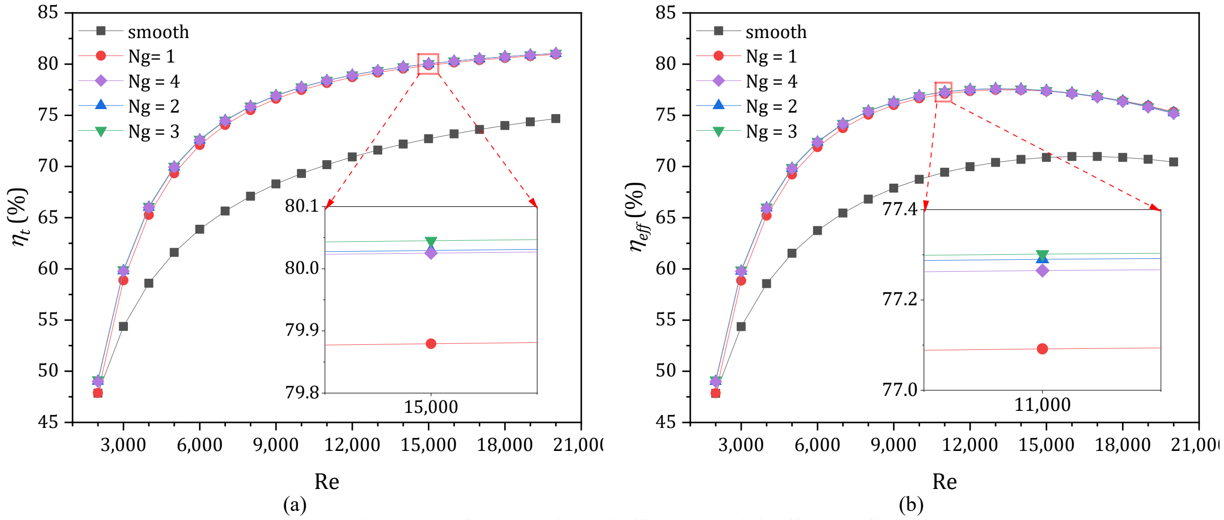

(a) (b)

Figure 7. The impact of N_g on (a)thermal efficiency, and (b)effective efficiency.

The influence of the w_g/e on the SAH's thermal efficiency for a wide range of Re is shown in Fig. 9a. With rising Re, the thermal efficiency rises dramatically as a result of the increased heat gain. Furthermore, as Re approaches 3000, the effect of DMAR on thermal efficiency becomes more substantial in comparison to the smooth duct. Furthermore, until $w_g/e = 1$, thermal efficiency improves as w_g/e increases, while the opposite tendency is observed for higher w_g/e values. In Fig. 9b, effective efficiency is plotted against Re for all w_g/e ratio values. Greater effective efficiency is associated with higher Re. This pattern continues until the Re reaches 13000, at which point efficiency begins to decline. At w_g/e =1, SAH-DMAR has a maximum effective efficiency of 77.6%, against 70.4% for traditional SAH. Thus, Re > 13000 is not recommended since the higher frictional losses outweigh the heat transfer enhancement.

Fig. 10a depicts the variation of T_p with Re for various rib pitch (p/e) values when the e/D of 0.045, the w_g/e of 1, the N_g of 3, and the α of 45°. The T_p drops as Re increases for all p/e values examined. The reason for this is that when Re rises, the turbulence intensity rises, implying that the air absorbs more heat from the absorber plate. For any Re, when the p/e increases, the T_p drops, reaches a minimum, and then rises. At a p/e of 12, T_p reaches its minimal value. The flow inter-rib reattachment and boundary layer regeneration are the causes of this fluctuation. The presence of ribs in the flow channel causes turbulence, which could improve heat transfer in terms of Q_u, as illustrated in Fig. 10b. Q_u has reached the highest value at p/e = 12 and corresponds to a higher Re in the investigated range of p/e. The number of re-attachment points produced by rib-roughness changes drastically as p/e changes. Even though the numbers of roughness components attached to the absorber plate are higher and they are closer together in p/e <12, there is little production of re-attachment points between the two following ribs, leading to a low Qu. The number of reattachment points is maximum when p/e = 12 is compared to other p/e values, such as 16.

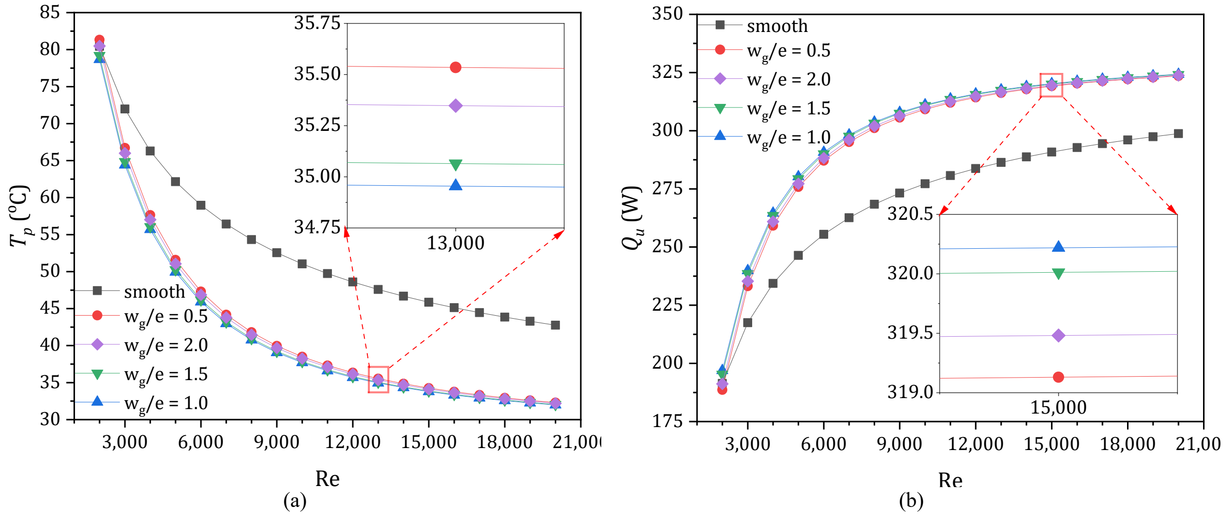

(a) (b)

Figure 8. The influence of w_g/e on (a) absorber plate temperature, and (b) useful energy gain.

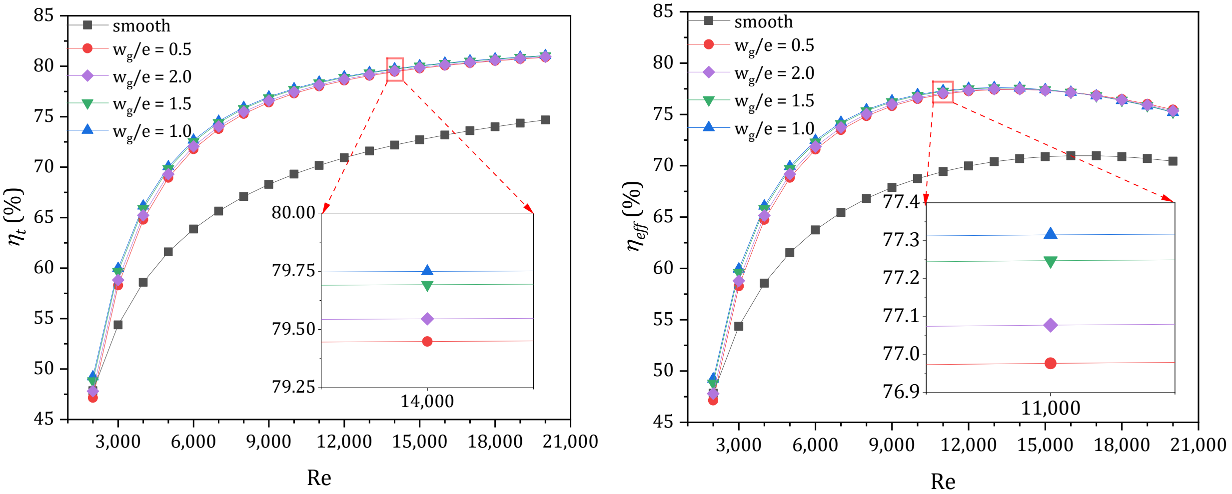

(a) (b)

Figure 9. The impact of w_g/e on (a)thermal efficiency, and (b)effective efficiency.

Fig. 11a depicts the thermal efficiency of a SAH with and without DMAR as a function of Re. When compared to smooth SAH, it is obvious that the thermal efficiency is considerably improved for all p/e values. Thermal efficiency improves as the pitch ratio is increased until p/e = 12, but for other pitch ratios, the opposite occurs. The maximum thermal efficiencies of SAH-DMAR and smooth SAH are 81.1 % and 74.7 %, respectively. Over a range of Re, Fig. 11b demonstrates the variation in the effective efficiency of a SAH with and without DMAR. The effective efficiency is clearly boosted over smooth SAH for all p/e values until Re exceeds 13000, after which it starts to fall due to the substantial extra pressure drop compared to low thermal enhancement. As a result, it is not recommended to use DMAR with SAH at Re > 13000. It is found that the effective efficiency of SAH-DMAR increased by 9.3% more than that for smooth duct when Re =13000. Based on the preceding findings, the highest effective efficiency is found at a p/e of 16.

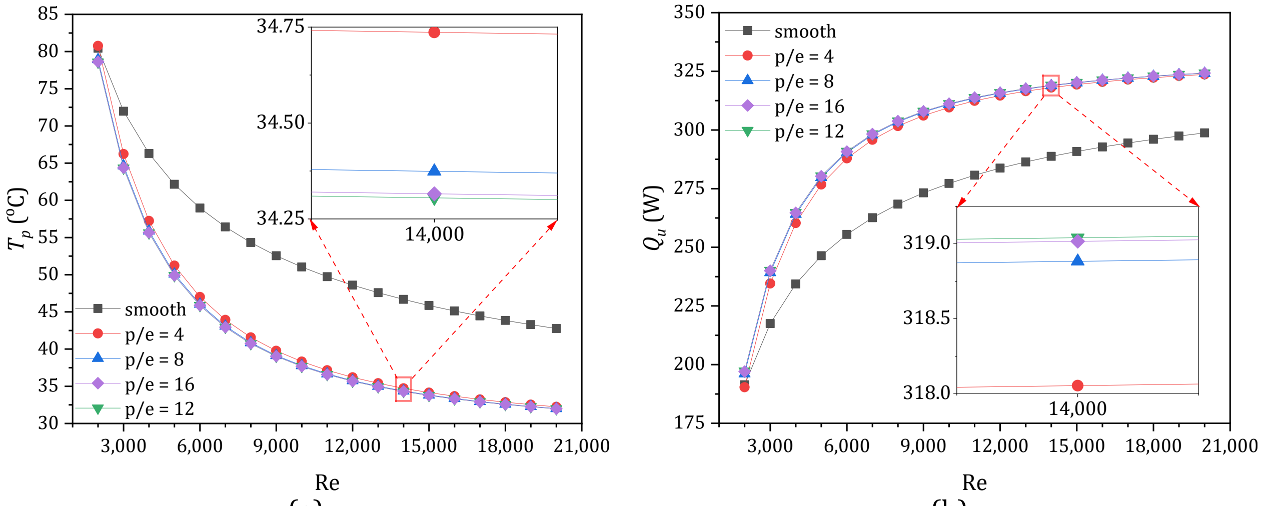

(a) (b)

Figure 10. The influence of p/e on (a) absorber plate temperature, and (b) useful energy gain.

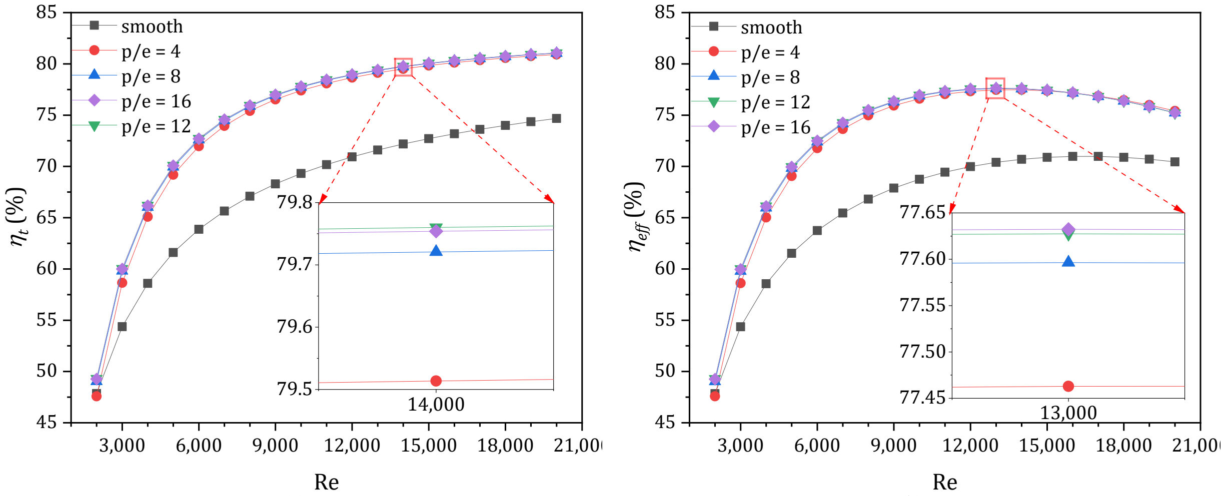

(a) (b)

Figure 11. The influence of *p/e* on (a)thermal efficiency, and (b)effective efficiency.

The influence of the angle of attack(α) is explored on T_p and Q_u of a solar air collector as illustrated in Fig. 12, where p/e, Ng, w_g/e, and e/D are at constant values of 16, 3, 1, and 0.045, respectively. The variations of T_p against the Re are seen in Fig. 12a. It may be seen that a roughness duct with DMAR transmits more useful energy gain to the airstream than that smooth duct, i.e., lower T_p for roughened SAH. It is discovered that the values of $T_p$are dropping with rises of Re in all cases. Consequently, the value of Q_u is raised with the growth of Re as depicted in Fig. 12b. Also, Q_u values are discovered to be enhanced with the subsequent rise in α. It occurs due to the shift in the path followed by the secondary flow across the absorber plate. Usually, the secondary flow occurred owing to the breakdown of viscous sub-layers flows or led by the rib element across the absorber plate, and it is transported along with the arc-shape rib element. Thus, the downstream eddies along DMAR which come in connection with the main airflow are transmitted to the heated surface which enhances the heat transfer rate.

The variation of thermal efficiency as a function of Re is shown in Fig. 13a for α values ranging from 30° to 75°. The greatest value of thermal efficiency is clearly discovered at 75°, while the lowest value is found at 30°. The behavior of thermal efficiency patterns may be explained by the fact that DMAR numbers become greatest in contact with the main airstream at α =75°, compared to the other values. In other words, at the heated surface, a significant recirculation flow zone occurs, allowing air to absorb more heat than a smooth duct. Fig. 13b depicts the effect of α on effective efficiency. Roughness ducts with DMAR have a higher effective efficiency than smooth ducts, as can be seen. For all values of Re, it is discovered that the values of effective efficiency rise as the value of α grows. The intense re-circulation flow zone that occurs at the heated surface causes powerful eddies that disrupt the axial airstream, and the pumping power required to move air across the duct increases due to the significant pressure drop. At Re = 13000, the highest increase in effective efficiency for SAH-DMAR is 9.4% higher than for smooth SAH.

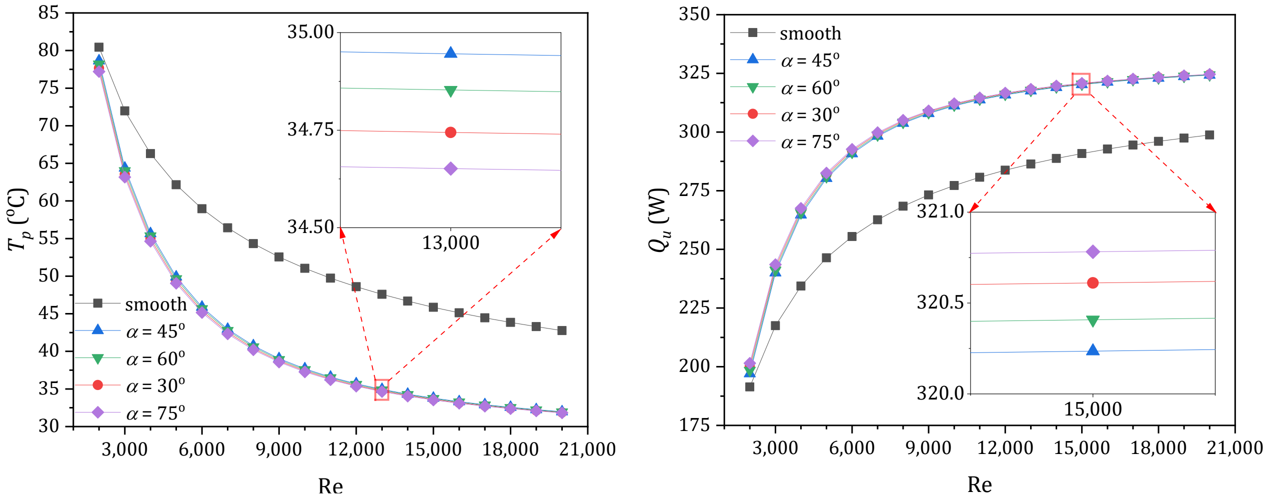

(a) (b)

Figure 12. Effect of α on (a) absorber plate temperature, and (b) useful energy gain.

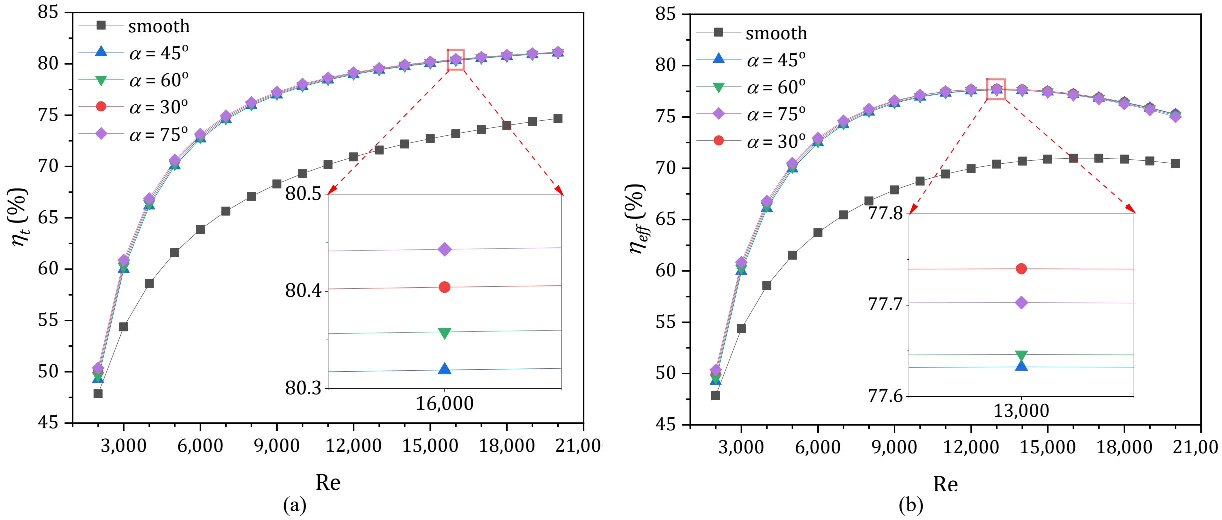

(a) (b)

Figure 13. The impact of α on (a)thermal efficiency, and (b)effective efficiency.

Table 2. Weather data for Baghdad on 3/1/2022

Time	8:00	9:00	10:00	11:00	12:00	13:00	14:00	15:00	16:00
I (W/m^2)	244.2	546.8	759.1	891.3	940.9	908.1	792.3	596.8	316.2
T_{am} (°C)	7.1	9.2	9.9	11.2	11.3	12.0	12.1	12.0	11.9

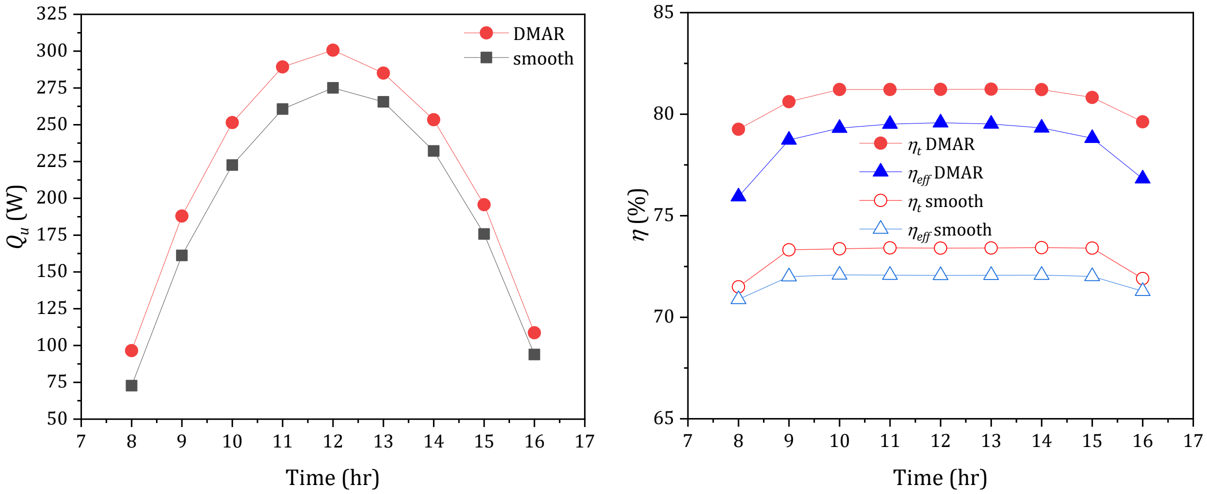

(a) (b)

Figure 14. Effect of optimum DMAR parameters on (a) useful energy gain, and (b) the thermal and effective efficiencies under real weather conditions on 3/1/2022.

Thermal efficiency enhancement criteria (*TEEC*) is a factor used to measure the augmentation in thermal efficiency of a SAH having an absorbing plate roughened by an artificial rib, which is calculated as

$$TEEC = \frac{\eta_{t,r} - \eta_{t,s}}{\eta_{t,s}} \tag{25}$$

where, $\eta_{t,r}$, and $\eta_{t,s}$are the thermal efficiency of roughened and smooth SAH, respectively.

The results of this study are compared to those of previously published investigations of different roughness geometries under similar conditions using Eq. 25. Fig. 15 depicts the variation of *TEEC* as a function of Re. According to the behavior of the curves, it can be reported that the validation results are in good agreement.

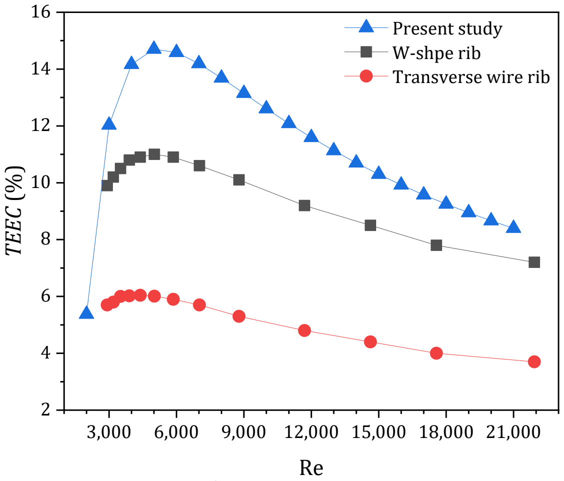

Figure 15. *TEEC* vs Re for comparison between the present study with W-shape rib [31] and transverse wire rib[32].

Performance evaluation criteria (*PEC*) is used to measure the enhancement in heat transfer rate against the penalty in pressure drop across the SAH as follows

$$PEC = \frac{\left(\frac{\mathrm{Nu_r}}{\mathrm{Nu_s}}\right)^3}{\frac{f_r}{f_s}} \tag{26}$$

where $\mathrm{Nu_r}$, $\mathrm{Nu_s}$, and fr, fs are Nusselt number and friction factor for roughened and smooth SAH, respectively.

The *PEC* obtained in this study is compared to previous research that used various rib shapes to enhance the performance of a SAH. Table 3 shows the comparison of the current work to previous ones, and as can be seen, the current method is satisfactory.

Table 3. Comparison to previously published studies

Rib shape	*PEC*
Arc shape [16]	2.78
Multiple V-shape [33]	3.51
Multi V-shape with gaps [34]	3.64
Multi-arc shape [35]	2.24
Multigap V-down ribs with staggered ribs [36]	2.23
S-shape [12]	3.34
Present study	3.51

4. Conclusions

In this study, the operating parameters of SAH with DMAR roughness on the absorbing plate were studied. The SAH's performance is assessed using a top-down iterative technique in MATLAB. The purpose of this study was to identify the optimum roughness parameters for maximum effective efficiency. The main conclusions of our investigation can be stated as follows:

1. The effective efficiency for SAH-DMAR was 9.4% higher than for smooth SAH. Optimum effective efficiency occurred atp/e, e/D, w_g/e, N_g, and α for DMARof 16, 0.045, 1, 3, and 75, respectively.
2. SAH-DMAR and smooth SAH have a maximum thermal efficiency of 81.1 % and 74.7 %, respectively.
3. The maximal heat gain for a SAH-DMAR is 324.2 W, against 298.7 W for a smooth duct.

4. Thermal and effective efficiencies of the SAH-DMAR are found to be 9.5 % and 8.6% higher than those of smooth duct, respectively when implemented in real weather conditions.

References

[1] A. Al aboushi, Solar Thermal Hybrid Heating System, Jordan Journal of Mechanical and Industrial Engineering. 11 (2017) 181–184.

[2] R. Al-Rbaihat, A. Sakhrieh, J. Al-Asfar, A. Alahmer, O. Ayadi, A. Al-Salaymeh, Z. Al-Hamamre, A. Al-Bawwab, M. Hamdan, Performance assessment and theoretical simulation of adsorption refrigeration system driven by flat plate solar collector, Jordan Journal of Mechanical and Industrial Engineering. 11 (2017) 1–11.

[3] K. Nidhul, A.K. Yadav, S. Anish, S. Kumar, Critical review of ribbed solar air heater and performance evaluation of various V-rib configuration, Renew. Sustain. Energy Rev. 142 (2021) 110871. https://doi.org/10.1016/j.rser.2021.110871.

[4] A.A. Farhan, H.A. Sahi, Energy Analysis of Solar Collector With perforated Absorber Plate, J. Eng. 23 (2017) 89–102.

[5] D.J. Hasan, A.A. Farhan, The Effect of Staggered porous fins on the performance of Photovoltaic panel in Baghdad, J. Eng. 26 (2020) 1–13. https://doi.org/10.31026/j.eng.2020.08.01.

[6] M. Al-Damook, Z.A.H. Obaid, M. Al Qubeissi, D. Dixon-Hardy, J. Cottom, P.J. Heggs, CFD modeling and performance evaluation of multipass solar air heaters, Numer. Heat Transf. Part A Appl. 76 (2019) 438–464. https://doi.org/10.1080/10407782.2019.1637228.

[7] S.Y. Taha, A.A. Farhan, Performance augmentation of a solar air heater using herringbone metal foam fins: An experimental work, Int. J. Energy Res. 45 (2021) 2321–2333. https://doi.org/10.1002/er.5927.

[8] S. Das, Simulation of optimal exergy efficiency of solar flat plate collector, Jordan Journal of Mechanical and Industrial Engineering. 10 (2016) 51–65.

[9] N. Minh Phu, N. Thanh Luan, A Review of Energy and Exergy Analyses of a Roughened Solar Air Heater, J. Adv. Res. Fluid Mech. Therm. Sci. 77 (2020) 160–175. https://doi.org/10.37934/arfmts.77.2.160175.

[10] S. Singh, S. Chander, J.S. Saini, Thermo-hydraulic performance due to relative roughness pitch in V-down rib with gap in solar air heater duct—Comparison with similar rib roughness geometries, Renew. Sustain. Energy Rev. 43 (2015) 1159–1166. https://doi.org/10.1016/j.rser.2014.11.087.

[11] H.K. Ghritlahre, An experimental study of solar air heater using arc shaped wire rib roughness based on energy and exergy analysis, Arch. Thermodyn. 42 (2021) 115–139. https://doi.org/10.24425/ather.2021.138112.

[12] K. Kumar, D.R. Prajapati, S. Samir, Heat transfer and friction factor correlations development for solar air heater duct artificially roughened with ‘S’ shape ribs, Exp. Therm. Fluid Sci. 82 (2017) 249–261. https://doi.org/10.1016/j.expthermflusci.2016.11.012.

[13] A.A. Farhan, H.E. Ahmed, M.A. Mussa, Thermal–Hydraulic Performance of a V-Groove Solar Air Collector with Transverse Wedge-Shaped Ribs, Arab. J. Sci. Eng. (2022). https://doi.org/10.1007/s13369-021-06442-5.

[14] S.S. Bhuvad, R. Azad, A. Lanjewar, Thermal performance analysis of apex-up discrete arc ribs solar air heater-an experimental study, Renew. Energy. 185 (2022) 403–415. https://doi.org/10.1016/j.renene.2021.12.037.

[15] N.K. Pandey, V.K. Bajpai, A. Sharma, S. Yadav, CFD and thermo-hydraulic analysis of multiple arc roughened absorber plate with gaps used in solar air heaters, Int. J. Ambient Energy. 0 (2020) 1–7. https://doi.org/10.1080/01430750.2020.1824941.

[16] S.K. Saini, R.P. Saini, Development of correlations for Nusselt number and friction factor for solar air heater with roughened duct having arc-shaped wire as artificial roughness, Sol. Energy. 82 (2008) 1118–1130. https://doi.org/10.1016/j.solener.2008.05.010.

[17] H.K. Ghritlahre, P.K. Sahu, S. Chand, Thermal performance and heat transfer analysis of arc shaped roughened solar air heater – An experimental study, Sol. Energy. 199 (2020) 173–182. https://doi.org/10.1016/j.solener.2020.01.068.

[18] A.P. Singh, Varun, Siddhartha, Heat transfer and friction factor correlations for multiple arc shape roughness elements on the absorber plate used in solar air heaters, Exp. Therm. Fluid Sci. 54 (2014) 117–126. https://doi.org/10.1016/j.expthermflusci.2014.02.004.

[19] N.K. Pandey, V.K. Bajpai, Thermo-hydraulic performance enhancement of solar air heater (SAH) having multiple arcs with gap shaped roughness element on absorber plate, Int. J. Eng. Sci. Technol. 8 (2016) 34–42. https://doi.org/10.4314/ijest.v8i1.3.

[20] Y. Agrawal, J.L. Bhagoria, V.S. Pagey, Enhancement of thermal efficiency of solar air collector by using discrete double arc reverse shaped roughness on the absorber plate, Mater. Today Proc. (2021). https://doi.org/10.1016/j.matpr.2021.10.362.

[21] R. Kumar, V. Goel, S. Bhattacharyya, V. V. Tyagi, A.M. Abusorrah, Experimental investigation for heat and flow characteristics of solar air heater having symmetrical gaps in multiple-arc rib pattern as roughness elements, Exp. Heat Transf. 00 (2021) 1–18. https://doi.org/10.1080/08916152.2021.1905752.

[22] R. Azad, S. Bhuvad, A. Lanjewar, Study of solar air heater with discrete arc ribs geometry: Experimental and numerical approach, Int. J. Therm. Sci. 167 (2021) 107013. https://doi.org/10.1016/j.ijthermalsci.2021.107013.

[23] M.A. Alfellag, H.E. Ahmed, M.G. Jehad, A.A. Farhan, The hydrothermal performance enhancement techniques of corrugated channels: a review, J. Therm. Anal. Calorim. (2022). https://doi.org/10.1007/s10973-022-11247-1.

[24] M.K. Sahu, R.K. Prasad, Thermohydraulic performance analysis of an arc shape wire roughened solar air heater, Renew. Energy. 108 (2017) 598–614. https://doi.org/10.1016/j.renene.2017.02.075.

[25] A. Cortés, R. Piacentini, Improvement of the efficiency of a bare solar collector by means of turbulence promoters, Appl. Energy. 36 (1990) 253–261. https://doi.org/10.1016/0306-2619(90)90001-T.

[26] J.A. Duffie, W.A. Beckman, N. Blair, Solar Engineering of Thermal Processes, Photovoltaics and Wind, fifth edit, JohnWiley& Sons, Inc., Hoboken,New Jersey, 2020.

[27] K.S. Ong, Thermal performance of solar air heaters: Mathematical model and solution procedure, Sol. Energy. 55 (1995) 93–109. https://doi.org/10.1016/0038-092X(95) 000 21 -I.

[28] K.G.T. Hollands, E.C. Shewen, Optimization of flow passage geometry for air-heating, plate-type solar collectors, J. Sol. Energy Eng. Trans. ASME. 103 (1981) 323–330. https://doi.org/10.1115/1.3266260.

[29] M. Hedayatizadeh, Y. Ajabshirchi, F. Sarhaddi, S. Farahat, A. Safavinejad, H. Chaji, Analysis of exergy and parametric study of a v-corrugated solar air heater, Heat Mass Transf. 48 (2012) 1089–1101. https://doi.org/10.1007/s00231-011-0957-7.

[30] R. Kumar, P. Chand, Performance prediction of extended surface absorber solar air collector with twisted tape inserts, Sol. Energy. 169 (2018) 40–48. https://doi.org/10.1016/j.solener.2018.04.021.

[31] A. Lanjewar, J.L. Bhagoria, R.M. Sarviya, Heat transfer and friction in solar air heater duct with W-shaped rib roughness

on absorber plate, Energy. 36 (2011) 4531–4541. https://doi.org/10.1016/j.energy.2011.03.054.

[32] S.K. Verma, B.N. Prasad, Investigation for the optimal thermohydraulic performance of artificially roughened solar air heaters, Renew. Energy. 20 (2000) 19–36. https://doi.org/10.1016/S0960-1481(99)00081-6.

[33] V.S. Hans, R.P. Saini, J.S. Saini, Heat transfer and friction factor correlations for a solar air heater duct roughened artificially with multiple v-ribs, Sol. Energy. 84 (2010) 898–911. https://doi.org/10.1016/j.solener.2010.02.004.

[34] A. Kumar, R.P. Saini, J.S. Saini, Development of correlations for Nusselt number and friction factor for solar air heater with roughened duct having multi v-shaped with gap rib as artificial roughness, Renew. Energy. 58 (2013) 151–163. https://doi.org/10.1016/j.renene.2013.03.013.

[35] A.P. Singh, Varun, Siddhartha, Effect of artificial roughness on heat transfer and friction characteristics having multiple arc shaped roughness element on the absorber plate, Sol. Energy. 105 (2014) 479–493. https://doi.org/10.1016/j.solener.2014.04.007.

[36] N.S. Deo, S. Chander, J.S. Saini, Performance analysis of solar air heater duct roughened with multigap V-down ribs combined with staggered ribs, Renew. Energy. 91 (2016) 484–500. https://doi.org/10.1016/j.renene.2016.01.067.

JJMIE
Volume 16, Number 4, September. 2022
ISSN 1995-6665
Pages 557 – 565

Jordan Journal of Mechanical and Industrial Engineering

Experimental Study of Thermal Conductivity Effect on the Performance of Thermal Energy Storage

Hassan Hadi Sadiq, Munther Abdullah Mussa*

Department of Mechanical Engineering, University of Baghdad, 10071 Baghdad, Iraq

Received 7 Apr 2022 *Accepted 6 Jul 2022*

Abstract

Renewable energy is an attractive energy source which helped to improve the global energy problems. Solar energy products are vital and have been supported by thermal energy storage. In this study, a latent heat thermal energy storage system (LHTESS) of horizontal shell-and-tube has been constructed. Two cases of paraffin wax with different thermal conductivities (TC) have been used as a phase change material (PCM), case1 and case2 of thermal conductivity of 0.265 W/m.K and 0.311 W/m.K respectively. Water has been used as a heat transfer fluid (HTF). In the current experiment, efforts have been made to investigate the influence of thermal conductivity on the thermal performance of thermal energy during the solidification process for both cases, case1 and case2. The investigation shows that case1 has got fully solid during 143 mins, while case2 has got full solidification during 116 mins. Also, the efficiency of the case2 is higher than case1. As a result, case2 is more efficient than case1.

Keywords: thermal performance, thermal conductivity effect, solidification, shell and tube.

Abbreviation

LHTESS	Latent heat thermal energy storage system
TES	Thermal energy storage
PCM	Phase change of material
TC	Thermal conductivity

Nomenclature

C_p	Specific heat (J/kg·K)
k	Thermal conductivity (W/m·K)
L	Latent heat (J/kg)
q	Instantaneous energy
Q	Accumulative energy
$\dot{m}$	Mass flow rate (kg/s)
T_{in}	Inlet temperature (K)
T_{out}	Outlet temperature (K)
Δt	Time (s)
$M_{H.E}$	Mass of heat exchanger (kg)
T_{end}	Temperature of the end process (K)
T_{ini}	Initial temperature of the process (K)
$Q_{H.E}$	Energy of heat exchanger
Q_{pcm}	Energy of phase change material
M_{pcm}	Mass of the PCM
$T_{solidus}$	Solidus temperature (K)
$T_{liquidus}$	Liquidus temperature (K)
Q_{max}	Maximum energy
D_{in}	Inner diameter of the shell
d_{in}	Inner diameter of the tube

Greek letter

ρ	Density (kg/m^3)
μ	Dynamic viscosity (kg/m·s)
η	Efficiency

Dimensionless

Re	Reynolds number

Subscript

in	Inlet
out	Outlet
ch&dis	Charge and discharge
H.E	Heat exchanger
end	End
ini	Initial
pcm	Phase change material
max	Maximum
in	Inner

1. Introduction

Over the last decade, demands for energy have increased, and that caused an energy crisis. Also, gas emissions (green-house effect), and fossil fuel depletion made the scientists look for other resources of energy. Renewable energy, such as solar, wind, and geothermal resources are promising. Solar energy is convenient for countries that have sunny weather as Iraq. The intermittency in solar energy products made researchers turn to search for solutions, as thermal energy storage systems showed the possibility to cover the discrepancy between energy demand and product. Thermal energy is divided into three types, sensible, latent, and chemical[1]. In this study, latent heat has been chosen. LHTESS is based on the phase transition of material solid-liquid,

---

* Corresponding author e-mail: munther@coeng.uobaghdad.edu.iq.

solid-solid, or liquid-gas. This method utilizes phase change of materials like paraffin wax and fatty acid. The main drawback of these materials is low thermal conductivity[2]. Hence, scientists investigate many methods to enhance thermal conductivity by adding material, such as nano-particles or increasing heat transfer surface area by adding fins. Agyenim et al. [3] studied the impact of integrating circular and longitudinal fins to shell and tubestorage unit on heat transfer rate. Erythritol has been selected as PCM which has a melting point of 117.7 ˚C and water as HTF. They demonstrated that the thermal energy storage(TES) with longitudinal fins performed the best result. Also, it improved the thermal response during charging and less in subcooling at melt during discharging. Ghozatloo et al. [4] established higher heat transmission via convection performance through a heat exchanger unit by utilizing graphene nanofluids. They concluded that mixing 0.075% of graphene withpure fluid will improve TC to 31.83%, in addition, the coefficient of convective heat transfer of graphene nanofluids at 38°C improved by 35.6% at a concentration of 0.1%. Rathod & Banerjee [5] analyzed the average heat transfer done through the melting and solidification process in shell and tube heat exchanger. Longitudinal fins have been welded on the tube. The analysis has been done at different values of inlet temperatures and flow rates. They concluded that the time needed for the melting process decreased by about 12.5% and 24.52% for a fluid inlet temperature of 80˚C and 85˚C respectively. Furthermore, the time taken for solidification reduces up to 43.6%. Al-Abidi et al. [6] inspected heat transfer improvement by using a triplex tube heat exchanger as TES. At each tube, four longitudinal fins have been welded to improve thermal performance. In addition, the impact of natural convection on the charging process has been inspected. They concluded that there is an enhancement in the temperature of charging reduced by 86 % with fins, and the efficiency for TES was 71.8%. Gasia et al. [7] inspected the impact of installing fins and the use of two different HTFs water and a commercial silicone; Paraffin wax RT58 as PCM, in addition to shell and tube LHTES unit, have been used. Their result showed that the fins design enhanced heat transfer by about 40% for commercial silicone, and 44% for water HTF. Yazici et al. [8] investigated the performance of melting heat transfer and energy storage efficiency of PCM (paraffin)/graphite matrix in a shell and tube for LHTES. Also, the influence of the inlet temperature of HTF on melting time was analyzed. They concluded that the effective TC increases 35 times heat transfer rate higher than pure paraffin. The overall melting time decreases by about 92%. Furthermore, total melting time was decreased by about 31% with the rise in HTF inlet temperature for the PCM/graphite matrix.Venkitaraj et al [9]studied the impact of injecting alumina (Al_2O_3) nanoparticles into pentaerythritol at 0.5 and 1.0 wt.% fractions. Their experiments were performed during the charging and discharging process in a shell and tube storage unit. Therminol-55 had been used as HTF with different flow rates of 2, 4, and 6 l/min. Their results showed that the charging / discharging efficiency reached maximum levels of 86.8% and 75.0 %, respectively, at 6 l/mins, according to their data. The overall energy efficiency of the thermal energy storage system improved from 38.3 % for pentaerythritol to 50.5 % and 58.5 % for pentaerythritol mixed with 0.5 wt. % and 1.0 wt. % of Al2O3 nanoparticles, respectively. Hassan et al [10] studied thermal performance during the charging process for latent heat unit using different fins geometry. Their experimental analysis had been performed out on a shell and three geometries of tubes, non-finned, longitudinal finned and circular finned tubes. All tubes have an inner diameter of 20 mm and thickness of 1.3 mm and length of 560 mm and were manufactured from steel. The shell with an internal diameter of 70 mm, 50 mm and a length of 50 mm thickness was made from Plexiglass. Commercial grade paraffin wax and water had been used as a PCM and HTF respectively. Their results showed that the overall charging time reduces to 69% and 55% using circular finned and longitudinal finned respectively. In addition, they determined that the most cumulative stored enery enhancement was achieved by employing circular finned of about 52% as compared with longitudinal finned. Yadav & Sahoo [11]investigated the impact of energy and exergy analysis on the lauric acid and paraffin wax PCMs-based on 0.1% vol. fraction of Al_2O_3 and CuO nano-additives TES system. The TES system is installed into the exhaust gas side of the four-stroke diesel engine. They showed that 0.1% vol. fraction of Al_2O_3 in lauric acid nano-enhanced 16.13%, 8.06%, 38.71%, 25.81%, and 32.26% less charging period than pure lauric acid, CuO–lauric acid, paraffin wax, Al_2O_3- paraffin wax, and CuO–paraffin wax, respectively. Jidhesh et al.[12] examined the enhancement of the charging and discharging rate of PCM. Paraffin had been used as the PCM. The steatite powder had been used as the additive material added with different weight fractions to enhance the thermal property of the PCM. The performance of the Paraffin/steatite composite had been investigated using a horizontal latent heat energy storage system. Their result showed that the solidification rate of the PCM was higher than the melting rate with an additive of steatite powder which increased in the paraffin accordingly. They concluded that the effect of increasing rate is mainly due to the property of the steatite material as it has a large latent heat retention rate. They observed that the solidification rate was improved by about 25%, 37% and 40% than the melting time by adding steatite powder to the paraffin with weight fractions of 10%, 20%, and 30% respectively. Mayil Velnathan & Valan [13] conducted an investigation on the thermal performance of a shell and helical tube LHTESS. Commercial grade erythritol having a melting temperature of 120 °C was employed as the PCM. The effect of the addition of graphene nanoparticles on the performance of the storage system such as heat flow rate, overall heat transfer coefficient, charging and discharging efficiency and effectiveness were evaluated and compared with the storage system with only base erythritol during both energy storage and retrieval processes. The efficiency of the new composite increased to 16.29% during the storage period and 28.48 % during the retrieval period compared to the base PCM system. Furthermore, they observed that the effectiveness was about 14% greater at the beginning of the melting process and about 12% greater at beginning of the solidification process for graphene-erythritol. Al-Maghalseh [14] studied the effect of natural convection of melting of PCM filled around horizontal pipe within a rectangular thermal storage unit. Four different configurations on the test model were carried out. Paraffin wax with meltin temperature 60°C and water have been used as a PCM and HTF respectivily. They demonstrated that as compared to case 1, the overall melting time was roughly decreased by 16.57 % with case 2, 31.83 % with case 3, and 41.3 % with case 4. Furthermore, while the conduction heat transfer was kept constant in all cases by applying the same operation and boundary conditions to the pipe and HTF, the rate of heat transfer enhancement is noticeably more obvious in natural convection in molten PCM.AL-Migdady et al. [15]investigated the cooling performance heat sinks filled with PCM. Two types of PCMs (RT35HC and RT44HC) have been used and metal foam integrated with different porosity (100%, 97% and 90%) as enhancement material. In addition, three different values of convective heat transfer coefficient between the heat sink boundaries and the surroundings. Their result showd that the better cooling was obtained in the heat sink filled with RT35HC compared to RT44HC. Moreover, using metal foam has better enhancement in decreasing the temperature in the case of porosity (97%, 90%) by 6°C and 5°C of RT35HC compared to the no-metal foam case. Whereas in case of RT44HC, the decrease in the temperature was (5 and 4)°C for the porosity(97% and 90%) compared to the no-metal foam case.Also, they found that the increase in the convective heat transfer coefficient reduced the melting rate of the PCM. In current study, the impact of TC of the PCM on TES will be investigated experimentally in shell and tube LHTES. Furthermore, thermal performance will be calculated through the discharge process.

2. Experimental work

In the current survey, Paraffin wax has been used as the PCM, and water as HTF. The choice of PCM
for shell and tube LHTES is based on thermal conductivity . Two types of wax have been used, Iraqi commercial paraffin with (k = 0.265 W/m.K), and commercial paraffin with (k = 0.311 W/m.K) and represented as case1 and case2 as shown in Figure 1 and Figure 2. The thermophysical properties of PCM have been depicted in Table 1.

2.1. Differential scanning calorimeter (DSC)analysis

Latent heat and specific heat of paraffin have been measured by DSC-60 Shimadzuand used as a PCM,Figure 3 represented the DSC measurement. A sample of size 5mg of paraffin in an aluminium pan has been used. The analysis has been conducted in the temperature range of 35-100˚Cat a rate of 12 ˚C/min with a nitrogen flow rate of 50 ml/min. The parameters have been determined by numerical integration of the area under the peak as illustrated in Figure 4.


Figure 1. Iraqi Paraffin


Figure 2. Commercial Paraffin

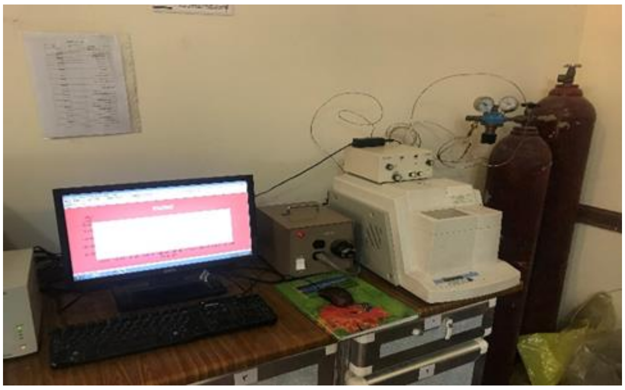
Figure 3. DSC instrument

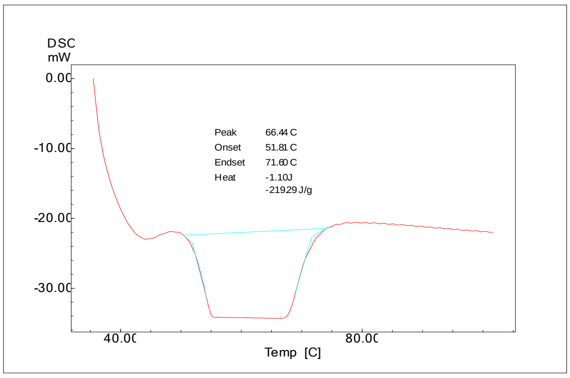

Figure 4. DSC analysis curve

Table 1. thermo-physical properties of PCM

Material	**Properties**						
	ρ_{solid}(kg/m^3)	ρ_{liquid}(kg/m^3)	C_p (J/kg·K)	k (W/m·K)	L (J/kg)	Melting temp. (K)	μ (kg/m·s)
Iraqi paraffin	852.14	766.11	2900	0.265	270715	334	0.0188
Commercial paraffin	813.795	733.33	2104	0.311	219290	331	0.0236
Water	-	998.2	4182	0.6	-	-	0.001003

2.2. Thermal conductivity measurement

In this study, Lee's Disc method has been utilized to measure the TC of organic paraffin. A steady-state is considered where the calculation can be made when the experimental test reaches equilibrium. Lee's method includes three-disc of brass; one of them prescribed as a heater with power input (1.5 Watt) as illustrated in Figure 5andFigure 6.The sample insert between disc2, and 3. T_1, $T_2$and T_3 are recorded after reaching the steady-state condition.

3. Mathematical Background

The instantaneous energy (q) and accumulative energy (Q) which are obtained or realized by water as HTF throughout the charging and discharging process described by as [16] :

$$q_{ch} = \dot{m}c_p(T_{in} - T_{out}) \quad (1)$$

$$q_{dis} = \dot{m}c_p(T_{out} - T_{in}) \quad (2)$$

$$Q_{ch\&dis} = \sum q_{ch\&dis}\,\Delta t \quad (3)$$

Where(c_p), ($\dot{m}$), and (T_{in}& T_{out}) are the specific heat, mass flow rate, and inlet/outlet temperature of the HTF respectively.

In the transient process, the accumulative energy that is realized or acquired by water ($Q_{ch\ \&\ dis}$) and the PCM ($Q_{pcm,\ ch\ \&\ dis}$) are opposedto the steady-state process. This part of heat exchange can be expressed as below:

$$Q_{H.E,ch} = M_{H.E}C_{p,H.E}(T_{end} - T_{ini}) \quad (4)$$

$$Q_{H.E,dis} = M_{H.E}C_{p,H.E}(T_{ini} - T_{end}) \quad (5)$$

Where ($M_{H.E}$), and ($C_{p,H.E}$) are the mass and specific heat of the exchanger respectively, and (T_{ini}& T_{end}) are the start/end temperature of the PCM through the charge/ discharge process.

Furthermore, the accumulative energy exchangeable with PCM ($Q_{pcm,\ ch\&dis}$) can be written as follows:

$$Q_{pcm,ch\&dis} = Q_{ch\&dis} - Q_{H.E,ch\&dis} \quad (6)$$

The thermal performance of LHTES can be described as follow:

$$\eta_{theory} = \frac{Q_{pcm,ch\&dis}}{Q_{max,ch\&dis}} \quad (7)$$

The maximum quantity of energy (Q_{max}) through the charging and discharging process which obtained from PCM can be written as:

$$Q_{max,ch} = M_{pcm}\left[C_{p,pcm}(T_{ini} - T_{solidus}) + L + C_{p,pcm}\left(T_{end} - T_{liquidus}\right)\right] \quad (8)$$

$$Q_{max,disch} = M_{pcm}\left[C_{p,pcm}\left(T_{ini} - T_{liquidus}\right) + L + C_{p,pcm}(T_{end} - T_{solidus})\right] \quad (9)$$

where (M_{PCM}), ($C_{p,PCM}$), (L), and ($T_{solidus}$& $T_{liquidus}$) are the mass, specific heat, latent heat, andsolidus/liquidustemperature respectively.

4. Experimental apparatus and procedure

In the present research shell and tube, horizontal concentric LHTES unit have been constructed to investigate the effect of TC of PCM on the TES system. Figure 7 and Figure 8 illustrate the schematic diagram, and test rig of the experiment respectively.The test rig consists of the measurement system, flow system and test section. The shell length is (800mm) and is made from aluminium with an inner diameter D_{in} of (80mm) and a thickness of (10mm). A tube of(26mm) inner diameter and made from copper located at the center of the shell where HTF through the tube and exchange heat with PCM, Figure 10.The paraffin wax is located in between the shell and tube. The outer surface of the shell has been insulated with two layers of asbestos tape of (5mm) thickness and thermal conductivity of (0.16 W/m.K).The charging system consisted of an electrical heater of power (1500W) installed on the shell's exterior surface. Acquisition system of data comprised of twentythermocouples K-type with accuracy (±2.5)utilized to record thePCM temperatureand distributed in two sections each section of 10 thermocouples located in a radial place as illustrated in Figure 9.Furthermore,two thermocouples are located at the inlet and outlet tube of HTF to record water temperature.Also, two data loggerswere employed to record the temperatures during the dischargecondition. Two cases of organic material paraffin with different thermal conductivities have been used as a PCM, case1 and case2 of thermal conductivity of 0.265 W/m.K and 0.311 W/m.K respectively. For the cas1,the heat exchanger was filled with 3kg of Iraqi paraffin, then for the case2,filled with 2.8kg of commercial paraffin. The PCM was melted inside the heat storage system by the electrical heater until reacheda temperature of(340K), and then HTF was pumped through the tube at a flow rate of (2l/min) and a constant temperature of (296K). The flow assumed laminar according to Reynolds number [17] (Re < 2300).

$$Re = \frac{4\dot{m}}{\pi d_{in}\mu}$$

Where $\dot{m}$is the mass flow rate, μ is the viscosity of water, and d_{in} is the inner diameter of the tube.

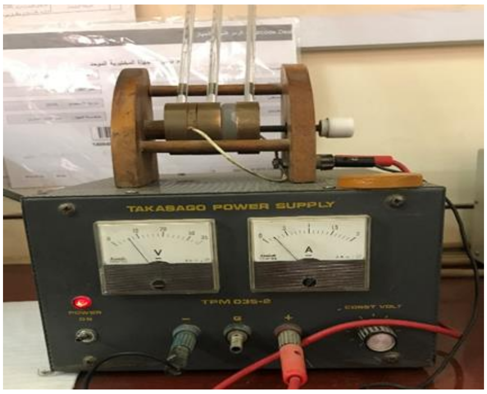

Figure 5. Disc Lee's instrument

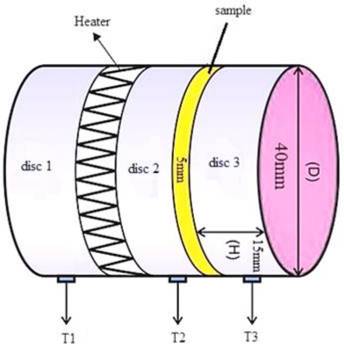

Figure 6. Schematic diagram of Disc Lee's

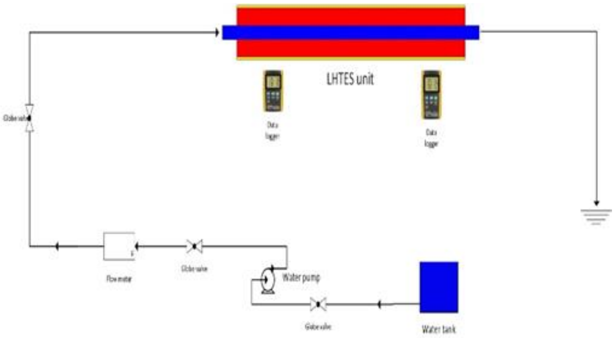

Figure 7. Schematic diagram of LHTES

Figure 8. Test Rig

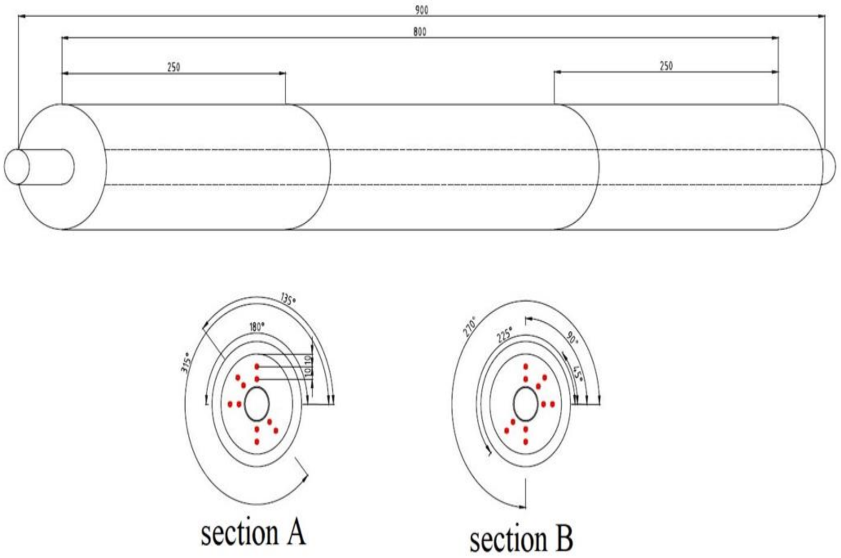

Figure 9. Thermocouple distribution

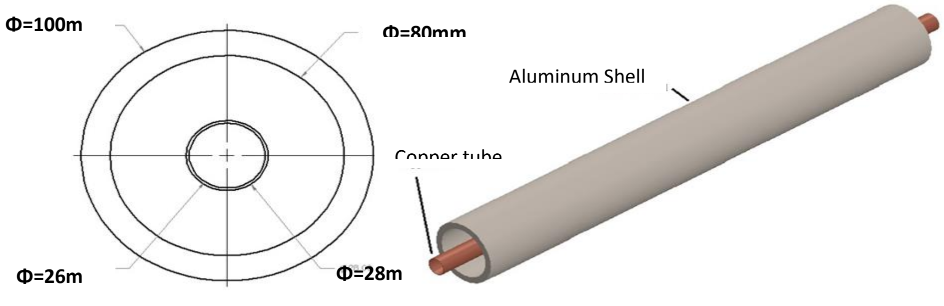

Figure 10. Shell and tube

5. Result and discussion

In the present research, the influence of TC of PCM on the performance of the energy storage experimentally has been studied. The experiment is conducted with two kinds of PCMs which are different in thermal conductivity, case 1=0.265 W/m.K and case 2=0.311 W/m.K. The mass flow and the temperature of the HTF at the inlet are considered constant with a value of 2 l/min and 296 K respectively. The variation of HTF temperature at the outlet of the storage unit during the discharge process at a constant inlet temperature and the constant flow rate has been illustrated in Figure 11. It can be shown that the drop in temperature for case2 is higher than that of the case1until 116 min. The temperature of case1 will be continue dropping until 145 min. More investigation has been performed on the heat gain as illustrated in Figure 12. It can be shown that the heat obtained by the HTF is faster and higher for case2 than case1. Furthermore, the maximum heat gain by HTF for case2 is after 60min whereas for case1 the maximum heat gain is after 90 min. The decrease in heat transfer is faster for PCM of high thermal conductivity. The mean temperature of the axial direction of sections A and B have been illustrated in Figure 13 and Figure 14, respectively. The temperature profiles for the same case of the PCM in the axial direction are remarkably similar. The difference in temperature was in between the two types of the PCMs when a comparison was made between the result of each. The calculations have been constructed from the average temperature reading of thermocouples. It is recognized that in the PCM for case2, the temperature decrease is faster than case1. For case1, the latest temperature of section A is 307.29K after 145min whereas it is 307.99K for case2 after 116min. In addition, for section B it is 308K for case1 after 145min and 308.9 for case2 after 116min. Figure 15 shows the evolution of the average temperature of the LHTES unit for the PCMs with different thermal conductivity. It could be noted that the duration of the decrease of the temperature will be decreased with increasing thermal conductivity. It is can be concluded that the rise in TC for PCM is shorter than the time needed to reach the final temperature of the solidification process. The increase in TC of the PCMs which is done by any method like using nanoparticles and material additives will affect on thermal properties of the material and one of them is latent heat. The discharge time of the PCM is influenced by the sensible and latent heat during solidification. Figure 16 illustrates the effect of the increase in TC of PCM on the latent heat. This enhancement in TC has a negative impact on the latent heat which causes reduction in it [18]. Hence, optimization should be considered to choosing the PCM in the application, a high TC mean reduces the dicharge time but reduction in the latent heat. The efficiency of LHTES for case1 is 66% after 145min whilst the efficiency for case2 is 76% after 116min. Its clear that in this study, case2 is highly efficient than case1. Figure 17 shows a statistical comparison of the variant in temperature at a specific time for both cases 1 and 2.

6. Conclusion

In the current study, the experiment focused on the measurements during the solidification process. Also, the influence of the PCM's thermal conductivity on the performance of the TES was investigated in this work. LHTES of horizontal concentric double pipe shell and tube heat exchanger has been designed and manufactured. Investigation of two types of PCM has been used with different thermal conductivities. It is concluded that the PCM's efficiency of high thermal conductivity has increased by 13.15% compared to the PCM of low thermal conductivity. Moreover, the solidification process is reaching the final temperature faster for PCM of higher thermal conductivity. In addition, the effect of TC of PCM on latent heat was analyzed. The main conclusion is that the PCM with higher thermal conductivity will have an efficient heat transfer and high efficiency which in turn preferred in many applications such as space heating. To verify the result of the present study a comparison was made with previous research. The temperature distribution profiles in Figure 15 agreed with the result of refence [19]who they studied the charastrastic of paraffin wax during the melting/soldification process as can be seen in the Figure 18.

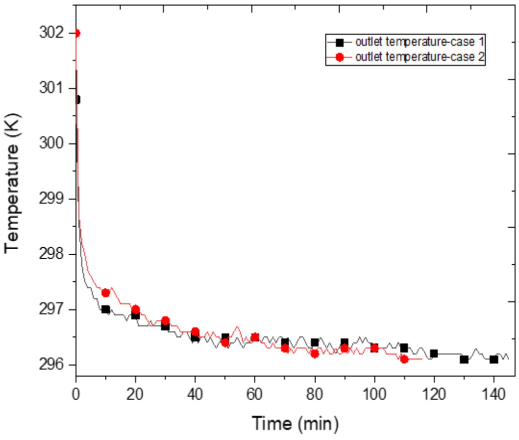

Figure 11. Outlet temperature of HTF

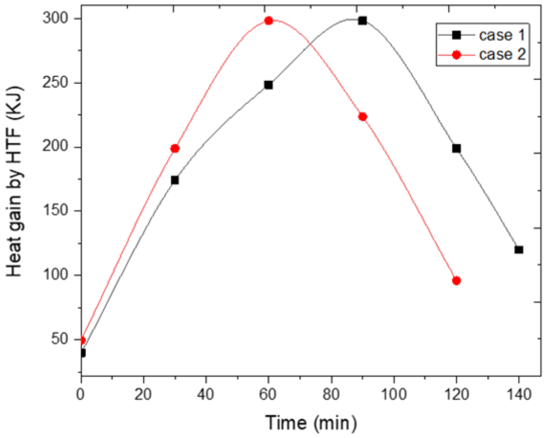

Figure 12. Heat gain by HTF

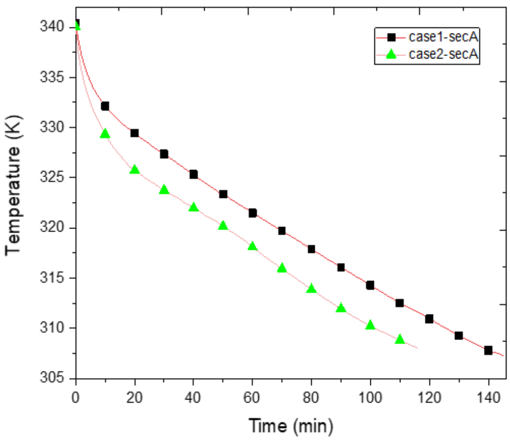

Figure 13. temperture variation of section A

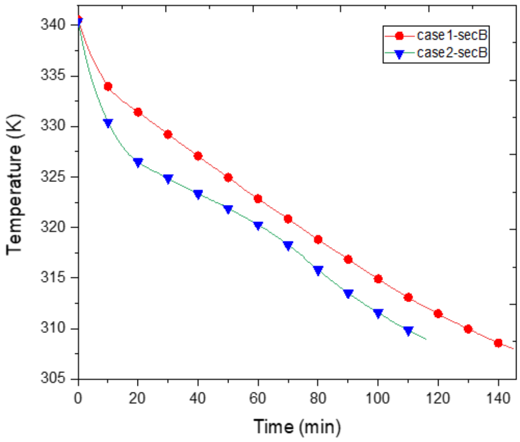

Figure 14. temperture variation of section B

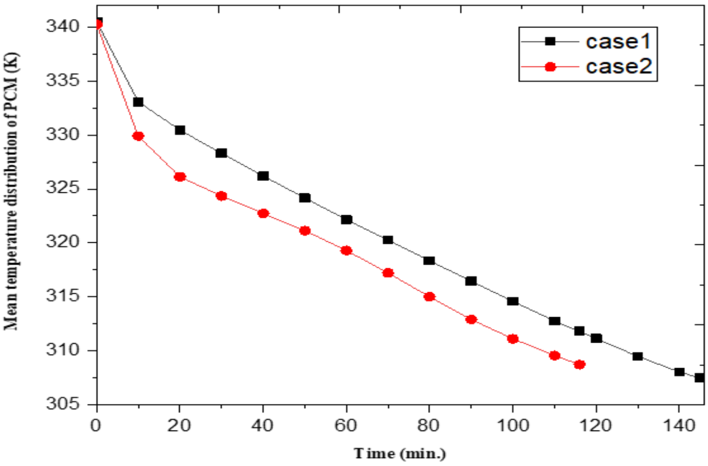

Figure 15. Average temperture variation in PCM

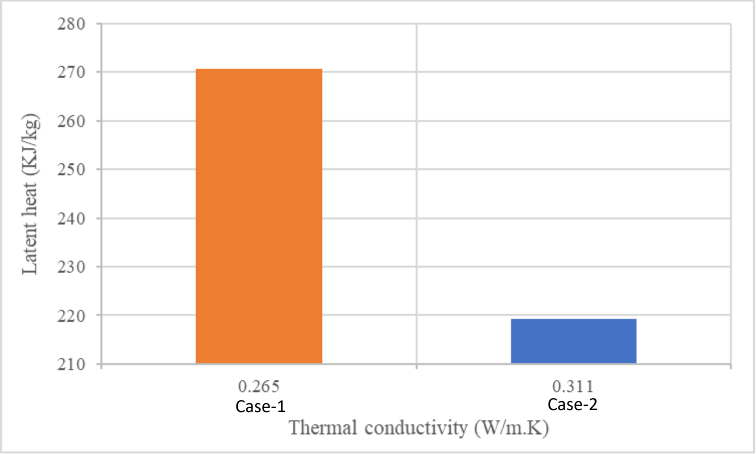

Figure 16. comparison Latent heat with Thermal conductivity

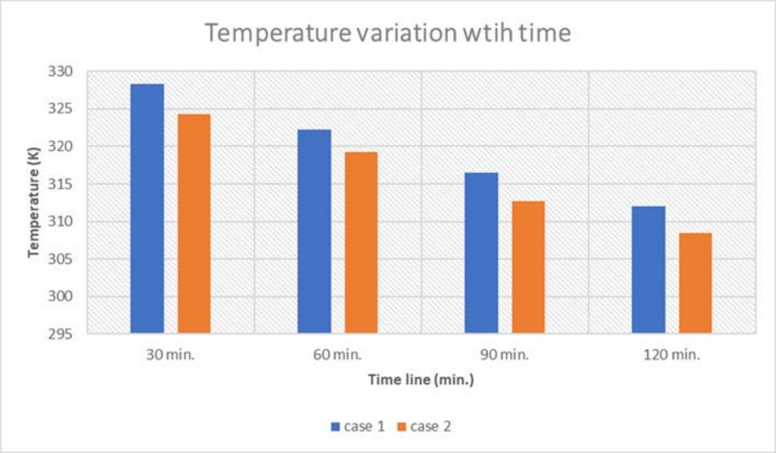

Figure 17. comparison of the variant in temperature at specific time

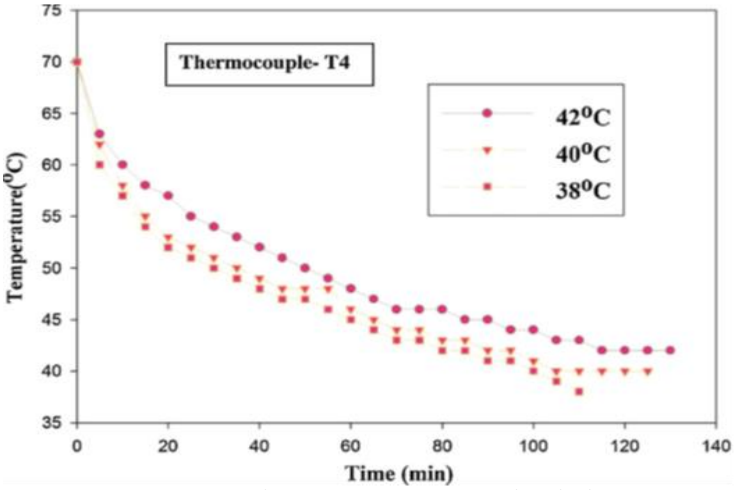

Figure 18. The result of temperature distribution profile of refrence [19]

Acknowledgement

The authors are grateful to the Department of Mechanical Engineering, College of Engineering, University of Baghdad, Iraq, for the assistance provided to achieve this research.

References

[1] A. Sharma, V. V. Tyagi, C. R. Chen, and D. Buddhi, “Review on thermal energy storage with phase change materials and applications,” *Renew. Sustain. Energy Rev.*, vol. 13, no. 2, pp. 318–345, 2009, doi: 10.1016/j.rser.2007.10.005.

[2] M. Kenisarin, K. Mahkamov, F. Kahwash, and I. Makhkamova, “Enhancing thermal conductivity of paraffin wax 53–57 °C using expanded graphite,” *Sol. Energy Mater. Sol. Cells*, vol. 200, p. 110026, 2019, doi: https://doi.org/10.1016/j.solmat.2019.110026.

[3] F. Agyenim, P. Eames, and M. Smyth, “A comparison of heat transfer enhancement in a medium temperature thermal energy storage heat exchanger using fins,” *Solar Energy*, vol. 83, no. 9. pp. 1509–1520, 2009. doi: 10.1016/j.solener.2009.04.007.

[4] A. Ghozatloo, A. Rashidi, and M. Shariaty-Niassar, “Convective heat transfer enhancement of graphene nanofluids in shell and tube heat exchanger,” *Exp. Therm. Fluid Sci.*, vol. 53, pp. 136–141, 2014, doi: https://doi.org/10.1016/j.expthermflusci.2013.11.018.

[5] M. K. Rathod and J. Banerjee, “Thermal performance enhancement of shell and tube Latent Heat Storage Unit using longitudinal fins,” *Appl. Therm. Eng.*, vol. 75, pp. 1084–1092, 2015, doi: https://doi.org/10.1016/j.applthermaleng.2014.10.074.

[6] A. Al-Abidi, S. Mat, K. Sopian, Y. Sulaiman, and A. Mohammad, “Heat Transfer Enhancement for PCM Thermal Energy Storage in Triplex Tube Heat Exchanger,” *Heat Transfer Engineering*, vol. 37, no. 7–8. pp. 705–712, 2016. doi: 10.1080/01457632.2015.1067090.

[7] J. Gasia, J. Diriken, M. Bourke, J. Van Bael, and L. F. Cabeza, “Comparative study of the thermal performance of four different shell-and-tube heat exchangers used as latent heat thermal energy storage systems,” *Renew. Energy*, vol. 114, pp. 934–944, 2017, doi: https://doi.org/10.1016/j.renene.2017.07.114.

[8] M. Y. Yazici, M. Saglam, O. Aydin, and M. Avci, “Thermal energy storage performance of PCM/graphite matrix composite in a tube-in-shell geometry,” *Therm. Sci. Eng. Prog.*, vol. 23, no. March, p. 100915, 2021, doi: 10.1016/j.tsep.2021.100915.

[9] K. P. Venkitaraj, S. Suresh, and B. Praveen, “Experimental charging and discharging performance of alumina enhanced pentaerythritol using a shell and tube TES system,” *Sustain. Cities Soc.*, vol. 51, no. July, p. 101767, 2019, doi: 10.1016/j.scs.2019.101767.

[10] A. K. Hassan, J. Abdulateef, M. S. Mahdi, and A. F. Hasan, “Experimental evaluation of thermal performance of two

different finned latent heat storage systems," *Case Stud. Therm. Eng.*, vol. 21, p. 100675, 2020, doi: 10.1016/j.csite.2020.100675.

[11] C. Yadav and R. R. Sahoo, "Thermal analysis comparison of nano-additive PCM-based engine waste heat recovery thermal storage systems: an experimental study," *J. Therm. Anal. Calorim.*, vol. 147, no. 3, pp. 2785–2802, 2022, doi: 10.1007/s10973-021-10611-x.

[12] P. Jidhesh, T. V Arjunan, and J. David Rathnaraj, "Experimental investigation on heat transfer characteristics of phase change composite for thermal energy storage system," *Mater. Today Proc.*, vol. 42, pp. 618–625, 2021, doi: https://doi.org/10.1016/j.matpr.2020.10.949.

[13] M. V and V. A. A, " Performance investigation of shell and helical tube heat energy storage system with graphene dispersed erythritol PCM ," *Energy Storage*, vol. 2, no. 6, 2020, doi: 10.1002/est2.198.

[14] M. M. Al-Maghalseh, "Investigate the natural convection heat transfer in a PCM thermal storage system using ANSYS/FLUENT," *Jordan Journal of Mechanical and Industrial Engineering*, vol. 11, no. Specialissue, pp. 217–223, 2017.

[15] A. K. AL-Migdady, A. M. Jawarneh, A. K. Ababneh, and H. N. Dalgamoni, "Numerical Investigation of the Cooling Performance of PCM-based Heat Sinks Integrated with Metal Foam Insertion," *Jordan Journal of Mechanical and Industrial Engineering*, vol. 15, no. 2, pp. 191–197, 2021.

[16] M. J. Hosseini, M. Rahimi, and R. Bahrampoury, "Experimental and computational evolution of a shell and tube heat exchanger as a PCM thermal storage system," *International Communications in Heat and Mass Transfer,* vol. 50. pp. 128–136, 2014. doi: 10.1016/j.icheatmasstransfer.2013.11.008.

[17] S. Seddegh, X. Wang, and A. D. Henderson, "A comparative study of thermal behaviour of a horizontal and vertical shell-and-tube energy storage using phase change materials," *Appl. Therm. Eng.*, vol. 93, pp. 348–358, 2016, doi: 10.1016/j.applthermaleng.2015.09.107.

[18] M. Khatibi, R. Nemati-Farouji, A. Taheri, A. Kazemian, T. Ma, and H. Niazmand, "Optimization and performance investigation of the solidification behavior of nano-enhanced phase change materials in triplex-tube and shell-and-tube energy storage units," *J. Energy Storage*, vol. 33, no. June, p. 102055, 2021, doi: 10.1016/j.est.2020.102055.

[19] S. P. Jesumathy, M. Udayakumar, S. Suresh, and S. Jegadheeswaran, "An experimental study on heat transfer characteristics of paraffin wax in horizontal double pipe heat latent heat storage unit," *J. Taiwan Inst. Chem. Eng.*, vol. 45, no. 4, pp. 1298–1306, 2014, doi: 10.1016/j.jtice.2014.03.007.

JJMIE

Volume 16, Number 4, September. 2022
ISSN 1995-6665
Pages 567 – 579

Jordan Journal of Mechanical and Industrial Engineering

Performance and Socioeconomics of 1st Wheeling PV Project Connected to Medium Grid in Jordan

Jamal O. Jaber[1*], Mohammad O. Awadi[2], Ali S. Dalabeeh[1], Ibrahim M. Mansour[3]

[1]Faculty of Engineering Technology, Al-Balqa' Applied University, Jordan
[2]Engineering Dept., Islamic Hospital, Amman, Jordan
[3]Faculty of Engineering Technology, Zarqa University, Zarqa – Jordan

Received 10 Apr 2022 Accepted 9 Jun 2022

Abstract

The issue of energy security is becoming very important due to higher standards of living and being the engine for economic development. Hence, recently solar PV systems witnessed high popularity worldwide since it has facilitated the utilization of the untapped potential of solar energy. On-grid PV schemes have become the first option for power generation, among other renewable energy sources, due to low cost of generated power as compared with other systems and short construction time. This paper presents the real performance data of the first large size solar PV project, in Jordan, connected to the medium voltage grid on wheeling basis. The PV station was designed to be installed on south-north axis with an east-west solar tracking system to enhance electrical energy production. The technical specification and calculated design parameters, such as different losses and energy yield, using the commercial software, PVsyst, were reported and compared with real data from the field. The annual electricity yield, in 2019, was about 3954 MWh with an overall performance ratio of 95%, exceeding all expectations. Unfortunately, little attention has been paid by governmental institutions and/or distribution companies, to the general performance of such plants and variation in rates of production. It is deemed that this paper will answer some of critique questions and fill the gap of information related to the performance of PV power stations, connected to the medium voltage network, under local conditions. More work should be aimed to check influencing factors on the performance of other large PV and wind plants in the country.

Keywords: PV modules, power generation, solar energy, performance, Jordan.

1. Background

Worldwide, all stakeholders including policymakers are keen to increase sustainability and reduce negative environmental impacts resulting from power generation through burning fossil fuels. Such trend could be accomplished by enhancing the utilization of clean, less costly systems such as using renewable energy (RE) sources in various applications. Jordan is considered unlucky, in terms of availability of conventional energy sources and security of supplies. Unfortunately, it suffers from the scarcity of conventional energy sources and being surrounded with all types of political conflicts and armed clashes in neighboring countries. On the other hand, it enjoys high solar radiation and good wind speeds in the western highlands that could be harnessed to generate electrical power, on commercial basis, Abu-Rummanet *al.* (2020). Equally important, being close to oil producing countries, mainly the Kingdom of Saudi Arabia and Iraq, Jordan was totally dependent on oil imports from these countries. Thus, the country was vulnerable to all types of shocks including regional political and armed conflicts, Jaber *et al.*(2015).

During the last decade with the aim of increasing energy security and local contribution of available energy sources, there was a clear shift towards renewable sources. The real of activities of harnessing renewable energy sources were started directly after the approval of the Renewable Energy and Energy Efficiency Law (REEE Law No. 13 for year 2012) in the 2nd half of 2012, Ministry of Energy and Mineral Resources (2012). This new law and its acts and directions aimed to (i) increasing the contribution of RE to the total energy mix in Jordan; (ii) promoting and exploiting RE for environmental protection and sustainable development purposes; and (iii) enhancing energy efficiency in all sectors of the economy. According to Article 10 of this law, rules and regulations to guide implementation of the REEL were issued by the Ministry of Energy and Mineral Resources and the Energy and Minerals Regulatory Commission. Such new legislation framework opened the doors for investors and developers to utilize RE sources and connect to the national and/or distribution grids. Consequently, long list of RE projects, in different regions of the country, are running now on commercial basis, and there are several large wind farm and PV projects are in the pipeline and expected to be

---

[*] Corresponding author e-mail: jojaber@gmail.com.

completed and connected to the grid before 2024, National Electric Power Company (2020). Almost all these projects, upon completion, will be connected to the 132 kV national grid. However, the study in hand is dealing with a mega PV project but connected to the medium voltage (33 kV) distribution grid.

Historically, Jordan is a net energy importing country with nearly 97% of its energy needs supplied from abroad such as crude oil, refined products, and recently natural gas. Such energy scenario will continue in the future but with a small contribution, of around 10%, from renewable sources. In 2019, the total energy demand was around 9.05 million ton of oil equivalent (toe), compared with about 9.71 million toe in the previous year 2018 and 9.00 & 7.35 million toe in 2015 and 2010, respectively, Ministry of Energy, Annual Report (2020). The primary energy consumption dropped by about 7% in 2019 due to slow down of economic activities as a result of the general situation in the MENA region. The 2020 was not as any year, due to the COVID-19 virus. All sectors in the economy were under extreme pressure to mitigate the devastative impacts of the pandemic: further drop in energy consumption due to the general lockdown of most activities except health and some basic services. This situation is expected to continue during the next two or three years, until things settle-down and go back to normal life. Such situation is considered as historic opportunity to revive the economy, and cut down GHG emissions, considering part or all mitigation measures listed in the 3rd National Communication, Ministry of Environment (2014). However, without the highly needed technical and financial assistance from developed countries, donors and international organizations, the Government of Jordan (GoJ) alone will not be able to implement the proposed measures and projects.

1.1. Energy Problem in Jordan

The indigenous energy sources covered only a small fraction, i.e. Jordan produced 0.136 million toe of natural gas and less than $0.12x10^{-2}$ million toe of crude oil. Thus, it is heavily dependent on imported fossil fuels (oil products and natural gas) to fulfill its domestic energy needs in industry, domestic heating, transport and power generation. The latter is considered the main driver for local energy demand, in addition to the transport sector, since these are chief fuel consumers. In 2019, transportation and power generation consumed about 35% and 30% of the total fuel consumption in the country, respectively. Main power stations are owned and operated by local generation companies, as IPPs, industrial self-generation for on-site consumption and a state company, i.e. Asamra. Maximum demand in 2019 was 3380 MW, while the contracted generation capacity was 4332 MW, i.e. 128% of the max demand, and the total installed capacity 5727 MW. Of which 2740 MW (48%) combined cycle plants, followed by renewable energy stations (i.e. 1100 MW solar PV plants, 370 MW wind and only 12 MW hydropower) which represents 26% of the installed capacity. The remaining, 26%, consists of steam (605 MW) and gas (83 MW) turbines as well as Diesel engine (814 MW) power plants (National Electric Power Company (2020), Ministry of Energy and Mineral (2020), Jaber *et al*. 2019). Fig. 1 shows the fuel-mix used to generate electrical power during 2008-2019, with natural gas being the prime fuel. The mix of power plants is based on firing natural gas (80%) as primary fuel and diesel oil or heavy fuel oil (HFO) as secondary fuel, followed by renewables (13%). This year, 2021, it is expected that the newly installed oil shale direct combustion power plant (2x235 MW) in the central part of the country will be commissioned and connected to the national grid. Currently, it is under testing and trial or non-commercial operation. Thereby, avoiding an additional fraction of the current oil and gas imports to the country. As can be seen in Fig. 1, the total generated power, in 2019, exceeded 20955 GWh, of which about 3000 GWh (14.3%) from renewable energy sources dominated by Solar PV (2086 GWh) and wind (892 GWh). While the generated electrical energy from hydropower sources was almost negligible: only 18.5 GWh. The major fraction (85.1%) of electricity generated by firing fossil fuels: 3338, 15.1 and 1.8 thousand toe of natural gas, heavy fuel oil and diesel, respectively, Ministry of Water and Irrigation 2020. It is worth mentioning that 99.8% of the population is served and have access to the electrical grid, even the Syrian refugee camps, Ministry of Energy and Mineral Resources (2020). It is true that, during the past decade, there was a growing interest in developing RE projects, especially those focused to meet self-consumption in various sectors. Either as net-metering system or wheeling basis. Consequently, the GoJ recently revised the regulatory framework to allow aggregation by groups of customers. However, still there are several obstacles that should be eliminated to open the door fully for developers and the private enterprises to invest in utilizing RE schemes for different applications. Currently, the most important barriers are distorted existing electricity tariff due to cross-subsidy, the ultimate authority given to electricity distribution companies regarding renewable energy systems without real monitoring or follow up by the Energy and Minerals Commission, and the imposed limitation on the capacity of wheeling project of 1 MW, Jaber *et al*. (2019). More importantly, is that none of the distribution companies nor the transmission company, i.e. National Electric Power Company (NEPCO), has invested in developing and improving the existing electrical grids to be smart and able to absorb the generated green electricity. Unfortunately, the latter sees renewable energy as a threat to its revenues.

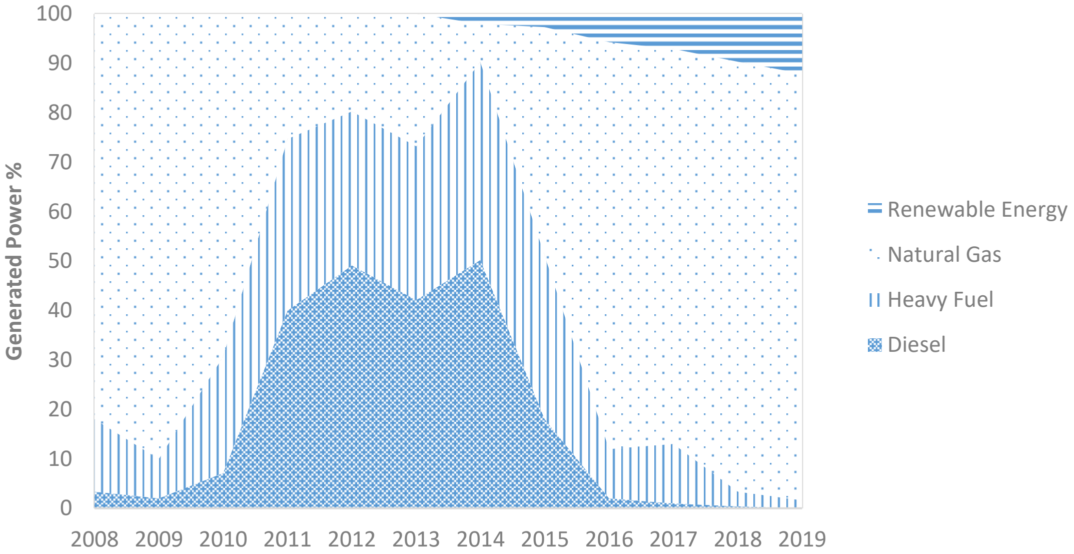

Figure 1. Fuel-mix used in power generation (National Electric Power Company (2020), Ministry of Energy and Mineral (2020), Jaber *et al*. 2019)

2. Introduction

As discussed previously that Jordan used to import all its energy needs as oil, from Iraq and Kingdom of Saudi Arabia (KSA), and natural gas and sometimes electricity, from Egypt, until 2015. Currently, around 14% comes from domestic renewable sources and the country is building more wind and solar power plants. It is planned to produce about 20% of expected electricity consumption in 2025, Ministry of Energy and Mineral Resources (2020-2025). The renewable energy sub-sector in Jordan is deemed to be a driver for job creation on temporary and permanent basis, especially for young technical and non-technical staff. In addition to economic benefits, the environmental advantages are numerous, but mainly the avoidance of burning fossil fuels. Thereby, the direct reduction of GHGs and other emissions. It should be mentioned here that common environmental difficulties and disasters, e.g. desertification and changes in rainfall patterns, have not received enough attention by concerned governmental institutions as well as from different categories of the society. Unfortunately, this is a very serious situation, and it may lead to more of environmental difficulties that would threaten the existence of our lives, such as the depletion of freshwater resources, and the continuous loss of biodiversity, bearing in mind that Jordan is considered the 2nd poorest country in the world in terms of available water resources, Ministry of Water and Irrigation (2020).

Jordan's ability to ensure less polluting, reliable, and low-cost energy sources for its growing economy and population, will require avoiding burning fossil fuels. Furthermore, the country should follow strong policies including technological jumps, in some sectors, such as transport, and more investment in clean energy and energy efficiency. In previously published papers, the role of renewable energy in the 21st century in Jordan was discussed, Jaber *et al*. (2004), and barriers facing utilization of renewable sources, Jaber *et al*. (2015)and energy education in schools of engineering, (Alawin *et al*. (2016), Jaber *et al*. (2017)) as well as knowledge and skill of fresh graduated engineers, Jaber *et al*. (2020). As in other developing countries, the interest was in using solar and wind energy, in particular PV modules, to generate electrical power in various sectors of the economy. Researchers, owners and operators of PV systems have focused their efforts and work on the simulation and direct effect of dust and birds' guano on the performance and the generated revenues Jaber *et al*. (2003) have investigated the integration of PV modules and gas turbine engine to meet max demand. PV system for water desalination Mohsen *et al*. (2001), and PV as sources of energy for residential space heating applications were studied under Jordan conditions, Jaber *et al*. (2008). The integration of PV modules with oil shale industry in central Jordan was investigated by Sladekand Jaber (2016). Repowering old thermal power plants, using steam turbines through employing a concentrated solar system was evaluated, and it was concluded that the payback period is relatively long, Abbas *et al*. (2016). Based on these papers and other reports, it was concluded that the GoJ should concentrate its efforts to help investors and developers working in RE to have access to easy financing long term plans regarding the unit prices of electricity generated via renewable energy sources and the gradual removal of all existing obstacles. Many Jordanian researchers studied the effect of climatic conditions, such as temperature, wind speed, and dust on the performance of PV modules. Since the accumulation of dust coupled with the lack of rain, in the MENA region, especially during the long summer season will reduce the generated electrical power. Saidan *et al*. (2016), have studied the rate of efficiency degradation of the of solar modules and found that the average drop in the productivity due to dust accumulation may reach approximately 6.24%, 11.8% and 18.74% for exposure periods of one day, one week and one month, respectively. Hammad *et al*. (2018), examined the cleaning frequency of PV modules, under local conditions, and reported that the optimal cleaning period is around two weeks during the summer season. Also, Al-Addoss *et al*., Al-Addous *et al*. (2019), studied the optimization of PV cleaning schedules for the best return-on-investment according to the average dust accumulation on models in PV power plants. They stated that average energy loss could hit 10% easily in semi-arid areas if cleaning schedules are not followed, Al-Kouz *et al*. (2019), predicted the conversion efficiency of a roof-top PV system as a function of dust accumulation and arrived at almost similar results: PV cleaning is recommended on bi-weekly basis. Obeidat *et al*. (2020), conducted a field survey and sensitivity analysis for five methods of cleaning PV modules. They concluded that manual cleaning on bi-weekly basis is the preferred option by experts in this field. Thus, cleaning of PV modules and its frequency are key features for a PV system, especially in semi-arid regions with frequent dust storms, as eastern and southern parts of Jordan. Other researchers studied the construction of a large central solar power plant, with thermal storage, in southern Jordan and reported that the cost of unit electricity produced is still higher than that generated by PV modules or conventional power stations, Al-Kouz *et al*. (2020). However, none of the researchers assessed the performance ratio and monthly or annual yield of large PV power plants in the country. Therefore, the paper in hand will try to answer these points and fill part of the gap in information regarding the performance ratio of mega-size PV stations connected to the medium-voltage grid. The prime aim of this field study is limited to assess the technical performance, losses and annual energy yield of the 1st PV power station connected, on wheeling basis, on 33 kV distribution network in the country.

On the international level, the green economy is gaining more momentum, and many governments in different parts of the world support and try hard to fight the global warming which is recognized as a threat to humanity. Thus, renewable projects, especially PV modules, are gaining extra thrust forward. This have activated scientist to pave the way for the development of research in renewable energy with some focus on solar energy (Goura, (2015), International Renewable Energy Agency (2021), International Renewable Energy Agency (2021), International Renewable Energy Agency (2021)). Cervone *et al*. (2015), discussed the impacts of regulatory rules on the economic performance of PV power plants, and developed a software instrument to analyze energy production of a PV power plant from the economic point of view with reference to prevailing regulatory rules. Daha *et al*. (2018), studied the impact of tropical desert maritime climate on the performance of a PV grid-connected power plant, in Djibouti, and reported the seasonal variation and energy loss due to soiling and weather conditions. Honrubia-Escribano *et al.* (2018), reviewed the influence of solar technologies on the economic performance of PV power plants in Europe. Oh *et al*. (2020), evaluated the performance and failure of PV system in 10 years field-aged 1 MW PV power plant and reported that output loss was mainly due inverter(s) failure and annual degradation in PV strings. Jed *et al*. (2020), evaluated the performance of a 954,809 kWp photovoltaic array made up of micro-amorphous silicon situated in Nouakchott (capital of Mauritania) based on measurements of one year of operation from September 2014 to August 2015 according to the IEC 61724 and concluded that the energy generated by the PV array and the energy fed to the utility grid are affected by solar insolation and the module temperature. Boretti and Castelletto (2021) reported the cost and performance of concentrated solar plants (CSP) and PV power stations in USA and concluded that combination of CSP and PV systems could provide a comparable performance at an acceptable cost. Şevik and Aktaş (2022) efficiency-enhancing and improvement activities such as manual and natural cleaning, thermal monitoring, and snow load removal in a 600 kW grid-connected photovoltaic (PV) power plant and found that up to 5.66% power reduction can occur for PV modules that have been dirty for close to one year. It was determined that the dust removal effect of the rain was up to 0.94%.

As in other countries around the world, there was a strong interest, during the last decade in Jordan, to use PV systems since it receives high solar radiation, all around the year of not less than 3000 hr. This is considered a tremendous amount of solar energy: the average daily solar radiation is about 5-7 kWh/m^2 day, Jaber *et al*. (2015). According to the Updated National Energy Strategy, the GoJ through the Ministry of Energy and Mineral Resources, has an ambitious plan to continue the construction of large grid connected power plants in close cooperation with private investors. There are about new 1500 MW of solar and wind are connected to the national and/or distribution grids and almost 1000 MW are in the pipeline and will be connected between 2021 and 2024, (National Electric Power Company (2020), Ministry of Energy and Mineral Resources (2020), Ministry of Energy and Mineral Resources (2020-2025)). These projects could substantially reduce Jordan's energy dependency and create significant fiscal benefits. On the other hand, other renewable sources, such as biomass and hydropower, are limited in Jordan due to the lack of surface water resources and the long dry summer season. The existing capacity, of only 12 MW of hydropower represents the current potential. In addition to few new small hydropower systems that has a good potential in selected sites in the western mountains and opportunity to construct pumped storage schemes powered by RE sources, Jaber (2012). However, at present there is no official interest in such projects. The planned Red-Dead Sea Water Conveyance project, which as very high potential to produce drinking water and generate electricity, was cancelled recently. The World Bank has confirmed that this project will no longer be among the projects intended to be implemented due to the lack of Jordanian governmental agreement on the parameters of the project, World Bank, Press release statement on Jordan's Red-Dead sea project (2021).

Based on the International Standard (IEC 61724), which defines classes of photovoltaic (PV) performance monitoring systems and serves as guidance for various monitoring system choices, the purposes of a performance monitoring system are diverse, IEC TS 61724-2 (2016-2017). These include (i) identification of performance trends in an individual PV system; (ii) localization of potential faults in a PV system; (iii) comparison of PV system performance to design expectations and guarantees; (iv) comparison of PV systems of different configurations; and (v) comparison of PV systems at different locations. Such wide concern drivers will lead to a diverse set of requirements, including sensors and/or analysis methods depending on the specific objective. Unfortunately, local regulations contain nothing regarding monitoring, performance and evaluation of PV power stations. Hence, the performance of PV plants, as a reliable future energy source, is not examined and weighed annually. This paper is the first of its kind in the country and, may be in the MENA region, and could be used as a reference to evaluate similar PV projects, connected to the national or distribution networks, in Jordan and the neighboring Arab countries. It has the main following objectives:

- assess the technical performance and annual energy yield,
- compare actual performance data, from the field, with the original design and simulation by the PVsyst.
- analyze the seasonal variation of the plant output and the performance ratio.

PV modules, which are semiconductors that have no moving parts, allow the conversion of solar insulation into DC electrical current. The latter can be converted to AC current by using special inverters. Such system is considered reliable, safe, environmentally sound method for power generation under different climatic conditions and almost maintenance free except cleaning and other minor jobs. It should be stressed here that it is not the aim of this investigation neither to discuss principles of design of PV plants nor to address the existing legal framework. Rather it is deemed to serve as a reference for monitoring large PV power plants and provide recommendations on how to maintain high performance ratio based on related international standards. The following section presents a short description about the studied PV plant, location and its layout. Followed by the technical specification of main components and then description of the adopted methodology. Finally, results and discussion of measured variables all year round, performance ratio and socio-economic impacts are presented.

3. Plant Description

3.1. Location

The solar PV plant is located south of Amman, about 30 km south-west of Queen Alia International Airport, in Umm Rassas (Lahoon) town. This is an old historical site, built during the Roman presence, in the country, more than 2000 years ago. The old town contains an old castle, churches, theater, and water collection system and currently it is a destination for foreign tourists. However, the PV power station is far from the historic town and inhabited area. It is owned and operated by the Islamic Charity Center Society (ICCS) and the generated electrical power used to supply the Islamic Hospital, in Amman, based on the Wheeling Directive, Energy and Minerals Regulatory Commission (2014).The project covers an area of 50,000 m^2, including the main sub-station which connects the project to the medium voltage (MV) 33 kV distribution grid, which belongs to Jordan Electrical Power Company (JEPCO) as shown in Fig. 2. The site topography is nearly flat; but contains a storm water drainage system to ensure that no water accumulation inside the project area.

The project included all needed infrastructure such as a ring service road, control room and special storage area, guard room, security lighting, cameras and monitoring system and as well as the security fence around the project area.

3.2. Project Capacity and Main Equipment

The original design of the plant was based on 6707 (Jinko Eagle-72) PV modules, which were planned to be fixed north-south on 33 trackers, i.e. moving galvanized steel-structure, with a single axis tracking (east-west). These were arranged to form 353 stings and each of these connected to the central inverter via combiner boxes and DC cables. All used equipment and components were specified and selected from well-known manufacturers, from Europe except PV modules, as shown in Table 1. Some minor stuff such as bolts, washers, earthing rods, cable ties and insulation materials were purchased from the local market, taking into account that specification should comply with the original desired technical specification.

3.3. Project Design

The PVsyst package, PVsyst (2015), is a simulation software developed specially to predict the overall performance of a PV solar system under specific conditions.

It is designed to be used by engineers and researchers as a very useful educative tool. The software includes a detailed contextual Help Menu that explains the procedures and models that are used, and offers a user-friendly approach with a guide to develop a project. The PVsyst has the ability to import metrological data as well as other technical and non-technical details from many different sources. By using this software, the designer or developer will be able to estimate with high degree of accuracy the performance of stand-alone or grid-connected PV system, based on the specification of selected modules, inverter, etc., using hourly simulation data. The obtained results of the PVsyst are used in the techno-economic feasibility study of a PV system regardless of its size, i.e. roof-top or central station. The results of the simulation were used to select main equipment and devices as summarized in Table 1.

The original design of the Solar PV power plant was modified to allow for the distribution company, JEPCO, to have an area of about 1050 m^2 of the original land to house the main switches and to be the connecting point to the MV grid. Moreover, JEPCO forced ICCS to construct a special building, of about 160 m^2, on this piece of land according to their reference specification, just to enclose energy meters and connection switches to the 33 kV grid. Unfortunately, the cost of this building exceeded US$125 thousand. The new design of the PV plant was based on having 353 strings, instead of 340 in the original design, and 19 panel per string that set up North-South and allowing sun tracking from East to West. The strings are connected in parallel to the central inverters. The converted AC 380 V power from the four central inverters is fed to two step-up medium voltage transformers, 2x1500 kVA in parallel, to raise voltage up to 33 kV as shown in Fig. 3. The total installed capacity is 2,146.24 kWp.

The four 500 kVA central inverters, two medium voltage transformers and the delivery and control unit are located nearly in the central area of the project to allow for minimal losses. The generated electrical power is pumped to JEPCO 33 kV grid via 3x95 mm^2 underground medium voltage copper cables. The main reason behind such design is to maximize efficiency by reducing electrical losses and to have smooth operation without any shading on the PV modules. The plant is designed to take back the needed power from the grid after the sunset until sunrise next morning, and during up normal conditions, to supply security lighting and control room appliances. This was based on JEPCO conditions to allow connection and operation of this project. It is important here to mention that related international and national codes were considered, especially the guidelines for renewable energy projects, Energy and Minerals Regulatory Commission (2012), and the local grid code, Energy and Minerals Regulatory Commission (2015), as well as instructions for RE project provided in the project approval letter. Such letter may include but not limited to fees to paid, connection point, connection agreement, electrical power supply to the site and other special conditions specified by the distribution company. It should be mentioned here that distribution companies have an ultimate authority to accept or reject a particular PV project or its proposed location. Moreover, the customer cannot argue nor re-submit another application claiming that network capacity, in that location, does not absorb the planned new PV plant capacity. Unfortunately, there is no real follow up by the Energy and Minerals Regulation Commission.

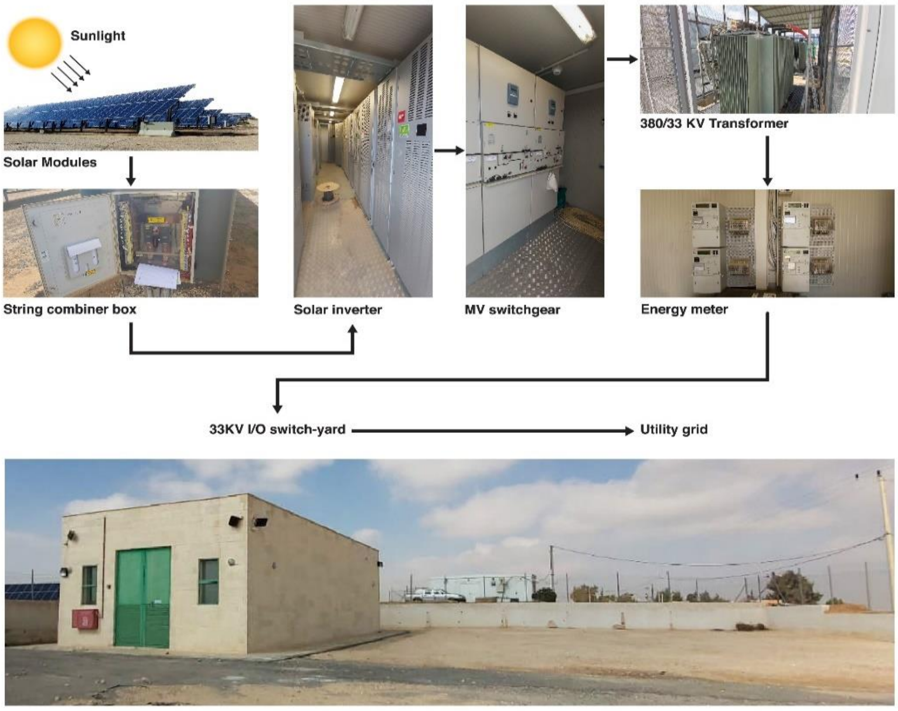

Figure 2. Um Rassas solar PV plant

Table 1. Specs of main equipment

No.	Item	Specification	Origin
1	PV modules	320 W Jinko, Type Eagle-72, Poly Crestline Module, Eff. 16% with a linear degradation rate over the lifetime of about 0.7% (2146.24kWp).	China
2	Inverters	FIMER, R6750TL, 4 Central Inverterswith active cooling (2484 kW), Eff. 98%.	Italy
3	Transformers	2x1500 kVA Step-up from 380 V to 33 kV, SEA and a small auxiliary transformer to supply internal consumption.	Italy
4	Delivery unit	Medium voltage (33 kV) switchgear and control unit, Siemens	Germany
5	DC and AC Cables	Solar cables (DC), low voltage (1000 V) and medium voltage (33 kV) cables (AC) as well as control and communication cables.	Grease
6	Conduits and Sleeves	High density polyethylene conduits and underground tubes.	Grease
7	Steel Structure	Mounting Systems, G235 Hot dip galvanized, steel structure with a single axis tracking system driven by 3-phase motor.	Germany
8	Tracking system	Single axis, screw-jack, Siemens SIMOGEAR Z59-LE90.	Germany
9	Closed Circuit Television (CCTV)	Cameras and recording system, remote zoom and focus (Full HD IR Bullet IP Camera) and weather station.	USA
10	Standby Generator	80 kVA Diesel generation set, Perkins, and Automatic Transfer System (ATS).	UK

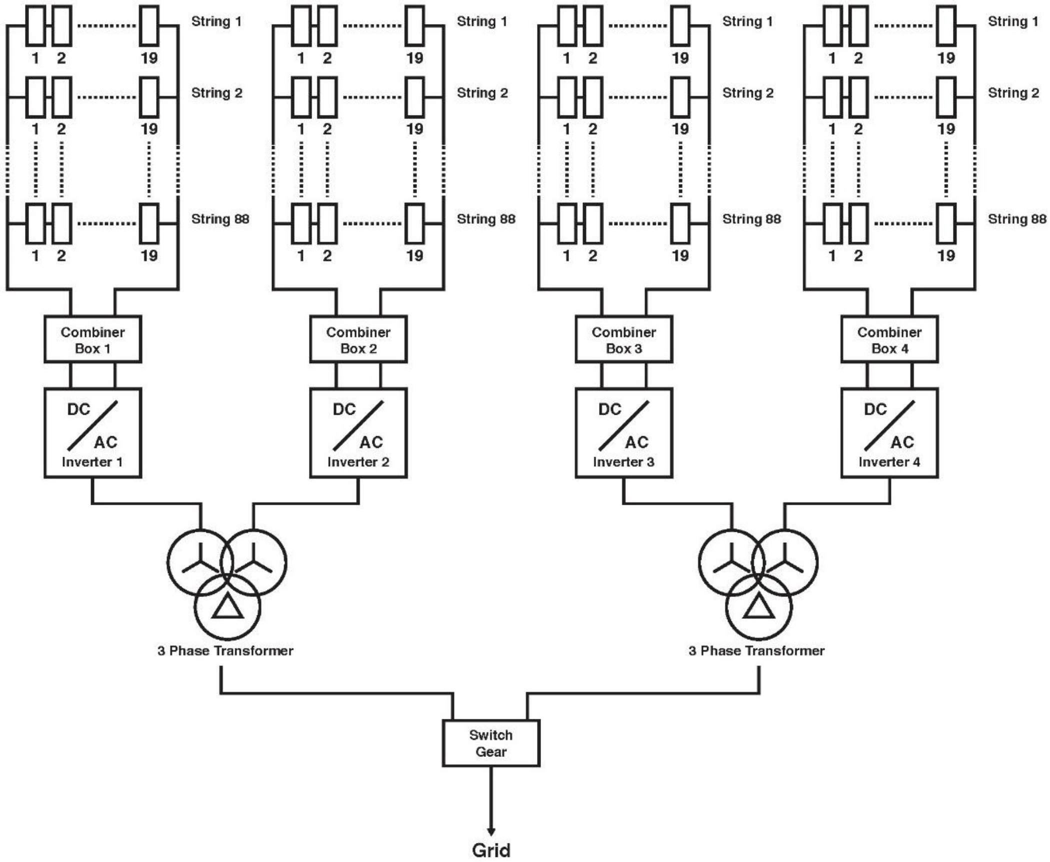

Figure 3. Main units and connection diagram of the solar PV plant

3.4. Annual Power Generation

As in other PV power plants, conversion efficiency and performance degradation over module's lifetime as well as PV cleaning are major factors affecting the generated electrical energy and its cost, (Kumar *et al*. (2015), Saidan *et al*. (2016), Hammad *et al*. (2018), Al-Addous *et al*. (2019), Al-Kouz *et al*. (2019), Obeidat *et al*. (2020)). The PV efficiency is defined as the conversion ratio of received solar intensity to electrical power and annual degradation of PV modules describes the decline in power production against time. A slight decline of these factors, in addition to PV cleaning frequency due to dust accumulation, may reduce the final output by 10-25%. Consequently, the cash flow and revenues of the PV project will be influenced significantly. Thus, such factors should be considered from early beginning and given high attention when designing a new PV power plant in order to reach and maintain high efficiency.

Umm Rasas power plant is located at a longitude of 35.927 N, Latitude 31.493 E and an altitude of about 750 m above sea level. The site is an open area, bare land except some desert plants. However, not close to the PV power plant, there are some farming activities based on irrigation from underground water, i.e. deep wells. In general, the site is characterized by long, hot, dry summers and short (December to March) but cool winters with heavy storms occasionally. The climatic conditions are influenced by the eastern Mediterranean and the Arabian desert. The coldest month is January, with temperatures ranging between 5 °C and 10 °C, and may drop to sub-zero for few days during night time, and August is the hottest month with average temperatures between 30 °C and 35 °C, or even higher touching 40s for a couple of days that may extend to September due to hot waves coming from the Indian continent. The average annual sunny days exceeds 300 days or approximately 3000 hours, Dept. of Statistics, Annual Statistical Report (2020). Equally important is that the 33 kV overhead lines are passing the main gate, of this project, to the distribution and switches sub-station not far from the site: only 500 m from the PV power plant. Hence, the solar PV power plant is located in a good and suitable site, from both technical and socioeconomic points of view.

In this project the tilt angle of PV modules is zero, i.e. horizontal, since the design is based on a single axis tracking system to enhance the production of electrical energy during morning and evening times. This new single axis and single post system are driven by a torque tube connected to a single electric motor on both sides, and a customized software with a tilt range from -45° (east) to +45° (west). All members of the structure are made of self-healing zinc-aluminum-magnesium coated steel to provide high durability and good resistance to corrosive environment. The steel structure carrying PV modules are forced to adjust back to a stew position, i.e. zero inclination, when the wind speed exceeds 100 km/h (i.e. about 27 m/s) to minimize the lift and drag forces and protect the system from any possible damage. It is important to mention here that in 2016-2017, large scale and even small roof-top PV systems, close to Umm Rassas and in other cities in Jordan witnessed serious damage due to a very high speed of surface wind associated with heavy rainstorm. However, there was no destruction nor losses in this project and all components are functioning properly as of today. The frequent technical problems in this project are limited to failure of cooling fans used in the ventilation system for inverters due to relatively high temperatures during daytime around the year and complete collapse of some PV modules. The average number of failed PV modules was about 50, i.e. less than 0.8%, per annum. These are still under the manufacture, JINKO Co., product warranty of ten years and should be reported to the manufacturing company. The panels have a standard efficiency of 16.49% and open circuit voltage (VOC) of 46.4 V, short circuit current (ISC) of 9.05 A, and operating temperature range from -40°C to 85°C with a junction box rating of IP67. In order to keep high power production, it should be stressed here that operation and maintenance team must develop and enact a plan aiming to inspect and test PV modules, frequently. Faulty modules should be removed and replaced with new ones. In 2019, the annual energy production was 3954 MWh, without deducting the losses in the distribution network. This value was almost like that predicted, 4024 MWh, by using the PVsyst. The following section will discuss the performance of the PV power plant over one year.

4. Results and Discussion

4.1. Performance Analysis

Appropriate design of a PV system is possible when every aspect of the system is analyzed and selected properly. The performance analysis of the grid connected PV power plant was conducted in terms of final yield, conversion efficiency and the annual performance ratio. While the economic analysis was based on the generated electricity and its cost savings. This is in full agreement with the developed performance parameters, by the International Energy Agency, (Ayompe *et al*. (2011), Besarati *et al*. (2013)), for solar PV grid connected power plants. As in other PV power systems, the PVsyst simulation software was used in the early beginning to predict the performance of this power plant. While the real data were collected, on daily basis, from the field over one year via the SCADA system and weather station installed on site as well as electrical energy meters.

The Irradiance is defined as the measure of power density of sunlight received at a location on the earth and is measured in watt per meter square. Based on the actual measurements from the site, the average annual solar irradiance in Umm Rassas site is quite high, i.e. 6.5 kWh/m^2.day, while the irradiance's maximum and minimum exist in July and January, respectively, as shown in Fig.4. The measured values are in full agreement with reported data in Jordan, Bani-Younes (2017). But the high solar irradiance in Umm Rassas is expected due to its location not far from the sun built and clear sky most of the year, i.e. long sunny hours.

4.2. Final yield and Performance ratio

The final yield (kWh/kWp) is defined as the annual net energy output of the PV power plant divided by the peak power of the installed PV array at standard conditions, i.e. 1000 W/m^2 solar irradiance and 25°C cell temperature. Fig. 5 shows the average monthly yield during the year 2019, compared with original simulation results using PVsyst. Again, it is clear that during the period April-October, the yield is high due high irradiance and daily long sunny hours. Equally important is the continuous efforts in keeping PV modules clean: the cleaning schedule is based on wet-manual cleaning method bi-weekly. As can be seen in Fig. 5, that real production during summer season is slightly higher than simulation results. While during colder months, early and late in the year, energy production was almost similar to that obtained from the simulation program. Again, such results could be attributed to using a sun tracking system and the frequent PV modules cleaning as well close follow up by the operation and maintenance (O&M) team. However, it is worth mentioning that the actual annual electrical energy yield, 3954 MWh, in 2019 almost similar to that predicted by PVsyst, 4024 MWh. Thus, the slight deviation, during summer and winter, could be ignored.

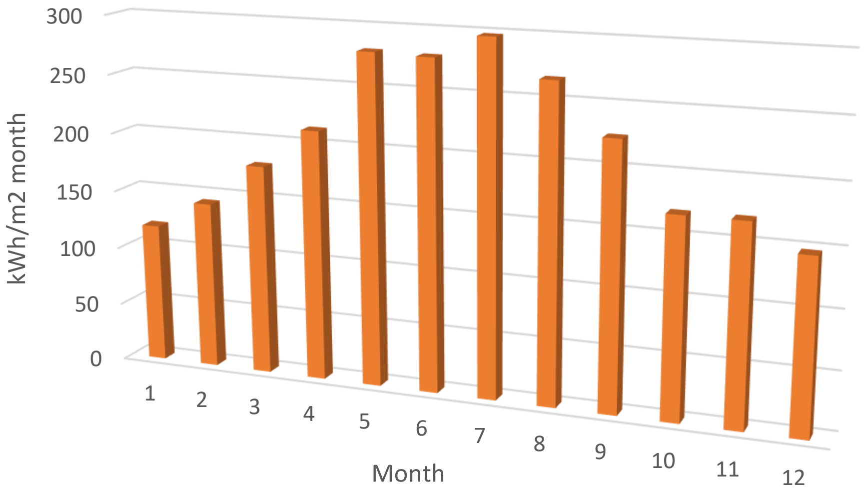

Figure 4. Monthly solar irradiance

The performance of PV modules under varying solar conditions will differ from the normal case. In particular, the intensity of solar radiation falling on a PV module changes in the time of day and varying in energy received by PV cells will affect its main parameters, such as I_{sc}, V_{oc}, power and conversion efficiency. The total energy generated by the PV plant and exported to the grid equals the daily monitored value of AC power output minus the losses in the system.

The performance ratio (PR) of the PV power plant is defined as the final yield of the plant divided by the reference yield. It is a comparison of the PV plant output to the output of the plant could be achieved by considering local solar irradiation, cell temperature, and other factors, such as grid availability, etc. According to the actual collected data during 2019, the actual calculated annual PR (0.950) is much higher than the simulated value (0.856) using the PVsyst package. The difference between the actual and simulated PR is due to the fact that the contracting company conducted the pre- and detailed-design, procurement and construction of this project. Moreover, the contractor provided a performance guarantee as part of the signed contract with the project owner. Fig. 6 illustrates the actual calculated PR over the average predicted PR. All values are high except in four months: January, February, November and December. This could be attributed to many factors, the most important is the high yield due to the efficient tracking system, continuous and daily monitoring and maintenance activities as well as cleaning the PV panels at least ten times a year during the summer season, i.e. twice a month. This is the only way to solve the problem of dust accumulation and consequently the drop in the generated power from the PV modules: cleaning is a key factor in maintaining the desired performance as well as plant economics. Several studies conducted to check the effect of dust accumulation on performance deterioration of solar cells, taking into account local conditions, and reported that appreciable losses incurred in the generated power due to the sun irradiance scattering effects on the surface of the solar panels (Kumar *et al*. (2015), Saidan*et al*. (2016), Hammad *et al*. (2018), Al-Addous *et al*. (2019), Al-Kouz *et al*. (2019), Obeidat *et al*. (2020)).

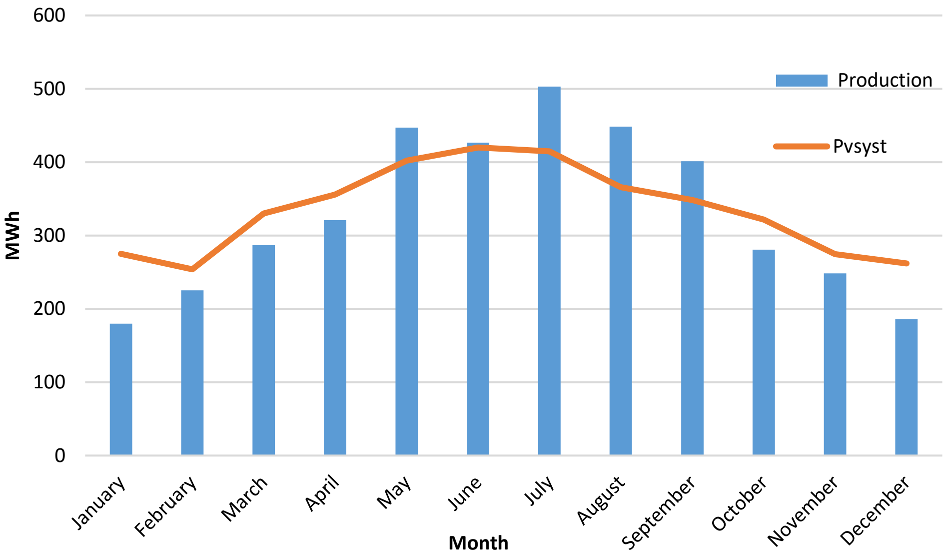

Figure 5. Average monthly energy yield

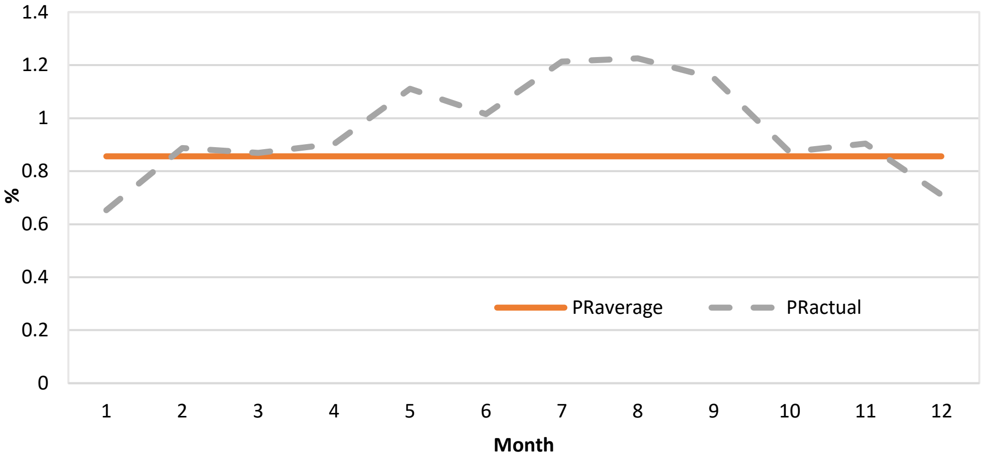

Figure 6. Actual and predicted average performance ratio

5. Socio-Economic Impacts

5.1. The economic impacts

This project contributed to economic and social development of Umm Rassas town and the final beneficiary of generated electric power, i.e. Islamic Hospital in Amman. During the construction of this project, more than 100 workers were involved in different jobs, including supervision and consultancy, engineers and technicians, guards and manual workers. Of them about 15-20 workers from Umm Rassas. On permanent basis there are 3 guards and two technicians to follow operation and maintenance issues on daily basis. PV modules cleaning is conducted by a special team, overnight, consisting of ten to twelve workers and large road water tank for about ten times a year.

According to the Wheeling Directive, Energy and Minerals Regulatory Commission (2014), the project owner should pay the wheeling fees, i.e. 0.007 JD/kWh, to the distribution company as well as bear the losses in the grid, i.e. 6% of the generated and transmitted electricity, regardless of the project location or how far from the load. Based on the prevailing electricity tariff and the specified category for hospitals, and after deducting energy losses in the distribution grid as well as distribution wheeling fees, the average annual savings exceeded 900 thousand JD, i.e. 1.25 million US$/year, at least. Such savings enabled the hospital management to keep the visit and prescription fees for all outside clinics fixed without any increase. This would help poor families and orphans having needed medical treatment at low and affordable cost. It is considered a unique and indirect impact of this project.

5.2. The social and environmental impacts

One of the aims of this project is to assess the sustainability of PV power plants, in Jordan, and their contribution in the national energy strategy and creation of jobs as well as poverty reduction. It is well known that appropriate feedback from the field will help in tuning and adjusting regional and national renewable energy policies and strategies, especially when it comes to socioeconomics of decentralized PV projects, Almasri *et al*. (2019). As in all power generation renewable energy projects, the impacts of the PV plant are grouped into the following categories according to the prevailed local regulation, Ministry of Environment (2020): environmental impacts (air, water and land), and social and economic dimensions. The first step was obtaining the environmental permit, after submitting the required EIA document to the Ministry of Environment. According to the Environmental Impacts By-Law, the Central Licensing Committee will review the submitted EIA and after approving the report including the environmental management plan, the permit could be issued to develop the project within certain time interval. This is a compulsory action for all development projects classified under list A. However, based on past field experience in large PV projects, it could be said that the relationship between a PV power plant and the local society and environment is always positive by all means. This is due to the fact that most of workers during the construction and testing phases are from nearby areas and no serious accidents or problems caused by such a new development. Bearing in mind that such projects are labor intensive during the construction phase and the value created in this phase arises mainly from labor-intensive works including civil engineering activities. Equally important is the technology transfer through foreign investment in such projects, which could lead to create new business relations such as manufacturing and/or assembly of certain parts locally under guidance and supervision of the mother company. At the end of the day, it is deemed that such project would strengthen local capabilities in engineering design, business development, and manufacturing and production.

Later on, during the commercial operation of this PV power station, three guards and two technicians are employed to look after the project. Technicians are highly skilled personal and responsible for integrating the PV solar power plant with the grid, facilitating the connection and looking after the PV plant. In this particular project, the major negative impact here is the reduction of grazing area according to cattle keepers and local residents. Thus, the positive socioeconomics of renewable energy projects is considered a key driver behind the development of such project in Jordan and other countries, Timilsina *et al*. (2011). Another possible but an important driver is the local content requirement which can support the expansion of related local industries and create new job opportunities. A special study, funded by the United States International Aid Agency (USAID) and conducted under Jordan Competitiveness Program (JCP) in 2015, showed that the introduction and enforcement of a rolling local contribution ratio, on renewable energy projects, starting from a low ratio would have a net positive impact on the economy, (El-Karmi *et al*. (2014), Interdisciplinary Research Consultants (2015)). However, the GoJ is still hesitating to introduce such a key incentive, especially for large power generation projects. This could be attributed to the low or absent official efforts in assessing the impact of renewable energy systems on value creation, which considered very critical for making informed policy decisions. Bearing in mind that such developments having a cross-sectoral nature and the analysis should look at various segments starting from job creation, added value to the economy, to welfare and responsibility towards local communities. Equally important is the absence of well-trained engineers and highly skillful workers in field of renewable energy in the local market, Jaber *et al.* (2020). Thus, the introduction of renewable energy courses and integrate vocational and technical as well as high education programs within the national renewable energy action plan is an essential step to promote renewable energy development in the country, Alawin *et al*. (2016).

The local applied research and development in renewable energy, and in particular, solar applications are still prowling due to lack of funding and inadequate study and training curricula related to RE sources and technologies. Thus, the value added through the created knowledge, that can lead to technological development, systems' improvement, reduce costs and better services at local conditions, is around zero. Without the development and adoption of a local RE plan, including serious funding to attract and bring together researchers and related industries to create applied research projects aimed to solve problems in the field, the innovation situation will remain stagnant with no real contribution.

The net positive environmental impact resulting from operating this PV power plant is emission reductions, mainly GHGs. Based on the annually generated power and the calculated rate of emission for 2019, the net reduction of GHGs is equivalent to approximately 1800 ton of CO_2, Jaber *et al*. (2019). It is too early to discuss the impacts of decommissioning phase of a PV power plant, in Jordan, at the end of its operational lifetime. But according to the submitted EIA reports, decommissioning of such plant will include recycling and final disposal of various components. The main issue is the disposal of PV modules since these are classified as an electronic waste and should be disposed-off in specified sites and following strict procedures, Ministry of Environment (2021). Thence, the importance of this phase will increase as the PV power plant reaches the end of its lifetime, i.e., within next two decades.

6. Conclusions

Jordan is highly susceptible to external energy sector shocks which impact its economy. However, it enjoys excellent conditions for the exploitation of solar energy due to its location close to the sun belt. Harnessing such resource would increase the green energy mix and lead the country to be more sustainable and energy secure. Given the importance of utilizing renewable energy sources, on the national and international levels, it is essential to have consistent and reliable information on renewable energy projects. Such info includes environmental and socio-economic viability, technological feasibility and technical details, etc. This paper tries to provide a project-based resource assessment which will help similar project developers and/or operators to monitor and evaluate their projects as well as investors and financiers to understand the performance and levels of revenues and possible risks. It contributes to the literature by reviewing the key performance indicators of mega PV projects, under local conditions, which has not been done in previous studies. Here the performance of 1st wheeling large scale PV, in Jordan, was analyzed and discussed based on real data obtained from the field. It was found that energy yield and performance ratio were high and reached expected values. This was not possible without frequent cleaning of PV modules on bi-weekly basis during summer season and continuous monitoring and O&M operations. Finally, such project and similar other ones, would enhance the diversification and reduction of energy imports, as well as the increase reliance on domestic energy resources. But this would require addressing and removing existing conflicts between stakeholders by adopting a more participatory approach to reform and improve energy sector governance.

Acknowledgment

Authors would like to thank the Islamic Charity Center Society (ICCS), Amman – Jordan, for providing the needed information to start this research work.

References

[1] Abu Rahmeha, T., Abbas, A., Jaber, J.O., Alawin, A. (2016), “Prospects of repowering of old thermal power stations by integrating CSP systems”, *Jordan Journal of Mechanical and Industrial Engineering*, 10, 85-98. http://jjmie.hu.edu.jo/vol%2010-2/JJMIE-19-16-01.pdf

[2] Abu-Rumman, G., Khdair, A.I., Khdair, S.I. (2020), “Current status and future investment potential in renewable energy in Jordan: An overview, *Heliyon*,6, e03346 (Cell Press). doi:10.1016/j.heliyon.2020.e03346.

[3] Alawin, A.A., Abu Rahmeh T., Jaber, J.O., Loubani,S., Abu Dalu, S., Awad, W., Dalabih, A. (2016), “Renewable energy education in engineering schools in Jordan: existing courses and level of awareness of senior students”, *Renewable & Sustainable Energy Reviews*, 65, 308-318. https://doi.org/10.1016/j.rser.2016.07.003

[4] Al-Addous, M., Dalala, Z., Alawneh, F., Class, C.B. (2019), “Modeling and quantifying dust accumulation impact on PV module performance”, *Solar Energy*, 194, 86–102.DOI: 10.1016/j.solener.2019.09.086

[5] Al-Kouz, W., Al-Dahidi, S., Hammad, B., Al-Abed, M. (2019), “Modeling and analysis framework for investigating the impact of dust and temperature on PV systems’ performance and optimum cleaning frequency”, *Applied Sciences*, 9, 1397. doi:10.3390/app9071397.

[6] Al-Kouz, W., Almuhtady, A., Nayfeh, J., Abu-Libdeh, N., Boretti, A. (2020), “A 140 MW solar thermal plant with storage in Ma’an, Jordan”, E3S Web of Conferences 181, 02001, http://doi.or g/10.1051/e3sconf/202018102001.

[7] Almasri, R., Alshamali, A., Chevillard, N. (2019), “Decentralized solar in Jordan”, EDAMA Association for Energy, Water & Environment, Report to the Friedrich-Ebert Stiftung, July 2019, Amman, Jordan. http://library.fes.de/pdf-files/bueros/amman/17271.pdf

[8] Ayompe, L.M., Duffy, A., McCormack, S.J., Conlon, M. (2011),“Measured performance of a 1.72 kW rooftop grid connected photovoltaic system in Ireland”,*Energy Convers. Manage*.,52, 816–825. DOI:10.1016/j.enconman.2010.08.007

[9] Baniyounes, A.M., (2017), “Renewable Energy Potential in Jordan”, *International Journal of Applied Engineering Research*, 12(9), 8323-8331.http://www.ripublication.com

[10] Besarati, S.M., Padilla, R.V., Goswami, D.Y., Stefanakos, E. (2013),“The potential of harnessing solar radiation in Iran: generating solar maps and viability study of PV power plants”, *Renewable Energy*, 53, 193–199.DOI: 10.1016/j.renene.2012.11.012

[11] Boretti, A., Castelletto, S. (2021)”, Cost and performance of CSP and PV plants of capacity above 100 MW operating in the United States of America”, *Renewable Energy Focus*, 39,90-98. https://doi.org/10.1016/j.ref.2021.07.006

[12] Cervone, A., Santini, E., Donatella, S.T., Romito, Z. (2015), “Impact of regulatory rules on economic performance of PV power plants”, *Renewable Energy*,74,78-86.https://doi.org/10.1016/j.renene.2014.06.037

[13] Daher, D.H., Gaillard, L., Amara, M., Ménézo, C. (2018), “Impact of tropical desert maritime climate on the performance of a PV grid-connected power plant”, *Renewable Energy*, 132,729-737. https://doi.org/10.1016/j.renene.2018.03.013

[14] Dept. of Statistics, Annual Statistical Report,(2020), Weather Conditions – Airport Station, Amman, Jordan (2021).http.d://dosweb os.gov.jo/

[15] El-Karmi, F.Z., Abu-Shikhah, N.M. (2014), “Promoting renewable energy in Jordan by employing economic incentives”, *Journal of Fundamentals of Renewable Energy Applications*,4(1), 1-7.DOI: 10.4172/2090-4541.1000130

[16] Energy and Minerals Regulatory Commission, (2012), Guidelines for selling electrical power generated from

renewable energy sources, 2012, Amman, Jordan.http://www.memr.gov.jo/

[17] Energy and Minerals Regulatory Commission, (2015), Intermittent Renewable Resources (Wind and PV) Distribution Connection Code at Medium Voltage (MV), 2015, Amman, Jordan.http://www.memr.gov.jo/

[18] Energy and Minerals Regulatory Commission, (2014), Wheeling Directive No. 2 Year 2014, Amman, Jordan.http://www.memr.gov.jo/

[19] Hammad, B., Al–Abed, M., Al–Ghandoor, A., Al–Sardeah, A., Al–Bashir, A. (2018), “Modeling and analysis of dust and temperature effects on photovoltaic, systems’ performance and optimal cleaning frequency: Jordan case study”, *Renewable and Sustainable Energy Reviews*, 82, 2218–2234. https://doi.org/10.1016/j.rser.2017.08.070

[20] Honrubia-Escribano, A., Ramirez, F.J., Gómez-Lázaro, E., Garcia-Villaverde, P.M., Ruiz-Ortega, M.J., Parra-Requena, G. (2018), “Influence of solar technology in the economic performance of PV power plants in Europe: A comprehensive analysis”,*Renewable and Sustainable Energy Reviews*, 82(1), 488-581. https://doi.org/10.1016/j.rser.2017.09.061

[21] Kumar, B.S., Sudhakar, K. (2015), “Performance evaluation of 10 MW grid connected solar photovoltaic power plant in India”, *Energy Reports*, 1, 184–192. https://doi.org/10.1016/j.egyr.2015.10.001

[22] International Electrotechnical Commission, IEC TS 61 724-2, Technical Specification, Photovoltaic system performance - Part 1: Monitoring and Photovoltaic system performance – Part 2: Capacity evaluation method (2016-2017). https://webstore.iec.ch/publication/25982

[23] Interdisciplinary Research Consultants, Mapping Report: Review and assess local manufacturers of various components of PV systems and their compliance with pertinent local and international standards, (2015), Jordan Competitiveness Program, funded by USAID, 2015, Amman, Jordan. (report submitted to the Ministry of Energy and Mineral Resources and Jordan Chamber of Industry in 2015).

[24] International Renewable Energy Agency (IRENA), Renewable energy and electricity interconnections for a sustainable northeast Asia, (2021), Abu Dubai, UAE.https://www.irena.org/-/media/Files/IRENA/Agency/Publication/2021/May/IRENA_Electricity_Interconnections_NortheastAsia_2021.pdf

[25] International Renewable Energy Agency (IRENA), Renewable power generation costs in 2020, (2021), Abu Dubai, UAE.https://www.irena.org/-/media/Files/IRENA/Agency/Publication/2021/Jun/IRENA_Power_Generation_Costs_2020.pdf

[26] International Renewable Energy Agency (IRENA), World energy transitions outlook: 1.5 C Pathway, (2021), Abu Dubai, UAE. https://www.irena.org/publications/2021/Jun/World-Energy-Transitions-Outlook

[27] Jaber, J.O., Bashir, A., Al Alwain, A., KhademEljamei, D. (2020), “Level of knowledge and skills of fresh engineering graduates in renewable energy: expectations and satisfaction of managers in the field”, *International Journal of Engineering Education*, 2, (2), 1-49. DOI: 10.14710/ijee.2.2.1-49

[28] Jaber, J.O., Elkarmi, F.Z., Alasis, E., Kostas, A. (2015), “Employment of Renewable Energy in Jordan: Current Status, SWOT and Problem Analysis”, *Renewable & Sustainable Energy Reviews*, 49, 490-,

[29] Jaber, J.O., Marahleh, G., Dlabeeh, A. (2019), “Emissions reduction resulting from renewable energy projects in Jordan”, *Journal of Energy Technologies and Policy*, 9(6), 42-51.DOI: 10.7176/JETP/9-6-06

[30] Jaber, J.O. ,Badran, O.O., Abu-Shikhah, N. (2004), “Sustainable energy and environmental impact: role of renewables as clean and secure source of energy for the 21st century in Jordan”, *Clean Technologies and Environment Policy*, 6, 174-186.https://doi.org/10.1007/s10098-003-0232-9

[31] Jaber, J.O. (2012), “Prospects and challenges of small hydropower development in Jordan”, *Jordan Journal of Mechanical and Industrial Engineering*,6,110-118. http://jjmie.hu.edu.jo/files/v6n2/JJMIE-265-10.pdf

[32] Jaber, J.O., Jaber, Q., Sawalaha,S., Mohsen, M.S. (2008), “Evaluation of conventional and renewable energy sources for space heating in the household sector”, *Renewable and Sustainable Energy Reviews*,12, 287-289.https://doi.org/10.1016/j.rser.2006.05.004

[33] Jaber, J.O., Odeh, S.D., Probert, S.D. (2003), “Integrated PV and gas turbine system for satisfying peak-demands”, *Applied Energy*, 76, 305-319.https://doi.org/10.1016/S0306-2619(03)00010-2

[34] Jaber, J.O., Awad, A., Abu Rahmeh, T., Alawin, A.A., Al-Lubani, S., Abu Dalu, S., Dalabih, A., Al-Bashir, A. (2017), “Renewable energy education in faculties of engineering in Jordan: relationship between demographics and level of knowledge of senior students, *Renewable & Sustainable Energy Reviews*, 73, 452-459.DOI: 10.1016/j.rser.2017.01.141

[35] Jed, M.E., Ihaddadene, R., Ihaddadene, N., Sidi, C.E.E., EL-Bah, M. (2020), “Performance analysis of 954,809 kWp PV array of Sheikh Zayed solar power plant (Nouakchott, Mauritania)”, *Renewable Energy Focus*, 32, 45-54.https://doi.org/10.1016/j.ref.2019.11.002

[36] Goura, R. (2015), “Analyzing the on-field performance of a 1-megawatt-grid -tied PV system in South India”,*Int. J. Sustainable Energy*,34, 1–9. https://doi.org/10.1080/14786451.2013.824880

[37] Ministry of Energy and Mineral Resources, Annual Report (2020), Amman, Jordan, 2021.http://www.memr.gov.jo/

[38] Ministry of Energy and Mineral Resources, Renewable Energy and Energy Efficiency Law, 2012, Amman, Jordan.http://www.memr.gov.jo/

[39] Ministry of Energy and Mineral Resources, Updated Energy Strategy 2020-2025, Amman, Jordan. http://www.memr.gov.jo/

[40] Ministry of Environment, Electric and Electronic Waste Management Regulations for the year 2021, Amman, Jordan.http://www.moenv.gov.jo/

[41] Ministry of Environment, Environmental Classification & Licensing By-Law No. 69 Year 2020, Amman, Jordan.http://www.moenv.gov.jo/

[42] Ministry of Environment, Jordan’s 3rd National Communication on Climate Change -2014, Amman, Jordan.

[43] Ministry of Water and Irrigation, Annual Report, (2020), Amman, Jordan, 2021.http://www.moenv.gov.jo/

[44] Mohsen, M., Jaber, J.O. (2001), “A photovoltaic powered system for water desalination, *Desalination*, 138, 129-136. https://doi.org/10.1016/S0011-9164(01)00254-5

[45] National Electric Power Company, Annual Report (2020), Amman, Jordan, 2021.https://www.nepco.com.jo/

[46] Obeidat, M.S., Al Abed Alhalim, E.M., Melhim, B.R. (2020), “Systematic approach for selecting a cleaning method to solar panels based on the preference selection index approach”, *Jordan Journal of Mechanical and Industrial Engineering*, 14(3), 279 – 287.http://jjmie.hu.edu.jo/vol14-3/02-11-19.pdf

[47] Oh, W., Choi, H., WonSeo, K., Kim, D., Kim, S.O., Lee, H.S., Hwang, H., Kim, D. (2020), “Evaluation based on performance and failure of PV system in 10 years field-aged 1 MW PV power plant”, *Microelectronics Reliability*, 114 (November Issue). https://doi.org/10.1016/j.microrel.2020.113763

[48] Timilsina, G.R., Kurdgelashvili, L., Narbel, P.A. (2011), "A Review of Solar Energy: Markets, Economics and Policies. Paper is funded by the Knowledge for Change Program (KCP),Policy Research working paper; No. WPS 5845. World Bank. https://openknowledge.worldbank.org/handle/10986/3612 License: CC BY 3.0 IGO.

[49] Saidan, M., Albaali, A.G., Alasis, E., Kaldellis, J.K. (2016), "Experimental study on the effect of dust deposition on solar photovoltaic panels in desert environment", *Renewable Energy*, 92, 499-505.DOI: 10.1016/j.renene.2016.02.031

[50] Şevik, S., Aktaş, A. (2022), "Performance enhancing and improvement studies in a 600 kW solar photovoltaic (PV) power plant; manual and natural cleaning, rainwater harvesting and the snow load removal on the PV arrays", *Renewable Energy*,181, 490-503. https://doi.org/10.1016/j.renene. 2021.09.064

[51] Sladek,T.A., Jaber, J.O. (2016), "Integrated development of renewable energy and oil shale", JIOSS 2016 - The 3rd Jordan International Oil Shale Symposium, Dead Sea, Hashemite Kingdom of Jordan 22 November 2016.http://toc.proceedings.com/37739webtoc.pdf

[52] World Bank, (2021), Press release statement on Jordan's Red-Dead sea project, 29 May 2021, https://en.royanews.tv/news/28334/2021-05-29.

JJMIE

Volume 16, Number 4, September. 2022
ISSN 1995-6665
Pages 581 – 590

Jordan Journal of Mechanical and Industrial Engineering

A Novel Design of the Articulated Lower Limb Prosthetic Foot Using Fiber-Reinforced Polymer

Sameer Hashim Ameen[1*],Randa Kamel Hussain[2], Rasool R. K. Al-Arkawazi[3]

[1,3]*Technical Instructors Training Institute, Middle Technical University, Iraq*

[2]*College of Science, Physics Dept., Mustansiriyah University, Iraq*

Received 8 May 2022 *Accepted 18 Jul 2022*

Abstract

The prosthetic foot (PF) is a device used to make the lower limb for the amputee patients perform approximately like the normal leg, while the articulated Ankle-Foot orthosis (AFO) is a brace for patients with severe drop foot. The articulated prosthetic lower limb prefers to add several functions to patients rather than a non-articulated prosthetic like a higher degree of freedom, comfort, and easier maintenance. A novel Articulated Ankle-Foot Prosthetic (AAFP) is designed, manufactured, computerized, and numerically analyzed by "LINKAGE PROGRAM" that is connected to the second program "KINOVEA PROGRAM" in order to investigate all the main characteristics items of the prosthetic foot. The AAFP is based on mixing between prosthetic foot (PF) and the articulated ankle-foot orthoses (AAFO), it consists of several links and one slider, all made from Carbon Fiber-Reinforced Polymer CFRP. The novel prosthetic foot is experimentally studied in terms of dorsiflexion angle, weight, sawing time, and stance time. The AAFP shows an excellent dorsiflexion angle and lighter weight in comparison with commercial feet. The dorsiflexion angle is 8o with a good increment reached to 2 % and 20 % in comparison to non-articulated foot and SACH foot respectively. A self-mechanically return mechanism foot, lighter weight, and a simpler design are obtained. It has a lighter weight of 39 % and 266 % of the total prosthetic foot weight in the comparison with nonarticulated and SACH feet respectively. Finally, the AAFP design is closely approached to the normal gait of a healthy person, by an approximately identical swing and stance phases time with a difference of no more than 2 % and 4.66 % respectively. The numerical analysis is based on the finite element method using AUTODESK INVENTOR PROGRAM. The numerical results showed that the induced stresses and strains in the prosthetic foot give a similar factor of safety as steel but with a lighter weight when the present novel design is made from Carbon Fiber-Reinforced Polymer (CFRP). Higher deformation is obtained from using CFRP (PP: 5, CF: 1 by weight) in comparison with steel, so a more elastic and damping response is offered against ground reaction forces.

Keywords: Ankle- Foot prosthetic, articulated foot, CFRP, dorsiflexion angle, swing time, Autodesk Inventor.

Nomenculture

A : Cross-Sectional area of the link (m2).
CF : Carbon Fiber.
CFRP : Carbon Fiber-Reinforced Polymer.
E : Modulus of Elasticity of Link Material (N/m2).
HDPE : High density polyethelene.
K : Spring Constant (N/m).
KE : Kinetic Energy (Joule).
L : Link Length (m).
m : Mass (kg).
PE : Potential Energy (Joule).
PP: Polypropylene.
U : Total Energy (Joule).
v : Speed of the foot mechanism (m/sec).
W : Frictional force (N).

1. Introduction

The great support provided by both biomechanics and biomaterials for the disabled in the lower and upper extremities was done by orthoses and prostheses (O&P) assistants.

The artificial devices which are substituted for missing body parts or supported (due to accident or diseases) are aimed to support, stabilize, and return motion. Orthoses (braces) hold up and adjust the structural and utility characteristics of disabled neuromuscular and musculoskeletal systems. For disabled with impairments that subscribe to practical activity limitations, orthoses are used to direct forces on the limb for biomechanical requirements[1].

The prosthesis is an artificial substitution for a missing limb, the remaining part of the amputee is devoted as the residual limb. The mechanical loads are passed from the residual limb to the prosthesis by the socket. The socket is

---

* Corresponding author e-mail: dr.sameer.hashim@mtu.edu.iq.

a cup-like structure that dresses appropriately for the residual limb.

The design and the cost of these prosthetic and orthotic devices represent the important elements in the development of the biomechanical industry, guiding an excess in the quality of life of amputee patients.

In fact, the choice of artificial or as called adaptive foot for amputee patients is yet complicated. To guarantee effective rehabilitation, the clinical examination of the amputee patients is necessary by the prosthetist. The prosthetist recommendation for the appropriate prosthesis is chosen for each case depending on the objective items like stability in the gait cycle and accurate fit of the prosthetic leg in lower limb amputee case [2].

The absence of one or both legs sure makes an imbalance in the amputee patient's gait cycle. The more important factors that affect the function of the lower limb prosthetic is the dorsiflexion angle of the foot, impact resistance, the foot life against loadings, and the material that the Solid Ankle Cushion Heel (SACH) foot is manufactured from. The SACH foot represents the traditional foot especially used by old man amputee patients who have a short stride in the gait cycle [3].

A significant improvement is obtained from using multi-axes in SACH foot [4]. These axes provide several degrees of freedom for the non-articulated foot which is reflected in a good enhancement observed in the overall gait cycle of amputee patients, but still, they have several disadvantages such as having a bulky volume, and poor dorsiflexion angle. To overcome the mentioned challenges, the composite material is a good replacement for traditional polyethylene in manufacturing the SACH foot. Other attempts to improve the mechanical properties are carried out by using date palm wood. The maximum dorsiflexion angle and fatigue life achieved are 7.5o and 1029135 cycles respectively [5].

The composite material is presented in recent research as an optimum solution for higher mechanical strength and lighter weight [6]. The carbon-reinforced polymer material demonstrates excellent mechanical properties when a polymer (as a matrix) is mixed with different compositions of carbon fibers. The great enhancement in modulus of elasticity, ultimate tensile strength, and impact resistance is obtained as carbon fiber increases, with a significant decrease in elongation [7].The fiber-reinforced polymer in nature forms like straw or rice husk may work to improve the mechanical properties of the material to a great extent [8].The finite element method with experimental design together works to obtain the required optimum contributions [9], [10].

Figure 1 shows the different designs of prosthetic feet AMP, energy-saving, and Adjustable AFO respectively. The mechatronics foot is demonstrated as an excellent development in the manufacturing of the prosthetic foot for amputee patients. A small motor, 60 watts, works to generate a maximum torque of 120 N.m in both clockwise and anticlockwise directions, assisting to make the required movement of the Ankle Mimicking Prosthetic (AMP) foot. Figure 1-a shows the schematic diagram of the AMP foot after being converted to simple springs and damper [11]. The partitioned foot supplied its power and motion from the ankle, acquired stability and tendency to the normal foot. The heavy-weight mechatronics foot consists of two motors with several springs and links [12].

Some of the novel energy storage prosthetic feet types depend on the storing of the kinetic energy generated during the stance phase and releasing some amount of it in the next gait phases [13], [14]. The "energy storage and return foot" ESAR enhanced the stride length for the patient to a good extent with symmetrical steps in gait cycle [15].

The ankle-foot prosthetic is a good replacement device for the traditional solid prosthetic foot in both; cost in the manufacturing material and the walking speed, depending mainly on its mechanism on the energy-saving or as called "energy return" by using springs elements to return back of the foot to its original position after mid-stance phase for the patient as shown in Figure 1-b [16].

The return of the energy as a mechanism is done (in a dynamic foot) by saving the potential energy in the stance phase before releasing some of its value in the next gait cycle phase [17].

The articulated ankle-foot orthosis is a suitable device for patients suffering from severe from post-stroke. The articulated AFO provides a solution for resistance to dorsiflexion and plantar flexion by applying the mechanical forces required to gain the normal reflection for the ankle and knee joints [18]. An articulated AFO has a spring to resist plantar flexion of the foot at a beginning of the mid-stance phase which effected the height of the center of mass of the patient, in addition to knee and ankle reflection [19].

The advantage of AFO has adjustability in the degree of freedom constructed under several ground cases of gait including ascending and descending stairs. The design of AFO has a damper that controlled ankle joint movement as shown in Figure 1-c. The AFO device is manufactured from composite material while the bearing weight of the patient is supported by two steel links distributed on two sides of the leg. The adjustable device provides 8 and 26 degrees of freedom in plantar flexion and dorsiflexion respectively [20], [21].

The hydraulic damper is a perfect choice, especially wherever a higher range of motion and patient walk down in inclination is required. A computerized design may give a understanding of motion and the requirements of a prosthetic foot. The programs MATLAB and SIM HYDRAULIC are used to simulate the activity functions of the prosthetic feet with lower volume and weight [22].

This work aimed to design " Articulated Ankle-Foot Prosthetic " (AAFP) based on mixing between traditional prosthetic foot and articulated ankle-foot orthoses. It depends on the links and single slider only in design, without any springs and/or dampers. This novel design is done by LINKAGE PROGRAM that enables editing of the precise sketching before obtaining the final design that comes as a later step to the KINOVEA PROGRAM as a video clip of foot movement. The KINOVEA PROGRAM analyzes the video clip and converts it to required items. The numerical investigations are done using AUTODESK INVENTOR PROGRAM, all stresses, deformations, and factors of safety are determined by using present material (CFRP) for manufacturing of new prosthetics, in addition to steel and high-density polyethylene HDPE for comparison purposes.

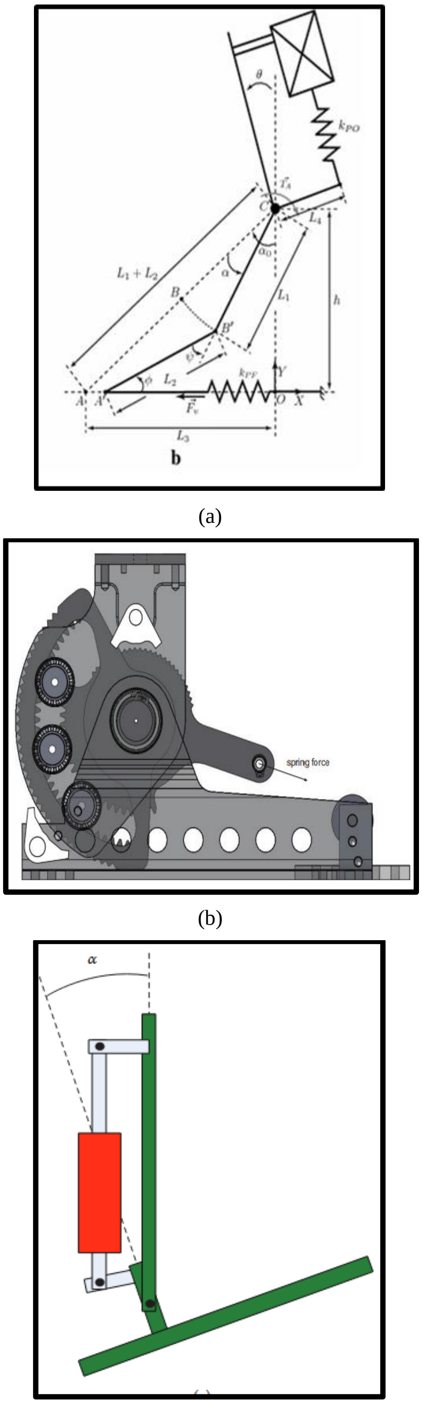

(a)

(b)

(c)

Figure 1. Different prosthetic foot.

(a) AMP Foot [. 8.], (b) Energy return Foot [.12.], (c) Ajustable AFO [.16.].

2. Methodology

The mechanism of the foot is designed according to what is called the " LINKAGE PROGRAM ". This program is similar to Computer-aided design "CAD" but in an easier form. This program has the ability to change the dimensions of the links and their quantity quickly with animation for each try. The program is exporting its file as a video clip which later represents an input to KINOVEA PROGRAM. The latest program has treated the videos by converting them to a separate sequence of images, in addition to measuring angles, distances, and times. The accurate results determined from the KINOVEA PROGRAM are the dorsiflexion angle response with time in the swing phase of the gait cycle. The results are bolstered by the evaluation of the horizontal movement of the slider, in addition to a determination of the cartesian displacements of the cross-links, in addition to measuring the time for the swing and stance phases. The present work procedures are demonstrated as block diagrams including design, experimental tests, and numerical results which are illustrated as shown clearly in Figure 2.

Regenerator at a flow rate of u_2 and an initial temperature of T_0 . After heating in the regenerator area and the porousmedium combustion area, it flows out of the middle cross-

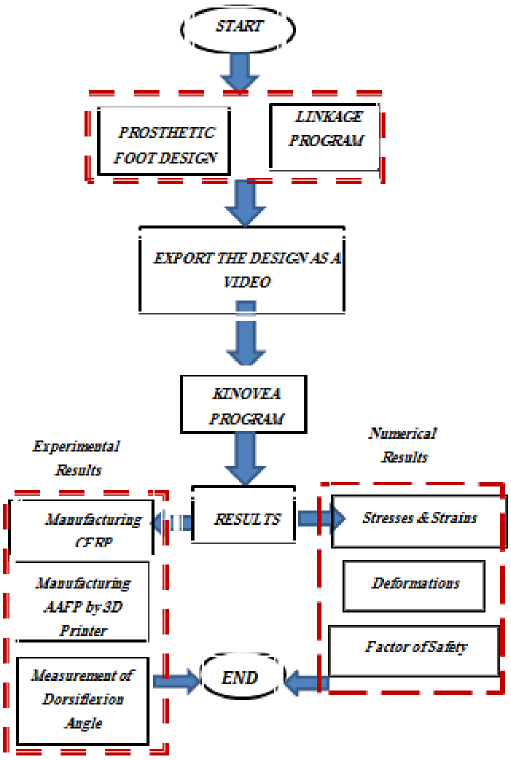

Figure 2. Flow chart of the current work.

3. Theory

One of the principal strategies in the formulation of the dynamic equations that are required to describe the overall motion of the prosthetic foot mechanism is the converting of the bearing load, the weight of the patient, to electrical power [23].The electrical power is generated is approximately 0.8 w which required in order to lift the foot upward.

In the present work, the formulation of equations is dependent mainly on the energy conservation law. The patient weight, which causes the potential energy in the foot, is converted to kinetic energy needed to make the dorsiflexion of the foot under the principle of return foot.

The total energy developed in the foot is divided into kinetic and potential energies as follows [24]:

$$U = KE + PE \tag{1}$$

The potential energy in the proposal AAFP is represented by the vertical extension of cross-links in the **y-axis as follows:**

$$PE = \frac{1}{2} K y^2 \tag{2}$$

The spring constant K is substituted by an equivalent link constant as follows:

$$K = K_{eq} = \frac{E.A}{L} \tag{3}$$

The sum of all equivalent link constants is represented the total link constant as follows:

$$K_{total} = \sum_{i=1}^{n} K_i = \sum_{i=1}^{n} \frac{E_i A_i}{L_i} \tag{4}$$

Where i = 1, 2, 3, ……, n

The kinetic energy in the slider can be formulated as follows:

$$KE = \frac{1}{2} m v^2 \tag{5}$$

The derivatives of Equation 1 items gives:

$$\Delta KE + \Delta PE = W \tag{6}$$

If the frictional forces (µ.N) in the slider are not to be ignored and other additional frictional forces in pins of links, otherwise Equation 6 is equal to zero.

4. Proposed Design

The present proposed design is carried out using the Linkage program by connecting several links (15 links) to form a final structure. The dimensions of the foot are (2.0 * 2.5 * 28) cm of 244 g weight. The re-motion of these links several times is required to achieve the best dorsiflexion angle obtained from the program. All dimensions, front and side views of the final design, are shown in Figure 3. The present novel mechanism design is working closely with the normal foot, which makes a dorsiflexion angle reaching 8 degrees in the swing phase, and returns to the null position (horizontal position with zero angles) in the stance phase immediately with no needing for the extra equipment like springs or dampers.

The main idea of the present prosthetic foot is constructed and presented as clearly shown in Figure 4-a, which illustrates the sketch of the mechanism animation of the foot. The white arrows represent the swing phase motion, while the red arrows refer to the stance phase. Figure 4-b shows the new prosthetic foot (AAPF) in the swing phase and its connection to the socket for amputee patients in the lower limb. In the stance phase, the red arrows represent the mechanism of motion that occurred, where the upper disc (up of the prosthetic foot) is attached to the lower disc and after that, the required supporting of patient weight by prosthetic foot is obtained. In conjunction with supporting the loading, the inclined foot is returned back to the null position (horizontally laid to the ground) by the kinematics of the cross-links.

Finally, the mechanism of the present foot can be summarized as follows:

1. Loading phase is working to generate what is called "stance Phase" by making the inclination of the foot zero.
2. The swing phase occurs when lifting the prosthetic foot from the ground in an unloading case.
3. The foot lift (at this instant the dorsiflexed angle in the foot is generated) starts and develops during the swing phase until reached maximum lift value before returning back to zero dorsiflexion angles at end of the stance phase.

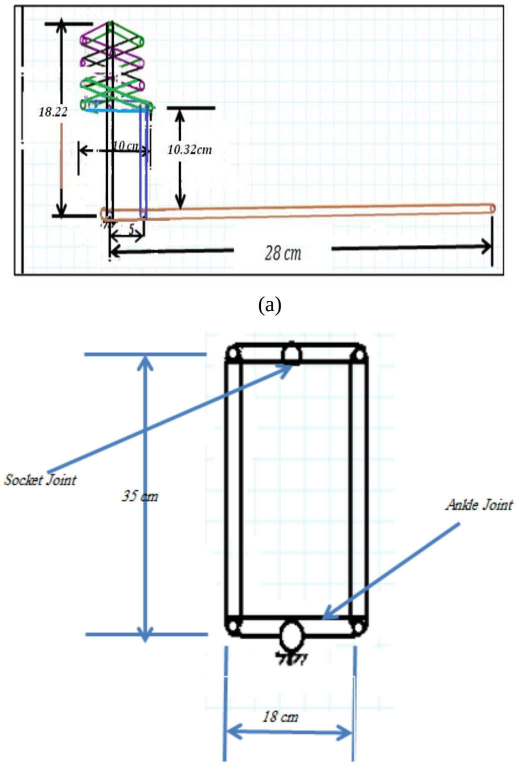

(a)

(b)

Figure 3. Dimensions of articulated prosethetic lower limb.
(a) Front view, (b) Side view

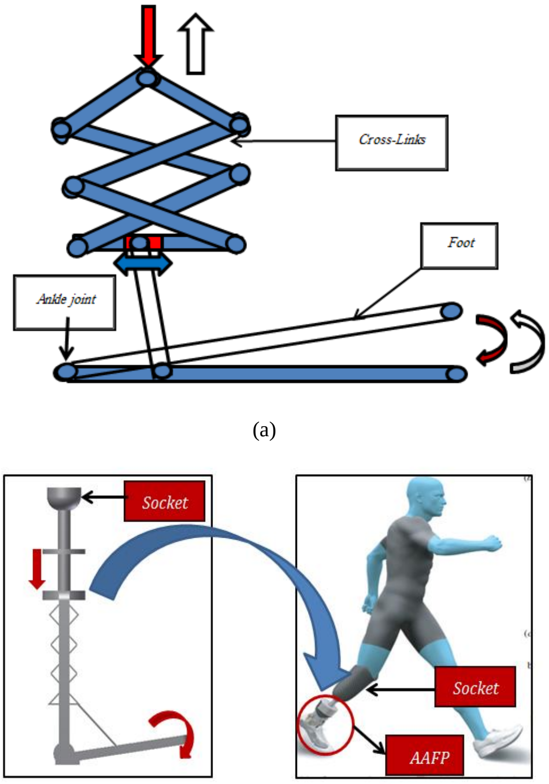

(a)

(b)

Figure 4. Ankle-Foot Prosthetic.
(a) Mechanism of Prosthetic animation (b) Connection AAFP to socket.

5. Results

5.1. Experimental results

5.1.1. Manufacturing the foot

The 3D printer represents the most accurate manufacturing machine in recent years for fabricating several mechanical parts, especially in prosthetics and orthotics fields. The prosthetic model manufactured from CFRP is shown in Figure 5 after being painted red color.

Figure 5-a represents details of the new prosthetic foot pre-manufacturing before executing the printing order, while Figure 5-b is the final shape.

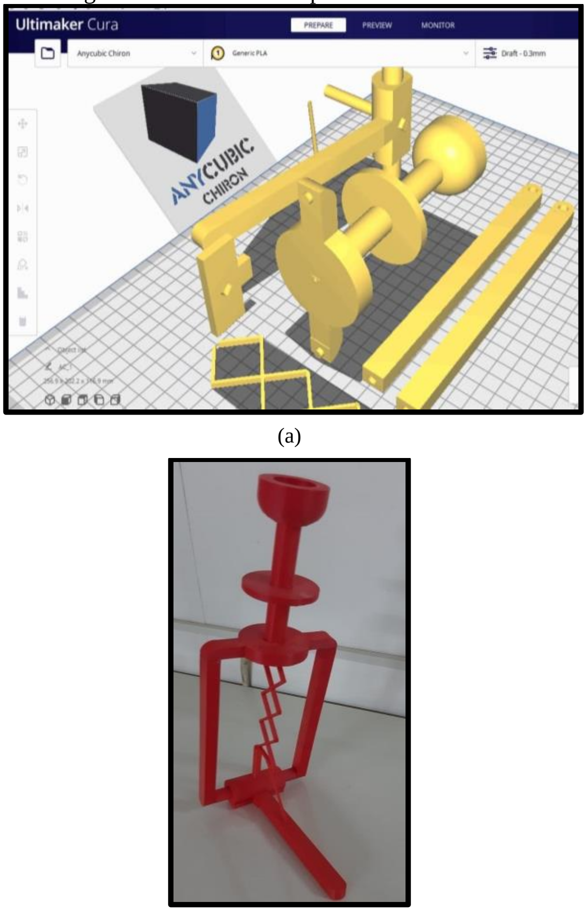

(a)

(b)

Figure 5. Manufacturing the prosthetic.

(a) Details, (b) Assembly

5.1.2. Manufacturing the CFRP material

The CFRP is produced using a rig as shown in Figure 6. The new rig consists of three heaters working to molten and mix the polypropylene particles with carbon fiber pieces. All heaters are adjustable regarding temperatures according to the material used. The last heater (at bottom of the rig) is adjusted to maintain a temperature more than the first two heaters by 20^o C to make the molten mixture like a fluid to easily occupy the shape of a die at end of the rig. The final shape of CFRP is demonstrated in Figure 7. The different compositions (PP / CF) by a percentage of weight are taken into account. The composite material (PP: 5 to CF: 1) represents the best-mixed materials for better modulus of elasticity and ultimate strength.

The investigated mechanical properties of the new material are shown in Table 1 by using the compression test of the black specimen shown in Figure 7.

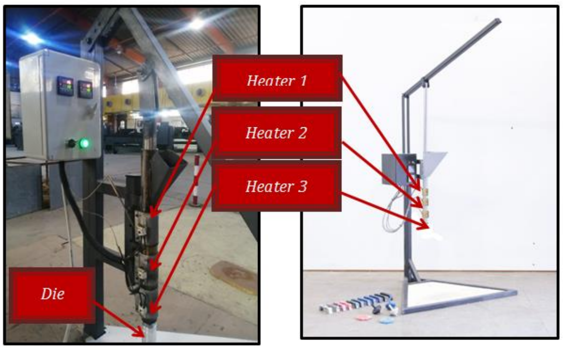

(a) (b)

Figure 6. CFRP Production Rig.

(a) Real Image, (b) Schematic drawing

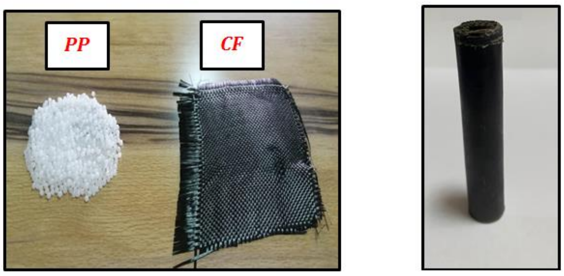

Figure 7. CFRP Specimen.

Composition, (b) Final product

Table 1. Mechanical poperties of materials under study.

Materials	Modulus of Elasticity (GPa)	Ultimate Tensile Strength (N / mm^2)	Poisson's ratio
CFRP	21.55	831	0.33
Steel[22]	200	450	0.30
HDPE[22]	1016	16.14	0.34

5.1.3. Dorsiflexion angle and swing time

The main goal of any prosthetic foot is the dorsiflexionangle which lifts the toes up during the swing phase and then becomes flat in the mid-stance phase.

The Kinova program converts the video clip to images that can be measured in foot inclination angle sequence with time as shown in Figure 8. All results are collected in one chart and compared with articulated ankle-foot orthoses [21] as clearly shown in Figure 9. The present foot presents a similar dorsiflexion response as the nonarticulated one. The time is taken logarithm because of the different time intervals in seconds for the present work while in milliseconds in reference. The dorsiflexion angle of the proposed prosthetic foot converges its temporal response closely to the response of a drop foot patient that wears an AFO.

The proposed AAFP exhibits a maximum dorsiflexion angle with less weight reaches to 8^o and 244 gm respectively as compared with a nonarticulated prosthetic foot and SACH foot, where an 86.13 kg.f (846 N) of the weight of the amputee patient is applied at the heel in the stance phase at the gait circle. From Table 2, the suggested design acquired the foot a good increment in dorsiflexion angle reached 2.5 % and 20 % in contrast with non-articulated foot and SACH foot respectively. The new design is just a collection of 15 steel links with different dimensions. The links are made from steel with a cross-sectional area of (2.0 x 2.5 mm), the total mass of about 244 g indicated a saving in weight in contrast with a heavyweight of the non-articulated prosthetic and SACH foot by 39 % and 266 % respectively.

Table 3 presents another advantage of the new AAFP which has a swing time very close to the natural foot of a healthy person running with wide strides. The time in Figure 6-d is half of a swing time. Hence, the good convergence of the foot swing time with the runner's foot reached only 2 % as a difference which makes excellent insurance of the safety of the present kinematic foot that is approximately equal to the natural one. In the stance phase, the duration time for present AAFP is greatere than for healthy persons only by 4.66 % as shown in Table 3 which lists the gait phases time.

Table 2. Comparison of different items with Ref. [27]

Items	Present Foot	Non-articulated Foot	SACH Foot
Dorsiflexion Angle (Degree)	8.0	7.8	6.4
Wight (g)	185	400	650

Table 3. Comparison of the selected gait phases time with Ref.[28]

Items	Present Foot	Natural Foot
Swing Time (seconds)	8.72	8.90
Stance Time (seconds)	9.81	10.29

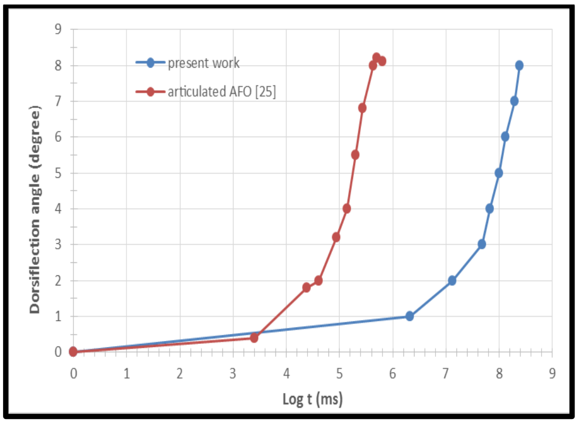

Figure 9. Dorsiflexion angle versus time.

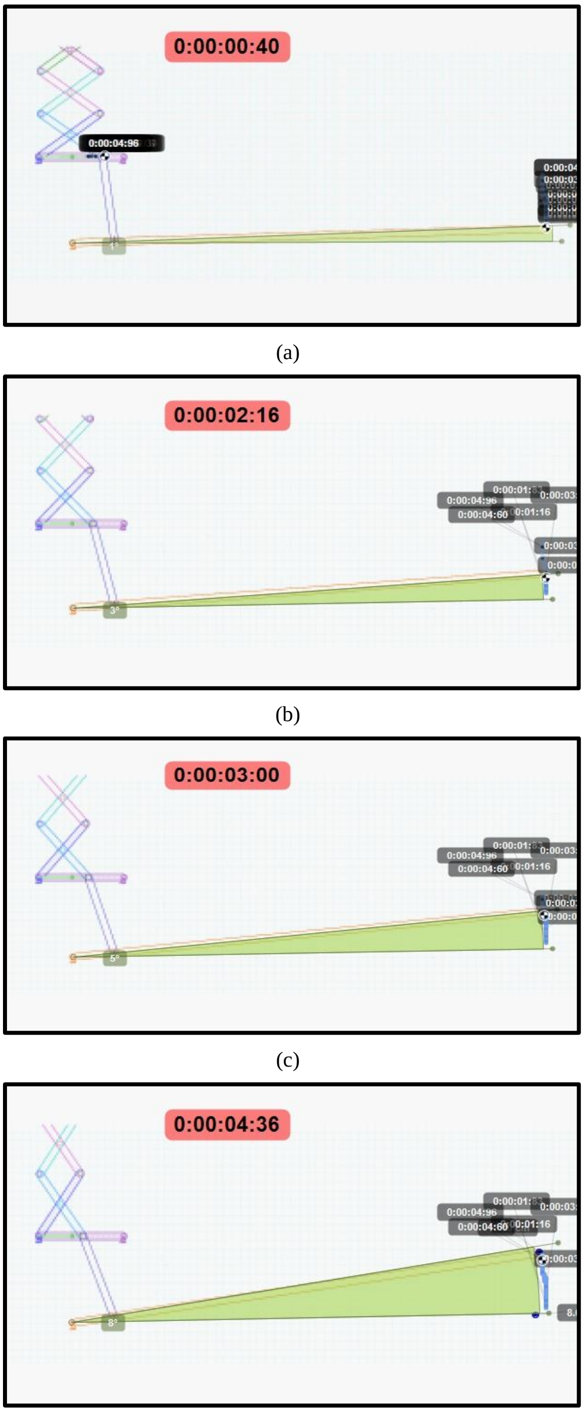

(a)

(b)

(c)

(d)

Figure 8. Dorsiflexion angle in swing phase.

(a) 1 degree, (b) 3 degrees, (c) 5 degrees, (d) 8 degrees.

5.1.4. Cross-Links lift and slider movement

To assess and evaluate the maximum elongation in a vertical direction or as called vertical lift of the whole prosthetic foot is evaluated according to the measure of the track path of the point A indicated in Figure 10. The criteria for the determination and assessment of the vertical lift and upward and downward movements are to achieve the "optimum" dorsiflexion and also plantarflexion of the foot that can be reached from cross-link movement. The dorsiflexion angle is obtained from the upward movement of cross-links while plantarflexion is obtained from downward movement.

The vertical displacement versus the time of point A in Cartesian coordinate when it moves upward in the swing phase is illustrated in Figure 11. The red and blue curves represent the y and x-axes movement. This means each pin that connected the cross-links move upward and downward by 1.0 cm, therefore the three pins in our design move a total distance of 3.0 cm. The time consumed in turning from stance phase to swing phase is 4.6 seconds only. Therefore, a 0.64 cm/sec constant linear vertical speed of the cross-links has represented the foot speed.

The cross-links are a good replacement for ordinary spring and damper with an excellent saving in weight and volume obtained, with reasonable kinematic items like distance and speed.

The vertical movement of the cross-links produced a horizontal movement for the small slider as shown in Figure 12 for one stroke. The horizontal reciprocated distance of the slider works to produce the required inclination of the laid link (foot). Figure 13 shows the linear response of the horizontal motion with time, by reaching a maximum slider movement of 2.2 cm.

The combined animation of cross-links and slider exhibits a linear distance of 3.0 and 2.2 cm respectively which works, as a result, making up an 8^o dorsiflexion angle of the foot.

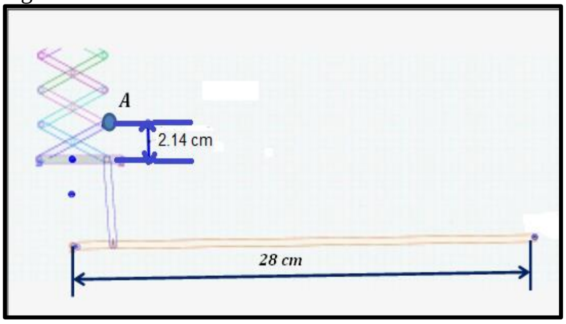

Figure 10. Null position of a prosthetic foot.

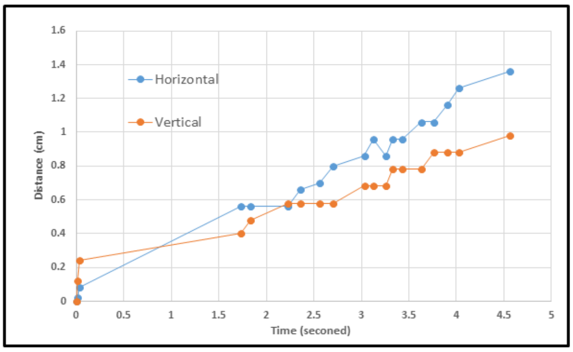

Figure 11. Movement of pin A in cartesian coordinate.

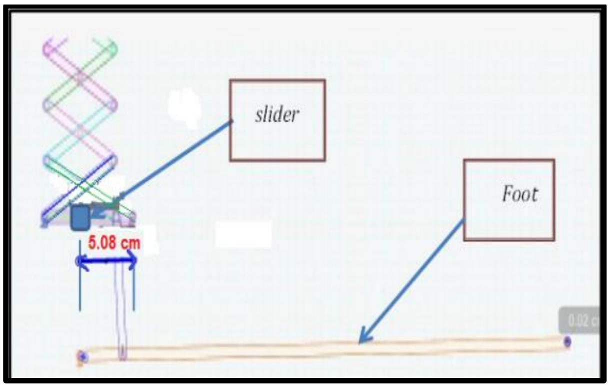

Figure 12. Movement of the slider in a horizontal coordinate.

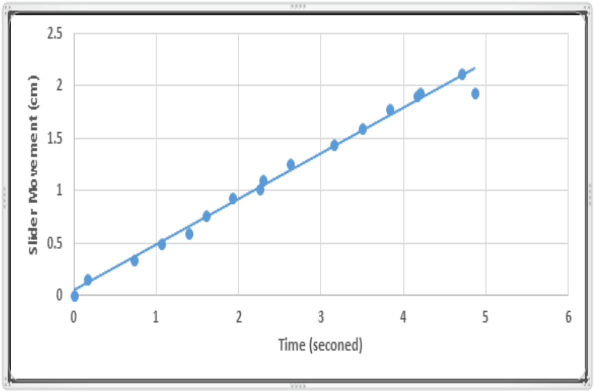

Figure 13. Horizontal movement of the slider versus time.

5.2. Numerical Results

The mechanical properties of the thermoset CFRP which represented the prosthetic foot material are shown in Table 1 in addition to comparison materials (steel and HDPE). The orientation of carbon fiber is selected to be 90^o (which exhibits a higher strength in comparison to other angles) and all mechanical properties are achieved by tensile test as listed from reference.

The loading applied to the prosthetic foot is 846 N which represents the patient weight. The concentrated force is converted to a bearing pressure (107.77 KPa) subjected to a lower disc that has a 10 cm diameter as shown in Figure 14-a, while the fixed support is located at the bottom face of the prosthetic heel made from silicon (for damping purposes) as shown in Figure 14-b. The total number of nodes generated in the mesh model is 5786 nodes.

The values of Von-Mises stress, deformation, shear stress, equivalent strain, and factor of safety that are presented as colored fringes across the main body of the present prosthetic foot made from CFRP are seen in Figures 15, 16, 17, 18, and 19 respectively. The maximum values of different items mentioned later are collected in Table 4 for prosthetic feet made from CFRP, steel, and HDPE materials**.**

The numerical results present higher Von-Mises stress of present CFRP prosthetic foot in comparison with the same foot made from steel, but less than prosthetic foot made from HDPE. These stresses developed in the new foot for different materials which were taken for comparison purposes. A safe design for both CFRP and steel only (reached to more than 15) in comparison to failed foot that made from HDPE.

The new material offers higher deformation and strain reaching maximum values of 0.03137 mm and 94.6 * 10^{-5} respectively so that a more elastic foot during gait phases. Other materials present lower deformations, then as a result more brittle feet are gained against shook pulses from the ground. The CFRP foot exhibits intermediate shear stress between both steel and HDPE.

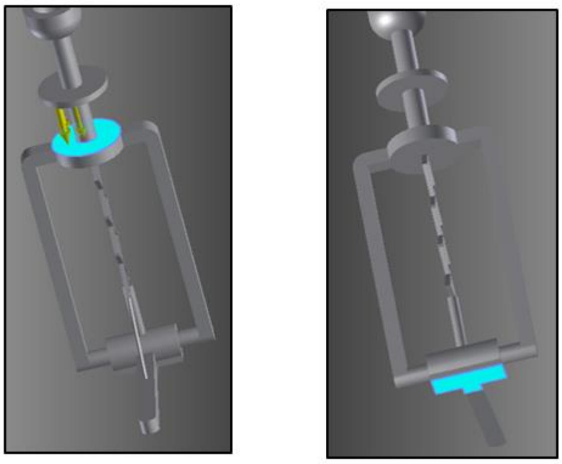

(a) (b)

Figure 14. Loading and Fixation of the prosthetic foot.

(a) Bearing pressure of 107.77 KPa, (b) Fixed support

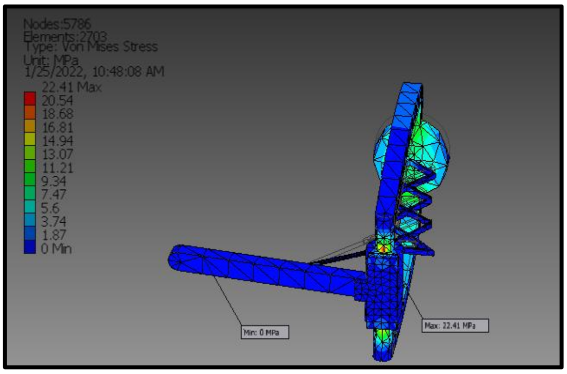

Figure 15. Von-Mises stress in prosthetic foot made from CFRP in MPa.

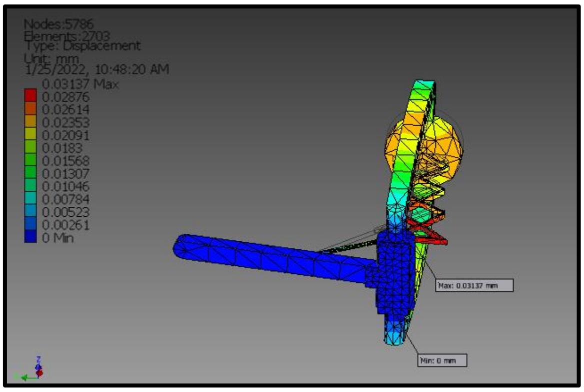

Figure 16. Deformation in prosthetic foot made from CFRP in mm.

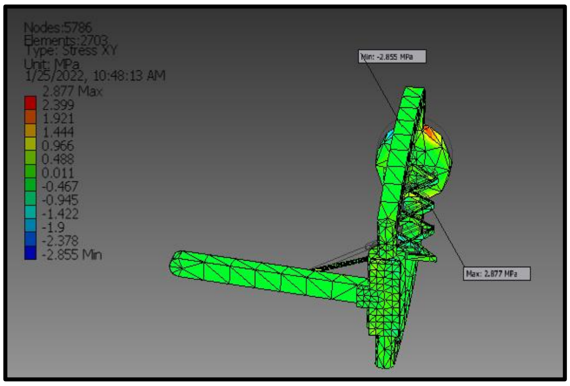

Figure 17. Shear stress in prosthetic foot made from CFRP in MPa.

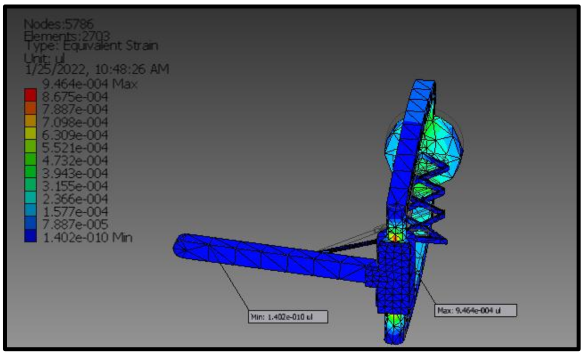

Figure 18. Equivalent strain in prosthetic foot made from CFRP.

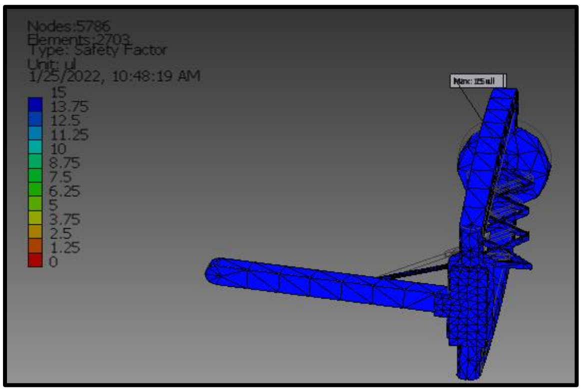

Figure 19. Factor of safety in prosthetic foot made from CFRP.

Table 4. Numerical values of items under study.

Items	CFRP	Steel	HDPE
Maximum Von-Mises stress (MPa)	22.41	10.88	31.19
Maximum Deformation (mm)	0.03137	0.001609	0.001014
Maximum shear stress (MPa)	2.877	1.455	4.272
Maximum equivalent strain	94.6 * 10^{-5}	4.65 * 10^{-5}	2.802 * 10^{-5}
Minimum Factor of Safety	15	15	0.39

6. Conclusions

The main conclusions obtained from the present AAFP can be summarized as follows:

1. High dorsiflexion angle is obtained which reached 8º, showing a good increment of about 2 % that for the nonarticulated foot, and a superior increment reached about 20 % versus SACH foot.
2. Lightweight in comparison to nonarticulated and SACH feet of 39 % and 266 % respectively, in addition to higher resistance to that patient's weight forces and impact resistance are gained due to being manufactured from CFRP.
3. Simplicity in design with mechanically foot return accomplished by no need for any complementary heavy pieces of equipment like springs or dampers.
4. Swing and stance phases time is approached closely to the normal foot, which the differences are 2 % and 4.66 % respectively.
5. Safe rigid design (like steel) but lighter weight and more elastic accomplished with using CFRP material in manufacturing the foot.

References

[1] V. Rajťúková, M. Michalíková, L. Bednarčíková, A. Balogová, and J. Živčák, "Biomechanics of lower limb prostheses," *Procedia engineering,* vol. 96, pp. 382-391, 2014.

[2] T. H. Weerakkody, T. D. Lalitharatne, and R. Gopura, "Adaptive foot in lower-limb prostheses," *Journal of Robotics,* vol. 2017, 2017.

[3] K. K. Resan, H. Ali, A. Hilli, and M. M. Ali, "Design and analysis of a new prosthetic foot for people of special needs," *the Iraqi Journal for Mechanical and Material Engineering,* vol. 11, 2011.

[4] F. Paradisi, A. S. Delussu, S. Brunelli, M. Iosa, R. Pellegrini, D. Zenardi, *et al.*, "The conventional non-articulated SACH or a multiaxial prosthetic foot for hypomobile transtibial amputees? A clinical comparison on mobility, balance, and quality of life," *The Scientific World Journal,* vol. 2015, 2015.

[5] H. S. Mohammed and J. M. Salman, "Design and Modeling the Prosthetic Foot from Suitable Composite Materials," *American Journal of Engineering and Applied Science,* vol. 13, pp. 516-522, 2020.

[6] F. Alfaqs, "Dynamic Behavior of Thin Graphite/Epoxy FRP Simply Supported Beam Under Thermal Load Using 3-D Finite Element Modeling," Jordan Journal of Mechanical and Industrial Engineering, vol. 15, No.3, PP. 301-308, Aug., 2021.

[7] A. Hadi and J. K. Oleiwi, "Improving tensile strength of polymer blends as prosthetic foot material reinforcement by carbon fiber," *Journal of Material Science & Engineering,* vol. 4, pp. 2169-0022.1000158, 2015.

[8] S. G. Ghalme, "Improving Mechanical Properties of Rice Husk and Straw Fiber Reinforced Polymer Composite through Reinforcement Optimization," Jordan Journal of Mechanical and Industrial Engineering, vol. 15, No.5, PP. 411-417, December, 2021.

[9] E. Al-Momani and I. Rawabdeh, "An application of finite element method and design of experiments in the optimization of sheet metal blanking process," Jordan Journal of Mechanical and Industrial Engineering, vol. 2, No. 1, pp. 53-63, March, 2008.

[10] A. Hadoush, "Finite Element Formulation of Internally Balanced Blatz Ko Material Model" , Jordan Journal of Mechanical and Industrial Engineering, Vol. 14, No.2, PP. 215-221, June, 2020.

[11] P. Cherelle, V. Grosu, M. Cestari, B. Vanderborght, and D. Lefeber, "The AMP-Foot 3, new generation propulsive prosthetic feet with explosive motion characteristics: design and validation," *Biomedical engineering online,* vol. 15, pp. 21-36, 2016.

[12] A. J. Young, A. M. Simon, and L. J. Hargrove, "A training method for locomotion mode prediction using powered lower limb prostheses," *IEEE Transactions on Neural Systems and Rehabilitation Engineering,* vol. 22, pp. 671-677, 2013.

[13] W. L. Childers and K. Z. Takahashi, "Increasing prosthetic foot energy return affects whole-body mechanics during walking on level ground and slopes," *Scientific reports,* vol. 8, pp. 1-12, 2018.

[14] X. Bonnet, H. Pillet, P. Fode, F. Lavaste, and W. Skalli, "Finite element modelling of an energy–storing prosthetic foot during the stance phase of transtibial amputee gait," *Proceedings of the Institution of Mechanical Engineers, Part H: Journal of Engineering in Medicine,* vol. 226, pp. 70-75, 2012.

[15] H. Houdijk, D. Wezenberg, L. Hak, and A. G. Cutti, "Energy storing and return prosthetic feet improve step length symmetry while preserving margins of stability in persons with transtibial amputation," *Journal of NeuroEngineering and Rehabilitation,* vol. 15, pp. 1-8, 2018.

[16] B. Brackx, M. Van Damme, A. Matthys, B. Vanderborght, and D. Lefeber, "Passive ankle-foot prosthesis prototype with extended push-off," *International journal of advanced robotic systems,* vol. 10, p. 101, 2013.

[17] N. P. Fey, G. K. Klute, and R. R. Neptune, "The influence of energy storage and return foot stiffness on walking mechanics and muscle activity in below-knee amputees," *Clinical Biomechanics,* vol. 26, pp. 1025-1032, 2011.

[18] T. Kobayashi, M. S. Orendurff, G. Hunt, L. S. Lincoln, F. Gao, N. LeCursi, *et al.*, "An articulated ankle–foot orthosis with adjustable plantarflexion resistance, dorsiflexion resistance and alignment: a pilot study on mechanical properties and effects on stroke hemiparetic gait," *Medical engineering & physics,* vol. 44, pp. 94-101, 2017.

[19] A. Daryabor, M. Arazpour, G. Aminian, M. Baniasad, and S. Yamamoto, "Design and evaluation of an articulated ankle foot orthosis with plantarflexion resistance on the gait: A case series of 2 patients with hemiplegia," *Journal of biomedical physics & engineering,* vol. 10, p. 119, 2020.

[20] M. Alam, I. A. Choudhury, and A. B. Mamat, "Mechanism and design analysis of articulated ankle foot orthoses for drop-foot," *The Scientific World Journal,* vol. 2014, 2014.

[21] A. K. Lapre, "Semi-active damping for an intelligent adaptive ankle prosthesis," 2012.

[22] A. Naseri, M. Mohammadi Moghaddam, M. Gharini, and M. Ahmad Sharbafi, "A Novel Adjustable Damper Design for a Hybrid Passive Ankle Prosthesis," in *Actuators,* 2020, p. 74.

[23] C. Pylatiuk, F. Metzger, R. Wiegand, and G. Bretthauer, "Kinetic energy scavenging in a prosthetic foot using a fluidic system," *Biomedizinische Technik/Biomedical Engineering,* vol. 58, pp. 353-358, 2013.

[24] L. Bowen, J. Vinolas, and J. L. Olazagoitia, "Design and potential power recovery of two types of energy harvesting shock absorbers," *Energies,* vol. 12, p. 4710, 2019.

[25] M. J. Jweeg and S. H. Ameen, "Experimental and Theoretical Investigations of Dorsiflexion Angle and Life of an Ankle-Foot-Orthosis Made From (Perlon/Carbon fiber/Acrylic) and Polypropylene Materials," *Journal of the Japanese Society for Experimental Mechanics,* vol. 11, pp. s305-s310, 2011.

[26] S. H. Ameen, D. M. N. Mahmood, and S. A. Hussein, "Towards an Efficient Electric Pole's Material for Iraqi Electric Network," *Al-Nahrain Journal for Engineering Sciences,* vol. 20, pp. 1198-1206, 2017.

[27] M. M. Ali, "Design and Analysis of a Non-articulated Prosthetic Foot for People of Special Needs," M. Sc. Thesis in Mechanical Engineering, AL-Nahrain University, 2010.

[28] L. C. Smith and B. Hanley, "Comparisons between swing phase characteristics of race walkers and distance runners," *International Journal of Exercise Science,* vol. 6, pp. 269-277, 2013.

JJMIE

Volume 16, Number 4, September. 2022
ISSN 1995-6665
Pages 591 – 600

Jordan Journal of Mechanical and Industrial Engineering

Moving Trajectory Tracking Method of Multi Degree of Freedom Manipulator Based on Particle Filter Algorithm

Pengzhan Zhao

School of Information and Intelligent Manufacturing, Chongqing City Vocational College, Chongqing, 402160, China

Received 16 May 2022 *Accepted 27 Jul 2022*

Abstract

In this study, a moving track tracking method of multi degree of freedom manipulator based on particle filter algorithm is proposed. By constructing the transformation matrix and the Jacobian matrix, the kinematics of the multi degree of freedom manipulator is analyzed. According to the three coordinates of the end of the multi degree of freedom manipulator, the forward kinematics model is solved and the inverse kinematics model is obtained. Particle filter algorithm is adopted to track the moving trajectory of multi degree of freedom manipulator, and the trajectory tracking error is corrected. Experiments show that this method has the advantages of small difference between the trajectory of the multi degree of freedom manipulator and the actual target trajectory, such as high trajectory tracking accuracy and short tracking time, and can meet the requirements of people for the trajectory control accuracy of the joint manipulator. It is expected that this paper can provide valuable references and help for the application field of robots as well as the actual life and production activities.

Keywords: Particle filter algorithm; Multiple degrees of freedom; Mechanical arm; Moving track; Kinematic model.

1. Introduction

The 20th century is the golden age of the rapid development of human science and technology, and major breakthroughs have been made in many fields. Among them, the breakthrough of robot technology is one of the best representatives. Since the 1950s, remarkable achievements have been made in just over a decade. Nowadays, the field of robot service is more and more extensive. For example, its shadow can be seen from the machining of mechanical parts in industry to the sweeping robot in life [1-3]. With the enrichment of application scenarios, the definition of robot has become more and more clear. Especially after entering the new century, the application field of robot has become more and more colorful. Robot control technology as the core technology of robot technology, more and more experts and professionals engaged in this field have invested in the research and work of related contents, and achieved a lot of results. As a kind of robot with obvious structural characteristics, the most basic function of articulated manipulator is to accept instructions and complete basic operations, such as positioning and trajectory tracking. Therefore, the realization of accurate positioning and tracking task is the premise for the articulated manipulator to complete various complex and specific tasks. In practical application, considering the complex structure of the manipulator, the motion system is highly combined, the interference of the working environment and the existence of uncertain factors, such as joint friction. Conventional control strategies are more and more difficult to meet people's requirements for the trajectory control accuracy of articulated manipulator [4,5].

Articulated manipulator is the basic unit of many robots with complex structure. At the same time, it is also the most widely used robot in the field of application. At present, the proportion of articulated robots in the field of robots in the world is more than 50%. The world's first articulated manipulator was born in a laboratory engaged in radioactive material research in the United States. The purpose is to help workers avoid damage to their health caused by direct contact with radioactive materials. The articulated manipulator is mainly composed of base, vertical arm, horizontal arm, terminal unit (hook, claw, suction cup, welding gun, etc.) and joints connecting each arm. Each joint of the manipulator can move independently or cooperatively. The superposition of all these joint movements determines the action of the manipulator [6]. The primary problem to be solved is to realize the positioning control of the manipulator to ensure that the manipulator maintains a desired attitude at the correct time and the operation terminal of the manipulator is in a correct position. In addition, sometimes we need to plan the whole movement process of the manipulator task, that is, the path planning of the manipulator [7]. Accurate trajectory tracking and positioning control is the focus of this paper. Robot control technology, as the brain of robot, plays a very important role. Therefore, the research on robot control technology is of positive significance to industrial production and daily life. In terms of manipulator positioning and trajectory tracking control, people have high requirements for control accuracy and speed. However, many advanced control algorithms need a large number of complex online operations, which greatly

---

* Corresponding author e-mail: zhaopz0000@163.com.

limits the working efficiency of the control system [8]. Moreover, it can be seen from the previous introduction that a large number of advanced control algorithms will use the specific model knowledge of the manipulator or rely on the experience accumulation of experts. However, the structure of the articulated manipulator itself is complex and establishment of an accurate mathematical model is difficult. Moreover, with the operation of the equipment, the state of the manipulator is constantly changing, and there are insufficient experienced relevant talents, which makes it difficult for many excellent control algorithms in theory to be applied in industrial practice. In addition, China has a weak foundation in the field of robot control. Domestic robot control is basically monopolized by foreign companies, and faces foreign technical barriers, which has seriously affected the development of robot control technology in China [9].

In view of the current difficulties in the field of manipulator control, reference [10] proposes a variable gain iterative learning trajectory tracking control method for a three degree of freedom manipulator. The Lagrange method is used to establish the dynamic equation, design a variable gain iterative learning controller for the three degree of freedom manipulator structure, and analyze the convergence to realize the trajectory tracking control of the manipulator. Reference [11] proposes a manipulator trajectory tracking control method based on hybrid interpolation, constructs a three degree of freedom manipulator dynamic model, determines the position and attitude of the manipulator in combination with the reference coordinate system, uses the Lagrange function method to analyze and display the structure of the manipulator, selects the first-order differential Prewitt operator with direction for edge detection, and uses cubic convolution and bicubic interpolation algorithm, Process the edge pixels of the manipulator trajectory, extract the edge information in the movement process of the manipulator, and provide the basis for the tracking of the manipulator trajectory. The fuzzy variable structure compensation method is used to achieve the tracking control of the manipulator trajectory. Reference [12] proposes automatic trajectory tracking control of multi axis series manipulator based on joint angle compensation. Firstly, the spatial pose description and coordinate transformation of multi axis series manipulator are described by rotation matrix, and then the joint angle at the end of multi axis series manipulator is compensated and calculated by joint angle compensation. The expected trajectory of multi axis series manipulator is planned according to the calculation results, and finally the motion variable of multi axis series manipulator is controlled by synovial controller, In this way, the automatic trajectory tracking control of multi axis series manipulator based on joint angle compensation is completed. Reference [13] proposes a manipulator trajectory tracking method based on adaptive robust control. The manipulator structure is designed independently by SolidWorks, the controller is designed according to the designed manipulator parameters, the manipulator control system model is established by Simulink, and the trajectory tracking control is verified under two moving target trajectories of straight line and curve. The adaptive robust control method can control the end trajectory of the manipulator more accurately. Reference [14] proposes a robot trajectory tracking control method based on variable gain active disturbance rejection technology. However, the motion trajectory of the multi degree of freedom manipulator tracked by the above five methods is quite different from the actual target trajectory, the tracking accuracy is low, and it takes a long time to track the motion trajectory, resulting in poor tracking effect and low efficiency.

To this end, this paper presents a moving trajectory tracking method of multi degree of freedom manipulator based on particle filter algorithm, and the feasibility of this method is verified by simulations. This study has a very positive significance for the application field of robot and the actual life and production activities.

2. Moving trajectory tracking method of multi degree of freedom manipulator

2.1. Kinematic analysis and model establishment

Motion trajectory refers to the spatial characteristics of the action composed of the route that a part of an object passes from the starting position to the end, which is expressed by the direction, form and amplitude of the motion trajectory. From the perspective of mechanics, the object has only 6 degrees of freedom in space. The general special manipulator has only 2 ~ 4 degrees of freedom, while the general manipulator has mostly 3 ~ 6 degrees of freedom. The realization of trajectory tracking control of multi degree of freedom manipulator is based on kinematic analysis, which is to transform the expected trajectory in Cartesian space and the joint angle in joint space [15].

(1) Transformation matrix

Usually, a fixed coordinate system is defined on each link of a multi degree of freedom manipulator, and the two adjacent coordinate systems can represent each other. Generally, their relative positions are described by the transformation matrix between the two adjacent links. The connecting rod is numbered from the fixed base of the multi degree of freedom manipulator. Generally, the coordinate system at the fixed base is O_0, and so on. Therefore, the coordinate system on the connecting rod i is O_i, and Fig. 1 shows the schematic diagram of the position and attitude of the connecting rod [16].

The coordinate system of all links can be established in sequence according to the following steps:

1. Find out the joint axis corresponding to each connecting rod and extend it in the direction of its axis.
2. Find out the common vertical line between joint axis $i-1$ and joint axis i or the intersection of joint axis $i-1$ and joint axis i, and establish the coordinate system with the intersection of the common vertical line and joint axis or the intersection of joint axis $i-1$ and joint axis i as the origin of connecting rod coordinate system O_i.
3. Specify that the direction of the Z_i axis is the direction of the i axis [17].
4. Specify that axis X_i points from joint axis $i-1$ to joint axis i along the direction of the common vertical line between joint axis $i-1$ and joint axis i. if joint axis $i-1$ and joint axis i intersect, specify that axis

X_i is perpendicular to the plane of joint axis $i-1$ and joint axis i.

5. The Y_i-axis direction is determined by the right-hand rule based on the X_i-axis and Z_i-Axis directions.
6. In special cases, when the first joint variable is 0, coordinate system O_0 and coordinate system O_1 coincide. For coordinate system O_n, the origin and the direction of axis X_n can be arbitrarily selected. When selecting, the connecting rod parameter is usually 0.

According to the provisions established by the coordinate system, when the Z_i axis coincides with the axial direction of joint i, the direction of Z_i can be selected from axial direction and reverse extension line direction, and either one can be selected without affecting the final result. When the two joint axes intersect, it is impossible to determine which joint axis is in the front and which is in the back. The direction of the X_i axis cannot be defined according to the rules. It can be selected arbitrarily among the two possibilities. Then, on the basis of the previous determination, the direction of the Y axis is determined based on the right-hand rule. When the joint axis $i-1$ is parallel to the joint axis i, the origin position of the coordinate system O_i can be selected arbitrarily [18]. Therefore, the choice of coordinate system is arbitrary.

In Figure 1, a_i represents the positive direction along the X_i axis, and the distance from the Z_{i-1} axis to the Z_i axis; α_i represents the positive rotation around the X_i axis, and the angle value from Z_{i-1} to Z_i; d_i represents the direction along the Z_{i-1} direction as Positive, the distance from X_{i-1} to X_i; θ_i represents the angle value of the positive rotation around the Z_{i-1} axis, from X_{i-1} to X_i. a_{i+1} is usually set to $a_i > 0$ because a_i corresponds to distance, but the value of α_i, d_i, θ_i can be positive or negative. The coordinate system O_i can be regarded as the coordinate system O_{i-1} rotates α_i degrees around X_{i-1}, denoted as A_{Rx}; then translates a_i along X_{i-1}, denoted as A_{Tx}; then translates d_i along Z_i, denoted as A_{Tz}; and finally rotates around Z_i by O_i degrees, Denoted as A_{Rz}. According to these four steps, the method of relative position movement of two adjacent links is recorded as the standard D-H method [19].

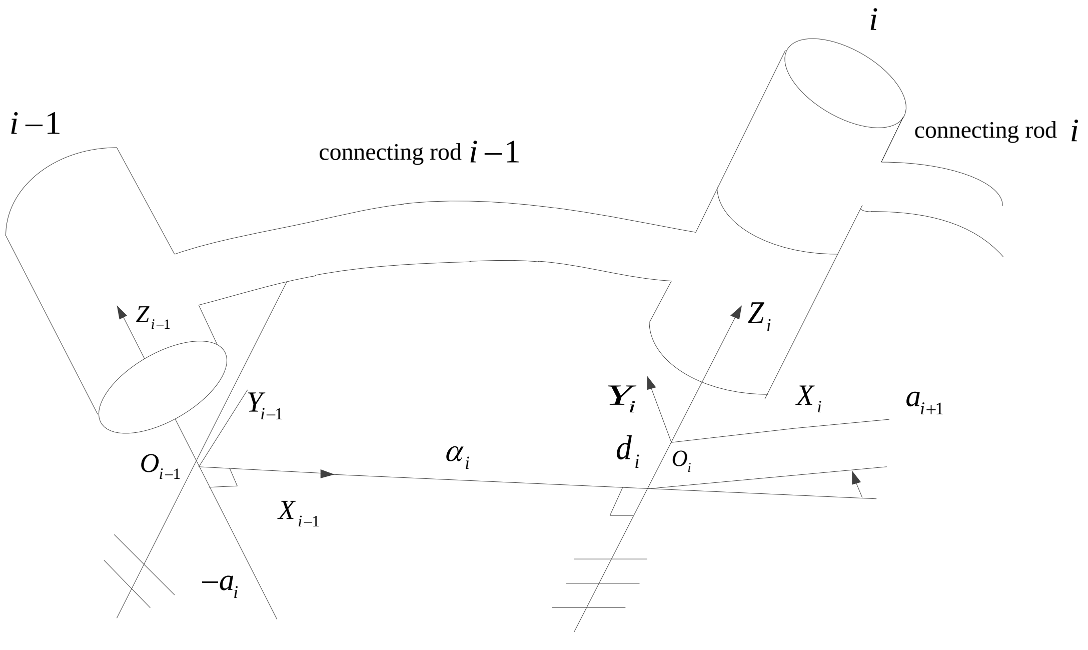

Figure 1. Schematic diagram of four parameters and coordinate system of connecting rod

The specific forms of A_{Rz}, A_{Tz}, A_{Tx} and A_{Rx} are as follows:

$$A_{Rz} = \begin{pmatrix} \cos\theta_i & -\sin\theta_i & 0 & 0 \\ \sin\theta_i & \cos\theta_i & 0 & 0 \\ 0 & 0 & 1 & 0 \\ 0 & 0 & 0 & 1 \end{pmatrix} \tag{1}$$

$$A_{Tz} = \begin{pmatrix} 1 & 0 & 0 & 0 \\ 0 & 1 & 0 & 0 \\ 0 & 0 & 1 & d_i \\ 0 & 0 & 0 & 1 \end{pmatrix} \tag{2}$$

$$A_{Tx} = \begin{pmatrix} 1 & 0 & 0 & a_i \\ 0 & 1 & 0 & 0 \\ 0 & 0 & 1 & 0 \\ 0 & 0 & 0 & 1 \end{pmatrix} \tag{3}$$

$$A_{Rx} = \begin{pmatrix} 1 & 0 & 0 & 0 \\ 0 & \cos\alpha_i & -\sin\alpha_i & 0 \\ 0 & \sin\alpha_i & \cos\alpha_i & 0 \\ 0 & 0 & 0 & 1 \end{pmatrix} \tag{4}$$

The coordinate system O_{i-1} corresponding to the connecting rod $i-1$ is transformed into the transformation matrix A_i of the coordinate system O_i corresponding to the connecting rod i to express as follows:

$$A_i = A_{Rz} \times A_{Tz} \times A_{Tx} \times A_{Rx} = DH(\theta_i, d_i, a_i, \alpha_i) \tag{5}$$

It is easy to find by substituting A_{Rz}, A_{Tz}, A_{Tx} and A_{Rx} into the above equation:

$$A_i = \begin{pmatrix} \cos\theta_i & -\cos\alpha_i \sin\theta_i & \sin\alpha_i \sin\theta_i & \alpha_i \cos\theta_i \\ \sin\theta_i & \cos\theta_i \cos\alpha_i & -\sin\alpha_i \cos\theta_i & \alpha_i \sin\theta_i \\ 0 & \sin\alpha_i & \cos\alpha_i & d_i \\ 0 & 0 & 0 & 1 \end{pmatrix} \tag{6}$$

(2) Jacobian matrix

The relationship between the linear velocity of the end of the multi-degree-of-freedom manipulator in Cartesian space and its joint angular velocity in joint space is represented by the Jacobian matrix.

The equation assumption of the desired trajectory of the end of the manipulator is shown in equation (7):

$$x = x(q) \tag{7}$$

In the formula, x represents the trajectory of the end of the manipulator in Cartesian space, and q denotes the rotation angle of each joint of the manipulator in the joint space [20]. The relationship between q and x is obtained by derivation of time on both sides of the above formula, as shown in formula (8):

$$x' = J(q)q' \tag{8}$$

In the formula, x' is the velocity of the end of the manipulator in Cartesian space; q' is the angular velocity of the rotation of each joint of the manipulator in the joint space; $J(q)$ is the Jacobian matrix of the manipulator. The elements in row i and column j of this matrix are:

$$J_{ij}(q) = \frac{\partial x_i(q)}{\partial q_j} \tag{9}$$

According to the above analysis, the inverse kinematics model of the multi degree of freedom manipulator is established, which lays the foundation for the next multi degree of freedom manipulator trajectory tracking.

Set θ_i to represent the joint angle (joint displacement), b and c to represent the distance between the center of gravity of the second link and the third link relative to the joint axis, and m_i, I_i, L_i to represent the mass, moment of inertia and length of each link, respectively [21]. Obtain the three coordinate values of the end of the manipulator:

$$\begin{cases} x = (L_2 \cos\theta_2 + L_3 \cos(\theta_2 + \theta_3)) \cos\theta_1 \\ y = (L_2 \cos\theta_2 + L_3 \cos(\theta_2 + \theta_3)) \sin\theta_1 \\ z = L_1 + L_2 \sin\theta_2 + L_3 \sin(\theta_2 + \theta_3) \end{cases} \tag{10}$$

Where x, y, z is the coordinate value of the end of the manipulator in the X-axis, Y-axis and Z-axis directions, respectively.

The inverse kinematics model can be obtained by solving the forward kinematics model, which is easily obtained by dividing the second formula by the first formula in formula (10):

$$\theta_1 = \arctan(\frac{y}{x}) \tag{11}$$

It is also easy to obtain from formula (10):

$$\begin{cases} \dfrac{x}{\cos\theta_1} = L_2 \cos\theta_2 + L_3 \cos(\theta_2 + \theta_3) \\ z - L_1 = L_2 \sin\theta_2 + L_3 \sin(\theta_2 + \theta_3) \end{cases} \tag{12}$$

By squaring both sides of the above equation (12) and adding them together, we can obtain:

$$\theta_3 = \arctan\left[((x/\cos\theta_1)^2 + (z - L_1)^2 - L_2^2 - L_3^2) / 2L_2L_3\right] \tag{13}$$

Expand the right side of the equal sign in formula (12) to get:

$$\begin{cases} \dfrac{x}{\cos\theta_1} = (L_2 + L_3 \cos\theta_3) \cos\theta_2 - L_3 \sin\theta_3 \sin\theta_2 \\ z - L_1 = (L_2 + L_3 \cos\theta_3) \sin\theta_2 + L_3 \sin\theta_3 \sin\theta_2 \end{cases} \tag{14}$$

Solving the above equation system can get:

$$\theta_2 = \arctan\left(\frac{(z - L_1)(L_2 + L_3 \cos\theta_3) - (x/\cos\theta_1) L_3 \sin\theta_3}{(x/\cos\theta_1)(L_2 + L_3 \cos\theta_3) + (z - L_1) L_3 \sin\theta_3} \right) \tag{15}$$

Finally, the solution of the positive kinematics formula (10) can be obtained by sorting out:

$$\begin{cases} \theta_1 = \arctan(\frac{y}{x}) \\ \theta_2 = \arctan\left(\frac{(z-L_1)(L_2+L_3\cos\theta_3)-(x/\cos\theta_1)L_3\sin\theta_3}{(x/\cos\theta_1)(L_2+L_3\cos\theta_3)+(z-L_1)L_3\sin\theta_3}\right) \\ \theta_3 = \arctan\left[((x/\cos\theta_1)^2+(z-L_1)^2-L_2^2-L_3^2)/2L_2L_3\right] \end{cases} \quad (16)$$

2.2. Trajectory tracking of multi-degree-of-freedom manipulator based on particle filter algorithm

The particle filter algorithm is a very common algorithm in the tracking field of multi-degree-of-freedom manipulators in recent years. Particle filter is a method for Bayesian estimation based on sampling Monte Carlo. Monte Carlo method is a statistical method, which is based on the probability model and estimates the unknown characteristic quantity through many simulation experiments [22]. Bayesian estimation is the use of Bayesian theorem combined with new evidence and previous prior probability to get a new probability [23].The core is to use Monte Carlo method to modify the prior probability density obtained by the target motion model based on statistical principles based on the theorem of large numbers [24]. The basic process is: first, based on the prior conditional distribution of state variables, and sampling according to certain rules in the prior probability distribution, the samples are particles. Then use the new measurement value for correction, and this posterior density distribution will be used as the prior probability density of the next recursive process to complete the parameter estimation process.

The probability density function $P(x_t | z_{1:t})$ is represented by a finite set of weighted particles $(s_t^{(i)}, w_t^{(i)})$. Among them, $s_t^{(i)}$ is the sampled particle, and $w_t^{(i)}$ is the corresponding weight of the particle. The algorithm is divided into the following three basic steps:

(1) Sampling

Select N particles from the previous set of particles $s_{t-1}^{(n)}$ to form a new set of sample particles $s_t^{(n)}$. State variables with high weights will be sampled multiple times, while state variables with low weights may not be sampled. This ensures the validity of the sample. The number of particles usually depends on the dimensionality of the state space [25]. The larger the number of particles, the better the true posterior density is reflected, and the more accurate the tracking results are. However, too many particles will increase the amount of calculation, make the processing time of the system longer, and affect the rapidity of tracking; while too few particles will make the predicted state variables too small, so that the particles that match the actual state of the observed object cannot be generated.

(2) Prediction

In order to generate more effective prediction particles, the standard random variable η is added to the particles obtained in step (1), so that the particles repeatedly sampled at the same place are separated, which is:

$$s_t^{(n)} = s_t^{(n)} + \eta \quad (17)$$

This new set of particles can be viewed as an approximate set of samples randomly selected from the prior probability density function $P(x_t | z_{1:t-1})$.

(3) Update

According to a set observation model, the similarity of each sample is calculated, and the weight of the sample is configured accordingly. The observation model must be able to truly reflect the similarity between the particle state and the actual observed state, and be simple and universal. At the same time, the type and parameters of the introduced noise must be moderate, so that the prediction process of the particle is neither so large that it exceeds the range of motion, nor so small that it cannot keep up with the motion of the object [26]. Finally, normalize the weights such that:

$$\sum_{i=0}^{N} \omega_t^{(n)} = 1 \quad (18)$$

Therefore, this paper uses the particle filter algorithm to track the movement trajectory of the multi-degree-of-freedom manipulator.

Using particle filter algorithm to track the trajectory of multi degree of freedom manipulator requires the particle filter tracking framework to be built. The particle filter tracking framework provides attachment conditions for the construction of the multi-DOF manipulator trajectory tracking environment. To guarantee that the hidden layer organization can maintain a benign distribution state, the framework structure mainly includes target change description, state Variables work together to handle two main functions. Among them, the target change description is the basic execution function of the particle filter tracking framework. The hidden layer organization will make every part that affects the movement trajectory of the manipulator set as a co-node. In a period of time, the displacement difference between the head node and the tail node is the motion displacement of the movement trajectory of the robot arm, and the motion curve between the head node and the tail node is the movement trajectory of the robot arm. The specific tracking process is shown in Figure 2.

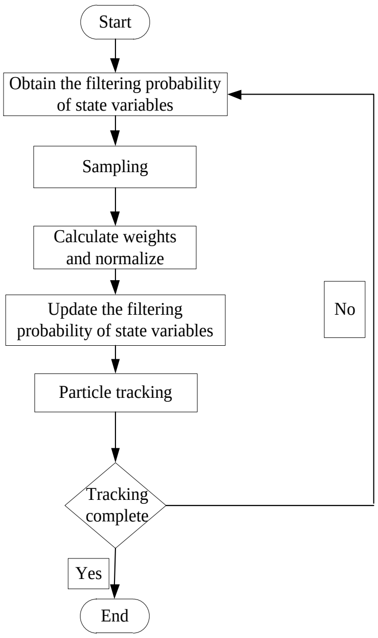

Figure 2. Particle filter tracking flow chart

Assuming that at time $k-1$, the filtering probability distribution of the state variable x_{k-1} of the manipulator is:

$$P(x_{k-1}|z_{0:k}) = \sum_{i=1}^{G} \omega_{k-1} N(x_{k-1}, u_{k-1}, \sum k-1) \quad (19)$$

When the measured observations at time k are obtained, the probability distribution can be expressed as:

$$P(x_k|z_{0:k}) = C_k \sum_{i=1}^{G} \omega_{ki} N(x_{k-1}, u_{k-1}, \sum k-1) \quad (20)$$

Sample x_{ki}^j is drawn using the importance function, weights ω_{ki}^j are calculated, and Monte Carlo estimates of the mean u_{ki} and covariance $\sum k-1$ of x_{ki} are obtained. Then the filtering probability distribution of the state variables of the manipulator at time k after the update is approximately expressed as:

$$P(x_k|z_{0:k}) \approx \sum_{i=1}^{G} \omega_{ki} N(x_k, u_{ki}, \sum ki) \quad (21)$$

Then the predicted probability distribution of the state variable at time $k+1$ is:

$$P(x_k|z_{0:k}) = \sum_{i=1}^{G} \omega_{(k+1)i} N(x_{k+1}, u_{(k+1)i}, \sum (k+1)i) \quad (22)$$

Assuming that there are G sums of Gaussian terms, the importance function required for the sample collection of the manipulator is $q = P(x_k|z_{0:k-1})$, and the importance function is sampled to obtain the sample point set x_{ki}^j and calculate the sample weight ω_{ki}^j, the main process is as follows:

1. Measurement update process:

- The approximate filtering probability distribution of the state variables of the $k-1$ manipulator is known. When the measured observation value of the moving manipulator at time k is obtained, the probability distribution function can be expressed by equation (18).
- Calculate the Monte Carlo estimation of the filter mean u_{ki} and covariance $\sum ki$ of the multi-degree-of-freedom manipulator sample point set x_{ki}^j at time k:

$$u_{ki} = \frac{\sum_{j=1}^{M} \omega_{ki}^j x_{ki}^j}{\sum_{j=1}^{M} \omega_{ki}^j} a \quad (23)$$

$$\sum ki = \frac{\sum_{j=1}^{M} \omega_{ki}^j (x_{ki}^j - u_{ki})(x_{ki}^j - u_{ki})^T}{\sum_{j=1}^{M} \omega_{ki}^j} \quad (24)$$

Update the weights and normalize the weights:

$$\bar{\omega}_{ki} = \frac{\bar{\omega}_{ki}}{\sum_{i=1}^{G} \bar{\omega}_{ki}} \quad (25)$$

2. Forecast update process:

- (1) Based on the measurement and observation of the multi-degree-of-freedom manipulator at time k, the state particle $x_{(k+1)i}$ at time $k+1$ is obtained by sampling from the state transition distribution $p(x_{(k+1)i} / x_{ki})$ of $i = 1, 2, ..., G$ in turn.

  (2) Update the weights

$$\bar{\omega}_{(k+i)i} = \omega_{ki} \quad (26)$$

3. Calculate the Monte Carlo estimation of the filter mean $\bar{u}_{(k+i)i}$ and the covariance $\sum (k+1)i$ of the multi-degree-of-freedom manipulator sample point set x_{ki}^j at time $k+1$:

$$\bar{u}_{(k+i)i} = \frac{1}{M} \sum_{i=1}^{M} x(k+1)i \quad (27)$$

$$\sum (k+1)i = \frac{1}{M} \sum_{i=1}^{M} (\bar{u}_{(k+i)i} - x_{(k+i)i}) \quad (28)$$

4. From equation (21), we can get the approximate filtering probability distribution of the state variables of the manipulator at time k+1, and the measurement update process at time k+1 is returned.

According to the above update process, set the tracking conditions for the movement trajectory of the manipulator:

$$w = \frac{x_1 x_1}{2} \sum_{i=1}^{M} \zeta (e_1 - e_2)^2 \quad (29)$$

In the formula, i represents the lower limit execution parameter of the transport trajectory node, e_1, e_2 represents the filter coefficient related to the change description and state variable co-processing, and ζ represents the standard power term coefficient of data processing.

The tracking error of the movement trajectory of the multi-degree-of-freedom manipulator is a physical parameter condition related to the particle filter, which can fully express the highest quality value focal element of the positioning removal advantage, and can also define the low quality assumption coefficient of the autonomous robot movement and displacement tending to the degenerate value. Let d represent the ideal calibration physical vector of the particle filter, and ζ represent the operating conditions of the moving trajectory of the manipulator. Combined with the above equations, the tracking error coefficient of the moving trajectory of the manipulator can be expressed as:

$$\varphi = 1 - \prod (1 - d g^{\varepsilon} \gamma j) \quad (30)$$

In the formula, g represents the maximum displacement difference allowed by the movement trajectory of the manipulator, ε represents the power term parameter related to the displacement difference, and γ represents the relevant correction coefficient. On the basis of formula (30), set θ to represent the upper threshold of paranoid co-processing, and φ to represent the lower threshold of paranoid co-processing, then formula (31) reflects the complete multi-DOF manipulator trajectory tracking error correction result.

$$m = \int_{\varphi}^{\theta} \frac{\lambda - u}{\sqrt{kz - x_v}} \tag{31}$$

Where λ denotes the maximum value of the tracking error coefficient of the movement trajectory of the manipulator in the ideal state, K represents the permission coefficient of cooperative processing, z represents the order of magnitude condition of the movement trajectory of the manipulator, and x_v represents the correction offset of Co-processing variance at v.

3. Simulation experiment analysis

The 6-DOF AUBO i5 lightweight robotic arm has the characteristics of light weight and high precision. The positioning accuracy can reach 0.05mm. It adopts open software architecture and can integrate existing software and algorithms; the mobile target is the built-in gc-cc-306 high-precision micro magnetic basic sensor electric drive device box, as shown in Figure 3.

In order to verify the effectiveness of the proposed tracking method, a six-degree-of-freedom AUBO i5 light manipulator was selected as the experimental object to conduct a simulation experiment. Figure 4 shows the scene diagram of the experimental platform, and the location distribution of each part is shown in the mark. The moving target moves in the plane space relative to the base frame, and its motion trajectory is tracked. The experimental operation procedure is controlled by the upper computer program developed based on the VS++ platform.

The binocular camera in the experimental platform consists of two CMOS cameras, the model is Micron AR0330, as shown in Figure 5; the parameters are: focal length 8 mm; pixel size 5.07 μm*3.38 μm; the highest resolution is 2048*1536; It is connected to the host computer through a USB type data line, and the sampling frequency is 30 frames per second.

(a) Robotic arm

(b) Moving objects

Figure 3. Robotic arm and moving target

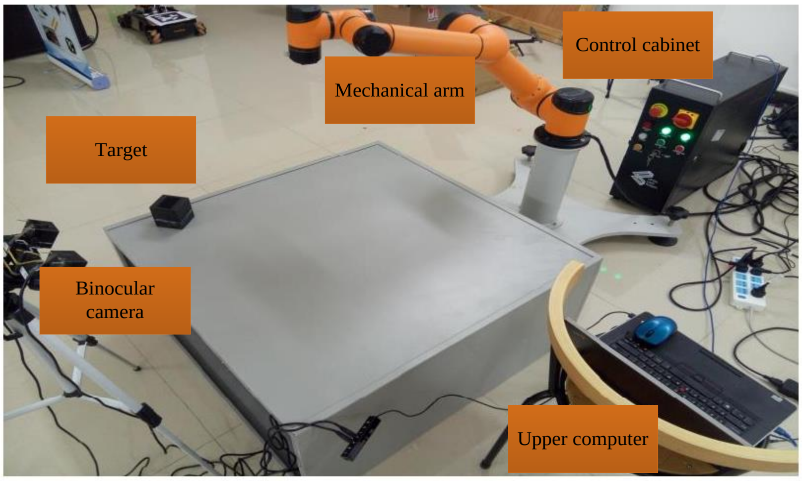

Figure 4. Experimental platform

Figure 5. Camera equipment

The actual motion trajectory of the 6-DOF manipulator target is a cosine curve, as shown in Figure 6. After obtaining the image information, the vision system performs image preprocessing to obtain image features, then stereo matches depth information, and then combines the information with the motion model to obtain the estimated value and filters to obtain the required amount of feedback. The feedback amount is transmitted to the upper computer control program, the joint variable information is obtained through the kinematics solution of the robot arm, and then the API function interface provided by the robot controller is called to realize the realization, and finally the motion of the robot arm is realized through the servo driver. The whole process is closed-loop continuous reciprocating.

Through this method and literature [8], a variable gain iterative learning trajectory tracking control method for 3-DOF manipulator is proposed, and the automatic trajectory tracking control and reference of multi axis series manipulator based on joint angle compensation proposed in literature [9] The robot arm trajectory tracking method based on adaptive robust control proposed in document [10] tracks the motion trajectory of the six degree of freedom robot arm, and the robot trajectory tracking control method based on variable gain active disturbance rejection technology proposed in document [11] tracks the robot arm trajectory, and compares the tracking trajectory results with the actual target trajectory. The comparison results are shown in Figure 7.

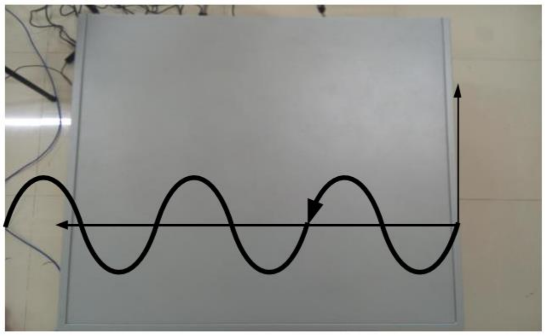

Figure 6. Target trajectory

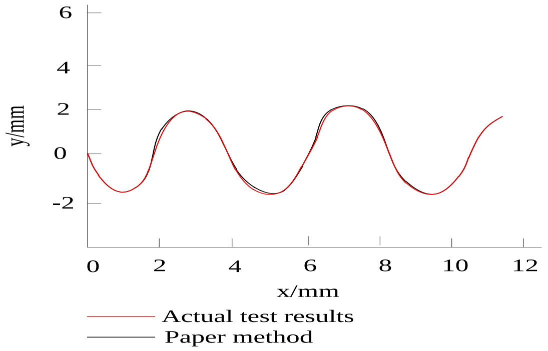

(a) Tracking results of our method

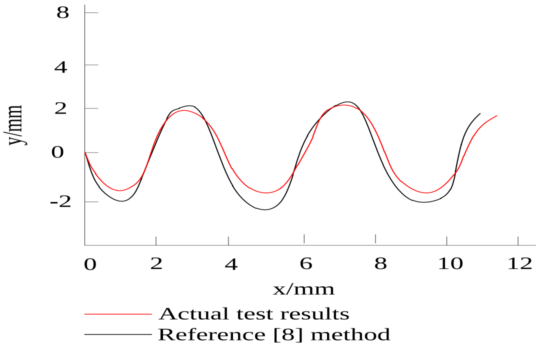

(b) Tracking results of the method in Reference [8]

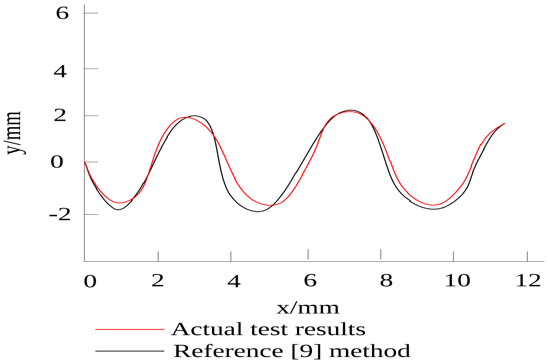

(c) Tracking results of the method in Reference [9]

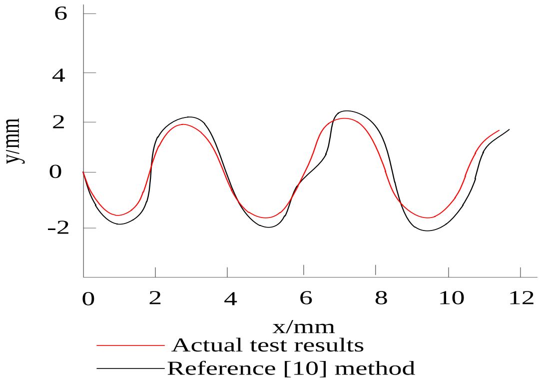

(d)Tracking results of the method in Reference [10]

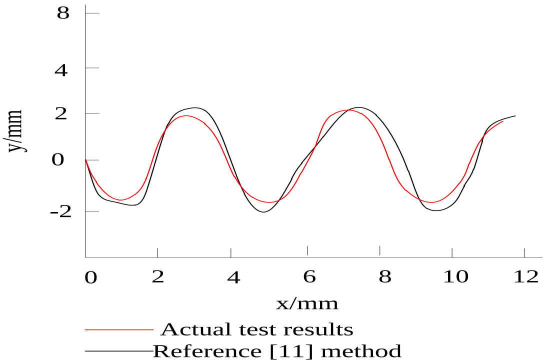

(e) Tracking results of the method in Reference [11]

Figure 7. The tracking results of the three methods and the actual target trajectory error

According to Figure 7, Compared with the methods proposed in references [8], [9], [10] and [11], the error between this method and the actual target trajectory tracking results is small, close to 100%, indicating that this method has high accuracy for the trajectory tracking of six degree of freedom manipulator.

The tracking time of the proposed method is compared with the methods in references [8], [9], [10] and [11], as shown in Figure 8.

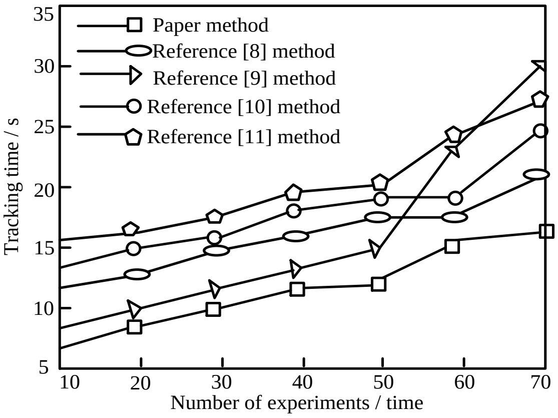

Figure 8. Tracking time of the movement trajectory of the 6-DOF manipulator by the three methods

According to Figure 8, the proposed method takes less than 15s to track the movement trajectory of the 6-DOF robot arm, while the tracking time of the reference [8],[9],[10] and [11] method and the reference [9] method is within 30s ,28s, 25s and 20s, respectively.

4. Conclusion

The control of multi-degree-of-freedom manipulators can usually be divided into two types: fixed-point position control and movement trajectory tracking control. Fixed-point position control is mainly used to complete point-to-point operations, such as handling, loading and unloading, spot welding, etc. The tracking control of the movement trajectory of the multi-degree-of-freedom manipulator needs to design a control strategy to make each joint of the manipulator run according to the expected movement trajectory. During the operation, it is necessary to ensure that the tracking error is as close to zero as possible and the system is stable, mainly to meet some accuracy requirements. Nowadays, high and repetitive jobs such as part machining, assembly, grinding, etc. with the increasing demand for socialized mass production, multi-degree-of-freedom manipulators are playing an increasingly important role in various fields, many of which require high-speed, high-precision tracking control of moving tracks. However, the multi-degree-of-freedom manipulator system is a complex nonlinear system. Its parameter uncertainty, strong coupling, internal friction and external disturbance make it difficult to establish an accurate dynamic model. Therefore, this paper proposes a multi-DOF manipulator trajectory tracking method based on the particle filter algorithm. However, when analyzing the tracking problem of multi-degree-of-freedom manipulators, the control algorithm only learns a specific trajectory and realizes the trajectory tracking. When the expected trajectory changes, the algorithm must perform new learning, and the control algorithm lacks due generalization ability, which needs further research and discussion.

Acknowledgment

Project Scientific and Technological Research Program of Chongqing Municipal Education Commission "Research on Teaching Virtual Simulation System of Intelligent Manufacturing Production Line Based on Digital Twins" (No.KJQN202203903)."

References

[1] Q. Wang, L. Xi, "Motion Planning of Palletizing Manipulator Joint Velocity Deviation Correction Based on SSD". Computer Simulation, Vol. 38, no. 7, 2021, 340-344.

[2] J.W. Guo, Y.B. Lv, H. Zhang, "Coordinated Gait Control of Snake Like Robot Based on Electromechanical Tracking". Jordan Journal of Mechanical and Industrial Engineering, Vol. 16, No.1, 2022, 87-95.

[3] G.B. Si, X.F. Jin, C.X. Wang, "Gait Control System of Autonomous Mobile Robot Based on PMAC". Jordan Journal of Mechanical and Industrial Engineering, Vol. 16, No.1, 2022, 31-40.

[4] F. Reynoso, P. Suarez, O. Sanchez et al, "A Custom EOG-Based HMI Using Neural Network Modeling to Real-Time for the Trajectory Tracking of a Manipulator Robot". Frontiers in Neurorobotics, Vol. 14, 2020, 578834-578842.

[5] Z.H. Meng, "Trajectory Tracking Control Algorithm of Six Degrees of Freedom Industrial Robot". Jordan Journal of Mechanical and Industrial Engineering, Vol. 16, No.1, 2022, 97-104.

[6] L. Kshetrimayum, K. R. Binoy, S. Bidyadhar, "Use of memristive chaotic signal as a desired trajectory for a two-link flexible manipulator using contraction theory based on a composite control technique". The European Physical Journal - Special Topics, Vol. 228, No. 10, 2019, 2215–2231.

[7] L. Chen, Y. Ma, Y. Zhang et al., "Obstacle Avoidance and Multitarget Tracking of a Super Redundant Modular Manipulator Based on Bezier Curve and Particle Swarm Optimization". Chinese Journal of Mechanical Engineering, Vol. 33, No. 05, 2020, 111-129.

[8] X.Q. Ma, L.J. Wang, "Control algorithm of stacking manipulator based on dead time compensation". Mechanical design and research, Vol. 37, No.1, 2021, 215-218

[9] W. Yintang, G. Linqi, L. Fucai et al., "Model-free adaptive control of space manipulator under different gravity environment". High tech communication: English version, Vol. 26, No. 1, 2020, 8-16.

[10] G. Wang, Y.J. Song, W.S. Tang, et al., "Trajectory tracking control of three degree of freedom manipulator based on iterative learning". Journal of Jilin University: Information Science Edition, Vol. 39, No. 4, 2021, 389-396

[11] Z.Y. Che, J.R. Wang, X.S. Wu, "Trajectory tracking control method of manipulator based on hybrid interpolation". Science and Technology Bulletin, No. 10, 2020, 6-9.

[12] M.Z. Duan, W. Zhang, "Automatic trajectory tracking control of multi axis series manipulator based on joint angle compensation." Automation application, No. 3, 2021, 20-22.

[13] C. Zhang, Z. Zhang, "Application of Adaptive Robust Control of the Manipulator Trajectory Tracking". Modular Machine Tool & Automatic Manufacturing Technique, No. 1, 2019, 86-89, 93.

[14] L. Zhang, K. Lu, C.X. Gao, et al., "Path Tracking Control Method of Robot Based on Time-Varying Gain Active Disturbance Rejection Control". Acta Electronica Sinica, Vol. 50, No. 1, 2022, 89-97.

[15] G. M. Andaluz, L. Morales, P. Leica, et al., “LAMDA Controller Applied to the Trajectory Tracking of an Aerial Manipulator”. Applied Sciences, Vol. 11, No. 13, 2021, 5885-5893.

[16] Welabo, G. Tesfamariamr, “Trajectory Tracking Control of UR5 Robot Manipulator Using Fuzzy Gain Scheduling Terminal Sliding Mode Controller”. Journal of Mechatronics and Robotics, Vol. 4, No. 1, 2020, 113-135.

[17] Y. Xia, W. Xie, J. Ma, “Research on trajectory tracking control of manipulator based on modified terminal sliding mode with double power reaching law”. International Journal of Advanced Robotic Systems, Vol. 16, No. 3, 2019, 172988141984789-172988141984789.

[18] Q. Yao, “Robust finite-time trajectory tracking control for a space manipulator with parametric uncertainties and external disturbances”. Proceedings of the Institution of Mechanical Engineers Part G Journal of Aerospace Engineering, 2021, 095441002110147-095441002110147.

[19] P. Wang, D. Zhang, B. Lu, “Trajectory tracking control for chain-series robot manipulator: Robust adaptive fuzzy terminal sliding mode control with low-pass filter”. International Journal of Advanced Robotic Systems, Vol. 17, No. 3, 2020, 172988142091698-172988142091698.

[20] M. Abdallah, R. Fareh, “Fractional order active disturbance rejection control for trajectory tracking for 4-DOF serial link manipulator”. International Journal of Modelling Identification and Control, Vol. 36, No. 1, 2020, 57-64.

[21] R. Liu, X. Chen, “Monte Carlo method in polymerization process”. Journal of chemical engineering of colleges and universities, Vol. 35, No. 3, 2021, 389-399

[22] X.Y. Han, Z.Z. Cai, Y.L. Zhu, “Bayesian estimation of dynamic panel model in threshold space and its application”. Research on quantitative economy and technical economy, Vol. 10, 2021,148-166

[23] L. Wang, S. Cui, C. Ma, et al., “Compound Impedance Control of a Hydraulic Driven Parallel 3UPS/S Manipulator”. Chinese Journal of Mechanical Engineering: English Edition, Vol. 33, No. 4, 2020,14-20.

[24] M. Zhu, L. Ye, X. Ma, “Estimation-based quadratic iterative learning control for trajectory tracking of robotic manipulator with uncertain parameters”. IEEE Access, 2020, 99.

[25] L. Su, Q. Hu, L. Zhang, “Recursive Decentralized Control for Trajectory Tracking of Flexible Space Manipulators”. IEEE Access, 2019, 39192-39206.

[26] Y. Dai, S. Yu, Y. Yan et al., “An EKF-based Fast Tube MPC Scheme for Moving Target Tracking of a Redundant Underwater Vehicle-Manipulator System”. IEEE/ASME Transactions on Mechatronics, 2019, 99.

JJMIE

Volume 16, Number 4, September. 2022
ISSN 1995-6665
Pages 601 – 613

Jordan Journal of Mechanical and Industrial Engineering

Utilizing AHP-TOPSIS as Multi-Criteria Decision Approaches to Select the Best Alternative for Waste to Energy Technology

Nader Al Theeb[*] , Hani Abu Qdais, Farah H. Abu Qdais, Omar Habibah

Jordan University of Science and Technology, Irbid, Jordan 22110

Received 12 Jun 2022 *Accepted 20 Jul 2022*

Abstract

The main purpose of this study is to provide the decision makers in Jordan with a methodology to choose the most competitive waste to energy technology. The study used a Multi-Criteria Decision Making (MCDM) procedure of both Analytical Hierarchy Process (AHP) alone using Expert Choice software and the combination of AHP and the technique for order of preference by similarity to ideal solution (AHP-TOPSIS). The integration between the AHP and the TOPSIS is the main contribution of this research. Four waste to energy options were evaluated using three main criteria: environmental, technical, and socioeconomic; with three sub-criteria under each main criterion. Results showed that the environmental criterion is the most important one among the three considered criteria; weight of this criterion is approximately 69.9%, followed by technical criterion, which take 20.8% as weight, and the socioeconomic criterion ranked least important with a weight of 9.3%. Additionally, landfill gas option is found as the first and most preferable waste to energy option with a global priority of 0.561 followed by anaerobic digestion with a weight of 0.296, while incineration and pyrolysis technologies ranked the least preferred options with priorities of 0.087 and 0.056, respectively.

Keywords: AHP, TOPSIS, Solid Waste, Renewable Energy.

Nomenclature

AHP: Analytic hierarchy process
TOPSIS: Technique for order of preference by similarity to ideal solution
MCDM: Multi-criteria decision-making
IN: Incineration plant
PY: Pyrolysis plant
AD: Anaerobic Digestion
LFG: Landfill Gas Recovery
D: Performance rating of alternative with respect to criteria
R: Normalized matrix
V: Weighted normalized matrix
PIS (A^*): Positive idle solution
NIS (N^{-*}): Negative idle solution
CC: Closeness coefficient
CR: Consistency ratio
RI: Random index
CI: Consistency index

1. Introduction

Jordan is a country in the MENA region, which stands for Middle East and North Africa, Jordan is a middle income country with a territory of 89,34 km^2.The country is characterized with scarcity in natural resources, mainly water and energy resources. Jordan population was 9.523 million inhabitants in 2016, distributed among 12 governorates [1].

Solid waste is managed by municipals in Jordan, which mainly depends on pipe options to transfer about 90% of solid waste to disposal locations [1]. Seventeen disposal locations are considered for operations in different cities of Jordan. In Al Ghabawil, there is the only engineered sanitary landfill that serves the capital of Jordan (Amman) and Zarqa, this location is the largest one in the country to afford the generated waste by these two large cities. The second largest landfill in the country is being rehabilitated to become a sanitary one. All the remaining disposal locations are considered as unsanitary landfills (dump sites).

Solid waste is disposed to all locations in Jordan with amount of 6,940 ton/day; as it was approximately measured in 2013, this causes an annual quantity of 2,533,100 tons/year. In 2011, due to the high number of Syrian refugees who entered Jordan, the amount of solid waste has been significantly increased which put pressure on the solid waste management [2].

Renewable energy sources, such as converting waste to energy, are clean and sustainable sources that can be used

---

[*] Corresponding author e-mail: naaltheeb@just.edu.jo.

as a replacement of the expensive and polluting fossil fuels. Several technologies can be utilized to convert the solid waste to energy. For example, Incineration, Pyrolysis, Anaerobic Digestion, and Landfill Gas Recovery. Each method has its own attractive attributes and drawbacks. Therefore, it is very important to choose the best technology or set of technologies, so the maximum energy with minimum effort can be achieved. In this research, the above-mentioned four technologies, are considered because they are suitable for the economy of Jordan and can be utilized. Additionally, they are the most common technologies.

Selecting the best technology to convert waste to energy is especially important for a country like Jordan that lacks its own energy resources and depends mainly on the imported fossil fuel to meet the increasing demand on energy. Given the fact that energy and waste sectors are responsible for more than 80% of the total greenhouse gases emitted in the country, waste to energy option is an attractive option to Jordan. To provide the decision makers in Jordan with a methodology to choose the best method to generate energy from waste, AHP-TOPSIS are utilized.

Both AHP and TOPSIS are multi-criteria decision-making method. The concept of AHP is to construct a pairwise comparison matrix based on soliciting experts' opinion with different backgrounds from academic, governmental and nongovernmental agencies who are involved in the waste and energy sectors in Jordan. The matrices are to compare between the alternatives for each criteria, then, set of calculations are performed to select the best choice, as will be more described later. In TOPSIS, alternatives are ranked based on their distance from the best or ideal one, and then the closest alternative to the ideal is taken.

2. Literature Review

Municipal solid wastes (MSW) are an important issue in any country. Wastes are generated and accumulated because of human activities. Population growth, urbanization and changes in lifestyles have resulted in an increase in the amounts of the generated solid waste, which poses serious challenges for many cities and authorities around the world. In developing countries, this is considered true [3]. In 2011, world cities generated about 1.3 billion tons of solid waste, this amount is expected to increase to 2.2 billion tons by 2025 [4 and 5]. Unless properly managed, solid waste will cause several environmental and public health problems and will significantly affect the economic development [4].

2.1. AHP and TOPSIS in Renewable Energy Problems

Researchers in many engineering fields, as in [6], have utilized AHP. In the energy sector, AHP and TOPSIS have been utilized to make decisions regarding the energy management because the sources of renewable energy are considered more important in these days compared to traditional resources such as fossil fuel or nuclear power plants. This is because of cleanness and availabilities of renewable sources in wide range of areas. The most important advantages of many renewable energy sources are their low greenhouse effect and other emissions in comparison with fossil fuel sources [7], they are less complex [8], and cost effective. As such, increased number of countries around the world consider renewable energy alternatives to decrease their dependency on the polluting imported fossil fuel [9]. However, none of the alternatives meets all advantages of the renewable energy resources [10]. Furthermore, due to the variations in economic, technical and environmental conditions, different countries have considered different options of renewable energy technologies [11].

In Jordan, a lot of research has been performed to manage the renewable energy and to benefit from it. For example, [12, 13, 14, 15, and 16]. In energy planning, selection of renewable energy technology is not an easy task that can be made based on a single criterion of decision-making. It is rather a multivariable complex problem where there is a need to prioritize certain renewable energy alternatives from various alternatives by considering consistency and multi interests and perspectives, using multi-criteria decision making (MCDM) [9]. Analytical hierarchy process (AHP) can be adopted as MCDM tool in many cases such determining the best energy source for a specific country, [17 and 18].

Several researchers used AHP in many fields evaluating and selecting various renewable energy technologies for different countries. An AHP model was developed in [19] to select and prioritize different renewable energy technologies to be used for Electricity production in Pakistan. Based on solicitation of experts' opinion, the researchers concluded that biomass and wind energy are the most preferable renewable energy sources. AHP and data envelopment analysis (DEA) have been used in [11] to evaluate and select renewable energy technologies in China. In this research, the results showed that solar and wind energies are the best alternatives for China based on environmental, economic, technical, and social criteria.

In [20], AHP have been used to rank and prioritize renewable energy options for sustainable electricity production in Malaysia. Solar energy is ranked first, and biomass is ranked second, these results were found according to the main criteria and their sub-criteria. Hydropower is set in the third rank, and finally the wind energy ranked the fourth as a least preferable option. In [18], opinions were solicited to rank the various renewable energy options in Colombia based on 5 criteria and 20 sub-criteria. In the results, technical criterion is found to be in the top of rank followed by environmental criteria, then the social, the risk and the economic criteria, which are ranked the lowest. The study concluded that the solar energy is ranked as the best alternative for Colombia.

To select the optimal waste to energy option in Sultanate of Oman, AHP model has been adopted in [21] that consisted of five criteria, six sub-criteria and eight alternatives. Among the assessed alternatives, the anaerobic digestion process was found to be the best solid waste to energy process for the country of Oman, followed by fermentation and incineration. [22] conducted another study that used AHP to select the best waste to energy technology for Dhaka city in Bangladesh. The AHP model consisted only of three criteria and three alternatives. There were no sub criteria. Among the three studied alternatives, the study concluded that the Plasma gasification ranked first followed by anaerobic digestion and pyrolysis. AHP with TOPSIS were integrated in [23] to evaluate the optimal collection strategy in reverse logistic for the Taiwan photovoltaic industry.

As noticed, utilizing MCDM in the field of generating energy from solid waste is still limited in Jordan. The purpose of the current study is to summarize and evaluate the solid waste management and energy sectors in Jordan, and to provide the policy makers in Jordan with a decision making tool to select the best Waste to Energy method of the country using two Multi-criteria decision tools, AHP and combination of AHP and TOPSIS.

3. Methodology of Multi-criteria Decision Making (MCDM)

3.1. The Analytic Hierarchy Process (AHP)

Multi-criteria decision-making (MCDM) process is utilized to select the best alternative in the presence of multiple, usually conflicting, criteria, [24]. The Analytic Hierarchy Process (AHP), which has been developed in [25], is one of the decision-making tools that serve such a purpose. AHP is performed by constructing pairwise comparison matrices based on experts' opinions. The comparisons are developed based on scaling the absolute judgments, which provides a measure of how much an alternative is important compared with others based on a specific criterion [26]. Table 1 shows the scale for measuring the opinions of experts; this scale is similar to the scale used in [25].

Table 1. Scale for pairwise comparison, [25].

Importance Scale	Definition of the Importance scale
1	Both criteria have the same importance
2	Intermediate value between the judgment in 1 and in 3
3	One criterion (row) has slightly weak importance over the other (column)
4	Intermediate value between the judgment in 3 and in 5
5	One criterion (row) is strongly important that the other criterion (column)
6	Intermediate value between the judgment in 5 and in 7
7	One criterion (row) importance is extremely stronger than the other criterion (column)
8	Intermediate value between the judgment in 7 and in 9
9	One criterion (row) importance is absolute stronger than the other criterion (column)

In this research, Experts who have long years of experience in solid waste management were interviewed to conduct the pairwise comparisons which were structured with four criteria, namely environmental, economic, social and technical aspects. These criteria were then expanded into a few more sub-criteria. Then, criteria and sub-criteria are compared based on different attributes and the pairwise comparison matrices are developed. This is done by soliciting experts' opinions and recording their judgments. Experts selected to perform, were from academics and researchers, energy business sector, regulators and nongovernment organizations (NGOs) that are dealing with energy issues. The solicitation of opinions was achieved via interviewing the experts and discussing with them the objectives of the study and asking them to fill the pairwise comparison matrices.

Judgments matrices were used to generate the priority vector to check the consistency of judgements by evaluating the consistency ratio (CR). The randomness in judgment can be measured by the consistency ratio, as in Equation 1:

$$CR = CI/RI \tag{1}$$

Where CI is the consistency index and RI is the random index, which expresses the expected value of the CI corresponding to the order of matrices. Table 2: represents the values of the RI versus the number of criteria (n).

Table 2. Random index (RI) values for different matrix sizes

n	1	2	3	4	5	6	7	8	9
RI	0	0	0.58	0.90	1.12	1.24	1.32	1.41	1.45

If the CR value is acceptable (Usually less than 10%), the experts' opinions and judgments are considered consistent, alternatively, the subjective experts' judgement should be repeated until the CR values lie within the expected range. The combined priorities of each waste to energy alternative can be determined by aggregating the weights in the hierarchy, this is called judgments synthetization, which leads to select the best technology.

To analyze the sensitivity of the decisions on the proper waste to energy alternatives, dynamic sensitivity analysis was carried out to construct the sensitivity figures; Expert Choice Software was used for this purpose. Finally, the AHP model outcome regarding the ranking of waste were presented and discussed. Comparisons with the findings of researchers on appropriate waste to energy technologies were conducted. Finally, based on the findings of sensitivity analysis, conclusions will be made and recommendations for future studies will be suggested.

The procedure of applying AHP in this research is shown in Figure 1. The methodology of applying the hierarchy is shown in Figure 2, which shows 3 criteria, 9 sub criteria and 4 alternatives that should be subjected to pairwise comparison.

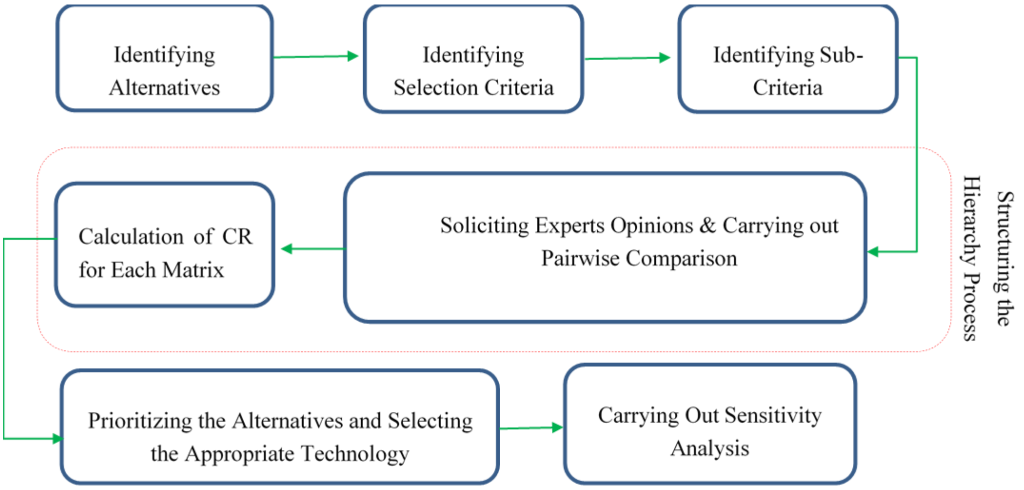

Figure 1. The methodology of AHP

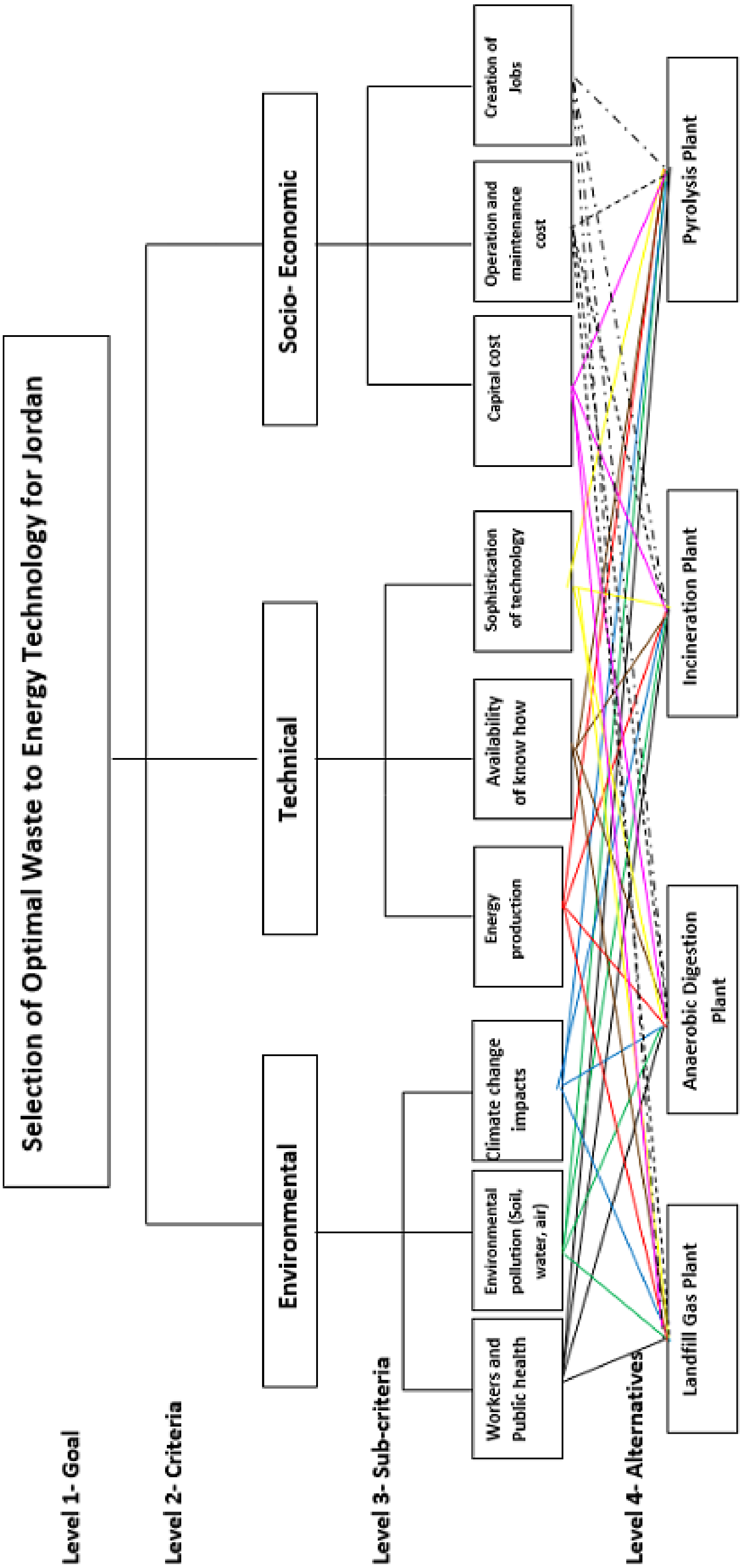

Figure 2. Analytical hierarchy model for the selection of Waste to Energy Technology

3.2. Technique of Order Preference Similarity to the Ideal Solution (TOPSIS)

TOPSIS is another known MCDM method, as proposed in [27], to find the best alternative. TOPSIS procedure starts with defining the ideal and least-ideal solutions. Then, the best solution is selected which is the one that has the minimum distance to ideal solution and maximum distance to the least-ideal solution [28]. Ideal solution is the solution that maximizes the benefits and minimizes the cost, whereas the least-ideal solution has the opposite definition. In TOPSIS, alternatives are arranged according to their "relative similarity to the ideal solution" [23]. The TOPSIS procedures are performed as in the next steps:

Step 1: Defining the matrix $D = [xij]$ which represents the performance rating of alternatives with respect to criteria, where the number of criteria is n and the number of alternatives is m.

$$D=\begin{bmatrix} x_{11} & x_{12} & \cdots & x_{1n} \\ x_{21} & x_{22} & \cdots & x_{2n} \\ \cdots & \cdots & \cdots & \cdots \\ x_{m1} & x_{m2} & \cdots & x_{mn} \end{bmatrix}$$

Step 2: Determination of the normalized decision matrix, $R = [rij]$, as follows:

$$R=\begin{bmatrix} r_{11} & r_{12} & \cdots & r_{1n} \\ r_{21} & r_{22} & \cdots & r_{2n} \\ \cdots & \cdots & \cdots & \cdots \\ r_{m1} & r_{m2} & \cdots & r_{mn} \end{bmatrix}$$

Where $rij = \frac{x_{ij}}{\sqrt{\sum_{k=1}^{m} x_{kj}^2}}$ $\forall$ i=1, 2,…, m , j=1,2,…,n (2)

Step 3: Calculation of the weighted normalized decision matrix $V = [vij]$, which is developed as in the next, where wi is the weight of the ith criterion.

$vij = rij \times wi\ \forall$ i=1, 2,…, m , j=1,2,…,n (3)

$$V=\begin{bmatrix} w_1.r_{11} & w_2.r_{12} & \cdots & w_n.r_{1n} \\ w_1.r_{21} & w_2.r_{22} & \cdots & w_n.r_{2n} \\ \cdots & \cdots & \cdots & \cdots \\ w_1.r_{m1} & w_2.r_{m2} & \cdots & w_n.r_{mn} \end{bmatrix}$$

Step 4: Positive ideal solution (PIS, A*) and negative ideal solution (NIS, A−) can be calculated as:

$$A^* = \{(\overset{MAX}{i} v_{ij} | \overset{MIN}{i} v_{ij} | j \epsilon c)\} \quad (4)$$

$$A^- = \{(\overset{MAX}{i} vij | \overset{MIN}{i} vij | j \epsilon c)\} \quad (5)$$

Step 5: Calculation the distances between each option and the NIS and PIS by using the Vertex method.

$$di^* = \sqrt{\sum_{j=1}^{n} (v_{ij} - v_j)^2} \quad \text{, i=1,2,…,m ; j=1,2,...,3} \quad (6)$$

$$di^- = \sqrt{\sum_{j=1}^{n} (v_{ij} - v_j)^2} \quad \text{, i=1,2,…,m ; j=1,2,...,3} \quad (7)$$

Step 6: The closeness coefficient of each alternative is calculated as in Equation 9. Finally, the alternatives are ranked in descending order of the CCi index.

$$CC_i = \frac{d^-}{d_i^- + d_i^*} \quad (8)$$

3.3. Integration of AHP and TOPSIS

To select the optimal waste to energy alternative in Jordan, AHP and TOPSIS decision-making processes were combined together. This has been achieved by using the weightings of the criteria and sub-criteria obtained from AHP analysis and fed into TOPSIS to rank the optimal waste to energy alternative. Figure 3 shows how the two decision-making tools were combined.

4. Results and Discussion

4.1. Screening of Alternatives and Criteria

Now, there are numerous waste to energy technologies and options that are available worldwide [29]. Furthermore, too many criteria and sub-criteria can be used in evaluating the waste to energy alternatives. However, there is no universal technology or group of technology that suits all countries [30]. Therefore, selection of alternatives and definition of criteria with their weights are central in AHP to assess the alternatives. To achieve that, a screening process should be carried out at the beginning of decision-making process to identify the alternatives that are feasible for the problem and the criteria and sub-criteria that will be used in the judgement [31].

Jordan is a developing country that is lacking indigenous energy resources. The World Bank classifies countries based on their economies into four categories, namely, high, upper middle, lower middle and low. In 2017, the Bank classified Jordan as a lower middle-income country. Therefore, alternatives and criteria of waste to energy are essential to adopt and select appropriate solutions in Jordan. As such, the following alternatives of waste to energy technologies were selected for this purpose, such as Landfill biogas, Anaerobic digestion, Incineration, and Pyrolysis.

Table 3 shows three evaluation criteria and sub-criteria used in the AHP process to select the best alternative of waste to energy in Jordan. As observed, three main criteria were selected, mainly the Environmental, Technical and Socio-Economic. Under each criterion, there are three relevant sub-criteria.

Table 3. Criteria and sub-criteria used in the AHP analysis

Criteria	Sub-criteria	Description
Environmental	Public and workers' health Water, air and soil pollution Climate change	Minimum adverse impacts of the selected technologies on the public as well as on the labor health Minimum potential release of pollutants into the ecosystem Minimum Greenhouse gas emissions by technology
Technical	Energy production Know how Sophistication of Technology	Maximum possible energy production from waste Availability of expertise and staff to run the technology. Complexity of the technology and requirements of spare parts
Socio-Economic	Capital cost Operation and maintenance Job creation	Minimum Initial investment cost needed Minimum operation & maintenance cost is established Maximum number of employment opportunities created by Y technology

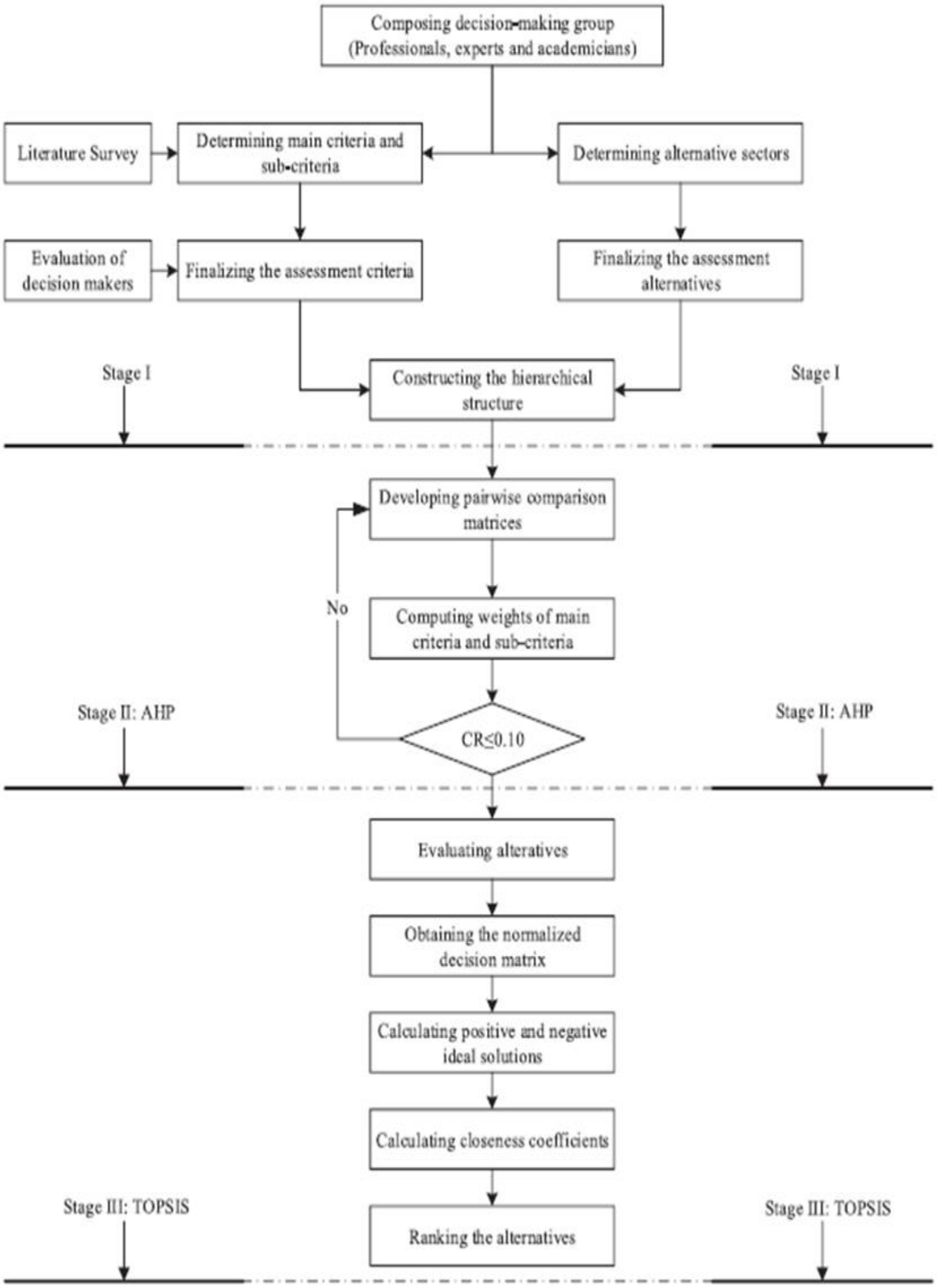

Figure 3. Flow diagram shows the procedure followed in integrating AHP with TOPSIS.

4.2. Soliciting of Expert Opinion

In AHP, expert opinion is a major step towards making judgement on the alternatives as well as the criteria importance by constructing pairwise matrices. In this study, judgments in the pairwise matrices are developed based on soliciting experts' opinions. Stakeholders, waste and energy experts, researchers, plants operators, public figures and policy makers who are familiar with the situation of the Jordanian waste and energy sectors, were consulted. In this study, opinions of 10 experts were solicited using a questionnaire. In AHP, number of experts is usually limited because the experts in the field with long experience are not easily found. Additionally, if the experts have an outstanding knowledge in the field, they are expected to provide consistent judgments that lead to the conclusions based on the low number of feedbacks; which is the case in this study, as we notice in the consistency results. Table 4 shows the categories of stakeholders whose opinions were solicited and their categories and number from each category.

The values of scores expressed through experts' opinions in each pairwise comparison matrices were aggregated using additive AHP procedure (by calculating the arithmetic mean for matrices developed by the experts) [31].

Table 4. List of stakeholder categories and their numbers whose opinions were solicited

No.	Stakeholders category	Profession	Number
1.	Waste and Environmental Academicians	Lecturers and Researchers	3
2.	Energy Academicians	Lecturers and Researchers	2
2.	Waste and municipal Professionals	Policy and Decision makers	2
3.	Community members	Business and NGOs members	3
	Total		10

4.3. Results of Pairwise Comparison

After the screening and constructing of the hierarchy structure, pairwise comparison was conducted to generate judgement matrices. This has covered the comparison between alternatives with respect to each sub-criterion, between sub-criteria with respect to main criterion, and between criteria with respect to the goal.

Initially, pairwise comparison of the selected criteria to achieve the goal was performed. Table 5 demonstrates a matrix with the derived priorities of the main criteria with respect to goal based on the pairwise comparison obtained from the experts. The value of the consistency ratio (CR) is 0.08, which is less than 0.1, consequently, the judgements in the matrix are consistent and logically satisfactory. Equation 1 is used here and in the next results to calculate the CR. In all of the next tables, the star symbol (*) represents the comparison value (x_{ij}) which can be found directly from the table and equals to $(1/x_{ji})$.

Table 5. Pairwise comparison matrix of main criteria with respect to goal

Criteria	Environmental	Technical	Socio-Economic	Priority vector
Environmental	1	4.5	5.6	0.699
Technical	*	1	3.0	0.208
Socio-Economic	*	*	1	0.093

The highest weight was given to the environmental criterion with value of 0.69. Then, the technical criterion that has a weight of 0.21, in addition to the criterion of socio economic that has the least weight of 0.09. This means that the environmental issues should take the maximum care and attention when the solid wastes are used to generate energy in Jordan. This is can be justified by the fact that Jordan is located in a semi-arid region where the environmental issues are of high concern for the decision makers of the country. For example, Jordan ranks the second poorest country worldwide in terms of renewable water resources [32]. Therefore, it is important to conserve and save every drop of water from pollution.

To choose the most suitable alternative of the waste to energy method for Jordan, three pairwise comparison matrices were developed. Each matrix represents the relative weights, resulted from the experts' feedback, of three sub-criteria with respect to one main criterion.

Tables 6, 7 and 8, show the pairwise comparisons, and Figures 4 a-c shows the weights for the environmental, technical, and socio-economic sub-criteria with respect to main criteria, respectively.

Table 6 presents pairwise comparison of environmental sub-criteria with respect to the main criteria. The consistency ratio of the pairwise matrix was calculated and found to be 0.09 of less than 0.1, which means that the judgments were consistent.

Table 6. Environmental criterion pairwise comparison matrix

Sub-Criteria	Workers & Public health	Environmental Pollution	Climate Change	Priority Vector
Workers & Public health	1	4.6	5.6	0.7
Environmental pollution	*	1	3.1	0.20
Climate change	*	*	1	0.1

Figure 4 (a) shows the weights of the environmental sub-criteria, where the workers and public health sub-criteria ranked first with 70% of the total weight, followed by environmental pollution criteria with 20% of the total weight and finally the climate change criteria which has the least weight of 10%. The high weight of the workers and public health sub-criteria may be justified as that the soliciting of the experts' opinion took place during the corona virus lockdown in Jordan, when the public health issues were priority for everybody in the country, which has been reflected on the solicited opinions and gave the public health the highest priority.

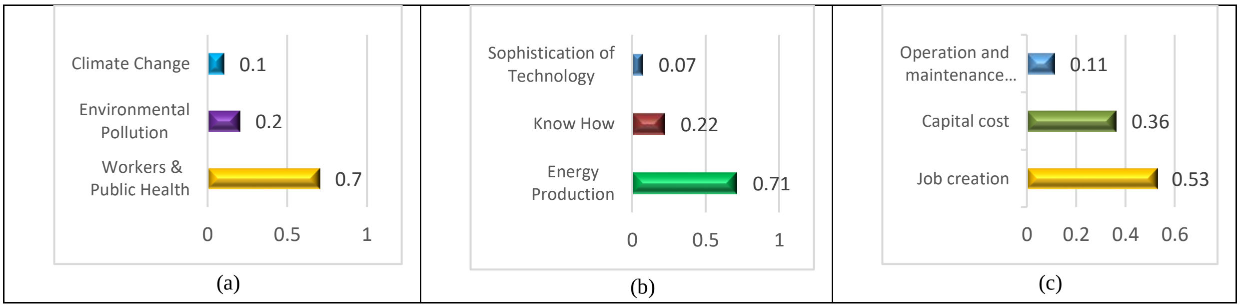

(a) (b) (c)

Figure 4. Relative weights of Environmental (a), Technical (b), and socio-economic (c) sub-criteria with respect to main criterion

The pairwise comparison results of technical sub-criteria with respect to the main criterion are presented in table 7. The CR was found to be 0.08 which is a satisfactory value as it is less than 0.1.

Table 7. Technical criterion pairwise comparison matrix

Sub-Criteria	Energy Production	Availability of know how	Sophistication of technology	Priority Vector
Energy Production	1	4.3	7.4	0.71
Availability of know how	*	1	4.2	0.22
Sophistication of technology	*	*	1	0.07

Figure 4(b) depicts the relative weights of Technical sub-criteria with respect to main criterion. It can be observed that energy production sub-criteria has the highest weight of 71%, followed by know how sub-criteria of 22% and technology sophistication with 7%. This can be understood from the energetic situation of Jordan, where more than 95% of the energy is imported, and therefore finding national resources of energy that can contribute to energy security of the country is a priority. As such, the experts gave the highest priority for energy production generated by each of the waste to energy alternative.

Table 8 presents the pairwise comparison matrix of sub-criteria with respect to socio-economic criterion. The calculated consistency ratio found was 0.08, which implies the acceptance of the experts' judgements.

Table 8. Pairwise comparison matrix of sub-criteria with respect to Socio-economic criterion

Sub-Criteria	Capital Cost	Operation & Maintenance Cost	Job Creation	Priority Vector
Capital Cost	1	4.2	2.0	0.53
Operation & Maintenance Cost	*	1	3.5	0.36
Job Creation	*	*	1	0.11

Figure 4(c) shows the results of the ranking of the socio-economic sub-criteria. Job creation has the highest priority with a weight of 53%, followed by capital cost of 36% and finally the operation and maintenance cost of 11%. Considering the fact that the unemployment rate in Jordan reached 19% in the year of 2019 (DOS, 2019), it is not surprising that job creation has the highest priority according to the experts' opinion, especially during the corona virus pandemic lockdown when many people lost their jobs which increased the percentage of the unemployment above the announced figure of 19%.

Taking into account that the waste to energy projects in Jordan are mainly financed through grants or soft loans, and the payback period of most renewable energy projects are short, the financial issues like capital and operation and maintenance costs have received less weight as compared to job creation sub-criteria.

4.4. Pairwise comparison of the alternatives under sub-criteria

The local priorities of alternatives under each sub-criterion are obtained from the pairwise comparison based on the experts' opinions. The results of comparison are presented in Figure 5. As it can be observed, the analysis revealed that all the alternatives have the same order of ranking under all the considered sub-criteria but with different priority values. The landfill biogas ranked first, followed by anaerobic digestion. On the other hand, the incineration and pyrolysis technologies, ranked third and fourth, respectively with relatively low weights. Considering the high tech nature of thermal process, and because the highest fraction of municipal solid waste in Jordan is food waste that comprises more than 50% of the total weight of the generated waste, the experts ranked biological processes like landfill biogas and anaerobic digestion of being the most preferable under all the sub-criteria as shown in Figure 5.

In order to have similar system boundaries for all alternatives, it is worth mentioning that all stages of solid waste storage, generation, storage, collection transfer and transport are the same for all alternatives. Consistency ratios for all pairwise comparison of the sub-criteria were calculated with values less than 0.1, except for the knowhow and operation and maintenance sub-criteria which both have a consistency ratio of 0.11, which is acceptable as it is slightly higher than 0.1.

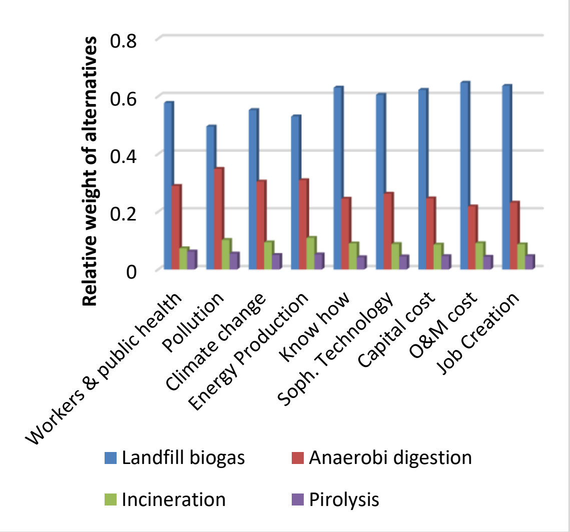

Figure 5. Ranking of waste to energy options based on each sub-criteria

4.5. Global Priorities of Alternatives

Relative (local) priorities of the criteria with respect to the main goal, as well as the relative priorities of the alternatives with respect to all sub-criteria were determined. Global priorities can be determined for waste to energy alternatives by multiplying the local priority vector of each criterion by local priority vector of alternatives, then the results are summed to get the global weight vector, as follows, [33 and 34]:

$$P_{Gi} = \sum P_{cj} P_{ij} \quad (9)$$

Where:

P_{Gi} is the global priority of the ith alternative with respect to the main goal

P_{cj} is the relative priority of the jth criteria with respect to the main goal

P_{ij} is the relative priorities of the ith alternative with respect to jth criteria

The landfill biogas plant option ranked first with a global priority of 0.561, followed by anaerobic digestion plant that was ranked second alternative with a weight of 0.296. The incineration plant and pyrolysis plants are the least preferred alternatives as judged by the low weight of 0.087 and 0.056 respectively.

As previously mentioned, both landfill biogas and anaerobic digestion are biological processes that depend on the biodegradation of organic fraction of the waste in the absence of oxygen which produce methane as a source of energy. On the other hand, the incineration and pyrolysis are thermal processes that depend on combustion of certain fraction of solid waste that has a relatively high heating value like plastics and wood. In terms of technology, thermal processes are sophisticated technologies as compared to biological processes that required qualified experienced personnel. Considering the high tech nature of thermal process, in addition to the fact that the highest fraction of municipal solid waste in Jordan is food waste comprising more than 50% of the total weight of the generated waste, the experts ranked biological processes, such as landfill biogas and anaerobic digestion, of being the most preferable under all the sub-criteria

5. Results of AHP and TOPSIS Integration

The second decision-making tool adopted in this study is the combination of AHP with TOPSIS. The criteria and weights obtained from AHP pairwise comparison were taken and fed into TOPSIS model to find their sub-criteria global weights, by using Equation 9, so as to prioritize waste to Energy options for Jordan. The sub-criteria were given letter symbols as in Table 9. Results in the global weight column are explained next.

Table 9. Criteria and Sub-criteria symbols

Criteria	Weight	Sub-criteria name	Sub-criteria Symbol	Global Weight	Type (Should be …….)
Environmental	0.699	Workers and Public Health	C11	0.488	Maximized
		Environmental Pollution	C12	0.146	Minimized
		Climate Change	C13	0.065	Minimized
Technical	0.208	Energy Production	C21	0.147	Maximized
		Availability of Know How	C22	0.046	Maximized
		Sophistication of Technology	C23	0.015	Maximized
Socio-Economic	0.093	Capital Cost	C31	0.033	Minimized
		Operation and Maintenance Cost	C32	0.011	Minimized
		Job Creation	C33	0.049	NA

First step is to find the global weights of the sub-criteria based on experts' opinion. Table 9 shows the global weights of the sub-criteria under each main criteria based on the expert's opinion. As can be seen from table, sub-criteria C11, C21and C33 has the highest weights under each criterion. After the weights of sub-criteria were calculated a decision matrix under TOPSIS has been developed. Table 10 shows the decision evaluation matrix that relates different alternatives to the nine sub-criteria.

Table 10. Decision evaluation matrix

	C11	C12	C13	C21	C22	C23	C13	C32	C33
Landfill Gas (LFG)	3.2	3	4.2	2	5.2	3.2	1.8	1.6	5.4
Anaerobic Digestion Plant (AD)	8.4	5.2	6.4	3.2	7.8	2	3.6	5.8	9.4
Incineration Plant (IN)	6.8	6.2	6.8	4.8	1.8	8.2	7	9.4	2.2
Pyrolysis Plant (PY)	3.8	8.8	9.2	7.4	2.6	5	9.2	7	2.8
Weights	0.488	0.146	0.065	0.147	0.046	0.015	0.033	0.011	0.049

After developing the decision matrix, the normalized matrix and the weighted normalized matrices are determined which are presented in tables 11 and 12, respectively. Equations 2 and 3 are used for this purpose.

Table 11. Normalized decision matrix.

	C11	C12	C13	C21	C22	C23	C13	C32	C33
LFG	0.269	0.243	0.305	0.208	0.525	0.310	0.147	0.121	0.473
AD	0.706	0.422	0.465	0.334	0.788	0.194	0.294	0.440	0.824
IN	0.572	0.503	0.494	0.500	0.182	0.795	0.572	0.714	0.193
PY	0.319	0.714	0.668	0.771	0.236	0.485	0.752	0.531	0.245
Weights	0.488	0.146	0.065	0.147	0.046	0.015	0.033	0.011	0.049

Table 12. Weighted normalized decision matrix.

	C11	C12	C13	C21	C22	C23	C13	C32	C33
LFG	0.131	0.035	0.019	0.031	0.024	0.004	0.004	0.001	0.023
AD	0.345	0.062	0.030	0.049	0.036	0.002	0.009	0.005	0.040
IN	0.279	0.073	0.032	0.074	0.008	0.012	0.019	0.008	0.009
PY	0.156	0.104	0.043	0.104	0.012	0.007	0.025	0.006	0.012
A_i^*	0.131	0.035	0.019	0.104	0.036	0.012	0.004	0.001	0.04
A_i^-	0.345	0.104	0.043	0.031	0.008	0.002	0.025	0.008	0.009

Finally, the closeness coefficient to the ideal solution for each waste to energy was calculated, by using equations 4-8, as presented in Table 13. As it can be seen from the table, the Landfill biogas alternative has the least distance to the ideal solution and consequently the highest closeness coefficient of 0.75, which implies that landfill biogas is the most preferable alternative under AHP-TOPSIS. This is in agreement with the findings under AHP model. However, the second ranked alternative under

TOPSIS was found to be pyrolysis, which ranked the least preferable under AHP.

Table 13. Distance and closeness to the ideal solution of the waste to energy alternatives

Alternative	d_i^*	d_i^-	CC_i	Ranking
LFG	0.076	0.228	0.75	1
AD	0.233	0.065	0.21812	4
IN	0.163	0.086	0.34538	3
PY	0.088	0.203	0.69759	2

6. Sensitivity Analysis

The results of analytical hierarchy process analysis are highly dependent on the preferences of experts where any changes in the relative importance of the various criteria and alternatives assigned by the experts may influence the results of AHP analysis in terms of ranking the alternatives or changes in the value of the global priorities of the alternatives [34]. As such, carrying out sensitivity analysis is an important step to check the consistency of the results as well as the robustness of the ranking. To analyze the sensitivity of the selected alternatives, performance sensitivity graphs were obtained according to different scenarios using Expert Choice software. In this study, sensitivity analysis was performed based on different scenarios.

The first scenario is called Baseline. Under this scenario, there is no change in criteria weights, which are exactly as assessed based on the experts' opinion as shown in the graph presented in Figure 6 (a). It is worth mentioning that this is a dynamic graph with two main vertical axes. The purpose of the axis on the left of the graph is to show the relative importance of each main criterion, while the second axis on the right is the alternative axis which is used to measure the total weight of each alternative.

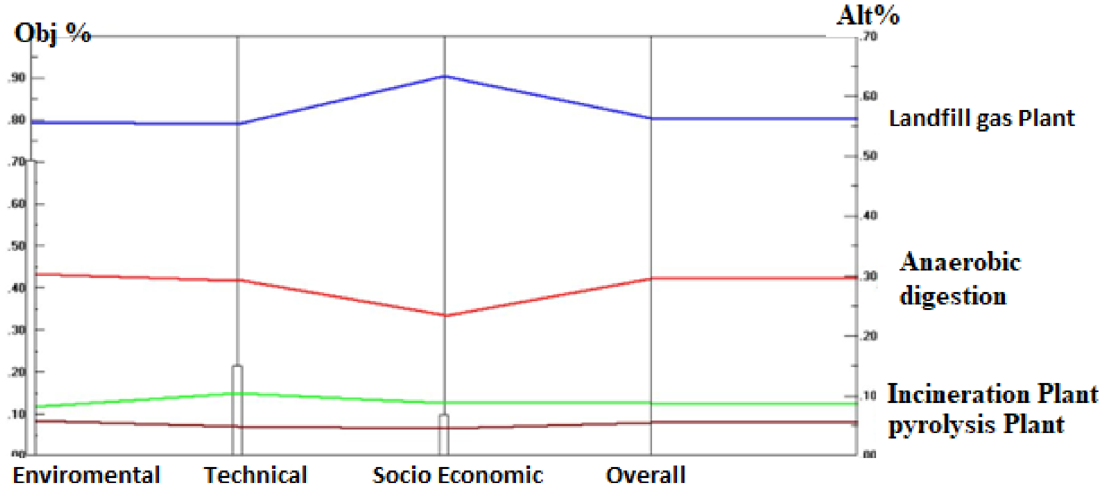

(a) Sensitivity analysis according to baseline scenario

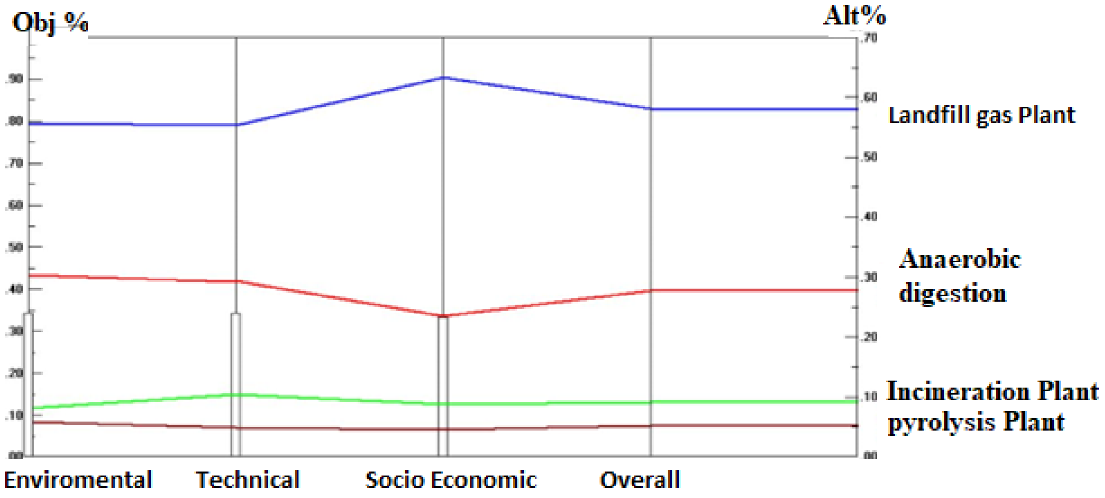

(b) Sensitivity analysis according to second scenario under which criteria have equal weights

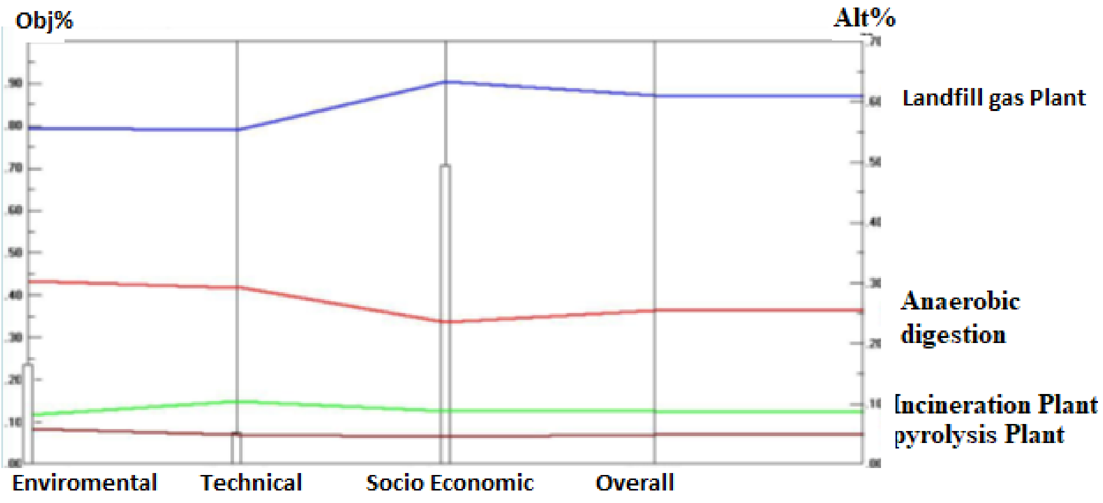

(c) Sensitivity analysis according to third scenario under which socio-economic criterion weight increased to 75%

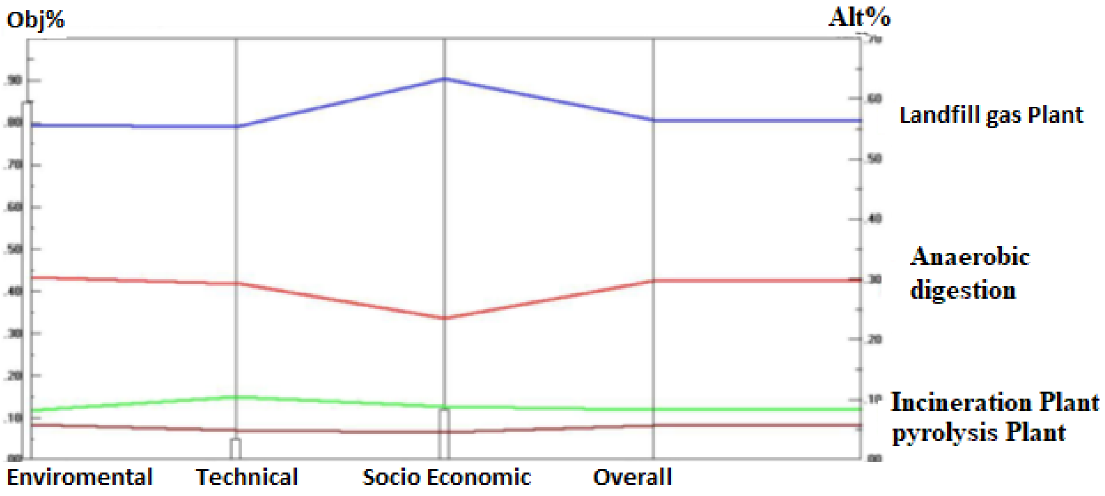

(d) Sensitivity analysis according to third scenario under which the technical criterion weight decreased to 5%

Figure 6. Sensitivity graphs

The second scenario is based on the assumption that all the three criteria used in evaluation of waste to energy alternatives have the same weight of 33.3%. Figure 6 (b) shows the sensitivity analysis of this scenario. It seems that the alternatives are not that sensitive under this scenario. The ranking remains the same, where landfill gas plant has the first priority; however, there are slight changes in the weight of alternatives.

The third scenario is used to change the criteria weights. According to this scenario, the criteria weights are randomly changing and the alternative weights are detected. Figures 6 (c-d) depict these changes. It can be observed that by changing the weight of the socio economic criterion from 9% to 70%, the weights of environmental criteria decreased to 24% and technical criterion to 5%. Moreover, the weight of the landfill gas alternative increases from 56% to 61%, while the weight of the anaerobic digestion alternative decreases to 25%. On the other hand, the weights of the incineration and pyrolysis alternatives did not witness significant changes.

7. Conclusions and Recommendations

In Jordan, energy and waste sectors are responsible for more than 80% of the total greenhouse gases emitted in the country from all sectors. Therefore, adopting waste to energy options is a win-win approach that will lead to the reduction in the amount of fossil fuel combustion and the polluting emissions associated with this use. In addition, it will reduce the amount of improper disposal of solid waste and the amounts of the greenhouse gases by utilizing the methane in energy production.

This study has focused on the selection of appropriate waste to energy option for Jordan using two decision making tools, namely analytical hierarchy process (AHP) and combination of analytical hierarchy process and technique for ordering preference by similarity to the ideal solution (TOPSIS). Four levels AHP model was constructed that consists of 3 criteria, 9 sub-criteria and 4 alternatives. Opinions of ten experts from various academics, researchers, governmental and nongovernmental agencies were solicited to carry out pairwise comparison of the criteria and alternatives using a specially designed questionnaire. Thirteen pairwise comparison matrices were generated. The analysis of priorities for criteria, sub-criteria and alternatives was conducted using Expert Choice software. Consistency analysis of the pairwise comparison matrices was conducted where in most cases the consistency ratio was less than 0.1.

Pairwise comparison of the criteria with respect to the goal of selecting appropriate waste to energy alternative revealed that the environmental criterion has the highest priority followed by technical criterion and the least priority was assigned to the socioeconomic criterion. As for the pairwise comparison of the sub-criteria under the main criteria, workers and public health sub-criteria had the highest priority under the environmental criteria, while the energy production had the first priority under technical criteria, and finally the job creation sub-criteria had the first priority under the socioeconomic criteria.

Under AHP, the global priority of alternatives revealed that landfill gas plant is the most preferred option with a weight of 56%, followed by anaerobic digestion with a weight of 29%, while the incineration and pyrolysis alternatives are the least preferred alternatives with 9% and 6%, respectively. This indicates that alternatives based on biological processes, as landfill gas and anaerobic digestion, are more preferable than alternatives based on thermal technologies, such as incinerator and pyrolysis. This maybe because that biological processes are less complicated and cheaper than thermal ones, which suit developing countries like Jordan.

Under AHP-TOPSIS analysis, the landfill gas alternative is also ranked the most preferred alternative, while the pyrolysis alternative is ranked the second, the incinerator is ranked third (same rank as under AHP), and finally the anaerobic digestion was the least preferred option.

Based on the findings of the current study, the following recommendations are made:

1. Jordan should consider waste to energy technologies more seriously and start adopting technologies like landfill gas and anaerobic digestion. Some recent research shows the economical advantages of utilizing such technology, as in [35].
2. In case the decision makers will follow the recommendations of the current study by adopting landfill biogas technology as an option of waste to energy in Jordan, the landfills should be designed and constructed as an engineered facility with proper lining, capping and containment systems, so as to maximize the amount of biogas generated and collected.
3. Further studies are recommended to cover other alternatives of waste to energy, such as refuse derived fuel, gasification by considering more criteria and sub-criteria and using other decision making tools rather than AHP and TOPSIS.

References

[1] DOS (2020), Department of Statistics, Jordan, http://dosweb.dos.gov.jo/ar/ (Accessed on 27/05/2020)

[2] Abu-Qdais H, Gibellini S, Vaccari M. Managing solid waste under crisis: The case of Syrian refugees in northern Jordan. InProceedings of the Sardinia 2017 Oct.

[3] Abu Qdais H. A., (2019) Developing a Decision Support Tool for Managing Sludge from Wastewater Treatment Plants in Jordan, Desalination and Water Treatment, 19, pp 95-104.

[4] World Bank (2018) What a Waste 2.0 A Global Snapshot of Solid Waste Management to 2050, International Bank for Reconstruction and Development / The World Bank 1818 H Street NW, Washington, DC 20433, USA.

[5] Wowrzeczka B. City of waste—importance of scale. Sustainability. 2021 Apr 1;13(7):3909.

[6] Jia L, Wang J, Rui L, Chu J. Design of Quantitative Risk Assessment System for Ship Longitudinal Motion Based on Analytic Hierarchy Process. JJMIE. 2022 Jan 1;16(1).

[7] Al Zou'bi, M. (2010) Renewable Energy Potential and Characteristics in Jordan. Jordan Journal of Mechanical and Industrial Engineering. Vol 4, No 1: 45– 48.

[8] Hrayshat, E. S. (2008) Analysis of Renewable Energy Situation in Jordan, Energy Sources, Part B, 3, pp 89–102. available online on: http://www.memr.gov.jo/EchoBusV3.0/SystemAssets/PDFs/EN/Bruchure%202018.pdf

[9] Cristobal San, J.R. (2011), Multi-criteria decision-making in the selection of a renewable energy project in spain: The Vikor method, Renewable Energy, 36(2): 498-502.

[10] Demirtas, O. (2013), Evaluating the best renewable energy technology for sustainable energy planning. International Journal of Energy Economics and Policy, 3, pp 23-33.

[11] Li Z. and Tao Y. (2014) The evaluation and selection of renewable energy technologies in China, Energy Periodica, 61: 2554-2557

[12] Alshorman AA, Al bkoor Alrawashdeh K, Alshorman M, Talat NT. Validation of Jordanian Green Building Based on LEED Standard for Energy Efficiency Methodology. Jordan Journal of Mechanical and Industrial Engineering. 2018 Jun 1;12(1).

[13] Al-Widyan MI, Soliman IA, Alajlouni AA, Zu'bi A, Omar I, Jaradat AI. Energy Performance Assessment of a Non-domestic Service Building in Jordan. Jordan Journal of Mechanical and Industrial Engineering. 2018 Sep 1;12(2).

[14] Alshorman AA, Al bkoor Alrawashdeh K, Alshorman M, Talat NT. Validation of Jordanian Green Building Based on LEED Standard for Energy Efficiency Methodology. Jordan Journal of Mechanical and Industrial Engineering. 2018 Jun 1;12(1).

[15] Liu D, Li S, Liu H. Experimental Study on Formaldehyde Emission from Environmental Protection and Energy-Saving Alcohol Fuel for Vehicles. JJMIE. 2021 Mar 1;15(1).

[16] Jarad H. Energy Savings in the Jordanian Residential Sector. Jordan Journal of Mechanical and Industrial Engineering. 2017 Jan 1;11(1).

[17] Abdullah L. and Najib L. (2016) Sustainable energy planning decision using the intuitionistic fuzzy analytic hierarchy process: choosing energy technology in Malaysia, International Journal of Sustainable Energy, 35(4), 360–377, available online on: http://dx.doi.org/10.1080/14786451.2014.907292

[18] Algarin C. R., Llanos A.P, Castro A. O. (2017) An Analytic Hierarchy Process Based Approach for Evaluating Renewable Energy Sources, International Journal of Energy Economics and Policy,7(4): 38-47.

[19] Amer M. and Daim T.U. (2011) Selection of renewable energy technologies for a developing county: A case of Pakistan, Energy for Sustainable Development, 15, pp 420-435.

[20] Ahmad S. and Tahar R. M. (2014) Selection of renewable energy sources for sustainable development of electricity generation system using analytic hierarchy process: A case of Malaysia, Renewable Energy, 63: 458-466.

[21] Qazi W. A, Abushammala M. and Azam M.H. (2018) Multi-criteria decision making of waste-to energy technologies for municipal solid waste management in Sultanate of Oman, Waste Management and Research, 36, pp 594-605

[22] Rahman S. M., Azeem A. and Ahmmed F. (2017) Selection of an appropriate waste to energy conversion technology for Dhaka City, Bangladesh., International Journal of Sustainable Engineering, 10, pp 99-104.

[23] Hsueh J. T. and Chun-Yueh Lin C. Y. (2017) Integrating the AHP and TOPSIS decision processes for evaluating the optimal collection strategy in reverse logistic for the TPI, International Journal of Green Energy. 14, pp 1209–1220

[24] Hwang, C.L., and Yoon K., (2012). Multiple attribute decision making: methods and applications a state-of-the-art survey Vol. 186. Springer Science and Business Media.

[25] Saaty, TL. (1980) The analytic hierarchy process: planning, priority setting, resource allocation. McGraw-Hill, New York, 287.

[26] Saaty, TL. (2008) Decision making with the analytic hierarchy process. International Journal of Services Sciences, 1, pp 82-93.

[27] Hwang CL, Yoon K. (1981) Methods for multiple attribute decision making. Multiple attribute decision making. New York: Springer, p. 58–191

[28] Chitsaz N. and Banihabib ME. (2015) Comparison of different multi criteria decision-making models in prioritizing flood management alternatives. Water Resources Management 29(8), pp 2503–25

[29] Klein A. (2002) Gasification: An alternative process for energy recovery and disposal of municipal solid wastes. Available at:
http://www.seas.columbia.edu/earth/kleinthesis.pdf
(accessed 23/05/ 2020).

[30] Atwadkar R.R. , Jadhav L. D. , M. M. Wagh M. M., and N. N. Shinde N. N. (2014) A Multi Criteria Ranking of Different Technologies for the Waste to Energy of Municipal Solid Waste in the City Of Kolhapur, International Journal of Emerging Technology and Advanced Engineering ,4, pp 937-942

[31] Lootsma F. A. (1999) Multi-Criteria decision analysis via ratio and difference judgement, Kluwer Academic Publishers, Dordrecht, Netherland.

[32] MWR (2016) Ministry of Water and Irrigation, National Water Strategy of Jordan, 2016 – 2025 Amman, Hashemite Kingdom of Jordan

[33] Ishizaka A. and Labib A. (2009) Analytical hierarchy process and expert choice: benefits and limitations, Operational Research Insight, 22(4), pp 201–220. DOI: 10.1057/ori.2009.10

[34] Khoshand A., Kamalan H. and Rezaeli H. (2018) Application of analytical hierarchy process (AHP) to assess options of energy recovery from municipal solid waste: a case study in Tehran, Iran, Journal of Material Cycles and Waste Management 20, pp 1689–1700

[35] Mabalane, P. N., Oboirien, B. O., Sadiku, E. R., & Masukume, M. (2021). A techno-economic analysis of anaerobic digestion and gasification hybrid system: energy recovery from municipal solid waste in South Africa. Waste and Biomass Valorization, 12(3), 1167-1184.

JJMIE

Volume 16, Number 4, September. 2022
ISSN 1995-6665
Pages 615– 625

Jordan Journal of Mechanical and Industrial Engineering

Assessment and Perception of Renewable Energy Awareness and Potential in Jordan

Yahia M. Al-Smadi*, Ahmad M. Alshorman, Walaa Hassan, Razan Bader, Islam Abu Awad, Sajedah Alzghoul, Huda Bataineh

Department of Mechanical Engineering, Jordan University of Science and Engineering, Irbid, Jordan

Received 2 Jun 2022 *Accepted 13 Jul 2022*

Abstract

The global fossil fuel crisis has generated the need to find alternative solutions through renewable energy sources. Since Jordan has a distinctive location, the potential for using renewable energy such as solar, wind, or other available sources has been studied extensively by researchers. The main objective of this study is to investigate the awareness level about the renewable energy in the Jordanian society. The research study group of people consisted of six hundred and sixty six surveys. The data showed that Jordanians have a high awareness and knowledge about renewable energy and its sources. More than 90% of the surveyed know about renewable energy's merits, and the environmental effect of fossil fuels. This paper also provides a comprehensive overview of the renewable energy technologies and projects established in Jordan, including their distribution, advantages and disadvantages and the challenges encountered by each project.

Keywords: Wind energy, Solar energy, Renewable Energy, Jordan, Energy Assessment.

1. Introduction

Fossil fuels, including oil, gas, and coal, are the primary non-renewable energy sources used worldwide for all technological and industrial development sectors. About 80% of the world's total energy consumption is generated from fossil fuels [1]. According to the International Energy Agency (IEA), the total world demand for primary energy sources will dramatically increase by 2040. In addition, experts estimate that the oil price for the next 22 years will reach $215/barrel [2].

Jordan is one of the countries that suffers from limited fossil fuel resources (i.e. oil and gas). In 2011, around 98% of the total energy consumed was imported from neighboring countries such as Iraq, Egypt, and the Arab Gulf countries to meet the energy demands. Jordan's commercial, industrial and domestic sectors consume around 15.08%, 22.07%, and 46.12% of the total energy, respectively, [3, 4, 5]. Many issues prevent Jordan from securely covering its energy requirements, such as the unsteady state of production in Iraq, the insufficient natural gas supply from Egypt, the rapid growth of commercial and industrial sectors, the high refugee influx, and the rapid increase in population which is expected to exceed 10 million in 2020. In addition to these local issues, the global climate change crisis has come about through the continuous increase of greenhouse gas emissions. The percentage of CO_2 is about 76% of total greenhouse gasses, most of which is released by non-renewable energy consumption in industrial or agricultural fields [6]. Therefore, the government of Jordan started to direct its attention toward renewable energy resources, including Biomass, Geothermal, Solar, and Wind energy [7]. The government passed a new law in 2012 titled "Renewable Energy and Energy Efficiency" that vigorously promotes, diversifies, and regulates the use of renewable energy across all industries. The law aims to:

1. Reduce greenhouse gas (GHG) emissions.
2. Accomplish 10% energy mix projects by 2020, along with the allocation of $15 billion.
3. Motivate investments in renewable energy, especially in the private sector [3, 8].

The 2018 annual report of the national electricity company in Jordan shows that the total electricity generated and imported in the Kingdom reached 20692 GWhs, with renewable energy resources contributing only 10.7% of the total electricity generated that year[9]. In 2019, the renewable energy resources' contribution reached 15.1% of the total electricity generated in Jordan, which is expected to reach 31% by 2030 [5]. It is essential to mention that Zarqa city in Jordan contains the Al-Hussain power plant and the Jordanian petrol refinery that contributes 70% of the overall contamination from fossil fuel combustion in Jordan. This paper investigates the level of awareness in the Jordanian society of renewable energy and its technologies. It also provides a comprehensive overview of planning and existing projects for renewable energy in Jordan. Such research helps government decision-makers develop instructions and laws that encourage the use and regulation of renewable energy projects. It also helps companies understand the reasons

---

* Corresponding author e-mail: ymsmadi@just.edu.jo.

for the turnout or shift away from using renewable energy sources instead of conventional energy resources. The paper is organized as follows; the main energy technologies and projects in Jordan are covered in section 2. The developments in the Jordanian industry's renewable energy use are discussed in section 3. The methodology and survey are in section 4. The conclusions are summarized in section 5.

2. Energy Technologies in Jordan

With the limited fossil fuel resources, Jordan has called attention to the local energy resources to bring down the high-cost energy bill. Jordan spared no effort to encourage investments in different renewable energy technologies and projects. In 2019, renewable energy contributed 15.1% of the total energy generated in Jordan. Solar energy contributed 10.4%, wind energy supplied 4.4% of the total energy generated, and other sources contributed only 0.3%.

2.1. Wind energy utilization in Jordan

Jordan has a considerable wind energy potential, estimated to be more than 250MW [10]. This energy could be utilized for power generation with an annual average wind speed between 7m/s and 9m/s above ground level. In Jordan, there are currently eight operational wind power plant stations in different regions: Hoffa, and Al-Ibrahimyya in Irbid city, Ras Muneef in Ajloun, Shammakh, Safawey, Umari, Twaneh, and Al-Jafr station. Only AlIbrahimyya and Hoffa stations (north region) are connected to the primary power grid. In 1988, Al-Ibrahimyya power plant (pilot wind farm) was built in cooperation with a Danish firm. Its capacity is 320KW, and its average annual energy production is around 650MWhs. Hoffa was constructed in 1996 with 1.2MW capacity in cooperation with the German government. Al-Khamshah and AlFujeij are two wind projects in progress with capacities of 30 – 40MW and 80 – 90MW, respectively. There are many benefits to using wind energy to generate electricity, including the fact that it is a free, renewable, clean, and abundant source of energy that does not pollute the atmosphere or produce atmospheric emissions, in contrast to the burning of fossil fuels, which releases nitrogen oxides (NO_X) and sulfur dioxide (SO_2), contributing to the greenhouse effect. Therefore, using wind energy may reduce fossil fuel consumption and environmentalpollution [10,11]

2.2. Solar energy utilization and distribution in Jordan

Jordan is one of the sun-belt countries with an annual average of global energy equaling 1800kWh/m^2/year [11]. Also, Jordan has more than 300 sunny days per year with solar radiation ranges between 5 – 7kWh/(m^{2}d); these significant facts make using solar energy in Jordan attractive.

The solar radiation in Jordan distributes as follows[3]:

- Southern region: 6-6.5 kWh/(m^{2}d).
- Eastern region: 5.5-6 kWh/(m^{2}d).
- Northern region: 5 -5.5 kWh/(m^{2}d).
- Middle region: 4.5-5 kWh/(m^{2}d).
- Eastern region: 4-4.5 kWh/(m^{2}d).

According to the 2019 annual report [5] of the Jordanian National Electric Power Company (NEPCO), many solar energy projects with large and small capacities are distributed in Jordan. For example, Mafraq development projects at the north-east of Jordan have a 153MW capacity, whereas Safawi projects in the east of Jordan have 51 MW. Also, the Quwireh. PV project in the south of Jordan has 95MW. Different universities have large projects with more than 40 MW capacity. Also, large industries such as Lafarge company has projects with 15MW, and many others. Simultaneously, the small projects with less than 5MW capacity are estimated at around 250MW. Even though the advantages of using photovoltaic technology are prominent, solar energy systems have major drawbacks making it challenging to rely on this source:

- Solar Energy storage systems are expensive due to the high cost of batteries [12].
- The efficiency is below expectations. However, research and development works are still active, thriving towards achieving higher operational efficiency [12].
- It occupies more space than non-renewable systems, reducing the cultivation area [13].
- Soiling has a significant impact on the efficiency of solar panels. Any dirt, snow, dust, or bird droppings may reduce the panel's performance by decreasing the output power [14].
- The dust distribution was investigated by Sanaz Ghazi in 2014, revealing that the Middle East and North Africa are the places with the highest dust accumulation[15]. Therefore, manual or automated cleaning mechanisms are essential and must be applied periodically [16]. However, the cleaning process is expensive in Jordan, especially in arid regions such as in Ma’an Governorate. A study was conducted on the cleaning process’s effect, concluding an average power degradation of 2.22% per month [17].

2.3. Biomass energy and its potential Use in Jordan

Biomass is a renewable energy source where carbon is derived from different organisms or their biological activities. Biomass includes plants (trees, crops, forests, and forest residues), animals, humans, and biological wastes (human, animal, and food waste). As a result, there is a wide variety of biomass types and classifications. Thus, Biomass can be classified as wood, and wood residues biomass, agriculture, herbs biomass, human and animal waste biomass, aquatic Biomass, and industrial biomass [18]. The Jordanian government aims to increase renewable energy use in general; however, most of the execution is concentrated on solar and wind energy. The focus on biomass is relatively scarce but has recently increased because biomass can compete with fossil fuels as another source of electricity generation [19].

2.3.1. Agricultural residues:

Jordan’s production of crops is estimated at 188,000tons. In contrast, its fruit production is estimated at 426.6tons and 1928.6thousandtons of vegetables [20]. The residue amounts of agriculture are calculated as the ratio between the residue's amount to the production amount (RPR) [21]. The RPR of wheat's estimated value is between 0.7and0.8 [22]. The estimated value of the RPR of maize is between 2.0 and 2.3. However, the value of PRP estimated for millet is between 1.75 and 2.0 [21, 23]. PRP value estimated for the olive tree is between 0.5 and 2.6 [23]. The estimated value of RPR for each barley, dentil, and clover trefoil is between 1.75 and 2 [21]. The total residues of the agricultural section were estimated at 997.25 thousand tons in 2011. The solid matter of this value contains 7.954Pj as energy content. This value covers about 2.48% of Jordan's energy consumption in the same year [21].

2.3.2. Olive cake:

The olive tree is considered a natural and essential source for olive oil in Jordan. Jordan's total number of olive trees in 2011 was approximately 17million [21]. Jordan's olive fruit production equals one-third of the total fruit production [20]. The olive cake is dried after its production as a byproduct of the oil extraction process. However, olive cake mass is considered as 35 to 45% of olive fruit mass. Moreover, the dried olive cake mass is 60 to 70% of this percentage [24]. In other words, each 100kg of olive fruit produces 26kg of dried olive cake[21]. The computed amount of olive cake in 2011 was 34,268 tons [20], with a maximum ash content of 3.27% and a calorific value of 24.5MJ/kg.

2.3.3. Animals' Manure:

Jordan depends on specific livestock and poultry species. In 2011, there were 6700 cows, 9210 horses and donkeys, 3017 sheep and goats, 13000 camels, and 37700 chickens. The total number estimated for livestock and poultry in 2011 was 3,106,710 [21]. The estimated amount of waste for these animals was 36000tons. This amount covers about 3.97% of the total energy consumption in Jordan in 2011 [21].

2.3.4. Municipal Sludge:

In Jordan, municipals collect sludge from slaughterhouses, vegetable markets, industrial organic waste, hotels, kitchens, and restaurants. The total amount of municipal sludge collected in the year 2011 was 1,960,000 tons[25]. The collected sludge's heating value from the mentioned places equals 11.49MJ/kg. This value covers 7.03% of Jordan's energy consumption in 2011 [21]. This good percentage makes animal waste an auspicious renewable energy source in the industrial section [21].

2.3.5. Medical Waste:

Medical waste is all solid, liquid, or gas waste produced from different healthcare centers. It also includes pharmaceutical industries, hospitals, laboratories, health centers, veterinary clinics, and the produced waste from the kitchens and offices of such buildings [26]. The total estimated amount of the medical section waste from these buildings is 9ton/day, which equals 3285ton/year [25]. Its average heating value is 14.2MJ/kg [21].

2.3.6. Industrial SectionWaste:

The total waste produced in Jordan's industrial section was 15,000 tons in 2007. However, this value is expected to increase and reach 59,000 tons by 2027 [21].

2.3.7. Wastewater:

In Jordan, there are only twenty-three wastewater treatment plants. The total flow rate daily is 216,412 m^3/day [27].Wastewater volume is increasing and is expected to reach 237MCM/year by 2020 [21]. The treatment plants only produce two million cubic meters of sewage yearly from Wastewater. This huge amount of sewage is a sufficient potential biogas energy source[28]. The dry solids of this sludge are 85,000tons, and the combustible material's heating value in the dry solid part of the sludge is 27.93MJ/kg. Hence, the amount of its potential energy is 2.52PJ [21].

Advantages and disadvantages of utilizing biomass and biomass fuel advantages:

- It is a renewable energy source.
- Natural production of CO_2 and climate benefits. It is a frugal renewable energy source with low carbon emission.
- It uses a non-edible material as a source of fuel.
- It helps in reducing fossil fuel consumption.
- Biomass energy has a low content of harmful elements.
- It riches of volatile matter.
- Its use does not need a high temperature in the degradable process.
- Biomass produces a large and continuous amount of energy due to its availability and continuous production.
- It helps in reducing SOx and NOx emissions, as well as waste reduction.
- Providing more jobs and extra incomes.
- Resuscitate degraded lands using digestate material rich in N_2[29].

Biomass and biomass fuel disadvantages:

- They are not always considered renewable energy sources due to their long-life cycle.
- There is a priority competition between the energy source and the edible source.
- It changes land use, which affects the natural ecosystem.
- Its use may lead to losing the controllability of feedstock supply.
- Some of the feedstock sources are unsustainable.
- There is an omission of production control and certification.
- There is limited knowledge about the validity of the technology. Also, there are few experiments and experiences of biofuel production.
- Relatively, it has a high initial cost.
- There is a low developing rate in biomass markets.
- Biomass production depends on the season, region, and time.
- There is a need for investment for harvesting, collection, storing.
- It has a high content of trace elements.
- Low pH and temperature [29].

2.3.8. Biomass Energy Projects in Jordan

The Ghabawi landfill was designed and constructed between 2001 and early 2003. The landfill depicts 9 excavated areas (called "cells") [30], each cell covers 120,000 to 200,000m^2. The first three cells produce around 4.8MWh. The landfill is fed with solid waste from Amman, the municipality of Zarqaa, AlMuaqqar, Alrusaifeh, and the small surrounding municipalities, with around 4300tons/day. They expect to cover and close the landfill by 2035.

2.4. Geothermal Energy Utilization in Jordan

The geothermal activities in Jordan can be expressed exclusively in two forms; direct usage of (thermal springs and hot deep wells) and using the earth's heat at the shallow ground for heating and cooling the buildings. Thermal springs form the primary source of geothermal energy in Jordan, with a temperature range between 20°C and 63°C [31]. The highest temperature of thermal springs reaches 63°C. Zarqa Ma'in and Zara at the Dead sea are the primary geothermal manifestation in Jordan. In contrast, other springs have temperatures below 45 °C [32]. Table 1 shows the thermal springs and hot thermal deep wells' flow rates and temperatures. Thermal springs have been used as curative water for medical purposes through hotels' spas constructed in the area [32]. Also, in Jordan, geothermal energy is used as a Ground Source Heat Pump (GSHP) for heating and cooling buildings. There are two operation projects, the first at the American University of Madaba (AUM) and another at The Higher Council for Science and Technology (HCST). Geothermal Energy systems are the most environmentally friendly, cost-effective, and energy-efficient heating and cooling technology. The United States Environmental Protection Agency (USEPA) reported that geothermal energy is the least polluting energy [34]. Installing a single geothermal unit is equivalent to planting 750 trees [35]. For district heating systems and GHPs, CO_2 equivalent emission is from 14 to 202g/kWht, lower than the modest land footprints [36].

Ground heat pumps used in geothermal systems need lower energy (electricity), a lower amount of refrigerant fluid, and a more straightforward design for air pumps. On the other hand, the earth is a more stable energy source than the air [38]. The most perceptible effect on the environment is that of drilling. Its operation for boreholes modifies the area's surface morphology and could damage local plants and wildlife, aside from the drilling's irritating noise. In the case of blowouts of fluids from the wells, fluids can pollute surface water and air. Also, the withdrawal of geothermal fluids may trigger the frequency of seismic events in tectonically active areas. Deep hot water often contains gases, such as carbon dioxide (CO_2), hydrogen sulfide (H_2S), ammonia (NH_3), methane (CH_4), and trace amounts of other gases. In addition to the dissolved chemicals whose concentrations usually increase with temperature, all of which are a source of pollution if discharged into the environment [34].

Table 1. Thermal springs and hot thermal deep wells in Jordan [33]

Spring/Well	Temperature range(°C)	Flow Rate(m^3/h)
Himmeh springs	38-44	300-3000
Mukheibeh wells	30-41	200-6000
North Shuneh well	57	700
Queen Alia airport	30-45	30-100
Zara springs	34-55	1-255
Zarqa Ma'in springs	30-63	1-350
Wadi Ibn Hammad springs	35-41	1-25
TS-1D thermal well	50	400
Burbeitta spring	39	315
Afra springs	45-47	376
Smeika thermal well	57	50
Himmeh springs	38-44	300-3000
Mukheibeh wells	30-41	200-6000
North Shuneh well	57	700

2.4.1. Geothermal Projects in Jordan

Project at American University of Madaba (AUM) The largest geothermal project in the Middle East is the American University of Madaba (AUM) project. The AUM's geothermal project was started in July 2011 and completed in August 2012. The project's goal was to utilize the earth heat for cooling and heating by ground source heat pump (GSHP). The system covers a 660kW cooling load and 470kW heating load with 420 boreholes 100m depth [37]. The system eliminates carbon dioxide emissions by approximately 300tons per year (saving 47%compared to other conventional systems) [37].

Project at Higher Council for Science and Technology (HCST). The Higher Council for Science and Technology (HCST) is within El-Hassan Science City Campus in Amman, Jordan. The HCST aims to achieve international standards and recognition in bright sciences and technologies and maximize the benefits of their applications for Jordan's sustainable socio-economic development. In other words, since most of the renewable energy (RE) sources are sustainable, and positively affect the economy of Jordan, HCST utilized all state-of-the-art energy efficiency (EE) measures and renewable energy (RE) technologies to transfer the main building into an Eco-green building. The HCST geothermal project was set in June 2016 as a model or a pilot demonstration plant, and it was completed in August 2017. Now, it continues to be operational in excellent conditions. Hence, the project confirmed the proposed technologies and systems' functionality, efficiency, and economics. The Eco-Building project consists of three parts: 1. Geothermal system heat pump (GSHP) for heating and cooling. 2. LED lighting. 3. Photo-Voltaic (PV) electricity generating of 52kW. The chosen building consists of six floors (two basement floors with a total area of 883m^2 and four floors with a total area of 3,427m^2). The Geothermal system is a type of Ground Source Heat Pump (GSHP) installed to cover 228kW cooling load and 262kWheating load and domestic hot water for the building.

The Ground Source Heat Pump (GSHP) incorporates 30 boreholes, each of which has dimensions (145mm diameter,130m deep and arranged in a 6m × 6m grid). It contains a double U probe pipe of 32mm (outer diameter). 60kW NIBE heat pumps, one master and five slaves, were installed to cover the building heating, cooling loads, and hot water demands. The GSHP can save 40% of the cooling system's energy and 46% of the heating system's energy compared with conventional cooling and heating systems. Therefore, it annually saves 19,784JD around 28,000USD, with a payback period of 14 years as calculated. Also, installing the GSHP system reduces the environmental pollution of burning diesel and the associated spilling of diesel tanks and reduces the amount of fossil fuel used before.

3. Industrial Sector

This section discusses Jordanian industry's use of renewable energy (RE) and its evolution from the early years of installing and operating projects to future projects. Several research studies have been performed to study the industrial sector in Jordan [38-43], focusing on each renewable energy source's efficiency. Several companies are advocating for the use of renewable energy, particularly solar and wind energy.These companies are under the Energy and Minerals Regulatory Commission (EMRC) instructions.

EMRC is the governmental commission regulating and monitoring the Kingdom's energy sector, natural resources, minerals, radio, and nuclear work .The total potential of electricity production in Jordan equals 18% of renewable energy (RE) at the end of the year 2018 with a total capacity of (855kW) which is a doubled value of 2017 [9, 5]. Table 2 shows the capacities of projects connected in 2021.

Due to the rapid increase in the Jordan population, energy consumption and demands are very high for both home and industrial use. Also, fossil fuel price is mounting continuously. As a result, the Jordanian government encourages and supports sectors to use renewable energy sources for electricity production, heating, cooling, pumping, and other general use. Many sectors develop their energy sources to utilize renewable energy for different user types. Figure 1 shows the sectors' usage of renewable energy units (The Capacity for each sector) in Jordan.

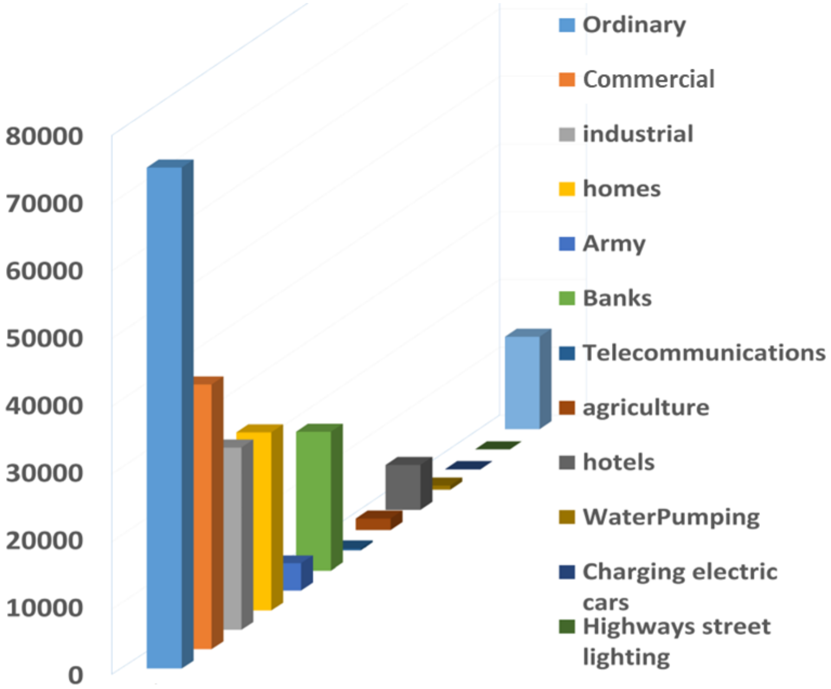

Figure 1. Capacity (kW) of connected renewable energy units for different sectors in Jordan

Table 2. The renewable energy project's status and capacity (PV and wind) in Jordan from 2018-2021.

Status	Capacity(MW)
Operated Project	630
Expected connected projects at the end of 2018	225
Expected connected projects at the end of 2019	196
Expected connected projects at in 2019 after the end of the green corridor	195
Expected connected projects in 2019/2020	100
Expected connected projects at in 2020 after the end of the green corridor	350
The total capacity of expected connected projects in 2021	50

It is obvious from figure 1 that most sectors that depend on renewable energy are the ordinary sectors, followed by the commercial and industrial sectors with capacities of 74382, 39360, and 27071MW, respectively. Also, the agriculture sector utilizes renewable energy with a capacity of 1698MW. In contrast, the lowest sector utilized RE is highway street lighting with a capacity of 2MW. The number of homes that utilized renewable energy is 2,845 with a capacity of 26339MW, indicating that the most significant contribution sectors are homes and domestic use. Hence, categorically, the public uses the most renewable energy sources.

4. Methodology

This paper sheds new light on the level of awareness and knowledge of Jordanian Citizens regarding renewable energy resources. Of the study population, 666 subjects completed and returned the questionnaire. The questionnaire consists of three sections: The questionnaire's first section investigates the general information regarding age, gender, and the participants' educational level. In the second section, several simple questions have been established to verify the participants' knowledge and awareness of renewable energy. Also, the third section concentrated on individuals who have their shops or residential groups. Finally, the survey ended with a question to determine the approval range from Jordanians to increase the reliance on renewable energy systems.

4.1. Part A: Public people awareness survey

A questionnaire was conducted based on closed format questions (Closed-ended Questions) of 15 questions using Google Survey. The closed-format questions include Dichotomous questions, Likert Scaling, Leading, Bipolar, and Rating. Only the Dichotomous, Likert, and multiple-choice questions have been used in this questionnaire to construct the survey structure. Four questions with the type of Dichotomous questions were answered with either ”yes” or ”no.” While in five questions of Likert Scaling, the respondents answered with either agree, disagree, and strongly agree, and disagree, in addition to neutral.

A public survey was conducted for Jordanian citizens of all ages and educational levels and distributed randomly. Also, the draft survey was sent to experts in renewable energy to detect, delete, and correct unclear and improperly written questions. Additionally, we implemented the survey in Arabic and English to make it easier for the participants to choose the preferred language and increase the collected data's quality and quantity. This study gathered information from various sources, including the industrial and public sectors, the Jordanian Renewable Energy Society, and the Ministry of Energy and Minerals. In addition, interviews with experts and decision-makers were conducted.

4.1.1. Analysis and Results

Section I: The first section of the survey discusses the general information regarding age, gender (Male and Female), and the educational level of the 666 recipients. As seen in figure 2, 56% of the participants were female, with ages ranging from less than 18 to above 50. Furthermore, about 43% of the female participants were between the age of 26 − 35. On the other hand, 43.8% of the total responses were from males, and 51% were from aged 25 to 35. The educational level distribution is also an essential factor in this survey. Figure 3 shows that the majority of the respondents hold bachelor's degrees. In comparison, only 5% of the respondents hold high school diplomas or below.

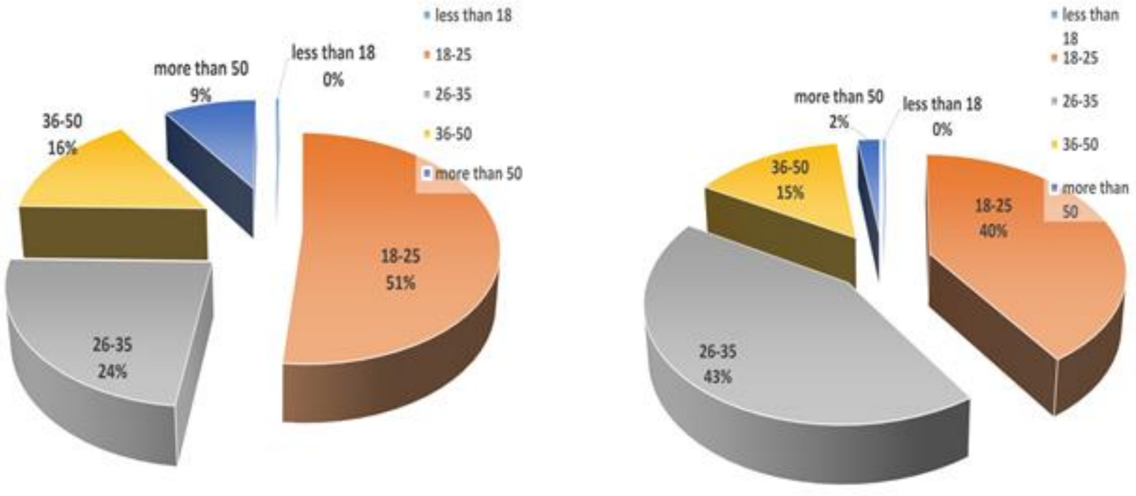

(a) (b)

Figure 2. Gender Age distribution a) male and b) female

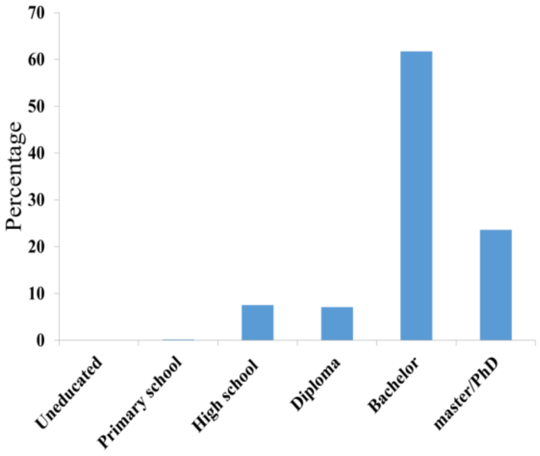

Figure 3. Educational Level Distribution

Section II : We primarily focused on testing (verifying) the level of awareness and knowledge of renewable energy in this section. For this purpose, we use Dichotomous questions shown in table 3, and Likert Scaling questions in Table 5. Interestingly, 98.9% answered that they have background knowledge of global warming, 90.80% of those surveyed indicated that they know the effect of burning fossil fuels on climate change. The terms of ”Renewable Energy” and its resources were impressively known by 99.4% of the total respondents. Further testing questions were conducted, as shown in Table 5. In Table 3, more than 73% of the respondents strongly agree (or agree) that the RE’s price will be much lower than conventional energy and will gradually become cheaper. On the other hand, less than 13% disagree (or strongly disagree), while 13.7% were neutral in response to this question. In response to the question: ’Compared to fossil fuel, do you think renewable energy-based technologies have a much lesser impact on the environment?’, the majority,approximately 95% replied by either strongly agree or agree. While less than 5% of those surveyed were neutral or disagreed that renewable energy has less impact than the conventional fossil fuel source of energy on the environment. When the participants were asked if they think investing in renewable energy is financially sustainable in the long run, the overall response to this question was very positive. Finally, respondents were asked to indicate whether they agree that renewable energy technologies are reliable or not. In response to this question, 55% agree, and37.2% strongly agree. A minority of participants (less than 4%) disagree or strongly disagree.

Section III: This questionnaire section required respondents to give information about the reliance on renewable energy at the shop markets and residential buildings. As shown in figure 4, when the participants were asked about support and increased reliance on Renewable energy resources, the majority (60%) of both genders (Male and Female) strongly agreed. A total of 73 shop or residential building owners were asked whether or not they installed a solar PV system and why they did not install it (if they do not use it). The results are divided into a category I of people who did not install the system and reasons for not installing. In contrast, category II refers to people who have the system and whether it meets their demand or not. Category I results show that most of the respondents (around 70%) do not have a PV system for several reasons shown in figure 6. These reasons can be summarized by the high costof installing these systems (around 65% agree on this), and 29% answered with the area’s limitation. Others replied that installing the system will not reduce the electricity bill. Simultaneously, only one participant responded that he does not care about environmental issues, and another did not answer. On the other hand, category II, shown in figure 5, shows that around 25% of the respondents installed the system and met their demands. At the same time, less than 10% did not meet their demand.

Table3. Jordanian Citizen level of knowledge of Renewable energy

		N=666				
		Scale				
	Question	Strongly Agree	Agree	Neutral	Disagree	Strongly Disagree
1	Do you think renewable energy will match the price of conventional energy and will eventually become cheaper?	31.70%	42%	13.70%	9.20%	3.40%
2	Compared to fossil fuel do you think renewable energy based technologies have much lesser impact on the environment?	59.60%	34.80%	3%	1.8%	0.8%
3	Do you think investing in renewable energy is financially sustainable in the long run?	41%	44%	9.90%	4.2%	0.9%
4	Do you think renewable energy technologies are reliable	37.20%	55%	4.2%	2.6%	1.1%

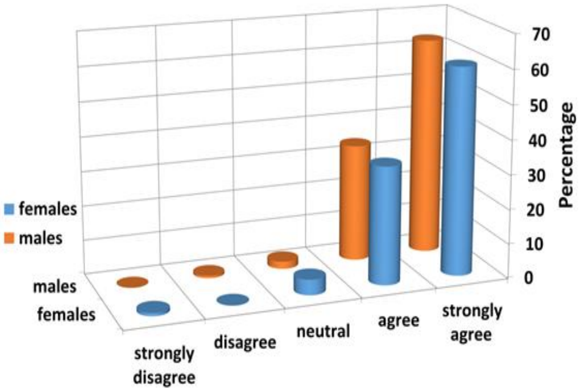

Figure 4. Support Renewable Energy

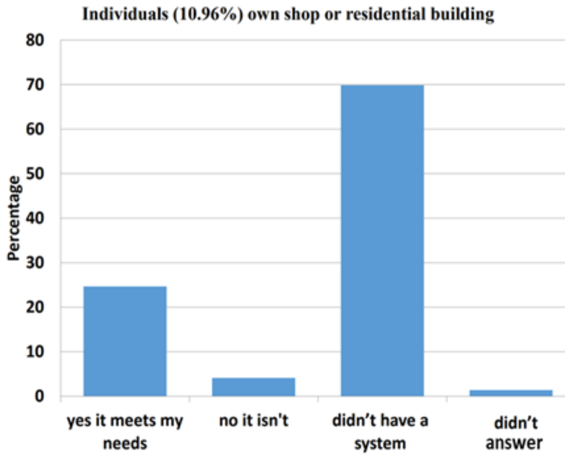

Figure 5. Individuals own shop or residential building.

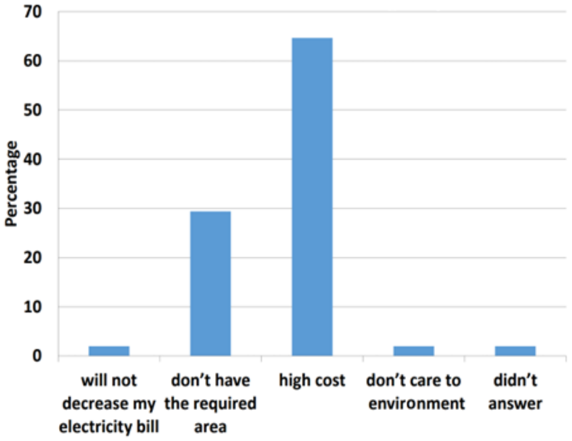

Figure 6. Reasons for not installing PV system

4.2. Part B: Mosques Gathering information

The mosque is a worship house sponsored by the Ministry of Awqaf Islamic Affairs and Holy Places. The mosque's geometric shape is characterized by the dome's existence on the roof and the minaret. The distribution and number of mosques in the Jordanian governorates and suburbs, as well as the mosques that utilize renewable energy systems, vary, with the majority implementing a renewable energy project. In the capital Amman, they reached 392 projects with a total capacity of 6576,715 kWp. Irbid is in second place where the number of renewable energy projects implemented by the end of 2017 in mosques is about 215 projects with the capacity of 3618.052 kWp. The rest of the executed projects are distributed in the other regions and the Jordanian governorates. See table 4 and figure 7. Due to the large increase in the electricity bill and the increase in the number of mosques in Jordan, the Jordanian Ministry of Awqaf Islamic Affairs and Holy Places has formed a Renewable Energy Committee that supervised 803 renewable energy projects on mosques with a total capacity of 13646.93 kWp at the end of 2017, that saved approximately 150,000 JD (around 210000 USD) per month. There are 141 renewable energy projects in the mosques around Jordan, with a total capacity of 2364kW. After implementing these projects, it is estimated that they will save 30000JD (42000 USD) per month. Also, due to Aqaba city's hot weather, the only coastal city in Jordan (located on the Red Sea's), Aqaba Governorate plans to support the implementation of 34 projects due to high electricity consumption in mosques especially in the summer semester. The total capacity of these 34 projects is 1568 kWp, with an almost year saving of 265000 JD (380000 USD). All these renewable energy systems projects implemented and planned to be implemented in mosques in Jordan, their capacities, and financialsavings are illustrated in table 6.

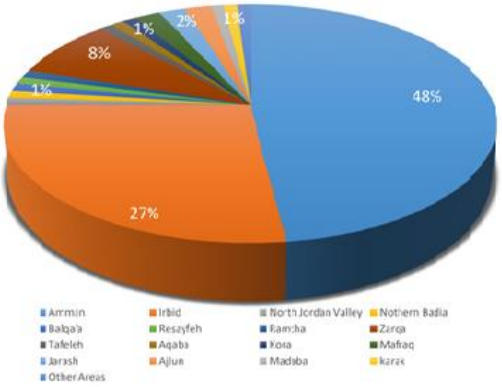

Figure 7. Distribution rates of renewable energy projects around Jordan at the end of 2017.

Table 4. The distribution of renewable energy projects in the mosques around Jordan that were implemented at the end of 2017.

Jordanian governorates	Number of projects	Project capacity (KWP)	Distribution rates (%)
Amman	392	6576.715	48.19
Irbid	215	3618.052	26.5
Northern Jordan Valley	8	145	1.06
Northern Badia	2	20.3	0.15
Balqa'a	23	360.5	2.6
Resayfeh	8	180.2	1.32
Ramtha	12	195.82	1.43
Zarqa'a	63	1134.45	8.31
Tafeleh	11	144.68	1.06
Aqaba	5	130.8	0.96
Kora	11	188.375	1.38
Mafraq	16	272.06	1.99
Jarash	11	179.535	1.31
Ajlun	15	332.463	2.44
Madaba	5	90.98	0.67
Karak	6	77	0.56

Table 5. Jordanian citizens' level of climate change knowledge and renewable energy

		N=666	
		Percentage (%)	
	Question	**Yes**	**No**
1	Have you heard of global warming or sometimes called climate change?	98.90%	1.10%
2	Do you think that burning fossil fuels is the cause of climate change?	90.80%	9.60%
3	Do you know the meaning of renewable energy?	98.80%	1.40%
4	Are you familiar with renewable energy resources such as solar, wind, and hydro?	99.40%	0.60%

4.3. Questionnaire survey analysis

All data were collected from the mosques' Imams (Imam is the one who leads Muslim worshippers in prayers and manages the mosque), where we distributed our survey to the mosques' sample in Jordan-Irbid. The main questions are about investigating the challenges and barriers faced by mosques that utilize renewable energy systems and their benefits. In our study, most mosques installed PV systems that use solar energy at a rate of 88%. On the other hand, only 8% of them utilize biofuels as alternative and renewable energy sources. However, none of the mosques in our survey utilizes wind energy. See figure 8. The capacity of the PV systems utilized in the mosques we studied ranges from 4.55 to 20.4kWp. Therefore, 56% of mosques are able to satisfy their total energy consumption with renewable energy. However, PV systems covered most of the electricity consumption for 44% of the mosques. All agreed on the benefit of using the solar system to generate electricity and a good positive that none of the mosques (0%) claimed that the system is no longer useful. The reasons for installing renewable energy systems in the mosques and encouraging Imams to request utilizing them to generate the electricity are:

- Increase electric tariff.
- Large consumption of the mosque of electricity.
- Renewable and not threatened with depletion.
- Environmentally friendly.

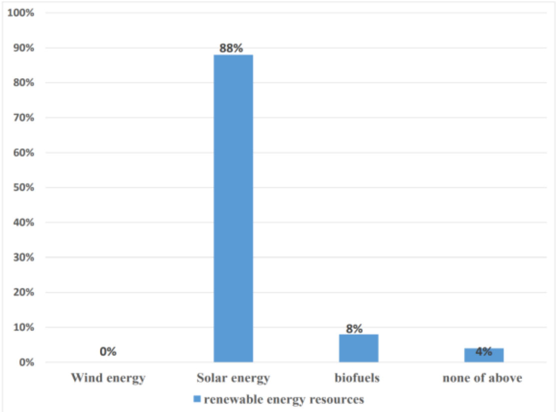

Figure 8. renewable energy resources that are utilized in the mosques

The increase in electricity tariffs in 28% of mosques is the main motive for using renewable energy systems. In comparison, 18% of mosques are directed to using renewable energy systems due to the high electricity consumption by the mosque. See figure 9. Based on experience in renewable energy systems, 52% plan to expand the system installed for the mosque, while 48% of mosques do not intend to expand the system. As for the benefits of such systems, the most important factor was the coverage of electricity consumption from the economic point of view. However, the managers of mosques face many obstacles after the installation and the use of the system; 40% complained of periodic maintenance required by the system and, therefore, the additional costs.

In comparison, 20% of mosques consider insufficient space a challenge. This may have led to 16% of mosques that did not cover the productivity of the renewable energy system required. 4% of them found the problem with the system's cost and its high structure, 12% did not face any obstacle. See figure 10.

Table 6. Summary of the economic feasibility of renewable energy projects in the Hashemite Kingdom of Jordan mosques until the end of December 2017.

Renewable energy projects	Projects number	Project capacity (KWP)	Financial saving (JD)
Implemented projects	803	13,646.93	150,000
Projects under construction	141	2,364.14	30,000
Planed projects to implement in Aqaba	34	1,568	22,000

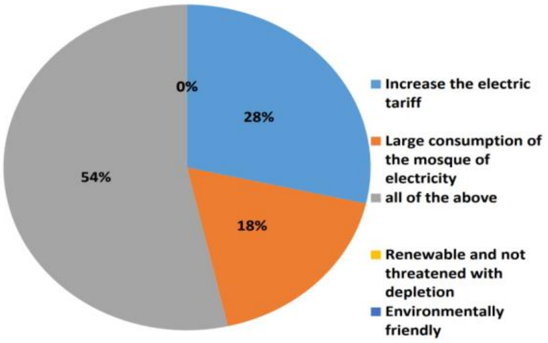

Figure 9. Reasons that the mosques install renewable energy systems

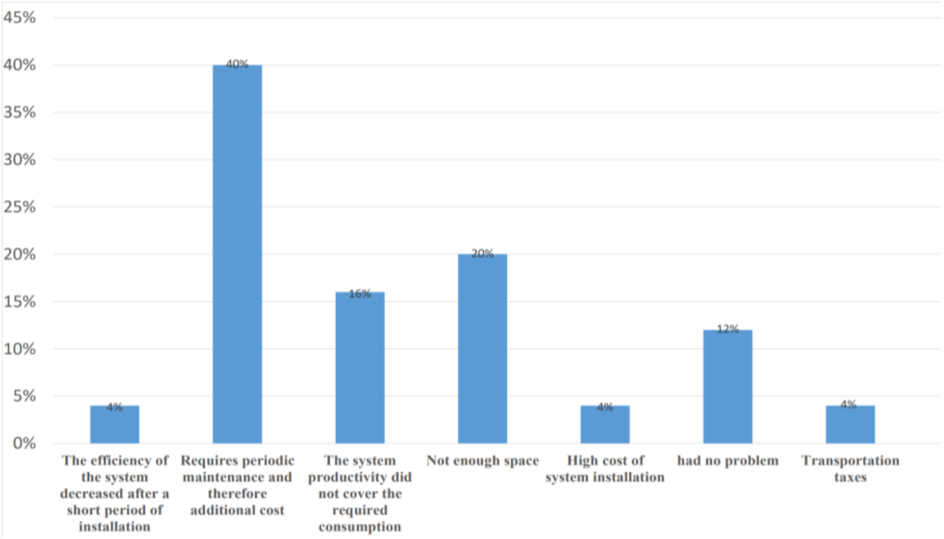

Figure 10. Problems and challenges while using the renewable energy system.

5. CONCLUSIONS

This paper studied an overview of renewable energy technologies used in Jordan regarding the installed projects' distribution, advantages, and disadvantages. It has been found that using PV systems for power generation and other applications through industries and in other sectors is dominant over all other technologies. Special attention regarding wind technology should be employed to enhance such potential benefits, especially on farms. Furthermore, the level of awareness of Jordanians to renewable energy was conducted by constructing a questionnaire. The data was then collected and analyzed for 666 respondents of different ages and educational levels for both genders. The results showed that the level of awareness in Jordanian society is high. More than 90% of the surveyed know about renewable energy, its merits, and the environmental effect of fossil fuels. Even though 70% of those who have a shop or a residential building did not install a PV system, the main cause was the high cost.

Regarding the high increase in renewable energy projects installed for mosques in Jordan, Amman has the highest number of projects (392) at the end of 2017. Irbid follows with 215 projects. All Imams of the mosques utilizing renewable energy systems are satisfied because of the reduction in the electricity bills. Finally, the number of people supporting renewable energy was high; therefore, the government should encourage people to install PV systems at their homes or facilities by providing continuous and necessary support.

References

[1] S. Mohr, J. Wang, G. Ellem, J. Ward, D. Giurco, "Projection of world fossil fuels by country". Fuel, Vol. 141, 2015, 120–135.

[2] F. Baghdadi, K. Mohammedi, S. Diaf, O. Behar, "Feasibility study and energy conversion analysis of stand-alone hybrid renewable energy system". Energy Conversion and Management, Vol. 105, 2015, 471–479.

[3] M. Al-Omary, M. Kaltschmitt, C. Becker, "Electricity system in Jordan: Status & prospects". Renewable and Sustainable Energy Reviews, Vol. 81, 2018, 2398–2409.

[4] J. Jaber, M. Mohsen, A. Al-Sarkhi, B. Akash, "Energy analysis of Jordan's commercial sector". Energy Policy, Vol. 31, No. 9, 2003, 887–894.

[5] NEPCO, National Electric Power Company.Annual report, Technicalreport, Jordan, 2019.

[6] X. Liu, S. Zhang, J. Bae, "The nexus of renewable energy-agricultureenvironment in BRICS". Applied energy, Vol. 204, 2017, 489–496.

[7] J. Jaber, F. Elkarmi, E. Alasis, A. Kostas, "Employment of renewable energy in Jordan: Current status, swot and problem analysis". Renewable and sustainable energy reviews,Vol. 49, 2015, 490–499.

[8] A. S. K. Dalabeeh, "Techno-economic analysis of wind power generation for selected locations in Jordan". Renewable Energy, Vol. 101, 2017, 1369– 1378.

[9] NEPCO, National Electric Power Company.Annual report, Technicalreport, Jordan, 2018.

[10] M. Ababneh, W. Kakish, O. A. Mohareb, I. Etier, "Investigation of wind energy in Jordan". International Conference and Exhibition on Green Energy and Sustainability for Arid Regions and Mediterranean Countries ICEGES, Amman, Jordan, 2009.

[11] F. Abdulla, M. Widyan, Z. Al-Ghazawi, S. Kiwan, H. Abu-Qdais, M. Hayajneh, A. Harb, M. Al-Nimr, "Status of Jordan renewable energy sector: problems, needs and challenges". Proceedings of the Regional Collaboration Workshop on Energy Efficiency and Renewable Energy Technology, 2004.

[12] S. Charfi, A. Atieh, M. Chaabene, "Modeling and cost analysis for different PV/battery/diesel operating options driving a load in Tunisia, Jordan and KSA". Sustainable cities and society, Vol. 25, 2016, 49–56.

[13] C. P. Castillo, F. B. e Silva, C. Lavalle, "An assessment of the regional potential for solar power generation in EU-28". Energy policy, Vol. 88, 2016, 86–99.

[14] M. R. Maghami, H. Hizam, C. Gomes, M. A. Radzi, M. I. Rezadad, S. Hajighorbani, "Power loss due to soiling on solar panel: A review" Renewable and Sustainable Energy Reviews, Vol. 59, 2016, 1307–1316.

[15] S. Ghazi, A. Sayigh, K. Ip, "Dust effect on flat surfaces–a review paper", Renewable and Sustainable Energy Reviews, Vol. 33, 2014, 742–751.

[16] R. Concei¸c˜ao, H. G. Silva, L. Fialho, F. M. Lopes, M. Collares-Pereira, "PV system design with the effect of soiling on the optimum tilt angle". Renewable energy, Vol. 133, 2019, 787–796.

[17] M. Z. Ahmed, H. A.-K. L. Al-Khawaldeh, A. Al-Tarawneh, "The effect of soiling and periodic cleaning on the performance of solar power plants in Ma'an, Jordan". Innovative Systems Design and Engineering,Vol. 9, No. 1, 2018.

[18] S. V. Vassilev, D. Baxter, L. K. Andersen, C. G. Vassileva, T. J. Morgan, "An overview of the organic and inorganic phase composition of biomass". Fuel, Vol. 94, 2012, 1–33.

[19] P. McKendry, "Energy production from biomass (part 1): overview of biomass". Bioresource technology, Vol. 83, No. 1, 2002, 37–46.

[20] D. of Statistical Studies, Annual report, technical report, Ministry of Agriculture, Amman, Jordan, 2011.

[21] Z. Al-Hamamre, A. Al-Mater, F. Sweis, K. Rawajfeh, "Assessment of the status and outlook of biomass energy in Jordan". Energy Conversion and Management, Vol. 77, 2014, 183–192.

[22] M. Seilmaier, W. Guggemos, M. Alberer, C. Wendtner, C. Spinner, "Infections among refugees". Notfall Rettungsmed, 2017.

[23] C. Di Blasi, V. Tanzi, M. Lanzetta, "A study on the production of agricultural residues in Italy". Biomass and Bioenergy, Vol. 12, No. 5, 1997, 321–331.

[24] R. K. Thakur, A. Natale, "Atrial fibrillation risk factors, Cardiac Electrophysiology Clinics", Vol. 13, No.1, 2021.

[25] H. A. Qdais, "Techno-economic assessment of municipal solid waste management in Jordan". Waste management, Vol. 27, No. 11, 2007, 1666–1672.

[26] Z. Al-Hamamre, M. Saidan, M. Hararah, K. Rawajfeh, H. E. Alkhasawneh, M. Al-Shannag, "Wastes and biomass materials as sustainablerenewable energy resources for Jordan". Renewable and Sustainable Energy Reviews, Vol. 67, 2017, 295–314.

[27] A.-z. Kamel, A. Nada, "Performance of wastewater treatment plants in Jordan and suitability for reuse". African Journal of Biotechnology, Vol. 7, No. 15, 2008.

[28] G. F. Parkin, W. F. Owen, "Fundamentals of anaerobic digestion of wastewater sludges". Journal of environmental engineering, Vol. 112, No. 5, 1986, 867–920.

[29] S. V. Vassilev, C. G. Vassileva, V. S. Vassilev, "Advantages and disadvantages of composition and properties of biomass in comparison with coal: An overview". Fuel, Vol. 158, 2015, 330–350.

[30] G. A. Municipality, "Greater Amman municipality (GAM) solid waste stakeholder engagement plan". Technical report, Greater Amman Municipality, February 2015.

[31] A. Al-Sarkhi, B. Akash, E. Abu-Nada, S. Nijmeh, I. Al-Hinti, “Prospects of geothermal energy utilization in Jordan”. Energy Sources, Part A, Vol. 30, No. 17, 2008, 1619–1627.

[32] A. Saudi, A. Swarieh, “Geothermal energy resources in Jordan”. World Geothermal Congress, 2015.

[33] Z. Abu-Hamatteh, K. Al-Zughoul, S. Al-Jufout, “Potential geothermal energy utilization in Jordan: Possible electrical power generation”. International Journal of Thermal and Environmental Engineering, Vol. 3, 2011, 9–14.

[34] A. Manzella, “Geothermal energy”. Institute of Geosciences and Earth Resources, Pisa, Italy, EPJ Web of Conferences, 2017.

[35] M. L’Ecuyer, C. Zoi, J. S. Hoffman, “Space conditioning: the next frontier: the potential of advanced residential space conditioning technologies for reducing pollution and saving consumers money, Office of Air and Radiation”. US Environmental Protection Agency, 1993.

[36] B. Goldstein, G. Hiriart, J. Tester, L. Gutierrez-Negrin, R. Bertani, C. Bromley, E. Huenges, A. Ragnarsson, M. Mongillo, J. W. Lund, et al., “Geothermal energy, nature, use, and expectations, in: Renewable Energy Systems”. Springer, 2013, 772–782.

[37] S. J. Nimri, “Geothermal system: A pioneer project at the American University of Madaba (AUM)”. ICERE 2015 International Conference on Environment and Renewable Energy at Vienna, Austria, May, 2015.

[38] E.A. Teshnizi, M. Jahangiri, A.A. Shamsabadi, L.M. Pomares, A. Mostafaeipour, M.E. Assad, “Comprehensive Energy-Econo-Enviro (3E) Analysis of Grid-Connected Household Scale Wind Turbines in Qatar”. Jordan Journal of Mechanical and Industrial Engineering, Vol. 15, No. 2, 2021, 215-231.

[39] A. Benatiallah, L.Kadi, B. Dakyo, “Modelling and Optimisation of Wind Energy Systems”. Jordan Journal of Mechanical and Industrial Engineering, Vol. 4, No. 1, 2010, 143-150.

[40] G. Halasa, “Wind-Solar Hybrid Electrical Power Generation in Jordan”. Jordan Journal of Mechanical and Industrial Engineering, Vol. 4, No. 1, 2010, 205-209.

[41] M. Al zou'bi , “Renewable Energy Potential and Characteristics in Jordan”. Jordan Journal of Mechanical and Industrial Engineering, Vol. 4, No. 1, 2010, 45-48.

[42] V. S. Kumar, A.F. Zobaa, R.D. Kannan, K. Kalaiselvi, “ Power Quality and Stability Improvement in Wind Park System Using STATCOM”. Jordan Journal of Mechanical and Industrial Engineering, Vol. 4, No. 1, 2010, 169-176.

[43] Y. Abdallat, A. Al-Ghandoor, I. Al-Hinti, “Reasons behind Energy Changes of the Jordanian Industrial Sector”. Jordan Journal of Mechanical and Industrial Engineering, Vol. 5, No. 3, 2011, 241-245.

JJMIE

Volume 16, Number 4, September. 2022
ISSN 1995-6665
Pages 627– 644

Jordan Journal of Mechanical and Industrial Engineering

Numerical Investigation of Buoyancy-driven Flow in a Crescent-shaped Enclosure

Houssem Laidoudi[1], Ahmed Kadhim Hussein[2,3], Ahmed B. Mahdi[4], Obai Younis[5,6,*], Emad Hasani Malekshah[7], Hussein Togun[8], Uddhaba Biswal[9]

[1] *Laboratory of Sciences and Marine Engineering, Faculty of Mechanical Engineering, USTO-MB, BP 1505, El-Menaouer, Oran, 31000, Algeria.*
[2] *College of Engineering - Mechanical Engineering Department – University of Babylon - Babylon City – Hilla – Iraq.*
[3] *College of Engineering, University of Warith Al-Anbiyaa, Karbala, Iraq*
[4] *Anesthesia Techniques Department, Al-Mustaqbal University College, Babylon, Iraq.*
[5] *Department of Mechanical Engineering, College of Engineering at Wadi Addwaser, Prince Sattam Bin Abdulaziz University, Wadi Addwaser, KSA*
[6] *Department of Mechanical Engineering, Faculty of Engineering, University of Khartoum, Khartoum, Sudan* [7] *Department of Power Engineering and Turbomachinery, Silesian University of Technology, Gliwice 44-100, Poland*
[8] *Department of Biomedical Engineering, University of Thi-Qar, Iraq*
[9] *Department of Mathematics, National Institute of Technology Rourkela, Rourkela 769008, Odisha, India*

Received 22 Jun 2022 *Accepted 18 Jul 2022*

Abstract

The buoyancy-driven flow in a crescent cavity is numerically analyzed by employing the finite volume method for the first time. The enclosure was filled with an incompressible fluid, whose thermal properties are given by Pr. The enclosure's left and right arcs have different temperatures. Two cases are adopted in the present work; in the first case, the left and right arcs were considered cold and hot. While for the second case, the thermal boundary conditions of the arcs were shifted. The results were illustrated for Prandtl number $0.71 \le Pr \le 50$ blockage ratio of the space $0.1 \le B \le 0.5$ and Rayleigh number $103 \le Ra \le 105$. For both considered cases, the velocity profiles increased with the increasing Ra and decreasing B. While the increase in Ra increases the values of Nu for both arcs. Also, the flow and thermal pattern are not affected by changing the fluid's thermal properties represented by Pr. Furthermore, when the influence of buoyant force is substantial, and the cavity width is wide, the shifting thermal boundary conditions become evident. These new results can be exploited in heat exchanger applications as well as insulating systems.

Keywords: Natural convection, Crescent-shaped cavity, FVM.

Nomenclature

Symbol	Description	Unit
B	The blockage ratio of the space	
g	Gravitational acceleration	m/s^2
d	Width of the gap inside the cavity	m
H	Cavity height	m
n	Normal vector	
Nu	Mean Nusselt number	
p	Pressure	N/m^2
P	Nondimesional pressure	
Pr	Prandtl number	
Ra	Rayleigh number	
T	Temperature	ºC
u	Velocity component in x-direction	m/s
U	Non-dimensional velocity component in X-direction	
v	Velocity component in y-direction	m/s
V	Non-dimensional velocity component in Y-direction	
x	Coordinate in the horizontal direction	m
X	Non-dimensional coordinate in the horizontal direction	
y	Coordinate in the vertical direction	m
Y	Non-dimensional coordinate in the vertical direction	

Greek Symbols

α	Thermal diffusivity	m^2/s
β	Thermal expansion coefficient	K^{-1}
ϕ	Non-dimensional temperature	
ν	Kinematic viscosity	m^2/s
ρ	Density	kg/m^3

Subscripts

c	Cold
h	Hot
l	Local

---

* Corresponding author e-mail: oubeytaha@hotmail.com.

1. Introduction

The buoyancy-driven convection, or sometimes called the free convection, in enclosures is a topic of great interest in heat transfer. This famous problem has received wide interest in the scientific community [1-3]. This is not a sudden chance, but it is due to its huge practical applications. These applications include nuclear reactors, thermal storage systems, cooling of electronic equipment, solar energy, heat exchangers, refrigerators, melting and solidification, drying and food technologies, wet clutches and airplane cabin insulation [4-9]. Unfortunately, most of the published papers on this problem are concerned with the classical well–known square or rectangular geometries. Whereas the papers concerned with the complicated geometries are much less than that related to the classical geometries. Samples of the complicated cavities include triangular [10-13] , vee-corrugated [14-16] , wavy [17] , elliptical [18] , parallelogrammic [19-22] , trapezoidal [23] , parabolic [24] , C-shape [25] , T-shape [26] , L-shape [27] , Γ- shape [28] , U-shape [29] and F-shape [30].

Dutta et al. [31] examined entropy production and natural convection inside a rhombic enclosure with a wavy and non-uniformly heated upper wall by numerical means. Whereas its lower and sidewalls were kept cold. They deduced that the *Nuav* was enhanced with the increase in the tilting angle. Hussein [32] explored the influence of the hot concentric circular cylinder on the free convection inside a parallelogrammic cavity loaded with air. He concluded that the increase in *Ra* enhanced the Nu_{av} values. The numerical investigation of the free convective flow inside a parallelogrammic enclosure with cold sidewalls was investigated by Salih and Mustafa [33]. The lower wall was partially heated, whereas the rest of this wall, together with the upper wall, were isolated. The authors deduced that Nu_{av} was enhanced by increasing the heat source length for all values of *Ra* and the cavity's inclination angle. The impact of various boundary conditions on free convection inside a porous parallelogrammic cavity was numerically addressed by Anandalakshmi and Basak [34]. The results revealed that the *Nuav* was enhanced for high *Da* for Rayleigh- Benard boundary condition. The numerical investigation of MHD buoyancy-driven convective flow inside an enclosure cavity elliptic shape was made by Adekeye et al. [35]. The cavity was loaded with a fluid saturated with a porous media, a hot top wall and a cold bottom wall. The authors reported that the impact of the tilted angle on the heat transmission rate was significant at $58^o \leq \phi \leq 90^o$. The numerical analysis of the free convection inside an octagonal enclosure included, inside it, a hot solid circular cylinder was presented by Hussain and Hussein [36]. All enclosure walls were cold. The cylinder was moved in three different directions (i.e., vertical, horizontal and diagonal). The study findings were presented for various *Ra* numbers and cylinder locations. It was found that the Nu_{av} attained its peak value at the highest *Ra*. Chen and Cheng [37] numerically and experimentally analyzed the buoyancy-driven convection of air in a tilted arc-shaped cavity. It was found that the increase in *Gr* intensified the Nu_{av}. Also, they observed that the vortex pattern was affected by the values of inclination angles. The numerical examination of the buoyancy-driven convective flow inside an inclined cavity of L –shape loaded with Newtonian fluid was performed by Tasnim and Mahmud [38]. They deduced that there was a linear relationship between (Nu_{av} and the tilted angle of the cavity at *AR* = 0.25 and $Ra = 10^3$ and 10^4 . Mustafa [39] explored air free convective flow confined in a parabolic enclosure with cold vertical walls numerically. The upper wall of the cavity was thermally isolated, while the lower one was hot. It was found that the highest *Ra* and small value of the parabolic equation maximized the Nu_{av} values. Wang et al. [40] numerically explored air convective flow inside a circular cavity containing a hot flat plate. The outer cavity wall was maintained at an isothermal cold temperature. The results indicated that the Nu_{av} was intensified when the flat plate was located vertically inside the cavity. Wang et al. [41] researched the impact of the orientation of the internal cylinder on the natural convective flow inside a cavity of a circular geometry numerically. The authors deduced that the local Nusselt number was enhanced when the cylinder was located in the corner-upward orientation. The numerical study of natural convection in a 3D spherical enclosure with cold external walls was performed by Welhezi et al. [42]. The cavity included a hot cubical body filled with various kinds of fluids. The results indicated that the Nu_{av} was maximized at *Pr* = 25 and Ra = 10^7. The numerical analysis of the free convective flow inside an isosceles triangular cavity was conducted by Roy et al. [43]. The enclosure's bottom wall was heated in a uniform and non-uniform manner. The local Nusselt number was shown to have an oscillating tendency. Saha [44] numerically analyzed transient laminar free convective flow inside a triangular cavity having hot inclined walls. The bottom wall of it was kept thermally insulated. He deduced that the instantaneous Nu_{av} strongly depended on *Pr*, *Ra* and the cavity aspect ratio. Oztop et al. [45] considered natural convection inside a tilted triangular cavity heated from below. The vertical wall was hot, while the inclined one was cold. The authors deduced that the heat transmission was influenced by the inclination angle and *Ra*. El-Hassan et al. [46] numerically researched natural convection inside a gamma of right-angled triangular enclosures. The upper walls were kept thermally insolated, whereas the inclined wall was cold and the vertical one was hot. They deduced that the *Nuav* was related to the cavity cross-sectional area. Yesiloz and Aydin [47] conducted a computational and experimental study on free convection inside a triangular enclosure loaded with water. The vertical, bottom, and inclined walls were cold, hot and thermally insulated, respectively. They recommended a correlation of *Nu* as a function of the *Ra*. The buoyancy-driven convective flow inside a tilted enclosure bounded by adiabatic horizontal flat walls was examined by Mushatet [48]. The enclosure's sidewalls were wavy and preserved at hot temperatures. He deduced that the local Nusselt number was reduced with higher values of wavy wall amplitude. Adjlout et al. [49] numerically analyzed free convection inside an inclined chamber with an insulated horizontal wall. The flat left and wavy right sidewalls were considered cold and hot, respectively. The results indicated that the increase in the number of undulations decreased the heat transmission rate when the tilt angle was more than 75^o . Koulali et al. [50] numerically examined natural convective flow inside a corrugated enclosure with two superimposed fluid layers. The upper and lower walls were kept adiabatic and under a constant heat flux, respectively, whereas the vertical walls were assumed cold. They found that the corrugated wall improved the heat transmission in the cavity. The numerical examination of the buoyancy-driven convective flow inside a tilted trapezoidal enclosure was performed by

Hussein et al. [51]. Both its sidewalls were assumed cold, whereas the lower and upper walls were hot and adiabatic, respectively. They concluded that the Nu_{av} attained its peak value at a tilt angle equal to (30º). Natarajan et al. [52] numerically explored the free convection inside a trapezoidal enclosure with cold sidewalls and a top adiabatic wall. The enclosure's bottom wall was heated either uniformly or non-uniformly. They concluded that the Nu_{av} was decreased for the non-uniform heating case. The numerical analysis of the buoyancy-driven convection inside an inclined trapezoidal enclosure was introduced by Lasfer et al. [53]. Both upper and lower walls were assumed adiabatic. Whereas the inclined left sidewall was hot, and the vertical right sidewall was cold. It was deduced that the Nu_{av} was a function of the aspect ratio, Ra and the inclination angle. Additional works related to the buoyancy-driven convection in complex shape cavities can be found in [54-63]. Based on the comprehensive literature and our wide experience in the convection heat transfer, there has been no research to date that has quantitatively explored free convection inside a crescent shape cavity. So, the contribution of the current work is to research this novel problem in more detail and with intense attention.

2. The physical model, governing equations and boundary conditions

Fig. 1 shows the physical model for a crescent-shaped cavity formed by meeting its inner and outer arcs. Also, the cavity height is defined by H, and the width of the gap inside the cavity is defined by d. The ratio d/H is called the blockage ratio B , and it is selected between (0.1 and 0.5). The cavity's left and right arcs have different temperatures. Two cases are adopted in the present work; in the first case, the left and right arcs were considered cold and hot. Whereas, in the second case, the left and right arcs were considered hot and cold, respectively. The cavity was filled with an incompressible fluid, whose thermal proprieties are given by Pr. The temperature difference between these arcs is responsible for making the thermal buoyancy force driving the natural convection inside the cavity.

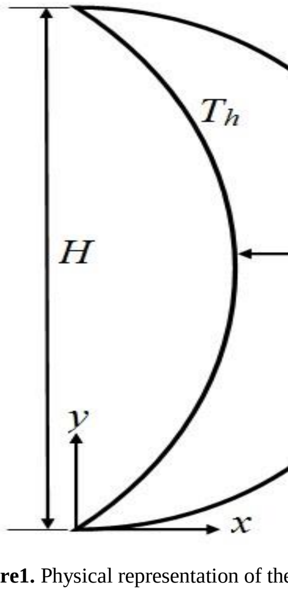

Figure1. Physical representation of the crescent cavity.

Before describing the mathematical model, it is worth presenting the assumptions are used in this work:-

1. No-slip condition is assumed between the fluid and the solid arcs of the cavity.
2. The flow is 2 D, steady, laminar and Newtonian.
3. The thermo-physical characteristics of the fluid are not related to temperature except the density, which was dealt with by the Boussinesq approximation.
4. In this type of work, the physical phenomena are not related to time, so the equations for this work are not related to time.

The dimensionless form of the governing continuity, momentum and energy equations in the Cartesian coordinate system read [3-6]:

$$\frac{\partial U}{\partial X}+\frac{\partial V}{\partial Y}=0 \tag{1}$$

$$\frac{\partial U}{\partial X}U+\frac{\partial U}{\partial Y}V=-\frac{\partial P}{\partial X}+Pr\left(\frac{\partial^2 U}{\partial X^2}+\frac{\partial^2 U}{\partial Y^2}\right) \tag{2}$$

$$\frac{\partial \mathrm{V}}{\partial \mathrm{X}}\mathrm{U}+\frac{\partial \mathrm{V}}{\partial \mathrm{Y}}\mathrm{V}=-\frac{\partial \mathrm{P}}{\partial \mathrm{Y}}+\mathrm{Pr}\left(\frac{\partial^2 \mathrm{V}}{\partial \mathrm{X}^2}+\frac{\partial^2 \mathrm{V}}{\partial \mathrm{Y}^2}\right)+Ra.\mathrm{Pr}.\phi \tag{3}$$

$$\frac{\partial \phi}{\partial X}U+\frac{\partial \phi}{\partial Y}V=\left(\frac{\partial^2 \phi}{\partial X^2}+\frac{\partial^2 \phi}{\partial Y^2}\right) \tag{4}$$

The last term in Eq.(3) illustrates Y-direction's connection between the momentum and energy equations. Eqs. (1-4) are presented in nondimensional form after converting the dimensional parameters in this way:

$$X=\frac{x}{H},Y=\frac{y}{H},U=\frac{uH}{\alpha},V=\frac{vH}{\alpha},P=\frac{pH^2}{\rho\alpha^2},\phi=\frac{T-T_c}{T_h-T_c} \tag{5}$$

While the Prandtl and Rayleigh numbers in the above equations are expressed as follows

[64] :

$$Pr=\frac{\nu}{\alpha},Ra=\frac{g\beta(T_h-T_c)H^3}{\nu\alpha} \tag{6}$$

$Pr =$ 0.71, 6.1 and 50. 0.71 for air, 6.1 for water and 50 for oil.

The Prandtl number expresses the thermal properties of the fluid. Whereas the Rayleigh number indicates the intensity of the thermal buoyancy inside the cavity. Convection heat transmission is evident in the cavity due to the temperature difference between the fluid and the enclosure's arcs. The values of the heat transfer rate are expressed by the local and mean Nusselt numbers as follows:

$$Nu_l=\left.\frac{\partial \phi}{\partial n}\right|_{wall} \tag{7}$$

$$Nu=\frac{1}{s}\int_0^s Nu_l\,ds \tag{8}$$

The Nu represents the mean of local values of the Nusselt number. That means the value of Nu increases with increasing the temperature gradient.

To complete the mathematical model, the appropriate boundary conditions must be specified as follows [3-6]:

For the cold arc of the cavity

$$U=0,V=0,\phi=0 \tag{9}$$

For the hot arc of the cavity

$$U=0,V=0,\phi=1 \tag{10}$$

3. Simulation procedure and the numerical test

To achieve the numerical simulation of the current study, a set of points must be accomplished and verified. These points can be summarized into two main parts as follows:

- Creating the grids and checking the density of their elements to minimize the error in the numerical results.
- Verifying the used numerical model.

The code Gambit is used to draw and create the grids of the studied space. Fig. 2 depicts the shape of the grid after its completion. The density of the elements was verified in each case from the value of the ratio (B). The results of this verification are shown in Table 1. It can be concluded that the element numbers for (case 2) are sufficient to reach satisfactory results. So, this step is called grid indpendency test.

The numerical code (ANSYS-CFX) was used as a solver in this investigation. The code transforms the differential equations (Eqs. (1-4)) into a matrix system by integrating the initial conditions (Eqs. 9 and 10), employing the finite volume approach. The high-resolution scheme solves the convective terms of the matrix system. While the SIMPLEC algorithm coupled the pressure and velocity. The results of the calculation can be adopted when the error becomes (10^{-8}) for momentum equations and (10^{-6}) for energy equations. To validate the numerical scheme used in this study, the natural convection problem in a square cavity at $Ra = 10^3$ and 10^5 as performed by Barakos et al. [65] is resolved again by employing the same numerical approach of the current paper. Also, this code was used to solve the previous problems considered by Kuehn and Goldstein [66] and Matin and Khan [67]. The comparison presented in Figs 3 and 4 shows that very good confidence was noticed. These comparisons confirm the accuracy of the method used.

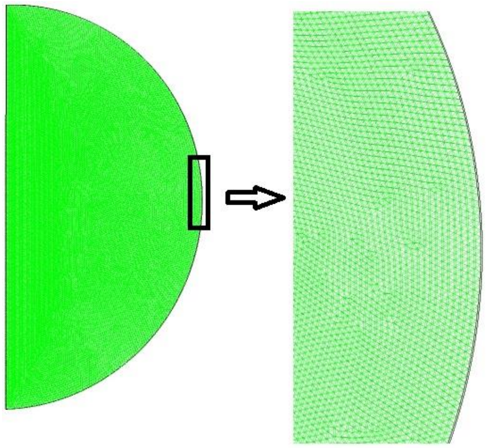

Figure 2. The shape of the created grid.

Table 1. Grid independency test for $Pr = 6.01$ and $Ra = 10^4$.

B	Case	Number of elements	Nu	difference
0.5	1	55275	4.4985	0.33%
	2	110550	4.5132	0.18%
	3	231100	4.5215	-
0.4	1	44220	4.3952	0.57%
	2	88440	4.4205	0.016%
	3	176880	4.4198	-
0.3	1	35376	4.2262	2.20%
	2	70752	4.3217	0.12%
	3	141504	4.3165	-
0.2	1	28301	4.1984	0.89%
	2	56602	4.2362	0.16%
	3	113204	4.2432	-
0.1	1	22641	4.1291	0.87%
	2	45282	4.0931	0.62%
	3	90564	4.0674	-

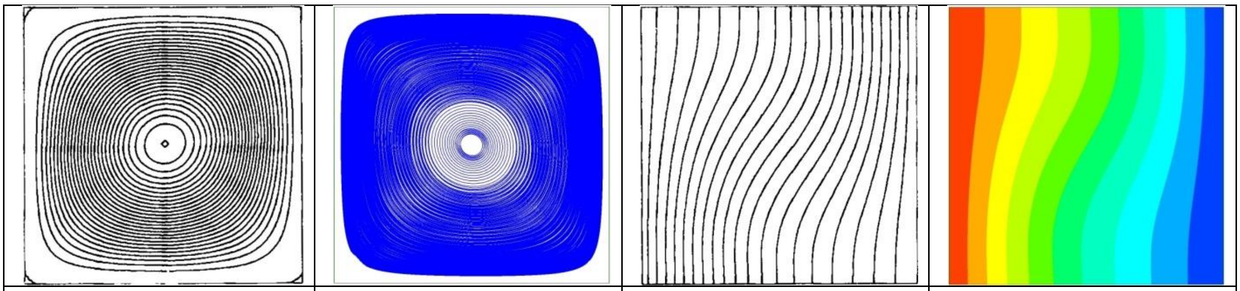

Barakos et al. [65] ($Ra = 10^3$) | Present result | Barakos et al. [65] ($Ra = 10^3$) | Present result

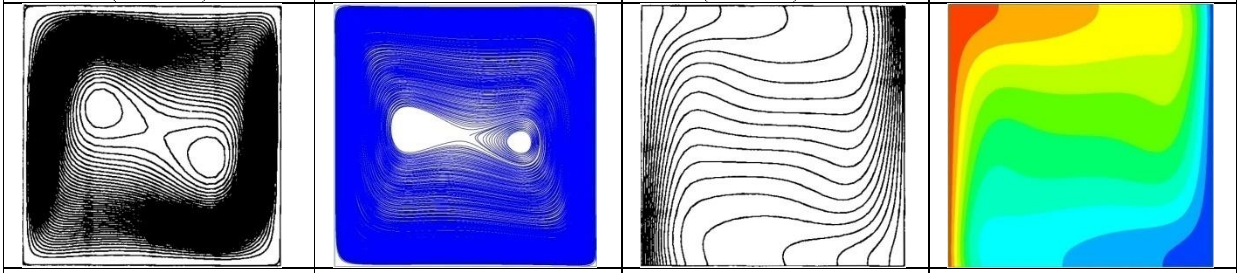

Barakos et al. [65] ($Ra = 10^5$) | Present results | Barakos et al. [65] ($Ra = 10^5$) | Present result

Figure 3. Comparison of streamlines (left) and isotherms (right) between current study results and Barakos et al. [65] results for $Pr = 6.1$.

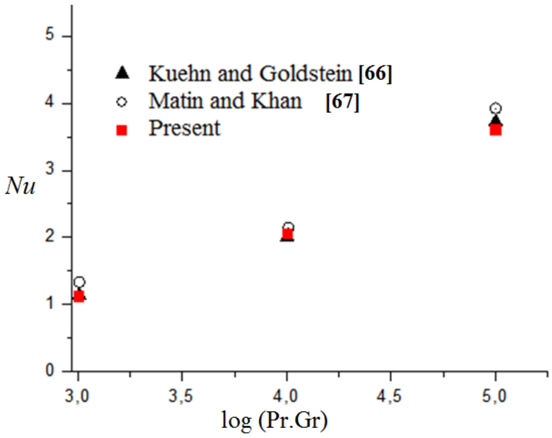

Figure 4. Comparison of *Nu* values of current study results and the results of Kuehn and Goldstein [66] and Matin and Khan [67] at *Pr* = 6.2.

4. Results and discussion

The buoyancy-driven flow of a fluid trapped in a room with a crescent shape cross-section was investigated numerically in the current study. The studied parameters are Prandtl number $0.71 \leq Pr \leq 50$, blockage ratio of the space $0.1 \leq B \leq 0.5$ and Rayleigh number $10^3 \leq Ra \leq 10^5$.

4.1. *Case 1 (Cold left arc and hot right arc):*

In this case, the left and right arcs of the cavity were preserved at constant cold and hot temperatures, respectively. Figs. 5 and 6 show the streamlines inside the crescent shape cavity for various values of *Ra*, *Pr* and *B* related to (case 1). Fig. 5 shows the impact of changing both the blockage ratio *B* and *Ra* numbers at a constant *Pr* number (i.e., *Pr* = 6.01). While, Fig. 6 presents the impact of changing *Pr* number and blockage ratio *B* at a constant *Ra* number (i.e., $Ra = 10^4$). It can be seen from both figures that the variation in the values of *B* has a clear effect on the cavity geometry. So, it switches from a semi-circle shape at the largest value of *B* or at *B* = 0.5 to a crescent shape at the lowest value of *B* or at *B* = 0.1. As the value of *B* decreases gradually, the left arc of the cavity becomes more concave to the internal space until it attains the crescent shape at *B* = 0.1. Therefore, the width of the gap inside the cavity decreases with decreasing the blockage ratio *B*.

Because of buoyancy force, the fluid layers near the hot right arc of the cavity become less dense and lighter, so they move upward to the top of the cavity. The fluid layers near the cold left arc become denser and heavy, moving downwards. Therefore, it can be observed from Figs. 5 and 6 that there is a circular flow inside the center of the cavity due to the flow movement between the hot and cold arcs of the cavity. The flow pattern in the cavity is uniform for lower values of *Ra* ($Ra < 10^4$). In this case, the viscous force is more predominant than buoyancy. Therefore, both the buoyancy force and the natural convection effects are weak. However, when the *Ra* value reaches $Ra = 10^5$, a definite disruption in the flow pattern may be observed. This is owing to the strong impacts of buoyant force and natural convection at high *Ra*.

Additionally, when the *Ra* number rises, the fluid velocity increases. Also, the flow vortices can be seen near the upper and lower edges of the cavity. Also, it can be observed from Figs. 5 and 6 that as the value of *B* decreases from *B* = 0.5 to 0.1 , the fluid movement becomes slow, and the flow pattern becomes approximately similar. Since the reduction in the value of *B* reduces the gap width inside the cavity and makes the region of the flow area inside it more restricted. Therefore, this hinders the movement of the flow. Furthermore, it can be observed from Fig. 6 that there is a small minor vortex at the bottom of the cavity and a major vortex at its center *B* = 0.1 and $Ra = 10^5$.

Concerning the effect of *Pr* on the streamline contours, it can be observed from Fig. 6 that there is no significant change in their pattern when the *Pr* increases from (Pr = 0.71) to *Pr* = 50. Therefore, it can be concluded that the flow pattern does not affect by changing the fluid's thermal properties represented by the *Pr*. Fig.7 illustrates the isotherms (dimensionless temperature) distribution of the fluid in the cavity in terms of the studied values of *B* and *Ra* number at *Pr* = 6.1. Since there is no effect of the *Pr* number values on the natural convection, as was observed in Fig. 6. Only one value of the *Pr* number was tested on the isotherms. When *Ra* number is low, the isotherm contours are symmetrical, close to each other, uniform and parallel to the arcs of the cavity. In this case, the heat is transmitted by conductive mode. Because of the high-temperature gradient in the cold arc's upper side and the hot arc's lower side, the isotherms' intensity increases in these regions. Therefore, the heat transmission was enhanced compared with the rest of the cavity. The clustering of isotherms at any point in the cavity arcs can be considered a good signal of a severe temperature gradient and a high heat transfer. At $Ra = 10^5$, the isotherm pattern changes significantly and elongates deeply, especially at the center of the cavity. Also, a thermal plume is evident within this space. In this case, convective heat transfer becomes significant.

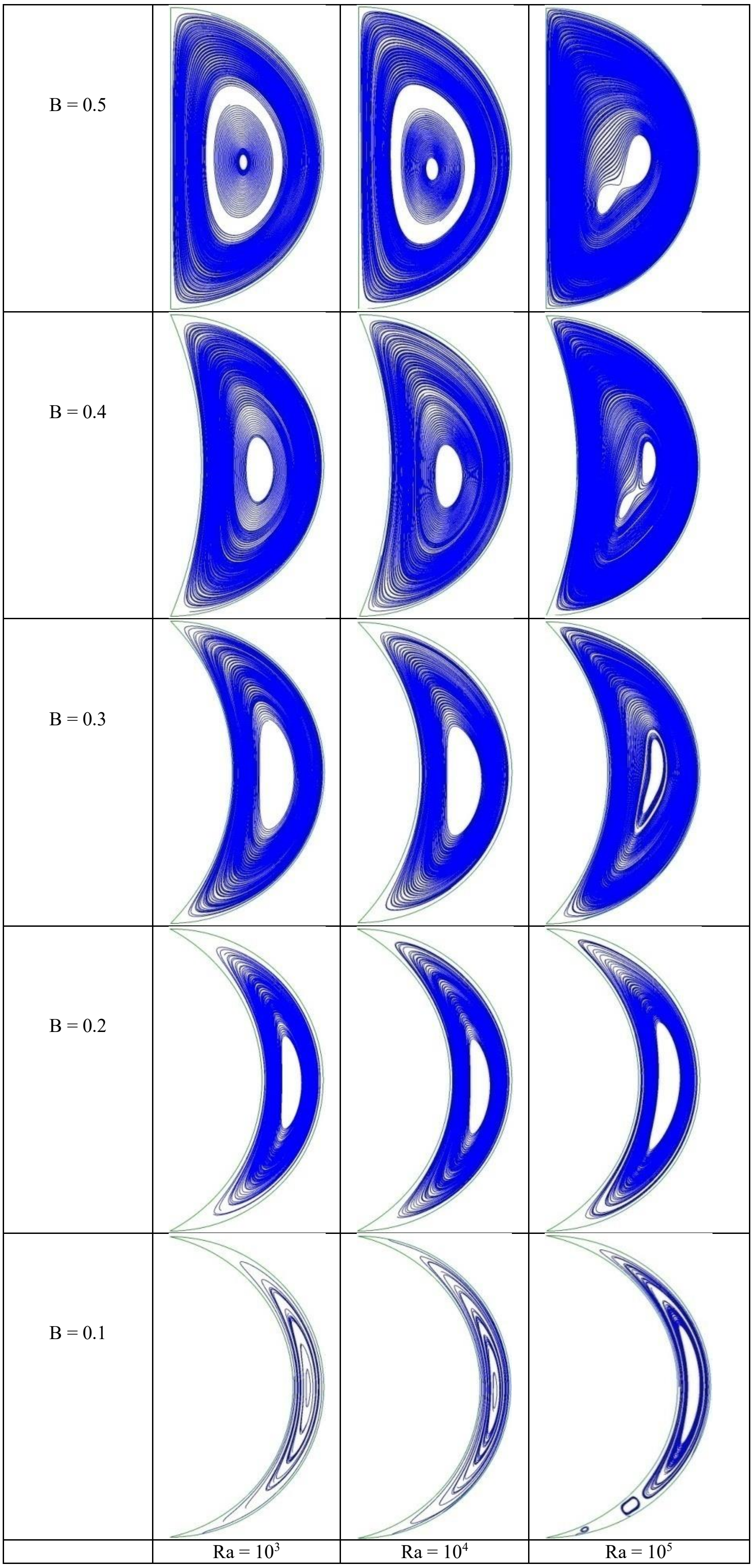

Figure 5. Streamlines inside the crescent shape cavity for various values of Ra and B at $Pr = 6.1$ related to (case 1).

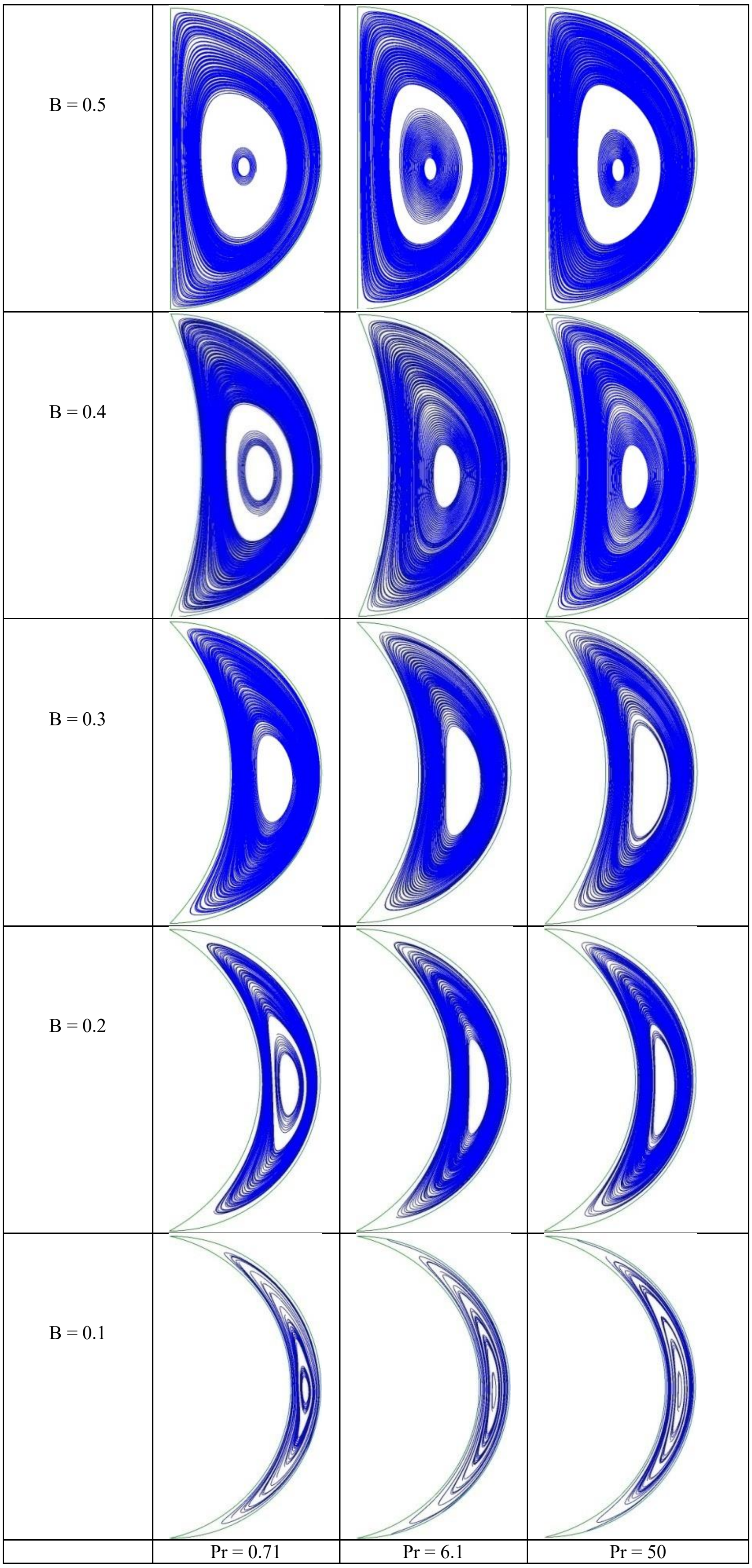

Figure 6. Streamlines inside the crescent shape cavity for various values of Pr and B at Ra = 10^4 related to (case 1).

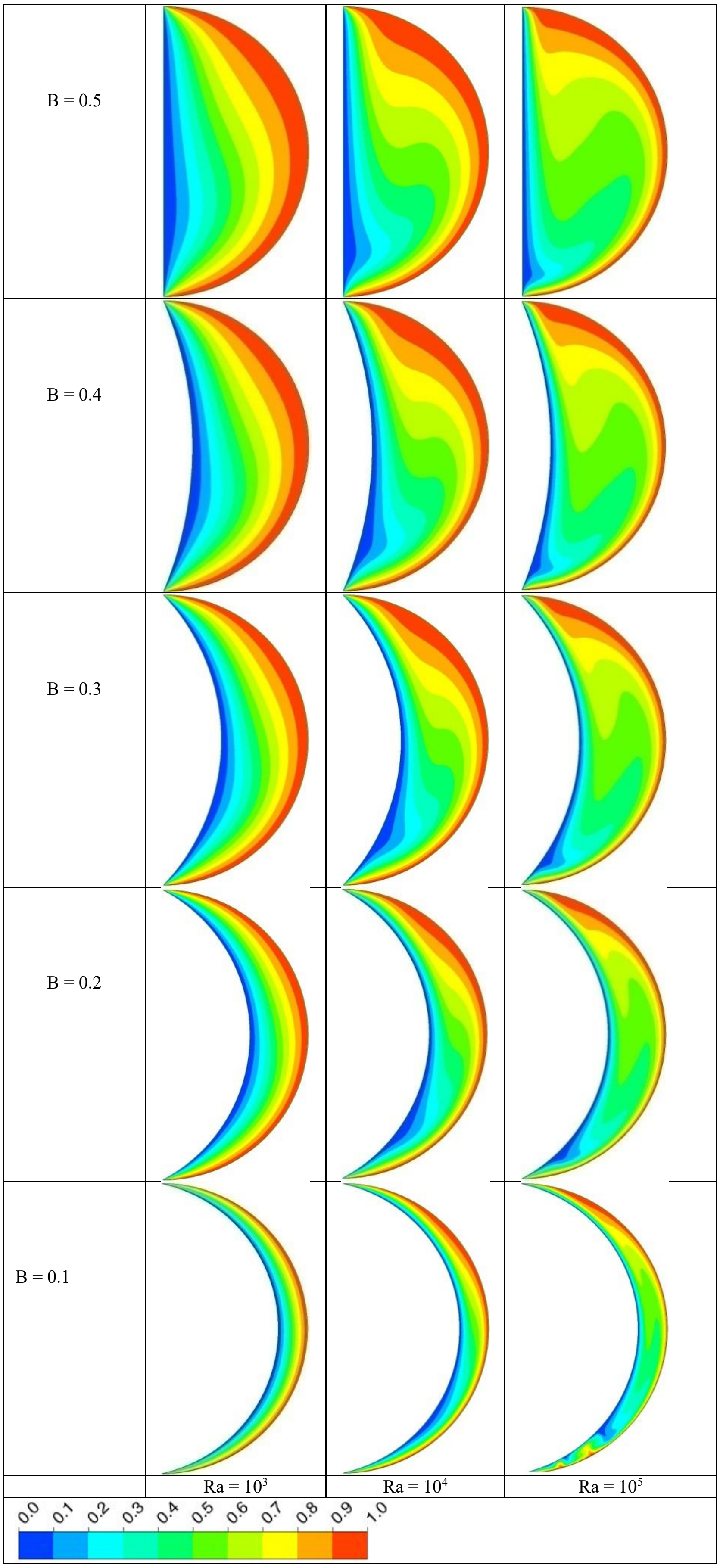

Figure 7. Isotherms inside the crescent shape cavity for various values of Ra and B at $Pr = 6.1$ related to (case 1).

Fig. 8 illustrates the distribution of dimensionless velocity component *V* along with the width gap spacing for various values of *Ra* and *B* at *Pr* = 6.1. The plus (+) and minus (-) signs indicate the direction of the movement of the fluid particles. This means that the flow direction is downward near the cold left arc. While near the hot right arc, its direction is upward. It could be observed that the flow velocity rises as *Ra* increases. In addition, at $Ra = 10^5$, the maximum velocity of the flow in the vicinity of the hot and cold arcs begins to increase by decreasing the value of *B* from *B* = 0.5 to 0.1. So, the peak value corresponds to the lowest value of *B*.

Fig. 9 shows the profiles of the mean values of *Nu* in terms of *Ra*, *Pr*, and *B*. It can be seen that the values of *Nu* are affected by the variation in both *Ra* and *B* whereas there is no clear effect of the variation in *Pr* on their values. It is useful to mention that the first group (the red lines) was related to the hot arc, while the second group (the blue lines) was related to the cold arc. The mean *Nu* values are taken in their absolute values, while the signs (+ and -) refer to the direction of the convection heat transfer. It is noticed that increasing *Ra* directly results in an increment in the values of *Nu* for both arcs. This is caused by a rise in the thermal buoyancy's magnitude, which arguments the heat transfer rates for both arcs. Concerning the effect of the parameter *B* on the values of *Nu*, it is observed that as *B* decreases from (0.5) to (0.1), the *Nu* for the hot arc decreases whereas its value for the cold arc begins to increase. This means that as the cavity width decreases, the heat transmission rate of the hot arc while the heat transmission rate of the cold arc increases.

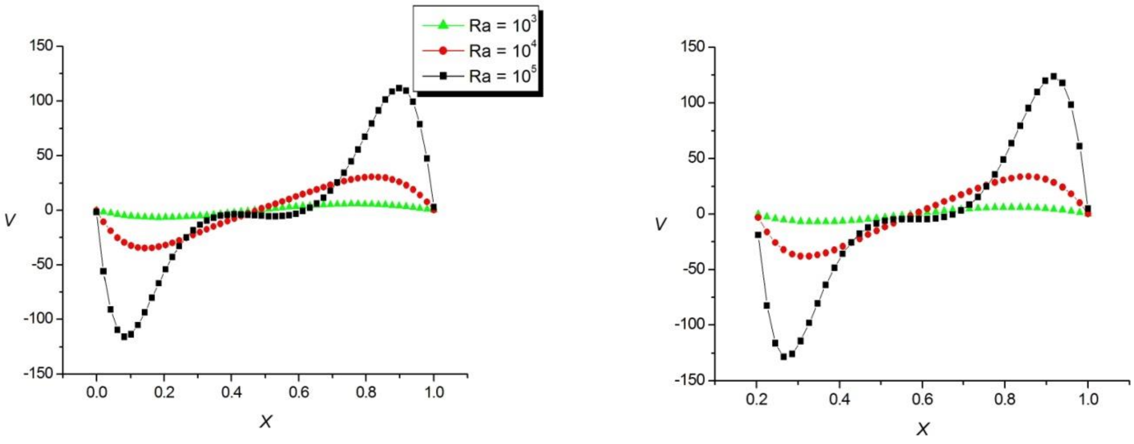

(a) B = 0.5

(b) B = 0.4

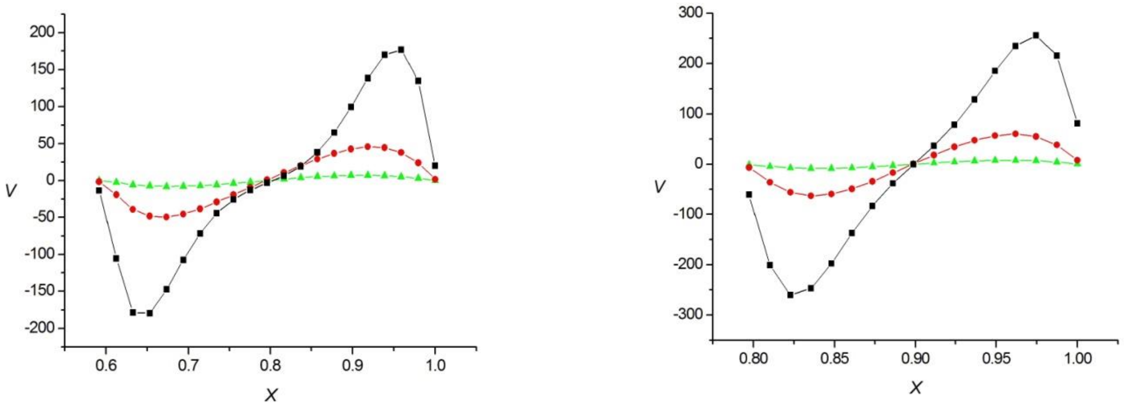

(c) B = 0.2

(d) B = 0.1

Figure 8. Dimensionless velocity profiles of *V* along *X* for various values of *Ra* and *B* at *Pr* = 6.1 related to (case 1).

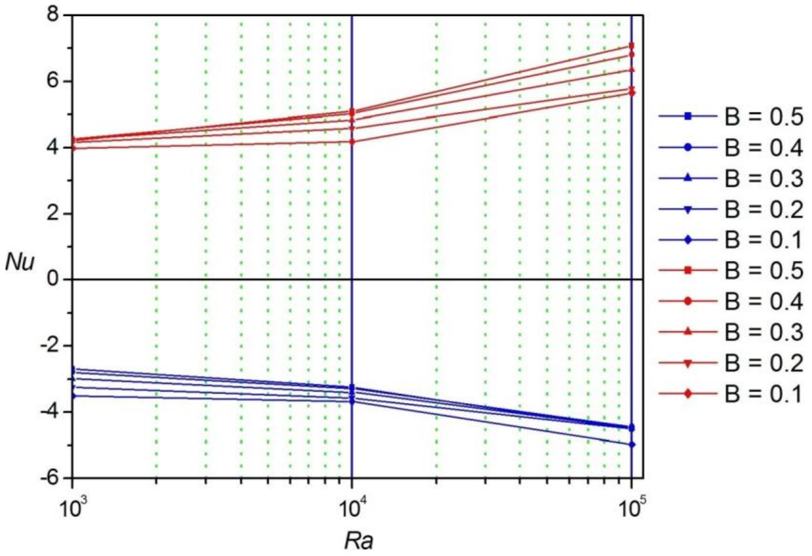

(a) Pr = 0.71

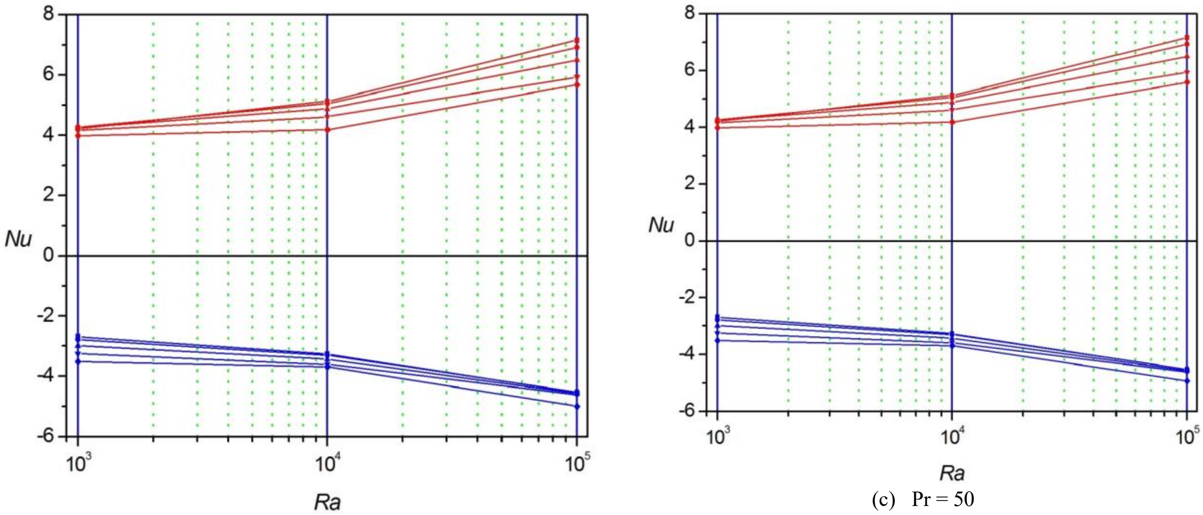

(b) Pr = 6.1

(c) Pr = 50

Figure 9. Profiles of mean Nu number versus Ra for different values of Pr and B related to (case 1).

4.2. *Case 2 (Hot left arc and cold right arc):*

In this case, the thermal distribution of the arcs was reversed. So, the left and right arcs were preserved at constant hot and cold temperatures, respectively. Figs. (10, 11 and 12) illustrate the streamlines and isotherms, respectively, inside the crescent shape cavity for various values of Ra, Pr and B related to (case 2). It can be observed from these figures that the pattern of the intra-compartment flow, in this case, is similar to that found in (case 1). However, a simple difference between them can be summarized in two points. The first point is that at $Ra = 10^5$, $B = 0.4$ and 0.5, the core of vortices is affected by shifting the thermal boundary conditions of the arcs. Therefore, it can be concluded that they move towards the cold arc of the cavity for both considered cases. While this difference begins to disappear with the decrease in B values. Therefore, it could be deduced that the change of the thermal boundary conditions becomes discernible when the buoyancy force has a substantial influence, and the cavity's width is big. The second point is that the minor vortices which are observed at $Ra = 10^5$ and $B = 0.1$ are replaced by their position from the bottom region in (Case 1) to the upper region in (Case 2). Once again, there is no discernible shift in the pattern of the streamlines when the (Pr) increases from $Pr = 0.71$ to 50.

With respect to the isotherm contours, it was seen that the thermal plume was adjacent to the hot left arc and extended further inside the cavity until it attained the cold right arc. It can be observed by comparing the results in Fig.12 with that displayed in Fig.7 that the pattern of isotherms is similar to each other except adjacent to the arcs boundaries. In a similar manner discussed in (Case 1), the isotherm contours are highly influenced by increasing the Ra. Therefore, they switch their pattern from uniform lines for low Ra to a ripple-like pattern at high values. This behavior is due to the high-temperature gradient between the cavity's left hot and right cold arcs.

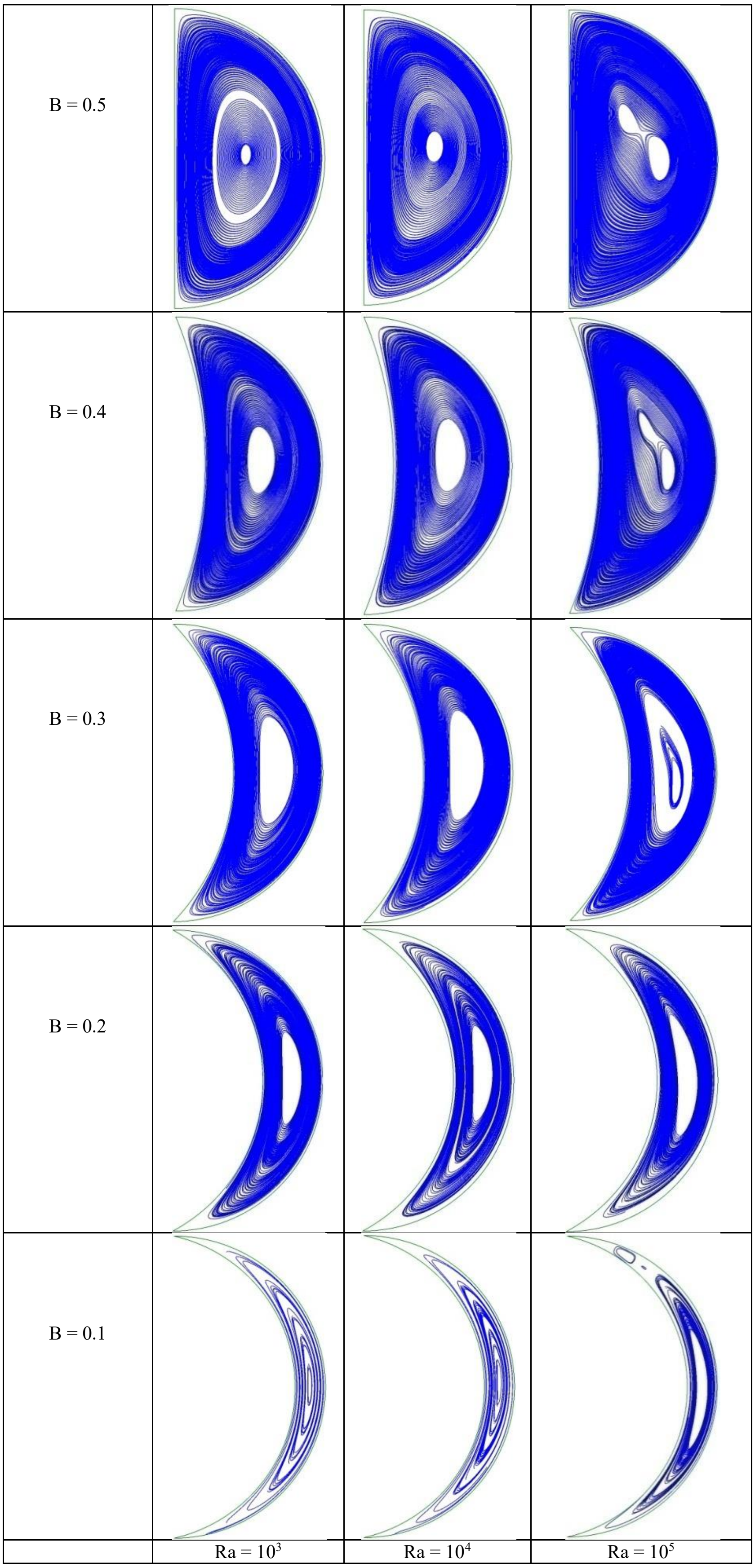

Figure 10. Streamlines inside the crescent shape cavity for various values of Ra and B at $Pr = 6.1$ related to (case 2).

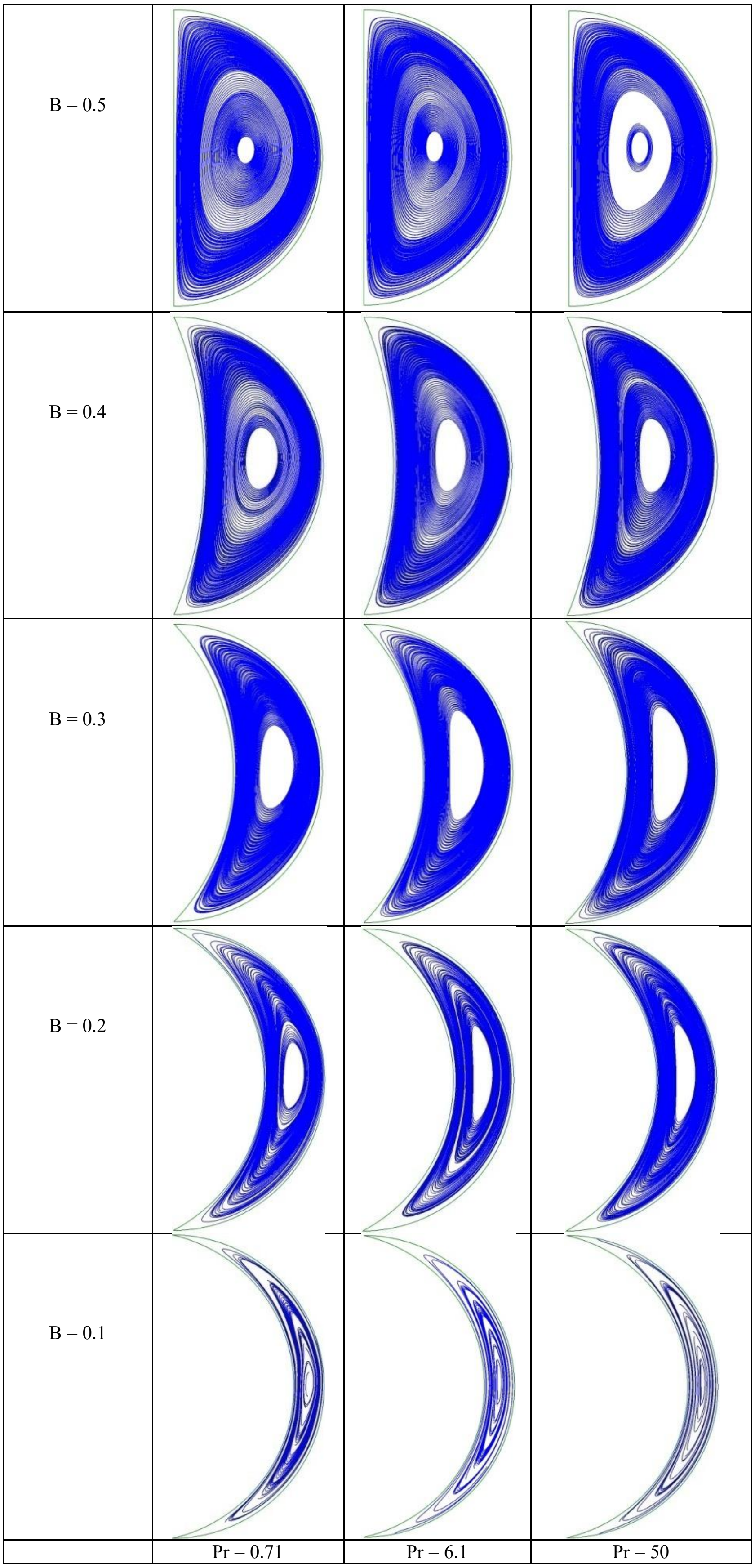

Figure 11. Streamlines inside the crescent shape cavity for various values of *Pr* and *B* at $Ra = 10^4$ related to (case 2).

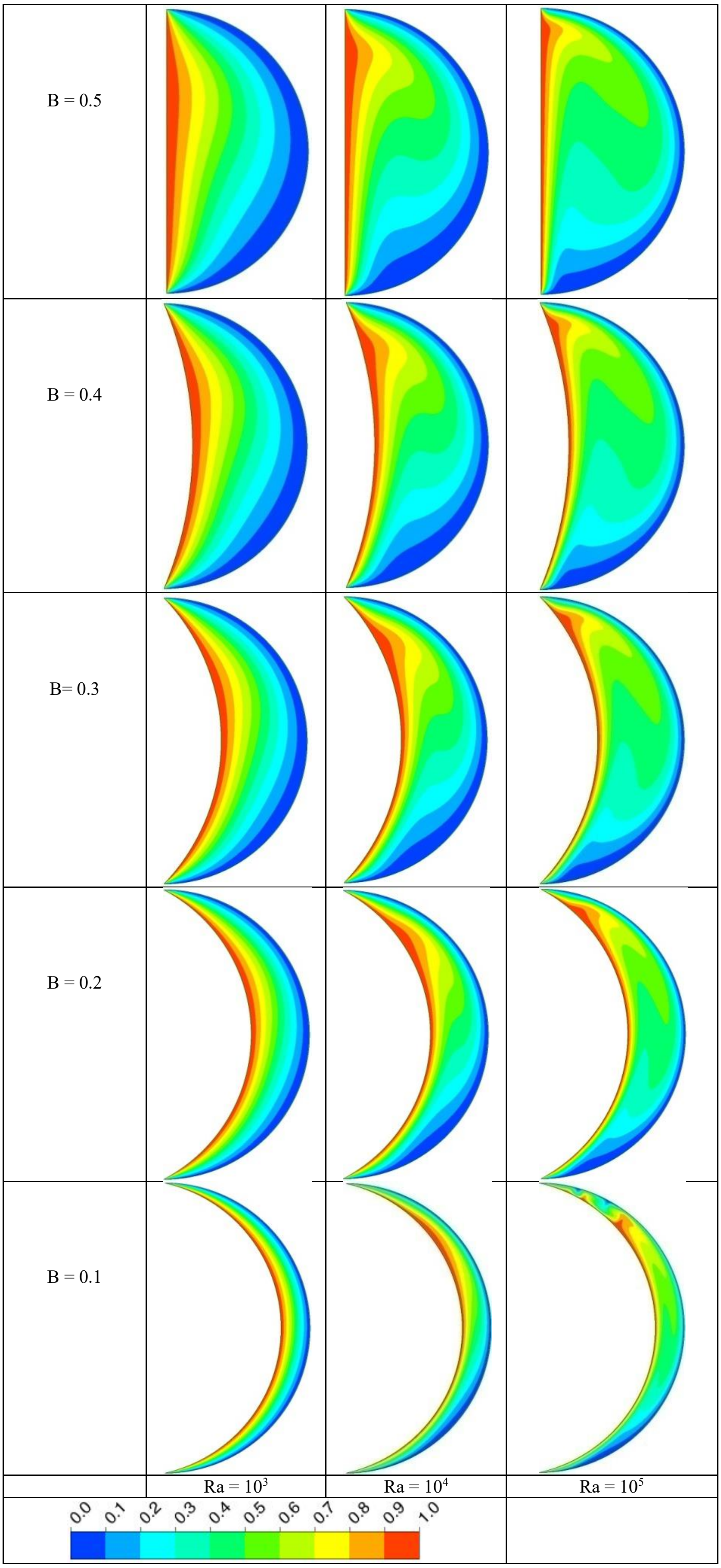

Figure 12. Isotherms inside the crescent shape cavity for various values of Ra and B at $Pr = 6.1$ related to (case 2).

The distribution of dimensionless velocity component V along with the width gap spacing for various values of Ra and B at Pr = 6.1 was displayed in Fig.13. The plus (+) and minus (-) signs indicate the direction of the movement of the fluid particles. This refers to the fact that adjacent to the cold right arc, the direction of the flow is downward, whereas, adjacent to the hot left arc, its direction is upward. Therefore, the velocity distribution was opposite to that noticed in Fig. 8. This result confirms that the velocity profiles are strongly affected by changing the thermal boundary conditions in cases 1 and 2. Similar to that found previously in (case 1), the velocity profiles increase with the increase in Ra and decrease in B. Therefore, their peak value can be found at $Ra = 10^5$ and $B = 0.1$.

The profiles of the mean values of Nu in terms of Ra, Pr and B were illustrated in Fig. 14. Again, the first set (the red lines) was related to the hot arc, whereas the second set (the blue lines) was related to the cold arc. Similar to that found previously in (case 1), the values of Nu are not varied clearly with the increase in Pr. This can be confirmed by the high similarity of Nu profiles for all selected values of Pr. The results indicated that Nu profiles for both cold and hot arcs increased with Ra. On another hand, the Nu was increased with the decrease in B for the hot arc, while an inverse effect can be seen for the cold arc. Furthermore, all observations and inferred analyzes agree with previous analyzes such as [68-75].

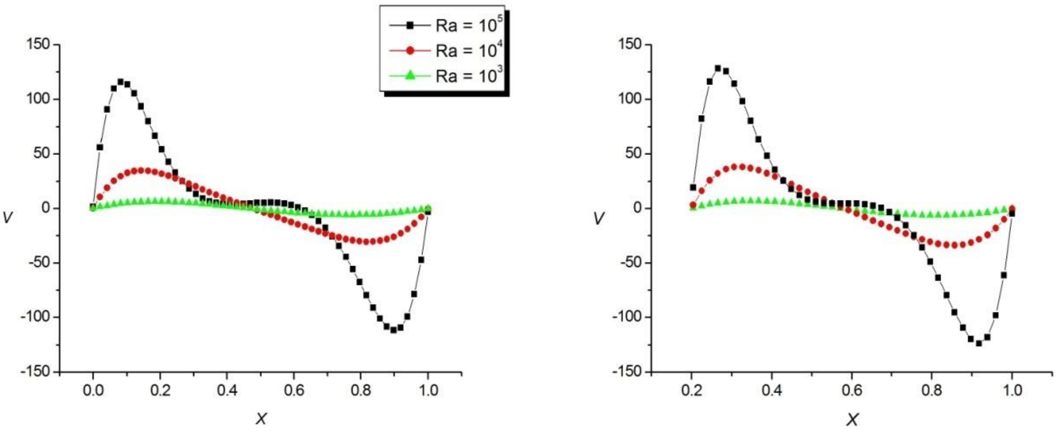

(a) B = 0.5 (b) B = 0.4

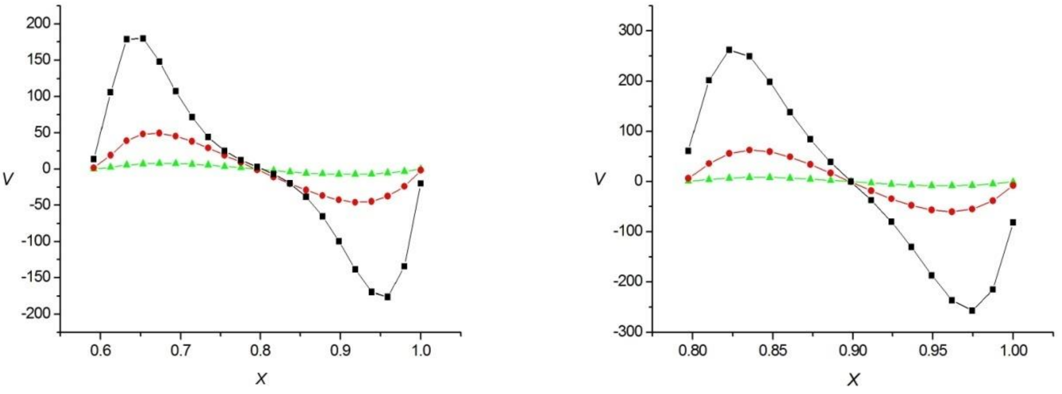

(c) B = 0.2 (d) B = 0.1

Figure13. Dimensionless velocity profiles of V along X for various values of Ra and B at Pr = 6.1 related to (case 2).

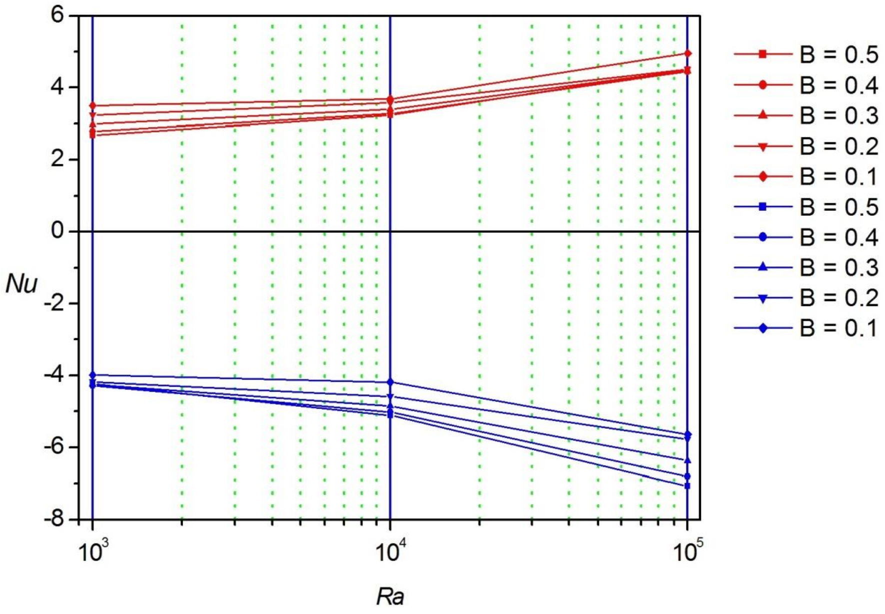

(a) Pr = 0.71

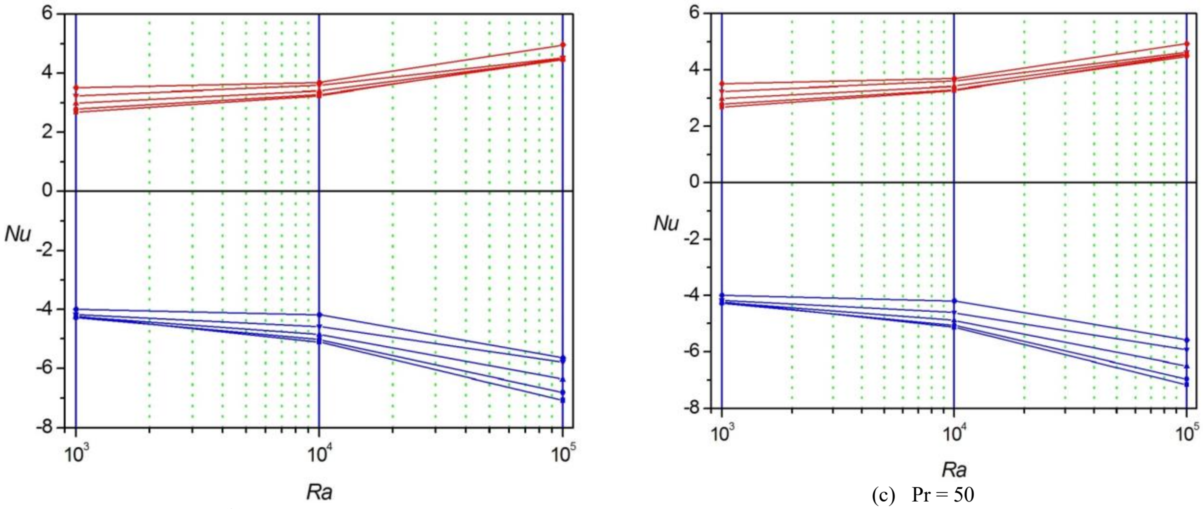

(b) Pr = 6.1

(c) Pr = 50

Figure 14. Profiles of mean Nu number versus Ra for different values of Pr and B related to (case 2).

5. Conclusions

The following are the key points that were extracted from the current work:

1. The flow velocity and buoyancy-driven convention increase as Ra increases in both considered cases.
2. For both considered cases, when the value of B decreases, the fluid movement becomes slow, and the flow pattern becomes approximately similar.
3. For both considered cases, the flow and thermal patterns were not affected by changing the fluid's thermal properties Pr.
4. For both considered cases, the velocity profiles increase with the increase in Ra and decrease in B. Therefore, their peak value can be found at $Ra = 10^5$ and $B = 0.1$. Also, the velocity profiles are affected strongly by changing the thermal boundary conditions.
5. For both considered cases, the increase in Ra increases the values of Nu for both arcs.
6. For (case 1), when the value of B decreases, the Nu for the hot arc decreases whereas its value for the cold arc begins to increase. For (case 2), the Nu was increased with the decrease in B for the hot arc, while an inverse effect can be seen for the cold arc.
7. When the influence of buoyancy force is substantial, and the cavity width is big, the shifting thermal boundary conditions become obvious.
8. These new kinds of results can be exploited in heat exchanger applications as well as insulating systems.
9. In future works, we seggest to use a fluid that combines rheological and nanoscale properties.

Acknowledgements

This publication was supported by the Deanship of Scientific Research at Prince Sattam bin Abdulaziz University, Alkharj, Saudi Arabia.

References

[1] Gourari , S., Mebarek-Oudina, F., Hussein, A.K., Kolsi, L., Hassen, W. and Younis, O. Numerical study of natural convection between two coaxial inclined cylinders, International Journal of Heat and Technology, Vol. 37, No. 3, 2019, pp. 779-786.

[2] Elkhazen, M., Hassen, W., Gannoun, R., Hussein, A.K. and Borjini, M. Numerical study of electro convection in a dielectric layer between two cofocal elliptical cylinders subjected to unipolar injection, Journal of Engineering Physics and Thermophysics, Vol. 92, No. 5, 2019, pp. 1318-1329.

[3] Al-Rashed, A., Kolsi, L., Hussein, A. K., Hassen, W., Aichouni, M. and Borjini, M. Numerical study of three-dimensional natural convection and entropy generation in a cubical cavity with partially active vertical walls, Case Studies in Thermal Engineering, Vol. 10, 2017, pp: 100-110.

[4] Ahmed, S., Hussein, A.K., Abd El-Aziz, M. and Sivasankaran, S. Conjugate natural convection in an inclined square porous enclosure with finite wall thickness and partially heated from its left sidewall. Heat Transfer Research, Vol.47, No.4, 2016, pp: 383-402.

[5] Hussain, S. and Hussein, A.K. Numerical investigation of natural convection phenomena in a uniformly heated circular cylinder immersed in a square enclosure filled with air at different vertical locations, International Communications in Heat and Mass Transfer, Vol. 37, No.8, 2010, pp: 1115–1126.

[6] Ghachem, K., Kolsi, L., Mâatki, C., Hussein, A.K. and Borjini, M. Numerical simulation of three-dimensional double diffusive free convection flow and irreversibility studies in a solar distiller, International Communications in Heat and Mass Transfer, Vol.39, 2012, pp: 869-876.

[7] Kolsi , L. , Hussein, A.K. , Borjini, M. , Mohammed , H. and Ben Aïssia ,H. Computational analysis of three-dimensional unsteady natural convection and entropy generation in a cubical enclosure filled with water-Al_2O_3 nanofluid, Arabian Journal for Science and Engineering, Vol. 39, 2014, pp: 7483-7493.

[8] Ahmed, S., Mansour, M., Hussein, A.K., Mallikarjuna, B., Al-Meshaal, M. and Kolsi, L. MHD mixed convection in an inclined cavity containing adiabatic obstacle and filled with Cu-water nanofluid in the presence of the heat generation and partial slip, Journal of Thermal Analysis and Calorimetry, Vol.138, No.2, 2019, pp: 1443-1460.

[9] Nikbakhti, R., Wang, X., Hussein, A.K. and Iranmanesh, A. Absorption cooling systems - Review of various techniques for energy performance enhancement, Alexandria Engineering Journal, Vol. 59, 2020, pp: 707-738.

[10] Sojoudi, A., Saha, S. and Gu, Y. Natural convection due to differential heating of inclined walls and heat source placed on bottom wall of an attic shaped space, Energy and Buildings, Vol. 89, 2015, pp: 153-162.

[11] Hussein, A.K., Rout, S., Fathinia, F., Chand, R. and Mohammed, H. Natural convection in a triangular top wall enclosure with a solid strip, Journal of Engineering Science and Technology, Vol.10, No.10, 2015, pp: 1326 - 1341.

[12] Hussein, A.K. and Hussain, S. Natural convection in a modified square enclosure with an inclined triangular top wall subjected to uniform heat flux in its left vertical wavy sidewall, Third Asian Symposium on Computational Heat Transfer and Fluid Flow, 22-26, September 2011, Kyoto, Japan, pp: 1-10.

[13] Hussein, A.K. Entropy generation due to the transient mixed convection in a three-dimensional right-angle triangular cavity, International Journal of Mechanical Sciences, Vol.146-147, 2018, pp: 141-151.

[14] Hussain, S., Hussein, A. and Mahdi, M. Natural convection in a square inclined enclosure with vee-corrugated sidewalls subjected to constant flux heating from below, Nonlinear Analysis: Modelling and Control, Vol. 16, No. 2, 2011, pp: 152-169.

[15] Hussein, A.K., Hussain, S., Saha, S., Saha, G. and Hasanuzzaman, M. Effects of a longitudinal magnetic field and discrete isoflux heat source size on natural convection inside a tilted sinusoidal corrugated enclosure, Journal of Basic and Applied Scientific Research, Vol.3, No. 10, 2013, pp: 402-415.

[16] Hussain, S., Hussein, A.K. and Mohammed, R. Studying the effects of a longitudinal magnetic field and discrete isoflux heat source size on natural convection inside a tilted sinusoidal corrugated enclosure, Computers and Mathematics with Applications, Vol. 64, 2012, pp: 476-488.

[17] Hussein, A.K. and Hussain, S. Heatline visualization of natural convection heat transfer in an inclined wavy cavities filled with nanofluids and subjected to a discrete isoflux heating from its left sidewall, Alexandria Engineering Journal, Vol.55, 2016, pp: 169-186.

[18] Mahfouz, F. Buoyancy driven flow within an inclined elliptic enclosure, International Journal of Thermal Sciences, Vol. 50 , 2011, pp : 1887-1899.

[19] Hussain, S., Hussein, A. and Kadim, K. Numerical simulation of natural convection in a parallelogrammic enclosure containing volumetric heat source with non-uniformly heated left sidewall, Heat Transfer-Asian Research, Vol. 43, No.6, 2014, pp: 542-560.

[20] Ghani, I., Khammas, F., Mustafa, A. and Hussein, A.K. MHD natural convection in a fully opened parallelogrammic enclosure filled with copper–water nanofluid and partially heated from its left sidewall, Journal of Advanced Research in Fluid Mechanics and Thermal Sciences, Vol. 74, No. 2, 2020, pp: 120 -145.

[21] Hussein, A.K. and Mustafa, A. Natural convection in a fully open parallelogrammic cavity filled with Cu-water nanofluid and heated locally from its bottom wall, Thermal Science and Engineering Progress, Vol. 1, 2017, pp: 66-77.

[22] Hussain, S. and Hussein, A.K. Natural convection heat transfer enhancement in a differentially heated parallelogrammic enclosure filled with copper-water nanofluid, Journal of Heat Transfer-Transactions of the ASME, Vol.136, 2014, pp: 082502-1- 082502-8.

[23] Hussein, A.K. Finite volume simulation of natural convection in a trapezoidal cavity filled with various fluids and heated from the top wall, Universal Journal of Fluid Mechanics, Vol.1, 2013, pp: 24-36.

[24] Hussein, A.K. and Mustafa, A. Natural convection in a parabolic enclosure with an internal vertical heat source filled with Cu–water nanofluid, Heat Transfer-Asian Research, Vol. 47, 2018, pp: 320-336.

[25] Ziapour, B. and Dehnavi, R. Finite-volume method for solving the entropy generation due to air natural convection in C-shaped enclosure with circular corners, Mathematical and Computer Modelling, Vol. 54, 2011, pp: 1286-1299.

[26] Hussein, A.K., Bakier , M., Ben Hamida , M. and Sivasankaran, S. Magneto-hydrodynamic natural convection in an inclined T-shaped enclosure for different nanofluids and subjected to a uniform heat source, Alexandria Engineering Journal, Vol. 55, 2016, pp: 2157-2169.

[27] Sourtiji, E. and Hosseinizadeh, S. Heat transfer augmentation of magneto-hydrodynamics natural convection in L-shaped cavities utilizing nanofluids, Thermal Science, Vol.16, No.2, 2012, pp: 489-501.

[28] Dehnavi, R. and Rezvani, A. Numerical investigation of natural convection heat transfer of nanofluids in a Γ shaped cavity, Superlattices and Microstructures, Vol. 52, 2012, pp: 312-325.

[29] Fard, A., Hooshmand, P., Mohammaei, M. and Ross, D. Numerical study on free convection in a U-shaped CuO/water nanofluid-filled cavity with different aspect ratios using double-MRT lattice Boltzmann, Thermal Science and Engineering Progress, Vol. 14, 2019, 100373.

[30] Yadollahi, A., Khalesidoost, A., Kasaeipoor, A., Hatami, M. and Jing, D. Physical investigation on silver-water nanofluid natural convection for an F-shaped cavity under the magnetic field effects, The European Physical Journal Plus, Vol. 132, 2017, pp: 372-384.

[31] Dutta , S. , Biswas , A. and Pati ,S. Analysis of natural convection in a rhombic enclosure with undulations of the top wall - a numerical study, International Journal of Ambient Energy, 2019, https://doi.org/10.1080/01430750.2019.1630304.

[32] Hussein, A.K. Computational analysis of natural convection in a parallelogrammic cavity with a hot concentric circular cylinder moving at different vertical locations, International Communications in Heat and Mass Transfer, Vol. 46, 2013, pp: 126-133.

[33] Salih, E. and Mustafa, A. Natural convection in a parallelogrammic enclosure partially heated from below, Zanco Journal of Pure and Applied Sciences, Vol.26, No.3, 2014, pp: 43-60.

[34] Anandalakshmi, R. and Basak ,T. Heatline-based thermal management for natural convection in porous rhombic enclosures with isothermal hot side or bottom wall, Energy Conversion and Management, Vo. 67, 2013, pp: 287-296.

[35] Adekeye , T. , Adegun, I. , Okekunle, P. , Hussein , A. K. , Oyedepo, S. , Adetiba , E. and Fayomi ,O. Numerical analysis of the effects of selected geometrical parameters and fluid properties on MHD natural convection flow in an inclined elliptic porous enclosure with localized heating, Heat Transfer-Asian Research, Vol. 46, No.3, 2017, pp: 261-293.

[36] Hussain, S. and Hussein, A.K. Natural convection analysis around a hot solid circular cylinder embedded inside an octagonal enclosure at various orientation locations, World Academy of Science, Engineering and Technology, Vol. 78, 2013, pp: 1238-1243.

[37] Chen, C. and Cheng, C. Buoyancy-induced flow and convective heat transfer in an inclined arc-shape enclosure, International Journal of Heat and Fluid Flow, Vol.23, 2002, pp: 823-830.

[38] Tasnim, S. and Mahmud, S. Laminar free convection inside an inclined L-shaped enclosure, International Communications in Heat and Mass Transfer, Vol.33, 2006, pp: 936-942.

[39] Mustafa, A. Natural convection in a parabolic enclosure heated from below, Modern Applied Science, Vol. 5, No. 3, 2011, pp: 213-220.

[40] Wang, A., Ying, C., Wang, Y., Yang, L., Ying, Y., Zhai, L. and Zhang, W. Effect of orientation and aspect ratio of an internal flat plate on natural convection in a circular enclosure, Processes, Vol. 7, 2019, pp: 1-15.

[41] Wang, Y., Chen, J. and Zhang, W. Natural convection in a circular enclosure with an internal cylinder of regular polygon geometry, AIP Advances, Vol. 9, 065023, 2019, doi: 10.1063/1.5100892.

[42] Welhezi, H., Ben-Cheikh, N. and Ben-Beya, B. Numerical analysis of natural convection between a heated cube and its spherical enclosure, International Journal of Thermal Sciences, Vol. 150, 2020, Article No. 105828.

[43] Roy, S., Tanmay, B., Thirumalesha, C. and Murali Krishna, C. Finite element simulation on natural convection flow in a triangular enclosure due to uniform and non-uniform bottom heating, Journal of Heat Transfer, Vol. 130, No.3, 2008, pp: 1761-1769.

[44] Saha, S. Unsteady natural convection in a triangular enclosure under isothermal heating, Energy and Buildings, Vol. 43, 2011, pp: 695-703.

[45] Oztop, H., Varol, Y., Koca, A. and Firat, M. Experimental and numerical analysis of buoyancy-induced flow in inclined triangular enclosures, International Communications in Heat and Mass Transfer, Vol. 39, 2012, pp: 1237-1244.

[46] El-Hassan, R., Campo, A. and Chang, J. Natural convection patterns in right-angled triangular cavities with heated vertical sides and cooled hypotenuses, Journal of Heat Transfer, Vol. 127, No.10, 2005, pp: 1181-1186.

[47] Yesiloz, G. and Aydin, O. Laminar natural convection in right-angled triangular enclosures heated and cooled on adjacent walls, International Journal of Heat and Mass Transfer, Vol. 60, 2013, pp: 365-374.

[48] Mushatet, K. Simulation of natural convection in an inclined square cavity with two wavy walls, Journal of Applied Sciences Research, Vol.6, No.12, 2010, pp: 2111-2122.

[49] Adjlout, L., Imine, O., Azzi, A. and Belkadi, M. Laminar natural convection in an inclined cavity with a wavy wall, International Journal of Heat and Mass Transfer, Vol. 45, 2002, pp: 2141-2152.

[50] Koulali , A. , Sahi , A. , Meziani , B. , Aissa , A. , Sadaoui , D. and Ali ,H. CFD analysis of natural convection between two superposed fluids: role of corrugated bottoms, Chemical Engineering Communications, 2021, https://doi.org/10.1080/00986445.2021.1976162

[51] Hussein, A.K. , Kolsi , L. , Chand, R. , Sivasankaran , S. , Nikbakhti , R. , Li , D. , Borjini, M. and Ben Aïssia ,H. Three-dimensional unsteady natural convection and entropy generation in an inclined cubical trapezoidal cavity with an isothermal bottom wall, Alexandria Engineering Journal, Vol.55, 2016, pp: 741-755.

[52] Natarajan, E., Basak, T. and Roy, S. Natural convection flows in a trapezoidal enclosure with uniform and non-uniform heating of bottom wall, International Journal of Heat and Mass Transfer, Vol.51, 2008, pp: 747-756.

[53] Lasfer, K., Bouzaiane, M. and Lili, T. Numerical study of laminar natural convection in a side-heated trapezoidal cavity at various inclined heated sidewalls, Heat Transfer Engineering, Vol. 31, No.5, 2010, pp: 362-373.

[54] Dutta, S., Goswami, N., Pati, S. and Biswas, A. Natural convection heat transfer and entropy generation in a porous rhombic enclosure: influence of non-uniform heating, Journal of Thermal Analysis and Calorimetry, Vol. 144, 2021, pp: 1493-1515.

[55] Garcia de Maria, J., Baïri, A. and Costa, V. Empirical correlations at high Ra for steady-state free convection in 2D air-filled parallelogrammic enclosures with isothermal discrete heat sources, International Journal of Heat and Mass Transfer, Vol. 53, 2010, pp: 3831-3838.

[56] Hussain, S., Hussein, A. and Kadim, K. Numerical simulation of natural convection in a parallelogrammic enclosure containing volumetric heat source with non-uniformly heated left sidewall, Heat Transfer-Asian Research, Vol. 43, No.6, 2014, pp: 542-560.

[57] Mahmud, S., Das, P., Hyder, N. and Islam, A. Free convection in an enclosure with vertical wavy walls, International Journal of Thermal Sciences, Vol. 41, 2002, pp: 440-446.

[58] Alnaqi, A., Hussein, A. K., Kolsi, L., Al-Rashed, A., Li, D. and Ali, H. Computational study of natural convection and entropy generation in the 3-D cavity with active lateral walls, Thermal Science, Vol. 24, No. 3B, 2020, pp: 2089-2100.

[59] Li, Z., Hussein, A.K., Younis, O., Rostami, S. and He, W. Effect of alumina nano-powder on the natural convection of water under the influence of a magnetic field in a cavity and optimization using RMS: Using empirical correlations for the thermal conductivity and sensitivity analysis, International

Communications in Heat and Mass Transfer, Vol. 112, Article No. 104497, 2020.

[60] Bendehina, A., Imine, O. and Adjlout, L. Laminar free convection in undulated cavity with non-uniform boundary conditions, Comptes Rendus Mecanique, Vol.339, 2011, pp: 42-57.

[61] Ghachem, K., Hussein, A.K., Kolsi, L. and Younis, O. CNT–water nanofluid magneto-convective heat transfer in a cubical cavity equipped with perforated partition, The European Physical Journal Plus, Vol. 136: 377, 2021, pp: 1-22.

[62] Zhang, X. and Hussein, A.K. Asymptotic solution of natural convection in a uniformly Joule-heating shallow cavity, Journal of Physics: Conference Series, Vol. 574 (012156), 2015, pp: 1-4.

[63] Li, Z., Hussein, A.K., Younis, O., Afrand , M. and Feng, S. Natural convection and entropy generation of a nanofluid around a circular baffle inside an inclined square cavity under thermal radiation and magnetic field effects, International Communications in Heat and Mass Transfer, Vol. 116, Article No. 104650, 2020.

[64] Hussein, A.K., Ashorynejad, H., Sivasankaran, S., Kolsi, L., Shikholeslami, M. and Adegun, I. Modeling of MHD natural convection in a square enclosure having an adiabatic square-shaped body using Lattice Boltzmann Method, Alexandria Engineering Journal, Vol.55, 2016, pp: 203-214.

[65] Barakos, G., Mitsoulis, E. and Assimacopoulos, D. Natural convection flow in a square cavity revisited: laminar and turbulent models with wall functions, International Journal for Numerical Methods in Fluids, Vol. 18, 1994, pp: 695-719.

[66] Kuehn, T. and Goldstein, R. An experimental study of natural convection heat transfer in concentric and eccentric horizontal cylindrical annuli, ASME Journal of Heat Transfer, Vol. 100, No.4, 1978, pp: 635-640.

[67] Matin, M. and Khan, A. Laminar natural convection of non-Newtonian power-law fluids between concentric circular cylinders, International Communications in Heat and Mass Transfer, Vol. 43, 2013, pp: 112-121.

[68] Kumar, M. and Mondal, P.K. Bejan's flow visualization of buoyancy-driven flow of a hydromagnetic Casson fluid from an isothermal wavy surface, Physics of Fluids, Vol., 33, 2021, pp: 093113.

[69] Kumar, M. and Mondal, P.K. Buoyancy driven flow of a couple stress fluid from an isothermal vertical plate: the role of spatially periodic magnetic field, Physica Scripta, Vol., 96, 2021, pp: 125014.

[70] DasGupta D., Mondal P.K., Chakraborty S. Thermocapillary-actuated contact-line motion of immiscible binary fluids over substrates with patterned wettability in narrow confinement, Physical Review E, 90, 2014, pp: 023011.

[71] Mondal P.K., Chaudhry S. Effects of gravity on the thermo-hydrodynamics of moving contact lines, Vol.30, 2018, pp: 042109.

[72] Rashid F.L., Talib S. M., Hussein A. K., ObaiY., An Experimental Investigation of Double Pipe Heat Exchanger Performance and Exergy Analysis Using Air Bubble Injection Technique, Jordan Journal of Mechanical and Industrial Engineering, Vol.16, 2022, pp:195-204.

[73] Yadav A. S., Effect of Half Length Twisted-Tape Turbulators on Heat Transfer and Pressure Drop Characteristics inside a Double Pipe U-Bend Heat Exchanger, Jordan Journal of Mechanical and Industrial Engineering, Vol. 3, 2009, pp: 17-22.

[74] Hossain R.A., Chowdhuri M.A.K, Feroz C. M., Design, Fabrication and Experimental Study of Heat Transfer Characteristics of a Micro Heat Pipe, Jordan Journal of Mechanical and Industrial Engineering, Vol. 4, 2010, pp:531-542.

[75] Murali G. J. , Katte S. S., Experimental Investigation of Heat Transfer Enhancement in Radiating Pin Fin, Jordan Journal of Mechanical and Industrial Engineering, Vol. 2, 2008, pp:163-167.

JJMIE

Volume 16, Number 4, September. 2022
ISSN 1995-6665
Pages 645– 652

Jordan Journal of Mechanical and Industrial Engineering

Assessment of Dust Properties in Ma'an Wind Farms in Southern Jordan

Mohammad Shalby[1], Ahmad Abuseif [1],Mohamed R. Gomaa[1,*], AhmadSalah[2], Abdullah Marashli[1], Hani Al-Rawashdeh[1]

[1]*Mechanical Engineering Department, Faculty of Engineering, Al-Hussein Bin Talal University, Ma'an, Jordan*
[2]*Electrical Engineering Department, Faculty of Engineering, Al-Hussein Bin Talal University, Ma'an, Jordan*

Received 22 Apr 2022 *Accepted 2 Aug 2022*

Abstract

Many wind turbines have been deployed in different regions of Jordan; most are located in southern Jordan, which has a desert climate. In one of these farms near Ma'an city, the operators noticed a frequent temperature increase (+2°C) due to clogged air nacelle filters during the dust period, which caused decreasing cooling efficiency. This led to the frequent shutdown to protect the turbine parts and replace filters. In contrast, this approach reduced the estimated total annual energy production by 6.4 million kWh. This work has carefully investigated wind farm sites to verify the sources and concentration of dust in the atmosphere around the farm. Also, the dust collected from the used (replaced) filter was analyzed by X-Ray Diffraction (XRD), sieves, and X-Ray Fluorescence (XRF) at Al- Hussein Bin Talal University and Asia Center in Amman laboratory. The results showed that Calcium (Ca) constituted 90% of the chemical elements in the dust sample collected from the filter. Also, the dust particles, which have a size of < 297 μm, could be passed through the filter. Indeed, the dust characteristics are similar to the dust sources surrounding the wind farm, which is evidence of the apparent influence of these sources on the wind farm. These filters must capture contaminants that affect the cooling system, and must be durable enough to withstand high airflow, heat, and U.V. radiation. Moreover, at the end of this study, the authors proposed recommendations to reduce dust effects, thereby reducing shutdown periods and additional maintenance costs.

Keywords: Dust analysis, Wind turbine, Air filter, Wind turbine performance.

1. Introduction

Global energy demand will increase by 4.6% in 2021. Therefore, Solar, wind, and ocean energies play an essential role in coping with growing energy needs and reducing fossil-fuel consumption and greenhouse gas emissions [1-6]. Among all the renewable energy sources, wind energy is the fastest-growing renewable energy source of its sustainability, availability, environment friendly, and cost-effectiveness. According to Global Energy Review 2021 [7], wind energy was introduced as the most significant increase in renewable generation, growing by almost 17%, significantly higher than in 2020. This type of renewables plays a vital role in the decarburization of the power sector [8, 9]. In 2020, 82.5 GW of new wind turbine power capacity was added, representing 33.2% of the total power generated from renewable energy [10]. Wind energy share of worldwide power generation is expected to increase to 14%, whereas Solar photovoltaics can grow to 7% by 2030 [11-14]. As is the case in many countries, Solar and wind–derived electrical generation has become increasingly important in the Jordan power grid. Indeed, the southern region of Jordan has one of the highest Solar irradiance levels globally of 4-7kWh per square meter, coupled with more than 300 days of sunshine. Moreover, this area possesses a high potential for wind energy resources, with annual average wind speeds exceeding 7m/s (at 10m height) in some regions [15,16].

Jordan's government invested 1.4$ billion in the energy sector to 20% of the energy mix, which Jordan plans to reach by 2020 [15,9]. Many wind farms have been commissioned from 2013 to 2021. Most of them were located in southern Jordan. This includes the Tafila (117 MW), Ma'an farm (66 MW), Al-Rajef project (82 MW), Shobak project (45 MW), Al-Fajeej Project (89 MW), Mas project (100 MW), Daihan project (51 MW), El-Abour project (51 MW) and an additional 100 MW from the third round of direct offers 2020–2021. Jordan is expected to generate 600–1000 MW from wind between 2019-2021 [17].

Generally, wind turbines are installed in various environments; thus, the equipment (electronic and control) that supports wind turbines must operate efficiently and probably under extreme conditions. Blowing sand and dust for inshore, rain, and salt fog for offshore turbines is a significant concern for wind turbine equipment. These contaminants can cause electronic failure and production power loss. The accumulation of dust is one of the major

---

* Corresponding author e-mail: Behiri@bhit.bu.edu.eg.

concerns for wind turbine equipment [18]. These contaminants can cause the increasing temperature inside the nacelle, which causes the failure of the wind turbine's electrical, electronic, and mechanical parts.

Many aspects have been studied in the literature to overcome the temperature increase in wind turbine nacelle [19]. For instance, many airflow configurations have been investigated [20,21]. Also, the distribution of temperature fields of the internal components of the wind turbine has been analyzed [22,23]. Other studies have been conducted on the current cabin cooling system to inspect the thermal performance of these systems under extreme temperatures [24-26]. A further aspect that has been studied is the influence of the working environment of wind turbines on heat generation [27-30].

The accumulated dust is one of the severe working environment aspects that causes the increasing temperature inside the nacelle to block the air circulation. However, there is a shortage of studies assessing wind turbine performance and the environmental impact on its performance [31-34]. Most of the previous studies have concentrated on the effects of dust accumulation on the blade surface roughness and its influence on the performance of wind turbines. This is because a few of these studies have been briefly reported in the literature to protect intellectual property in a competitive market environment. On the other hand, the impact of the dust accumulated in the nacelle filter on reducing the effectiveness of the internal ventilating system of the wind turbines also needs more investigation. As well known, wind turbine filters must capture contaminants while allowing adequate airflow to ensure equipment within the turbine remains cool. The air filter must also be durable enough to withstand high airflow, heat, and U.V. radiation. According to the statistics of Ma'an wind farm, the number of unit shutdowns caused by the over-temperature of components due to accumulated dust exceeds 60% of the total number of abnormal shutdowns.

In Ma'an wind farm, the accumulated dust removal is a costly process. It is usually treated through (manual dust removal), carried out by the operation and maintenance personnel on the top of the wind turbine. This requires workforce and material resources, long downtime, limited dust removal, and heat dissipation. One novelty of the current investigation is to assess the significance of the filter clogging, which is responsible for entering the fresh air into the turbine's nacelle. This study will help mitigate dust's negative impacts on turbine operation. In this context, this study aims to investigate and classify the accumulated dust collected from the nacelle filters and the area around the farm. Then, the authors present some recommendations to reduce accumulated dust removal costs.

2. Case study

The case study is Ma'an wind farm located in southern Jordan, near the Al-Hussein Bin Talal University campus (latitude: 30° 16' 9.7" and longitude: 35° 41' 50.1"). This location is known for having a large wind potential capacity. It has average wind speeds of about (5-7) m/s at 10 m height, as shown in Fig. 1 [35]. In addition, it has good infrastructure and electrical grid connections. Therefore, it was chosen for deployed wind turbines. Fig. 2 illustrates the wind turbine location. This wind farm works 40 wind turbines with 97 rotor diameters and total nominal power of 80 MW[36].

Although of these advantages, Ma'an has a desert climate and rare rainfall with an average of 44 mm a year only. Additionally, this city has many stone crushers, where Ma'an stone is considered a high-quality building stone in the Middle East. The development projects are underway in this city. Thus, the construction projects are becoming close to the wind farm.

According to these circumstances, wind farm operators have started to report increases in the internal temperature of the nacelle due to the air filter collaging. Fig. 3 illustrates the air filter used in the Ma'an farm.Fig. 3(a) the new air filter that would be fixed in place of the blocked one shown in Fig. 3(b). When the air filter is clogged with dust, as shown in Fig. 3(b), this leads to shutting down of the wind turbine frequently to clean the filter and protect the internal components of the wind turbine from the increasing temperature. Therefore, it became essential to identify dust sources that impact the rising temperature of the wind turbine. Theoretically, wind farm operators noticed that the dust directly impacts the nacelle air filter blocking. Practically, no investigation has been done on this dust type and its characteristics or source.

3. Dust Analysis Methodology

To investigate and classify the accumulated dust collected from the nacelle filters and the area around the farm. The method followed in this work is developed as illustrated in Fig. 4. Initially, some critical measures must be used to create parallel datasets of the turbine's status, ambient temperature, and turbine active power. The dataset contains data for four periods in the year 2021 during regular turbine operation in summer when temperatures and dust accumulation are the highest.

The dust collected from the wind turbine air filter (D-T) has been used to analyze the mineral percent, chemical composition, and size of particles. These tests have been conducted by using X-Ray Diffraction (XRD), sieves, and X-Ray Fluorescence (XRF) inside the laboratory of Al-Hussein Bin Talal University; see Figs. 5(a) and 5(b). The second test was conducted to determine the particle size of the dust collected from the air filter. This test was carried out at the laboratory of the Asia Center in Amman. The various sizes of sieves used in this test are shown in Fig. 5(c). The dust collected for a year from the environment around the farm by a particle matter device is shown in Fig. 5(d). It is used to measure the concentration of dust by weighing dust trapped in the filter.

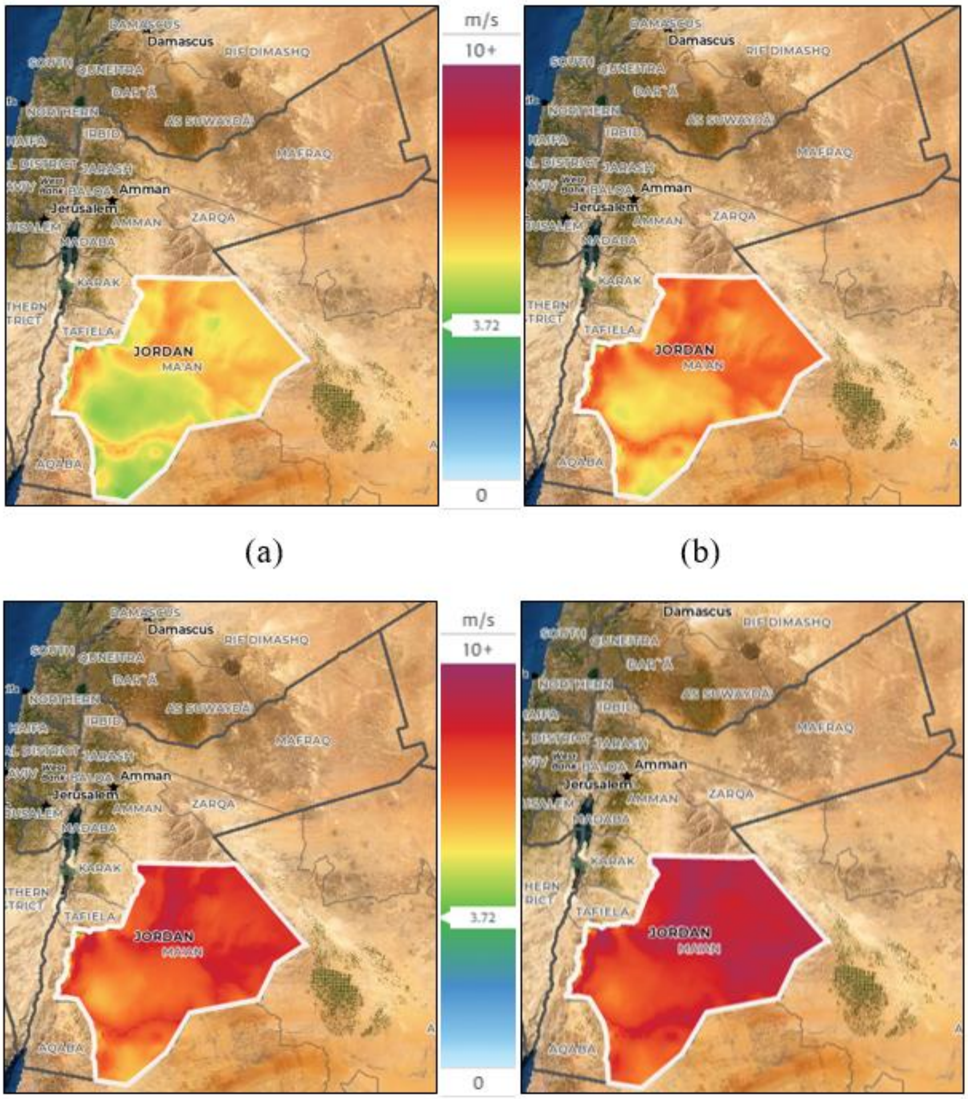

(a) (b)

(c) (d)

Figure 1. Mean wind speed in Jordan at altitude (a) 50 m; (b) 100m; (c) 150m; (d) 200m.

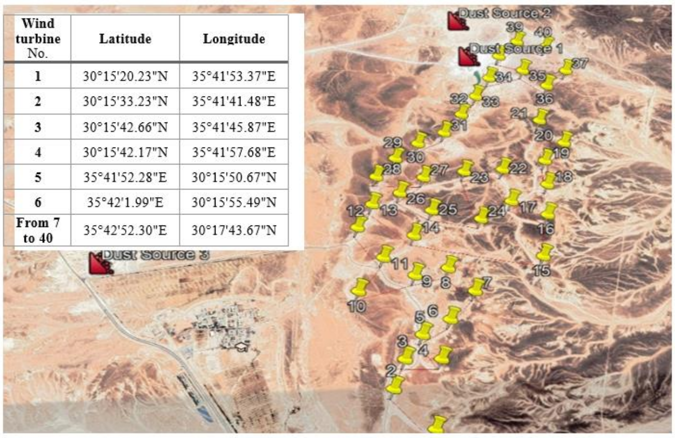

Wind turbine No.	Latitude	Longitude
1	30°15'20.23"N	35°41'53.37"E
2	30°15'33.23"N	35°41'41.48"E
3	30°15'42.66"N	35°41'45.87"E
4	30°15'42.17"N	35°41'57.68"E
5	35°41'52.28"E	30°15'50.67"N
6	35°42'1.99"E	30°15'55.49"N
From 7 to 40	35°42'52.30"E	30°17'43.67"N

Figure 2. Location of the Ma'an wind farm in southern Jordan.

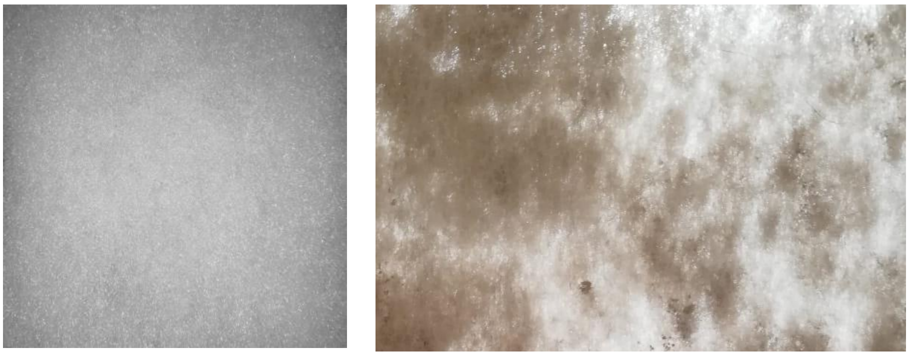

(a) (b)

Figure 3. The air filter used in the Ma'an wind farm; (a) the air filter before it was used, (b) the air filter after it was blocked of dust.

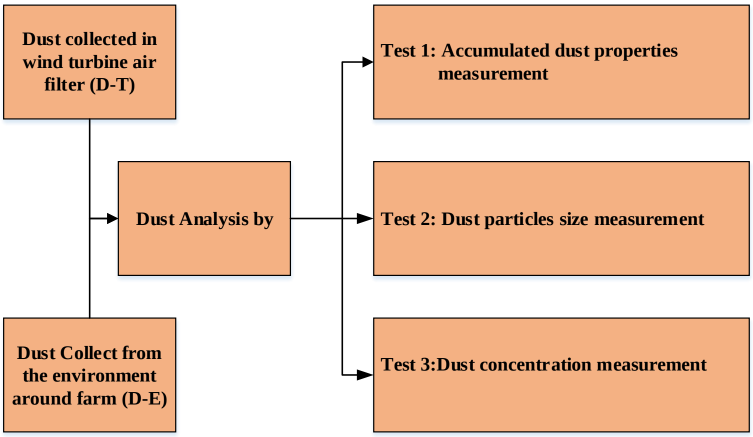

Figure 4. Method of Analysis.

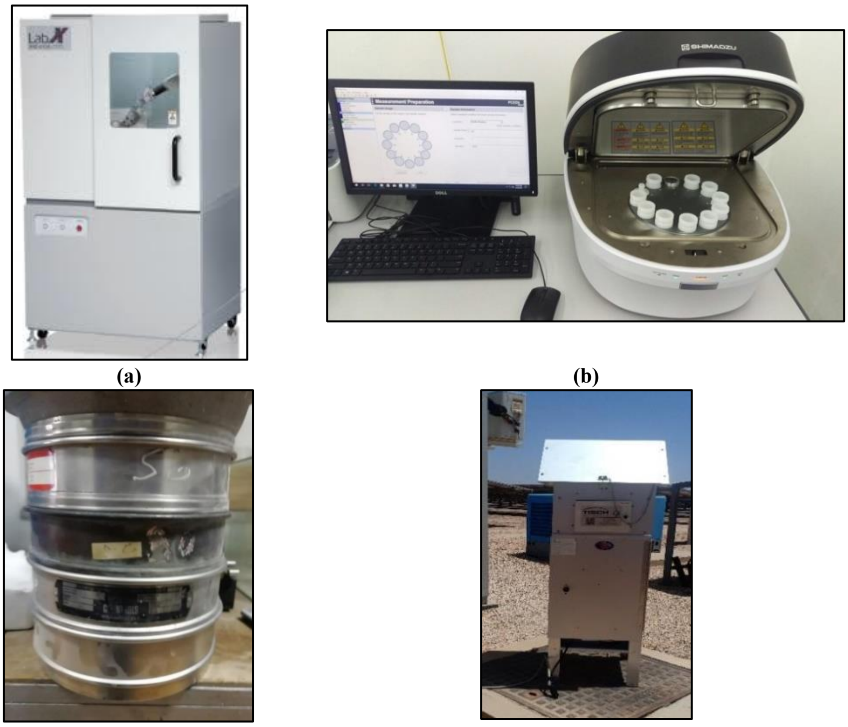

(a) **(b)**

(c) **(d)**

Figure 5. Instrumentations used in dust investigation; (a) X-Ray Diffraction (XRD)-LabX-6100; (b) Particles Matter Device; (c) X-Ray Fluorescence (XRF)-EDX 7000 (d) Sieves

4. Results and Discussions

The results in this section are limited to the dust specimens collected during four periods in the year 2020 during regular turbine operation in summer when temperatures and dust accumulation are the highest, as described in Section 3.

4.1. Dustchemical content analysis

The chemical content of the dust particles collected from the air filter (D-T) was investigated in the first analysis stage. This analysis has been conducted using X-Ray Diffraction (XRD) device (Fig. 5(a)). In this test, the molecular structure of crystalline dust material has been ascertained by diffraction x-rays through the dust sample. Figure 6 summarizes the test results. This figure indicates that the most dominant element was Calcium (Ca), which reached about 90%, and Silicon (Si) 6.10%. The reason of the high Ca content in the dust sample could be the stone crushers spread around the wind farm as the calcium is abundant in limestone and gypsum used in construction (see Fig.2, Dust source 1, and Dust source 2).

On the other hand, a comparison has been conducted between the chemical composition elements performed in this work and the dust analysis conducted in a previous study on dust accumulation on solar Photovoltaics [37, 38]. Fig.7 shows the comparison result. This figure illustrates variations between the chemical components of the dust accumulated in the wind turbine filter (D-T) and the dust sample collected over the PV panels (D-PV). The Ca reaches about 90% in D-T, while Ca is present at about 57.3% in the D-PV. However, the rest of the chemical components (e.g., S.I., Fe, ..etc.)in the D-PV specimen has a higher percentage than the D-T sample.

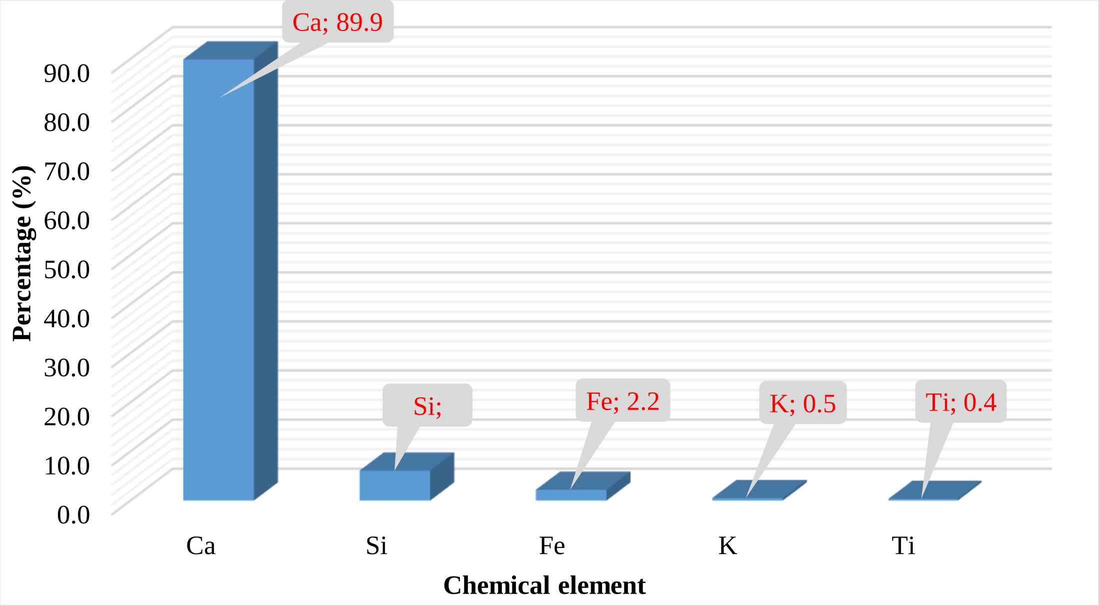

Figure 6. The chemical composition of the sample collected from D-T.

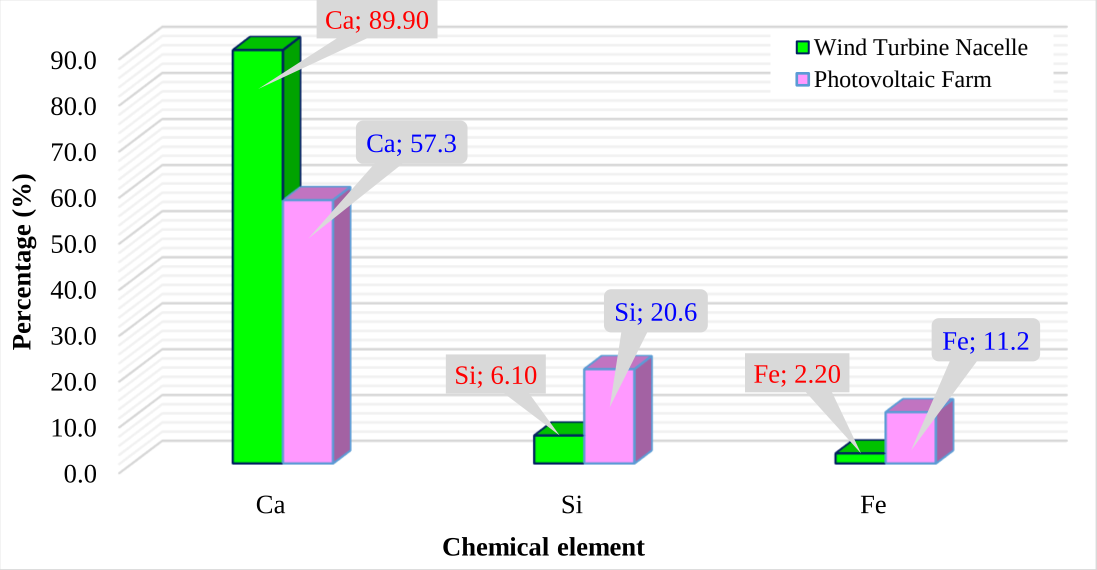

Figure 7. Comparison of the chemical elements between the samples collected from D-S and the D-T.

4.2. Dust particle size measurement

In this test, the accumulated dust particle size has been analyzed using different sieve sizes (See Fig.5.(c.)). The results of this test are illustrated in Table 1. The results showed that the dust particle size of about 149 µm was the most available in the dust sample with about 43.7%, then 74µm and 177µm, about 21.7% and 19.9%, respectively. The results of this test also illustrate that the current filter used in the wind farm can trap dust with a particle diameter of 74 to 590 µm. However, most of the dust particles (85%) trapped by air filters have a diameter of 74 to 177 µm.

Further, the current air filter is less efficient in trapping the dust with a particle diameter smaller than 297 µm. Accordingly, a part of dust particles (~< 297 µm) could be passed through the filter, damaging the wind turbine's internal component. Therefore, the concentrations of dust in the atmosphere with particle size (~< 74 µm) have to be studied.Accordingly, the dust particles with particle size (~< 74 µm) have been classified according to the international classification in Table 2. It is important to note that these results have been collected over four different periods during 2020, as presented in Section 2.

Table 1. Dust particle size trapped at the air filter (D-T)

Sieve number	Sizes of sieve opening (µm)	Weight (%)
30	590	2
40	420	9.8
50	297	2.9
80	177	19.9
100	149	43.7
200	74	21.7

Table 2. The average concentration of dust air particles

Particles Matters	Period 1	Period 2	Period 3	Period 4
PM2.5	21 µg/m^3	32 µg/m^3	71 µg/m^3	17µg/m^3
PM10	55 µg/m^3	80 µg/m^3	128µg/m^3	43µg/m^3

4.3. Effect of dust accumulation on the turbine performance

In literature [39,40], the nacelle temperature significantly impacts the turbine's productivity. Indeed, increasing temperatures inside the nacelle damage some turbine parts, such as the control unit, and decrease the lubricating oil efficiency. This frequently shuts down the turbine for maintenance work, thus reducing production. In this work, the temperature has been observed in the Ma'an wind farm for different periods in 2020. It has been found that the nacelle environment temperature rises by 14°C due to the air filter clogging due to dust accumulation. This issue often happens when the dust level is high in the atmosphere, as in Table 3.

According to the study periods, the wind turbine productivity reduced to 2000.6 kW when the dust concentration rate in the environment was high (71µg/m^3). In comparison, it was 2012.5 KW at an ambient temperature of about 27.9 but a low dust concentration rate of about (14 µg/m^3).

Many factors, like wind speed and direction, could impact wind turbine productivity. However, this study also proved that the increase in dust levels in the atmosphere directly affects wind turbine productivity and could be a significant factor, especially in a region like Ma'an city.

Table 3. The value of turbine productivity with the concentration of dust in the atmosphere

Period	Max average active power (kW)	Dust concentration rate (µg/m^3)	Ambient temperature (°C)
Period 1	2010.10	21	21.4
Period 2	2009.00	32	21.2
Period 3	2000.60	71	27.3
Period 4	2012.50	14	27.9

5. Conclusion

A good nacelle environment and reasonable nacelle temperature are robust guarantees for the safe operation of wind turbines. This study provided a detailed analysis of the dust accumulated in the wind turbine air filter on the Ma'an, southern Jordan farm. A chemical content variation was observed in dust particles collected from the wind turbine air filter. Also, the chemical content of the dust collected from the wind turbine air filter and the PV panels was similar but at different proportions. This study also proved that when the dust level is high in the atmosphere, the temperature increases inside the nacelle. Accordingly, productivity decreased during this period.

In the desert environments like southern Jordan, where most of the renewable energy projects are located (e.g., Solar farms, Wind farms), it is vital to maximizing power production. This needs a proper management of maintenance operations to keep the turbine nacelles operating normally. Despite dust accumulation negatively affecting wind turbine production, there is a shortage of studies on accumulated dust on the increasing temperature inside the wind turbine nacelle. According to the results of this work, the nacelle air filter needs frequent cleaning to allow the fresh air to complete the nacelle ventilation cycle and prevent too much dust accumulation, which is conducive to significant losses. In addition, the nacelle environment can be effectively improved, and the cabin temperature can be reduced by installing a proper filter. According to the dust particle size found in this work, another recommendation could be the possibility of using a backwash technique to clean such filters. This study could be helpful in the operation and maintenance of the wind turbine in a desert region like southern Jordan. However, further investigation is still needed to determine a suitable cleaning technique according to the weather conditions.

References

[1] Tayo, Ajadi et al., Global Trends in Renewable Energy Investment 2020. (cited 2021 27 Sep.); Available from: https://www.fs-unep-centre.org/wp-content/uploads/2020/06/GTR_2020.pdf.

[2] Dandan Liu, Shigang Li, Hui Liu. Experimental Study on Formaldehyde Emission from Environmental Protection and Energy-Saving Alcohol Fuel for Vehicles. Jordan Journal of Mechanical and Industrial Engineering 15 (1), 2021, P. 1-6.

[3] Mustafa Al-Qudah, Ahmad Sakhrieh, Ali Almarzouq, Ahmad Al-Omari. Thermal Analysis of a Combined Cycle Power Plant under Varying Operating Conditions. Jordan Journal of Mechanical and Industrial Engineering 14 (4), 2020, P. 387-392.

[4] Ahmad O. Hasan, Ahmed I. Osman, Ala'a H. Al-Muhtaseb, Hani Al-Rawashdeh, Ahmad Abu-jrai, Riad Ahmad, Mohamed R. Gomaa, Tanmay J. Deka, David W. Rooney. An experimental study of engine characteristics and tailpipe emissions from modern DI diesel engine fuelled with methanol/diesel blends. Fuel Processing Technology 220 (2021) 106901. https://doi.org/10.1016/j.fuproc.2021.106901.

[5] Mohamed R. Gomaa, Nesrien Al-Dmour, Hani A. AL-Rawashdeh, Mohammad Shalby. Theoretical model of a fluidized bed solar reactor design with the aid of M.C.R.T. method and synthesis gas production. Renewable Energy 148 (2020) 91-102. https://doi.org/10.1016/j.renene.2019.12.010.

[6] Abdullah Marashli, Enas Alfanatseh, Mohammad Shalby, Mohamed R. Gomaa. Modelling single-effect of Lithium Bromide-Water (LiBr–H2O) driven by an evacuated solar tube collector in Ma’an city (Jordan) case study. Case Studies in Thermal Engineering 37, (2022), 102239. https://doi.org/10.1016/j.csite.2022.102239.

[7] IEA, Global Energy Review 2021. 2021, International Energy Agency: France

[8] e Azevedo, H.D.M., et al., A review of wind turbine bearing condition monitoring: State of the art and challenges. 2016. 56: p. 368-379.

[9] Mohamed R. Gomaa, Hegazy Rezk, Ramadan J. Mustafa, Mujahed Al-Dhaifallah. "Evaluating the Environmental Impacts and Energy Performance of a Wind Farm System Utilizing the Life-Cycle Assessment Method: A Practical Case Study". Energies 2019, 12 (17), 3263. http://dx.doi.org/10.3390/en12173263.

[10] Van de Graaf, T., The International Renewable Energy Agency, in Elgar Encyclopedia of Environmental Law. 2021, Edward Elgar Publishing Limited. p. 99-107.

[11] Bhattacharya, M., et al., The effect of renewable energy consumption on economic growth: Evidence from top 38 countries. 2016. 162: p. 733-741.

[12] Mohamed R. Gomaa, Waleed Hammad, Mujahed Al-Dhaifallah, Hegazy Rezk. "Performance enhancement of grid-tied P.V. system through new design cooling techniques under dry desert condition: an experimental study and comparative analysis". Solar Energy 2020, 211, 1110–1127. https://doi.org/10.1016/j.solener.2020.10.062.

[13] Mohamed R. Gomaa, Mohamed A. Mohamed, Hegazy Rezk, Mujahed Al-Dhaifallah, Mohammed J. Al shammri. "Energy Performance Analysis of On-Grid Solar Photovoltaic System- a Practical Case Study". International Journal of Renewable Energy Research (I.J.R.E.R.) 2019, 9(3), 1292-1301.

[14] Khalideh Al bkoor Alrawashdeh, Nabeel.S.Gharaibeh, Abdullah A. Alshorman, Mohamad H. Okour. Magnus Wind Turbine Effect Vertical Axis Using Rotating Cylinder Blades. Jordan Journal of Mechanical and Industrial Engineering 15 (2), 2021, P. 233-241.

[15] Abu-Rumman, G., A.I. Khdair, and S.I.J.H. Khdair, Current status and future investment potential in renewable energy in Jordan: An overview. 2020. 6(2): p. e03346.

[16] Kiwan, S. and E.J.R.E. Al-Gharibeh, Jordan toward a 100% renewable electricity system. 2020. 147: p. 423-436.

[17] (M.E.M.R.), M.o.E.a.M.R., Annual Reports, Amman, Jordan. 2018.

[18] Mathavan, J.J. and A.J.R.i.M. Patnaik, Analysis of wear properties of granite dust filled polymer composite for wind turbine blade. 2020. 5: p. 100073.

[19] Jian, S., et al. Review of the cooling technology for high-power wind turbines. in 5th International Conference on Advanced Design and Manufacturing Engineering (I.C.A.D.M.E.). 2015.

[20] Moria, H., et al., Investigation Effects of Different Wind Turbine Designs on Air Flow and Generated Power. 2020. 8(3).

[21] Yahya, W., et al., Study the influence of using guide vanes blades on the performance of cross-flow wind turbine. 2021: p. 1-10.

[22] Yang, G., et al. Research on improvement of ambient temperature of wind turbine engine room. in I.O.P. Conference Series: Earth and Environmental Science. 2020. I.O.P. Publishing.

[23] Lee, J., et al., Thermal and mechanical design for refrigeration system of 10 MW class HTS wind power generator. 2020. 30(4): p. 1-5.

[24] Khalilzadeh, S. and A.H.J.J.o.C.P. Nezhad, using waste heat of high capacity wind turbines in a novel combined heating, cooling, and power system. 2020. 276: p. 123221.

[25] Nematollahi, O., et al., An evaluation of wind turbine waste heat recovery using organic Rankine cycle. 2019. 214: p. 705-716.

[26] Milanese, M., G. Colangelo, and D.J.T.S. Laforgia, High efficiency nanofluid cooling system for wind turbines. 2014. 18(2): p. 543-554.

[27] Benallal, A. and N.J.W.E. Cheggaga, Impact of dust events on the optimization of photovoltaic-wind hybrid system in desert. 2021: p. 0309524X20985777.

[28] Chen, S. and R.K. Agarwal. Numerical Investigation of Wind Turbine Airfoils under Clean and Dusty Air Conditions. in AIAA AVIATION 2020 FORUM. 2020.

[29] Al-Shemmeri, T., Wind turbines. 2010: Bookboon.

[30] Demir, E., Wind Turbine Power Curve Update Based on Atmospheric Conditions and Structural Fatigue. 2020, Izmir Institute of Technology (Turkey).

[31] Khalfallah, M.G. and Koliub, A.M., 2007. Effect of dust on the performance of wind turbines. Desalination, 209(1-3), pp.209-220.

[32] Deb, D., Patel, M. and Singh, H., 2017, March. Automated cleaning of wind turbine blades with no downtime. In 2017 IEEE International Conference on Industrial Technology (I.C.I.T.) (pp. 394-399). IEEE.

[33] Salem, H., Diab, A. and Ghoneim, Z., 2013, October. C.F.D. simulation and analysis of performance degradation of wind turbine blades in dusty envirnonments. In 2013 international conference on renewable energy research and applications (I.C.R.E.R.A.) (pp. 827-832). IEEE.

[34] Ren, N. and Ou, J., 2009. Dust effect on the performance of wind turbine airfoils. Journal of Electromagnetic Analysis and Applications, 1(2), pp.102-107.

[35] The Global Wind Atlas. 2021 (cited 2021 27 September); Available from: https://globalwindatlas.info/.

[36] The wind power, T.W. 2021 (cited 2021 12 July); Available from: https://www.thewindpower.net/windfarm_en_24721_maan.php.

[37] Al-twaissi W. 2020. Impact of accumulated dust on photovoltaics cells performance and efficiency in ma'an region. MSc. Thesies.

[38] Ramadan J. Mustafa, Mohamed R. Gomaa, Hegazy Rezk. "Environmental Impacts on the Performance of Solar

Photovoltaic Systems". Sustainability 2020, 12 (2), 608. https://doi.org/10.3390/su12020608.

[39] Al-Khayat, M., Al-Rasheedi, M., Gueymard, C.A., Haupt, S.E., Kosović, B., Al-Qattan, A. and Lee, J.A., 2021. Performance analysis of a 10-MW wind farm in a hot and dusty desert environment. Part 2: Combined dust and high-temperature effects on the operation of wind turbines. Sustainable Energy Technologies and Assessments, 47, p.101461.

[40] Al-Rasheedi, M., Al-Khayat, M., Gueymard, C.A., Haupt, S.E., Kosović, B., Al-Qattan, A. and Lee, J.A., 2021. Performance analysis of a 10-MW wind farm in a hot and dusty desert environment. Part 1: Wind resource and power generation evaluation. Sustainable Energy Technologies and Assessments, 47, p.101487.

المملكة الأردنية الهاشمية

الجامعة الهاشمية

المجلة الأردنية
للهندسة الميكانيكية والصناعية

JJMIE

مجلة علمية عالمية محكمة

تصدر بدعم من صندوق البحث العلمي

http://jjmie.hu.edu.jo/

ISSN 1995-6665

المجلة الأردنية للهندسة الميكانيكية والصناعية

المجلة الأردنية للهندسة الميكانيكية والصناعية: مجلة علمية عالمية محكمة تصدرعن الجامعة الهاشمية بالتعاون مع صندوق دعم البحث العلمي والابتكار- وزارة التعليم العالي والبحث العلمي في الأردن.

ترسل البحوث إلى العنوان التالي

الاستاذ الدكتور علي جوارنه
رئيس تحرير المجلة الأردنية للهندسة الميكانيكية والصناعية
الجامعة الهاشمية
كلية الهندسة
قسم الهندسة الميكانيكية
الزرقاء – الأردن
هاتف: 3903333 5 00962 فرعي 4147
Email: jjmie@hu.edu.jo
Website: www.jjmie.hu.edu.jo